Advances in Civil Engineering

# Advanced Infrastructure Systems Integrating Hardware and Software Platforms

Lead Guest Editor: Jianlong Zheng
Guest Editors: Yanyan Chen, Qingli Dai, Songtao Lv, Hui Yao, and Zhanping You

# Advanced Infrastructure Systems Integrating Hardware and Software Platforms

Advances in Civil Engineering

# Advanced Infrastructure Systems Integrating Hardware and Software Platforms

Lead Guest Editor: Jianlong Zheng
Guest Editors: Yanyan Chen, Qingli Dai, Songtao Lv, Hui Yao, and Zhanping You

# Contents

# Contents

Hindawi
Advances in Civil Engineering
Volume 2021, Article ID 8831094, 11 pages
https://doi.org/10.1155/2021/8831094

*Research Article*

# Investigating Driving Styles: A Validation Study of Multidimensional Driving Styles with British and Chinese Drivers

**Xu Sun,[1] Ying Jiang,[1] Gary Burnett,[2] and Qingfeng Wang[3]**

[1]*Faculty of Science and Engineering, University of Nottingham Ningbo, Ningbo 315100, China*
[2]*Human Factors Research Group, University of Nottingham, Nottingham, UK*
[3]*Nottingham University Business School China, University of Nottingham Ningbo, Ningbo 315100, China*

Correspondence should be addressed to Qingfeng Wang; qingfeng.wang@nottingham.edu.cn

Received 29 September 2020; Revised 26 August 2021; Accepted 19 September 2021; Published 30 September 2021

Academic Editor: Nicola Baldo



Culture has a significant impact on driving behaviour and can play an important role in driving safety. The adaptation of traffic-related psychological instruments, developed elsewhere in new national contexts, should consider the cultural context. This paper validates the multidimensional driving style inventory (MDSI) with two cultural samples consisting of 215 Chinese drivers and 240 British drivers. A factor analysis of the driving style yielded evidence that both datasets present some variations from the original version of the instruments in the factorial structure. The analysis of the UK sample is comparable to the previous MDSI by indicating six driving styles, namely, anxious, risky and dissociative, high-velocity and angry, patient, careful, and distress-reduction. The analysis of the Chinese participants' dataset showed its factorial structure with 40 items of the 44 original items divided over six styles. A new dimension, namely, an inattentive driving style, appeared in the Chinese sample. These differences raise the need to validate and adapt such instruments to consider cultural specificities. Implications were also derived for driver and road safety enhancement solutions through driver behaviour applications.

## 1. Introduction

Road traffic accidents are a major health and economic problem throughout the world, and research within traffic psychology has mainly focused on the human factors that are evident in car accidents, such as attitudes, driving behaviours, and sociodemographics (e.g., [1, 2]). Driving styles have been shown to be an important human factor related to traffic accidents [1]. Rothengatter and Huguenin [2] have suggested that 85% of traffic accidents can be attributed to human factors, but it remains necessary to explore this issue more deeply and broadly. Elander et al. [3] defined driving style as the method drivers choose to employ when they are driving, or how they drive habitually while facing various traffic conditions, including their choice of driving speed, the distance from vehicles ahead, and their habitual level of general attentiveness and assertiveness. It has been shown that drivers with certain driving styles, such as being reckless and careless, tend to exhibit unsafe driving behaviours [4]. Therefore, an investigation of driving styles can help us to better understand the causes of certain kinds of driving behaviour from a more general perspective. It can also help to provide important support for the classification of drivers, such that drivers with different driving styles could be monitored and alerted in advanced driver-assistance systems to reduce risky driving behaviours.

To identify people's driving styles, two approaches have been widely applied, including simulator experiments and self-reported surveys. Simulator experiments have the advantage of allowing researchers to establish customized environmental conditions; however, such experiments are usually expensive and are limited by the reality of a virtual environment [5]. Therefore, self-reported surveys have become a rather popular approach. The multidimensional driving style inventory (MDSI) is a self-report measure developed to assess driving styles [6]. A total of 44 items were developed by Taubman-Ben-Ari et al. [7] to measure driving styles according to a subjective approach, in which

participants were asked to rate, on a 6-point scale, the extent to which each item reflected their feelings, thoughts, and behaviours as drivers. The factor analysis revealed eight main driving style factors, which explained 56% of the variance of the 44 items, namely, dissociative, anxious, risky, angry, high-velocity, distress-reduction, patient, and careful. Based on an extensive literature review, Taubman-Ben-Ari et al. hypothesized four broad dimensions of driving styles. The first dimension is characterized by driving at high speed, passing other cars in no-passing zones, and driving while intoxicated, probably endangering both the driver and others. This dimension is represented in the MDSI by the risky and high-velocity driving styles. The second dimension is where drivers exhibit feelings of alertness and tension. This dimension is represented by anxious, dissociative, and distress-reduction styles. The angry driving style is the third general dimension, reflecting a tendency to drive aggressively on the road, such as sounding the horn or flashing lights at other drivers. Finally, there is the patient and careful driving style, in which drivers are well-adjusted, patient, and polite while following the rules. This is represented in the MDSI by the careful patient style.

Taubman-Ben-Ari et al. [7] have provided evidence of the reliability and validity of the MDSI as applied to the population of Israel. Furthermore, the MDSI has already been translated into several languages and has been verified in a variety of countries (e.g., Argentina, Belgium, the Netherlands, Spain, Romania, Malaysia, and Italy). Poó et al. [8] adapted and validated a Spanish version of the MDSI for use in Argentina, reducing the dimensions to six factors, by merging high velocity with risky, and patient with care. Trógolo et al. [9] also examined the validity of the MDSI with a sample of 1277 drivers from Argentina. Exploratory structural equation modelling (ESEM) was used to test the factor structure and measurement invariance of the MDSI. The findings suggested a 6-factor model represented by the risky, angry, dissociative, anxious, careful, and patient styles. Huysduynen et al. [10] further validated the MDSI for drivers in Belgium and the Netherlands. Their study found that the five factors identified among participants from the Netherlands and Belgium were more stable than the eight factors from the original study with the participants in Israel. The following five factors were identified: angry, anxious, dissociative, distress-reduction, and careful. Padilla et al. [11] validated the appropriateness of the MDSI to the Spanish spoken in Spain. The results revealed a 6-factor structure of the Argentinian version of the MDSI, with higher internal consistency values for each of the driving styles. Karjanto et al. [12] investigated the driving styles using the MDSI with 338 drivers in Malaysia. The findings revealed four driving styles out of the original eight factors, including careful, risky, anxious, dissociative, and angry styles. Holman and Havârneanu [13] developed a Romanian version of the MDSI to fit the Romanian driving context and cultural specificities. It divided driving behaviour into seven styles, among which the anxious, risky, angry, distress-reduction, and dissociative styles correspond to the original instrument. A supplementary driving style, namely the "violation of rules", contextually perceived as the irrational style, was introduced. Freuli et al. [14] validated the MDSI for the measurement of driving styles with 561 drivers from Italy. They confirmed the 8-factor structure of the original MDSI by removing the 4 items which did not properly contribute to the factors. Wang et al. [15] examined the reliability, structure, and validity of a Chinese version of the MDSI with 296 drivers from China, to determine which types of driving styles are typical among Chinese drivers. They revised the original MDSI by indicating four driving styles, namely, the risky, angry, high-velocity, careful, and anxious styles. Long and Ruosong [16] also validated a Chinese version of the MDSI with 760 drivers. Their study revealed a 6-factor structure of the MDSI including risky, anxious, angry, distress-reduction, careful, and dissociative driving styles. These studies have all supported the reliability and validity of the MDSI; however, the factor structure encountered across the studies has been inconsistent.

There is evidence that cultural factors influence both traffic performance and safety [17]. For example, Chinese drivers have a unique traffic culture that could promote different driving styles and behaviours [18, 19]. In studies concerned with displays of anger while driving, Chinese drivers reported less anger in response to discourtesy and illegal driving than their American counterparts, or drivers in New Zealand and Spain [20]. In terms of driving skills, Chinese drivers exhibit a different driving style and are involved in more crashes than those in the United States and Japan [21, 22]. In Western countries, the behaviour of drivers is controlled by traffic rules. Lajunen and Parker [23] examined the feasibility of using the Driving Anger Scale (DAS) developed by Deffenbacher et al. [24], and a sample of British drivers revealed that the subscale of "police presence" did not evoke any appreciable levels of anger, indicating that UK drivers' attitudes to traffic enforcement are more positive than US drivers. As traffic conditions and driving behaviour are different in different countries, it is not appropriate to expect that psychological instruments which have been developed elsewhere could work directly for traffic studies in other countries [25, 26].

Driving styles and the relationships between the different aspects of driving styles are still poorly understood [27] largely due to traffic culture, sociodemographic characteristics, and cultural differences [28]. This study aims to explore the effectiveness of the MDSI in two different geographical regions by conducting an independent validation of the questionnaire. It first validates the eight main factors and loadings through the distribution of the same questionnaire among drivers in China and the United Kingdom, thereby providing valid information on culturally relevant driving styles and becoming a valuable tool with which to support future studies of traffic psychology. It then explores the relationship between the identified driving styles and the sociodemographic characteristics. It concludes with a summary of the main findings and some suggestions for future directions of driving style research. This study contributes to efforts to promote road safety through an understanding of driving styles.

## 2. Research Experiment

*2.1. Participants.* A total of 455 drivers were sampled, with 215 from China and 240 from the United Kingdom, who completed the questionnaire on which this study is based. The two groups were different in terms of gender, experience, and age distribution. The sample from diverse geographical areas in China consisted of 137 men and 78 women, who ranged in age (from 18 to 65) and in driving experience (consisting of the number of years of driving experiences from 1–40 years). The sample from the United Kingdom consisted of 127 men and 113 women, who ranged in age from 20 to 76 and had driving experience ranging from 2 to 58 years. The samples were divided into three groups according to age ("young" = younger than 30 years old, "Middle age" = between 31 and 60 years old, and "old" = 61 years and older). The descriptive statistics for participant demographics are shown in Table 1.

It is expected that the demographic distribution of our sample reflects some degree of distribution within the respective driver population. For instance, a recent population-based controlled study in a capital city in China indicated a proportion of 18.5% young drivers, 61% of middle-aged drivers, and 20% older drivers [29]. In contrast, the age distribution of drivers in the United Kingdom is 27.5% for the under-30 group, 60% for the 31–60 group, and 12.5% for the group aged above 61 [30]. Another study investigating the influence of gender on advanced driver-assistance systems under Chinese road conditions had 50% more male drivers than female drivers [31]. While the sample demographics seem reasonable, there is a lack of official information on the overall driver population distribution in this context to confirm the complete appropriateness of our sample selection [32].

*2.2. Instruments.* Taubman-Ben-Ari et al. [7] summarized the various developed measures of driving behaviour into a multidimensional conceptualization of driving styles. They broadened the scope of analysis from the behaviours related to traffic accidents, to behaviours, and habits related to daily driving. The original items in the MDSI were adapted primarily from several existing surveys, including the Driver Style Questionnaire (DSQ, French et al. [33]), the Driver Behaviour Questionnaire (DBQ, Reason et al. [34]), and the Driver Behaviour Inventory (DBI, Gulian et al. [35]). Each questionnaire taps very different aspects of driving styles. For instance, the DSQ [33] assesses factors such as "speed," "seat belt use," and "traffic violations," but also "feelings of control" and "risk-taking behaviour." In contrast, the DBI [35] studies "driving stress" and "dimensions of driving aggression," such as frustration relating to overtaking manoeuvres. The well-known DBQ [34] has yet another focus; it examines "lapses" (e.g., switching on the wrong appliance), "errors" (e.g., failing to notice pedestrians crossing the road), and deliberate "violations" (e.g., speeding or tailgating). Taubman-Ben-Ari et al. [7, 36] integrated the various measurement scales into a multidimensional conceptualization of driving styles and eventually formed the original version of the MDSI. This original MDSI, consisting of 44 items was created based on eight factors and four domains of driving styles: (1) a reckless and careless driving style, (2) an anxious driving style, (3) an angry and hostile driving style, and (4) a patient and careful driving style. The reckless and careless driving style refers to deliberate violations of safe driving norms, and the seeking of sensations and thrills while driving. It is characterized by driving at high speeds, passing in no-passing zones, and driving while intoxicated. The anxious driving style reflects feelings of alertness and tension, as well as ineffective engagement in relaxing activities during driving. The angry and hostile driving style refers to expressions of irritation, rage, and hostility while driving, along with a tendency to act aggressively on the road, including cursing other drivers, honking the horn, or flashing headlights. The patient and careful driving style reflects well-adjusted driving behaviours, such as planning, paying full attention to the road, displaying patience, courtesy, and calmness behind the wheel and obeying the traffic rules.

The Chinese version of the MDSI was developed based on the original MDSI [7]. The translation was conducted independently by two researchers and was crossed checked by a professional translator. The final version consisted of 44 items based on eight driving style factors that previous instruments used to measure as separate concepts (e.g., driving stress, driver aggression, and risky driving). A pilot test was conducted with six Chinese drivers to check the translated MDSI. All participants indicated that the Chinese version of the MDSI was understandable. Participants were asked to rate each item on a 6-point Likert-type scale (ranging from "not at all" to "very much") according to their behaviours during driving. It also incorporates positive driving styles, or more specifically, the patient and careful driving styles, which had been omitted from most previous studies (e.g., [37]).

*2.3. Procedure.* Participants were first recruited online via social media, having passed through screening procedures to ensure they qualified for the study. All participants were required to satisfy the following conditions: (1) at least 18 years old; (2) having a valid driving license; and (3) having at least 1 year of driving experience. The questionnaire was distributed with the online survey tool Sojump (http://www.sojump.com) through snowball sampling, in which the questionnaires were first disseminated to a group of university students, who were then asked to share the questionnaires with their network. Sojump is a professional online survey platform that permits services of questionnaire design and data collection. The recruited participants were presented with a brief overview of the purpose of the research and the eligibility criteria, and they were asked questions concerning their sociodemographic characteristics as well as their driving styles and driving behaviours under various passenger conditions. The two groups completed the survey in their respective mother tongue through the online survey tool. It lasted for a period of 3 months for the data collection and 1 month for monitoring the data

Table 1: Participants' demographics.

| Demographic variables | China sample | UK sample |
|---|---|---|
| Gender | 137 men and 78 women | 127 men and 113 women |
| Age | Mean = 37.93, SD = 10.76 | Mean = 49.14, SD = 14.069 |
| <30 | 69 | 24 |
| 31–60 | 141 | 156 |
| >60 | 5 | 60 |
| Driving years | Mean = 9.06, SD = 6.785 | Mean = 27.46, SD = 15.019 |

acquired. Ethical approval for the project was granted by the Research Ethics Subcommittee of the University of Nottingham, Ningbo.

*2.4. Data Analysis.* A Kolmogorov–Smirnov test was firstly conducted, which showed that the sample data were normally distributed ($P < 0.05$). A factor analysis was then performed to validate the previously developed MDSI versions with our samples. The mean substitution was used for the treatment of missing data. The factor analysis performed employed a Varimax rotation, to reveal the underlying structure of the items. The rotation method Oblimin was employed, which allows for the factors in the final solution to be correlated. We examined differences in these factor scores through sociodemographic and driving-history variables, employing multivariate analyses of covariance (MANCOVA). The univariate effects of the variables that emerged as significantly associated with factor scores were then further examined through univariate ANOVAs and Pearson's correlations.

## 3. Results

*3.1. Factor Analysis of the Chinese Sample.* A factor analysis with the Varimax rotation of the answers from the 215 Chinese participants was conducted to explore whether the 44 MDSI items would form the distinguishable eight factors as presumed when compared to the results of Taubman-Ben-Ari et al. [7]. The findings reveal a distribution of the 44 items over eight factors (eigenvalue >1), explaining 56.1% of the variance. Two factors did not have sufficient items to make a meaningful contribution. Table 2 presents the loadings of each item.

Factor 1 consists of 11 items explaining 10.56% of the variance (Cronbach's alpha: .897). Four items in this factor were included in the anxious driving style, six in the dissociative driving style, and one in the high-velocity driving style of the original MDSI. Consequently, this factor was labelled as the angry and dissociative driving style. Factor 2 consists of seven items addressing risky, hostile, and thrill-seeking behaviour. This factor explains 4.33% of the variance (Cronbach's alpha .886). Among these items, three were included in the risky driving style while three were in the angry driving style and one in the careful driving style of the original MDSI. This factor was labelled as the risky and angry driving style. Factor 3 consists of eight items addressing a person's tendency to drive quickly and to be oriented towards high-velocity driving. This factor explains 3.05% of the variance (Cronbach's alpha: .705). Five of these items were included in the high-velocity driving style, two in the anxious driving style, and one in the dissociative driving style of the original MDSI, which was labelled the high-velocity driving style. Factor 4 consists of six items addressing a well-adjusted and adaptive driving style, including concentration, patience, and compliance with road traffic regulations. This factor explains 2.08% of the variance (Cronbach's alpha: .705) and was labelled the patient and careful driving style. Three items of this factor were included in the patient driving style: two were in the careful driving style and one in the dissociative driving style of the original MDSI. Factor 5 consists of six items addressing a person's tendency to engage in relaxing activities to reduce stress while driving. This factor explains 1.38% of the variance (Cronbach's alpha: .73), among which four items were included in the distressed driving style, two in the careful, and one in the patient driving styles of the original MDSI. This factor was labelled as the distress-reduction driving style. Factor 6 consists of four items addressing inattentive driving behaviours when driving, which can be observed as an instantaneous attention deviation from driving. This factor was labelled as the inattentive driving style. This factor explains 1.38% of the variance (Cronbach's alpha: .83). There were two items from the dissociative driving style: one item from the distress-reduction driving style and one from the careful driving style of the original MDSI. Factor 7 consists of two items from the anxious driving behaviour of the original MDSI addressing confident driving behaviour. This factor explains 1.05% of the variance (Cronbach's alpha: .584), which was labelled as confident driving behaviour. Factor 8 consists of two items that explain 1.02% of the variance (Cronbach's alpha: .11), among which one item was included in the anxious driving behaviour and one in the high-velocity driving behaviour of the original MDSI. This factor was labelled as others.

A constraint was set to have at least three items per factor. The reliability of these factors was tested by Cronbach's alpha. Nunnally [41] stipulated that if the constructs are generally above or close to 0.70, then it can be confirmed that the item measurements of the constructs are reliable. The items for Factor 7 achieved a low Cronbach's alpha figure, so it was removed from the analysis. The items in Factor 8 are heterogeneous, which makes it difficult to label, in combination with a low Cronbach's alpha, so this factor was also removed from the analysis.

As a follow-up to the results of the first-factor analysis, a second-factor analysis with a Varimax rotation consisting of six factors was conducted, in which items 4, 40, 2, and 7 were

Table 2: Factor model coefficients of the multidimensional driving styles of the Chinese sample.

| Factors and items | Loading |
|---|---|
| Factor 1: anxious and dissociated driving style | |
| [30] Feel nervous while driving | 0.771 |
| [35] Plan my route badly, so that I hit traffic that I could have avoided | 0.759 |
| [37] Nearly hit something due to misjudging my gap in a parking lot | 0.743 |
| [33] Intend to switch on the windscreen wipers but switch on the lights instead | 0.719 |
| [32] Feel distressed while driving | 0.707 |
| [29] Misjudge the speed of an oncoming vehicle when passing | 0.663 |
| [26] Forget that my lights are on the full-beam until flashed by another motorist | 0.647 |
| [9] Driving makes me feel frustrated | 0.635 |
| [19] *Attend to my hair/makeup while driving* | *0.546* |
| [24] It worries me when driving in bad weather | 0.522 |
| [31] *Get impatient during the rush hour* | *0.511* |
| Factor 2: risky and angry driving style | |
| [23] Like the thrill of flirting with death or disaster | 0.826 |
| [28] Get a thrill out of breaking the law | 0.774 |
| [38] Enjoy the excitement of dangerous driving | 0.734 |
| [21] Like to take risks while driving | 0.731 |
| [4] Enjoy the sensation of driving at the limit | 0.607 |
| [39] Honk my horn at others | 0.594 |
| [27] *When someone does something on the road that annoys me, I flash them with the high beam* | *0.579* |
| [11] *Swear at other drivers* | *0.30* |
| Factor 3: high-velocity driving style | |
| [15] In a traffic jam, I think about ways to get through the traffic faster | 0.691 |
| [8] When in a traffic jam and the lane next to me starts to move, I try to move into that lane as soon as possible | 0.686 |
| [3] Drive through traffic lights that have just turned red | 0.673 |
| [16] When a traffic light turns green and the car in front of me does not get going immediately, I try to urge the driver to move on | 0.665 |
| [1] Blow my horn or "flash" the car in front as a way of expressing frustration | 0.657 |
| [18] When someone tries to skirt in front of me on the road, I drive in an assertive way in order to prevent it | 0.651 |
| [34] Attempt to drive away from traffic lights in third gear (or in the neutral mode in automatic cars) | 0.468 |
| Factor 4: patient and careful driving style | |
| [17] At an intersection where I have to give right-of-way to oncoming traffic, I wait patiently for cross-traffic to pass | 0.762 |
| [12] When a traffic light turns green and the car in front of me does not get going, I just wait for a while until it moves | 0.743 |
| [40] Tend to drive cautiously | 0.655 |
| [22] Base my behaviour on the motto "better safe than sorry" | 0.606 |
| [13] *Drive cautiously* | *0.330* |
| Factor 5: distress-reduction driving style | |
| [36] Use muscle relaxation techniques while driving | 0.729 |
| [41] Plan long journeys in advance | 0.659 |
| [42] Always ready to react to unexpected manoeuvres by other drivers | 0.618 |
| [7] While driving, I try to relax myself | 0.507 |
| [6] *Do relaxing activities while driving* | *0.30* |
| Factor 6: inattentive driving style | |
| [20] Distracted or preoccupied, and suddenly realize the vehicle ahead has slowed down, and have to slam on the brakes to avoid a collision | *0.738* |
| [14] *Lost in thoughts or distracted, I fail to notice people at pedestrian crossings* | *0.579* |
| [10] I daydream to pass the time while driving | *0.546* |
| [25] Meditate while driving | 0.466 |
| *Factor 7* | |
| [2] *Feel I have control over driving [−]* | |
| [43] *Feel comfortable while driving* | |
| *Factor 8* | |
| [44] *Purposely tailgate other drivers* | |
| [5] *On a clear freeway, I usually drive at or a little below the speed limit* | |

The grey items were removed from the second analysis; the items in italics do not correlate with the same items in the original factor analysis.

excluded as they did not fit in the six main factors used in this analysis. The analysis revealed a distribution of 40 items over six factors explaining 58% of the variance. The loadings of the items for each of these factors are presented in Table 2.

Factor 1 consists of 11 items explaining 26.36% of the variance (Cronbach's alpha: .902) addressing anxious and dissociative driving behaviour. Among these items, four were included in the anxious driving style, six in the

dissociative driving style, and one in the high-velocity driving style of the original MDSI, which was labelled as the anxious and dissociative driving style. Factor 2 consists of eight items explaining 10.9% of the variance (Cronbach's alpha: .886). Four of these items were included in risky driving style: three in the angry driving style and one in the careful driving style of the original MDSI. This factor was labelled as the risky and angry driving style. Factor 3 consists of seven items explaining 7.58% of the variance (Cronbach's alpha: .76), among which five items were included in the high-velocity driving style, one in the anxious driving style, and one in the dissociative driving style of the original MDSI. This factor was labelled as the high-velocity driving style. Factor 4 consists of five items explaining 4.8% of the variance (Cronbach's alpha: .68). Three items were included in the patient driving style and two in the careful driving style of the original MDSI. Therefore, this factor was labelled the patient and careful driving style. Factor 5 consists of five items explaining 3.34% of the variance (Cronbach's alpha: 0.63), among which three items were included in the distress-reduction driving style, one in the careful and one in the patient driving style of the original MDSI. This factor was labelled the distress-reduction driving style. Factor 6 consists of four items explaining 3.07% of the variance (Cronbach's alpha: 0.71). This is a new factor including two items from the dissociative driving style: one item from the careful driving style and one from the distress-reduction driving style, which was labelled as the inattentive driving style.

*3.2. Driving Styles and Sociodemographic Factors of the Chinese Sample.* The relationship between the identified driving styles and the sociodemographic characteristics of gender, age, and driving experience were investigated by multivariate and univariate analyses of variance (ANOVA). The multivariate ANOVA indicated a significant gender difference $F$ (6, 215) = 1.257, $P < 0.01$. Univariate ANOVAs showed that gender differences were not significant in the anxious and dissociative driving style (1, 215) = 0.516, $P > 0.05$ (men mean = 2.53, SD = 1.04; women mean = 2.43, SD = 0.94), the distress-reduction driving style (1, 215) = 2.78, $P > 0.05$ (men mean = 4.14, SD = 0.93; women mean- = 3.94, SD = 0.98), the inattentive driving style (1, 215) = 0.912, $P > 0.05$ (men mean = 3.04, SD = 0.98; women mean = 3.02, SD = 0.87), but they indicated significant differences in the risky and angry driving style $F$ (1, 215) = 4.51, $P < 0.05$ (men mean = 2.27, SD = 0.08; women mean = 2, SD = 0.72), in the patient and careful driving style $F$ (1, 215) = 4.93, $P < 0.05$ (men mean = 4.12, SD = 0.90; women mean = 4.37, SD = 0.76), and in the high-velocity driving style $F$ (1, 215) = 8.203, $P < 0.05$ (men mean = 3.63, SD = 1.13; women mean = 3.1, SD = 1.03).

Pearson's correlations ([1]Pearson's correlation coefficients between .10 and .29 represent a small association, coefficients between 0.30 and 0.49 represent a medium association, and coefficients of 0.50 and above represent a large association [45].) were tested to explore the associations between age and the six driving styles. They indicated that age was inversely associated with the anxious and dissociative driving style, $r$ (207) = −0.312, $P < 0.05$, the risky and angry driving style, $r$ (207) = −0.346, $P < 0.05$, the high-velocity driving style, $r$ (207) = −0.238, $P < 0.05$, distress-reduction driving style, $r$ (207) = −0.205, $P < 0.05$, and the inattentive driving style, $r$ (207) = −0.314, $P < 0.05$ and that it was positively associated with the patient and careful driving style, $r$ (207) = .236, $P < 0.05$. This confirms that the older the participants, the lower the tendency to adopt anxious and dissociative, risky and angry, high-velocity, distress-reduction, and distracted driving styles, and the higher the tendency to embrace the patient and careful driving style.

Pearson's correlation also showed that driving experience was significantly inversely associated with the anxious and dissociative driving style, $r$ (207) = −0.237, $P < 0.05$, the risky and angry driving style, $r$ (215) = −0.241, $P < 0.05$, and the inattentive driving style, $r$ (207) = −0.313, $P < 0.05$, while it was positively associated with the patient and careful driving style, $r$ (207) = 0.287, $P < 0.05$. It revealed no significant relationships between age and the high-velocity style and the distress-reduction driving style.

*3.3. Factor Analysis of the UK Sample.* The factor analysis with the Varimax rotation was conducted on the answers from the 240 UK participants, revealing distribution of the 44 items over eight factors explaining 65.7% of the variance. Two factors did not have sufficient items to make a meaningful contribution. The item distribution can be found in Table 3.

Factor 1 consists of five items explaining 34.1% of the total variance (Cronbach's alpha: .502). These items were labelled as the anxious driving style, explaining a person's tendency to experience nervousness and stress while driving. Factor 2 includes 19 items explaining 8.48% of the total variance (Cronbach's alpha: .962). These items refer to a person's tendency to seek stimulation and engagement in risky driving and the tendency to be distracted during driving, which was labelled as the risky and dissociative driving styles. Among these items, four items are included in the risky driving style, and seven in the dissociative driving style of the original MDSI, while the remaining eight items were from the other styles of the original MDSI. Factor 3 includes five items explaining 7.3% of the total variance (Cronbach's alpha: .804). This factor describes a person's tendency to drive quickly, and this kind of hazardous driving behaviour, which may interfere with and endanger other road users, was labelled as the high-velocity and angry driving style. Three items are included in the high-velocity driving style and two in the angry style of the original MDSI. Factor 4 includes five items explaining 3.21% of the total variance (Cronbach's alpha: .623), describing people's tendency to be polite to other road users and exhibiting no sign of pressure on their time. Three items were previously included in the patient style in the MDSI, and two items were included in other driving styles. This factor was labelled as the patient driving style. Factor 5 includes three items explaining 2.09% of the total variance (Cronbach's alpha: .784), in which people tend to drive carefully and in a structured manner. This factor was labelled as the careful

Table 3: Factor model coefficients of the multidimensional driving styles of the UK sample.

| Factors and items | Loading |
|---|---|
| Factor 1: anxious driving style | |
| [43] *Feel comfortable while driving* | *0.753* |
| [30] Feel nervous while driving | 0.728 |
| [24] It worries me when driving in bad weather | 0.674 |
| [2] *Feel I have control over driving [−]* | *0.580* |
| [9] Driving makes me feel frustrated | 0.571 |
| [32] Feel distressed while driving | 0.569 |
| Factor 2: risky and dissociative driving style | |
| [23] Like the thrill of flirting with death or disaster | 0.857 |
| [19] Attend to my hair/makeup while driving | 0.835 |
| [14] *Lost in thoughts or distracted, I fail to notice people at pedestrian crossings* | *0.808* |
| [20] *Distracted or preoccupied and suddenly realize the vehicle ahead has slowed down and have to slam on the brakes to avoid a collision* | *0.802* |
| [34] *Attempt to drive away from traffic lights in third gear (or in the neutral mode in automatic cars)* | *0.794* |
| [29] Misjudge the speed of an oncoming vehicle when passing | 0.788 |
| [28] Get a thrill out of breaking the law | 0.787 |
| [21] Like to take risks while driving | 0.782 |
| [26] Forget that my lights are on the full-beam until flashed by another motorist | 0.777 |
| [3] Drive through traffic lights that have just turned red | 0.777 |
| [38] Enjoy the excitement of dangerous driving | 0.762 |
| [44] Purposely tailgate other drivers | 0.739 |
| [37] Nearly hit something due to misjudging my gap in a parking lot | 0.734 |
| [33] Intend to switch on the windscreen wipers but switch on the lights instead | 0.689 |
| [35] Plan my route badly, so that I hit traffic that I could have avoided | 0.642 |
| [27] When someone does something on the road that annoys me, I flash them with the high beam | 0.519 |
| [25] Meditate while driving | 0.457 |
| Factor 3: high-velocity and angry driving style | |
| [15] In a traffic jam, I think about ways to get through the traffic faster | 0.708 |
| [31] Get impatient during the rush hour | 0.699 |
| [16] When a traffic light turns green and the car in front of me does not get going immediately, I try to urge the driver to move on | 0.626 |
| [1] Blow my horn or "flash" the car in front as a way of expressing frustration | 0.623 |
| [18] When someone tries to skirt in front of me on the road, I drive in an assertive way in order to prevent it | 0.607 |
| [39] *Honk my horn at others* | *0.508* |
| [8] *When in a traffic jam and the lane next to me starts to move, I try to move into that lane as soon as possible* | *0.455* |
| Factor 4: patient driving style | |
| [12] When a traffic light turns green and the car in front of me does not get going, I just wait for a while until it moves | 0.714 |
| [17] At an intersection where I have to give right-of-way to oncoming traffic, I wait patiently for cross-traffic to pass | 0.610 |
| [41] Plan long journeys in advance | 0.591 |
| [42] *Always ready to react to unexpected manoeuvres by other drivers* | *0.440* |
| Factor 5: careful driving style | |
| [40] Tend to drive cautiously | 0.784 |
| [13] Drive cautiously | 0.756 |
| [22] *Base my behaviour on the motto "better safe than sorry"* | *0.585* |
| Factor 6: distress-reduction driving style | |
| [6] Do relaxing activities while driving | 0.768 |
| [7] While driving, I try to relax myself | 0.724 |
| [36] *Use muscle relaxation techniques while driving* | *0.655* |
| *Factor 7* | |
| [4] *Enjoy the sensation of driving on the limit* | |
| [5] *On a clear freeway, I usually drive at or a little below the speed limit* | |
| *Factor 8* | |
| [11] *Swear at other drivers* | |
| [10] *I daydream to pass the time while driving* | |

The grey items were removed from the second analysis; the items in italics do not correlate with the same items in the original factor analysis.

driving style. Two items were included in the careful style and the remaining item in the patient style of the original MDSI. Factor 6 includes three items explaining 1.5% of the total variance (Cronbach's alpha: .562), describing drivers' engagement in relaxing activities while driving, which was labelled as the distress-reduction driving style. These three items were included in the original MDSI, corresponding to the distress-reduction style. Factor 7 includes two items

explaining 1.1% of the total variance (Cronbach's alpha: .201). These items were part of the risky and anxious driving styles of the original MDSI. Factor 8 includes two items explaining 1.02% of the total variance, and these were included in the dissociative driving style of the original MDSI.

A constraint was again set to have at least three items per factor. The items in Factors 7 and 8 achieved a low Cronbach's alpha figure and were removed from the analysis. As a follow-up to the results of the first-factor analysis, a second-factor analysis with the Varimax rotation consisting of six factors was conducted, in which items 6, 7, and 12 were excluded. This analysis revealed a distribution of 41 items over six factors, explaining 62.86% of the variance. The loadings of the items on each of these factors are presented in Table 3.

Factor 1 includes six items explaining 35.43% of the total variance (Cronbach's alpha: .585). All items were included in the anxious driving style of the original MDSI. Factor 2 includes 17 items explaining 8.81% of the total variance (Cronbach's alpha: .960). These items address unsafe and risky driving behaviour, among which four items were included in the risky and dissociative driving styles, seven in the dissociative driving style of the original MDSI, and the remaining six items from other styles in the original MDSI. Factor 3 includes seven items explaining 7.4% of the total variance (Cronbach's alpha: .831). Four items are included in the high-velocity driving style, and three in the angry style of the original MDSI. Factor 4 includes four items addressing patient driving behaviour and attitudes. This factor explains 4.91% of the total variance (Cronbach's alpha: .623). Among these items, three were previously included in the patient style and one in the careful driving style of the original MDSI. Factor 5 includes three items explaining 3.48% of the total variance (Cronbach's alpha: .784). There are two items in the careful style and one in the patient style of the original MDSI. Factor 6 consists of three items explaining 2.83% of the total variance (Cronbach's alpha: .562), and this was labelled the distress-reduction driving style.

*3.4. Driving Styles and Sociodemographic Factors of the UK Sample.* The relationship between the identified driving styles and the sociodemographic characteristics of gender, age, and driving experience were investigated by multivariate and univariate analyses of variance (ANOVA). The multivariate ANOVA indicated no significant gender difference $F$ (6, 240) = 2–16, $P > 0.05$. Univariate ANOVAs showed that gender differences were significant in the risky and dissociative driving styles $F$ (1, 240) = 0.9.33, $P < 0.05$, (men mean = 1.92, SD = 1.06; women mean = 1.57, SD = 0.63) and not significant in the anxious driving style $F$ (1, 240) = 0.394, $P > 0.05$ (men mean = 3.36, SD = .71; women mean = 3.41, SD = 0.57), the high-velocity and angry driving style $F$ (1, 240) = 0.3.07, $P > 0.05$ (men mean = 2.79, SD = 1.06; women mean = 2.55, SD = 1.01), the patient driving style $F$ (1, 240) = 0.216, $P > 0.05$ (men mean = 4.54, SD = 0.91; women mean = 4.71, SD = 0.84), the careful driving style $F$ (1, 240) = 0.225, $P > 0.05$ (men mean = 4.59, SD = 0.97; women mean = 4.78, SD = 1.01), and the distress-reduction driving style $F$ (1, 240) = 0.764, $P > 0.05$ (men mean = 4.59, SD = 0.97; women mean = 4.78, SD = 1.01).

Pearson's correlations indicated inverse associations between age and the anxious driving style, $r$ (235) = −0.118, $P < 0.05$, the risky and dissociative driving style, $r$ (235) = −0.401, $P < 0.01$, the high-velocity and angry driving style, $r$ (235) = −0.481, $P < 0.05$, and the distress-reduction driving style, $r$ (235) = −0.315, $P < 0.01$. There was no significant relationship identified between age and the patient driving style, $r$ (235) = 0.06, $P > 0.05$, or age and the careful driving style, $r$ (235) = 0.09, $P > 0.05$. This provides evidence that the older the participant, the lower the tendency to adopt anxious, risky, high-velocity, and distress-reduction driving styles.

Pearson's correlation also showed that driving experience was inversely associated with the anxious driving style, $r$ (235) = −0.215, $P < 0.05$, the risky and dissociative driving style, $r$ (235) = −0.493, $P < 0.01$, the high-velocity and angry driving style, $r$ (235) = −0.419, $P < 0.05$, and the distress-reduction driving style, $r$ (235) = −0.328, $P < 0.01$. It revealed no significant relationships between age and the careful driving style, $r$ (235) = 0.32, $P > 0.05$, and between age and the patient driving style, $r$ (235) = 0.22, $P > 0.05$.

## 4. Conclusion and Discussion

The analysis of the Chinese participants' dataset showed its factorial structure is comparable to the previous MDSI, with 40 of the 44 original items divided over six factors. Two of the eight factors were identical to the factorial composition of the MDSI. Six factors in the original MDSI [7] were merged into three groups. Specifically, the "anxious and dissociative", the "risky and angry," and the "patient and careful" driving styles form single dimensions in the MDSI.

The present findings also suggest the inattentive style as a new dimension in the Chinese sample. The "inattentive" driving style refers to inattentiveness to driving procedures, which is caused by cognitive distraction. Inattention while driving can be understood as an instantaneous cognitive deviation from normal behaviour with the immediate following of sudden driver actions to correct behaviours resulting from inattention [37]. An inattentive driving style differs from a dissociative driving style owing to its cognitive nature, as opposed to a dissociative driving style which can be observed as the practice of driving while engaging in another physical activity. Inattention plays a significant role in the field of road safety problems [43], and it was not given enough attention when Taubman-Ben-Ari et al. [7, 36] proposed the central domains of driving styles. According to an empirical study [42], 78% of the 82 accidents recorded and 65% of the 761 near accidents were the direct result of driver inattention. Tango and Botta [40] estimated that 13.3% of accidents can be attributed to driver cognitive distraction, while 9.7% of crashes are categorized as incidents when the driver "looked but did not see." For example, with the pervasive use of mobile devices, the attention distraction caused by cell phone conversations has now become a common phenomenon [39].

Developing countries especially struggle to address road and vehicle safety concerns owing to an increased number of inattentive and careless drivers [37]. For example, the Ministry of Works of Malaysia has provided evidence that 41% of vehicle collisions are the direct result of driver carelessness [38]. The International Transport Forum's annual road safety report ranked South Africa as the country with the highest number of road fatalities [46], while there are studies of Chinese drivers' behaviour showing that inattentive driving made a significant contribution to traffic accidents (e.g., [47]). The complicated driving environment in China poses further challenges to these groups of inattentive drivers, including infrastructural issues, such as roads being constructed incorrectly [48], poorly designed, or a lack of road signs [49], and drivers having to share the road with a substantially large number of pedestrians and cyclists [50]. Uncertainty about the reactions and trajectories of vulnerable road users, such as those who are attempting to violate traffic control signals to cross at their own convenience, may further exacerbate the complexity of existing traffic situations [50]. It is evident that inattentive driving behaviour is considered a major safety problem, and there is significant benefit in identifying those drivers who engage in an inattentive driving style.

The results concerning the gender differences in the Chinese sample are consistent with previous literature, with men being more likely to engage in the risky and angry, and the high-velocity driving styles, while women are more likely to engage in patient and careful driving styles [51]. One possible explanation for this, as stated by Özkan and Lajunen [52], is that most male drivers exhibit high levels of masculine characteristics (e.g., being adventurous and aggressive), tending to view reckless driving as a challenge rather than a threat while interpreting the behaviour of other drivers as hostile. In contrast, the majority of female drivers are perceived as possessing highly feminine traits (e.g., caring for other people) so that they may prefer to drive in a safe and careful manner. There is no gender difference for the anxious and dissociative, or distress-reduction and inattentive driving styles, contrasting with Taubman-Ben-Ari and Skvirsky's study [36], which found female drivers scoring higher for the anxious style. The associations between age, driving experience, and the six driving styles were in line with previous studies, whereby age was inversely related to the maladaptive driving styles, namely anxious and dissociative, risky and angry, high-velocity, and inattentive [27] but also to the distress-reduction style, as in Poó et al. [8], while being positively related to the adaptive driving style, namely, patient and careful. This finding is also evidence of the influence of driving experience on driving styles, indicating that less-skilled drivers are more inclined to adopt anxious and dissociative, risky and angry, and inattentive driving styles [13]. It revealed no significant relationships between driving experience and the high-velocity and distress-reduction driving styles.

The analysis of the UK sample showed that most of the original factors could be replicated quite well, with 40 of the 44 original items divided over six factors. Four of the eight factors are identical to the factorial structure of the MDSI. Two factors in the original MDSI were merged into one group, namely the high-velocity and angry driving style. The findings also indicated that the risky driving style of the original MDSI was combined with the dimension of the dissociative driving style, which formed a new group. The gender difference was found to be consistent with Özkan and Lajunen's study [52], indicating that men are more likely to adopt risky and dissociative driving styles. The findings further revealed the association between age, driving experience, and driving style, indicating that young and less-skilled drivers are more inclined to adopt anxious, risky and dissociative, high-velocity, and angry driving styles, which is consistent with some previous investigations [4, 13, 27, 36]. However, there seems to be no clear relationship between age and experience and their effect on the adoption of careful and patient driving styles. This means that careful and patient styles may potentially be found among drivers of all ages and years of experience. A report has revealed that 91% of UK drivers self-report that they are "careful and competent" drivers [53]. Drivers who drive carefully and act patiently, even when traffic conditions do not satisfy their expectations, emphasize safety on the roads. The International Traffic Safety Data and Analysis Group accident database evaluated 37 countries and ranked the United Kingdom as one of the countries with the lowest number of road fatalities, with a ratio of 4 deaths per 100,000 inhabitants in 2011 [46].

Our findings imply that there is a need to explore and induce driver and road safety enhancement solutions through the investigation of driver styles. An increasing number of studies have employed psychological responses to collect data about drivers (e.g., [9, 11, 14]). Such responses in drivers could then be translated into adaptive and maladaptive driving styles. If such an assessment of driving styles could be identified, driver behaviour could potentially be improved by focusing education on shifting these responses from maladaptive to adaptive driving styles. For example, Ellison et al. [54] built a driver model to evaluate driver behaviour to improve road safety. This study also highlights how driving-related behaviours have been shown to vary across countries, including drivers' tendencies to obey or break traffic rules. As traffic conditions, living environments, and cultural backgrounds vary around the world, drivers exhibit different styles when participating in a traffic environment [13]. Any such differences also raise the need to adapt psychological responses to give consideration to cultural specificities [18, 19].

This study has some limitations. First, it relied on self-reported driving behaviour, and the results obtained from driving style questionnaires could be used as predictors of actual driving behaviour. However, there is a need to further investigate how the results of the self-reported behaviour are correlated with actual behaviour in a vehicle or driving simulator. This will validate the trustworthiness of the metric due to the reporting bias and will enhance the understanding of driving styles. Second, the study followed the guideline of Child [55]. Any factor loading scores less than 0.3 were removed. Scores greater than 0.4 were considered stable [56], which appeared in the British sample. In the Chinese sample,

there were three items (i.e., one in Factor 2, one in Factor 4, and one in Factor 5), indicating that the factors account for approximately 30% of the relationship within the data. For small samples, 0.3 should be used with caution, although it was observed that for each of these factors, there were at least 3 non-cross-loading items with an acceptable loading score of 0.4 or above. Finally, both studies were conducted on convenience samples, which are not representative of the entire Chinese and UK populations, and while efforts were made to include drivers varying as much as possible in terms of their age and driving experience, some caution must be urged in generalizing the results.

## Data Availability

The data are not publicly available due to restrictions, e.g., there contained information that could compromise the privacy of research participants. The data that support the findings of this study are available from the corresponding author upon reasonable request.

## Conflicts of Interest

The authors declare that they have no conflicts of interest.

## References

[1] F. Hartwich, M. Beggiato, and J. F. Krems, "Driving comfort, enjoyment and acceptance of automated driving–effects of drivers' age and driving style familiarity—'," *Ergonomics*, vol. 61, no. 8, pp. 1017–1032, 2018.

[2] T. Rothengatter and R. D. Huguenin, *Traffic and Transport Psychology Theory and Application: Proceedings of the ICTTP 2000*, Elsevier, Amsterdam, Netherland, 2004.

[3] J. Elander, R. West, and D. French, "Behavioral correlates of individual differences in road-traffic crash risk: an examination of methods and findings," *Psychological Bulletin*, vol. 113, no. 2, pp. 279–294, 1993.

[4] H. Gwyther and C. Holland, "The effect of age, gender and attitudes on self-regulation in driving," *Accident Analysis & Prevention*, vol. 45, pp. 19–28, 2012.

[5] H. Hooft van Huysduynen, J. Terken, and B. Eggen, "The relation between self-reported driving style and driving behaviour. a," *Transportation Research Part F: Traffic Psychology and Behaviour*, vol. 56, pp. 245–255, 2018.

[6] A. H. Goodwin, R. D. Foss, and N. P. O'Brien, *The Effect of Passengers on Teen Driver Behavior (No. DOT HS 811 540)*, National Highway Traffic Safety Administration, Washington, DC, USA, 2012.

[7] O. Taubman-Ben-Ari, M. Mikulincer, and O. Gillath, "The multidimensional driving style inventory-scale construct and validation," *Accident Analysis & Prevention*, vol. 36, no. 3, pp. 323–332, 2004.

[8] F. M. Poó, O. Taubman-Ben-Ari, R. D. Ledesma, and C. M. Díaz-Lázaro, "Reliability and validity of a Spanish-language version of the multidimensional driving style inventory," *Transportation Research Part F: Traffic Psychology and Behaviour*, vol. 17, pp. 75–87, 2013.

[9] M. A. Trógolo, J. D. Tosi, F. M. Poó, R. D. Ledesma, L. A. Medrano, and S. Dominguez-Lara, "Factor structure and measurement invariance of the multidimensional driving style inventory across gender and age: an ESEM approach," *Transportation Research Part F: Traffic Psychology and Behaviour*, vol. 71, pp. 23–30, 2020.

[10] H. H. V. Huysduynen, J. Terken, J. Martens, and B. Eggen, "Measuring driving styles : a validation of the multidimensional driving style inventory," in *Proceedings of the 7th International Conference on Automotive User Interfaces and Interactive Vehicular Applications*, pp. 257–264, Nottingham, England, September 2015.

[11] J. L. Padilla, C. Castro, P. Doncel, and O. Taubman-Ben-Ari, "Adaptation of the multidimensional driving styles inventory for Spanish drivers: convergent and predictive validity evidence for detecting safe and unsafe driving styles," *Accident Analysis & Prevention*, vol. 136, Article ID 105413, 2020.

[12] J. Karjanto, N. M. Yusof, J. Terken et al., "The identification of Malaysian driving styles using the multidimensional driving style inventory," in *Proceedings of the 8th International Conference on Automotive User Interfaces and Interactive Vehicular Applications*, pp. 245–252, Ann Arbor, MI, USA, October 2016.

[13] A. C. Holman and C. E. Havârneanu, "The Romanian version of the multidimensional driving style inventory: psychometric properties and cultural specificities," *Transportation Research Part F: Traffic Psychology and Behaviour*, vol. 35, pp. 45–59, 2015.

[14] F. Freuli, G. De Cet, M. Gastaldi et al., "Cross-cultural perspective of driving style in young adults: psychometric evaluation through the analysis of the multidimensional driving style inventory," *Transportation Research Part F: Traffic Psychology and Behaviour*, vol. 73, pp. 425–432, 2020.

[15] Y. Wang, W. Qu, Y. Ge, X. Sun, and K. Zhang, "Effect of personality traits on driving style: psychometric adaption of the multidimensional driving style inventory in a Chinese sample," *PLoS One*, vol. 13, no. 9, Article ID e0202126, 2018.

[16] S. Long and C. Ruosong, "Reliability and validity of the multidimensional driving style inventory in Chinese drivers," *Traffic Injury Prevention*, vol. 20, no. 2, pp. 152–157, 2019.

[17] M. Houtenbos, "Expecting the unexpected," Thesis, Delft University of Technology, Leidschendam, The Netherlands, 2008.

[18] D. Yang, X. Qiu, D. Yu, and R. Sun, "Study on the driving style heterogeneity and drivers' driving styles choice in China," in *Proceedings of the Annual Meeting Transportation Research Board 01558168*, Washington, DC, USA, January 2015.

[19] Z. Feng, S. Lu, and W. Zhang, "Difference and similarity comparisons of traffic accident characteristics in China and Europe," in *Proceedings of the 14th COTA International Conference of Transportation Professionals*, pp. 2666–2676, American Society of Civil Engineers, Changsha, China, 2014.

[20] F. Li, X. Yao, L. Jiang, and Y. Li, "Driving anger in China: psychometric properties of the driving anger scale (DAS) and its relationship with aggressive driving," *Personality and Individual Differences*, vol. 68, pp. 130–135, 2014.

[21] P. Atchley, J. Shi, and T. Yamamoto, "Cultural foundations of safety culture: a comparison of traffic safety culture in China, Japan and the United States," *Transportation Research Part F: Traffic Psychology and Behaviour*, vol. 26, pp. 317–325, 2014.

[22] W. Zhang, O. Tsimhoni, M. Sivak, and M. J. Flannagan, "Road safety in China: analysis of current challenges," *Journal of Safety Research*, vol. 41, no. 1, pp. 25–30, 2010.

[23] T. Lajunen and D. Parker, "Are aggressive people aggressive drivers? a study of the relationship between self-reported general aggressiveness, driver anger and aggressive driving," *Accident Analysis & Prevention*, vol. 33, no. 2, pp. 243–255, 2001.

[24] J. L. Deffenbacher, M. E. Huff, R. S. Lynch, E. R. Oetting, and N. F. Salvatore, "Characteristics and treatment of high-anger drivers," *Journal of Counseling Psychology*, vol. 47, no. 1, pp. 5–17, 2000.

[25] O. Şimşekoğlu, T. Nordfjærn, M. F. Zavareh, A. M. Hezaveh, A. R. Mamdoohi, and T. Rundmo, "Risk perceptions, fatalism and driver behaviors in Turkey and Iran," *Safety Science*, vol. 59, pp. 187–192, 2013.

[26] T. Nordfjærn and T. Rundmo, "Perceptions of traffic risk in an industrialized and a developing country," *Transportation Research Part F*, vol. 12, pp. 91–98, 2009.

[27] F. Sagberg, G. B. Selpi, G. F. Bianchi Piccinini, and J. Engström, "A review of research on driving styles and road safety," *Human Factors: The Journal of the Human Factors and Ergonomics Society*, vol. 57, no. 7, pp. 1248–1275, 2015.

[28] T. Özkan, T. Lajunen, J. E. Chliaoutakis, D. Parker, and H. Summala, "Cross-cultural differences in driving behaviours: a comparison of six countries," *Transportation Research Part F: Traffic Psychology and Behaviour*, vol. 9, no. 3, pp. 227–242, 2006.

[29] B. Shen, W. Qu, Y. Ge, X. Sun, and K. Zhang, "The relationship between personalities and self-report positive driving behavior in a Chinese sample," *PloS One*, vol. 13, Article ID e0190746, 2018.

[30] K. R. Thompson, A. M. Johnson, J. L. Emerson, J. D. Dawson, E. R. Boer, and M. Rizzo, "Distracted driving in elderly and middle-aged drivers," *Accident Analysis & Prevention*, vol. 45, no. 2, pp. 711–717, 2012.

[31] G. Li, S. Eben Li, and B. Cheng, "Field operational test of advanced driver assistance systems in typical Chinese road conditions: the influence of driver gender, age and aggression," *International Journal of Automotive Technology*, vol. 16, no. 5, pp. 739–750, 2015.

[32] W. J. Stevenson, *Operations Management*, McGraw-Hill Education, New York, NY, USA, 12th edition, 2014.

[33] D. J. French, R. J. West, J. Elander, and J. M. Wilding, "Decision-making style, driving style, and self-reported involvement in road traffic accidents," *Ergonomics*, vol. 36, no. 6, pp. 627–644, 1993.

[34] J. T. Reason, A. Manstead, S. G. Stradling, J. Baxter, and K. Campbell, "Errors and violations on the road—a real distinction," *Ergonomics*, vol. 33, no. 11, pp. 1315–1332, 1990.

[35] E. Gulian, G. Matthews, A. I. Glendon, D. R. Davies, and L. M. Debney, "Dimensions of driver stress," *Ergonomics*, vol. 32, no. 6, pp. 585–602, 1989.

[36] O. Taubman-Ben-Ari and V. Skvirsky, "The multidimensional driving style inventory a decade later: review of the literature and re-evaluation of the scale," *Accident Analysis & Prevention*, vol. 93, pp. 179–188, 2016.

[37] G. Albertus, M. Meiring, and H. C. Myburgh, "A review of intelligent driving style analysis systems and related artificial intelligence algorithms," *Sensors*, vol. 15, pp. 30653–30682, 2015.

[38] I. Mohamad, M. Ali, and M. Ismail, "Abnormal driving detection using real time global positioning system data," in *Proceedings of the 2011 IEEE International Conference on Space Science and Communication (IconSpace)*, pp. 1–6, IEEE, Penang, Malaysia, July 2011.

[39] K. L. Young, C. M. Rudin-Brown, C. Patten, R. Ceci, and M. G. Lenné, "Effects of phone type on driving and eye glance behaviour while text-messaging," *Safety Science*, vol. 68, pp. 47–54, 2014.

[40] F. Tango and M. Botta, "Real-time detection system of driver distraction using machine learning," *IEEE Transactions on Intelligent Transportation Systems*, vol. 14, no. 2, pp. 894–905, 2013.

[41] J. C. Nunnally, *Psychometric Theory*, McGraw-Hill, New York, NY, USA, 2nd edition, 1978.

[42] O. Bagdadi, "Assessing safety critical braking events in naturalistic driving studies," *Transportation Research Part F: Traffic Psychology and Behaviour*, vol. 16, pp. 117–126, 2013.

[43] V. L. Neale, T. A. Dingus, S. G. Klauer, J. Sudweeks, and M. Goodman, "An overview of the 100-car naturalistic study and findings," in *Proceedings of the 19th International Technical Conference on the Enhanced Safety of Vehicles*, pp. 6–9, ESV, Washington, DC, USA, June 2005.

[44] M. A. Regan and E. Mitsopoulos, "Understanding passenger influences on driver behaviour: implications for road safety and recommendations for countermeasure development," Report 180, Monash University Accident Research Centre, Melbourne, Australia, 2001.

[45] P. Bobko, *Correlation and Regression: Applications for Industrial Organizational Psychology and Management*, Sage Publications, Thousand Oaks, CA, USA, 2nd edition, 2001.

[46] International Traffic Safety Data and Analysis Group, International Traffic Safety Data and Analysis Group, 2020, http://www.internationaltransportforum.org/jtrc/safety/safety.html Road Safety Annual Report.

[47] A. Lindgern, F. Chen, P. W. Jordan, and H. Zhang, "Requirements for the design of advanced driver assistance systems—the differences between Swedish and Chinese drivers," *International Journal of Design*, vol. 2, no. 2, pp. 41–54, 2008.

[48] J. Li, Z. Henk Van, and S. Lu, "Calibration of a traffic simulation for a Chinese city," in *Proceedings of the 14th Meeting of the Euro Working Group on Transportation*, Elsievier, Poznan, Poland, September 2011.

[49] Y.-H. Huang, W. Zhang, M. Roetting, and D. Melton, "Experiences from dual-country drivers: driving safely in China and the US," *Safety Science*, vol. 44, no. 9, pp. 785–795, 2006.

[50] P. Wang, P.-L. P. Rau, and G. Salvendy, "Road safety research in China: review and appraisal," *Traffic Injury Prevention*, vol. 11, no. 4, pp. 425–432, 2010.

[51] D. Shinar and R. Compton, "Aggressive driving: an observational study of driver, vehicle, and situational variables," *Accident Analysis & Prevention*, vol. 36, no. 3, pp. 429–437, 2004.

[52] T. Özkan and T. Lajunen, "Why are there sex differences in risky driving? the relationship between sex and gender-role on aggressive driving, traffic offences, and accident involvement among young Turkish drivers," *Aggressive Behavior*, vol. 31, no. 6, pp. 547–558, 2005.

[53] 91% of UK drivers say they're "careful and competent": Available at https://www.autoexpress.co.uk/car-news/105267/91-of-uk-drivers-say-theyre-careful-and-competent.

[54] A. B. Ellison, S. P. Greaves, and M. C. J. Bliemer, "Driver behaviour profiles for road safety analysis," *Accident Analysis & Prevention*, vol. 76, pp. 118–132, 2015.

[55] D. Child, *The Essentials of Factor Analysis*, Bloomsbury Academic, London, UK, 3rd edition, 2006.

[56] E. Guadagnoli and W. F. Velicer, "Relation of sample size to the stability of component patterns," *Psychological Bulletin*, vol. 103, no. 2, pp. 265–275, 1988.

Hindawi
Advances in Civil Engineering
Volume 2021, Article ID 5571271, 10 pages
https://doi.org/10.1155/2021/5571271

*Research Article*

# An Attention-Based Model for Travel Energy Consumption of Electric Vehicle with Traffic Information

**Shen Li,[1] Hailong Zhang,[2] Huachun Tan,[2] Zhiyu Zhong,[3] and Zhuxi Jiang[3]**

[1]*Department of Civil & Environmental Engineering, University of Wisconsin-Madison, Madison, WI, USA*
[2]*School of Transportation, Southeast University, Nanjing, China*
[3]*China Engineering Laboratory for Electric Vehicles, School of Mechanical Engineering, Beijing Institute of Technology, Beijing, China*

Correspondence should be addressed to Hailong Zhang; bit.zhl203@gmail.com

Received 13 January 2021; Revised 19 August 2021; Accepted 20 August 2021; Published 28 September 2021

Academic Editor: Hui Yao



Mileage anxiety is one of the most important factors that affect the driving experience due to the limitation of battery capacity. Robust and accurate prediction of the energy consumption of the journey of the electric vehicle can guide the driver to allocate the power rationally and relieve the anxiety of the mileage. Since vehicle sharing is the biggest application scenario of electric vehicles, it is a critical challenge in share mobility research area. In this paper, a travel energy consumption prediction model of electric vehicles is proposed in order to improve the mobility of shared cars and reduce the anxiety of drivers because they are worried about insufficient power. A recurrent neural network with attention mechanism and deep neural network is used to build the model. To validate the proposed model, a simulation is demonstrated based on both traffic and vehicle information. After the simulation, experimental results show that the proposed model has high prediction accuracy, and we also show through visualization how the model finds high relevant road segments of the road network while dealing with corresponding traffic state input.

## 1. Introduction

In recent years, people have paid sufficient attention to environmental pollution problems and the depletion of oil resources caused by excessive use of fossil fuel. The development of pure electric vehicles to replace the traditional energy vehicles is one of the important ways to solve these problems. The current commercialized application of electric vehicles is car sharing, which has many benefits such as being environmentally friendly, saving energy, and reducing emission [1]. However, the imperfection of the current battery technology and the battery capacity constraint still leads to car sharing user experience mileage anxiety while driving a shared electric car.

There are many existing applications for car sharing system using electric vehicles showing the strong correlation between electric vehicles and car sharing technologies, but with the lack of discussion on range anxiety caused by limitation of the current battery technology and the battery capacity constraint [2, 3]. Neubauer and Wood published a paper to examine the sensitivity of BEV utility to range anxiety and different charging infrastructure scenarios, including variable time schedules, power levels, and locations (home, work, and public installations). The results indicated that the effects of range anxiety can be significant but are reduced with access to additional charging infrastructure [4]. Some state-of-the-art works have made effort to address the aforementioned problem by improving the battery performances during the battery manufacturing production chain. In [5], a random forest based feature analyses and modelling method is proposed for battery manufacturing, and the coupling effects of the battery features are mined and quantified by using the ML technologies. Further in [6], a Gaussian process regression model is used to analyze the influence of battery electrode mass load under the underlying correlation of four intermediate production feature

variables. Meanwhile, applying advanced battery management technology is the other approach to reduce mileage anxiety. For instance, King et al. used on-demand vehicle access method to alleviate electric vehicle range anxiety, and with the help of battery management strategy, the driving range of EVs get is further improved [7]. In [8], a multi-objective constrained nonlinear optimization is applied to adjust batteries charging patterns, which effectively improve the energy-saving performance of EV. In [9], a battery changing management strategy is proposed to cooptimize the energy consumption and battery degradation. In [10], battery charging process considering internal temperature control is addressed by generalized predictive control (GPC). Energy consumption prediction is a core technology for battery management of EVs; besides the driver, accurate prediction of energy consumption can effectively alleviate the driver's anxiety and help them concentrate on driving the vehicle. However, the energy consumption of an electric car is affected by many factors, such as traffic status, vehicle status, and weather. For this reason, travel energy consumption prediction has long been considered as a difficult problem.

There has been much research on this issue. Cartenì et al. proved that the performance of electric vehicle has huge impact on car sharing models. The results indicated that the most statically significant attributes for those models are travel cost and travel time [11]. Ralf made a research on the estimation on energy consumption of the navigation route. A rule-based method was used in this work, which was conditioned on historical traffic and speed limit. However, the design of rules and the setting of coefficients needed experts, which should be changed under different situations [12]. De Cauwer et al. constructed energy consumption calculation models based on traffic information, vehicle parameters, road topology, and other information. The models are constructed by multiple linear regression, which was based on vehicle dynamics equation as underlying physical model. The model is complex and requires extensive feature preprocessing of the data [13]. Moreover, there are many similar works on the vehicle's energy consumption prediction [14, 15]. However, there is a complex and coupling relationship between driving condition and energy consumption of EVs. The tradition method cannot handle the nonlinear regression with spatiotemporal features especially considering traffic information. Since 2006, deep learning has been applied in many fields and has achieved very successful results [16], such as object recognition [17, 18], machine translation [19], and speech recognition [20]. Deep learning creates abstract high-level features by combining lower-level features to discover the distributed representation of the data, and in the high-level feature space, we can perform some operations that cannot be done in lower-level space. A deep convolutional neural network based energy consumption prediction method was proposed considering the influence of vehicle speed, tractive effort, and road elevation [21]. Recurrent Neural Networks are adapted to estimate the energy consumption of EVs during the specific route [22]. However, these methods cannot guarantee the prediction accuracy and robustness because they do not take the impact of traffic flow on vehicle operating conditions into account, where the traffic information on the driving route is merely considered in the existing ones at best. In fact, the traffic states of the whole road networks, especially the neighbor roads of the driving route, would make great influence on the energy consumption of EVs. However, the information of the whole road networks is tremendous to capture and distill the useful knowledge for deep neural networks. However, working with such high-dimensional information necessitates a powerful mechanism to steer the model to information important to the task at hand. Thus, an adaptive weighting mechanism should be applied when exacting features of road networks. Fortunately, the attention mechanism has a great promotion effect in sequence learning task and has many successful applications in the field of image caption [23], NLP [24] graph transformers [25], and other areas [26, 27], which is a kind of encoder that imitates the behavior of human attention. However, the attention mechanism based energy consumption prediction method has not been constructed; further, as a result of this, the traffic information of the road networks is still not fully unutilized to further improve the prediction accuracy for energy consumption of EVs. Motivated by that, we proposed an attention based prediction model to improve the robustness and accuracy by extracting traffic state information in different sections of the road network during the forecasting process.

Accordingly, a deep learning method is used to construct an electric vehicle travel energy consumption prediction model based on traffic conditions and vehicle states in this paper, which aims to make a robust and accurate prediction of the vehicle energy consumption during the journey. In the proposed model, we utilize traffic information and vehicle status information, which are two different types of information. Since traffic conditions of the road network are continuously changing during the trip, traffic conditions during the trip as a sequential input were considered. And the recurrent neural network is used, which is suitable for dealing with sequential input, to extract the features of the traffic status of the whole trip. Then, the deep neural network was applied to fuse the vehicle state features with the traffic state features and output the prediction results of energy consumption of the trip. For the traffic feature extraction, the traffic information of the road network is used as the input of the model. The traffic conditions of the road network can help provide information on the traffic state changes during the driving of the vehicle in the task of predicting travel energy consumption. More specifically, the congestion, the morning peak hour, and the evening peak hour are major scenarios that would be tested in the paper. Besides, an attention mechanism was employed to help the model extract the information that has a great influence on the current task from the traffic state of road network. Therefore, we extract the feature of these two kinds of information separately and fuse the extracted feature information in the hidden space. Finally, we use the fused feature to predict the energy consumption of the trip. Furthermore, we show how attention mechanism can help the energy

consumption forecasting model extract traffic state information and how its attention degree changes in different sections of the road network during the forecasting process.

In the following sections of the article, first, we described the construction of the model. Then, we conducted a comparative experiment and analyzed the influence of input of different information and the model structure on the accuracy of the model. Finally, we visualize the attentional mechanisms of the model and illustrate the characteristics of attentional mechanisms in extracting traffic characteristics.

## 2. Methodology

The travel energy consumption of a vehicle is mainly determined by the driving cycles of the vehicle, and the operating conditions of the vehicle are affected by traffic conditions and the status of the vehicle. Therefore, in order to accurately predict the energy consumption of electric vehicle travel, we need to use these two kinds of information. In this section, a prediction method of travel energy consumption of electric vehicles based on deep learning model combined with attention mechanism is proposed. Figure 1 gives the framework of the proposed deep learning architecture. The details are given as follows.

RNN is a kind of neural network, which is suitable for dealing with sequential input data. The connection between hidden layers makes RNN have memory of preceding input data [25]. Road network is composed of numerous road segments, and the vehicle travel is a sequential composition of several road segments. We use traffic states of the road segments, in which the car during the travel is the input of RNN. In this paper, we use traffic flow, velocity, density, and the length of road segment as traffic state input. The traffic states input of a travel is represented as $X$.

$$X = \{x_1, x_2, \ldots, x_n\}, \quad x_t \in R^d, \tag{1}$$

where $n$ is the number of road segments of the travel and $d$ is the size of input vector. In this paper, $d$ is equal to 4 as we described above.

Vehicle travel energy consumption is directly affected by vehicle driving cycles, and vehicle driving cycles are mainly affected by traffic states. For the travel energy consumption prediction task, the future traffic state information corresponding to the traveling route of the vehicle is the key information. However, future traffic states of each road have a complex correlation with the current traffic states of road network. In order to make a reasonable and precise explanation of the total traffic state of vehicle travel, we utilize not only the traffic states of the route, but also the traffic states of road network as input. We represent current time traffic states of road network as

$$\mathrm{TS} = \{\mathrm{ts}_1, \mathrm{ts}_2, \ldots, \mathrm{ts}_m\}, \quad \mathrm{ts} \in R^d, \tag{2}$$

where $m$ is the number of roads of road network and $\mathrm{ts}_i$ is the traffic state vector of $i$-th road segment of the road network.

For each trip, the current traffic conditions of some sections of the road network may affect the traffic conditions on the vehicle's path in the future. However, it is difficult to determine which roads we should pay more attention to. In order to help the model find out high relevant roads to the prediction task, we employ attention mechanism in our model. Attention is implemented as a hidden layer, which computes a categorical distribution (or hierarchy of categorical distributions) to make a soft-selection over source elements [28]. For each road segments in the road network, the attention mechanism produces $m$-dimensional positive weight $a_t$. Each dimension of $a_t$, shown as $a_{t,i}$, can be interpreted as the relative importance to give to road segment $i$ in blending the $\mathrm{ts}_i$,'s together.

$$A = \{a_1, a_2, \ldots, a_n\}, \quad a_t \in R^m. \tag{3}$$

The $a_t$ is computed by an attention model $f_{att}$ for which we use a multilayer perceptron (MLP) conditioned on $x_t$ and previous hidden states $h_{t-1}$.

$$\begin{aligned} z_t &= f_{att}(x_t, h_{t-1}), \\ a_{t,k} &= \frac{\exp(z_{t,k})}{\sum_{k=1}^{m} \exp(z_{t,k})}. \end{aligned} \tag{4}$$

Once weights are computed, the traffic state representation feature $s_t$ can be computed by

$$s_t = w_s x_t \oplus (a_t \cdot \mathrm{TS}), \tag{5}$$

where $w_s$ is the learned weights and $\oplus$ is the concatenation of two vectors.

The initial hidden state $h_0$ is computed through one MLP conditioned on $x_1$.

$$h_0 = f_{\mathrm{init}}(x_1). \tag{6}$$

The traffic states feature vector of the whole trip can be computed in a recursive way.

$$h_t = \tanh(Wh_{t-1} + Us_t + b), \quad t = 1, \ldots, n. \tag{7}$$

We use the final hidden states $h_n$ as the output of traffic information extractor.

The other important factor of travel energy consumption is vehicle state. For electric vehicle, State of Charge (SOC), cell temperature, and cell voltage are key influence factors of vehicle energy consumption. In order to combine vehicle states into prediction model, we employ a MLP as vehicle states extractor. The vehicle state $v_s \in R^k$ is a $k$ dimensional vector, which contains all key factor of vehicle energy system, which can be collected. The final output of $v_h$ is computed through a MLP conditioned on $v_s$.

$$v_h = P\mathrm{ReLU}(w_{vh} v_s + b_v), \tag{8}$$

where $w_{vh}$ and $b_v$ are the learned weights and bias and $P$ReLU [29] is the activation function.

The task of energy consumption predictor is to make the prediction conditioned on the output of traffic information extractor and vehicle states extractor. We concatenate traffic information extractor's output $h_n$ and vehicle states extractor's output $v_h$ as $C$ and use it as the input of the predictor. We use a deep neural network (DNN) to make the

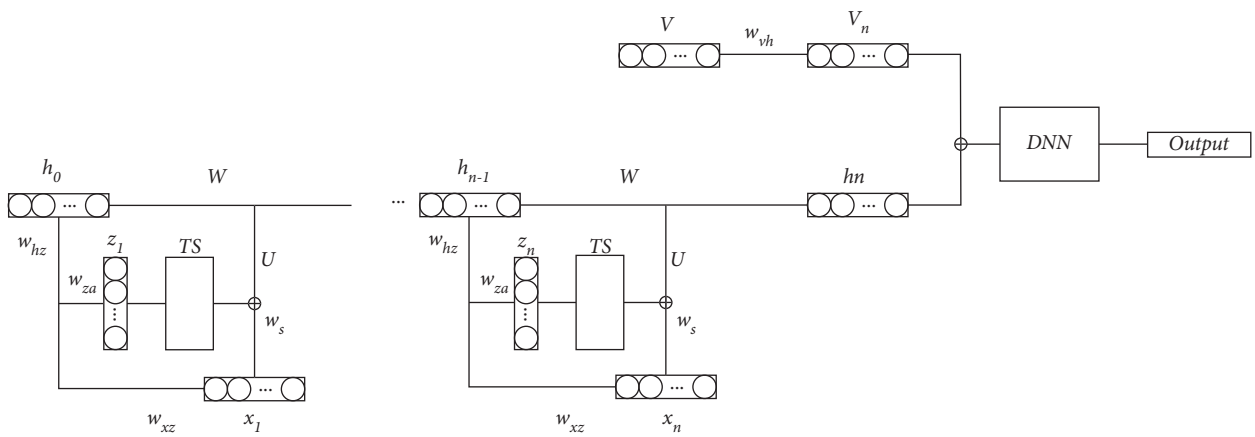


Figure 1: Graphical structure of travel energy consume prediction model. Our model employs attention mechanism in RNN to extract features from traffic states of road network. We use a one hidden layer neural network (NN) to extract features of vehicle states and concatenate the output of RNN and NN as the input of the DNN. The output of DNN is the final prediction result of our model.

prediction, and 3 hidden layers should be enough in this task. The output of energy consumption predictor $y_{\text{pred}}$ is the prediction result of the task. The model can be trained jointly by minimizing the residual between model's prediction result and ground truth, and the loss function is

$$\text{loss} = \frac{1}{N}\sum_{i=1}^{N}\left(y_{\text{truth}} - y_{\text{pred}}\right), \tag{9}$$

where $N$ is the number of training sets.

In the training process, the sequenced traffic information is input into RNN, and $h_n$ is outputted by the last layer, then the feature vector $v_s$ mapped to the vehicle state vector is fused with $h_n$ as a input vector of DNN, and the final energy consumption prediction result $y_{\text{pred}}$ is obtained by DNN. Thus, the loss function can be calculated with the ground truth $y_{\text{truth}}$. Though backpropagation, the neural network parameters can be optimized with the optimizer RMSprop [30], where the learning rate is set as 0.00001 before the $10^{\text{th}}$ epoch and 0.000001 after that. After 100 epochs, the training process will be terminated, and the trained neural network will be tested under the test dataset.

## 3. Experiments Design

In this section, we introduce the process of the construction of dataset and implement detail of the model.

*3.1. Data Description.* Our model is a data-driven model and needs two kinds of data, traffic information of road network and the vehicle state. However, it is difficult for us to obtain traffic status data and vehicle status data corresponding to each other. We have built a simulation platform for electric vehicle operation data collection and travel energy consumption calculation.

We utilize *Quadstone Paramics* traffic simulation software to construct a traffic simulation model, from which we can collect traffic states of all road segments of road network and driving cycles of vehicles. Moreover, we build a vehicle simulation model by *Simulink/MATLAB*, from which we can collect vehicle states and compute travel energy consumption. The logic diagram of the simulation platform is shown in Figure 2.

*3.2. Traffic Simulation Model.* *Quadstone Paramics* is a traffic microsimulation software, which is widely used in many aspects of transportation. A Paramics model is represented by a combination of "nodes, links, and traffic zones" to construct the road network in the real world. Through the set of OD matrices, users can adjust the traffic flow on different roads. Users can also change the individual vehicle movements by adding plug-ins in the model.

As shown in Figure 3, we construct the road network of traffic simulation model based on the road network of Beijing Northwest Third Ring Road. Each road segment of the road network has an index from 1 to $n$, where $n$ is the amount of road segments in the road network. In this paper, we construct a road network with 330 road segments and 27 travel regions. From traffic simulation model, we get traffic information of road network and driving cycles of vehicles, which run on the road. Traffic information contains the average traffic flow, velocity, and density of every road segment in the road network every minute. And, we randomly choose numerous vehicles running on road from the traffic simulation model and record its driving cycles by granularity of 0.5 s and the index of the road segments the vehicles have passed.

When making a prediction, we should choose a possible route at first and construct traffic states input based on this route. We also add vehicle location information $\text{loc}_t$ to traffic state input $x_t$, and one-hot encoding vector is employed to represent location information (e.g., in the case road, the network has 5 road segments, $\text{loc}_t = [1, 0, 0, 0, 0]$ for the index of $t_{\text{th}}$ road segment of the route is No. 1).

*3.3. Vehicle Simulation Model.* As shown in Figure 4, we build a vehicle simulation model based on electric vehicle in *Simulink/MATLAB*.

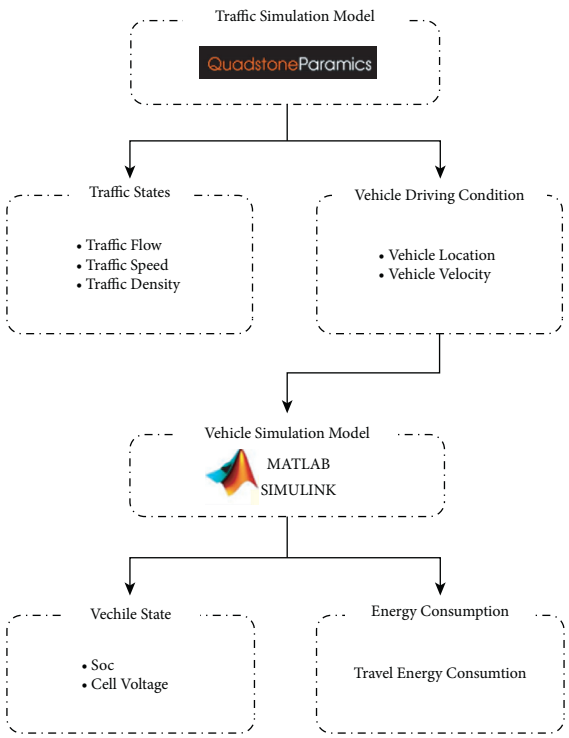


Figure 2: EV running data acquisition simulation platform.

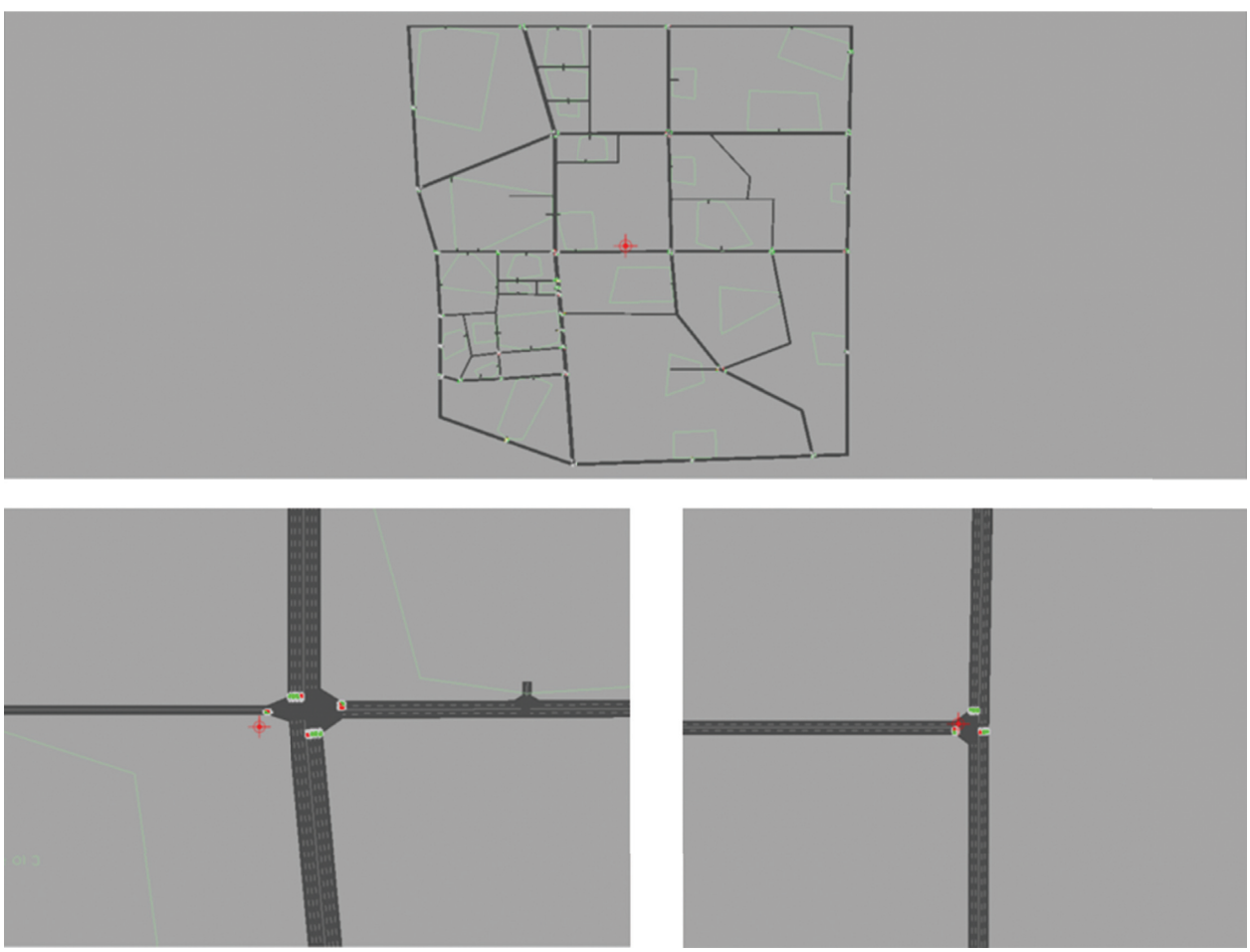

Figure 3: Road network of traffic simulation model.

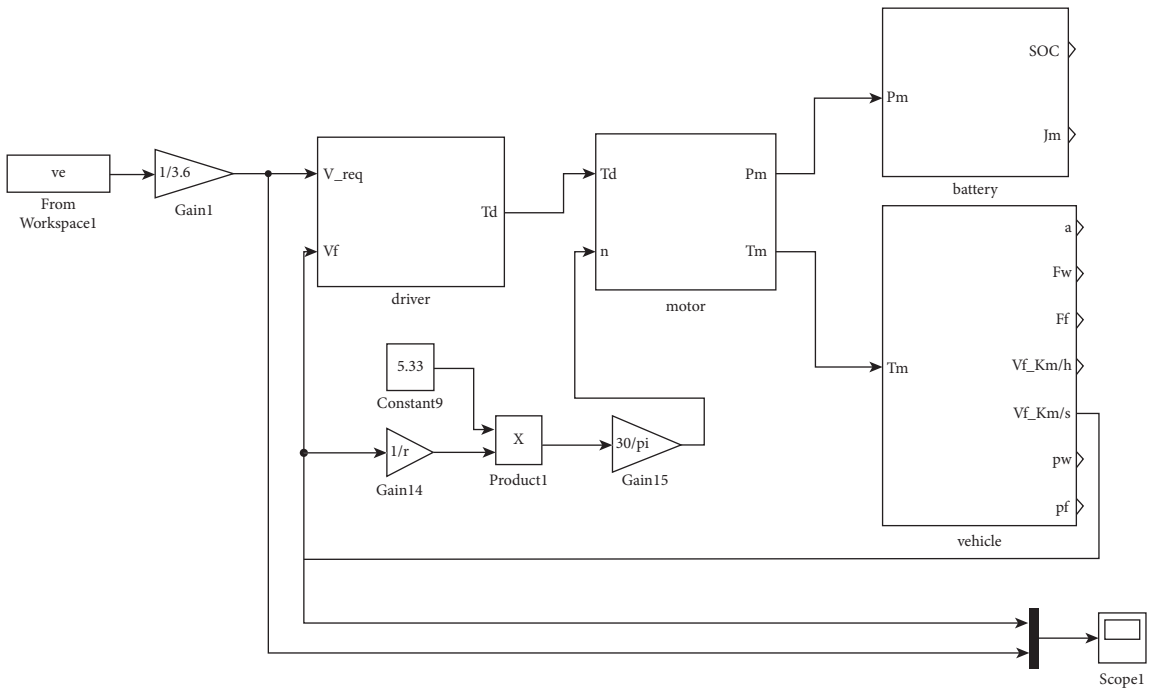


Figure 4: EV simulation model.

*3.3.1. Driver Simulation Model.* The driver controls vehicle vertical dynamic by the accelerator or brake pedal based on the difference between the actual speed of the feedback and the expected speed of the vehicle, thereby determining the driving or braking torque, and real-time following the speed. Commonly using the PI controller to simulate the driver's operation, the driver's PI controller principle is shown in the following formula:

$$\begin{aligned} v_e &= v_{\text{ref}} - v_f, \\ \text{Acc} &= \frac{1}{A}\left(k_p \times v_e + \lambda_i k_i \int_0^t v_e \mathrm{d}t\right), \\ \lambda_i &= \begin{cases} 0, & \left|k_i \int_0^t v_e \mathrm{d}t\right| > A, \\ 1, & \left|k_i \int_0^t v_e \mathrm{d}t\right| \le A, \end{cases} \end{aligned} \tag{10}$$

where $v_{\text{ref}}$ is the reference speed, $v_f$ is the real speed, and $v_e$ is the error between $v_{\text{ref}}$ and $v_f$, Acc is the angel of the accelerator or brake pedal normalized into [−1, 1], in which [0, 1] represents acceleration and [−1, 0] represents deceleration, $A$ is the full range of pedal angel, $k_p$ is the proportional factor, $k_i$ is the integral factor, and $\lambda_i$ is the Integral antisaturation coefficient. The driver model adjusts the output driving or braking torque as follows:

$$T_d = \text{Acc} \times T_{\text{tol}}. \tag{11}$$

$T_d$ is the motor torque, where $T_d \ge 0$ represents the driving torque, and $T_d \le 0$ represents the brake torque.

*3.3.2. Motor Model.* The drive motor uses a quasi-steady state method to simulate the motor and its controller, and the quasi-steady state equation is shown in the following equation:

$$p_m = \frac{T_m n_m}{\eta_m (T_m, n_m)}. \tag{12}$$

In the formula, $n_m$ is the rotation speed of the drive motor, $T_m$ is the torque of the drive motor, and $\eta_m$ is the efficiency of the main drive motor. Its efficiency MAP is shown in Figure 4:

*3.3.3. Battery Model.* The battery model uses a $R_{\text{int}}$ model, which is an equivalent circuit model characterized by open circuit voltage and resistance. The calculation formulas of current and power under this model are as follows:

$$\begin{aligned} P_b &= V_{\text{oc}} I_b - I_b^2 R_{\text{int}}, \\ I_b &= \frac{V_{\text{oc}} - \sqrt{V_{\text{oc}}^2 - 4R_{\text{int}} P_b}}{2R_{\text{int}}}. \end{aligned} \tag{13}$$

Among them, $V_{\text{oc}}$ is the open circuit voltage, and $R_{\text{int}}$ is the internal resistance of the battery; they are the function of battery SOC and temperature $T$. The energy consumption of the battery can be calculated by the following formula:

$$\text{Jm} = \frac{1}{3.6 \times 10^6} \int_0^t V_{\text{oc}} I_b \mathrm{d}t. \tag{14}$$

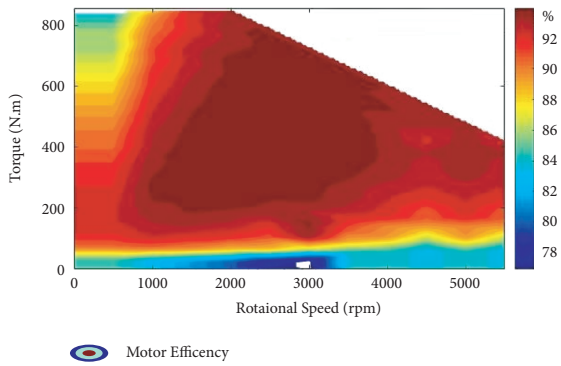


Figure 5: Motor efficiency map.

*3.3.4. Vehicle Dynamic Model.* The dynamic model of the vehicle can calculate the acceleration and speed of the vehicle according to the driving resistance balance equation:

$$a = \frac{F_d - F_f - F_w}{\delta m} = \frac{F_d - fmg\cos\alpha - mg\sin\alpha - (C_d A/21.15)v^2}{\delta m}, \quad (15)$$

$$v = 3.6\int_0^t a\,\mathrm{d}t.$$

In the formula, $f$ is the rolling resistance, $\alpha$ is the road ramp angle (the default value is 0), $m$ is the curb mass, $g$ is the acceleration of gravity, $C_d$ is the air resistance coefficient, and $A$ is the windward area of the vehicle.

We randomly set the initial SOC and collect the status of various key components in the running process of the vehicle and calculate the travel energy consumption. The travel energy consumption results of the vehicle are used as the ground truth of prediction model. We used the data collected by real vehicles to verify the accuracy of the vehicle simulation model. The test results show that the error in the calculation of travel energy consumption of our vehicle simulation model is within ±3%. Therefore, we can treat the simulation data as a replacement of real data.

We made a four-hour traffic simulation and collected 31175 vehicle driving cycles using the traffic simulation model. Furthermore, we compute the energy consumption of these driving cycles by utilizing the vehicle simulation model. For stabilizing the training process, we normalize the data by rescaling data to [0, 1].

## 4. Results Analysis

We divide the dataset into numerous batches with a size of 30. We make the dataset by combining traffic states information and vehicle states information together. The model can realize an end to end training by minimizing the loss function, and we use RMSProp to optimize the model.

We employ the deterministic "soft" attention [23] in our model, which computes the weighted expectation of road network's traffic states. Ideally, the attention mechanism should be able to find out high relevant roads to the prediction task, by setting high value to the corresponding road of the weight vector. The visualization of attention mechanism is shown in Figure 5.


Figure 6: Visualization of the attention for each traffic state input. (The color of road segment represents the level of attention, red represents high attention, yellow represents medium attention, and green represents low attention. The black dash line represents the driving route of shared electric vehicle, and the blue triangle represents the current position of shared electric vehicle.)

As we can see in Figure 6, during the whole trip, the attention mechanism promotes the prediction model, paying more attention to the traffic state of currently located and roads, where the vehicle on it can reach the road in a short time. Furthermore, at the initial stage of the trip (before 5 min in Figure 6), the model pays more attention to roads near to the location of the vehicle. As the vehicle travels on the preset route (10~15 min in Figure 6), attention is attached to the mainline far away from the vehicle location. The pattern learned by attention mechanism agrees with the principle of traffic evolution process. As the traffic flow of the road network changes dynamically, the near future traffic state of a road is mainly affected by the current traffic state of the road itself and roads, where the vehicle on it can reach the road in a short time, where the far future traffic state of a road is further affected by the traffic state of a wider range of road network. Besides, the attention mechanism also helps

Table 1: Comparison of different models of travel energy consumption prediction.

| | MAE | MSE | MAPE |
|---|---|---|---|
| RNN (att) + DNN | **0.074682** | **0.163005** | **0.105525** |
| RNN + DNN | 0.078688 | 0.171749 | 0.111659 |
| RNN + DNN (without vehicle data) | 0.082078 | 0.179148 | 0.118443 |
| DNN | 0.131376 | 0.286749 | 0.173804 |

The bold values represent the algorithm with the least error; that is, the prediction effect of the algorithm is the best.

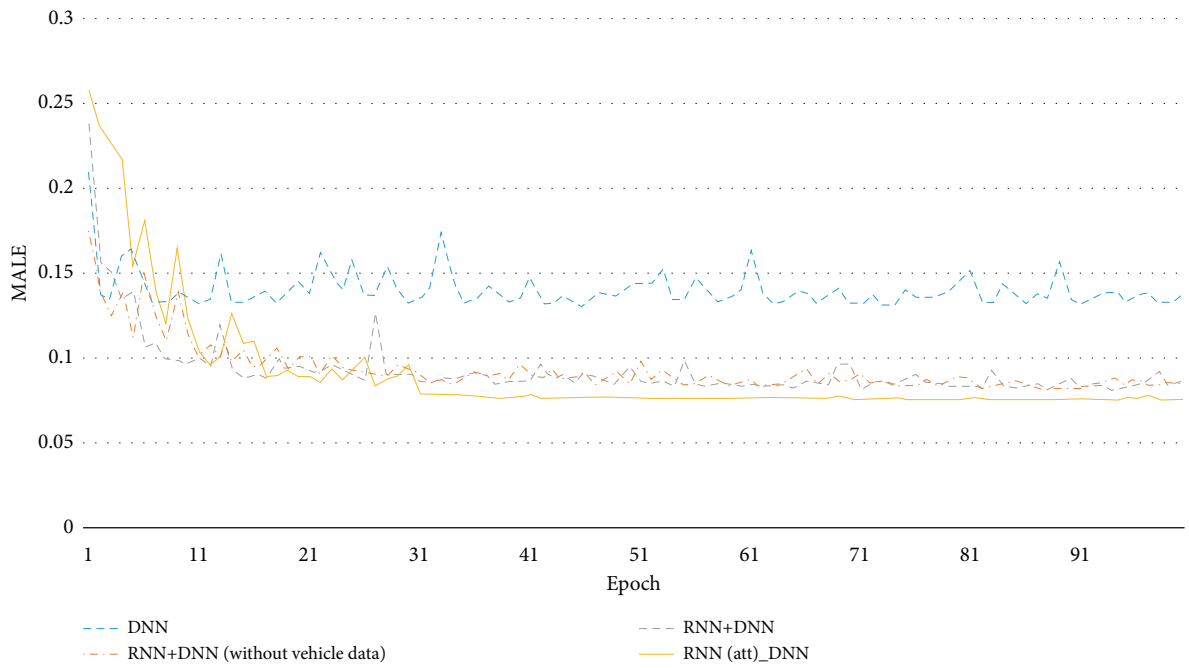


Figure 7: Training process of different methods.

the RNN based prediction model with recursively feeding traffic states input into the model.

In order to explore whether the attention mechanism helps improve the model's performance on prediction, we make a comparison experiment by removing attention mechanism from our model but using the same dataset for training and testing. Furthermore, we explore the importance of traffic information and vehicle information to our model by making a simply modification to our model and training the model by using traffic information and vehicle states separately. For verification, the results are shown in Table 1 and Figure 7.

The experiment result shows that the model with attention mechanism has a better performance than the model without attention. Combined with the visualization of the attention, we can know that the attention mechanism exactly helps the model extract the feature of traffic state. We verify the importance of vehicle state information by removing vehicle states extractor from the model, and we train the model using traffic state and distance data. For the verification of the importance of traffic states information, we use vehicle states and distance to finish the prediction task. For the selection of model, we choose a DNN with three hidden layers. From the results, we know that traffic states information is the key information of the travel energy consumption prediction, and the model has a poor performance without traffic states information. The performance of the model trained without vehicle states information also has a decline. In this paper, the impact of removing traffic information is greater than removing vehicle state information from the model.

## 5. Conclusion

In this paper, a method of traffic state feature extraction was proposed based on attention mechanism, which can extract effective key features from high-dimensional traffic network state data and reduce the interference of irrelevant features on travel energy consumption prediction model. Furthermore, a deep learning prediction method for energy consumption of electric vehicles based on traffic information is demonstrated. The method integrates vehicle status information and traffic network status features. The experimental result shows that the travel energy consumption prediction proposed in this paper has a high prediction accuracy. The idea of this paper can help the future work in travel energy prediction and traffic state prediction. Besides pure electric vehicle, how other vehicle models affect the proposed method needs to be further investigated in future studies.

However, there are still some limitations of this paper. The proposed prediction model is trained with data produced form simulation because the match data of traffic networks and electric vehicles is hard to be obtained in the real world. For future research, the model will be further researched and tested with real data. Besides, the effects of air condition usage and driver styles will be taken into consideration for a more accurate energy consumption prediction.

## Data Availability

The EV data collected from ROEWE used to support the findings of this study were supplied by SAIC under license, and so these cannot be made freely available. Requests for data, (6/12 months) after publication of this article, will be considered by the corresponding author.

## Conflicts of Interest

The authors declare that they have no conflicts of interest.

## Acknowledgments

This work was financed by the National Science Foundation of China (no. 61620106002) and the National Key R&D Program of China (no. 2019YFB1600100).

## References

[1] A. Luè, A. Colorni, R. Nocerino, and V. Paruscio, "Green move: an innovative electric vehicle-sharing system," *Procedia—*, vol. 48, pp. 2978–2987, 2012.

[2] S. Carrese, T. Giacchetti, M. Nigro, and S. M. Patella, "An innovative car sharing electric vehicle system: an Italian experience," *Urban Transport XXIII*, vol. XXIII, no. 176, p. 245, 2017.

[3] R. Mounce and J. D. Nelson, "On the potential for one-way electric vehicle car-sharing in future mobility systems," *Transportation Research Part A: Policy and Practice*, vol. 120, pp. 17–30, 2019.

[4] J. Neubauer and E. Wood, "The impact of range anxiety and home, workplace, and public charging infrastructure on simulated battery electric vehicle lifetime utility," *Journal of Power Sources*, vol. 257, pp. 12–20, 2014.

[5] K. Liu, X. Hu, H. Zhou, L. Tong, and J. Marco, "Feature analyses and modelling of lithium-ion batteries manufacturing based on random forest classification," *IEEE*, no. 99, 2021.

[6] K. Liu, Z. Wei, Z. Yang, and K. Li, "Mass load prediction for lithium-ion battery electrode clean production: a machine learning approach," *Journal of Cleaner Production*, vol. 289, no. 1, 2020.

[7] C. King, W. Griggs, F. Wirth, K. Quinn, and R. Shorten, "Alleviating a form of electric vehicle range anxiety through on-demand vehicle access," *International Journal of Control*, vol. 88, no. 4, pp. 717–728, 2015.

[8] K. Liu, C. Zou, K. Li, and T. Wik, "Charging pattern optimization for lithium-ion batteries with an electrothermal-aging model," *IEEE transactions on industrial informatics*, vol. 14, 2018.

[9] K. Liu, X. Hu, Z. Yang, Y. Xie, and S. Feng, "Lithium-ion battery charging management considering economic costs of electrical energy loss and battery degradation," *Energy Conversion and Management*, vol. 195, pp. 167–179, 2019.

[10] K. Liu, K. Li, and C. Zhang, "Constrained generalized predictive control of battery charging process based on a coupled thermoelectric model," *Journal of Power Sources*, vol. 347, pp. 145–158, 2017.

[11] A. Cartenì, E. Cascetta, and S. De Luca, "A random utility model for park & carsharing services and the pure preference for electric vehicles," *Transport Policy*, vol. 48, pp. 49–59, 2016.

[12] A. Ralf, "Apparatus of calculating a navigation route based on estimated energy consumption," US Patent 20090254266, 2009.

[13] C. De Cauwer, J. Van Mierlo, and T. Coosemans, "Energy consumption prediction for electric vehicles based on real-world data," *Energies*, vol. 8, no. 8, pp. 8573–8593, 2015.

[14] C. De Cauwer, W. Verbeke, T. Coosemans, S. Faid, and J. Van Mierlo, "A data-driven method for energy consumption prediction and energy-efficient routing of electric vehicles in real-world conditions," *Energies*, vol. 10, no. 5, p. 608, 2017.

[15] Z. Yi and H. Bauer Peter, "Adaptive multi-resolution energy consumption prediction for electric vehicles," *IEEE Transactions on Vehicular Technology*, vol. 66, no. 99, p. 1, 2017.

[16] B. Yoshua, "Learning deep architectures for AI," *Foundations and trends® in Machine Learning*, vol. 2, no. 1, pp. 1–127, 2009.

[17] G. Ross, "Fast R-CNN," in *Proceedings of the IEEE International Conference on Computer Vision*, Santiago, Chile, December 2015.

[18] S. Ren, K. He, R. Girshick, and J. Sun, "Faster R-CNN: towards real-time object detection with region proposal networks," *IEEE Transactions on Pattern Analysis and Machine Intelligence*, vol. 39, no. 6, pp. 1137–1149, 2017.

[19] R. Collobert and J. Westonet, "A unified architecture for natural language processing: deep neural networks with multitask learning," in *Proceedings of the 25th International Conference on Machine Learning*, pp. 160–167, Helsinki, Finland, July 2008.

[20] H. Geoffrey, L. Deng, D. Yu et al., "Deep neural networks for acoustic modeling in speech recognition: the shared views of four research groups," *IEEE Signal Processing Magazine*, vol. 29, no. 6, pp. 82–97, 2012.

[21] S. Modi, J. Bhattacharya, and P. Basak, "Estimation of energy consumption of electric vehicles using deep convolutional neural network to reduce driver's range anxiety," *ISA Transactions*, vol. 98, pp. 454–470, 2020.

[22] M. Laroui, A. Dridi, H. Afifi, H. Moungla, M. Marot, and M. A. Cherif, "Energy management for electric vehicles in smart cities: a deep learning approach," in *2019 15th International Wireless Communications & Mobile Computing Conference (IWCMC)*, pp. 2080–2085, IEEE, Tangier, Morocco, June 2019.

[23] K. Xu, J. Ba, R. Kiros et al., "Show, attend and tell: Neural image caption generation with visual attention," in *Proceedings of the International Conference on Machine Learning*, pp. 2048–2057, Lille, France, July 2015.

[24] C. Ronan, W. Jason, K. Michael, K. Kavukcuoglu, and P. Kuksa, "Natural language processing (almost) from scratch," *Journal of Machine Learning Research*, vol. 12, no. 1, pp. 2493–2537, 2011.

[25] D. Bahdanau, K. Cho, and Y. Bengio, "Neural machine translation by jointly learning to align and translate," 2014, https://arxiv.org/abs/1409.0473.

[26] Y. Lecun, L. Bottou, Y. Bengio, and P. Haffner, "Gradient-based learning applied to document recognition," *Proceedings of the IEEE*, vol. 86, no. 11, pp. 2278–2324, 1998.
[27] K. Yoon, D. Carl, L. Hoang, and A. M. Rush, *Structured attention networks*, Springer, Berlin, Germany, 2017.
[28] D. C. Plaut and T. Shallice, "Deep dyslexia: a case study of connectionist neuropsychology," *Cognitive Neuropsychology*, vol. 10, no. 5, pp. 377–500, 1993.
[29] K. He, X. Zhang, S. Ren, and J. Sun, "Delving deep into rectifiers: surpassing human-level performance on ImageNet classification," pp. 1026–1034, 2015, https://arxiv.org/abs/1502.01852.
[30] J. Max, S. Karen, V. Andrea, and A. Zisserman, "Deep structured output learning for unconstrained text recognition," *Eprint Arxiv*, vol. 24, no. 6, pp. 603–611, 2014.

Hindawi
Advances in Civil Engineering
Volume 2021, Article ID 6640527, 14 pages
https://doi.org/10.1155/2021/6640527

*Research Article*

# Analysis of Differences in ECG Characteristics for Different Types of Drivers under Anxiety

**Yongqing Guo**,[1,2] **Xiaoyuan Wang**,[2,3] **Qing Xu**,[4] **Quan Yuan**,[4] **Chenglin Bai**,[5] **and Xuegang (Jeff) Ban**[6]

[1]*School of Transportation and Vehicle Engineering, Shandong University of Technology, Zibo 255049, China*
[2]*Joint Laboratory for Internet of Vehicles, Ministry of Education-China Mobile Communications Corporation, Tsinghua University, Beijing 100048, China*
[3]*College of Electromechanical Engineering, Qingdao University of Science & Technology, Qingdao 266000, China*
[4]*State Key Laboratory of Automotive Safety and Energy, School of Vehicle and Mobility, Tsinghua University, Beijing 100084, China*
[5]*School of Physics Science and Communication Engineering, Liaocheng University, Liaocheng 252000, China*
[6]*Department of Civil and Environmental Engineering, University of Washington, Seattle, WA, USA*

Correspondence should be addressed to Xiaoyuan Wang; wangxiaoyuan@qust.edu.cn

Received 23 December 2020; Accepted 7 August 2021; Published 24 August 2021

Academic Editor: Hui Yao



Anxiety is a complex emotion characterized by an unpleasant feeling of tension when people anticipate a threat or negative consequence. It is regarded as a comprehensive reflection of human thought processes, physiological arousal, and external stimuli. The actual state of emotion can be represented objectively by human physiological signals. This study aims to analyze the differences of ECG (electrocardiogram) characteristics for various types of drivers under anxiety. We used several methods to induce drivers' mood states (calm and anxiety) and then conducted the real and virtual driving experiments to collect driver's ECG signal data. Physiological changes in ECG during the experiments were recorded using the PSYLAB software. The independent sample *t*-test analysis was conducted to determine if there are significant differences in ECG characteristics for different types of drivers in anxious state during driving. The results show that there are significant differences in ECG signal characteristics of drivers by gender, age, and driving experience, in time domain, frequency domain, and waveform under anxiety. Our findings of this study contribute to the development of more intelligent and personalized driver warning system, which could improve road traffic safety.

## 1. Introduction

According to the statistics, more than 90% of traffic accidents are caused at least in part by human mistakes [1, 2], of which many errors result from drivers' negative emotional motivations such as anxiety, anger, and contempt. Driver's emotion as a psychological response has a substantial effect on the cognitive processes, including driver's perception, judgment, action, and behavior. Therefore, it is of great significance to identify driver's psychological and physiological characteristics in emotional states, in order to create safe and efficient driving.

Human emotions have a huge impact on how we live. The choices we make and the actions we take are influenced by the different types of emotions that we experience. There have been numerous studies to investigate the complex interactions between human emotion and physiological response in social, cultural, and economic fields, including household income [3], cultural diversity [4], physical health [5, 6], purchasing consumption [7, 8], Internet application [9], and environmental impact [10–12]. For example, Jaeger et al. [10] found that anxious emotion makes people want to eat more spicy snacks and single snack intake compared to their calm state. The study by Zhang et al. [7] and Wang

et al. [8] suggested that high brightness evokes people's positive emotions and low brightness evokes people's negative emotions.

In the transportation field, researchers and scholars have conducted the studies of the correlation between emotional state and driving behavior and explored the influence of human-vehicle-environment factors toward driver' mood [13–15]. For example, while driving, driver's anxious emotion is more likely to be induced by environmental factors such as noisy and high arousal sound [14], low road visibility [16], and driver' factors such as less driving experience [17].

Emotional states are combinations of psychological arousal and physiological response. Human emotions result in physical and physiological changes that influence behavior through autonomic nervous responses, such as electrocardiogram [18, 19], respiration frequency [20, 21], pulse [22], skin electricity [23, 24], electromyogram [25], and skin temperature [26]. Existing research focuses on the impact of human emotion on the ECG signal properties. For example, a study by Ba et al. showed that emotion is correlated with skin resistance, heart rate, and breathing rate [27]. Takahashi et al. [28] found that the heartbeat interval becomes shorter and the ratio of low frequency band to high frequency band becomes higher in anger than in calm. Herrero-Fernández [29] found that the QT interval variability of ECG waveform is positively associated with the level of anger, and the RR interval variability of ECG waveform is negatively associated with the level of anger.

The detection and warning systems for traffic safety based on drivers' ECG signals have received increasing attention. Isikli Esener [30] recognized drivers' distress level using subspace-based feature extraction on ECG signals and other physiological measurements. Balasubramanian and Bhardwaj [31] used a noncontact ECG measurement approach to determine the fatigue levels of drivers. Zhao et al. [32] measured drivers' mental fatigue according to their ECG signals. Gromer et al. [33] applied a low-cost ECG sensor to detect drivers' drowsiness, by extracting the main ECG parameters including heart rate, QRS-complex, and heart rate variability. Taherisadr et al. [34] proposed an ECG-based driver distraction detection system using convolutional neural networks.

In conclusion, there have been few attempts in the past to analyze the influence of driver's emotions on their behavioral based on physiological signals. Hence, it is essential for transportation researchers to identify driver's ECG characteristics in emotional states to gain a deep understanding of how driver's emotions affect their behavior and reactions. This study focuses on examining the differences of ECG characteristics for various types of drivers in anxious state during driving.

## 2. Research Method

*2.1. Participants.* This study included 27 male drivers and 21 female drivers (age range: 22–50 y; mean age: 33.4 y). Participants were classified into three groups according to their driving propensities, which were determined by the propensity questionnaire [1]. The three groups were extraversion, middle type, and introversion, respectively. In this study, if drivers drove less than 10,000 kilometers, they would be considered as novice drivers, experienced drivers otherwise. Participants drove approximately 14,000 km miles on average. Prior to the experiment, they were told not to take any drugs that affect the brain and nervous system within one week and not to have tea, coffee, and wine that affect the mood and mental state within 48 hours. Moreover, they were asked to avoid any vigorous and high-intensity workout. Researchers provided a detailed description of the experimental design to the participants. Summary information of participants is presented in Table 1.

## 3. Experimental Material and Equipment

*3.1. Emotional Induction Materials.* The materials used for emotional induction in this study were primarily obtained from the International Affective Picture System (IAPS) and the Chinese Affective Picture System (CAPS). The two databases were designed for the experimental study of emotions, by providing a set of standardized emotional stimuli according to three dimensions: pleasure, arousal, and dominance. Different types of emotion-inducing materials were applied, including audio, visual olfactory, and taste materials. Moreover, participants were also asked to carry out difficult assignment with stress, in order to induce their anxious emotion. Parts of the anxiety induction material are shown in Figure 1.

*3.2. Real Driving Experiment.* The experimental route consists of a single loop, including two long sides with a length of 1.613 km (between Beijing Road and Nanjing Road) and two short sides with a length of 0.623 km (between Qingnian Road and Xincun West Road, as shown in Figure 2). The experimental equipment mainly includes two experimental vehicles, laser radar, laser ranging sensor, high-precision global positioning system, noncontact multifunction speedometer, vehicle recorder, PSYLAB human factor engineering equipment, pedal force manometer, high-definition camera, laptop, and unmanned aerial vehicle (Figure 3). The unmanned aerial vehicle was used for recording the experimental process. Screenshots of real experimental scenes (in Xincun West Road) are illustrated in Figure 4.

*3.3. Virtual Driving Experiment.* In the virtual driving experiments, a high-fidelity simulator from Japanese manufacturer FORUM 8 was used, which allowed users to construct 3D traffic environment. The Road Builder and UC-win/Road software were used in the driving simulator to build an experimentation platform of the road system with human, vehicle, and road components (Figure 5). The driving simulator was able to collect data on interactions between drivers and vehicles under various traffic conditions. It enables researchers to collect details of useful parameters for drivers' action and vehicle performance, including distance traveled, offset from lane center, speed, acceleration, deceleration, braking, lane-changing, and

Table 1: Statistics of drivers' information.

| | | |
|---|---|---|
| Number of drivers | 28 | 20 |
| Gender | Male; female | Male; female |
| Age | Youth (22–27 y) | Middle age(45–50 y) |
| Driving experience | Novice (driving mileage ≤ 10,000 km)<br>Experienced (driving mileage > 10,000 km) | Novice (driving mileage ≤ 10,000 km)<br>Experienced (driving mileage > 10,000 km) |
| Driving tendency | $T_1$ (extraversion); $T_2$ (middle type); $T_3$ (introversion) | $T_1$ (extraversion); $T_2$ (middle type); $T_3$ (introversion) |

(a) (b)

Figure 1: Parts of the anxiety induction material. (a) Anxiety induction visual materials. (b) Pictures of different people in anxiety.


Figure 2: Real driving experimental route.

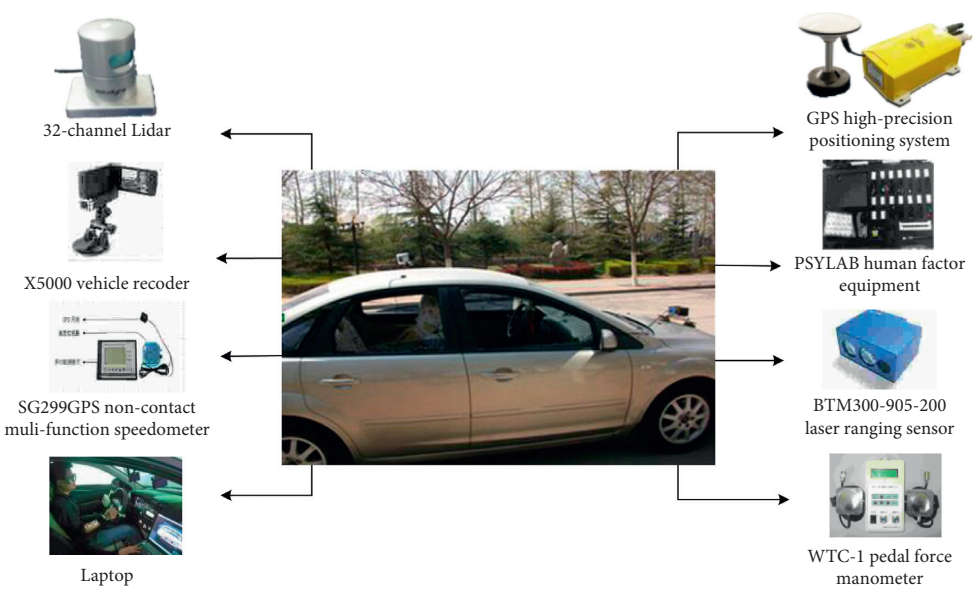


Figure 3: Real driving experimental equipment.


(a) (b)

Figure 4: Screenshots of experimental scenes (in Xincun West Road).

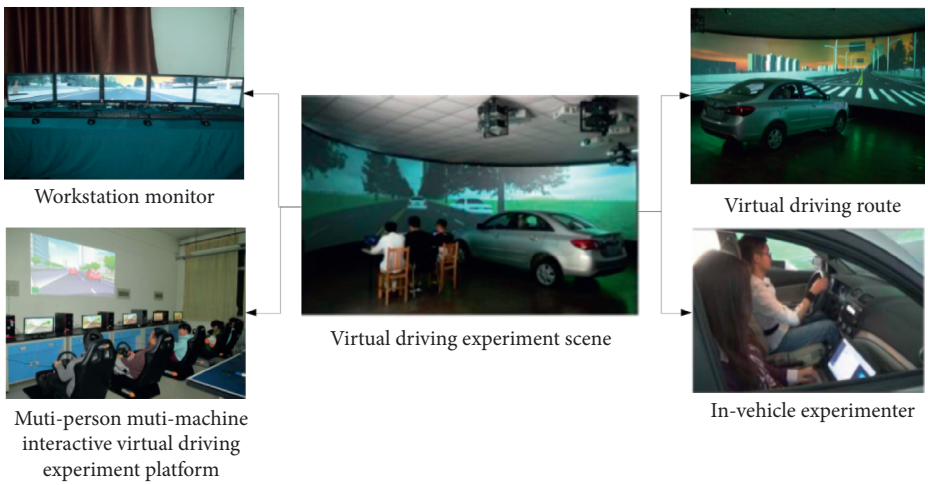


Figure 5: Virtual driving experimental equipment.

steering angle. The driving simulator can reproduce the road situations similar to reality. Under the virtual environment, the subject can drive just like on the ordinary road, with the same responses as real-life driving. The wearable wireless ECG sensors are shown in Figure 6. The simulation-based experiment route and street view are shown in Figure 7.

*3.4. Experimental Process.* The real driving experiments in anxiety were carried out during morning peak hours of 7 : 00–9: 00 and evening peak hours of 17 : 00–19 : 00 from Monday to Friday. The experimental process is shown in Figure 8.

*3.5. Assessing the Level of the Induced Anxiety.* Participant's level of anxiety was detected, based on Beck Anxiety Inventory (BAI), self-perception, facial expression, and behavioral action. The BAI reflects the intensity of physical and cognitive anxiety (Table 2). In this study, the emotion-induction experiments end when subjects obtained a score of 26 points or more. During the driving experiment, experimenters irregularly communicate to the subjects to get their emotional states. After the driving experiment, subjects were asked to watch the recorded video to report their emotional experience during driving. For more details about the process of evaluating driver's anxiety level, please refer to our another article by Guo et al. [35].

## 4. ECG Signal Data Collection and Preprocessing

*4.1. ECG Signal Data Preprocessing.* The raw ECG signals contain motion artifact, power frequency interference, and sensor internal interference noise. The PSYLAB software was used for reducing the noise in the ECG signal, as shown in Figure 9. The definitions of the parameters for denoising preprocess are given in Table 3. The comparison of ECG signal before and after denoising is shown in Figure 10. It was seen that after noise reduction, the noise can be controlled to an acceptable level. For more details about the ECG signal preprocessing, please refer to another article by Wang et al. [36].

*4.2. ECG Signal Data Collection.* Each subject was involved in driving experiments multiple times. A total of 3849 groups of effective data were obtained, including 983 clusters from the real driving experiments and 2866 clusters from the driving simulators. The variables and symbols in the experiment are given in Table 4. Parts of the experimental data are given in Figure 11 and Table 5.

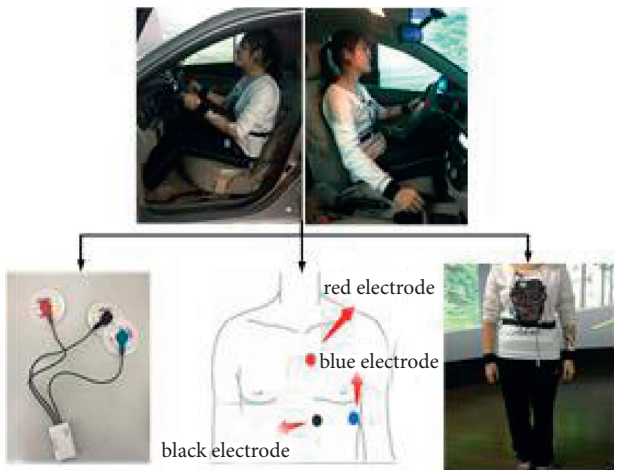


Figure 6: The wearable wireless ECG sensors.

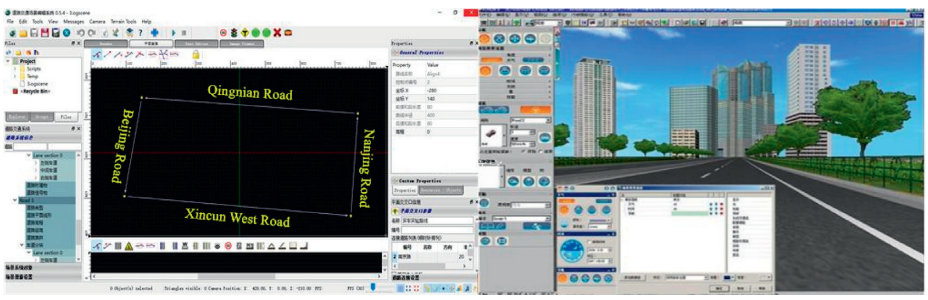


(a) (b)

Figure 7: The simulation-based experiment route and street view.

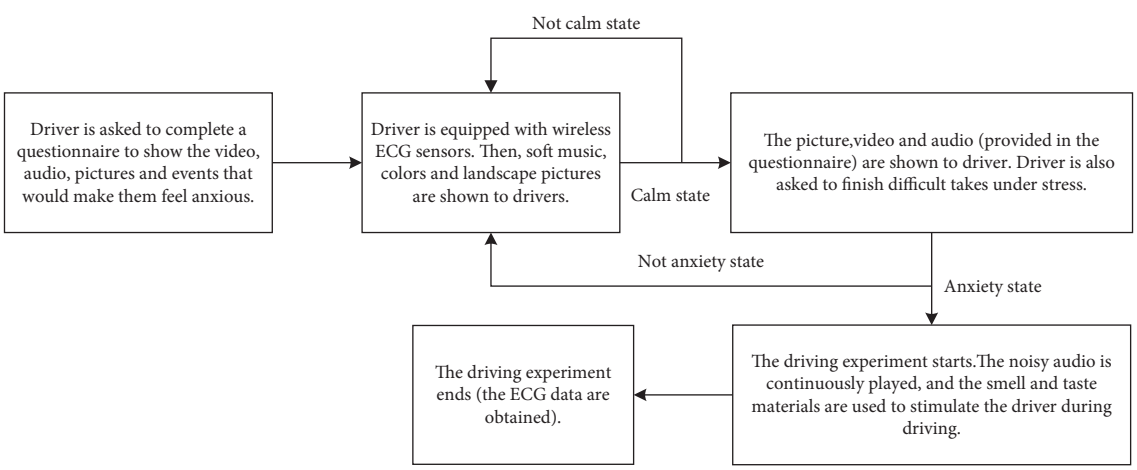


Figure 8: The experimental process of real driving in anxiety.

## 5. Results and Discussion

*5.1. Driver's ECG Characteristics by Gender.* Statistical analysis was performed using SPSS Statistics 23.0 where the confidence interval was set at 95%. The independent $t$-test was used to determine whether there are differences in ECG indicators between female and male drivers, and the results are given in Table 6.

The results show that there are significant differences between male and female drivers in the five ECG indicators: AVHR, AVNN, RWAVE, TWAVE, and S ($p < 0.05$). No significant difference was found between male and female drivers in the other indicators. The results in Figure 12 and Table 6 show that female drivers have higher average heart rate and S-point peaks and lower average heartbeat, $R$ wave peaks, and T-point peaks than male drivers. The results

Table 2: Beck anxiety inventory (BAI).

| |
|---|
| (1) Body numbness or thorns |
| (2) Feel feverish |
| (3) Leg tremble |
| (4) Cannot relax |
| (5) Fear of bad things |
| (6) Feel dizzy |
| (7) Palpitation |
| (8) Restless |
| (9) Frightened |
| (10) Tension |
| (11) Suffocation |
| (12) Hand trembling |
| (13) Body shake |
| (14) Afraid of out of control |
| (15) Difficult breathing |
| (16) Fear to die |
| (17) Feel panic |
| (18) Abdominal discomfort |
| (19) Faint |
| (20) Flush |
| (21) Sweat |

*Note.* The 21 symptoms have four levels of induction. The score of each symptom can be expressed as "1 point-none;" "2 points-mild, no major annoyance;" "3 points-moderate, feel uncomfortable but still tolerable;" "4 points-heavy, can only barely endure." The total score of 21 symptoms is 15–25 points for mild anxiety, 26–35 points for moderate anxiety, and more than 36 points for severe anxiety.

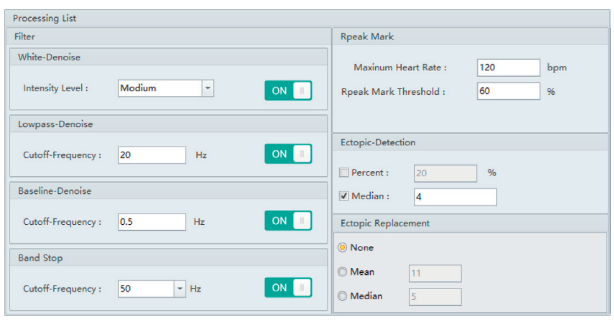


Figure 9: Denoising preprocess interface for original ECG signal.

Table 3: The definitions of parameters for denoising preprocess.

| White-denoise | Baseline-denoise | Lowpass-denoise | Band stop |
|---|---|---|---|
| Remove white noise from ECG signals | High frequency signal is retained and low frequency signal is cut off | Low frequency signal is retained and high frequency signal is cut off | Remove power frequency interference |

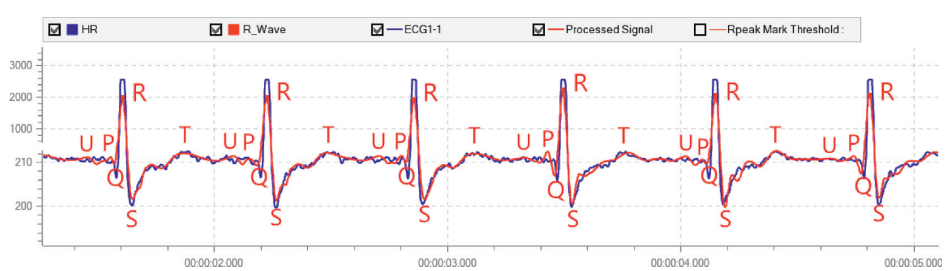


Figure 10: Comparison of ECG signal before and after denoising.

indicate that compared to male drivers, female drivers tend to have a faster heart rate, a shorter heartbeat interval, and a more obvious manifestation of myocardial ischemia in anxiety while driving.

Under moderate and high levels of anxiety, female drivers are more likely to experience dizziness, slow response, and fidgeting due to rapid heartbeat and poor blood flow to the heart. Moreover, females are more likely to have

Table 4: Variables and symbols in the experiment.

| Variable | Symbol |
|---|---|
| Gender | G |
| Age (year) | A |
| Driving experience (ten thousand kilometers) | D |
| Driving tendency | T |
| Emotion | Em |
| R wave average peak ($uV$) | RWAVE |
| T wave average peak ($uV$) | TWAVE |
| Q wave average peak absolute value ($uV$) | Q |
| S wave average peak absolute value ($uV$) | S |
| Average heart rate (bpm) | AVHR |
| Atrioventricular interval (ms) | AVNN |
| Standard deviation of NN intervals for period of interest (ms) | SDNN |
| Percent of NN intervals>50 ms (%) | $PNN_{50}$ |
| Root mean square of successive (ms) | RMSSD |
| Ratio of ultralow frequency band to very low frequency band | UVLF/VLF |
| Ratio of low frequency band to high frequency band | LF/HF |
| Total power ($ms^2$) | TP |

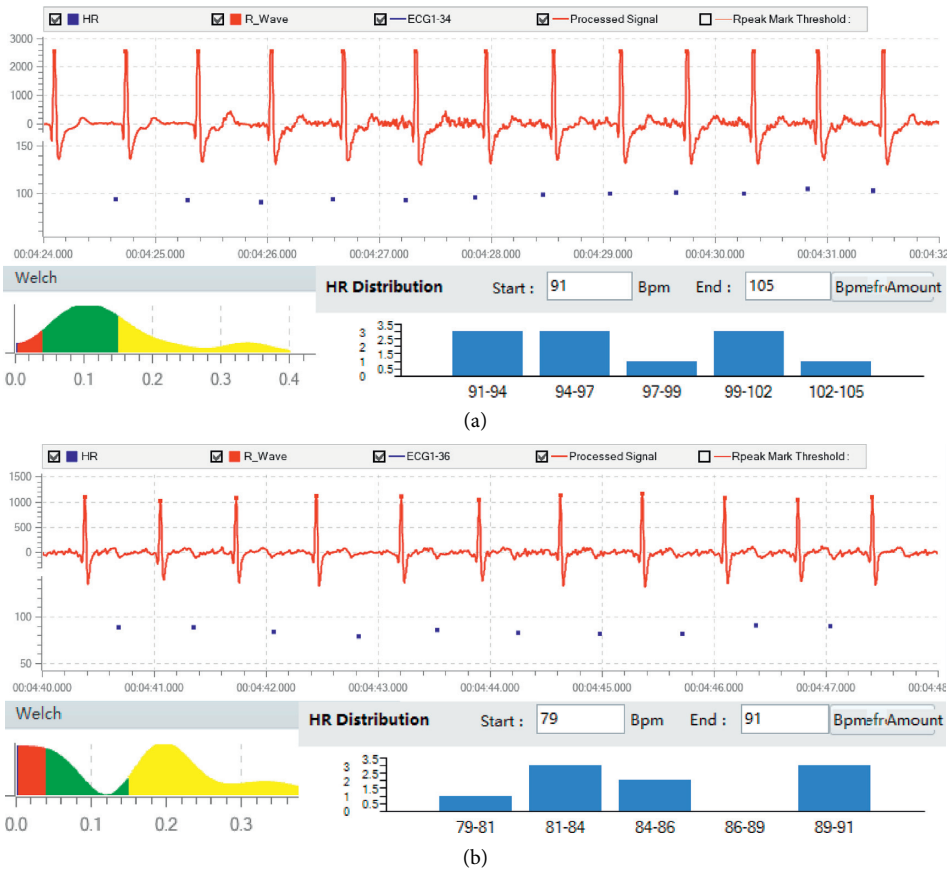


Figure 11: Distribution of driver's ECG data distribution in anxiety. (a) Driver's heart rate and frequency distribution (male * 27 y * novice * middle type). (b) Driver's heart rate and frequency distribution (female * 27 y * experienced * introversion).

chest distress, shortness of breath, as well as discomfort in the arms, neck, and shoulders as with myocardial ischemia. These symptoms might contribute to distraction, difficulty keeping the eyes from focusing, and slow reaction during driving. The results in Figure 12 suggest that these gender differences in the symptoms may be more pronounced in middle-aged drivers than in young ones, especially for novice and introverted drivers.

Table 5: Statistics of driver's ECG characteristic data.

| No. | G | D | Em | AVHR | AVNN | SDNN | PNN50 | RMSSD | RWAVE |
|---|---|---|---|---|---|---|---|---|---|
| | Male | 0.4 | | 95 | 632.60 | 129.36 | 15.56 | 158.32 | 2559.27 |
| 1 | A | T | Anxiety | TWAVE | Q | S | UVLF/VLF | LF/HF | TP |
| | 22 | Extraversion | | 392.78 | −431.67 | −1554.49 | 0.07 | 1.07 | 2641.22 |
| No. | G | D | Em | AVHR | AVNN | SDNN | PNN50 | RMSSD | RWAVE |
| | Male | 0.50 | | 88 | 680.96 | 57.79 | 11.90 | 32.10 | 2559.17 |
| 2 | A | T | Anxiety | TWAVE | Q | S | UVLF/VLF | LF/HF | TP |
| | 27 | Middle type | | 363.74 | −469.37 | −1513.37 | 0.13 | 9.56 | 1123.26 |
| No. | G | D | Em | AVHR | AVNN | SDNN | PNN50 | RMSSD | RWAVE |
| | Female | 0.30 | | 102 | 586.65 | 45.39 | 5.70 | 12.91 | 2234.62 |
| 3 | A | T | Anxiety | TWAVE | Q | S | UVLF/VLF | LF/HF | TP |
| | 24 | Extraversion | | 360.99 | −399.78 | −1260.28 | 0 | 12.89 | 749.11 |
| | ... | | | ... | | ... | | ... | |
| No. | G | D | Em | AVHR | AVNN | SDNN | PNN50 | RMSSD | RWAVE |
| | Female | 1.30 | | 84 | 713.37 | 31.37 | 2.50 | 27.41 | 1171.33 |
| $n-1$ | A | T | Anxiety | TWAVE | Q | S | UVLF/VLF | LF/HF | TP |
| | 50 | Introversion | | 110.52 | −209.44 | −685.18 | 0.01 | 7.18 | 565.47 |
| No. | G | D | Em | AVHR | AVNN | SDNN | PNN50 | RMSSD | RWAVE |
| | Male | 3.80 | | 81 | 743.24 | 161.12 | 47.37 | 232.41 | 1920.80 |
| n | A | T | Anxiety | TWAVE | Q | S | UVLF/VLF | LF/HF | TP |
| | 50 | Introversion | | 255.69 | −235.46 | −880.28 | 0.06 | 1.73 | 5497.79 |

Table 6: Independent $t$-test results of ECG characteristics for male and female drivers in anxiety.

| | | $t$ | df | Significance (2-tailed) | Mean difference | Standard error difference | 95% confidence interval of the difference | |
|---|---|---|---|---|---|---|---|---|
| | | | | | | | Lower | Upper |
| AVHR | M-F | −4.196 | 8 | **0.003*** | −2.778 | 0.662 | −4.304 | −1.251 |
| AVNN | M-F | 5.218 | 8 | **0.001*** | 22.135 | 4.242 | 12.353 | 31.918 |
| SDNN | M-F | 0.9 | 8 | 0.394 | 17.703 | 19.671 | −27.658 | 63.064 |
| $PNN_{50}$ | M-F | 2.291 | 8 | 0.051 | 10.841 | 4.732 | −0.718 | 21.754 |
| RMSSD | M-F | 1.713 | 8 | 0.125 | 53.675 | 31.333 | −18.579 | 125.93 |
| RWAVE | M-F | 4.197 | 8 | **0.003*** | 341.24 | 81.302 | 153.761 | 528.726 |
| TWAVE | M-F | 9.601 | 8 | **0.000*** | 109.6 | 11.416 | 83.281 | 135.932 |
| Q | M-F | −1.698 | 8 | 0.128 | −28.3 | 16.672 | −66.753 | 10.137 |
| S | M-F | −15.118 | 8 | **0.000*** | −219.3 | 14.509 | −252.808 | −185.892 |
| UVLF/VLF | M-F | −0.364 | 8 | 0.725 | −0.009 | 0.024 | −0.065 | 0.047 |
| LF/HF | M-F | 0.034 | 8 | 0.973 | 0.104 | 3.035 | −6.894 | 7.104 |
| TP | M-F | 0.88 | 8 | 0.404 | 298.59 | 339.158 | −483.501 | 1080.699 |

*Note.* The significance level is 0.05. M-F, male-female.

*5.2. Driver's ECG Characteristics by Age.* The independent $t$-test results (in Table 7) show that there are significant differences between middle-aged and young drivers in the seven ECG indicators AVHR, AVNN, RWAVE, TWAVE, Q, S, and UVLF/VLF ($p < 0.05$). There is no significant difference between middle-aged and young drivers in the other indicators. The results in Figure 13 and Table 7 show that young drivers have higher average heart rate, $R$ wave peaks, and T-point peaks than middle-aged drivers. Furthermore, young drivers have lower average heartbeat interval, Q-point peaks, S-point peaks, and the ratio of ultralow frequency band to very low frequency band than middle-aged drivers. The results indicate that compared to middle-aged drivers, young drivers tend to have a faster heart rate, a shorter heartbeat interval, a higher pulse pressure, a greater sympathetic nerve activity, and a higher rate of left ventricular hypertrophy and hyperkalemia in anxiety.

In moderate and severe cases, young drivers are more likely to feel dizziness and chest distress due to rapid heartbeat and poor blood flow to the heart. Young drivers are also more likely to suffer from muscle stiffness as with hyperkalemia. These symptoms might contribute to slow response and maintain head-down position (vision at low location). As a result, young drivers might pay less attention on traffic environment of the sides and the straight ahead in the far while driving. These age differences in the symptoms are more obvious in female drivers than in male ones.

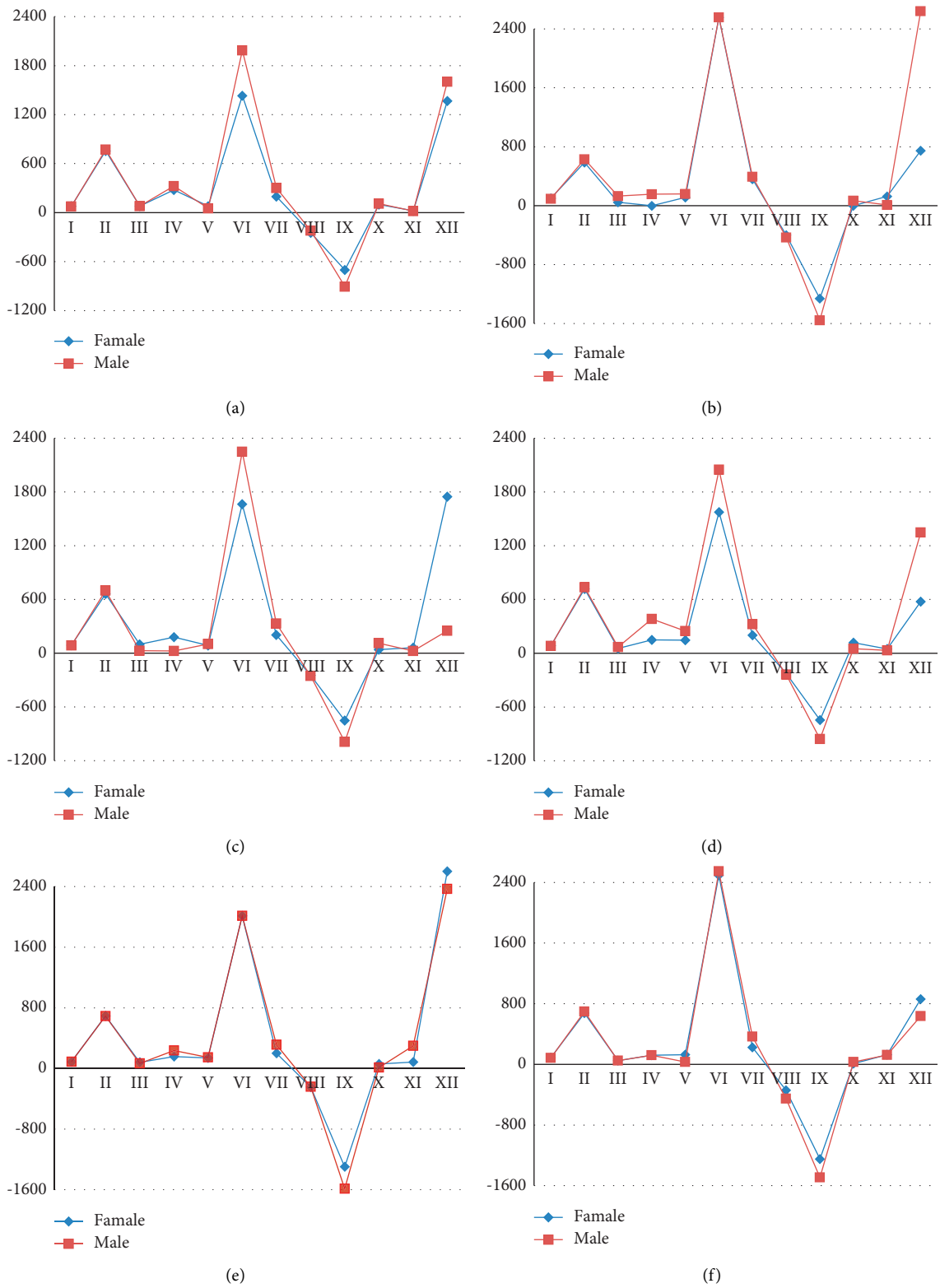


Figure 12: Male and female drivers' ECG characteristics in anxiety. (a) 45–50 years old * novice * extraversion. (b) 45–50 years old * novice * middle type. (c) 45–50 years old * novice * introversion (d) 22–27 years old * novice * extraversion. (e) 22–27 years old * novice * middle type. (f) 22–27 years old * novice * introversion (I, AVHR; II, AVNN; III, SDNN; IV, $PNN_{50}$; V, RMSSD; VI, RWAVE; VII, TWAVE; VIII, Q; IX, S; X, UVLF/VLF*1000; XI, LF/HF*100; XII, TP).

Table 7: Independent $t$-test results of ECG characteristics for young and middle-aged drivers in anxiety.

| | | $t$ | df | Significane (2-tailed) | Mean difference | Standard error difference | 95% confidence interval of the difference | |
|---|---|---|---|---|---|---|---|---|
| | | | | | | | Lower | Upper |
| AVHR | M-Y | −5.358 | 5 | **0.003*** | −8.5 | 1.586 | −12.578 | −4.422 |
| AVNN | M-Y | 5.604 | 5 | **0.002*** | 69.225 | 12.352 | 37.473 | 100.977 |
| SDNN | M-Y | −0.461 | 5 | 0.664 | −13.6 | 29.487 | −89.403 | 62.193 |
| $PNN_{50}$ | M-Y | 2.082 | 5 | 0.092 | 10.488 | 5.038 | −2.462 | 23.439 |
| RMSSD | M-Y | −0.553 | 5 | 0.604 | −10.84 | 19.621 | −61.286 | 39.589 |
| RWAVE | M-Y | −5.907 | 5 | **0.002*** | −715.7 | 121.187 | −1027.313 | −404.273 |
| TWAVE | M-Y | −3.812 | 5 | **0.012*** | −71.08 | 18.646 | −119.01 | −23.15 |
| Q | M-Y | 7.604 | 5 | **0.001*** | 171.05 | 22.495 | 113.231 | 228.882 |
| S | M-Y | 41.944 | 5 | **0.000*** | 545.87 | 13.015 | 512.423 | 579.333 |
| UVLF/VLF | M-Y | 6.29 | 5 | **0.001*** | 0.062 | 0.01 | 0.036 | 0.087 |
| LF/HF | M-Y | −1.651 | 5 | 0.16 | −3.937 | 2.384 | −10.064 | 2.191 |
| TP | M-Y | −0.645 | 5 | 0.547 | −367.1 | 568.955 | −1829.7 | 1095.386 |

*Note.* The significance level is 0.05. M-Y, middle aged-young.

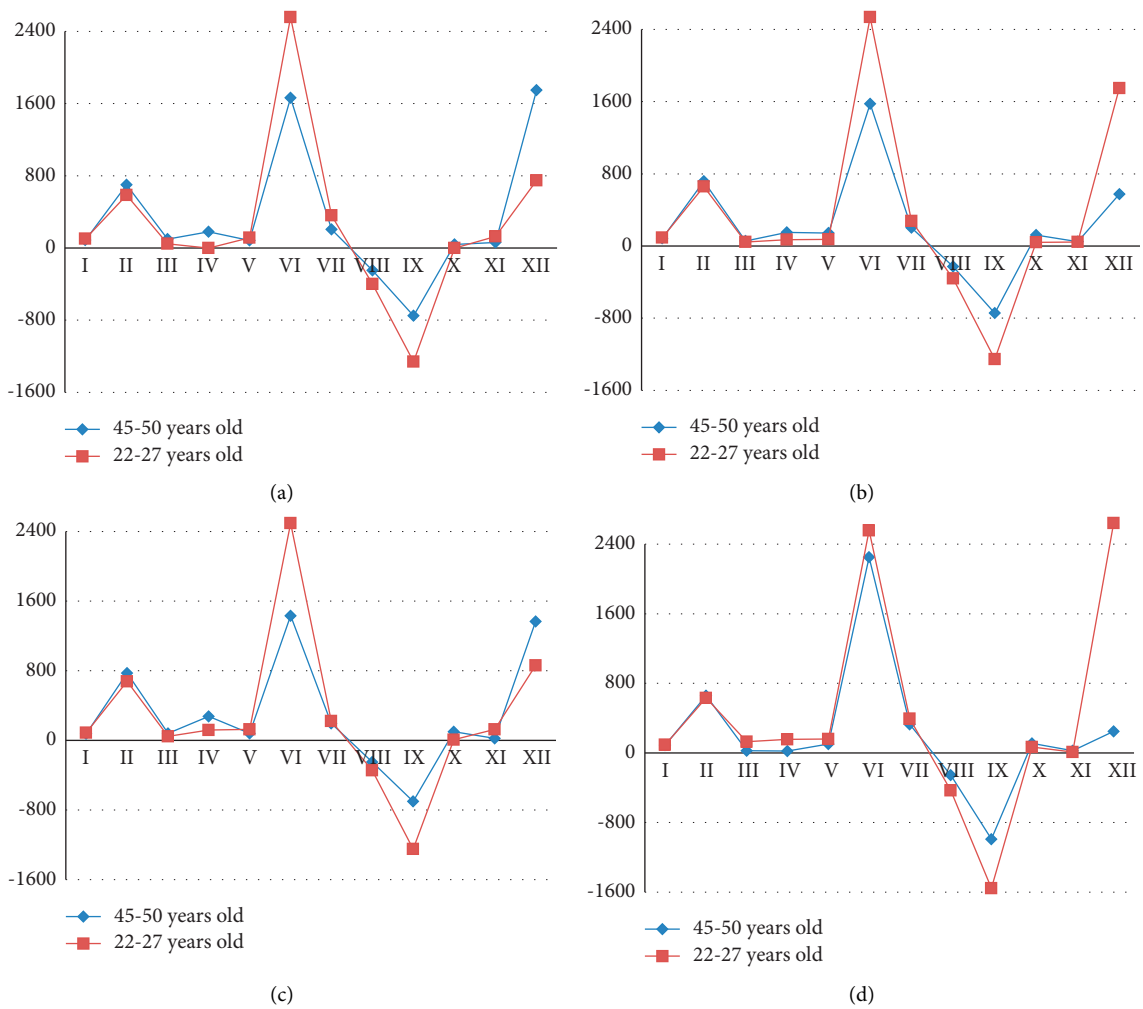


Figure 13: Continued.

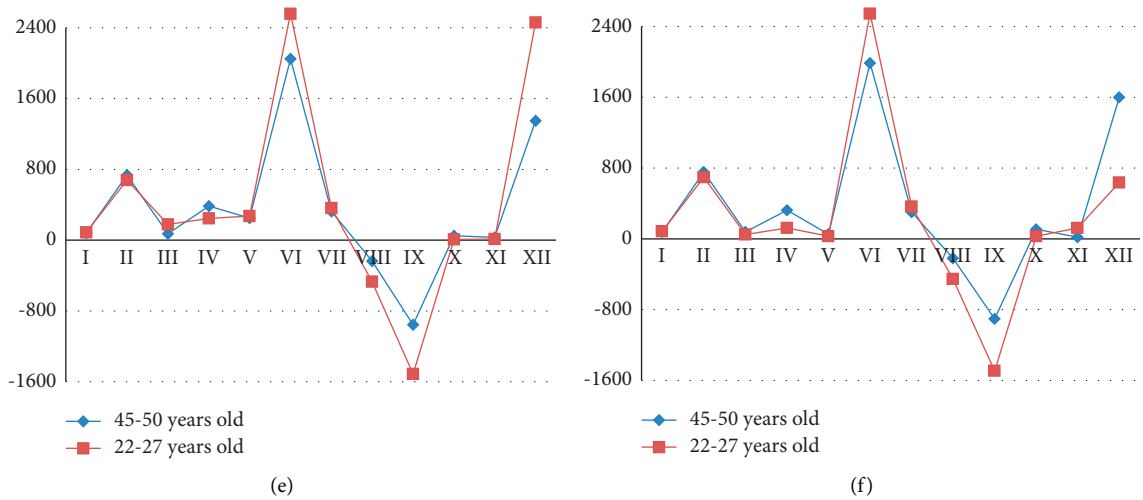


Figure 13: Young and middle age drivers' ECG characteristics in anxiety. (a) Female * novice * extraversion. (b) Female * novice * middle type. (c) Female * novice * introversion. (d) Male * novice * extraversion. (e) Male * novice * middle type. (f) Male * novice * introversion (I, AVHR; II, AVNN; III, SDNN; IV, $PNN_{50}$; V, RMSSD; VI, RWAVE; VII, TWAVE; VIII, Q; IX, S; X, UVLF/VLF*1000; XI, LF/HF*100; XII, TP).

Table 8: Independent *t*-test results of ECG characteristics for novice and experienced drivers in anxiety.

| | | *t* | df | Significance (2-tailed) | Mean difference | Standard error difference | 95% confidence interval of the difference | |
|---|---|---|---|---|---|---|---|---|
| | | | | | | | Lower | Upper |
| AVHR | N-E | 2.928 | 5 | **0.033*** | 2.000 | 0.683 | 0.244 | 3.756 |
| AVNN | N-E | −2.535 | 5 | **0.042*** | −18.510 | 7.304 | −37.289 | 0.259 |
| SDNN | N-E | 0.821 | 5 | 0.449 | 7.620 | 9.28 | −16.234 | 31.474 |
| $PNN_{50}$ | N-E | −0.221 | 5 | 0.834 | −1.010 | 4.577 | −12.775 | 10.755 |
| RMSSD | N-E | −0.777 | 5 | 0.472 | −19.730 | 25.394 | −85.011 | 45.545 |
| RWAVE | N-E | 3.414 | 5 | **0.019*** | 98.015 | 28.706 | 24.223 | 171.807 |
| TWAVE | N-E | 2.323 | 5 | 0.068 | 29.490 | 12.693 | −3.139 | 62.119 |
| Q | N-E | −1.011 | 5 | 0.358 | −7.527 | 7.446 | −26.667 | 11.613 |
| S | N-E | −2.814 | 5 | **0.037*** | −34.020 | 12.093 | −65.113 | −2.941 |
| UVLF/VLF | N-E | 0.989 | 5 | 0.368 | 0.030 | 0.03 | −0.048 | 0.108 |
| LF/HF | N-E | −1.510 | 5 | 0.192 | −6.453 | 4.275 | −17.443 | 4.536 |
| TP | N-E | −1.010 | 5 | 0.359 | −428.700 | 424.638 | −1520.36 | 662.77 |

*Note.* The significance level is 0.05. N-E, novice-experienced.

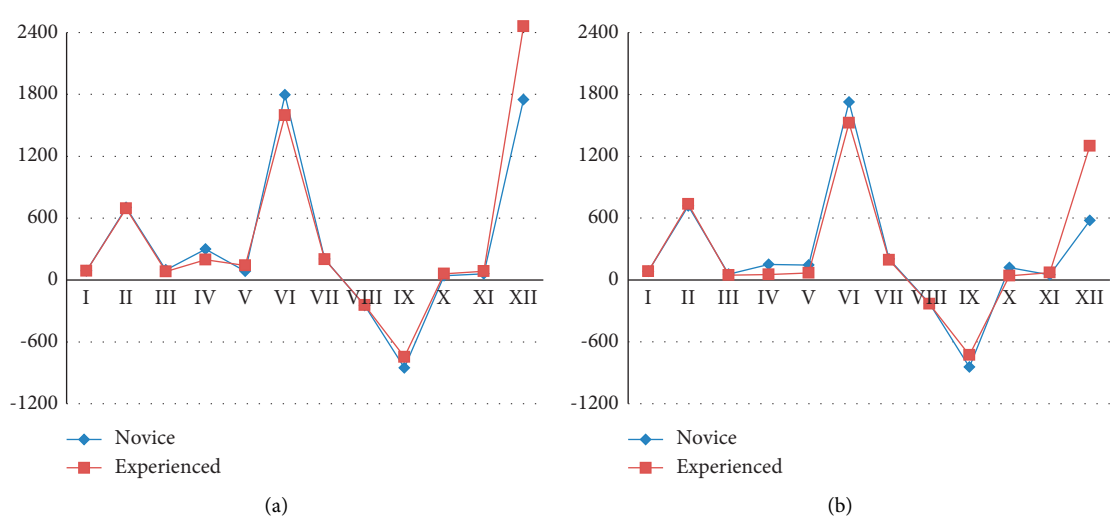


Figure 14: Continued.

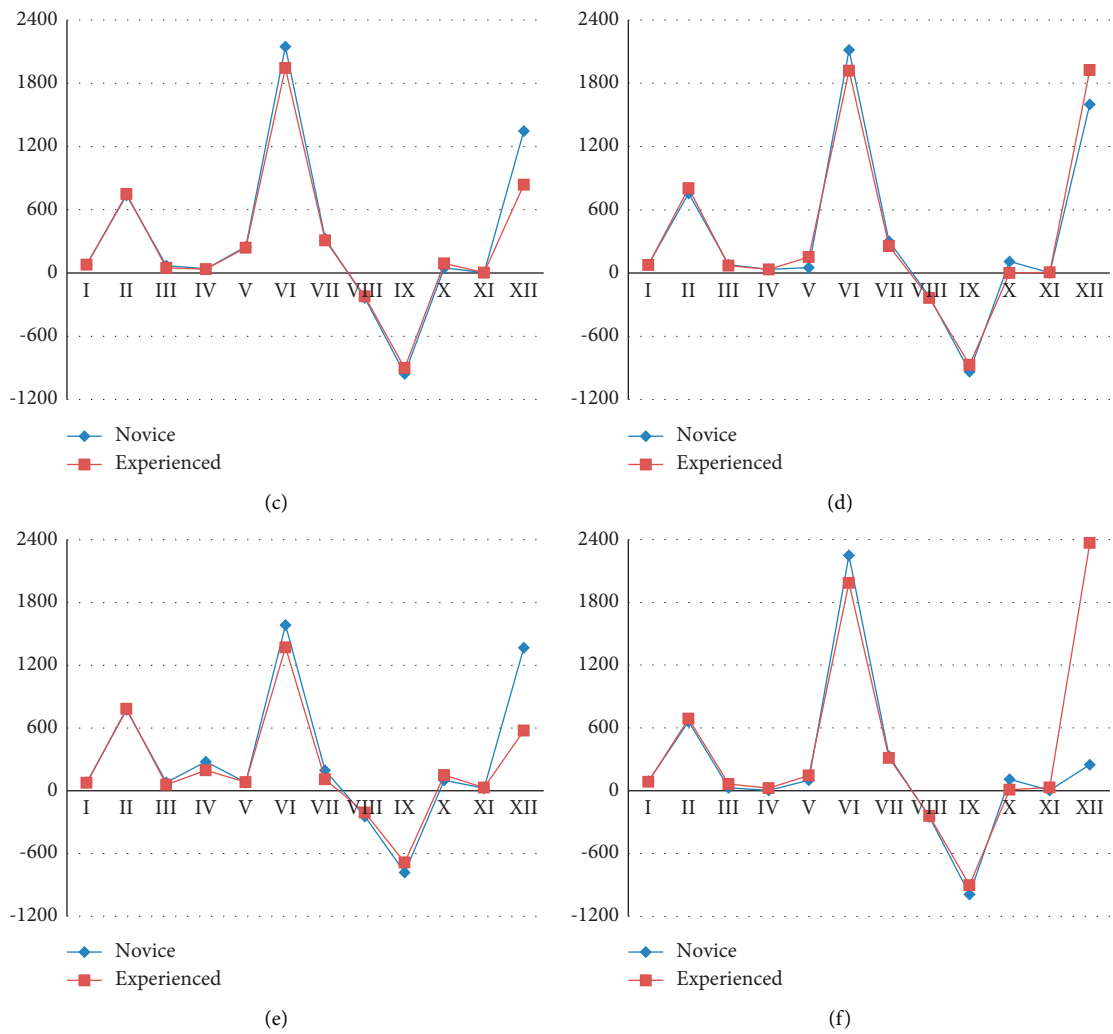


Figure 14: Novice and experienced drivers' ECG characteristics in anxiety. (a) Female * 45–50 years old * extraversion. (b) Female * 45–50 years old * middle type. (c) Female * 45–50 years old * introversion. (d) Male * 45–50 years old * extraversion. (e) Male * 45–50 years old * middle type. (f) Male * 45–50 years old * introversion (I, AVHR; II, AVNN; III, SDNN; IV, $PNN_{50}$; V, RMSSD; VI, RWAVE; VII, TWAVE; VIII, Q; IX, S; X, UVLF/VLF*1000; XI, LF/HF*100; XII, TP).

Moreover, it should be noted that high levels of sympathetic nerve activity, left ventricular hypertrophy, and pulse pressure occur rarely in young individuals during driving.

*5.3. Driver's ECG Characteristics by Driving Experiences.* The independent *t*-test results (Table 8) show that there are significant differences between novice and experienced drivers in the four ECG indicators, AVHR, AVNN, RWAVE, and S ($p < 0.05$). No significant difference was found between novice and experienced drivers in the other indicators. The results in Figure 14 and Table 8 show that novice drivers have higher average heart rate and *R*-wave peaks and lower average heartbeat interval and S-point peaks than experienced drivers. The results indicate that compared to experienced drivers, novice drivers tend to have a faster heart rate, a shorter heartbeat interval, and an aberrant ventricular conduction in anxiety.

In moderate and severe cases, novices are more likely to experience sweating and nervous intense due to rapid heartbeat. Novices are also more likely to suffer from shortness of breath as with aberrant ventricular conduction. These symptoms might cause long fixation duration and behavioral inflexibility to react to sudden events during driving.

## 6. Conclusion

This study identified the differences of ECG characteristics for different types of drivers under anxiety. The real and virtual driving experiments were designed and conducted to collect driver ECG signal data. The data were analyzed by gender, age, and driving experience. The main findings are demonstrated as follows.

(1) Compared to male drivers, female drivers tend to have a faster heart rate, a shorter heartbeat interval, and a more obvious manifestation of myocardial ischemia in anxiety. Under moderate and high levels of anxiety, female drivers are more likely to

experience dizziness, slow response, and fidgeting due to rapid heartbeat. Moreover, females are more likely to have chest distress, shortness of breath, as well as discomfort in the arms, neck, and shoulders as with myocardial ischemia.

(2) Compared to middle-aged drivers, young drivers tend to have a faster heart rate, a shorter heartbeat interval, a higher pulse pressure, a greater sympathetic nerve activity, and a higher rate of left ventricular hypertrophy and hyperkalemia in anxiety. In moderate and severe cases, young drivers are more likely to feel dizziness and chest distress due to rapid heartbeat. Young drivers are also more likely to suffer from muscle stiffness as with hyperkalemia.

(3) Compared to experienced drivers, novice drivers tend to have a faster heart rate, a shorter heartbeat interval, and an aberrant ventricular conduction in anxiety. In moderate and severe cases, novices are more likely to experience sweating and nervous intense due to rapid heartbeat. Novices are also more likely to suffer from shortness of breath as with aberrant ventricular conduction.

Our findings of this study suggest that ECG signals closely reflect driver's emotional state and can be used to detect driver's physical state. The findings also contribute to the development of the intelligent and personalized driver warning system, which could improve road traffic safety. Further studies are required to gather additional ECG data for different types of drivers and determine the factors affecting the ECG characteristics in emotional states.

## Data Availability

The data used to support the findings of this study are available from the corresponding author upon request.

## Conflicts of Interest

The authors declare that there are no conflicts of interest.

## Acknowledgments

This study was supported by the Joint Laboratory for Internet of Vehicles, Ministry of Education–China Mobile Communications Corporation (ICV-KF2018-03), Qingdao Top Talent Program of Entrepreneurship and Innovation (19-3-2-8-zhc), the National Natural Science Foundation of China (71901134, 61074140, and 61573009), and the National Key R&D Program of China (2017YFC0803802).

## References

[1] X. Y. Wang, J. L. Zhang, and X. G. Ban, *Vehicle Driving Tendency Identification Based on Collaborative Simulation of Dynamic Human-Vehicle Environment*, Science Press, Beijing, China, 2013.

[2] H. F. Jia, Y. X. Si, and M. Tang, "Study on driver information processing mode based on cognitive psychology," *China Safety Science Journal*, vol. 16, no. 1, pp. 22–25, 2006.

[3] L. X. Yan, C. Z. Wu, and S. Gao, "Study on the relationship between driver's individual factors and driving anger," *Journal of Transport Information and Safety*, vol. 31, pp. 119–124, 2013.

[4] M. Schmidt-Daffy, "Velocity versus safety: impact of goal conflict and task difficulty on drivers' behaviour, feelings of anxiety, and electrodermal responses," *Transportation Research Part F: Traffic Psychology and Behaviour*, vol. 15, no. 3, pp. 319–332, 2012.

[5] J. Naveteur, S. Cœugnet, C. Charron, L. Dorn, and F. Anceaux, "Impatience and time pressure: subjective reactions of drivers in situations forcing them to stop their car in the road," *Transportation Research Part F: Traffic Psychology and Behaviour*, vol. 18, no. 22, pp. 58–71, 2013.

[6] B. Geethanjali, K. Adalarasu, M. Jagannath, and N. P. Guhan Seshadri, "Music induced emotion using wavelet packet decomposition-An EEG study," *Biomedical Signal Processing and Control*, vol. 45, pp. 115–128, 2018.

[7] X. Zhang, B. Zuo, K. Erskine, and T. Hu, "Feeling light or dark? emotions affect perception of brightness," *Journal of Environmental Psychology*, vol. 47, pp. 107–111, 2016.

[8] L. Wang, Y. Bie, and S. Li, "The impact of roadside landscape colors on driver's mean heart rate considering driving time," *Transportation Research Part F: Traffic Psychology and Behaviour*, vol. 42, pp. 151–161, 2016.

[9] N. Dubovski, E. Ert, and M. Y. Niv, "Bitter mouth-rinse affects emotions," *Food Quality and Preference*, vol. 60, pp. 154–164, 2017.

[10] S. R. Jaeger, S. M. Lee, K.-O. Kim, S. L. Chheang, D. Jin, and G. Ares, "Measurement of product emotions using emoji surveys: c," *Food Quality and Preference*, vol. 62, pp. 46–59, 2017.

[11] M. Kirwan, S. M. Pickett, and N. L. Jarrett, "Emotion regulation as a moderator between anxiety symptoms and insomnia symptom severity," *Psychiatry Research*, vol. 254, pp. 40–47, 2017.

[12] D. Clingingsmith, "Negative emotions, income, and welfare: causal estimates from the PSID," *Journal of Economic Behavior & Organization*, vol. 130, pp. 1–19, 2016.

[13] B. Q. Ford and I. B. Mauss, "Culture and emotion regulation," *Current Opinion in Psychology*, vol. 3, pp. 1–5, 2015.

[14] E. Vingilis, Z. Yıldırım-Yenier, P. Fischer et al., "Self-concept as a risky driver: m," *Transportation Research Part F: Traffic Psychology and Behaviour*, vol. 43, pp. 15–23, 2016.

[15] G. E. Kang and M. M. Gross, "The effect of emotion on movement smoothness during gait in healthy young adults," *Journal of Biomechanics*, vol. 49, no. 16, pp. 4022–4027, 2016.

[16] C. E. Gallagher, M. C. Watt, A. D. Weaver, and K. A. Murphy, ""I fear, therefore, I shop!" exploring anxiety sensitivity in relation to compulsive buying," *Personality and Individual Differences*, vol. 104, pp. 37–42, 2017.

[17] Y. L. Chen, C. L. Chang, and C. S. Yeh, "Emotion classification of YouTube videos," *Decision Support Systems*, vol. 101, 2017.

[18] K. N. Minhad, S. H. M. Ali, and M. B. I. Reaz, "Happy-anger emotions classifications from electrocardiogram signal for automobile driving safety and awareness," *Journal of Transport & Health*, vol. 7, pp. 75–89, 2017.

[19] B. Reimer, B. Mehler, J. F. Coughlin, N. Roy, and J. A. Dusek, "The impact of a naturalistic hands-free cellular phone task on heart rate and simulated driving performance in two age groups," *Transportation Research Part F: Traffic Psychology and Behaviour*, vol. 14, no. 1, pp. 13–25, 2011.

[20] F. H. Wilhelm, J. A. Rattel, M. Wegerer et al., "Attend or defend? sex differences in behavioral, autonomic, and

respiratory response patterns to emotion-eliciting films," *Biological Psychology*, vol. 130, pp. 30–40, 2017.

[21] E. Rendon-Velez, P. M. van Leeuwen, R. Happee, I. Horváth, W. F. van der Vegte, and J. C. F. de Winter, "The effects of time pressure on driver performance and physiological activity: a driving simulator study," *Transportation Research Part F: Traffic Psychology and Behaviour*, vol. 41, pp. 150–169, 2016.

[22] W. Handouzi, C. Maaoui, A. Pruski, and A. Moussaoui, "Objective model assessment for short-term anxiety recognition from blood volume pulse signal," *Biomedical Signal Processing and Control*, vol. 14, pp. 217–227, 2014.

[23] A. Goshvarpour, A. Abbasi, and A. Goshvarpour, "An accurate emotion recognition system using ECG and GSR signals and matching pursuit method," *Biomedical Journal*, vol. 40, no. 6, pp. 355–368, 2017.

[24] M. P. Barnard and P. Chapman, "The effects of instruction and environmental demand on state anxiety, driving performance and autonomic activity: are ego-threatening manipulations effective?" *Transportation Research Part F: Traffic Psychology and Behaviour*, vol. 55, pp. 123–135, 2018.

[25] K. Rymarcayk, C. Biele, A. Grabowska, and H. Majczynski, "EMG activity in response to static and dynamic facial expressions," *International Journal of Psychophysiology*, vol. 79, no. 2, pp. 330–333, 2011.

[26] B. Scott-Parker, "Emotions, behaviour, and the adolescent driver: a literature review," *Transportation Research Part F: Traffic Psychology and Behaviour*, vol. 50, pp. 1–37, 2017.

[27] Y. Ba, W. Zhang, A. H. S. Chan, T. Zhang, and A. S. K. Cheng, "How drivers fail to avoid crashes: a risk-homeostasis/perception-response (RH/PR) framework evidenced by visual perception, electrodermal activity and behavioral responses," *Transportation Research Part F: Traffic Psychology and Behaviour*, vol. 43, pp. 24–35, 2016.

[28] R. Takahashi, M. Kobayashi, T. Sasaki, Y. Yokokawa, H. Momose, and T. Ohhashi, "Driving simulation test for evaluating hazard perception: elderly driver response characteristics," *Transportation Research Part F: Traffic Psychology and Behaviour*, vol. 49, pp. 257–270, 2017.

[29] D. Herrero-Fernández, "Psychophysiological, subjective and behavioral differences between high and low anger drivers in a simulation task," *Transportation Research Part F: Traffic Psychology and Behaviour*, vol. 42, no. 2, pp. 365–375, 2016.

[30] I. Isikli Esener, "Subspace-based feature extraction on multi-physiological measurements of automobile drivers for distress recognition," *Biomedical Signal Processing and Control*, vol. 66, no. 5, Article ID 102504, 2021.

[31] V. Balasubramanian and R. Bhardwaj, "Can cECG be an unobtrusive surrogate to determine cognitive state of driver?" *Transportation Research Part F: Traffic Psychology and Behaviour*, vol. 58, pp. 797–806, 2018.

[32] C. Zhao, M. Zhao, J. Liu, and C. Zheng, "Electroencephalogram and electrocardiograph assessment of mental fatigue in a driving simulator," *Accident Analysis & Prevention*, vol. 45, pp. 83–90, 2012.

[33] M. Gromer, D. Salb, T. Walzer, N. M. Madrid, and R. Seepold, "ECG sensor for detection of driver's drowsiness," *Procedia Computer Science*, vol. 159, pp. 1938–1946, 2019.

[34] M. Taherisadr, P. Asnani, S. Galster, and O. Dehzangi, "ECG-based driver inattention identification during naturalistic driving using mel-frequency cepstrum 2-D transform and convolutional neural networks," *Smart Health*, vol. 9-10, pp. 50–61, 2018.

[35] Y. Guo, X. Wang, Q. Xu, F. Liu, Y. Liu, and Y. Xia, "Change-point analysis of eye movement characteristics for female drivers in anxiety," *International Journal of Environmental Research and Public Health*, vol. 16, no. 7, Article ID 1236, 2019.

[36] X. Wang, Y. Guo, C. Chen, Y. Xia, and Y. Liu, "Analysis of female drivers' ECG characteristics within the context of connected vehicles," *Journal of Intelligent and Connected Vehicles*, vol. 2, no. 2, pp. 55–66, 2019.

Hindawi
Advances in Civil Engineering
Volume 2021, Article ID 5590759, 8 pages
https://doi.org/10.1155/2021/5590759

*Research Article*

# Acceleration and Deceleration Parameter Calibration of Tunnel Entrance Based on the Naturalistic Driving Test of Passenger Car

**Shijian He**,[1] **Xinsha Fu**,[2] **Zhihua Tan**,[3] **Jijing Wang**,[1] **and Ting Ge**[4]

[1]*School of Traffic and Transportation Engineering, Changsha University of Science and Technology, Changsha 410076, China*
[2]*School of Civil Engineering and Transportation, South China University of Technology, Guangzhou 510640, China*
[3]*School of Physical Education, Changsha University of Science and Technology, Changsha 410076, China*
[4]*School of Civil Engineering, Suzhou University of Science and Technology, Suzhou 215011, China*

Correspondence should be addressed to Zhihua Tan; luck@csust.edu.cn

Received 4 February 2021; Revised 18 May 2021; Accepted 17 July 2021; Published 24 July 2021

Academic Editor: Sanjay Nimbalkar



The precise calibration of acceleration and deceleration parameters is crucial for improving the accuracy of operating speed prediction and analysis tools at tunnel entrances. Therefore, acceleration and deceleration data of passenger car captured from 20 drivers at 30 tunnel entrances were collected from 200 m outside to 200 m inside the tunnel portal and averaged across four study zones. The results show that, first, the distribution of deceleration rates based on speed differs from that of acceleration rates based on speed in all zones. Second, significant differences in the probability density distribution of deceleration were found between each zone ($p < 0.001$), but differences in acceleration could not be found between any zones ($p > 0.05$). Third, the feature values (breakpoints) of the acceleration/deceleration cumulative frequency curves were located near the 95th percentile, differing from the traditional 85th percentile found with the extant model. The feature values of acceleration in the four zones coincided at 0.5 m/s$^2$ and those of deceleration were 0.93, 0.85, 0.70, and 0.47 m/s$^2$ under zones 1–4, respectively. This study provides accurate feature values of acceleration and deceleration for modelling an updated tunnel entrance operating speed prediction model.

## 1. Introduction

Operating speed consistency analysis remains an important method for freeway safety evaluation. The core of this method is a common operating speed prediction model that is used to obtain continuous operating speed profiles worldwide. This method examines the differences between vehicle operating speeds and road design speeds per adjacent road segments. Present, operating speed prediction models provide an ubiquitous worldwide quantitative evaluation index. Operating speed prediction is of great significance to accident risk analysis. Thus, improving model accuracy is an enduring focus of research in the field of freeway safety design and auditing.

Since operating speeds were first scientifically estimated [1] and evaluation standards of speed consistency were put forward [2], several operating speed prediction models have been designed and deployed. Most versions of the common model have two common characteristics. They are applied to specific road segment types (e.g. tangents [3], horizontal curves [4–6], curved slope segments [7, 8], and interchange ramps [9]), and the road segments almost always depend on single or multiple geometric elements. Hence, these elements (e.g. radius, curve change ratio, curve length, and tangent length) are the key variables [10–12]. Speed prediction models differ slightly per country and region, and the selection and combination of these geometric variables differ based on terrain and traffic characteristics [13–15].

The reliance on geometric elements stems from their relationship to operating speeds and accident occurrence. Hence, the characteristics of acceleration and deceleration values are most pertinent [16]. For example, the radius of a horizontal curve affects both the distribution and amplitude of deceleration and acceleration depending on speed [17]. In turn, the operating speed of the horizontal curve segment can be predicted based on the radius [18]. Deceleration and

acceleration values were generally assumed in previous studies to be a certain value or in each range. For example, Lamm and Choueiri [2] estimated the deceleration and acceleration rates to be 0.8 m/s$^2$ and Calvi et al. [19] estimated them to be 0.85 m/s$^2$. Alternatively, the rates on freeways in China are assumed to range from 0.15 to 0.50 m/s$^2$ [13].

However, the common operating speed prediction models are not very effective at tunnel entrances because the major influencing variables of operating speeds at tunnel entrances are the environmental transitions and not the geometric transitions and the pavement [20–23]. In China, operating speeds at tunnel entrances are predicted by directly discounting the prediction of the front-facing geometric road segment. However, this method fails to identify accident risks [13]. Some freeway accident investigations in China have shown that rear-end accidents, which can be attributed to large speed mutations and insufficient deceleration distances, occur frequently near tunnel entrances [24–27]. This may imply that the current assumptions of deceleration and acceleration do not match the actual situations at tunnel entrances. Therefore, a highly accurate operating speed prediction model of tunnel entrances is needed, and the calibration of deceleration and acceleration measurements at those locations is a prerequisite.

This study aims to calibrate deceleration and acceleration measurements at tunnel entrances, and there are two main issues that need to be solved. First, we must discover whether the assumptions of the existing model differ from the actual situations at the tunnel entrances. Second, we must explore the value range of deceleration and acceleration at those locations. Therefore, this study reports on a naturalistic driving study conducted to obtain drivers' real driving behaviours collected using a speed detector and video recordings. Indicators of 20 drivers at 30 tunnel entrances along the no. G55 mountainous freeway in Guangdong province were statistically analysed.

## 2. Methods

*2.1. Test Road.* To avoid the interference of various ancillary elements, such as alignment condition, road pavement condition, and road width, and to obtain sufficient samples, naturalistic driving tests were conducted on a road section of a mountain freeway (no. G55 in western Guangdong province) comprising 15 tunnels × 2 directions (160 km). As illustrated in Figure 1, the test road runs between the major interchange at Huaijinan and the one at Sihui. Tunnel lengths range between 215 and 1660 m ($M = 642$, SD = 377). The design speed of the test area is 100 km/h, and there are three lanes per direction.

To reduce the interference of traffic volume on the results of this study, the testing was conducted between 7 and 11 am because the traffic headway during this period is generally greater than 6 s, which can be treated as a free-flow condition.

*2.2. Apparatus.* Data collection of real-time vehicle parameters from a controller area network supported by onboard diagnostic (OBD) sensors is common to naturalistic driving studies. Such experiments well support the analysis of online driving behaviour variables with high realism. Thus, the present study used a high-precision apparatus (Figure 2) that included an OBD sensor, a smartphone, and a video recorder to collect data parameters of acceleration and deceleration.

The OBD sensors and smartphone connections relied on bluetooth connections, from which acceleration and deceleration data were exported at a sample frequency of 2 Hz. Speed data were synchronously recorded alongside acceleration/deceleration data at the same frequency, and the real-time driving position was recorded using the video recorder. Then, the position curves were obtained by calculating the product of speed over time, and the positions of acceleration and deceleration were determined by synchronizing the video recorder and the OBD sensor data.

*2.3. Participants.* Drivers were recruited from the South China University of Technology and road-testing management companies using online advertising and e-mail. Twenty drivers (26–40 years old ($M = 32.7$, SD = 3.2)) were selected. They each had held valid driving licenses between 2 and 12 years ($M = 6.5$, SD = 3.5). Hence, they could legally drive a passenger car with fewer than seven seats on a freeway. Their annual accumulated freeway mileage per year ranged from 2,100 to 12,000 km ($M = 5800$, SD = 3250). Written consent was obtained, and this study conformed to ethical guidelines.

*2.4. Data Preparation.* Each driver was instructed to drive one round trip along the test road using normal driving styles. Thus, 30 group data were acquired per tunnel and driver (600 total data items). After eliminating anomalies (e.g. equipment failures, spurious values, and time misalignments), 546 groups were used for analysis.

In the present study, a tunnel entrance was defined as the road segment beginning at 200 m in front of the tunnel portal to 200 m past the portal on the inside. As given in the previous research studies [16, 17, 26, 27], this area was divided into four zones of 100 m each. Acceleration and deceleration data were analysed separately per zone, resulting in 501, 393, 1268, and 1771 data items for zones 1–4, respectively. For deceleration, 3167, 3347, 2269, and 1628 respective data items were acquired.

## 3. Results and Discussion

*3.1. Speed-Related Variations of the Distribution Characteristics of Acceleration and Deceleration.* It is clear by definition that speed is the key constituent of acceleration and deceleration measures. Thus, in the tunnel entrance road segments, drivers adjusted their speeds to adapt to the environmental changes from an open road to a semiclosed tube. The fundamental motivation of this type of speed adjustment differs from that of adjustments along open roads, owing to the distinctive road geometries involved. In this study, the relationships of acceleration/deceleration to driving speed in each zone were analysed to verify whether


Figure 1: Test road along the no. G55 freeway, Guangdong, China.

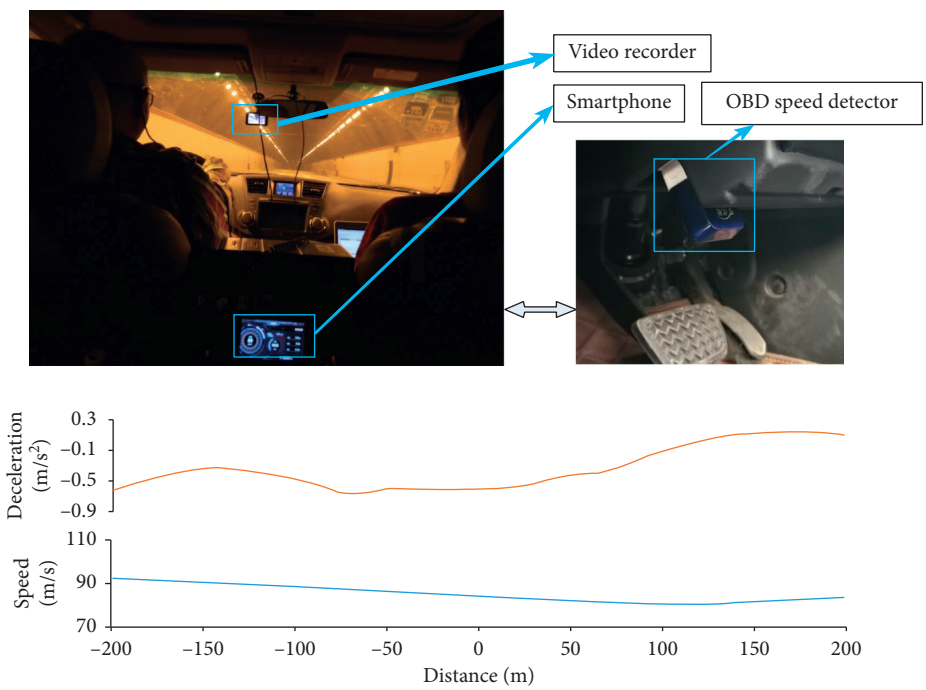


Figure 2: Data sample and apparatus of the naturalistic driving test.

the effects were consistent with those found in previous open road studies.

Figure 3 illustrates how the distribution of acceleration and deceleration varies based on driving speed. Figures 3(a)–3(d) represent the distribution of acceleration and deceleration in zones 1–4 (averaged across all tunnels), respectively. The positive values in this figure represent acceleration, and the negative values represent deceleration; the red line represents the boundary of the distribution triangle.

In each zone, the distributions of deceleration and acceleration differed with driving speed. Specifically, in zones 1–3, the range of the distribution triangle of deceleration was significantly larger, and the shapes were different from those of acceleration. In these zones, the distribution triangle of deceleration was nearly isometric and that of acceleration sloped with a high axis located at the side of low driving speed. In zone 4, the distribution triangle of deceleration was antisymmetrical to that of acceleration. This result demonstrates that the acceleration and deceleration distributions vs. driving speed were not similar in any zone. Therefore, acceleration and deceleration should be calibrated separately for the road segments of tunnel entrances, which diverge from the existing assumptions made by specifications in China.

Second, the distribution triangles of acceleration in each zone can be considered the same because their shapes and ranges are very similar. This implies that the

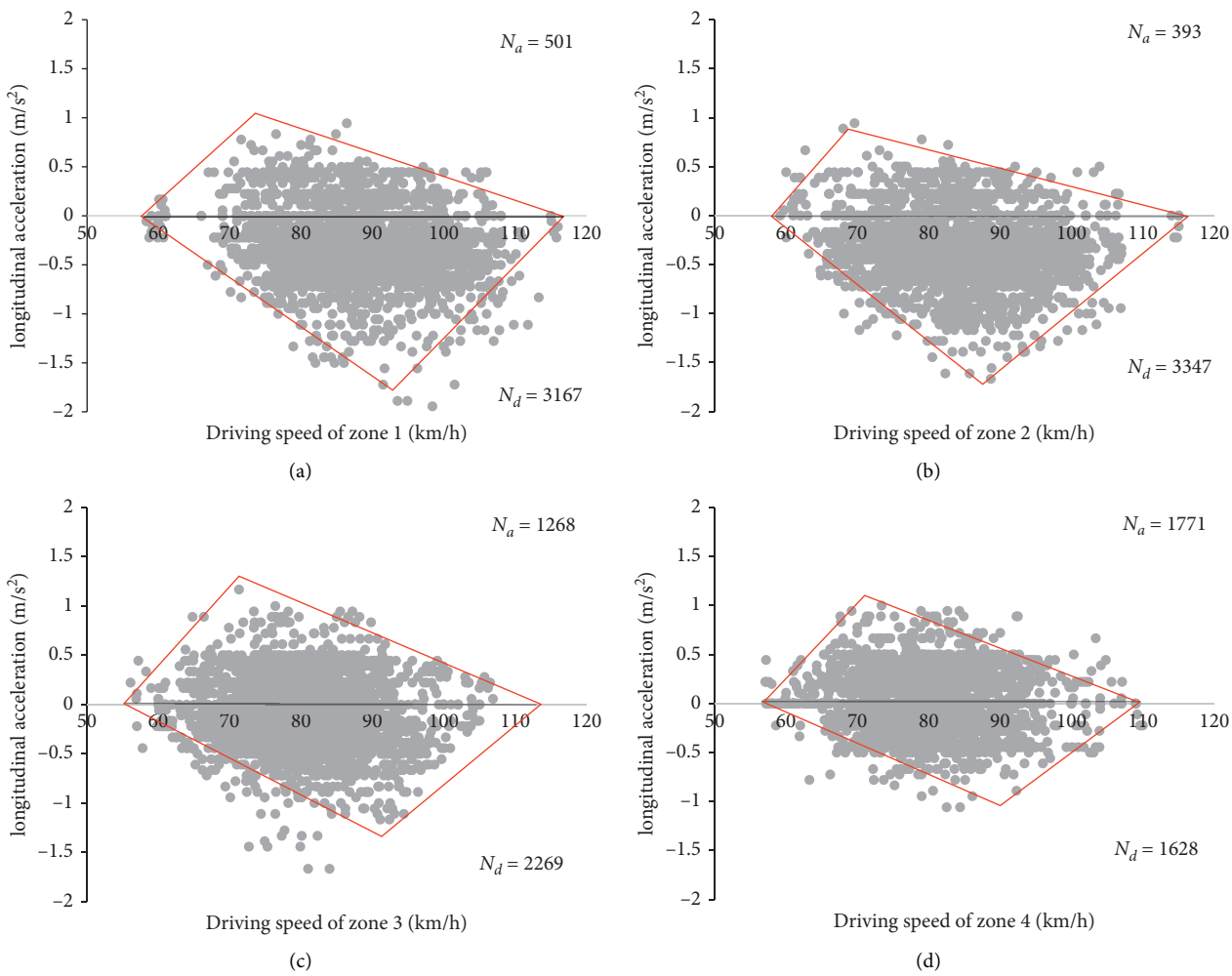


Figure 3: Distributions of acceleration and deceleration with the driving speed. (a) Zone 1. (b) Zone 2. (c) Zone 3. (d) Zone 4.

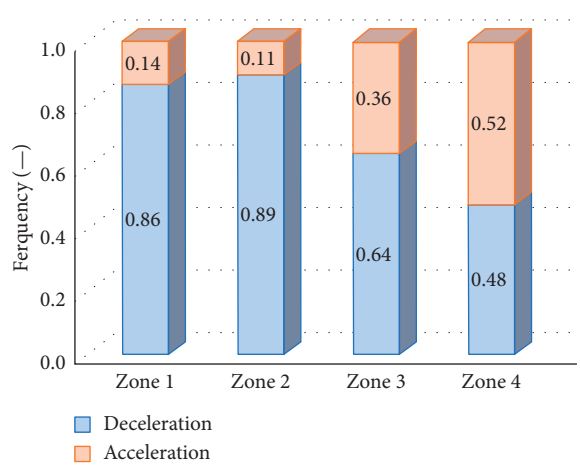


(a)

Figure 4: Continued.

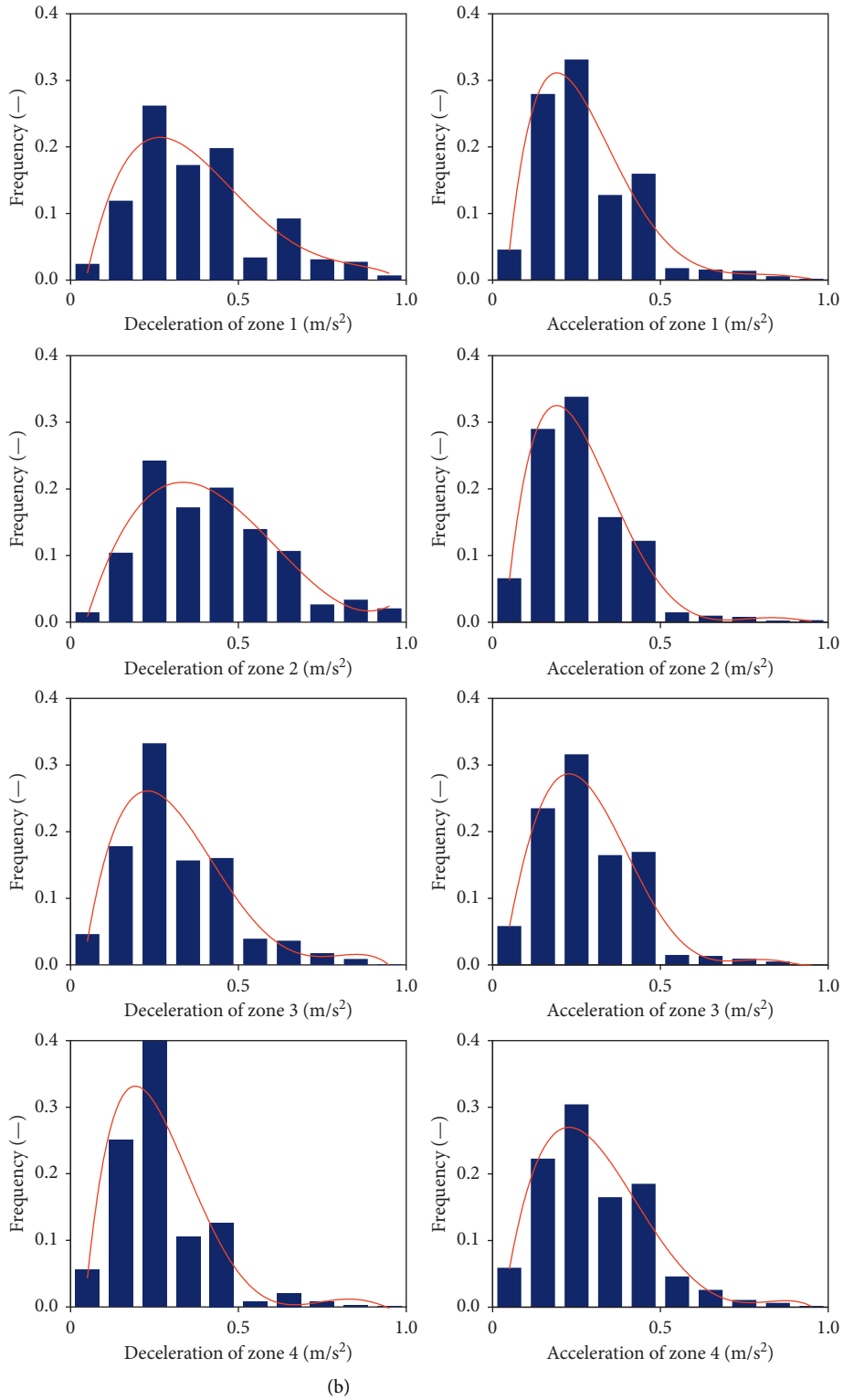


Figure 4: Distribution characteristics of acceleration and deceleration in different zones. (a) Proportions of acceleration and deceleration in the four zones. (b) Probability density distributions of acceleration and deceleration in the four zones.

distribution of acceleration vs. driving speed was not affected by zone division. However, the distribution triangles of deceleration in each zone were dissimilar in aspects of both shape and range. Furthermore, the distribution triangle of deceleration in zone 4 was obviously different. This illustrates that the distribution of deceleration vs. the driving speed was affected by zone division.

Table 1: Kruskal–Wallis $H$ test results of the probability density distribution of acceleration and deceleration.

| Zones | Acceleration ($m/s^2$) | | Deceleration ($m/s^2$) | | $P_{a,a}$ [1] | | | | $P_{d,d}$ [2] | | | | $P_{a,d}$ [3] |
|---|---|---|---|---|---|---|---|---|---|---|---|---|---|
| | Mean | SD | Mean | SD | Zone 1 | Zone 2 | Zone 3 | Zone 4 | Zone 1 | Zone 2 | Zone 3 | Zone 4 | |
| Zone 1 | 0.28 | 0.15 | −0.41 | 0.25 | 1 | 0.66 | 0.65 | 0.48 | 1 | 0.001 | <0.001 | <0.001 | <0.001 |
| Zone 2 | 0.26 | 0.14 | −0.43 | 0.26 | | 1 | 0.35 | 0.24 | | 1 | <0.001 | <0.001 | <0.001 |
| Zone 3 | 0.29 | 0.17 | −0.33 | 0.2 | | | 1 | 0.75 | | | 1 | <0.001 | <0.001 |
| Zone 4 | 0.3 | 0.17 | −0.26 | 0.14 | | | | 1 | | | | 1 | <0.001 |

[1] $P_{a,a}$ is the significance test indicator of the probability density distribution of acceleration between zones. [2] $P_{d,d}$ is the significance test indicator of the probability density distribution of deceleration between zones. [3] $P_{a,d}$ is the significance test indicator of the probability density distribution of acceleration and deceleration.

*3.2. Distribution Characteristics of Acceleration/Deceleration in Different Zones.* In previous operating speed prediction models, most acceleration and deceleration values are assumed to either be a constant or within a given range, depending on the models' horizontal curve segment, tangent segment, and slope segment specifications. However, the various assumptions made by the different models have one thing in common: the distribution characteristics of acceleration and deceleration in the road segments are assumed to be the same. Therefore, in view of the peculiarity of tunnel entrances, it is necessary to analyse each zone separately as we have done.

Figure 4(a) shows the proportions of the number of accelerations and decelerations in the four zones. With the zone changes, proportions of variability regarding acceleration and deceleration were observed. From zones 1–4, the proportion of deceleration increased first and decreased later, whereas with acceleration, the situation was the opposite. Specifically, the proportions of deceleration were 0.86, 0.89, 0.64, and 0.46 for zones 1–4, respectively, whereas the proportions of acceleration were 0.14, 0.11, 0.36, and 0.54, respectively. This indicates that the probabilities of acceleration and deceleration are not the same in all the zones. The data indicate that drivers had a high probability of deceleration just before the tunnel portal, but it decreased after entering the tunnel. The probabilities of acceleration and deceleration were balanced in zone 4, which may explain the relevant result observed by Bella et al. (2007), who found that the speed difference prior to entering the tunnel portal (zones 1 and 2) was significantly larger than that after entering (zones 3 and 4).

Figure 4(b) shows the probability density distributions of acceleration and deceleration with absolute value less than 1 $m/s^2$ in the four zones. The bars reflect the frequencies of acceleration or deceleration over a range of 0.1 $m/s^2$. Moreover, Table 1 presents the results of the Kruskal–Wallis (K-W) $H$ test for the probability density distributions of acceleration and deceleration in the four zones. The results of the K-W test indicate that the significance test indicator of the probability density distribution of acceleration between zones ($P_{a,a}$) was larger than 0.05, demonstrating that the distributions in the four zones were subject to the same form. This may be due to the unchangeable vehicle engine torques and the stable designs of continuously variable transmission. Second, the probability density distribution of deceleration in the four zones were not subject to the same form because the probability density distribution of acceleration between zones ($P_{d,d}$) was lower than 0.05. This implies that there were significant differences in the drivers' deceleration behaviours in the different zones. Finally, in each zone, there were significant differences between the probability density distributions of acceleration and deceleration ($P_{a,d} < 0.001$). These results further illustrate that acceleration and deceleration should be calibrated separately in the different zones.

*3.3. Feature Value Calibration of Acceleration/Deceleration in Different Zones.* Following the observations, we conducted an in-depth analysis of the feature values and calibrated them to the different zones of this study. Figure 4 shows that the acceleration and deceleration values in each zone exceeded the commonly accepted range of values (0.15–0.50 $m/s^2$) for both acceleration and deceleration recommended by the Specifications for Highway Safety Audit of China. Hence, the upper limit values were calibrated by analysing the breakpoints of their cumulative frequency curves because those points are recognized feature values in existing operating speed prediction models. Until now, the 85th percentile point of the cumulative frequency curve has been assumed to be the standard breakpoint, and extant operating speed prediction models are calibrated based on this.

Figure 5 shows the cumulative frequency curves of the acceleration and deceleration for each zone. Notably, the breakpoints were neither observed at the 85th percentile of the cumulative frequency curves of acceleration nor at the deceleration. They were instead found at the 95th percentile, highlighting a notable model discrepancy. This suggests that modifications are necessary for tunnel entrances.

The 95th percentile breakpoint rates of acceleration were nearly the same (0.5 $m/s^2$) in the different zones (0.50, 0.50, 0.50, and 0.47 $m/s^2$ for zones 1–4, respectively). Thus, they were not larger than 0.5 $m/s^2$. Hence, realistic expectations of acceleration at tunnel entrances fall within the suggestion range assumed by the Specifications for Highway Safety Audit of China.

However, these rates varied in the different zones (0.93, 0.85, 0.70, and 0.47 $m/s^2$ for zones 1–4, respectively). Only in zone 4, the 95th percentile rate of deceleration falls within the suggested range, whereas that of deceleration in the other zones was greater than the upper limit of the suggestion range. The largest 95th percentile

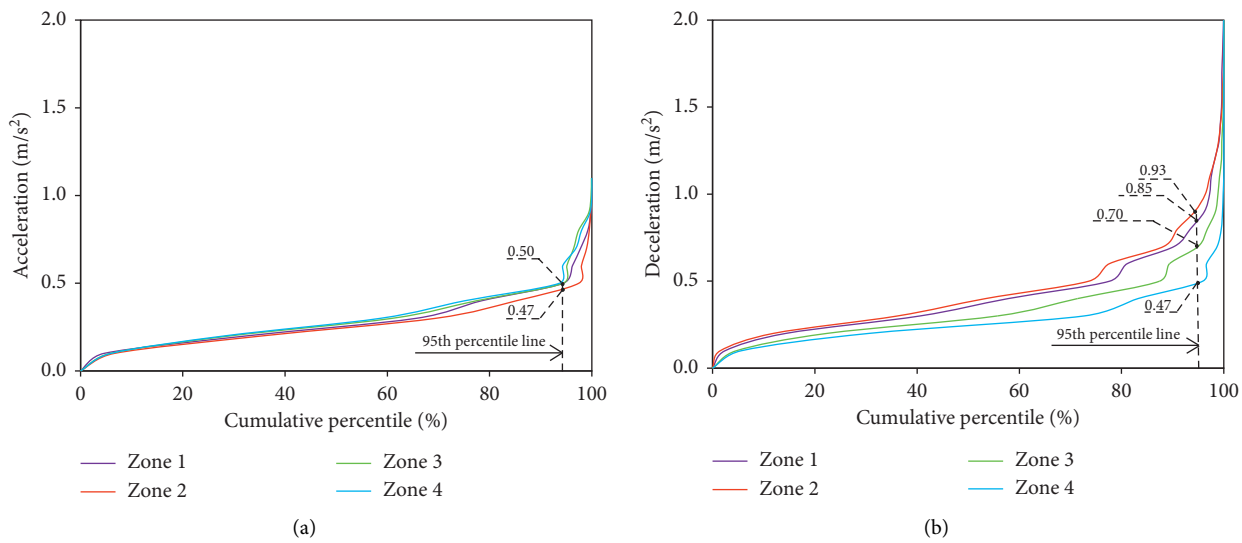


Figure 5: Cumulative frequency curves of acceleration and deceleration for each zone. (a) Acceleration. (b) Deceleration.

rate of deceleration was found in zone 2 (0.93 m/s$^2$), which exceeded the upper limit (0.5 m/s$^2$) of the suggested range by 86%. This implies that the suggested range of acceleration and deceleration at tunnel entrances should be considered separately.

The calibration determined the 95th percentile rate of acceleration (0~0.5 m/s$^2$ in all zones) can be used for modifying operating speed prediction models. Thus, if the worst condition in the tunnel entrance zones is considered, the largest 95th percentile rate of deceleration (0.93 m/s$^2$ in Zone 2) can be used to establish boundary conditions of deceleration for operating speed prediction. Furthermore, in the simulation cabin, Lamm and Choueiri [2] estimated the deceleration and acceleration rates to be 0.8 m/s$^2$ and Calvi et al. [19] estimated them to be 0.85 m/s$^2$. Thus, the rates in simulation cabin are obviously different from the 95th percentile breakpoint rates of the naturalistic driving test. The 95th percentile breakpoint rates of acceleration and deceleration may provide reference for simulation parameter correction.

## 4. Conclusion

This study found that the differences of acceleration and deceleration distributions at tunnel entrances are extremely important to calibrating and improving the common operating speed prediction model currently in use. To obtain the actual acceleration and deceleration characteristics of vehicles, naturalistic driving tests and continuous online data observations were carried out on a freeway segment spanning 30 tunnels. The distribution characteristics in four specified zones at each tunnel entrance were observed, and the feature values were analysed. The main conclusions of the research are as follows:

(1) In the four sections of each tunnel entrance, the distributions of deceleration differed from those of acceleration, which contradicts the assumptions of common operating speed prediction models. Moreover, the distribution of acceleration and deceleration according to driving speed may be affected by zone divisions. Therefore, acceleration and deceleration should be calibrated separately in the different zones of tunnel entrances.

(2) From the area outside the tunnel (zone 1) to that completely inside the tunnel (zone 4), the proportion of deceleration increased first and decreased afterward. Specifically, the proportions were 0.86, 0.89, 0.64, and 0.46 in zones 1–4, respectively, whereas the proportion of acceleration was reversed. Furthermore, there were no significant differences in the probability density distribution of acceleration in any zone. However, there were significant differences of the probability density distribution of deceleration in all zones. Furthermore, the probability density distributions of acceleration and deceleration were different in all zones. Thus, value calibration of acceleration and deceleration should be performed separately.

(3) For both acceleration and deceleration, the breakpoints were not found at the 85th percentile of the cumulative frequency curves, as expected from past utilisation of the common model. Instead, they were predominately found near the 95th percentile. The breakpoint values of acceleration were close to 0.5 m/s$^2$ in the different zones, whereas the breakpoint values of deceleration varied (i.e., 0.93, 0.85, 0.70, and 0.47 m/s$^2$ under zones 1–4, respectively). The largest breakpoint value of deceleration (0.93 m/s$^2$) was found in zone 2: a fact that can be used as a modified parameter for operating speed prediction models at tunnel entrances.

In the present study, owing to the technical limitations of the transmission and collection of continuous online data from trucks, data of acceleration/deceleration were collected

using passenger cars only. Therefore, future works should calibrate acceleration and deceleration parameters of heavy trucks at tunnel entrances.

## Data Availability

The data used to support the findings of this study are available from the corresponding author upon request.

## Conflicts of Interest

The authors declare that they have no conflicts of interest.

## Acknowledgments

This study was funded by the National Natural Science Foundation of China (51778242, 51978283, and 51808370).

## References

[1] J. C. Glennon, T. R. Neuman, and J. E. Leisch, "Safety and operational consideration for design of rural highways curves," Report FHWA/RD-86/035, Federal Highway Administration, McLean, VA, USA, 1986.

[2] R. Lamm and E. M. Choueiri, "Recommendations for evaluating horizontal design consistency based on investigations in the state of New York," *Transportation Research Record*, vol. 1122, pp. 68–78, 1987.

[3] M. D. Luca, F. Russo, O. Cokorilo, and G. Dell'Acqua, "Modeling operating speed using artificial computational intelligence (ACI) on low-volume road," in *Proceedings of the Transportation Research Board 93rd Annual Meeting*, Washington, DC, USA, 2014.

[4] M. Christopher and J. M. Mason, "Geometric design guidelines to achieve desired operating speed on urban streets," in *Proceedings of the 65th ITE Annual Meeting: 1995 Compendium of Technical Papers*, Institute of Transportation Engineers, Denver, CO, USA, 1995.

[5] S. M. Easa and A. Mehmood, "Establishing highway horizontal alignment to maximize design consistency," *Canadian Journal of Civil Engineering*, vol. 34, no. 9, pp. 1159–1168, 2007.

[6] A. Jacob and M. V. L. R. Anjaneyulu, "Operating speed of different classes of vehicles at horizontal curves on two-lane rural highways," *Journal of Transportation Engineering*, vol. 139, no. 3, pp. 287–294, 2013.

[7] G. M. Gibreel, S. M. Easa, and I. A. El-Dimeery, "Prediction of operating speed on three-dimensional highway alignments," *Journal of Transportation Engineering*, vol. 127, no. 1, pp. 21–30, 2001.

[8] J. Morrall and R. J. Talarico, "Side friction demanded and margins of safety on horizontal curves," *Transportation Research Record*, vol. 1435, pp. 145–152, 1994.

[9] Z.-y. Zhang, X.-y. Hao, W.-b. Wu, and D. Wang, "Research on the running speed prediction model of interchange ramp," *Procedia—Social and Behavioral Sciences*, vol. 138, pp. 340–349, 2014.

[10] C. Han, H. Huang, J. Lee, and J. Wang, "Investigating varying effect of road-level factors on crash frequency across regions: a Bayesian hierarchical random parameter modeling approach," *Analytic Methods in Accident Research*, vol. 20, pp. 81–91, 2018.

[11] J. J. Tang, W. Q. Yin, C. Y. Han, L. L. Zheng, and H. L. Huang, "A regional quantile analysis for the varying effect of road-level risk factors on crash rate," *Analytic Methods in Accident Research*, vol. 29, Article ID 100159, 2020.

[12] J. J. Tang, L. L. Zheng, C. Y. Han, Y. Zhang, Y. J. Zou, and H. L. Huang, "Statistical and machine-learning methods for clearance time prediction of road incidents: a methodology review," *Analytic Methods in Accident Research*, vol. 27, Article ID 100123, 2020.

[13] J. Xu, L. Wei, W. Xu, and Y. M. Shao, "Acceleration and deceleration calibration of operating speed prediction models for two-lane mountain highways," *Journal of Transportation Engineering, Part A: Systems*, vol. 143, no. 7, Article ID 04017024, 2017.

[14] H. Wen and E. T. Donnell, "Models of acceleration and deceleration rates on a complex two-lane rural highway: results from a nighttime driving experiment," *Transportation Research Part F: Traffic Psychology & Behaviour*, vol. 13, no. 6, pp. 397–408, 2010.

[15] Y. Hassan, "Traffic and speed characteristics on two-lane highways: field study," *Canadian Journal of Civil Engineering*, vol. 30, no. 6, pp. 1142–1154, 2003.

[16] S. Bassan, "Overview of traffic safety aspects and design in road tunnels," *IATSS Research*, vol. 40, no. 1, pp. 35–46, 2016.

[17] X. S. Fu, S. J. He, J. T. Du, and T. Ge, "Effects of in-vehicle navigation on perceptual responses and driving behaviours of drivers at tunnel entrances: a naturalistic driving study," *Journal of Advanced Transportation*, vol. 2019, Article ID 9468451, 13 pages, 2019.

[18] F. Bella and M. Silvestri, "Driver's braking behavior approaching pedestrian crossings: a parametric duration model of the speed reduction times," *Journal of Advanced Transportation*, vol. 50, no. 4, pp. 630–646, 2016.

[19] A. Calvi, A. Benedetto, and M. R. De Blasiis, "A driving simulator study of driver performance on deceleration lanes," *Accident Analysis & Prevention*, vol. 45, pp. 195–203, 2012.

[20] C. Caliendo, M. L. De Guglielmo, and M. Guida, "A crash-prediction model for road tunnels," *Accident Analysis & Prevention*, vol. 55, pp. 107–115, 2013.

[21] T. O. Nævestad and S. Meyer, "A survey of vehicle fires in Norwegian road tunnels 2008–2011," *Tunnelling and Underground Space Technology*, vol. 41, pp. 104–112, 2014.

[22] C. C. Liu, S. T. Lv, D. Z. Jin, and F. T. Qu, "Laboratory investigation for the road performance of asphalt mixtures modified by rock asphalt/styrene butadiene rubber," *Journal of Materials in Civil Engineering*, vol. 33, no. 3, Article ID 04020504, 2021.

[23] C. C. Liu, S. T. Lv, X. H. Peng, J. L. Zheng, and M. Yu, "Analysis and comparison of different impacts of aging and loading frequency on fatigue characterization of asphalt concrete," *Journal of Materials in Civil Engineering*, vol. 32, no. 9, Article ID 04020240, 2020.

[24] Z.-l. Ma, C.-f. Shao, and S.-r. Zhang, "Characteristics of traffic accidents in Chinese freeway tunnels," *Tunnelling and Underground Space Technology*, vol. 24, no. 3, pp. 350–355, 2009.

[25] Q. Meng and X. Qu, "Estimation of rear-end vehicle crash frequencies in urban road tunnels," *Accident Analysis & Prevention*, vol. 48, pp. 254–263, 2012.

[26] J. Wang, A. Pervez, Z. Wang, C. Han, L. Hu, and H. Huang, "Crash analysis of Chinese freeway tunnel groups using a five-zone analytic approach," *Tunnelling and Underground Space Technology*, vol. 82, pp. 358–365, 2018.

[27] J. S. Yeung and Y. D. Wong, "Road traffic accidents in Singapore expressway tunnels," *Tunnelling and Underground Space Technology*, vol. 38, pp. 534–541, 2013.

Hindawi
Advances in Civil Engineering
Volume 2021, Article ID 5584325, 12 pages
https://doi.org/10.1155/2021/5584325

*Research Article*

# Development and Performance Evaluation of Thin-Layer Color Antiwearing Paving Materials

**Zhaohui Liu,[1] Xiangming Deng,[1,2] Hao Guo,[3] Yingchun Zhang,[3] Di Wei,[1] and Dongmei Zhang[1,4]**

[1]*School of Traffic and Transportation Engineering, Changsha University of Science & Technology, Changsha 410114, Hunan, China*
[2]*Guangxi Communications Investment Group Corporation Ltd, Nanning 530007, Guangxi, China*
[3]*Hunan Provincial Communications Planning, Survey and Design Institute Co., Ltd, Changsha 410200, Hunan, China*
[4]*Hunan International Scientific and Technological Innovation Cooperation Base of Advanced Construction and Maintenance Technology of Highway, Changsha University of Science and Technology, Changsha 410114, Hunan, China*

Correspondence should be addressed to Dongmei Zhang; dmzhang@csust.edu.cn

Received 3 February 2021; Revised 24 February 2021; Accepted 31 May 2021; Published 11 June 2021

Academic Editor: Yinshan Tang



To develop a color antiwearing wear layer based on epoxy resin adhesives, the effect of single formula composition on the properties of adhesives was analyzed through drawing strength tests, shear strength tests, and bending strength tests. It was found that when the mass ratio of the epoxy resin curing agent and the dosage of the toughening agent increased, the bonding performance and toughness of the adhesive firstly increased and then decreased. With the increase of the mass ratio of phenolic aldehyde amine to polyamide, the bonding performance and toughness of the adhesive were improved, but the effect was significantly reduced when the ratio was more than 2. With the increase of diluent content, the bonding performance and toughness of the adhesive were reduced. Based on response surface optimization, the optimum formulation was recommended. The content of the mass ratio of the epoxy resin to the curing agent and mass ratio of curing agent phenolic amine to polyamide, toughening agent content, and diluent content was determined to be 2.971%, 1.887%, 2.455%, and 1.000%, respectively. And, the dosage of each material was consistent with the effect of the dosage of a single formula on the properties of adhesives. The performance of the color antiwearing thin layer was tested by the adhesion test and antiwearing durability test. It was found that temperature had a significant effect on the adhesion, the adhesion of the thin layer was significantly reduced at low temperature, and the sensitivity to impact load was enhanced, while the adhesion and sensitivity to impact load were effectively improved at more than 20°C. At the same time, the antiwearing of the thin layer decreased rapidly at the initial stage under the reciprocating load but tended to be stable when the load exceeds 500 times.

## 1. Introduction

Road traffic safety has always been the focus of scientific research workers [1, 2]. The State Council's "Thirteenth Five-Year Modern Comprehensive Transportation System Development Plan" pointed out that future highway construction should be "innovation-driven, green, and safe" as the basic principles, firmly establish the concept of safety first, and comprehensively improve the safety and reliability of transportation, and to ensure the safety of users to reach the destination has become the basic property of the highway [3]. However, the road traffic accident is still a difficult problem that cannot be avoided all over the world. According to the data of "road traffic and transportation safety development report (2017)," there are 8.643 million traffic accidents in China in 2016, resulting in direct property losses of 1.21 billion yuan [4]. The analysis of the causes of a large number of traffic accidents shows that, in addition to the vehicle and the climate, the driver is also one of the important accident risk factors. For example, long-term driving distraction can easily cause visual fatigue. Besides, some

expressways contain a lot of curved road sections, appearing in the form of a combination of curved road sections and long downhills. The "nonorthogonality" of these linear designs bury hidden dangers for driving stability and safety [5, 6]. It is urgent to improve road traffic safety. The color antiwearing thin layer provides a new idea for improving road driving safety. It coats the road surface with adhesives and colored antiwearing aggregates to form a 4–10 mm thick structural layer, and through the change of color and the improvement of vibration, the driver is reminded to enter the dangerous road section from the visual and tactile aspects, respectively. Also, the structure layer has good antiwearing performance, which improves driving safety in a diversified way [7].

The research and application of the color antiwearing thin layer originated from Europe, the United States, and other developed countries in the 1950s, and it is applied to traffic engineering fields involving safety management [8–11], such as parking lot, tunnel entrance and exit, ramp, and deceleration belt. However, the research in this field started late in China; until the beginning of the 21st century, color pavement technology is applied to public places such as carriageway and residential area. With the maturity of the preparation, production, and construction technology of colored paving materials, the colored pavement is developing towards lightness, high performance, and safety [12]. The development of color thin layer binder has experienced three stages; they are color coating, color asphalt, and polymer resin [13]. At present, epoxy resin, polyurethane, and methyl methacrylate are widely studied. Chen et al. [14] developed a kind of antiwearing layer adhesive material for pavement, which was composed of epoxy resin, curing agent, toner, and quartz sand. The bonding material had excellent mechanical properties, deformation properties, and durability. Quan et al. [15] developed a one-component polyurethane adhesive, which was composed of polyaspartic resin, DOP, and MD polyether prepolymer, and had the characteristics of transparency, wears resistance, and good sealing performance. Wu [16] prepared a thermoplastic elastomer-modified polymethyl methacrylate color nonslip coating, which mainly included modified MMA resin liquid, rubber particles, dibutyl phthalate, and formyl peroxide, and had nonpolishing, nonslip, quiet, and other characteristics. With the development of the types of adhesives, the pavement properties of adhesives have been paid more and more attention. Zhong et al. [17] adopted pure shear strength test methods to compare the shear strength of epoxy resin and modified emulsified asphalt under different temperature conditions to evaluate the interlayer adhesion. They found that epoxy resin had good adhesion to asphalt concrete, and its shear strength was higher than emulsified asphalt. Xue et al. [18] measured the adhesion between color antiwearing thin layers under different resin coating amounts by paint and varnish pull-apart adhesion test method. It was found that, with the increase of resin adhesive coating amount, the adhesion between layers gradually tends to a fixed value. Li et al. [19] compared the interfacial bond strength of the original pavement with or without groove through the pull-out test and shear test, which found that the shear strength and pull-out strength can be increased by one-third under the groove condition. Wu et al. [20] determined that the structure depth of the colored antiwearing wearing course was 1.81 mm and the friction coefficient BPN was 59.8, which was higher than that of the general asphalt pavement. Zhang et al. [21] compared the friction coefficient of the color antiwearing thin layer with SMA-13 and AC-13 pavement under dry and wet conditions and found that the epoxy color antiwearing wear layer had the best performance and could shorten the braking distance by 40%. Liu et al. [22] compared the skid resistance performance of colored antiwearing thin layers from different aggregate sources and found that the antiwearing performance of bauxite particles, ceramic particles, quartz sand, and colored sand decreased in turn.

To sum up, there is still a need for further research in formulation development, thin-layer material adhesion, and skid resistance durability. Therefore, this paper through the single factor studied epoxy resin curing agent mass ratio, mass ratio of two types of curing agents, toughening agent dosage, and diluent dosage on the properties of adhesive, and then, the response surface method was used to obtain the optimal ratio. Finally, the adhesion between epoxy resin adhesive and ceramic particles was explored, and the antiwearing durability was evaluated.

## 2. Experimental

*2.1. Materials.* Since the adhesive of the epoxy resin was generally composed of epoxy resin and curing agent, to improve its comprehensive performance, it needed to be realized by adding tougheners, diluents, etc. The information on epoxy resin, curing agent, toughening agent, diluents, and other materials selected is shown in Table 1.

The color ceramic was the aggregate in the test, and its main technical indexes are shown in Table 2.

### 2.2. Test Methods

*2.2.1. Drawing Strength Test.* The microdrawing instrument of Shijiazhuang Zhuopu Technology Co., Ltd. was used. The epoxy resin adhesive was evenly stirred and applied on the surface of the clean steel plate, and then, the drawing head with a diameter of 100 mm was placed. After standing at room temperature and curing for 24 hours, the drawing strength was tested with a tensile rate of 10 mm/min. The principle of the equipment is shown in Figure 1.

The calculation formula is shown in the following formula:

$$\tau = \frac{4 \times F}{3.14 \times D^2}. \quad (1)$$

In formula (1), $\tau$ is drawing strength (MPa), $F$ is the maximum drawing value (N), and $D$ is the diameter of the puller (mm).

*2.2.2. Shear Strength Test.* The epoxy resin adhesive was evenly applied on the 100 mm × 100 mm surface of three 100 mm × 100 mm × 50 mm cement concrete specimens. After 24 hours of static curing at room temperature, it was

Table 1: Materials.

| Type | Name | Manufacturer |
|---|---|---|
| Main agent | Epoxy resin (E−51) | Zhenjiang Danbao Resin Co. Ltd |
| Curing agent | Polyamide (650 low molecular weight)<br>Phenolic aldehyde amine (T−31) | Zhengzhou Xinjiuda Chemical Products Co. Ltd |
| Toughening agent | Dibutylphthalate | Shandong Yousseo Chemical Technology Co. Ltd |
| Diluent | Butyl glycidyl ether | Changzhou Runxiang Chemical Co. Ltd |
| Coupling agent | Silane coupling agent (KH550) | |
| Filler | Nano-$SiO_2$<br>Nano-$CaCO_3$ | Tianjin Jinxi Chenguang Chemical Welfare Factory<br>Tianjin Tianchenggong Chemical Co. Ltd |

Table 2: Technical indicators of the color ceramic.

| Technology index | Test results |
|---|---|
| Apparent specific gravity | 2.51 |
| Moisture content (%) | 1.1 |
| Mohs hardness | 6.5 |
| Grain size (mm ) | 1~3 |

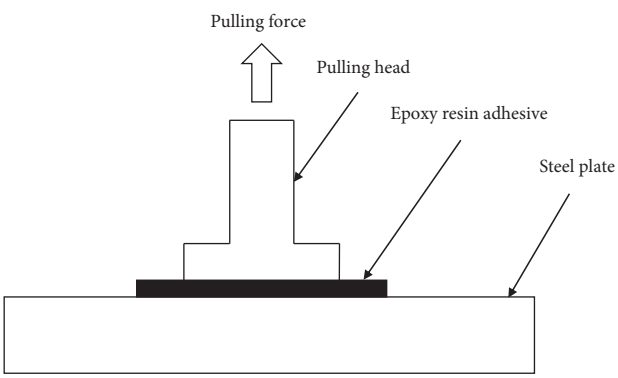


Figure 1: Drawing strength test principle.

placed in a self-made shear fixture, and its shear strength was tested at 1 mm/min:

$$\tau = \frac{F}{S}. \quad (2)$$

In formula (2), $\tau$ is shear strength (MPa), $F$ is shear force (kN), and $S$ is the stress area ($m^2$).

The test principle is shown in Figure 2.

*2.2.3. Bending Strength Test.* Based on "test method of resin casting performance (GB/T 2567–2008)," cuboid epoxy resin castables were prepared, and then, a three-point bending test was carried out.

*2.2.4. Adhesion Test.* According to the low-temperature adhesion test of asphalt and aggregate (T0660-2000), a 2 mm thick epoxy resin adhesive was applied on the central surface of the clean steel plate. Afterward, the color ceramic particles were evenly spread at a spreading amount of 1.8 kg/$m^2$ to form a circle with a radius of 70 mm. After curing at room temperature for 24 hours, the steel balls were dropped from different heights to observe the number of ceramic particles dropped after impact.

*2.2.5. Antiwearing Durability Test.* The self-made indoor accelerated wear equipment (Figure 3) was used, which was mainly composed of a drive system, temperature control system, wheelset system, and control system. The asphalt mixture rut board specimen (300 mm × 300 mm × 50 mm) was prepared, and the surface was laid with a color anti-wearing thin layer. The frequency conversion and wear times were set according to the test speed requirements, and the texture depth in the circular wear zone and the mass loss per unit area of the specimen were measured after different wear times.

## 3. Development of Epoxy Resin Adhesive

*3.1. Effect of Single Material Composition on the Properties of Adhesives.* To get a good application in the pavement, the thin layer material should have excellent bonding performance and effectively deform with the pavement structure without damage. Therefore, a single factor test was designed to analyze the effects of the mass ratio of the epoxy resin to the curing agent (phenolic amine and polyamide) and mass ratio of phenolic amine to polyamide, toughening agent, and diluent on the drawing strength, shear strength, and bending strength of the adhesive. In the test, the content of silane coupling agent (KH550), nano-$SiO_2$, and nano-$CaCO_3$ were 0.5% (extra-mixing). The test factor level design and test results are shown in Table 3, and the following conclusions are drawn .

(1) When the mass ratio of the epoxy resin curing agent increased, drawing strength, shear strength, and bending strength of adhesive firstly increase and then decrease (Figure 4). The reason is that, at the beginning of the mass ratio increase, the amine group in the curing agent causes the epoxy group in the epoxy resin to form a hydroxyl group and then react with the epoxy group to form a network polymer, which improves the overall performance of the adhesive [23, 24]. However, when the mass ratio is further increased, the excess epoxy resin makes the curing agent not have enough amine groups to cure and crosslink with it, and the epoxy resin itself has a low viscosity, which reduces the bonding performance and toughness. In this respect, the mass ratio of the epoxy resin to the curing agent should be about 3.

(2) As the mass ratio of phenolic amine to polyamide increases, the drawing strength and shear strength of

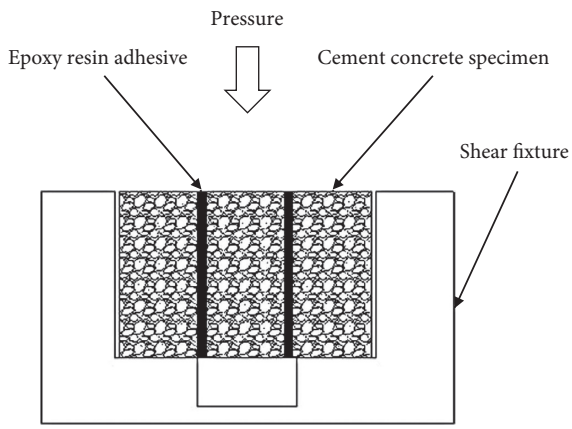


Figure 2: Shear strength test principle.

Table 3: Single factor test.

| Serial number | Mass ratio of epoxy resin to curing agent | Mass ratio of phenolic amine to polyamide | Toughening agent dosage (%) | Diluent content (%) | Drawing strength (MPa) | Shear strength (MPa) | Bending strength (MPa) |
|---|---|---|---|---|---|---|---|
| 1 | 2.0 | 1.5 | 3 | 2 | 4.13 | 1.84 | 59.66 |
| 2 | 3.0 | 1.5 | 3 | 2 | 6.22 | 2.89 | 75.69 |
| 3 | 4.0 | 1.5 | 3 | 2 | 5.19 | 2.34 | 62.3 |
| 4 | 5.0 | 1.5 | 3 | 2 | 3.88 | 1.77 | 48.6 |
| 5 | 3.0 | 1.0 | 3 | 2 | 5.34 | 2.23 | 72.5 |
| 6 | 3.0 | 1.5 | 3 | 2 | 6.22 | 2.89 | 78.36 |
| 7 | 3.0 | 2.0 | 3 | 2 | 6.54 | 2.95 | 80.69 |
| 8 | 3.0 | 2.5 | 3 | 2 | 6.46 | 2.77 | 81.1 |
| 9 | 3.0 | 1.5 | 2 | 2 | 5.88 | 2.44 | 76.2 |
| 10 | 3.0 | 1.5 | 3 | 2 | 6.22 | 2.89 | 80.36 |
| 11 | 3.0 | 1.5 | 4 | 2 | 6.01 | 2.84 | 77.6 |
| 12 | 3.0 | 1.5 | 5 | 2 | 4.87 | 2.56 | 69.1 |
| 13 | 3.0 | 1.5 | 3 | 1 | 6.41 | 3.04 | 79.65 |
| 14 | 3.0 | 1.5 | 3 | 2 | 6.22 | 2.89 | 75.6 |
| 15 | 3.0 | 1.5 | 3 | 3 | 5.51 | 2.55 | 68.45 |
| 16 | 3.0 | 1.5 | 3 | 4 | 3.84 | 1.76 | 54.14 |

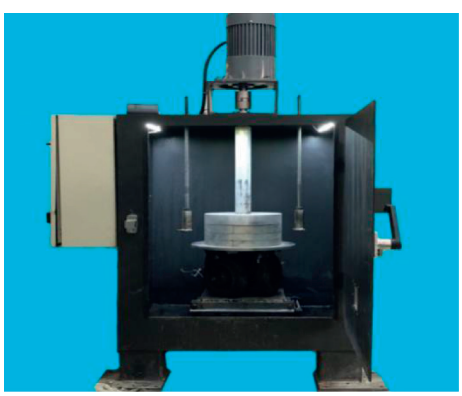

Figure 3: The accelerated wear equipment.

the adhesive gradually increase at the initial stage, but slightly decrease when the mass ratio exceeds 2 (Figure 5). On the contrary, the bending strength gradually increases, but the increase rate slows down when the mass ratio exceeds 2. This is due to the synergistic effect of polyamide and phenolic amine, which can improve the curing degree of the epoxy system and make the network structure formed by the reaction of active groups and epoxy firmer. However, it is possible that phenolic amine can only enhance the performance of the epoxy system within a certain dosage range, and the brittleness of the cured product beyond this range is gradually reflected [25, 26]. Therefore, from this perspective, the mass ratio of phenolic amine to polyamide should not exceed 2.

(3) With the increase in the amount of the toughening agent, the drawing strength, shear strength, and bending strength of the adhesive first increase and then decrease (Figure 6). The reason is that, at the initial stage of the increase in the amount of the toughening agent, the molecular weight of dioctyl phthalate (DBP) is relatively small, which can intersperse between the molecular chains of the epoxy cured product, increasing the mobility of the molecular chains and the spatial freedom of the epoxy resin molecular chain, and improve the toughness

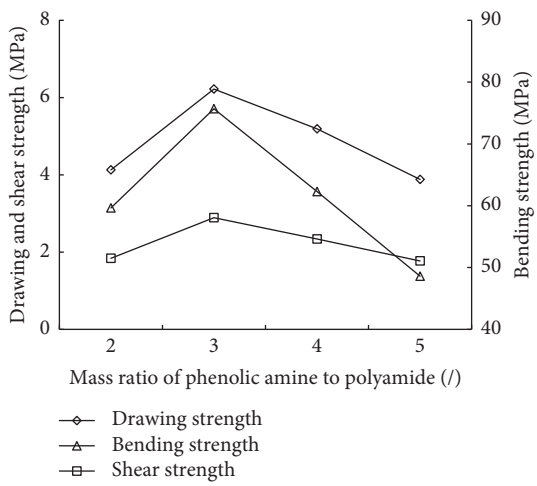


Figure 4: Mass ratio of the epoxy resin to the curing agent.

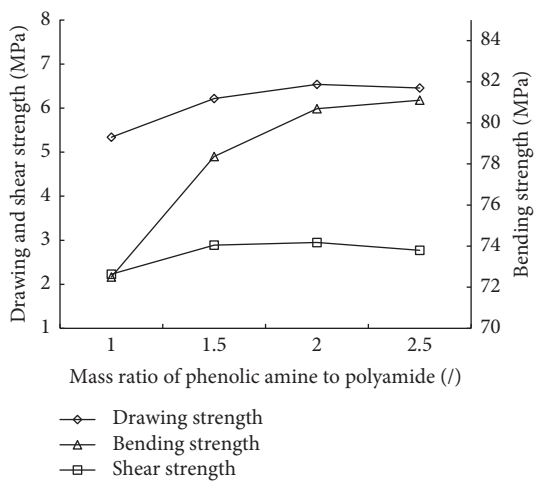


Figure 5: Mass ratio of phenolic amine to polyamide.

and strength. When the dosage is further increased, excessive DBP is incorporated into the epoxy system, and it cannot participate in the curing reaction of the epoxy resin, and there are a large number of small molecules in the cured product. Due to the low viscosity, the mechanical properties of adhesives are reduced to some extent [27]. Therefore, the optimal content of diluent is 3%.

(4) The increase of the content of diluent harms the properties of epoxy resin adhesive. With the increase of the diluent content, the drawing strength, shear strength, and bending strength of the adhesive all show a decreasing trend (Figure 7). This may be because the butyl glycidyl ether diluent belongs to a linear small molecule compound, and the linear chain segment in the molecule after curing reaction weakens the rigid structure of the whole crosslinking network and reduces the mechanical properties. However, from the perspective of construction workability, it is still recommended to add an appropriate amount of diluent [28].

*3.2. Optimization of Adhesive Formulation Based on Response Surface Methodology.* Response surface method is a statistical method of experimental design, which uses a reasonable experimental design to obtain the mathematical expression between design variables and response values through limited experiments, and obtains the optimal number of parameter groups through regression equation analysis, which is widely used in biology, chemistry, industry, engineering, and other fields [29–31]. To optimize the composition ratio of the epoxy resin adhesive, the drawing strength, shear strength, and bending strength are used as response values, and the three-level response surface with four factors including the mass ratio of the epoxy resin to the curing agent, the mass ratio of phenolic amine to polyamide, the content of toughening agent, and the diluent is designed. The factor levels are shown in Table 4, and the test results are shown in Table 5.

Since the single factor method cannot explain the interaction between factors and cannot give a clear model between factors and response values, the Design Expert software is used to perform multiple fitting regression on the test results in Table 5 to obtain the quadratic multinomial regression model which is the model of drawing strength ($X$), shear strength ($Y$), and bending strength ($Z$) on the mass ratio of the epoxy curing agent, the mass ratio of phenolic amine to polyamide, the content of toughening agent, and the diluent:

$$\begin{aligned}
X &= -12.51925 + 8.6345\mathrm{A} + 4.53733\mathrm{B} + 1.05617\mathrm{C} \\
&\quad + 0.743\mathrm{D} + 0.09\mathrm{AB} + 0.0475\mathrm{AC} + 0.0525\mathrm{AD} - 0.15\mathrm{BC} - 0.44\mathrm{BD} \\
&\quad + 0.18\mathrm{CD} - 1.512\mathrm{A}^2 - 1.048\mathrm{B}^2 - 0.21825\mathrm{C}^2 - 0.26575\mathrm{D}^2, \\
Y &= -7.351 + 4.92233\mathrm{A} + 2.378\mathrm{B} + 0.54317\mathrm{C} + 0.36767\mathrm{D} - 0.02\mathrm{AB} \\
&\quad - 0.0075\mathrm{AC} - 0.0225\mathrm{AD} - 0.045\mathrm{BC} - 0.185\mathrm{BD} + 0.0975\mathrm{CD} \\
&\quad - 0.81358\mathrm{A}^2 - 0.55433\mathrm{B}^2 - 0.10733\mathrm{C}^2 - 0.11233\mathrm{D}^2, \\
Z &= -183.50475 + 119.314\mathrm{A} + 66.373\mathrm{B} + 18.22067\mathrm{C} + 9.466\mathrm{D} \\
&\quad + 1.11\mathrm{AB} + 0.1775\mathrm{AC} + 1.0375\mathrm{AD} - 3.334\mathrm{BC} - 6.045\mathrm{BD} + 2.945\mathrm{CD} \\
&\quad - 20.69025\mathrm{A}^2 - 14.376\mathrm{B}^2 - 3.234\mathrm{C}^2 - 4.10025\mathrm{D}^2,
\end{aligned} \tag{3}$$

where $X$ is the drawing strength, MPa, $Y$ is the shear strength, MPa, $Z$ is the bending strength, MPa, A is the mass ratio of the epoxy resin to the curing agent, B is the mass ratio of phenolic amine to polyamide, C is the amount of the toughening agent, %, and D is the dilutant dosage, %.

To test the validity of the regression equation and further determine the influence degree of various factors on the drawing strength, shear strength, and bending strength, the regression equation is analyzed by variance with the drawing strength as an example. The results are shown in Table 6, and from this, we can see the following conclusions.

(1) Model $P < 0.0001$, indicating that this model has a significant effect on the drawing strength. The regression model $R^2 = 0.9814$ indicated that 98.14% of the variation of the response value of the model comes from the selected factors. The model fits well,

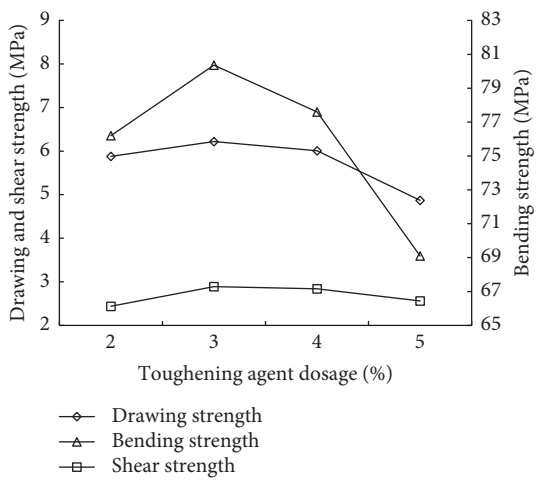


Figure 6: Toughening agent dosage.

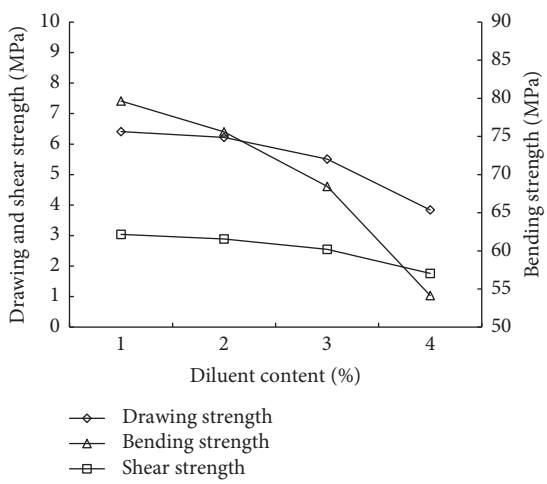


Figure 7: Diluent content.

Table 4: Experimental factors and levels of the response surface.

| Factors | Level | | |
|---|---|---|---|
| | −1 | 0 | 1 |
| Mass ratio of epoxy resin to curing agent | 2.0 | 3.0 | 4.0 |
| Mass ratio of phenolic amine to polyamide | 1.0 | 1.5 | 2.0 |
| Toughening agent dosage (%) | 2.0 | 3.0 | 4.0 |
| Diluent content (%) | 1.0 | 2.0 | 3.0 |

and the regression equation can describe the relationship between the various factors and the response value. The test method is reliable.

(2) According to the $P$ value in the regression model, the influence of a single factor on the response value from large to small is D, B, A, and C. The $P$ value of D is less than 0.0001, which indicates that it has the most significant impact on the drawing strength, the interaction term BD has a more significant impact, and the others are not significant. The quadratic term $A^2$ has the most significant impact, and the others are highly significant, which indicates that various factors have an interactive impact on the drawing strength, rather than a simple linear relationship.

The response surface graph can vividly describe the interaction between the factors. The steeper slope of the response surface indicates that the response value is more sensitive to changes in the ratio. On the contrary, the slope of the curve is gentler, and the change of the ratio has little influence on the response value. The influence of factor interaction on the response value is shown in Figures 8–13 , and from this, we can see the following conclusions.

(1) The interaction surface of the epoxy curing agent mass ratio and phenolic polyamide mass ratio, epoxy curing agent mass ratio and toughening agent content, epoxy curing agent mass ratio, and diluent content is steep, which indicates that the interaction effect on drawing strength is significant. The reason is that the mass ratio of the epoxy resin to the curing agent plays a leading role in the performance of the adhesive, and the effects of different levels of toughener and diluent depend on the level of the mass ratio of the epoxy resin to the curing agent.

(2) The interaction surface of phenolic polyamide mass ratio and toughening agent content, phenolic polyamide mass ratio and diluent content, toughening agent content, and diluent content is gentle, indicating that the interaction on drawing strength is not significant.

As shown in Figure 14, the drawing strength is compared by the test results and the prediction results of the response surface curve model. The results show a good linear relationship, so the model can predict the drawing strength under unknown conditions and seek the optimal solution. Therefore, A is 2.969%, B is 1.903%, C is 2.502%, and D is 1.000%.

In the same way, the shear strength regression equation is analyzed by variance, and based on the model prediction equation, A is 2.977%, B is 1.823%, C is 2.497%, and D is 1.000%. The bending strength regression equation is analyzed by variance, and based on the model prediction equation, the optimal ratio was A is 2.971%, B is 1.940%, C is 2.352%, and D is 1.000%.

On comprehensive consideration of drawing strength, shear strength, and bending strength, using Design Expert software, the three quadratic regression equations are combined. The maximum response value is solved within the variable range of factors, and the optimal ratio of epoxy resin binder is finally obtained. A is 2.971%, B is 1.887%, C is 2.455%, and D is 1.000%.

## 4. Study on Road Performance of Color Antiwearing Thin Layer

*4.1. Adhesion.* The adhesion between adhesive and aggregate is an important index to evaluate the antiwater damage and antiloose ability of the color antiwearing thin layer. Therefore, the steel plates are placed in −15°C, 20°C, 60°C, and 70°C environmental boxes for heat preservation, and the

Table 5: Response surface experimental results.

| Serial number | Mass ratio of epoxy resin to curing agent | Mass ratio of phenolic amine to polyamide | Toughening agent dosage (%) | Diluent content (%) | Drawing strength (MPa) | Shear strength (MPa) | Bending strength (MPa) |
|---|---|---|---|---|---|---|---|
| 1 | 3.0 | 1.5 | 3.0 | 2.0 | 6.14 | 2.94 | 81.35 |
| 2 | 3.0 | 1.5 | 2.0 | 1.0 | 5.98 | 2.84 | 79.14 |
| 3 | 2.0 | 1.0 | 3.0 | 2.0 | 4.36 | 1.96 | 55.96 |
| 4 | 3.0 | 1.0 | 3.0 | 1.0 | 5.47 | 2.68 | 71.63 |
| 5 | 2.0 | 1.5 | 3.0 | 3.0 | 4.14 | 1.99 | 52.69 |
| 6 | 3.0 | 2.0 | 4.0 | 2.0 | 5.56 | 2.61 | 72.45 |
| 7 | 3.0 | 1.5 | 3.0 | 2.0 | 6.07 | 2.95 | 80.11 |
| 8 | 3.0 | 1.5 | 3.0 | 2.0 | 6.10 | 2.96 | 81.33 |
| 9 | 3.0 | 2.0 | 3.0 | 1.0 | 6.49 | 3.12 | 86.34 |
| 10 | 3.0 | 1.5 | 2.0 | 3.0 | 5.05 | 2.44 | 65.23 |
| 11 | 3.0 | 1.5 | 3.0 | 2.0 | 6.11 | 2.76 | 81.45 |
| 12 | 3.0 | 1.0 | 4.0 | 2.0 | 5.51 | 2.59 | 74.35 |
| 13 | 4.0 | 1.5 | 3.0 | 1.0 | 4.28 | 2.01 | 56.3 |
| 14 | 3.0 | 1.5 | 4.0 | 3.0 | 5.62 | 2.68 | 74.10 |
| 15 | 4.0 | 2.0 | 3.0 | 2.0 | 4.39 | 1.88 | 58.60 |
| 16 | 4.0 | 1.5 | 4.0 | 2.0 | 4.44 | 2.01 | 57.44 |
| 17 | 2.0 | 1.5 | 2.0 | 2.0 | 4.41 | 1.95 | 58.63 |
| 18 | 2.0 | 1.5 | 3.0 | 1.0 | 4.57 | 2.06 | 60.14 |
| 19 | 4.0 | 1.0 | 3.0 | 2.0 | 4.08 | 1.77 | 54.20 |
| 20 | 4.0 | 1.5 | 2.0 | 2.0 | 4.36 | 1.93 | 57.36 |
| 21 | 3.0 | 1.5 | 4.0 | 1.0 | 5.83 | 2.69 | 76.23 |
| 22 | 3.0 | 2.0 | 3.0 | 3.0 | 5.25 | 2.45 | 69.36 |
| 23 | 2.0 | 2.0 | 3.5 | 2.0 | 4.49 | 2.11 | 58.14 |
| 24 | 3.0 | 1.0 | 3.5 | 3.0 | 5.11 | 2.38 | 66.74 |
| 25 | 3.0 | 2.0 | 2.5 | 2.0 | 5.76 | 2.77 | 75.98 |
| 26 | 2.0 | 1.5 | 4.5 | 2.0 | 4.30 | 2.06 | 56.86 |
| 27 | 3.0 | 1.0 | 2.5 | 2.0 | 5.41 | 2.66 | 71.2 |
| 28 | 4.0 | 1.5 | 3.5 | 3.0 | 4.06 | 1.85 | 53.00 |
| 29 | 3.0 | 1.5 | 3.5 | 2.0 | 6.00 | 2.88 | 80.00 |

Table 6: Variance analysis of the regression model.

| Source | Quadratic sum | Degrees of freedom | Mean square | *F*-value | *P* |
|---|---|---|---|---|---|
| Model | 16.5698 | 14 | 1.1836 | 52.6813 | < 0.0001 |
| A-a | 0.0363 | 1 | 0.0363 | 1.6158 | 0.2244 |
| B-b | 0.3333 | 1 | 0.3333 | 14.8370 | 0.0018 |
| C-c | 0.0070 | 1 | 0.0070 | 0.3119 | 0.5853 |
| D-d | 0.9577 | 1 | 0.9577 | 42.6272 | < 0.0001 |
| Ab | 0.0081 | 1 | 0.0081 | 0.3605 | 0.5578 |
| Ac | 0.0090 | 1 | 0.0090 | 0.4017 | 0.5364 |
| Ad | 0.0110 | 1 | 0.0110 | 0.4907 | 0.4951 |
| Bc | 0.0225 | 1 | 0.0225 | 1.0015 | 0.3339 |
| Bd | 0.1936 | 1 | 0.1936 | 8.6173 | 0.0109 |
| Cd | 0.1296 | 1 | 0.1296 | 5.7686 | 0.0308 |
| $A^2$ | 14.8290 | 1 | 14.8290 | 660.0569 | < 0.0001 |
| $B^2$ | 0.4453 | 1 | 0.4453 | 19.8189 | 0.0005 |
| $C^2$ | 0.3090 | 1 | 0.3090 | 13.7526 | 0.0023 |
| $D^2$ | 0.4581 | 1 | 0.4581 | 20.3903 | 0.0005 |
| Residual error | 0.3145 | 14 | 0.0225 | | |
| Mismatch items | 0.3032 | 10 | 0.0303 | 10.7141 | 0.0176 |
| Pure error | 0.0113 | 4 | 0.0028 | | |
| Total deviation | 16.8843 | 28 | | | |

steel balls are allowed to fall freely from 50 cm to 100 cm heights, respectively. The number of ceramic particles falling is observed. The test results are shown in Figure 15, and from this, we can see the following conclusions.

(1) Ambient temperature has an important influence on the adhesion of epoxy resin adhesive and ceramic particles, and the adhesion of the thin layer decreases at low temperature. At −15°C, the number of ceramic

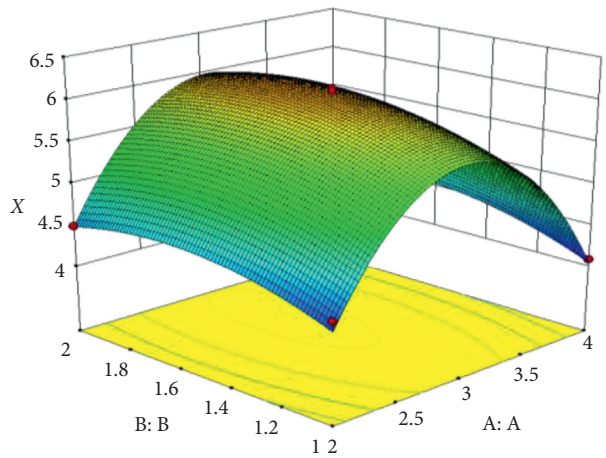


Figure 8: The interaction term AB.

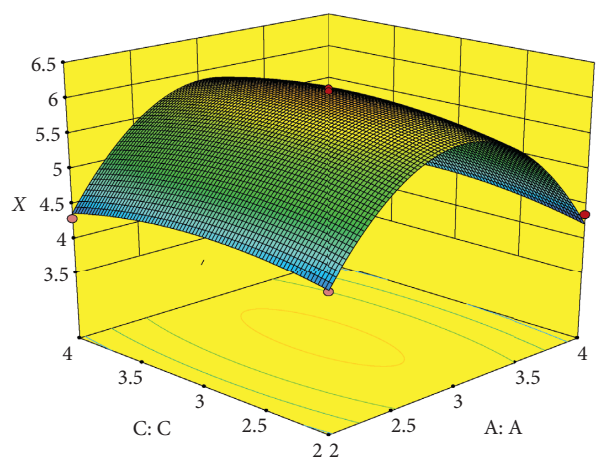


Figure 9: The interaction term AC.

particles falling is 2–10 times that of 20°C, 60°C, and 70°C. This is mainly because the macromolecular chain in the adhesive is frozen under a low-temperature environment, and the crack propagation ability is reduced, and it shows brittle failure under external force. Therefore, winter is the main period for the spalling of the antiwearing thin layer, and the temperature range in an unfavorable season should be considered in the performance evaluation of the antiwearing thin layer.

(2) When the impact load is increased, the adhesion between the epoxy resin adhesive and the ceramic particles decreases, showing that the number of ceramic particles dropped increases. The impact load has a certain temperature sensitivity on the adhesion of epoxy resin adhesive and ceramic particles. When the drop height of the steel ball increases from 50 cm to 100 cm, the number of falling ceramic particles increases by 11 at −15°C. When the temperature exceeds 20°C, the number of ceramic particles dropped increases by 1-2 with the increase of impact load, and the effect of impact load on adhesion decreases.

*4.2. Antiwearing Durability.* The color antiwearing thin layer is affected by wheel impact and other effects in the use process, and the aggregate will drop and polish, which will affect its use effect, so its antiwearing durability is one of the important performances. Therefore, based on the self-made indoor accelerated wear simulation equipment, different degrees of accelerated wear tests are carried out to test the texture depth and mass loss per unit area after wear. The weight ratio of binder to aggregate is 60 : 40. In the test, the ambient temperature is 30°C, the grounding pressure is 0.7 MPa, and the rotation speed is 60 r/min. The test results are shown in Table 7, and from this, we can see the following conclusions.

(1) With the increase of wear times, the wearing resistance of the color antiwearing thin layer decreases gradually. The texture depth decreases from 1.52 mm to 1.14 mm with only 500 times of wear at the initial

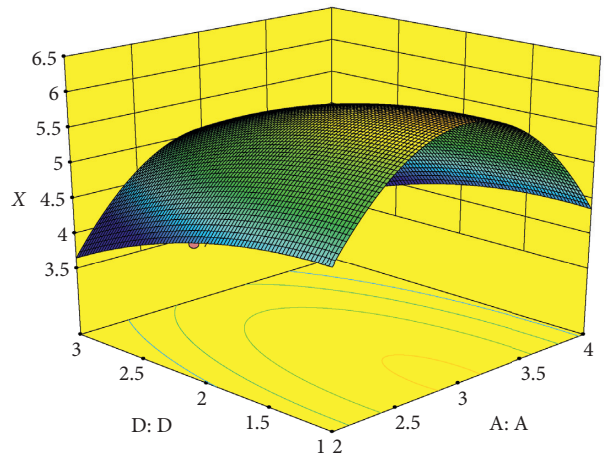


Figure 10: The interaction term AD.

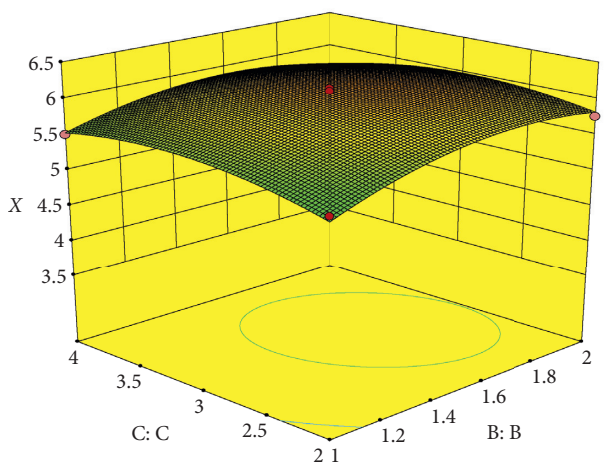


Figure 11: The interaction term BC.

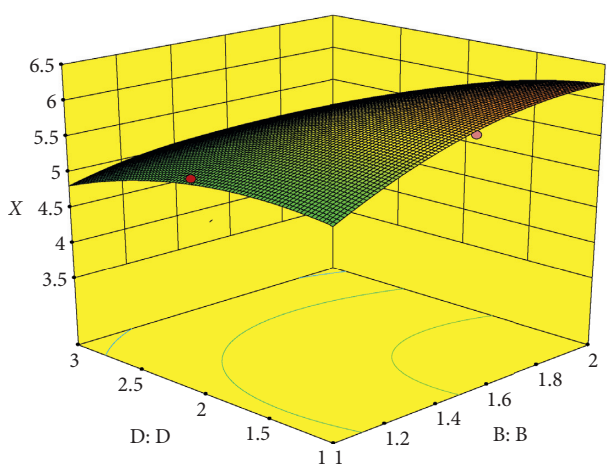


Figure 12: The interaction term BD.

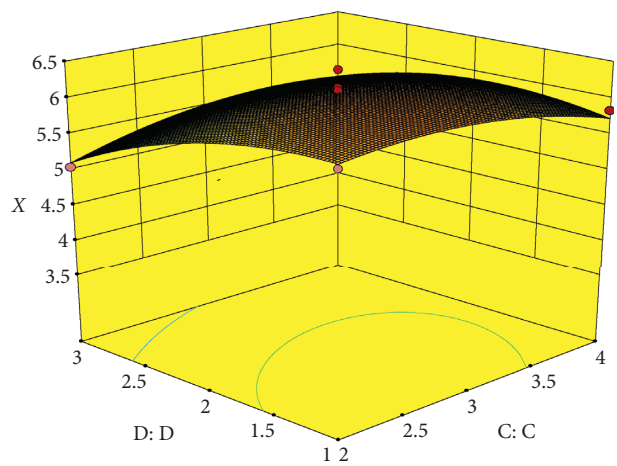


Figure 13: The interaction term CD.

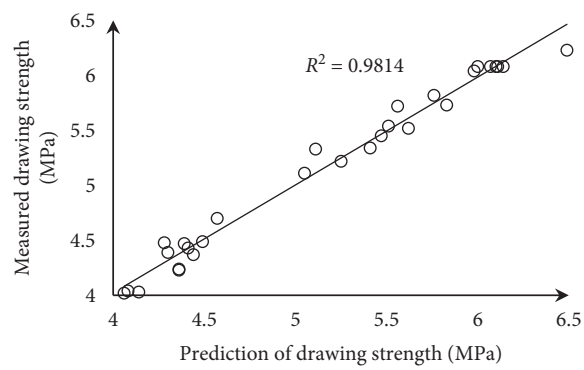


Figure 14: The drawing strength of the test results and the prediction results.

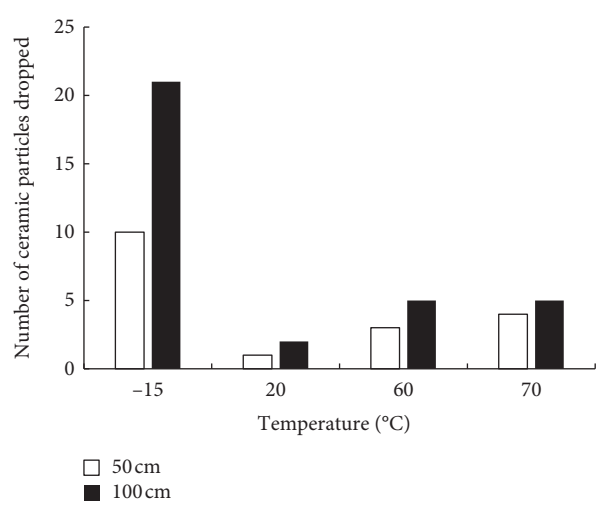


Figure 15: The adhesion of epoxy resin adhesive and ceramic particles.

stage. However, in the later stage, the wear rate is significantly slower, increasing from 500 times to 20,000 times of wear, and the texture depth decreased from 1.14 mm to 0.99 mm (Figure 16). Therefore, the design and evaluation of the antiwearing thin layer should pay attention to the changes in the wear process, rather than focusing on the antiwearing performance at the initial stage.

Table 7: Test results of antiwearing durability.

| Wear times | Texture depth (mm) | Mass loss per unit area (g/cm$^2$) |
|---|---|---|
| 0 | 1.52 | — |
| 500 | 1.14 | 0.015 |
| 2000 | 1.08 | 0.022 |
| 5000 | 1.03 | 0.026 |
| 10000 | 1.01 | 0.028 |
| 20000 | 0.99 | 0.029 |

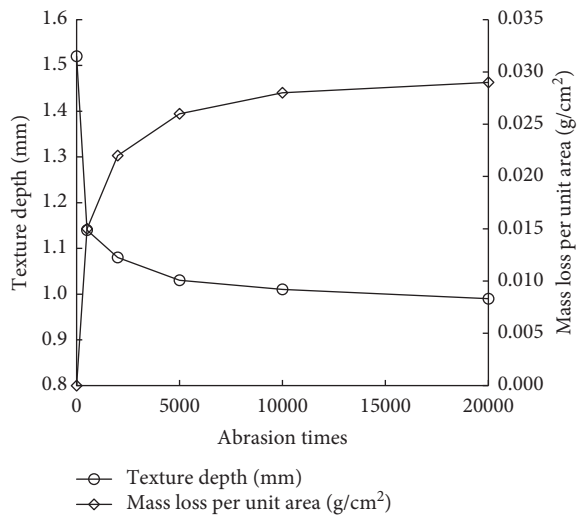


Figure 16: The texture depth and mass loss per unit area of the color nonslip layer under different wear times.

(2) Under the action of traffic load, the wearing resistance performance of the color antiwearing thin layer decreases, which is mainly caused by the drop of aggregate particles in the initial stage, and the mass loss per unit area increases significantly. The mass loss per unit area increases from 0 to 0.015 g/cm$^2$ after 500 wear times. With the further increase of wear times, the mass loss per unit area slows down, which is mainly caused by the surface structure polishing of ceramic particles.

## 5. Conclusion

(1) With the increase of the mass ratio of the epoxy resin to the curing agent and the dosage of the toughening agent, the bonding properties and toughness of epoxy resin adhesives were firstly improved and then decreased. The toughening effect of phenolic amine in the curing agent was only reflected in a certain range. When it exceeded this range, the increase of bending strength was limited, while the drawing strength and shear strength decreased slightly. Diluent harmed the mechanical properties of epoxy resin adhesive, but it was recommended to add an appropriate amount of diluent to improve the construction workability.

(2) Based on the response surface optimization results, the recommended mass ratio of the epoxy resin to a curing agent, mass ratio of phenolic amine to polyamide, toughening agent, and diluent were 2.971%, 1.887%, 2.455%, and 1.000%, respectively.

(3) Adhesion tests showed that temperature had a significant effect on the adhesion between the adhesive and the painted ceramic particles. The adhesion of the thin layer was decreased at low temperature, and the sensitivity to impact load was enhanced. However, both aspects were improved when the temperature exceeded 20°C. The accelerated wear test showed that, with the increase of wear times, the structure depth of the color antiwearing thin layer specimen first decreased rapidly and then decreased slowly, and the mass loss per unit area first increased rapidly, then increased slowly, and finally tended to a certain value. This showed that the color antiwearing thin layer could still maintain good skid resistance performance after repeated wear, which provided a guarantee for driving safety.

## Data Availability

All the data in this paper are checked, which are obtained from tests in this study, and no other data were used to support this study.

## Conflicts of Interest

The authors declare that there are no conflicts of interest regarding the publication of this paper.

## Acknowledgments

This research was financially supported by the National Natural Science Foundation of China (nos. 51878075 and 52008045), Guangxi Natural Science Foundation (2018GXNSFAA294146), Open Fund of Hunan International Scientific and Technological Innovation Cooperation Base of Advanced Construction and Maintenance Technology of Highway Changsha University of Science and Technology (kfj190801), Natural Science Foundation of Hunan Province (2020JJ5595), Guangxi Major Science and Technology Project (Gui Ke AA18242032 and Gui Ke AB19245019), and Scientific Research Project of Hunan Education Department (19C0067).

## References

[1] C. C. Liu, S. T. Lv, D. Z. Jin, and F. T. Qu, "Laboratory investigation for the road performance of asphalt mixtures modified by rock asphalt/styrene butadiene rubber," *Journal of Materials in Civil Engineering*, vol. 33, no. 3, 2021.

[2] S. T. Lv, J. Yuan, X. H. Peng, L. You et al., "Standardization to evaluate the lasting capacity of rubberized asphalt mixtures with different testing approaches," *Construction and Building Materials*, vol. 269, Article ID 121341, 2020.

[3] W. Li, "The future transportation is comprehensive and intelligent—take the 'thirteenth five-year' modern comprehensive transportation system development plan and related research as reference," *China Highway*, vol. 25, no. 5, pp. 72–74, 2018.

[4] M. Gsul, Y. H. Hu, and X. Zhou, "Road traffic safety development report (2017)," *China Emergency Management*, vol. 12, no. 2, pp. 48–58, 2018.

[5] M. J. Feng, T. Wang, and X. S. Wang, "Safety evaluation of combined horizontal and vertical alignments on mountainous freeways," *Journal of Beijing University of Technology*, vol. 44, no. 6, pp. 919–925, 2018.

[6] Y. Yan, Y. Zhang, and G. P. Li, "Comprehensive evaluation of the highway alignment consistency based on the driving speed index characteristic features," *Journal of Safety and Environment*, vol. 17, no. 3, pp. 835–839, 2017.

[7] Q. Li, Y. W. Wang, and G. Q. Li, "Application research on colorful resin anti-sliding thin layer covering technology in Qinghai provincial road S103," *Journal of China & Foreign Highway*, vol. 38, no. 3, pp. 39–43, 2018.

[8] R. W. Lee, J. W. Kim, and D. W. Kim, "Development of color pavement in Korea," *Journal of Transportation Engineering*, vol. 111, no. 3, pp. 292–302, 1985.

[9] M. Xu, X. Pan, and Q. Deng, "Setting method of thin-layer antiskid colored pavement in tunnel based on increasing luminance of pavement," in *Proceeding of the Twelfth COTA International Conference of Transportation Professionals*, Beijing, China, August 2012.

[10] S. Varamini, M. K. Farashah, and S. L. Tighe, "Colored asphalt bus rapid transit lanes in the regional municipality of York: integrating laboratory performance testing into sustainable pavement asset management," in *Proceeding of the 2016 Conference of the Transportation Association of Canada (TAC)*, Toronto, Canada, September 2016.

[11] F. Liu, D. Qu, Z. Tan, C. Yang, and Y. Liu, "Experimental investigation of the effects of four anti-slide particles on the operational performance of coated coloured pavement," *Procedia Engineering*, vol. 161, pp. 589–594, 2016.

[12] Y. Guo, *Study on Development and Performance of Color Ultra-Thin Functional Layer*, Chongqing Jiaotong University, Chongqing, China, 2018.

[13] M. Zhong, "Application of modified epoxy resin thin layer paving in bridge deck maintenance," in *Proceeding of the 2013 Large-Scale Bridge Academic Exchange Conference in Two Provinces and Two Districts*, Guangzhou, China, June 2013.

[14] F. Chen, F. Li, and X. F. Huang, "Adhesive material of anti-slip layer for road Surface and preparation method," China 201410003219.7, 2014.

[15] H. H. Quan, "Color non-slip pavement cured by one-component polyurethane adhesive," China 201420509612.9, 2014.

[16] C. Y. Wu, "Thermoplastic elastomer modified polymethyl methacrylate colored non-slip coating," China 201410712911.7, 2014.

[17] M. Zhong, "Application of modified epoxy resin thin layer paving in bridge deck maintenance," *Journal of China & Foreign Highway*, vol. 33, no. 6, pp. 290–294, 2013.

[18] C. L. Xue, Y. H. Cao, and C. J. Li, "Development and performance research of environment-friendly color non-slip pavement materials," *Highway Traffic Technology (Applied Technology Edition)*, vol. 13, no. 4, pp. 128–131, 2017.

[19] H. Li, *Study on Development and Performance of Color Ultra-Thin Functional Layer*, Hunan University, Changsha, China, 2014.

[20] J. M. Wu, W. Wang, and S. F. Li, "Research on the road performance of epoxy thin layer paving material," *Highway*, vol. 61, no. 10, pp. 225–228, 2016.

[21] D. B. Zhang, C. Xie, and P. Wang, "Application research of chemco epoxy adhesive in colored pavement," *Highways & Automotive Applications*, vol. 32, no. 1, pp. 85–87, 2016.

[22] F. Liu and J. Sun, "What hat are you wearing?" *Auditing Leadership*, vol. 33, no. 1, pp. 183–186, 2015.

[23] J. Li, Y. B. Cai, and J. Li, "Research progress in the biomass curing agents for epoxy resins," *China Adhesives*, vol. 27, no. 11, pp. 58–62, 2018.

[24] P. Wang, G. Sui, and X. P. Yang, "The effect of the stoichiometric ratio of epoxy and amine on the mechanical properties of epoxy/curing agent fabrications," *Composites Science and Engineering*, vol. 40, no. 2, pp. 22–27, 2013.

[25] Y. T. Zhao, Q. H. Rao, and H. L. Zhang, "Research progress of polyamide and cardanol modified amine curing agents for epoxy resin," *Thermosetting Resin*, vol. 32, no. 2, pp. 48–51, 2017.

[26] G. D. Qiu, Y. Qian, B. Zhu, and A. Zhu, "Synthesis and properties of cardanol modified phenolic amide curing agents for epoxy resin," *Paint & Coatings Industry*, vol. 45, no. 8, pp. 34–39, 2015.

[27] Z. P. Liu, H. Niu, and W. J. Li, "Performance research on epoxy/SiC composite material," *New Chemical Materials*, vol. 43, no. 11, pp. 194–196, 2015.

[28] Q. Sun, J. Wang, and H. P. Cai, "Investigation on the effect of reactive diluent type on properties of epoxy resin system," *Composites Science and Engineering*, vol. 38, no. 6, pp. 6–8, 2011.

[29] S. B. Ma, J. Q. Gao, and J. H. Wei, "Structure optimization of stone roadbed asphalt pavement based on response surface method," *Journal of Chongqing Jiaotong University (Natural Science)*, vol. 38, no. 3, pp. 44–50, 2019.

[30] Z. W. Shi and F. Xie, "Experimental research of abrasion resistance of steel fiber reinforced concrete based on response surface analysis method," *Journal of Highway and Transportation Research and Development*, vol. 32, no. 7, pp. 23–27, 2015.

[31] S. B. Ma, Q. F. Yu, and K. Wei, "Research on asphalt pavement overhaul based on response surface," *Highway Engineering*, vol. 40, no. 3, pp. 175–180, 2015.

Hindawi
Advances in Civil Engineering
Volume 2021, Article ID 6657786, 8 pages
https://doi.org/10.1155/2021/6657786

*Research Article*

# Analysis Model of Risk Factors of Urban Bus Operation Based on FTA-CLR

**Jianfeng Xi**,[1] **Yunhe Zhao**,[1] **Tongqiang Ding**,[1] **Jian Tian**,[2] **and Lianjie Li**[1]

[1]*College of Transportation, Jilin University, Changchun 130022, China*
[2]*China Academy of Transportation Sciences, Beijing 100029, China*

Correspondence should be addressed to Tongqiang Ding; dtq8@163.com

Received 8 December 2020; Revised 27 April 2021; Accepted 13 May 2021; Published 27 May 2021

Academic Editor: Hui Yao



In order to comprehensively analyze the risk factors and accurately find the high risk factors related to accidents, an analysis model of risk factors of urban bus operation is proposed, in which the advantages of the structural analysis of the Fault Tree Analysis (FTA) and the correlation analysis of the Cumulative Logistic Regression (CLR) are combined. Firstly, based on the accident data in Northeast China, FTA is used to compile the urban bus operation fault tree. In the fault tree, 16 bus operation risk factors are classified, while the risk factors are sorted and compared from three aspects: structural importance, probability importance, and critical importance. And then, the 11 higher risk factors are selected according to the discriminant principle. Secondly, bus operation accidents are divided into fatal accidents, injury accidents, and major economic loss accidents. The CLR model is used to fit the much higher risk factors that lead to urban bus operation accidents from above 11 higher risk factors. Finally, the scientific rationality and applicability of the model are verified, through the goodness of fit test and the comparison test with the actual probability of occurrence.

## 1. Introduction

Due to the large number of passengers transported by bus, casualties are extremely likely to occur in event of an operation accident. Furthermore, the characteristics of urban bus operation accidents are different from other forms of road traffic, so the risk factors of bus operation accidents have become people's main concerns. Some scholars conduct research on the influence degree of road infrastructure on public transportation safety, the characteristics and weights of basic indicators of urban public transportation, factors affecting the safety of bus operations, and preventive and improvement measures [1–3]. Some scholars explore the relationship between the personality characteristics of bus drivers, driving behaviors, and accident risk [4, 5]. Other scholars explore bus accidents in the United States and find out that the severity of bus accidents is related to the age, gender, and dangerous driving behavior of bus drivers [6]. For the analysis of traffic safety and the causes of traffic accidents, the scholar uses the Fuzzy Fault Tree Analysis to evaluate the safety of the public transportation system [7].

A considerable number of authors research on bus crash severity in recent years. In order to cluster bus crash data by dividing them into homogeneous categories, some scholars analyse data involved bus crashes in the State of Victoria, Australia, in which the factors affecting fatality in bus involved crashes are extracted by implementing association rules discovery on the clusters [8]. In order to solve the problem of the lack of reporting of some of the factors involved in the crash and the nonuniform distribution of factors affecting the crashes leading to the inherent heterogeneity of crash data, the Latent Class Cluster (LCC) regression approach is used to reveal important, formerly hidden relationships in traffic safety analyses [9, 10]. Furthermore, Fault Tree Analysis (FTA) and Bayesian network are widely used in accident Analysis, and many successful applications are found in the fields of transportation, fuel cell degradation, biogas system, chemical safety, and power distribution [11–14]. In particular, some scholars compile a road traffic fault tree using the Fault Tree Analysis method, find out the influencing factors of road traffic accidents, and

analyse the key influencing factors of the severity of the accident with the Logistic model [15]. Due to the fact that our focus is to excavate and rank all the accident risk factors for urban bus operations as well as the insufficient data about the type and severity of injuries of urban bus operations, the FTA with the advantages of structural analysis is a suitable method.

Then, other scholars believe that it is necessary to classify traffic accidents in order to enhance the homogeneity of accident data [16]. Some scholars use the Probit model, the Binomial Logistic model, and the Multinomial Logistic model to analyse the factors affecting the severity of accidents at three-way and four-way no signal intersections [17]. Because of the good applicability of the Logistic Regression model, it can better assess risk factors of bus involved accident severity including both discrete and continuous variables. Feng et al. divide drivers in US bus accidents into three categories, no traffic violation records, traffic violation records (middle-aged), and traffic violation records (young and old), and analyse the factors affecting the severity of accidents in each category of drivers [18]. Nasri and Aghabayk investigate the underlying risk factors associated with the severity of urban transit bus accidents in Mashhad, Iran, by estimating a binary logit model, in which the accident severity is divided into PDO (Property Damage Only) and injury or fatal categories, and the effect of several risk factors on the probability of bus accidents with higher severity is examined [19]. Some scholars use the real bus operation accident data in Guangdong Province of China as an example and use the Binomial Logistic model to analyse the factors affecting the severity of bus accidents from four scenarios: overall accidents, intervehicle accidents, vehicle-pedestrian accidents, and single-vehicle accidents [20].

FTA can well dig out all the risk factors of accidents based on urban bus operation characteristics, classify all factors, and present them clearly in a structured manner. In addition, CLR would get the desirable analysis results depending on the suitable set of risk factors. In this research, it is not only necessary to dig out all the accident risk factors of urban bus operation but also it is needed to sort all risk factors and find higher risk factors by the Pearson $\chi^2$ statistic and Deviance statistic goodness of fit test. Therefore, this paper combines FTA and CLR to find out the higher risk factors of urban bus operation accidents.

## 2. Materials and Methods

Because the operating environment of urban buses is more complex and involves many influencing factors, FTA can classify the risk factors that lead to accidents of urban bus operation. The determination of the minimum cut set can present the set of each risk factor to clarify the structural importance of each risk factor. However, the analysis of structural importance only analyses the impact of each risk factor on bus operation accidents according to the structure of the fault tree. What we are concerned about is the impact of the occurrence probability of each risk factor on the probability of bus operation accidents and how to measure which is easier to reduce the risk factors with high probability or low probability. Therefore, the probability importance and critical importance of each risk factor have practical significance to the extraction of high risk factors. There are a number of requirements and assumptions in using Logistic Regression models. The most important ones of them are IIA (Independence of Irrelevant Alternatives), linearity of independent variables and log odds, little or no multicollinearity among the independent variables, and the independence of the observations. Even so, it is flexible in application and simple in calculation, which can make the results of the analysis more objective. The utilized data in this article could meet these requirements and assumptions. The existing classification of the severity of traffic accidents is mostly based on the most severe injury imposed on the passengers. In fact, heavy economic losses should also be an important consideration in the severity of the accident. Since the dependent variable is set for multiple values, and the independent variable includes both discrete and continuous variables, the Cumulative Logistic model in the multivariate Logistic model is the most appropriate.

Based on the above reasons, an analytical model of the risk factors of urban bus operation is constructed. The steps of the FTA-CLR analysis model are as follows.

The first step is to compile the fault tree. Based on the bus operation accident data in a certain area, the accident is regarded as the top event. According to accident types and causes, risk factors are classified and connected with "OR" 

or "AND" 

.

Then, the next top events are analysed until the basic events can no longer be separated.

The second step is the calculation of importance. Three kinds of importance are calculated, which are structural importance, probability importance, and critical importance.

*2.1. Structural Importance.* Boolean algebra [21] is used to solve the minimum cut set of the fault tree of bus operation accidents. Formula (1) [22] is used to calculate the coefficient of structural importance of risk factors. The greater the value of $I_\varphi(i)$, the greater the structural importance coefficient. According to the criterion of structural importance, if the minimum cut set contains only one basic event, the structural importance of the risk factor represented by the basic event is the largest. If the minimum cut set contains inconsistent basic events, the structural importance of the risk factors represented by the basic events of the minimum cut set with fewer basic events is large:

$$I_\varphi(i) = \sum_{X_i \in G_r} \frac{1}{2^{n_i - 1}}, \tag{1}$$

where $I_\varphi(i)$ represents the structural importance coefficient of the basic event $X(i)$. $n_i$ represents the minimum cut set capacity of the basic event $X(i)$. $G_r$ represents the minimum cut set containing the basic event $X(i)$.

*2.2. Probability Importance.* Formula (2) [23] is used to find out the degree which means the change in the probability of the i-th basic event on the change in the probability of the top event. It is the coefficient of probability importance of risk factors. The larger the value of $I_g(i)$, the higher the probability of the basic event:

$$I_g(i) = \frac{\partial P(T)}{\partial q_i}, \tag{2}$$

where $I_g(i)$ is the probability importance coefficient of the basic event $X(i)$. $P(T)$ represents the occurrence probability function of the top event. $q_i$ represents the probability of occurrence of the i-th basic event $X(i)$, which is calculated based on the data of bus operation accidents.

*2.3. Critical Importance.* Formula (3) [23] is used to measure the importance of each basic event in terms of sensitivity and its own probability of occurrence. It is the coefficient of the critical importance of risk factors. The larger the value of $I_g^c(i)$, the greater impact on the probability of occurrence of the top event:

$$I_g^c(i) = \frac{q_i}{p(T)} I_g(i), \tag{3}$$

where $I_g^c(i)$ represents the critical importance coefficient of the i-th basic event. $p(T)$ represents the probability of occurrence of the top event.

The third step is sorting and analysis. The risk factors are sorted by structural importance coefficient, probability importance coefficient, and critical importance coefficient. After the coefficients are normalized, higher risk factors are selected according to the discriminant principle. Discriminant principle: ① the order of structural importance coefficient and probability importance coefficient is the main basis, and the critical importance coefficient is the auxiliary basis and ② in the order of the main basis, the cumulative sum of the normalized index of each importance is above 90%.

The fourth step is to analyse the severity of bus operation accidents based on the CLR. The probability calculation model is shown in formula (4) [15]. The mixed stepwise selection method [15] is used to gradually eliminate independent variables with insignificant coefficients. That is independent variables with a significant level of Sig. < 0.05, and through correlation analysis to determine significantly related risk factors:

$$P\left(Y \le \frac{j}{X}\right) = \frac{e^{\alpha_i + \sum_{j=1}^{j} \beta_{ij} X_i}}{1 + e^{\alpha_j + \sum_{j=1}^{j} \beta_{ij} X_i}}, \tag{4}$$

where $\sum_{j=1}^{j} P(y = j/X) = 1, j = 1, 2, \ldots, j-1$, $P(Y \le j/X)$ is cumulative probability. $X$ contains $i$ independent variables, such as $X_1, X_2, \ldots, X_{\mathrm{i}}$. $I$ is the number of independent variables. $\alpha_{\mathrm{i}}$ is a constant term. $\beta_{ij}$ is the regression coefficient.

The fifth step is the model test. According to the Pearson $\chi^2$ statistic and Deviance statistic goodness of fit test [24], if the significance level of the Pearson $\chi^2$ statistic and Deviance statistic is more than 0.05, it indicates that the model fits well. Then, compare the predicted probability of the accident type calculated by the model with the actual probability to determine its accuracy.

The FTA-CLR model analysis process is shown in Figure 1.

## 3. Results and Discussion

*3.1. Compilation of Fault Tree.* Taking the data of bus operation accidents in Northeast China as an example, the basic events of urban bus operation accidents are summarized, and the fault tree of urban bus operation is compiled.

Because the cause of urban bus operation accidents is related to many factors, accidents of urban bus operation are divided into two types: traffic accidents and service accidents. Therefore, the accident is regarded as the top event; the fault tree of traffic accidents and the fault tree of service accidents are compiled separately. There are three main forms of bus operation accidents: vehicle-fixed object, vehicle-pedestrian, and vehicle-vehicle. Any one of them will cause accidents, so the OR door is used to connect. Continue to use this method to analyse subtop events until the basic events can no longer be separated. At this point, the construction of the fault tree of traffic accidents is completed. The construction method of fault tree of service accidents is the same. The fault tree of traffic accidents and the fault tree of service accidents are shown in Figures 2 and 3, respectively.

*3.2. Calculation of Importance.* Because service accidents of the urban bus generally do not cause serious accidents, this paper only analyses the risk factors that may cause serious accidents in urban bus operation. The minimum cut set of the fault tree of traffic accidents in urban bus operation is obtained as follows:

G1 = $\{X_1\}$, G2 = $\{X_2\}$, G3 = $\{X_3\}$, G4 = $\{X_4\}$, G5 = $\{X_5\}$, G6 = $\{X_8\}$, G7 = $\{X_{12}\}$, G8 = $\{X_{13}\}$, G9 = $\{X_{14}\}$, G10 = $\{X_2X_{10}\}$, G11 = $\{X_9X_{10}\}$, G12 = $\{X_4X_{11}X_{10}X_{15}\}$, G13 = $\{X_6X_{11}X_{10}X_{15}\}$, G14 = $\{X_7X_{11}X_{10}X_{15}\}$, G15 = $\{X_{16}X_{11}X_{10}X_{15}\}$.

A total of 15 minimum cut sets of risk factors of traffic accidents in urban bus operation are obtained, of which there are 9 minimum cut sets of a single factor. It shows that if one of the influencing factors exists in the actual operation of the urban bus, it is very likely to cause traffic accidents. Then, it is of practical significance to find out the higher risk factors leading to bus operation accidents.

The structural importance coefficients of the risk factors affecting accidents of urban bus operation are obtained. As shown in the second column of Table 1, the order is as follows:

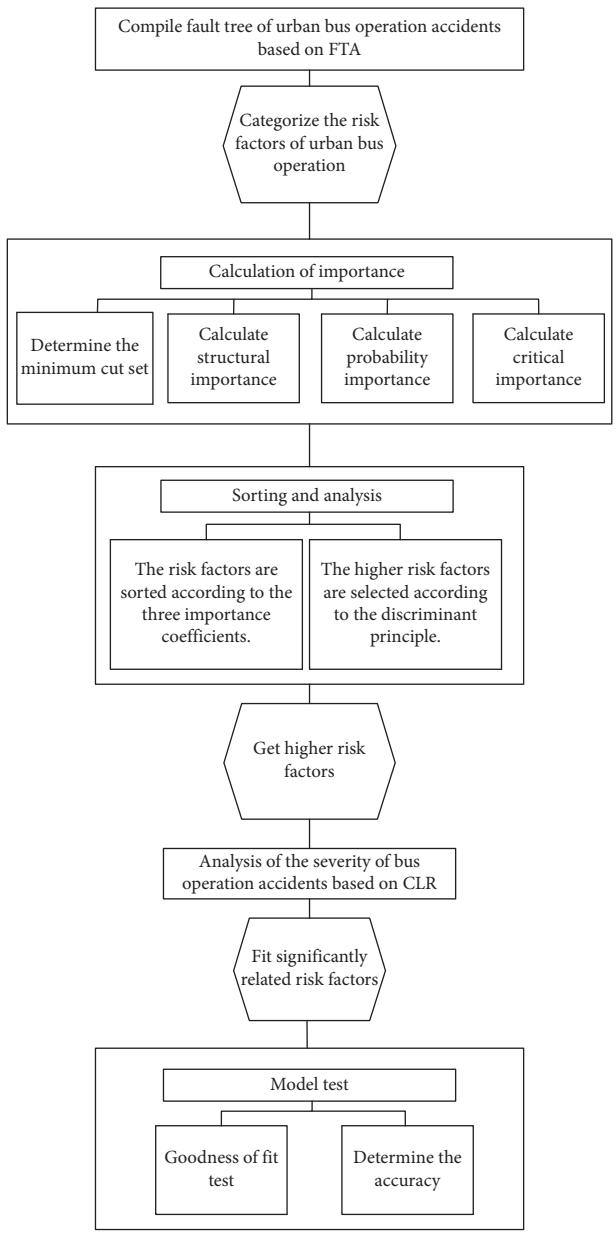


Figure 1: FTA-CLR model analysis process.

$$I_\varphi(2) = I_\varphi(10) > I_\varphi(4) > I_\varphi(1) = I_\varphi(3) = I_\varphi(5) = I_\varphi(8) = I_\varphi(12) = I_\varphi(13) = I_\varphi(14) > I_\varphi(9) = I_\varphi(11) = I_\varphi(15) > I_\varphi(6) = I_\varphi(7) = I_\varphi(16). \tag{5}$$

The probability importance coefficients of the risk factors affecting accidents of urban bus operation are obtained. As shown in the third column of Table 1, the order is as follows:

$$I_g(13) > I_g(2) > I_g(10) > I_g(1) > I_g(4) > I_g(14) > I_g(5) > I_g(3) = I_g(8) > I_g(9) = I_g(12) > I_g(15) > I_g(11) > I_g(6) = I_g(7) = I_g(16). \tag{6}$$

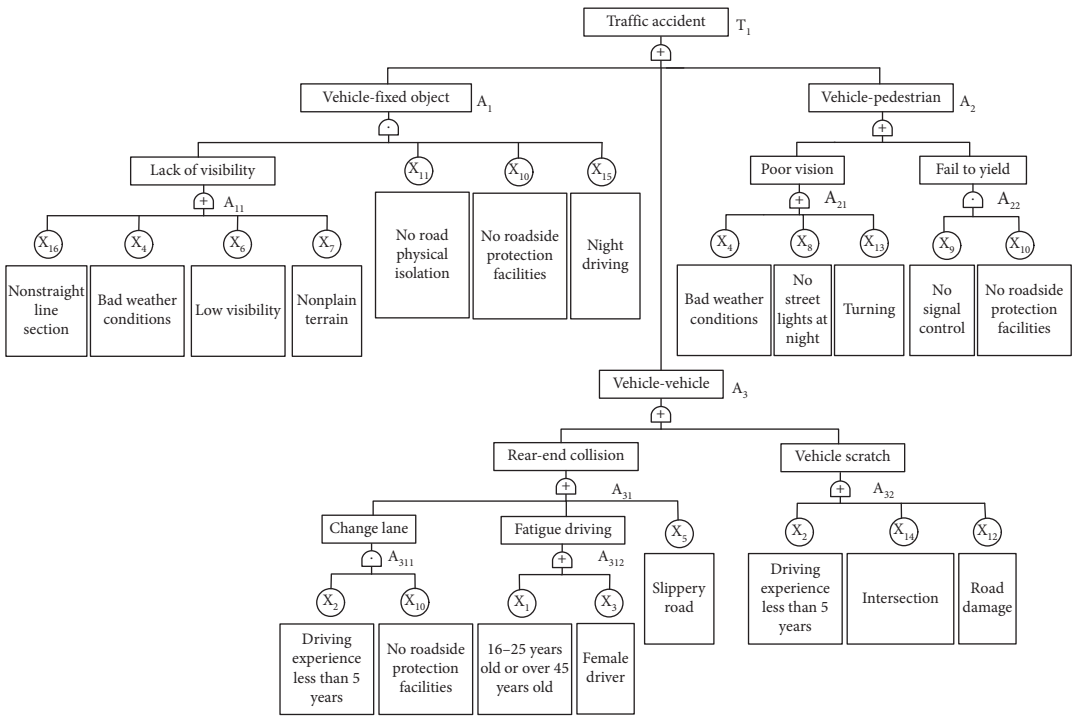


Figure 2: Fault tree of traffic accidents in urban bus operation.

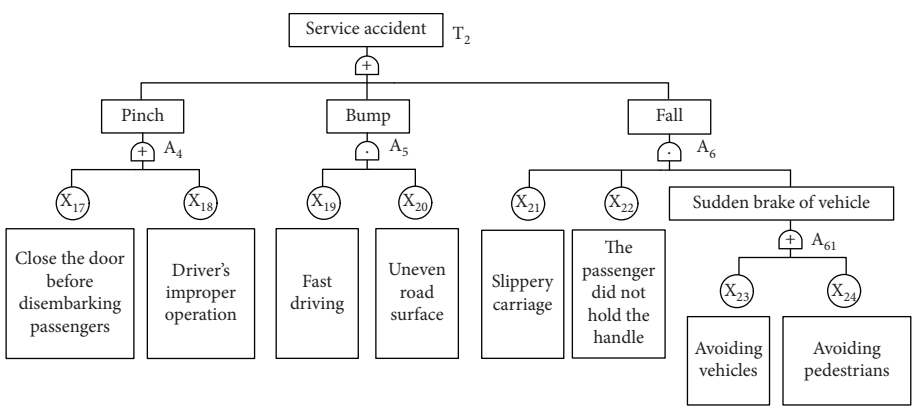


Figure 3: Fault tree of service accidents in urban bus operation.

The critical importance coefficients of the risk factors affecting accidents of urban bus operation are obtained. As shown in the fourth column of Table 1, the order is as follows:

$$I_g^c(13) > I_g^c(2) > I_g^c(10) > I_g^c(9) > I_g^c(1) = I_g^c(4) > I_g^c(14) > I_g^c(5) > I_g^c(11) = I_g^c(15) > I_g^c(3) = I_g^c(8) > I_g^c(6) > I_g^c(12) > I_g^c(7) > I_g^c(16). \tag{7}$$

*3.3. Sorting and Analysis.* 16 risk factors are obtained by classifying the basic events determined by the bus traffic fault tree. The analysis of structural importance, probability importance, and critical importance is carried out. According to the sorting order of the main basis, the cumulative sum of the normalized index of each importance is shown in Table 2.

It can be seen that the cumulative sum of the normalized index of each importance of the first 11 risk factors is above 90%. At the same time, from the first 11 to 12 risk factors, the increase of the cumulative sum of the normalized index based on the critical importance is not obvious. Therefore, the first 11 risk factors are selected as higher risk factors. They are 16–25 years old or older, have less than 5 years of

Table 1: Importance coefficient of risk factors of urban bus operation accidents.

| Risk factors | Structural importance coefficient | Probability importance coefficient | Critical importance coefficient |
|---|---|---|---|
| Age $X_1$ | 1 | 0.0115 | 0.0028 |
| Driving experience $X_2$ | 1.5 | 0.0386 | 0.0257 |
| Gender $X_3$ | 1 | 0.0093 | 0.0005 |
| Weather $X_4$ | 1.125 | 0.0113 | 0.0020 |
| Road table conditions $X_5$ | 1 | 0.0103 | 0.0015 |
| Visibility $X_6$ | 0.125 | 0.0007 | 0.0004 |
| Terrain $X_7$ | 0.125 | 0.0007 | 0.0002 |
| Lighting conditions $X_8$ | 1 | 0.0093 | 0.0005 |
| Traffic signal mode $X_9$ | 0.5 | 0.0091 | 0.0034 |
| Roadside facilities protection type $X_{10}$ | 1.5 | 0.0168 | 0.0127 |
| Road physical isolation $X_{11}$ | 0.5 | 0.0010 | 0.0007 |
| Road condition $X_{12}$ | 1 | 0.0091 | 0.0003 |
| Driving state $X_{13}$ | 1 | 0.0441 | 0.0357 |
| Intersection or section $X_{14}$ | 1 | 0.0106 | 0.0018 |
| Driving period $X_{15}$ | 0.5 | 0.0051 | 0.0007 |
| Road alignment $X_{16}$ | 0.125 | 0.0007 | 0.0001 |

Table 2: The cumulative sum of the normalized index.

| Number of risk factors | Structural importance (%) | Probability importance (%) | Critical importance (%) |
|---|---|---|---|
| 10 | 86 | 91 | 97 |
| 11 | 90 | 96 | 98 |
| 12 | 93 | 98 | 98 |

Table 3: Coding and meaning of independent variables.

| Symbol | Meaning | Coding and assignment |
|---|---|---|
| $X_1$ | Age | 16–25 years old = 1; 26–35 years old = 2; 36–45 years old = 3; 46–55 years old = 4; 56 years old and above = 5 |
| $X_2$ | Driving experience | 1–5 years = 1; 5–10 years = 2; 10–15 years = 3; 15–20 years = 4; more than 20 years = 5 |
| $X_3$ | Gender | Female = 0; male = 1 |
| $X_4$ | Weather | Sunny = 0; nonsunny (rain, snow, fog, overcast, strong wind, etc.) = 1 |
| $X_5$ | Road table conditions | Dry = 0; not dry (rain, snow, ice) = 1 |
| $X_8$ | Lighting conditions | Daytime = 1; street light at night = 2; No street light at night = 3 |
| $X_9$ | Traffic signal mode | Signal control = 0; no signal control = 1 |
| $X_{10}$ | Roadside facilities protection type | Without roadside protection = 0; With roadside protection = 1 |
| $X_{12}$ | Road condition | Road surface is intact = 0; Road surface damage = 1 |
| $X_{13}$ | Driving state | Nonstraight = 0; straight = 1 |
| $X_{14}$ | Intersection or section | Road section = 0; intersection = 1 |

driving experience, female driver, nonsunny and low visibility, slippery road, no street lighting at night, no signal control, no protective facilities on the roadside, damaged road surface, driving straight, and driving at intersections.

### 3.4. Severity Analysis Based on CLR

*3.4.1. Dependent Variable.* When studying the significantly related risk factors of urban bus accidents, this paper lists only major economic losses into the classification of urban bus accidents. This paper comprehensively divides the severity of bus operation accidents into three levels. The code is $Y = 1$ for fatal accidents, $Y = 2$ for injury accidents, and $Y = 3$ for only major economic loss accidents.

*3.4.2. Independent Variable.* Based on the analysis of the importance of basic events in the bus operation fault tree compiled in this paper, from the perspective of people,

Table 4: Model calibration results.

| Parameter | | Reference category | Fatal accident | | Injury accident | |
|---|---|---|---|---|---|---|
| | | | B | Sig. | B | Sig. |
| Driving experience | 1–5 years | More than 20 years | −16.293 | 0.006 | −16.747 | 0.001 |
| | 5–10 years | | −17.140 | 0.006 | −17.111 | 0.001 |
| | 10–15 years | | −17.269 | 0.006 | −17.330 | 0.000 |
| | 15–20 years | | −17.648 | 0.006 | −18.139 | 0.001 |
| Lighting conditions | Daytime | No street light at night | −0.748 | 0.000 | 0.049 | 0.000 |
| | Street light at night | | −0.156 | 0.000 | 0.704 | 0.000 |
| Traffic signal mode | Signal control | No signal control | 0.074 | 0.021 | 17.392 | 0.000 |
| Driving state | Nonstraight | Straight | −0.995 | 0.015 | −0.601 | 0.005 |
| Constant | | | 19.408 | 0.000 | 20.049 | 0.005 |

Table 5: Accuracy of predicting severity of urban bus operation accidents.

| Loss accident | Fatal accident (%) | Injury accident (%) | Only major economic (%) |
|---|---|---|---|
| Predicted probability | 26.49 | 65.54 | 7.97 |
| Actual probability | 28.99 | 67.96 | 3.05 |
| Error | 2.5 | 2.42 | 4.92 |

vehicles, roads, and environment in the transportation system, 11 independent variable factors are determined. The independent variable coding is shown in Table 3.

*3.4.3. Fitting.* The independent variables with significance level Sig. < 0.05 are gradually eliminated. Through correlation analysis, 4 significantly related risk factors are determined. There are driving experience ($X_2$), lighting conditions ($X_8$), traffic signal mode ($X_9$), and driving state ($X_{13}$). The model calibration results are shown in Table 4.

*3.5. Model Test.* In this way, the Cumulative Logistic probability prediction model of urban bus fatal accidents and injury accidents is obtained. The results of goodness of fit test show that the Pearson $\chi^2$ statistic has a significant level of 0.998 > 0.05, and the Deviance statistic has a significant level of 0.969 > 0.05. It shows that the model fits well.

Then, 1390 cases of the data of urban bus accidents with complete information in Northeast China are selected. The Cumulative Logistic probability prediction model constructed in this paper is used to predict and calculate. The predicted probabilities of fatal accidents, injury accidents, and only major economic loss accidents are compared with the actual probability of occurrence, as shown in Table 5. From the comparative analysis, it can be seen that the errors are less than 5%, which shows that the accuracy of the constructed model for predicting the severity of urban bus operation accidents is relatively high.

## 4. Conclusions

(1) Combining the respective advantages of the Fault Tree Analysis and Cumulative Logistic Regression, an analysis model of risk factors of urban bus operation based on FTA-CLR is proposed. It could analyse the risk factors of urban bus operation accidents in more detail.

(2) Taking the accident data of urban bus operation in Northeast China as an example, the risk factors are analysed according to the steps of the FTA-CLR analysis model, in which the driving experience, lighting conditions, traffic signal mode, and driving state are the first 4 higher factors. Through the goodness of fit test and the actual probability of occurrence comparison test, the scientific rationality and applicability of the model are verified.

(3) The analysis results of the model could provide a reference for identifying high risk factors of urban bus operations in different regions. The analysis of risk factors can also provide some bases for taking the countermeasures of urban bus accidents.

## Data Availability

The data used to support the findings of this study are available from the corresponding author upon request.

## Conflicts of Interest

The authors declare that they have no conflicts of interest.

## Acknowledgments

The work was funded by the National Natural Science Foundation of China (Grant no. 51308249).

## References

[1] P. Chen, X. Liu, and J. G. Qiao, "The research of public traffic safety evaluation system," *Applied Mechanics and Materials*, vol. 253-255, pp. 1855–1859, 2012.

[2] Y. Zhou and Q. Zhang, "The safety evaluation of the urban public transport based on the gray model," in *Proceedings of the 2011 International Conference on Remote Sensing, Environment and Transportation Engineering (RSETE)*, Nanjing, China, June 2011.

[3] J. G. Strathman, P. Wachana, and S. Callas, "Analysis of bus collision and non-collision incidents using transit ITS and other archived operations data," *Journal of Safety Research*, vol. 41, no. 2, pp. 137–144, 2010.

[4] L. Mallia, L. Lazuras, C. Violani, and F. Lucidi, "Crash risk and aberrant driving behaviors among bus drivers: the role of personality and attitudes towards traffic safety," *Accident Analysis & Prevention*, vol. 79, no. 35, pp. 145–151, 2015.

[5] X. Shi and L. Zhang, "Effects of altruism and burnout on driving behavior of bus drivers," *Accident Analysis & Prevention*, vol. 102, pp. 110–115, 2017.

[6] S. Kaplan and C. G. Prato, "Risk factors associated with bus accident severity in the United States: a generalized ordered logit model," *Journal of Safety Research*, vol. 43, no. 3, pp. 171–180, 2012.

[7] L. Li, *Study on the Safety Evaluation of Urban Conventional Public Transport Operation System*, Jilin University, Jilin, China, 2020.

[8] S. A. Samerei, K. Aghabayk, A. Mohammadi, and N. Shiwakoti, "Data mining approach to model bus crash severity in Australia," *Journal of Safety Research*, vol. 76, pp. 73–82, 2021.

[9] L. Yang and W. David, "Modelling severity of pedestrian-injury in pedestrian-vehicle crashes with latent Class clustering and partial proportional odds model: a case study of North Carolina," *Accident Analysis and Prevention*, vol. 131, pp. P284–P296, 2019.

[10] S. Ming, X. Suna, and D. Shan, "Pedestrian crash analysis with latent class clustering method," *Accident Analysis & Prevention*, vol. 124, pp. P50–P57, 2019.

[11] G. Zhang, V. V. Thai, K. F. Yuen, H. S. Loh, and Q. Zhou, "Addressing the epistemic uncertainty in maritime accidents modelling using Bayesian network with interval probabilities," *Safety Science*, vol. 102, pp. 211–225, 2018.

[12] L. Placca and R. Kouta, "Fault tree analysis for PEM fuel cell degradation process modelling," *International Journal of Hydrogen Energy*, vol. 36, no. 19, pp. 12393–12405, 2011.

[13] S. Cheng, Z. Li, H.-P. Mang, K. Neupane, M. Wauthelet, and E.-M. Huba, "Application of fault tree approach for technical assessment of small-sized biogas systems in Nepal," *Applied Energy*, vol. 113, pp. 1372–1381, 2014.

[14] F. A. Rahman A. Varuttamaseni et al., "Application of fault tree analysis for customer reliability assessment of A distribution power system," *Reliability Engineering & System Safety*, vol. 111, pp. 76–85, 2013.

[15] H. Liu, *Analysis of the Influencing Factors for Crash Severity and the Establishment of Prediction Model*, Jilin University, Jilin, China, 2014.

[16] M. Bédard, G. H. Guyatt, M. J. Stones, and J. P. Hirdes, "The independent contribution of driver, crash, and vehicle characteristics to driver fatalities," *Accident Analysis & Prevention*, vol. 34, no. 6, pp. 717–727, 2002.

[17] K. Haleem and M. Abdel-Aty, "Examining traffic crash injury severity at unsignalized intersections," *Journal of Safety Research*, vol. 41, no. 4, pp. 347–357, 2010.

[18] S. Feng, Z. Li, Y. Ci, and G. Zhang, "Risk factors affecting fatal bus accident severity: their impact on different types of bus drivers," *Accident Analysis & Prevention*, vol. 86, pp. 29–39, 2016.

[19] M. Nasri and K. Aghabayk, "Assessing risk factors associated with urban transit bus involved accident severity: a case study of a Middle East country," *International Journal of Crashworthiness*, vol. 25, pp. 1–11, 2020.

[20] Q. Lin and Y. Deng, "Analysis of factors affecting city bus accident severity based on logistic model: a case in Guangdong Province," *Acta Scientiarum Naturalium Universitatis Sunyatseni*, vol. 59, no. 4, pp. 120–127, 2020.

[21] Q. Bu, Y. Wang, and D. Wang, "Application research of fault tree analysis," *Journal of Southwest Petroleum University*, vol. 29, no. 4, pp. 141–144, 2007.

[22] He Wang, L. Hao, L. Lin et al., "Analysis of grain depot fire accident based on fault tree," *Journal of the Chinese Cereals and Oils Association*, vol. A2, pp. 21–24, 2019.

[23] W. Huang, P. Xu, and Q. Yu, "Causation mechanism analysis of urban haze based on FTA method: taking tianjin as A case study," *CIESC Journal*, vol. 69, no. 3, pp. 982–991, 2018.

[24] X. Huang, *The Real Estate Warning Study Based on Multivariate Logistic Regression Model*, Jinan University, Jilin, China, 2012.

Hindawi
Advances in Civil Engineering
Volume 2021, Article ID 6642594, 12 pages
https://doi.org/10.1155/2021/6642594

*Research Article*

# Experimental and Numerical Simulation Study on the Shear Strength Characteristics of *Magnolia multiflora* Root-Soil Composites

**ZiFan Sui,[1] Wen Yi,[1] YunGang Lu,[2] and Liang Deng[2]**

[1]*Central South University of Forestry & Technology, Changsha 410004, Hunan, China*
[2]*Hunan Expressway Group Co., Ltd., Changsha 410026, Hunan, China*

Correspondence should be addressed to Wen Yi; yiwengangbiao@163.com

Received 21 December 2020; Revised 17 April 2021; Accepted 6 May 2021; Published 19 May 2021

Academic Editor: Hui Yao



The shear strength of the soil refers to the ultimate strength of the soil against shear failure, which is one of the important indicators used to measure slope stability. This paper presents a simulation of direct shear tests on root-soil composites with different root embedding angles under different stress conditions. By comparing and analyzing the simulation results of ABAQUS software and the laboratory test results, the enhancement effect of plant roots on soil shear strength was explored. Conclusions can be drawn as follows: the excellent agreement between numerical models and laboratory shear tests suggested that the developed model can quickly and conveniently predict the shear strength of the root-soil composites. The shear strength was related to the rooting arrangement. For a single root system, when the inclination angle of the root was about 64° to the shear direction, the shear resistance of soil was much improved, while the root reinforcement had less effect when the inclination angle was greater than 90°. In the case of multiple roots, the hybrid rooting method can more effectively improve the shear resistance of the root-soil composite. Therefore, in the practical application of using the root to strengthen the soil, the angle of a single root and arrangement of multiple roots should be comprehensively considered.

## 1. Introduction

Before the end of 2019, the total mileage of highways in China has exceeded 5.0125 million kilometers. However, Slopes are inevitably generated during mountain road constructions; these kinds of the slope are prone to landslides and other geological problems, such as soil erosion. All these problems seriously affect road traffic safety and the ecological environment [1, 2]. To solve these problems, soil bioengineering techniques have emerged, which can not only stabilize the slope but also prevent soil erosion, save engineering costs, and beautify the road landscape [3–6].

The interaction between soil and plant roots mainly contributes to plant slope protection [7]. According to the theory of composite materials, plant roots can be treated as flexible reinforcement materials, which improve the shear strength of soil [8, 9]. Since 1970, many works studied the stress-strain and strength characteristics of the reinforced soil and the effect of the roots on the soil through experiments such as direct shear tests and triaxial tests [10–14]. In the 1980s, Wu et al. [15] proposed a cementing relationship between the roots and soil and make the research on the mechanical mechanism of root fixation to a higher level. Wu et al. [16, 17] elaborated the concept of the "soil-root composites" and analyzed the relationship between the shear strength and normal pressure, root content, water content, and other factors through laboratory tests. The results suggested that the mechanical reinforcement of the root system was related to the strength of soil and roots and the environmental conditions, especially the changes in stress and moisture [18, 19]. At the same time, in order to effectively improve the reinforcement effect of the roots on the soil, Ted et al. [20–22] have carried out research on plant root growth regulation. By changing factors such as moisture and phosphate content in the soil, people can control the growth direction of plant roots to achieve the desired effect.

Most scholars have researched the shear performance of root-soil composites through experimental methods. The mechanism of shear behavior depends on the interaction of friction and constraint between root and soil. The shear characteristics of the root-soil composite are affected by many factors, such as the internal friction angle, cohesion force, and water content of the soil [23]. The improvement of shear strength of the soil is the main feature of the root reinforcement, which is influenced by moisture content, diameter, and root morphology of a single root [24]. Besides, considering the fact that plants require time to grow, the root used in the soil sample in the direct shear test is not entirely the same as the root in the original soil. These modeling conditions are difficult to be reconstructed in shear tests in the laboratory. Furthermore, the growth rate of root biomass was uneven, and the proportion of adventitious roots was prominent during the juvenile period [25]. Therefore, it is more complicated and inaccurate to study the individual action of root using experimental methods.

Various finite element numerical analysis software products have been used to analyze actual engineering problems [26]. Considering the difficulties in testing root-soil composites, an increasing number of research cases adopted numerical simulation software to analyze the mechanical interaction between roots and soil [27, 28]. Moreover, the finite element numerical simulation can accurately simulate the characteristics of the root-soil composite material due to its broad applicability and easy parameter definition. In 2010, Lin et al. [29] established a 3D model of Makino bamboo T-shaped taproot and fibrous root, which was used in the numerical simulation study of the pullout test and analyzed the effect of the bamboo root system on the slope stability. In 2011, Mickovski et al. [30] compared and analyzed the difference between 2D and 3D simulations of plant roots. Considering the complexity of the spatial distribution of roots, it is generally believed that the accuracy of the 3D model is higher. There are four main types of calculation models commonly used in root-soil interaction [31]: the first type assumes that the root system of the plant and the soil are separated from each other, ignoring the movement between the two [32]. The second category regards the effects of plant roots as external loads imposed on the soil [33]. The third category comprehensively considers the frictional contact relationship between the soil and the root system [34]. The fourth category regards the combination of root and soil as a composite material [24]. Depending on the research focus, it is particularly important to choose a suitable calculation mode.

In order to quickly and conveniently analyze the effect of root on soil reinforcement, we explore the best arrangement of the root system in soil and enrich the theory of root-soil consolidation and numerical simulation-related research. In this study, through ABAQUS finite element software, the direct shear friction test of the *Magnolia multiflorum* root and soil interface was simulated numerically, and the results were compared with laboratory test results to analyze the feasibility of the numerical simulation model, which laid a foundation for the exploration of the best root percentage and the best root distribution method. The paper is organized as follows: the root-soil composite material was sampled on-site, and the cohesion force, friction angle, root diameter, length, and other related parameters were measured through the indoor test. On this basis, a finite element model of the root-soil composite material was constructed. Subsequently, the effectiveness of the finite element model was verified by comparing test data with simulation results. Simultaneously, the best embedding angle of a single root system and the best rooting method of multiple root systems were discussed with the help of the model.

## 2. Materials and Methods

*2.1. The Mechanism of Root Strengthening Soil.* The root embedded in the soil will be stretched and produce tension when the soil is sheared. The tension force can be decomposed into the horizontal direction and vertical direction, the horizontal force can be directly used to resist shear deformation, and the vertical force can be converted to positive stress to increase the friction force. When the root was inserted vertically into the soil, the incremental shear strength of the root-soil composite can be calculated by the following equation.

When the root system is orthogonal to the shear plane (Figure 1(a)),

$$\Delta S = \left(\frac{T}{A_S}\sin\theta + \frac{T}{A_S}\cos\theta \cdot \tan\varphi\right), \tag{1}$$

$$\sin\theta = \frac{x}{\sqrt[2]{x^2 + H^2}}, \tag{2}$$

$$\cos\theta = \frac{H}{\sqrt[2]{x^2 + H^2}}. \tag{3}$$

When the root system is oblique to the shear plane (Figure 1(b)),

$$\Delta s = \frac{T}{A_s}\sin\left(90^\circ - \psi\right) + \frac{T}{A_s}\cos\left(90^\circ - \psi\right) \cdot \tan\phi, \tag{4}$$

$$\psi = \arctan\left(\frac{x}{(x + H)/\tan\, a}\right), \tag{5}$$

where $\Delta S$ is the cohesion increment, $T$ is the tension force generated by root, $A_S$ is the cross-sectional area, $\theta$ is the angle between the root with the vertical direction after deformation, $\varphi$ is the internal friction angle, $x$ is the maximum shear displacement, $H$ is the length of the sheared part of the root, $\psi$ is the angle between the root and the shear surface after shear deformation, and a is the angle formed between the root of the initial state and the shear surface ($^{0^\circ} \ll a \ll 180^\circ$).

The shear strength of the soil and its increment of cohesion force can be calculated for different root angles. The results were further explored to determine the most appropriate root embedding angle, which would improve the shear resistance of soil and enhance the stability of the slope most. Based on the results of the field tests, Likitlersuang

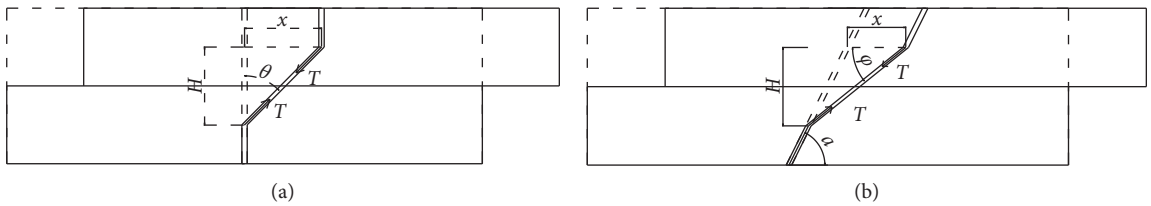


Figure 1: Root deformation diagram: (a) the root is orthogonal to the shear plane; (b) the root intersects the shear plane obliquely.

et al. [35] calculated the displacement of the root-soil composite at maximum shear strength as shown in

$$x = \frac{0.72A_r}{A_s + 13.3}, \tag{6}$$

where $A_r$ is the total area of the root system on the shear plane.

There have been few studies on the thickness of the shear zone $H$. A fixed value of $H = 5$ mm is usually taken in the calculation, which will produce errors with the actual test situation. The actual deformation of the root in the soil can be observed, and the thickness of the shear zone can be calculated by

$$H = \frac{X}{\tan\left(90^\circ - \psi\right)}. \tag{7}$$

After understanding the reinforcement mechanism of the root system to the soil, further relevant experiments and numerical simulation studies were carried out, and the feasibility of the model was verified by comparing the errors between the simulated values and the experimental and theoretical values.

*2.2. Introduction of the Study Area.* The study area is located in the Yueyang section of the Da-Yue highway (east longitude 112°10′3″ to 114°9′6″, north latitude 28°25′33″ to 29°48′47″), which has a humid continental monsoon climate. Its annual average temperature is between 16.5°C and 17.2°C, the highest temperature ranges from 39.3°C to 40.8°C, the lowest extreme temperature ranges from −11.4°C to −18.1°C, and the average annual precipitation is from 1289.8 to 1556.2 mm. There is more rainfall in the eastern part than the western part of the test section. The same area has more rainfall in spring and summer than autumn and winter. The studied slope is relatively high, with the highest point at 36.31 meters. Considering the effect and aesthetics of slope protection, we selected *Magnolia multiflorum*, *Robinia pseudoacacia, Cynodon dactylon*, and *Cobus chrysanthemum* as the slope protection plants. The landscape of the slope before and after protection is shown in Figure 2.

We used a ring knife to select soil on the test slope as the test soil. By referring to "Test Methods of Soils for Highway Engineering" in China, the soil water content was measured as 15.3%–21.4% by oven drying method. The natural density of the soil was tested as 1.65 g/cm$^3$–1.82 g/cm$^3$ through the cutting ring method, and the particle composition of the soil was obtained through the sieving analysis test and is listed in Table 1. The plasticity index of the soil measured by the photoelectric liquid-plastic-limit combined analyzer is 22.9%, which is greater than 17%, so the soil is determined to be clay.

*2.3. Collection of the Root Sample.* The horizontal excavation method was used to collect the plant roots for experimental research. After excavating, the roots were wrapped in the soil sample and placed in a shear box and were watered for proper conservation. In this test, the diameter of *Magnolia multiflorum* was measured as 0.6–0.8 mm by using the vernier caliper, as shown in Figure 3. In order to prevent the root system from losing nutrients, it should be noted that the test should be completed within one month after roots were collected.

*2.4. Direct Shear Test of Root-Soil Composites.* The direct shear test was used in this paper because of its simple and easy operation. ZJ strain-controlled quadruple direct shear instrument produced by the Nanjing Soil Instrument Factory was chosen.

An iron wire was inserted to ensure the buried root position while preparing cylindrical specimens with a diameter of 61.8 mm and a height of 20 mm. The moisture content of the soil sample is consistent with that of the slope site soil, and its value is 18.62%, the iron wire was removed to insert the root, and the hole was compacted with soil. Then, the sample was covered with filter paper and pervious stone before being pushed into the shear box. During the test, vertical pressures of 100 kPa, 150 kPa, 200 kPa, and 250 kPa were applied to each group of specimens. The transmission was opened to shear at a speed of less than 0.02 mm/min until the shear damage occurred; during the process, the device automatically records the shear stress. In the shearing process, as the shear deformation of the root-soil composite increased, the shear strength of the root-soil composite was equal to shear stress when the shear failure occurred. The test process is shown in Figure 4.

*Magnolia multiflorum* roots were used as the test subjects, and three kinds of root angle of 90°, 90° + 45°, and 45° root were used. To obtain the shear strength of soil, it is necessary to draw its stress-strain curve in the direct shear test. During the test, for specimens without root or the root-soil composite, as dislocation appeared between the upper and lower shear boxes, the shear stress increased approximately linearly with the change in displacement and finally reached a stable value which was the shear strength. The relationship between shear strength and shear displacement was fitted as follows [36]:

(a) (b)

Figure 2: Landscape of studied slope: (a) before slope protection; (b) after planting plants.

Table 1: Results of sieving analysis test.

| Screen hole diameter (mm) | Percentage (%) | Screen hole diameter (°) | Percentage (%) |
|---|---|---|---|
| 40 | 0 | 1 | 11.8 |
| 20 | 5.0 | 0.5 | 15.3 |
| 10 | 14.2 | 0.25 | 5.7 |
| 5 | 17.8 | 0.075 | 1.5 |
| 2 | 28.3 | <0.075 | 0.3 |

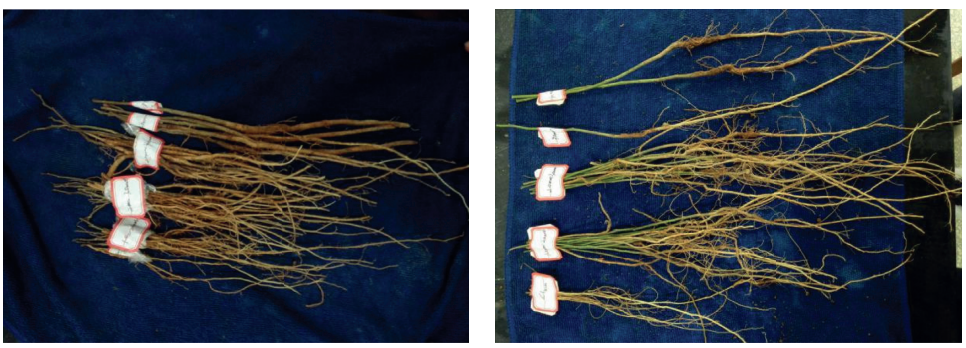

(a) (b)

Figure 3: Morphological characteristics of different root systems: (a) root system with a length of about 20 mm; (b) root system with a length of about 28.8 mm.

$$\frac{\Delta l}{\tau} = a\Delta l + b, \tag{8}$$

where $\Delta l$ is the shear displacement and $a$ and $b$ are the constants.

Multiple groups of laboratory direct shear tests were performed to record the corresponding shear strength under each vertical pressure. The direct shear test results were analyzed, and the relationship curve between the shear strength and normal stress of the root-soil composites was fitted in Table 2. According to the analysis, the shear strength increased with the increase of vertical load under the same root number and root pattern. The results showed that as the vertical load increased, the shear strength increased, which was a linear relationship for cohesive soils that can be expressed by equation (2). Comparing equation (2) with the fitting formula in Table 3, the cohesive force and internal friction angle of the material can be calculated. The cohesion force and the internal friction angle of the ordinary soil and root-soil composites can be used for slope stability analysis.

$$\tau = c + \sigma \tan \varphi, \tag{9}$$

where $\tau$ is the shear strength, $c$ is the cohesion, and $\varphi$ is the internal friction angle.

*2.5. Numerical Modeling of the Direct Shear Test.* The solid model with a diameter of 61.8 mm and a height of 20 mm was established to maintain the same size as the actual soil sample. It meshed with a three-dimensional first-order hexahedron element (C3D8), including a total of 564 nodes and 870 nodes. In the finite element simulation, the Mohr-Coulomb ideal plasticity model was applied. The specific values are shown in Table 2.

Plant roots can be divided into three types according to their morphology: straight type, scattered type, and

Figure 4: Shear test process of root-soil composites: (a) perforated cloth root of the direct shear specimen; (b) finished sample. (c) direct shear devices; (d) specimens after shear failure.

Table 2: Soil parameters in the numerical simulation.

| Parameter | Value | Unit |
|---|---|---|
| Soil density | 1450 | kg/m$^3$ |
| Elastic modulus | 10 | MPa |
| Poisson's ratio | 0.3 | — |
| Cohesion | 24.44 | kPa |
| Friction angle | 29.44 | ° |
| Coefficient of friction | 0.564 | — |
| Moisture content | 18.62 | % |

Table 3: Laboratory results of the direct shear test.

| Plant species | Root angle with the horizontal direction | Curve fitting | $R^2$ (%) | $c$ (kPa) | tan$\varphi$ | $\varphi$ (°) |
|---|---|---|---|---|---|---|
| No root | — | $y = 0.5646x + 4.435$ | 99.43 | 4.435 | 0.564 | 29.449 |
| M. multiflora | 90° + 90° | $y = 0.6890x + 7.792$ | 99.62 | 7.792 | 0.689 | 34.567 |
| | 45° + 45° | $y = 0.7197x + 7.085$ | 99.47 | 7.085 | 0.719 | 35.743 |
| | 45° + 90° | $y = 0.7532x + 8.292$ | 99.53 | 8.292 | 0.753 | 36.987 |

horizontal type [37]. The root is an ideal linear elastic material and follows the generalized Hooke's law [38]. In the stability analysis of ecological slope protection, since only root tension is considered (similar to the characteristics of steel cables), truss flexible rod element T2D2 is usually used for simulation. However, in the indoor direct shear test, in addition to the tensile force caused by the displacement between the upper and lower soil bodies, the shear force should also be considered. Therefore, this study used the B31 beam element with a vertical length of 20 mm or inclined length of 28.28 mm and a diameter of 0.7 mm to simulate the plant root system with different angles (90° + 90°, 90° + 45°, 45° + 45°). The elastic modulus of the root of Magnolia multiflorum is 0.64–2.33 GPa, Poisson's ratio is 0.3, and the density is 1691 kg/m$^3$. The specific root distribution is shown in Figure 5.

The contact in the simulation of the direct shear test mainly includes the contact of the soil and the contact between the roots and the soil. The "Surface-to-Surface contact" was adopted between the soils, the upper and the down soil contact surfaces are selected as "Master surface" and "Slave surface," respectively. The "Penalty formula" is used to calculate the friction force in the tangential behavior, and the contact type in the normal behavior is "hard"

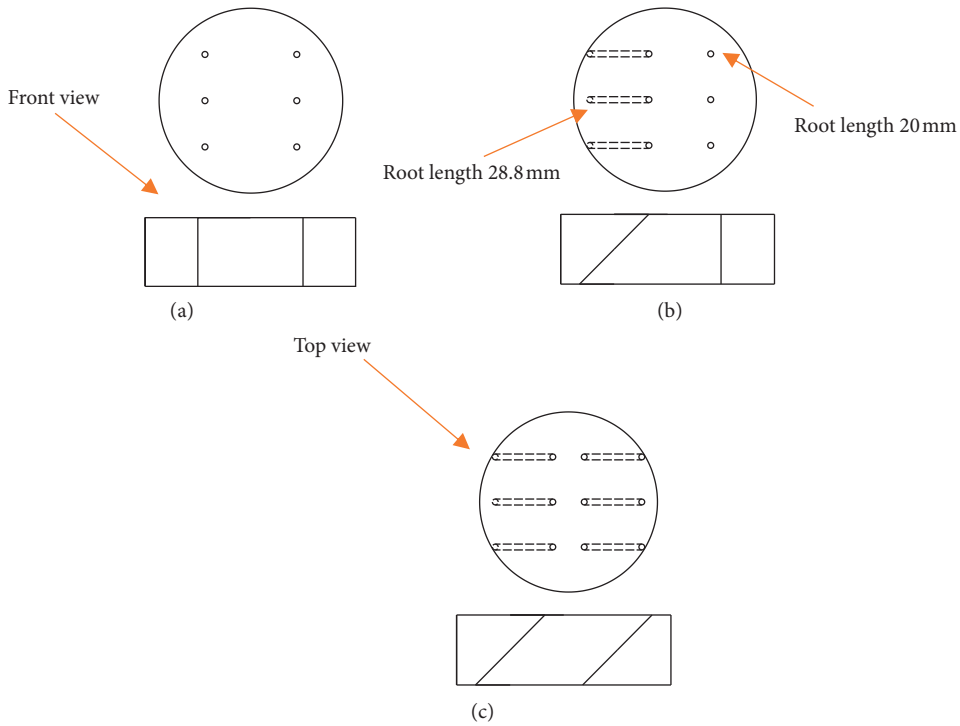


Figure 5: Top view and main view of three root insertion modes: (a) 90° + 90°; (b) 90° + 45°; (c) 45° + 45°.

contact. The contact between the roots and soil was modeled by the embedded region constraints model in the ABAQUS constraint menu, and the roots were treated as embedded bodies.

The simulation did not take into account the shear rate, which simplified the test process appropriately, because the time of soil failure will not affect the results. Stress boundary conditions were used to simulate the vertical pressure, and displacement boundary conditions were used to play the role of the shear box. The numerical simulation was carried out following three steps: the initial step, load step, and shear step. The first step is to define the properties of the soil-soil and soil-root contact surfaces and fix the displacement of the specimen in the $x$ and $y$ directions and the vertical displacement of the lower soil. In the second step, a vertical load was applied to the top surface of the upper soil. Since the amount of soil in the direct shear test is small, the influence of the soil gravity factors was ignored for simplification. The last step is to release the $x$-direction constraint of the lower soil and apply a horizontal displacement of 10 mm to simulate the shearing process. Taking the 90° embedded root system as an example, after the shearing was completed, the root-soil composite model is shown in Figure 6.

Taking the model under 250 kPa vertical load as an example, the equivalent stress cloud diagram of the composite and root in the shear direction is shown in Figure 7. It can be seen that the stress concentration of the soil appeared on the shear surface, and the stress is mainly concentrated in the soil in contact with the root. The peak shear stress of specimens with roots was much greater than that without roots. When the root system was embedded at 90° and 45°, the peak shear stress of the root system was the largest. After the simulation was finished, the shear stress on the shear plane and the $x$-direction displacement of the lower soil were output, the relationship between the shear stress and shear displacement under normal stress is plotted, and its peak or the stable value was taken as its shear strength.

## 3. Results

*3.1. Shear Stress and Shear Displacement Curves.* The shear stress and the shear displacement are recorded in Figure 8. The comparison between curves of laboratory test and numerical simulation indicated that the error between results of laboratory test and numerical simulation of the specimen without root was small, and the embedding of the root increased the error; especially when the embedded root system is inclined to the soil, the error is greater. Besides, in the initial stage of the stress-strain curve, two curves were not entirely consistent, and the finite element simulation curve rose relatively faster and reaches the peak intensity soon. The reason for this phenomenon is that in order to simplify the simulation process, the shear rate was not controlled deliberately, which has little influence on the peak value of the curve. Although the shear stress and displacement curves were not completely coincident, the variation trend of each curve was similar, and the predicted shear strength had a good agreement with the laboratory result.

*3.2. Relationship between Shear Strength and Vertical Load.* According to the results of the direct shear test in the laboratory and numerical simulation, their shear strength

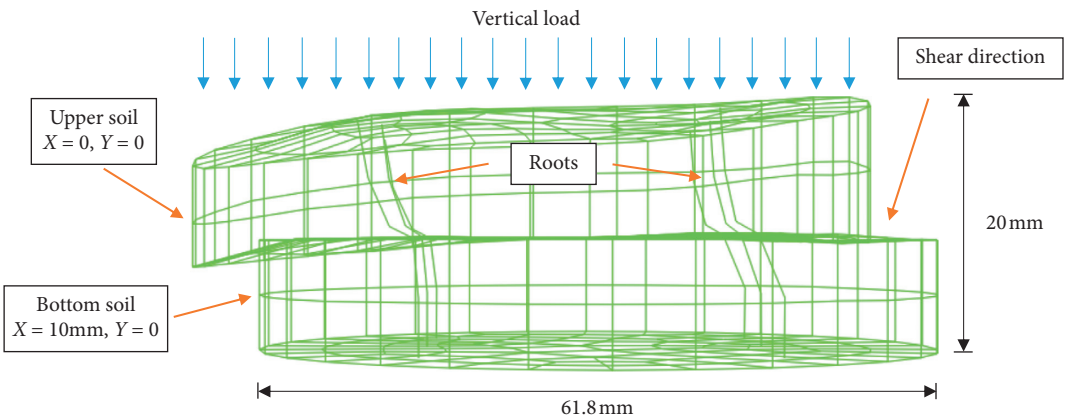


Figure 6: Numerical simulation of the laboratory direct shear test.

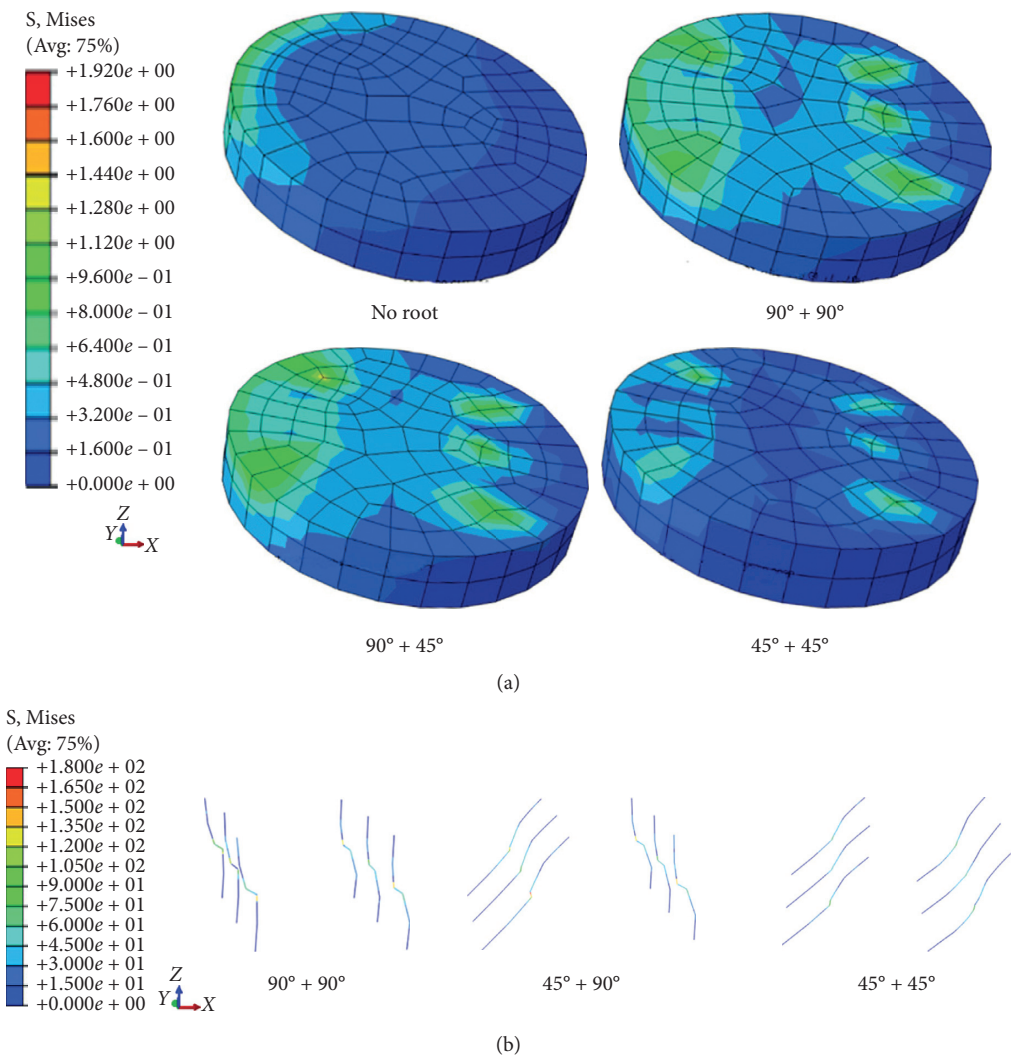


Figure 7: The stress cloud diagram of the composite and plant roots: (a) equivalent stress of bottom soil; (b) equivalent stress of plant roots.

had no significant difference, as shown in Figure 9. For the multiple groups of tests, the simulation results are relatively good, with an average relative error of 2.9%, and a maximum relative error of 5.2%. The simulation curves of the specimen without the root were nearly coincident with the test curve; after adding the root, the error started to increase, especially after plant roots are inserted into the soil at different angles. Under normal circumstances, the simulation process is considered feasible if the differences between simulation results and test results are within ±20% [39]. There are two

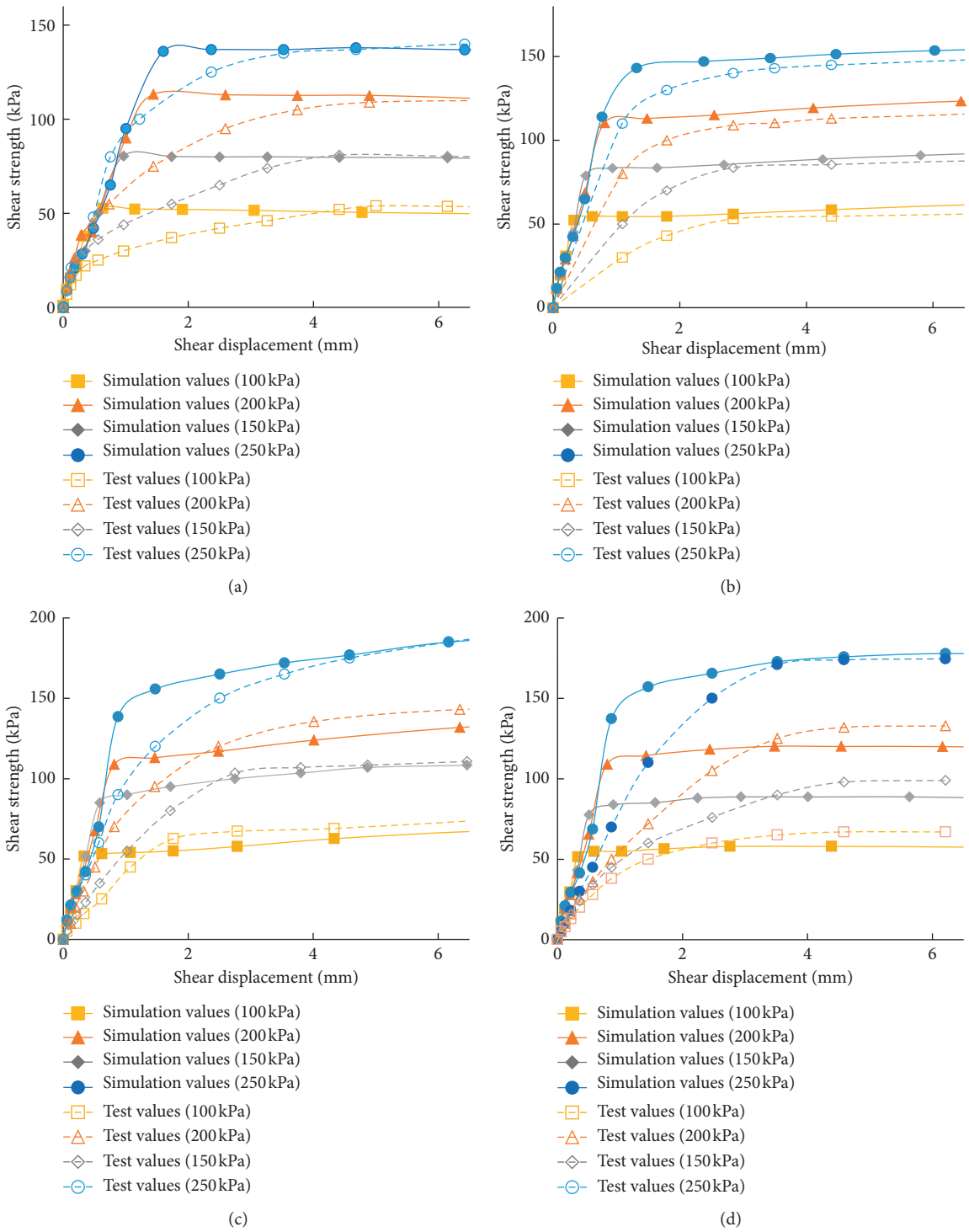


Figure 8: Shear stress-displacement curves of root-soil composites with different root arrangement: (a) ordinary soil; (b) 90° + 90°; (c) 90° + 45°; (d) 45° + 45°.

main reasons for this error: (1) it is difficult to precisely control the inclination angle of the root inserted into the soil while root embedding in the soil at various angles in the laboratory test, and (2) there are also differences between the B31 beam element and the actual root during the finite element numerical simulation.

*3.3. Relationship between Shear Strength and Root Embedding Angle.* To make the experimental results more apparent and the data laws more straightforward, the root diameter was appropriately increased, the incremental cohesion force of "*a*" from 0° to 90° was recorded sequentially, and the data records are shown in Table 4.

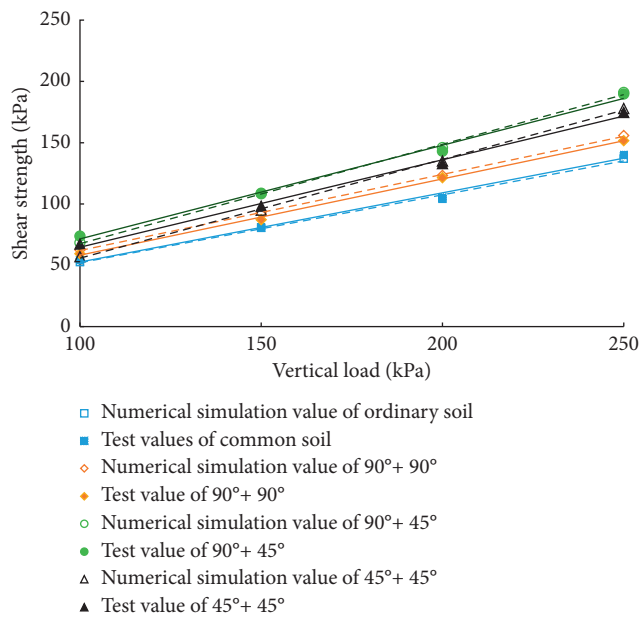


Figure 9: Relationship curve between shear strength and vertical load.

Table 4: Incremental cohesion values at various angles.

| Angle (°) | Increase in cohesion (kPa) |
|---|---|
| 10 | 7.13 |
| 20 | 7.37 |
| 30 | 7.51 |
| 40 | 7.59 |
| 50 | 7.63 |
| 60 | 7.65 |
| 70 | 7.65 |
| 80 | 7.65 |
| 90 | 7.64 |

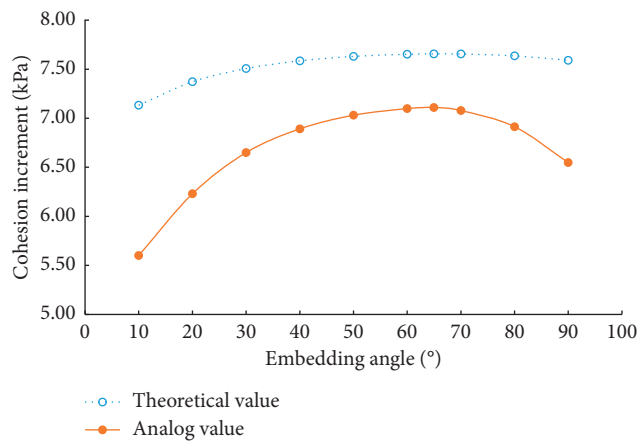


Figure 10: Relationship curve between root embedding angle and cohesion incremental.

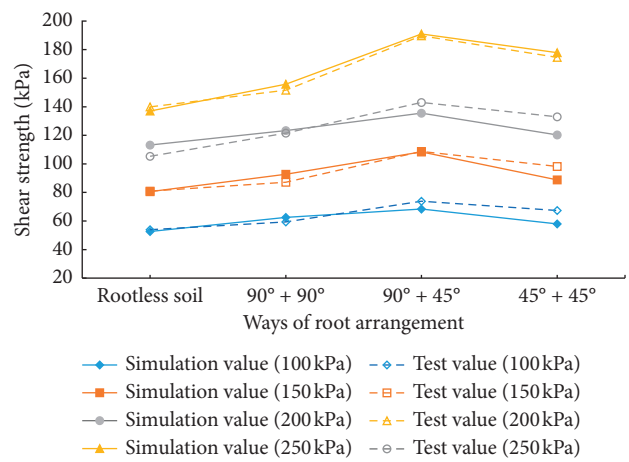


Figure 11: The relation curve between cloth root and shear strength.

Finite element simulations were based on theoretical studies to analyze the effect of plant embedding angle on the shear strength of the root-soil composite and were also further combined with theory to verify the accuracy of the model. The roots were embedded in the soil model at different angles, the shear strength of the soil without roots was compared with that of the composite material, the effect of roots on the cohesion increment of the soil was analyzed, and the correlation curve between the root angle and the cohesion increment is plotted in Figure 10.

It can be seen that the simulation results and the theoretical analysis results showed the same pattern. The cohesion increment was the greatest when the root system was embedded at an angle of about 64°. The curve of formula (4) was drawn as the solid line in Figure 10, it can be seen that the curve first rose and then dropped, and the cohesive force reached its peak at 29°. Besides, when the inserted angle of the root was greater than 90°, the shear strength increment was small or even less than the soil without root; combining this with finite element simulation results, it can be seen that when "$\alpha$" > 90°, the root was compressed and cannot withstand the pressure so that the material properties cannot be fully developed, and the reinforcement effect of the root was not pronounced.

*3.4. Optimal Arrangement of Roots in the Soil.* The above study combines theoretical analysis with finite element simulations to explore the effect of a single embedding angle on cohesion increment. It was determined that the angle of root entry had an effect on the viscous cohesion increment of the composites. In the actual project, the number of roots planted on the slope is relatively large, and there are various combinations between roots and roots; for example, the same single inclination arrangement can be used, or mixed roots can be used, and the development of suitable rooting method to effectively expand the root reinforcement effect on the soil is crucial. The study of single and mixed rooting methods was carried out using both laboratory tests and numerical simulations. Due to the limitation of the size of the straight shear test block, only two better inclination angles of 45° and 90° have been used for this combination. The plotting of the rooting method and shear strength

correlation curve is as follows (Figure 11), where the dashed line is the test result, and the solid line is the simulation result. The analysis of the data shows that when the soil contains multiple roots, different rooting methods will also affect the shear strength of the soil. Three types of rooting methods were used, with the 90° + 45° mixed rooting method having significantly better shear resistance than single-rooted soils.

## 4. Conclusions

This study conducted a finite element simulation of the direct shear test of the root-soil composite material. The simulation results were compared with the laboratory results to verify the feasibility of the model. At the same time, some application prospects of the model were proposed here; that is, the effect of root embedding angle on cohesive force increment was analyzed through numerical simulation, and the effect of root arrangement in soil on shear strength was explored. For some cases that are not easy to realize by experimental methods, numerical simulation can show its unique advantages. The following conclusions can be drawn:

(1) The root system of *Magnolia multiflorum* effectively improved the shear strength of the soil, and its enhancement effect was about 10%–40%. In the direct shear test, the shear stress presented a trend of rapid increasing first and then gradually slowing down until it is stable. The maximum or stable value was considered as the shear strength of the material. The tensile force of the plant root system resisted part of the shear force; therefore, the shear resistance of the root-soil composite has been improved. Under the same rooting method, the shear strength increases with the increase of vertical pressure, showing a linear relationship. Combining this with the Coulomb formula, it can be seen that plant roots have little effect on the friction angle of the soil and have a good effect on the cohesion enhancement, which can significantly increase the stability of the slope

(2) The shear strength is not only affected by factors such as the root diameter and root cross-section ratio but is also related to the manner of root distribution and the angle between the root and shear surface. Through theory, experiment, and simulation results, it can be seen that the root was inserted into the soil at different angles, and there is a difference in the improvement of the root-soil composite shear strength. When the inclination angle of the root is around 64°, the shearing strength of the soil was much improved, and when the inclination angle of the root was greater than 90°, the effect of roots on the soil was not pronounced. Besides, in the case of multiple root distributions, the shear strength of the 45° + 90° distribution was the largest; that is, the shear strength of the mixed root distribution manner is larger than that of the single root distribution manner

(3) This paper explored the above problems by means of numerical simulation, and the conclusions obtained are consistent with the theoretical analysis and experimental results, the average value of the relative error of shear strength obtained from the multiple sets of tests was 2.9%, and the maximum relative error was 5.2%. After multiple verifications, it is feasible to study the shear strength of the root-soil composite by numerical simulation. The research results and research methods of this article have a good guiding significance for the development of related research on root growth regulation and slope protection

## Data Availability

All data used to support the findings of this study are included within the article.

## Conflicts of Interest

The authors declare no conflicts of interest.

## Authors' Contributions

Conceptualization was done by ZiFan Sui and Wen Yi; methodology was prepared by ZiFan Sui; resources and software were provided by ZiFan Sui; validation was conducted by ZiFan Sui, Wen Yi, and YunGang Lu; formal analysis was done by ZiFan Sui; investigation was performed by ZiFan Sui; data curation was done by Liang Deng; the original draft was written by ZiFan Sui; reviewing and editing were done by ZiFan Sui; visualization, supervision, and project administration were carried out by ZiFan Sui; funding acquisition was contributed by Wen Yi. All authors have read and agreed to the published version of the manuscript.

## Acknowledgments

This research was funded by the Introduction of Key Technologies for Landscape Restoration of Deep Cut Slopes, under grant number 2015-4-38, and Research on Key Technology of Ecological Landscape Restoration of Highway Slope Road in Ecological Fragile Area, under grant number 201803.

## References

[1] L. Yang, M. Yang, and G. Yang, "Modeling fractures and cracks on tree branches," *Computers & Graphics*, vol. 80, pp. 63–72, 2019.

[2] Y. Yao, J. Ni, and J. Li, "Stress-dependent water retention of granite residual soil and its implications for ground settlement," *Computers and Geotechnics*, vol. 129, Article ID 103835, 2021.

[3] G. B. Bischetti, M. Di Fi Dio, and F. Florineth, "On the origin of soil bioengineering," *Landscape Research*, vol. 39, no. 5, pp. 583–595, 2014.

[4] Y. P. Dhital, R. B. Kayastha, and J. Shi, "Soil bioengineering application and practices in Nepal," *Environmental Management*, vol. 51, no. 2, pp. 354–364, 2013.

[5] L. Giupponi, G. Borgonovo, A. Giorgi, and G. B. Bischetti, "How to renew soil bioengineering for slope stabilization: some proposals," *Landscape and Ecological Engineering*, vol. 15, no. 1, pp. 37–50, 2019.

[6] F. Rey, C. Bifulco, G. B. Bischetti et al., "Soil and water bioengineering: practice and research needs for reconciling natural hazard control and ecological restoration," *Science of the Total Environment*, vol. 648, pp. 1210–1218, 2019.

[7] H. Zhu, L. M. Zhang, T. Xiao, and X. Y. Li, "Enhancement of slope stability by vegetation considering uncertainties in root distribution," *Computers and Geotechnics*, vol. 85, pp. 84–89, 2017.

[8] A. Gonzalez-Ollauri and S. B. Mickovski, "Plant-soil reinforcement response under different soil hydrological regimes," *Geoderma*, vol. 285, pp. 141–150, 2017.

[9] N. Pollen and A. Simon, "Estimating the mechanical effects of riparian vegetation on stream bank stability using a fiber bundle model," *Water Resources Research*, vol. 41, no. 7, Article ID W07025, 2005.

[10] M. Pallewattha, B. Indraratna, A. Heitor, and C. Rujikiakamjorn, "Shear strength of a vegetated soil incorporating both root reinforcement and suction," *Transportation Geotechnics*, vol. 18, pp. 72–82, 2018.

[11] T. C. Hales and C. F. Miniat, "Soil moisture causes dynamic adjustments to root reinforcement that reduce slope stability," *Earth Surface Processes and Landforms*, vol. 42, no. 5, pp. 803–813, 2017.

[12] T. Watson, "In situ shear tests of soil blocks with roots," *Canadian Geotechnical Journal*, vol. 35, no. 4, pp. 579–590, 1998.

[13] T. H. Wu, P. E. Beal, and C. Lan, "In-situ shear test of soil-root systems," *Journal of Geotechnical Engineering*, vol. 114, no. 12, pp. 1376–1394, 1988.

[14] C.-C. Fan and M.-H. Tsai, "Spatial distribution of plant root forces in root-permeated soils subject to shear," *Soil and Tillage Research*, vol. 156, pp. 1–15, 2016.

[15] T. H. Wu, W. P. McKinnell III, and D. N. Swanston, "Strength of tree roots and landslides on Prince of Wales island, Alaska," *Canadian Geotechnical Journal*, vol. 16, no. 1, pp. 19–33, 1979.

[16] T. H. Wu, R. M. Mcomber, R. T. Erb, and P. E. Beal, "Study of soil-root interaction," *Journal of Geotechnical Engineering*, vol. 114, no. 12, pp. 1351–1375, 1988.

[17] G. B. Bischetti, E. A. Chiaradia, T. Epis et al., "Root cohesion of forest species in the Italian alps," *Plant & Soil*, vol. 324, no. 1-2, pp. 71–89, 2009.

[18] M. Zhun, S. A. Laurent, G. Marie et al., "Engineering ecological protection against landslides in diverse mountain forests: cchoosing cohesion models," *Ecological Engineering*, vol. 45, pp. 55–69, 2012.

[19] P. P. Capilleri, M. Cuomo, E. Motta, and M. Todaro, "Experimental investigation of root tensile strength for slope stabilization," *Indian Geotechnical Journal*, vol. 49, no. 6, pp. 687–697, 2019.

[20] W. T. Ted, R. Mily, G. Donald et al., "Regulation of root angle and gravitropism," *G3: Genes, Genomes, Genetics*, vol. 8, no. 12, pp. 3841–3855, 2018.

[21] L. C. Williamson, S. P. Ribrioux, A. H. Fitter, and H. M. O. Leyser, "Phosphate availability regulates root system architecture in arabidopsis," *Plant Physiology*, vol. 126, no. 2, pp. 875–882, 2001.

[22] T. C. Hales, C. R. Ford, T. Hwang, J. M. Vose, and L. E. Band, "Topographic and ecologic controls on root reinforcement," *Journal of Geophysical Research*, vol. 114, no. F3, Article ID F03013, 2009.

[23] C. Wang, W. Ng, N. Jun Jun, and K. L. Anthony, "The effects of plant growth and spacing on soil hydrological changes: a field study," *Géotechnique*, vol. 70, no. 10, pp. 1–41, 2019.

[24] S. Yang, G. Xiaowei, and X. Xiaochuan, "Ecological restoration and mechanical reinforcement effect of slope of tailings reservoir," *Environmental Earth Sciences*, vol. 80, no. 3, pp. 256–262, 2021.

[25] D. Zhang, J. Cheng, Y. Liu et al., "Spatio-temporal dynamic architecture of living brush mattress: root system and soil shear strength in riverbanks," *Forests*, vol. 9, no. 8, p. 493, 2018.

[26] G. B. Bischetti, E. A. Chiaradia, V. D'Agostino, and T. Simonato, "Quantifying the effect of brush layering on slope stability," *Ecological Engineering*, vol. 36, no. 3, pp. 258–264, 2009.

[27] A. Cislaghi, M. Bordoni, C. Meisina, and G. B. Bischetti, "Soil reinforcement provided by the root system of grapevines: quantification and spatial variability," *Ecological Engineering*, vol. 109, pp. 169–185, 2017.

[28] M. Yang, P. Défossez, F. Danjon, and T. Fourcaud, "Tree stability under wind: simulating uprooting with root breakage using a finite element method," *Annals of Botany*, vol. 114, no. 4, pp. 695–709, 2014.

[29] D.-G. Lin, B.-S. Huang, and S.-H. Lin, "3-D numerical investigations into the shear strength of the soil-root system of Makino bamboo and its effect on slope stability," *Ecological Engineering*, vol. 36, no. 8, pp. 992–1006, 2010.

[30] S. B. Mickovski, A. Stokes, R. van Beek, M. Ghestem, and T. Fourcaud, "Simulation of direct shear tests on rooted and non-rooted soil using finite element analysis," *Ecological Engineering*, vol. 37, no. 10, pp. 1523–1532, 2011.

[31] W. Chungen, H. Kaicheng, Z. Nan et al., "Discussion on ecological protection technology of high and steep slope of expressway," *IOP Conference Series: Earth and Environmental Science*, vol. 632, no. 2, pp. 220–222, 2021.

[32] M. Li, Y. Yang, S. Wu, and G. Xu, "On ecological slope protection technology of highway construction in Tibet," *E3S Web of Conferences*, vol. 233, pp. 1151–1155, 2021.

[33] W. Shaowei, C. Degou, L. Song, and Y. Jianping, "Performance test and stability analysis of jute ecological bcag on subgrade slope," *E3S tWeb of Conferences*, vol. 233, pp. 1133–1137, 2021.

[34] W. Dongdong, Y. Zaijian, C. Yitong et al., "Characterisation of soil erosion and overland flow on vegetation-growing slopes in fragile ecological regions: a review," *Journal of Environmental Management*, vol. 285, no. 1, pp. 115–120, 2021.

[35] S. Likitlersuang, A. Takahashi, and K. H. Eab, "Modeling of root-reinforced soil slope under rainfall condition," *Engineering Journal*, vol. 21, no. 3, 2017.

[36] T. S. Nguyen, "Stability analysis of vegetated residual soil slope under rainfall conditions," *Environmental Geotechnics*, vol. 7, no. 5, pp. 1–45, 2018.

[37] K. H. Eab, A. Takahashi, and S. Likitlersuang, "Centrifuge modelling of root-reinforced soil slope subjected to rainfall infiltration," *Géotechnique Letters*, vol. 4, no. 3, pp. 211–216, 2014.

[38] K. H. Eab, S. Likitlersuang, and A. Takahashi, "Laboratory and modelling investigation of root-reinforced system for slope

stabilisation," *Soils and Foundations*, vol. 55, no. 5, pp. 1270–1281, 2015.

[39] U. Leknoi and S. Likitlersuang, "Good practice and lesson learned in promoting vetiver as solution for slope stabilisation and erosion control in Thailand," *Land Use Policy*, vol. 99, 2020.

Hindawi
Advances in Civil Engineering
Volume 2021, Article ID 6654213, 9 pages
https://doi.org/10.1155/2021/6654213

*Research Article*

# Effects of Biostabilization on Engineering Properties of Geomaterials

**Shengting Li,[1] Chenyi Luo,[2] Yi Yang,[3] Lvzhen Yang,[4] Lijian Wu,[1] Tuo Huang,[5] and Zhuangji Wang[6]**

[1]*Key Laboratory of Transport Industry of Road Structure and Material, Ministry of Transport, Research Institute of Highway, Beijing 100088, China*
[2]*School of Life Science, Beijing University of Chinese Medicine, Beijing 102488, China*
[3]*Xiandai Investment Co., Ltd., School of Traffic and Transportation Engineering, Changsha University of Science & Technology, Changsha, Hunan 410076, China*
[4]*School of Road and Bridge Engineering, Hunan Communication Polytechnic, Huangxing Zhen, Changsha, Hunan 410132, China*
[5]*School of Traffic and Transportation Engineering, Changsha University of Science & Technology, Changsha, Hunan 410076, China*
[6]*Department of Plant Science and Landscape Architecture, University of Maryland, College Park, MD 20742, USA*

Correspondence should be addressed to Lvzhen Yang; 17101030071@stu.csust.edu.cn and Zhuangji Wang; cauwzj@gmail.com

Received 14 October 2020; Revised 30 January 2021; Accepted 19 April 2021; Published 29 April 2021

Academic Editor: Eleftherios K. Anastasiou



Biostabilization is a newly proposed method to improve the strength and durability of geomaterials, and it can serve as an alternative to chemical and mechanical stabilization. The objectives of this study are to perform biostabilization treatments for selected roadway construction geomaterials and to evaluate the biostabilization effects on engineering properties of the geomaterials. Three types of geomaterials were selected, and two of them were compacted soil from unpaved road surface. *Bacillus pasteurii*, the biostabilization bacterium, was used to induce mineral precipitates within the geomaterial pore spaces, where the biostabilization effects were performed. Two types of liquid incubation media, containing $NH_4Cl$ or $(NH_4)_2SO_4$, were applied for bacteria culturing. Unconfined compression, scanning electron microscopy (SEM), energy-dispersive X-ray spectroscopy (EDS), and X-ray diffraction (XRD) measurements were conducted to evaluate the biostabilization results. From unconfined compression, sample strength performance was improved by the biostabilization treatments; the benefits of biostabilization were pronounced by a relatively long culturing time and an oven-dry procedure; the liquid culturing medium containing $NH_4Cl$ performed better than the medium containing $(NH_4)_2SO_4$. After biostabilization, SEM photographs provided direct evidence for the precipitates induced by bacteria within the geomaterial pore space. The precipitates either connected the adjoined particles or partially covered the particle surface, which increased the surface roughness. EDS and XRD results indicated that calcite, dolomite, and albite were the major precipitates produced during biostabilization treatments. In conclusion, biostabilization ameliorated the microstructures of the geomaterials and improved their strength. Future research topics should include the applications of biostabilization for in situ road construction.

## 1. Introduction

Geomaterials, such as soils and aggregates, are widely applied in roadway infrastructure systems. Soils are used for embankment fills and subgrades, while aggregates are used for pavement bases and in Portland cement concrete (PCC) or asphalt concrete. The quality of geomaterials directly influences the longevity of infrastructure systems; hence, enhancing the stability of geomaterials is a prominent issue considered during construction. For example, at sites with marginal or weak soils, mechanical and chemical stabilization should be applied [1]; when aggregates with high porosity are used in PCC or asphalt concrete [2, 3], chemical treatments with sodium silicate solutions are usually

performed to seal the pores, improve the strength and durability of PCC or asphalt concrete, and prevent concrete deterioration [4]. However, the applicability of those operations was limited by the cost, suitability, availability, constructability, and environmental concerns.

Biostabilization has been proposed as an alternative to improve the mechanical properties of geomaterials in a sustainable and environment friendly way [5, 6]. In biostabilization, naturally occurring or engineered bacteria are injected into the geomaterials, and precipitates of inorganic cementing materials, induced by microbe-produced polymers, serve as binding agents to bond soil particles and plug pores among coarse aggregates [7].

Previous studies involving biostabilization were mostly directed to laboratory studies of carbonate precipitates as the cementation material, with emphasizing on the selection of materials and procedures, the morphology of carbonate precipitates, as well as the evaluation of biostabilization effects. For example, DeJong et al. [5] recommended to use *Bacillus pasteurii* as the bacteria and considered the stabilization procedures as two steps, i.e., bacteria incubation and cementation treatments. Whiffin et al. [8] reported the use of *Sporosarcina pasteurii* as an alternative bacterium in biostabilization. Ramakrishnan et al. [6] reported the use of water, urea, and phosphate buffer as three growth media and concluded that *Bacillus pasteurii* grew in phosphate buffer provided optimal biostabilization results in concrete based on the evaluation of precipitate sizes and concrete strength against adverse environments, e.g., sulfate, alkaline, and freeze-thaw cycles. Bachmeier et al. [9] reported that immobilization of bacteria-produced urease, an enzyme inducing urea decomposition and carbonate precipitates, could result in smaller and less organized crystals comparing with free urease. Jonkers et al. [10] monitored the change of cement pore size under biostabilization and reported a shift of the pore size distribution from a range of 0.1–1.0 $\mu$m to a range of 0.01–0.1 $\mu$m, demonstrating the shrinkage of pore size after biostabilization treatments. Burbank et al. [11] and Meyer et al. [12] presented the effects of biostabilization on soil resistance to seismic-induced liquefaction and dust control through wind tunnel testing, and both effects implied that biostabilization enhanced the binding strength among soil particles.

Evaluations of biostabilization results fall into two scales. The microstructures and chemical compositions of biostabilized and untreated geomaterials are characterized by scanning electron microscopy (SEM) and X-ray diffraction (XRD) measurements. For example, DeJong et al. [7] applied SEM and observed calcite precipitates in the pore spaces of biostabilized silica sand. XRD is used to quantitatively analyze the mineral constituents of precipitates. For example, Bang and Ramakrishnan [13] measured the weight fraction of the calcite precipitates for samples under biostabilization or control treatments and verified the causal relation between bacteria activity and amount of calcite precipitates. For macroscale, pore size distribution is one of the critical characteristics, which was measured with mercury porosimetry [10], and the decreasing of porosity implies positive effects of biostabilization.

Biostabilization is pollution-free [6]; and the nonpathogenic bacteria used in biostabilization are native to subsurface soil environment [5]. Applications of biostabilization can substantially reduce the use of nonrenewable resources and energy, as well as decrease the production of nonbiodegradable wastes. Hence, biostabilization mitigates environmental burden of geo- and civil engineering operations [10].

The current designs and tests of biostabilization are mostly based on laboratory experiments under controlled environments. To assist implementations, an experiment based on samples from roadway sites should be appreciated. For example, some of the county roads are remained unpaved in China, where compact soils (gravel) are applied on road surface. Rainfall, strong wind, drought, and freezing-thawing could cause road surface damages, while biostabilization could be one of the potential ways to alleviate such damages. Thus, the objectives are to perform biostabilization treatments for selected geomaterials and (2) evaluate the biostabilization effects on engineering properties of geomaterials.

## 2. Materials and Methods

*2.1. The Procedures of Biostabilization.* Calcite (calcium carbonate, $CaCO_3$) precipitate in biostabilization treatments is defined as "microbiologically induced calcite precipitation (MICP)," which belongs to a broader category of science called biomineralization. MICP process can be presented with a simplified reaction as follows [11]:

$$(NH_2)_2CO + 2H_2O \longrightarrow 2NH_4^+ + CO_3^{2-}, \quad (1)$$

where $NH_4^+$ increases the pH values in the liquid phase and $CO_3^{2-}$ can react with calcium ions ($Ca^{2+}$) and produce $CaCO_3$ precipitates as follows:

$$Ca^{2+} + CO_3^{2-} \longrightarrow CaCO_3. \quad (2)$$

A bacterial species named *Bacillus pasteurii* was adopted in this study following the suggestion by DeJong et al. [7] because (1) *Bacillus pasteurii* is an aerobic and urease production bacterium, naturally occurring in soil; (2) *Bacillus pasteurii* cells do not aggregate, ensuring a relatively high cell surface to volume ratio and free urease redistribution during biostabilization treatments; and (3) *Bacillus pasteurii* provides two sources of $CO_2$, cellular respiration and urea decomposition [5].

In this study, the freeze-dried bacteria were procured from America Type Culture Collection (ATCC). Following the ATCC instructions, 1.0 L liquid culturing medium was made with 20.0 g yeast extract, 10.0 g $(NH_4)_2SO_4$ or $NH_4Cl$, and 0.13 M Tris buffer (pH = 9.0). Yeast extract provides nutrients and Vitamin B for bacteria reproduction, where Vitamin B also promotes the growing speed of *Bacillus pasteurii*. $(NH_4)_2SO_4$ or $NH_4Cl$ serves as nitrogen sources for amine groups, enzyme, and other proteins of bacteria. ATCC recommends the used of $(NH_4)_2SO_4$ during incubation of bacteria; however, $SO_4^{2-}$ can be harmful to some civil engineering materials, so the culturing medium with

$NH_4Cl$ is proposed. In this study, both types of $NH_4^+$, i.e., $(NH_4)_2\ SO_4$ and $NH_4Cl$, were considered. Before culturing, *Bacillus pasteurii* was first rehydrated using the culturing medium (5-6 ml) under a 30°C ± 2°C and aerobic environment, and one single colony was obtained from the rehydrated bacteria via the streak plate method. Then, the selected colony was transferred into a flask and mixed with the culture medium. Such a mixture was placed in a shaking incubator under a 30°C ± 2°C and aerobic environment for 2 days to culture enough bacteria.

After the 2-day culturing, the concentration of *Bacillus pasteurii* was increased. Before application, the concentration of bacteria was adjusted to $1.6 \times 10^8$ cells $mL^{-1}$ by adding new culturing liquid. The final concentration of *Bacillus pasteurii* was calibrated by optical density (OD) via a UV-visible spectrophotometer. Culturing liquid under the target bacteria concentration was then injected into geomaterial samples, and those samples were stored under a 30°C ± 2°C and aerobic environment for 5 days to finish a single-round of biostabilization treatment. In this study, we also allowed a duplication of the 5-day biostabilization treatment. Therefore, samples under single-round and double-round of culturing were obtained. Before the performance evaluations, the biostabilized geomaterials were saturated with water and air-dried or oven-dried at 110°C to simulate a range of ambient (weather) conditions occurred on gravel roads.

*2.2. Geomaterial Samples.* Three types of geomaterials were tested in this study: (1) the standard silica sand was the clean, dry, and free-flowing uncemented sand, with a porosity of 40%, a specific gravity of 2.65 Mg $m^{-3}$, and a uniformity coefficient of 1.4; (2) surface materials from an unpaved road were sampled, with classification as poorly graded and silty sand (SP-SM soil); and (3) soils from a highway construction site were obtained and classified as silty sand (SM soil). DeJong et al. [5] and DeJong et al. [7] adopted the silica sand to demonstrate the positive effects of biostabilization. The SM soil samples in this study were subjected to frequent freeze-thawing cycles, which may lead to damages such as frost boils, rutting, and potholes. Photographs for the three types of geomaterials are shown in Figure 1.

PVC molds were used to hold the geomaterial samples. The mold was a column with 7.3 cm in height and 3.5 cm in cross-sectional diameter. Each mold included two pieces, and stainless-steel clamps were used to join the tops of those two pieces and rubber bands were used to bind the bottoms of those two pieces together. The two-piece design of PVC molds allowed the geomaterial samples to be easily transported out of the molds after biostabilization, and the interior surface of PVC molds was covered by the aluminum foil to minimize the sample lost during transportation. PVC molds were filled with the geomaterial samples and stored within glass beakers. Before injecting the bacteria liquid, aluminum foil was also wrapped around the bottom of PVC molds to reduce liquid leaking, and the glass beakers and PVC molds were placed into an autoclave for a 25-minute sterilization, with temperature equal to 120°C.

*2.3. Testing Methods.* After the biostabilization treatment, geomaterial samples were transported out of the PVC molds. Since the two-piece design of PVC molds was easy to split, after releasing the stainless-steel clamps, the undisturbed geomaterial samples could be demolded easily. Multiple tests were performed to evaluate the biostabilization effects on the engineering properties of the geomaterials.

Unconfined compression test is a simple method to assess the undrained strength and the stress-strain characteristics of the geomaterials, and it can verify the biostabilization effects on bonding geomaterial particles. A Geotest Instrument Corporation model S2010 device with 907.2 kg capacity was used in this study, and the procedures followed the ASTM D2166–16 Standard Test Method for Unconfined Compressive Strength of Cohesive Soil [14]. The load applied in the measurement could be read from the device in an increment of 4.5 kg. The compression strength ($\sigma_c$, kPa) under a given load can be determined with the following equation:

$$\sigma_c = \frac{P}{A}, \tag{3}$$

where $P$ (g) represents the load and $A$ ($cm^2$) is the mean cross-sectional area of the sample. Noted that the device provided values when gauge readings $\geq 22.5$ kg, and any gauge readings $< 22.5$ kg would be marked as $\sigma_c = 0$, indicating negligible compressive strength.

The scanning electron microscope (SEM) provides a nondestructive way to measure the surface morphology of geomaterial samples. Accelerated electrons in SEM carrying certain amount of kinetic energy are dissipated as a variety of signals due to the interactions between electrons and samples. These signals include secondary electrons, backscattered electrons, diffracted backscattered electrons, photons, visible light, and heat. SEM images are produced by the secondary electrons and backscattered electrons [15]. Diffracted backscattered electrons can be used to determine microstructures and mineral constituents.

Energy-dispersive X-ray spectroscopy (EDS) is a technique for analyzing the element abundance of the geomaterial samples with or without biostabilization treatments. EDS measurements are based on the X-ray emission spectrums from the samples, and each chemical element corresponds to a specific set of peaks in the observed spectrums, depending on its atomic structure [15, 16]. At ground state, an atom has electrons in quantized energy levels forming layered electron shells bound to the nucleus. To obtain the characteristic X-ray emissions, a high-energy beam of charged particles or a beam of X-ray strikes the geomaterial samples, excites electrons in inner (low-energy) shells, ejects them from inner shells, and creates electron vacancies. Electrons from outer (high-energy) shells can migrate to inner shells and fill those vacancies. Energy differences between high-energy and low-energy shells can be released as X-ray emissions. The energy of such X-ray emissions is measured by an energy-dispersive spectrometer, and the measured results correspond to the element abundance of the give geomaterial samples.

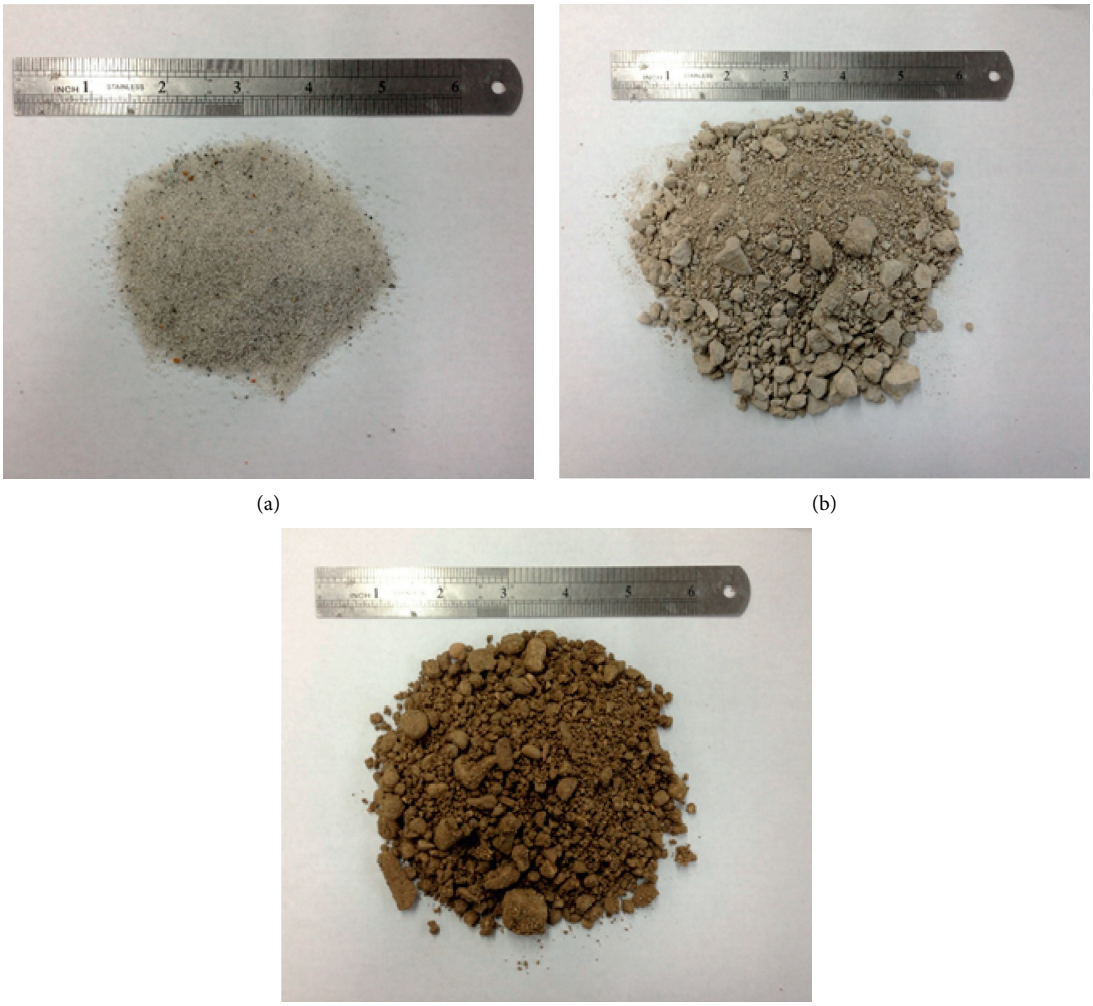

(a) (b) (c)

Figure 1: Three types of geomaterials included in this study: standard silica sand (a), surface material (SP-SM soil) (b) from an unpaved road, and surface material (SM soil) (c) from a highway construction sites.

X-ray diffraction (XRD) was used to determine the chemical compositions of the geomaterial samples with and without biostabilization. XRD characterizes chemical components based on the crystalline species [17, 18]. Crystals are composed of regularly aligned atoms, and planes of atoms in crystals are separated by a constant distance. Such a constant distance is the characteristic factor of the crystalline species. When monochromatic X-rays with finite energy and wavelength strike the crystal in a specific direction, presented by the angle ($\theta$) between the X-rays and the normal direction of the crystal surface, the X-rays scattered by crystal planes may be superposed and reinforced based on $\theta$, expressed via Bragg's law. Because minerals have their unique $\theta$ when diffraction occurs, depending on their interatomic distances within a mineral crystal, unique arrays of diffraction maxima can be obtained from XRD. Although the geomaterials contain particles or fine powders, there are still sufficient crystals properly oriented so that every set of crystal plane will be capable of diffraction, which ensured the operability of XRD measurements in determining the mineral species.

## 3. Result and Discussion

*3.1. Unconfined Compression Tests.* Geomaterial samples were treated using the liquid medium with $NH_4Cl$ or $(NH_4)_2SO_4$ for single-round or double-round of culturing and then saturated, air-dried, or oven-dried before the unconfined compression tests. Because the untreated, loose silica sand had no cohesion, therefore, no unconfined compressive strength, comparing with the SP-SM soil and SM soil, it was used as a reference to represent the "absolute effect" of the biostabilization. The results of unconfined compression tests are presented in Figure 2; log-scale was used in the $y$-axis due to the data range. Because the unconfined compressive strength ($\sigma_c$) is drawn in log-scale, $\sigma_c = 0$ cannot be directly presented; hence, negligible unconfined compression ($\sigma_c = 0$) is placed at the level of $x$-axis. In additional, experiments on

the silica sand treated in the liquid medium without the bacteria were performed to present the cohesion induced by the culturing procedures, and only two positive compression strength were observed from oven-dried samples, with values equal to 46.1 kPa and 19.6 kPa for $NH_4Cl$ and $(NH_4)_2$ $SO_4$ media, respectively.

In Figure 2, the saturated samples did not present any strength. For air-dried and oven-dried samples, besides the coherence due to the drying procedures, biostabilization contributed to the increase of $\sigma_c$ values. In general, the double-round culturing performed better than the single-round culturing, which is as expected because the longer the culturing period was, the stronger the MICP reaction were performed.

Oven-dried samples tended to produce larger $\sigma_c$ values comparing to the air-dried samples. One possible reason is when the water evaporated quickly under relatively high temperature, the water films between soil particles were shrunk and particles were pushed together, which enhanced the particle connections and made the soil matrix dense, while in air-dried samples, soil structures as well as the water films on particle surface tended to be retained. However, because of biostabilization, $\sigma_c$ values of oven-dried silica sand samples were 2–40 times larger comparing to the values from the oven-dried silica sand samples treated without bacteria, while no effective $\sigma_c$ values were observed for air-dried silica sand samples treated without bacteria. Thus, positive effects of biostabilization can be demonstrated.

Comparing the liquid media with $NH_4Cl$ or $(NH_4)_2$ $SO_4$, the trends of $\sigma_c$ values in saturated, air-dried, and oven-dried samples among the three geomaterials were similar; measurements under the saturated condition did not report effective $\sigma_c$, and $\sigma_c$ achieved maximum values under oven-dried conditions. However, since sulfates promote the formation of sulfuric acid, which could damage concrete, $\sigma_c$ values for samples with $(NH_4)_2$ $SO_4$ in the culturing medium tended to be lower than ones with $NH_4Cl$. Thus, $NH_4Cl$ would be a better choice for the biostabilization culturing medium.

*3.2. SEM Photograph.* Among all the samples, the oven-dried silica sand treated with the $NH_4Cl$ liquid medium (Figure 2(a)) showed a large increase in unconfined compressive strength, especially for the samples with double-round culturing. Therefore, it would be interesting to perform analyses for their microstructure and chemical compositions. Another benefit of using silica sand in these measurements is the original microscale shape of silica sand is relatively uniform, and the chemical compositions of silica sand are relatively simple, comparing to SP-SM soil and SM soil. Since all the three types of geomaterials were processed with the same biostabilization process, the consequences obtained from silica sand can be easily generated to the SP-SM soils and the SM soils.

Figure 3(a) shows the uniform and regular-shaped silica sand particles and the pore spaces between particles, which provides a reference for the morphology of silica sand. The surface of individual particle is relatively smooth with no additional substances. Some cracks, embossing, and cavities existed but can only be observed in 3000× SEM photographs, which is much smaller than the size of biostabilization-induced precipitates. Thus, we omit such photographs for simplicity.

For the silica sand after biostabilization treatments, SEM photographs were taken at multiple magnifications, and 100×, 300×, and 600× pictures are presented in Figures 3(b)–3(d), respectively. When sand particles are closed to each other, the pore spaces between them were partially filled and some particle-particle bridges were formed by precipitates induced by bacteria. However, most of the pore spaces were too large and the separation of particles was too wide, where filling or connections cannot be formed directly. In those cases, precipitates were observed on particle surface, which increased the particle surface roughness. This provided an explanation for the increasing unconfined compressive strength in silica sand after biostabilization, especially when silica sands were oven-dried.

*3.3. EDS and XRD Tests.* Figure 4 presents a (1500×) SEM picture that focused on a portion of particle surface. The shape and texture of the precipitates can be observed, including round, flat, clubbed, and irregular shapes. Four possible substances in Figure 4 are labelled, with the corresponding EDS results presented in Table 1. The element analysis for the untreated silica sand is also presented. Untreated silica sand consists of silicon, oxygen, and aluminum, while silica sand after biostabilization showed relatively complicated chemical compositions.

To examine the chemical compositions within the precipitates, XRD tests (Figure 5) were performed. Four main minerals were detected, including calcite ($CaCO_3$), dolomite [$CaMg$ $(CO_3)_2$], quartz ($SiO_2$), and albite [(Na, Ca) (Si, Al)$_4$ $O_8$]. Combining with the EDS results, calcite, dolomite, and albite were produced from the biostabilization. As shown in Figure 4, Label 1 indicated calcite and Label 3 indicated albite, while more than one mineral constituent existed at the other two locations.

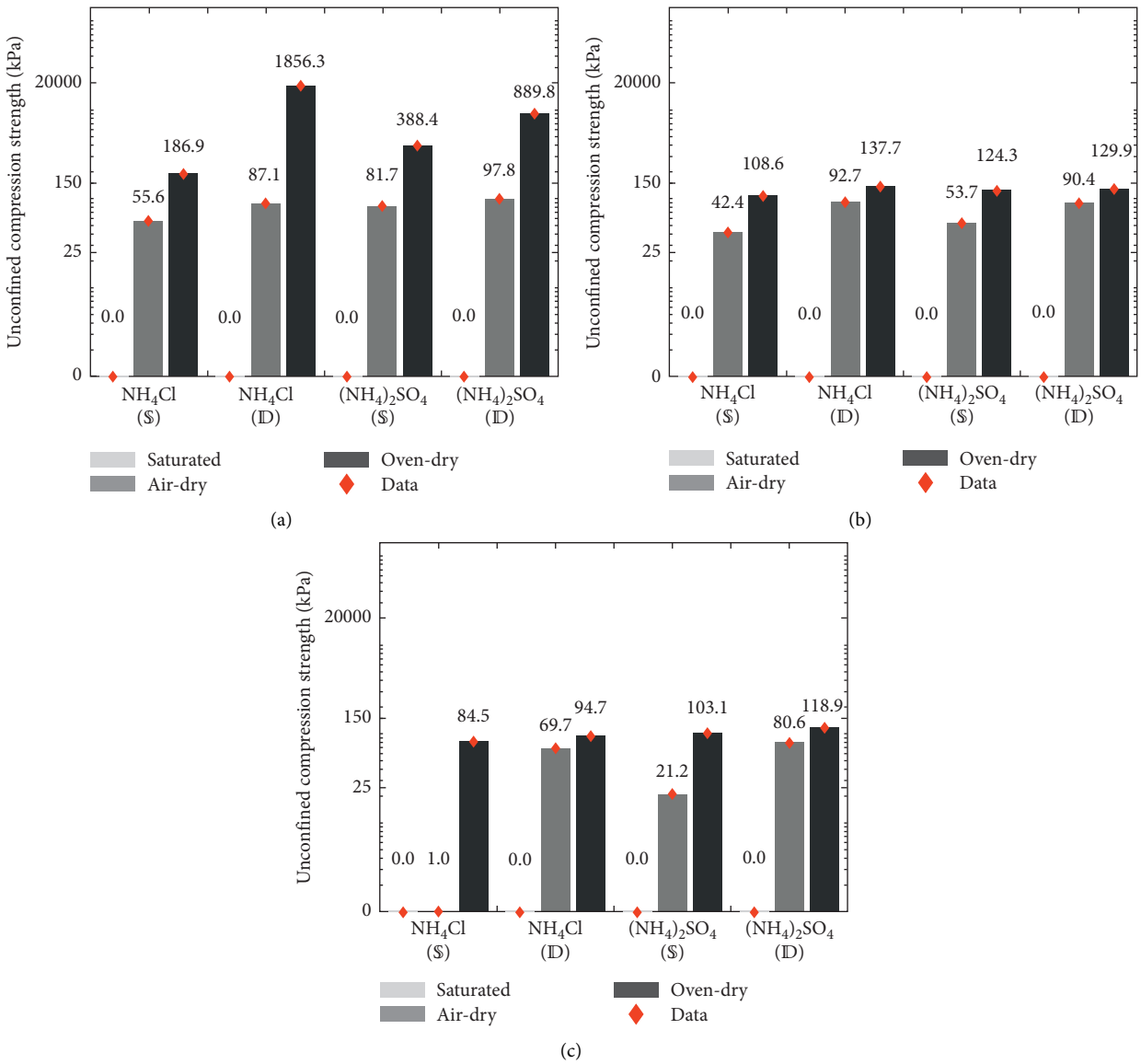


Figure 2: The results of unconfined compression tests for silica sand (a), SP-SM soil (b), and SM soil (c) after single-round of culturing (𝕊) and double-round of culturing (𝔻). Red diamonds mark the measured $\sigma_c$ results. Because the unconfined compressive strength ($\sigma_c$) is drawn in log-scale, zero values (negligible unconfined compression) are placed at the level of horizontal axis.

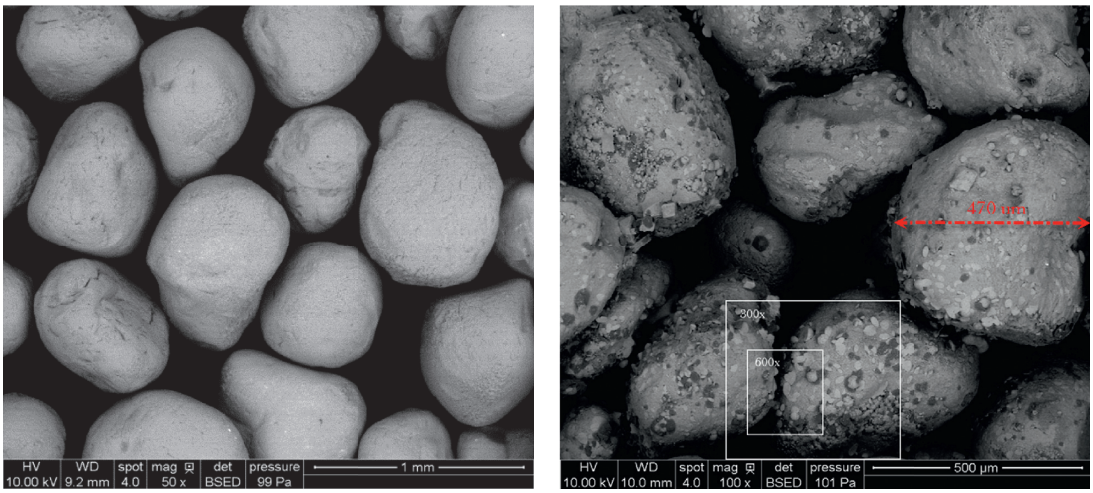


Figure 3: Continued.

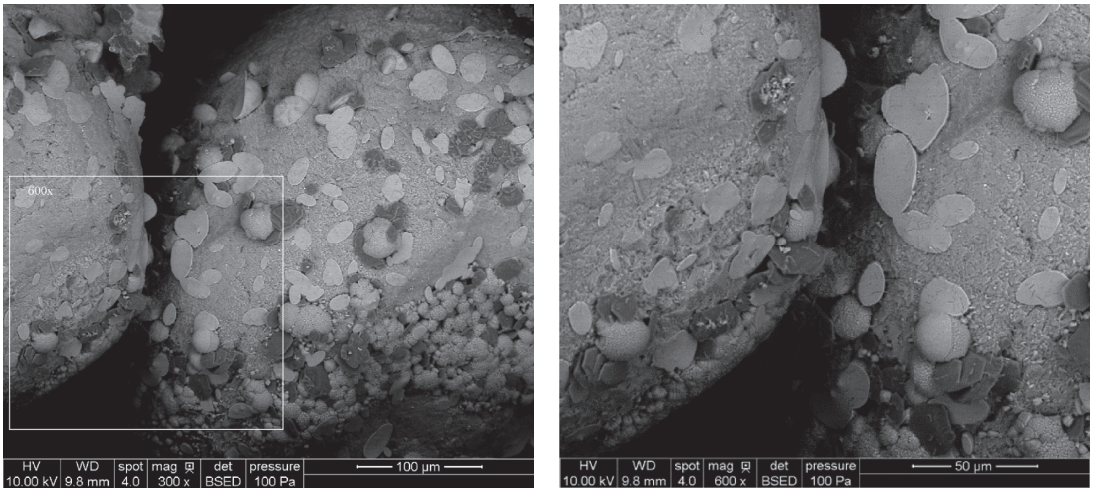


(c) (d)

Figure 3: The SEM photograph of original silica sand and silica sand after biostabilization: untreated silica sand (50×) (a); silica sands after biostabilization (100×) (b), (300×) (c), and (600×) (d). The white squares in (b) and (c) identify the magnified regions for (c) and (d), respectively.

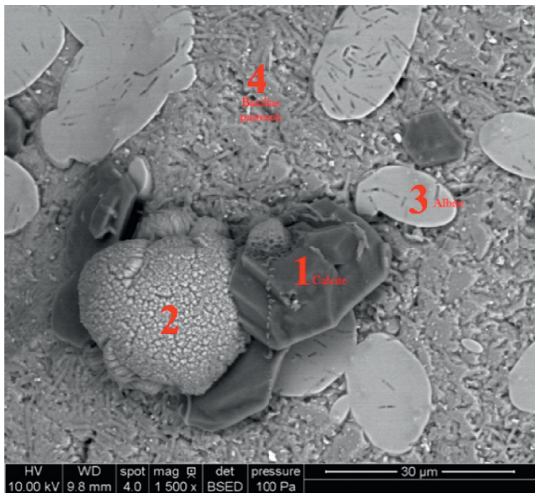


Figure 4: The SEM photograph of silica sand after biostabilization (1500×). Four red labels present 4 possible precipitation substances produced in biostabilization.

Table 1: Element abundance analyses with EDS for the 4 labelled substances in Figure 4 and the untreated silica sand.

| Element | Untreated silica sand | | Label 1 | | Label 2 | | Label 3 | | Label 4 | |
|---|---|---|---|---|---|---|---|---|---|---|
| | Atomic % | Weight % | Atomic % | Weight % | Atomic % | Weight % | Atomic % | Weight % | Atomic % | Weight % |
| O | 57.39 | 43.43 | 53.19 | 35.35 | 57.26 | 37.72 | 52.69 | 35.20 | 52.13 | 36.86 |
| Na | | | 0.43 | 0.41 | 0.20 | 0.19 | 0.75 | 0.72 | 0.09 | 0.09 |
| Al | 0.47 | 0.60 | 0.18 | 0.20 | 0.08 | 0.09 | 0.27 | 0.30 | 0.19 | 0.23 |
| Si | 42.14 | 55.98 | 15.98 | 18.65 | 11.92 | 13.78 | 18.95 | 22.22 | 37.95 | 47.10 |
| P | | | 0.04 | 0.05 | 0.09 | 0.11 | 0.01 | 0.01 | | |
| S | | | 1.49 | 1.99 | 2.56 | 3.38 | 10.32 | 13.81 | 1.58 | 2.25 |
| Cl | | | 22.84 | 33.64 | 6.77 | 9.88 | 3.65 | 5.40 | 3.75 | 5.88 |
| K | | | 0.42 | 0.68 | 0.34 | 0.54 | 1.04 | 1.69 | 0.39 | 0.67 |
| Ca | | | 5.43 | 9.04 | 20.79 | 34.31 | 12.34 | 20.65 | 3.92 | 6.93 |
| Total | 100.00 | 100.00 | 100.00 | 100.00 | 100.00 | 100.00 | 100.00 | 100.00 | 100.00 | 100.00 |

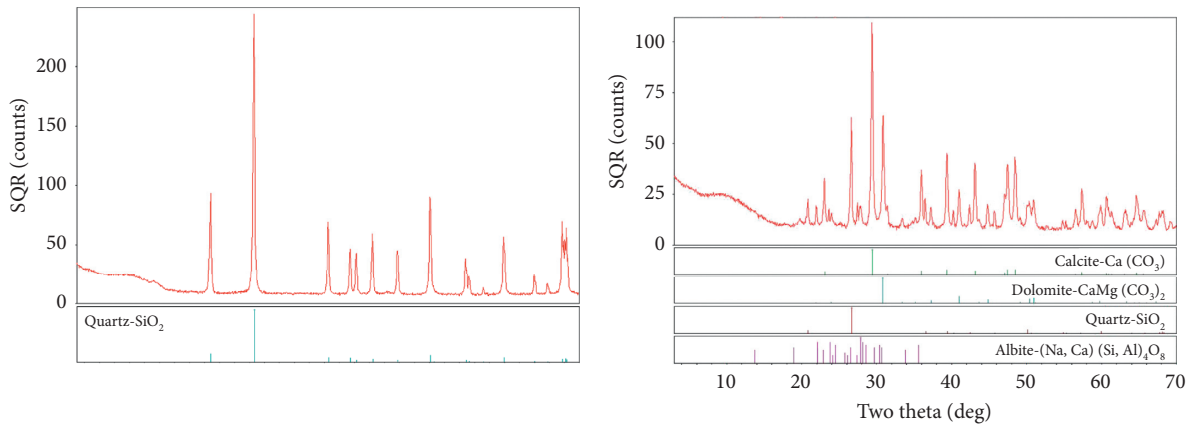


(a) (b)

Figure 5: XRD results for untreated silica sand (a) and silica sand after biostabilization (b).

## 4. Summary and Conclusions

Biostabilization was reported as a novel method to enhance unconfined compressive strength and improve other engineering properties of geomaterials. Biostabilization utilized certain types of bacteria to induce precipitates on geomaterials, which bonded the particles and partially filled the pore spaces. In this study, biostabilization was applied on three types of geomaterials, i.e., silica sand, SP-SM soils, and SM soils, where the two soil samples were from roadway surface. Biostabilization was performed using *Bacillus pasteurii*, and the selected geomaterial samples after biostabilization were tested for unconfined compressive strength, surface morphology, and chemical compositions.

Based on the results, biostabilization increased the averaged unconfined compressive strength by 3–6 times. Additional culturing period (double-round culturing) and dying with relatively high temperature (i.e., oven-dried samples) could magnify the biostabilization effects. By SEM and chemical analysis, the precipitates induced by bacteria included calcite, dolomite, and albite, and the precipitates adhered to particle surface to provide connections between adjoint particles and partially filled the pore spaces and increased the particle surface roughness, which explained the increasing of unconfined compressive strength from microscale perspectives.

Biostabilization, as a new geomaterials improvement technology, was studied to develop a series of standard procedures for bacteria culturing, biostabilization treatments for geomaterials, and performance evaluation. Results from this study verified the effectiveness of the biostabilization method in improving the geomaterial stability, quantified by unconfined compressive strength.

Comparing to literature results, this study adopted the soil and highway embankment and the subgrade filling-material as the geomaterial samples. New mineral composites, such as dolomite, calcium phosphate, and albite, were detected after the biostabilization treatments. The findings in this study provided evidence for the effects of biostabilization and reinforced our understanding to the biostabilization method. Future research could include the investigation of in situ biostabilization applications for soils, especially for gravels utilized in roadway infrastructure systems or the roadside soils received alkaline substances during road maintenance [19, 20].

## Data Availability

The original data used to support the findings of this study are available from the first author upon request.

## Additional Points

*Highlights/Core-Ideas.*(1) Biostabilization on three types of geomaterials was performed.(2) Precipitates produced by biostabilization included calcite, dolomite, and albite.(3) Pore space of samples was partially filled by precipitates after biostabilization.(4) Particle bonding and surface roughness were improved by biostabilization.(5) Unconfined compressive strength of samples after biostabilization was increased.

## Conflicts of Interest

The authors declare that they have no conflicts of interest.

## Acknowledgments

The authors would like to thank the Fundamental Scientific Research Fund Project of Central \Government Public Welfare Research Institutes (grant no. 2020-9052) for sponsoring this study.

## References

[1] Y. Yang, S. Li, C. Li et al., "Comprehensive laboratory evaluations and a proposed mix design procedure for cement-stabilized cohesive and granular soils," *Frontiers in Materials*, vol. 7, p. 239, 2020.

[2] S. Lv, J. Yuan, X. Peng et al., "Standardization to evaluate the lasting capacity of rubberized asphalt mixtures with different testing approaches," *Construction and Building Materials*, vol. 269, Article ID 121341, 2021.

[3] C. Liu, S. Lv, D. Jin, and F. Qu, "Laboratory investigation for the road performance of asphalt mixtures modified by rock asphalt–styrene butadiene rubber," *Journal of Materials in Civil Engineering*, vol. 33, Article ID 04020504, 2021.

[4] V. J. Marks and W. Dubberke, "Durability of concrete and the Iowa pore index test," *Transportation Research Record*, vol. 853, pp. 25–30, 1982.

[5] J. T. DeJong, M. B. Fritzges, and K. Nüsslein, "Microbially induced cementation to control sand response to undrained shear," *Journal of Geotechnical and Geoenvironmental Engineering*, vol. 132, no. 11, pp. 1381–1392, 2006.

[6] S. K. Ramakrishnan, R. K Panchalan, and S. S. Bang, "Improvement of concrete durability by bacterial mineral precipitation," in *Proceedings of the 11th International Conference on Fracture*, Turin, Italy, December 2001.

[7] J. T. DeJong, B. M. Mortensen, B. C. Martinez, and D. C. Nelson, "Bio-mediated soil improvement," *Ecological Engineering*, vol. 36, no. 2, pp. 197–210, 2010.

[8] V. S. Whiffin, L. A. Van Paassen, and M. P. Harkes, "Microbial carbonate precipitation as a soil improvement technique," *Geomicrobiology Journal*, vol. 24, no. 5, pp. 417–423, 2007.

[9] K. L. Bachmeier, A. E. Williams, J. R. Warmington, and S. S. Bang, "Urease activity in microbiologically-induced calcite precipitation," *Journal of Biotechnology*, vol. 93, no. 2, pp. 171–181, 2002.

[10] H. M. Jonkers, A. Thijssen, G. Muyzer, O. Copuroglu, and E. Schlangen, "Application of bacteria as self-healing agent for the development of sustainable concrete," *Ecological Engineering*, vol. 36, no. 2, pp. 230–235, 2010.

[11] M. B. Burbank, T. J. Weaver, T. L. Green, B. C. Williams, and R. L. Crawford, "Precipitation of calcite by indigenous microorganisms to strengthen liquefiable soils," *Geomicrobiology Journal*, vol. 28, no. 4, pp. 301–312, 2011.

[12] F. D. Meyer, S. Bang, S. Min, and L. D. Stetler, "Microbiologically induced soil stabilization: application of *Sporosarcina pasteurii* for fugitive dust control," *Geo-Frontiers: Advances in Geotechnical Engineering*, vol. 2011, 2011.

[13] S. S. Bang and V. Ramakrishnan, "Microbiologically enhanced crack remediation (MECR)," in *Proceedings of the International Symposium on Industrial Application of Microbial Genomes*, vol. 1, pp. 3–13, 2001.

[14] ASTM D-2166, *Standard Test Method for Unconfined Compressive Strength of Cohesive Soil*, ASTM International, West Conshohocken, PA, USA, 2016.

[15] J. I. Goldstein, D. E. Newbury, J. R. Michael, N. W. M. Ritchie, J. H. J. Scott, and D. C. Joy, *Scanning Electron Microscopy and X-Ray Microanalysis*, Springer, New York, NY, USA, 2017.

[16] R. Jenkins and J. L. De Vries, *Practical X-Ray Spectrometry*, Macmillan Education, London, UK, Second edition, 1970.

[17] B. D. Cullity, *Elements of X-Ray Diffraction*, Addison-Wesley Publishing Company, Inc, Boston, MA, USA, 1956.

[18] L. D. Whittig and W. R. Allardice, "X-ray diffraction techniques," *Methods of Soil Analysis: Part 1 Physical and Mineralogical Methods*, vol. 5, pp. 331–362, 1986.

[19] C. Luo, Z. Wang, F. Kordbacheh et al., "The influence of concrete grinding residue on soil physical properties and plant growth," *Journal of Environmental Quality*, vol. 48, no. 6, pp. 1842–1848, 2019.

[20] C. Luo, Z. Wang, F. Kordbacheh et al., "A greenhouse study of concrete grinding residue influences on seedling emergence and early growth of selected prairie species," *Water, Air, & Soil Pollution*, vol. 231, p. 253, 2020.

Hindawi
Advances in Civil Engineering
Volume 2021, Article ID 5533441, 9 pages
https://doi.org/10.1155/2021/5533441

*Research Article*

# Modification Mechanism of Asphalt Modified with Rock Asphalt and Styrene-Butadiene Rubber (SBR)

**Xiangming Deng,[1,2,3] Hui Huang,[2,4] Bin Wang,[2,4] and Jie Chen[2,4]**

[1]*Changsha University of Science and Technology, Changsha 410114, China*
[2]*Guangxi Key Lab of Road Structure and Materials, Nanning 530007, China*
[3]*Guangxi Communications Investment Group Corporation Ltd., Nanning 530022, China*
[4]*Guangxi Transportation Science and Technology Group Co., Ltd., Nanning 530007, China*

Correspondence should be addressed to Hui Huang; 88974719@qq.com

Received 4 February 2021; Revised 23 March 2021; Accepted 12 April 2021; Published 21 April 2021

Academic Editor: Jian Ji



High-performance asphalt binder plays an important role in the durable asphalt pavement. Asphalt modified by rock asphalt (RA) is one of the high-performance modified asphalt materials. It was used in road engineering as a relatively environmentally friendly material, because rock asphalt takes some advantages of large reserves, easy treatment, and efficient modification. Moreover, the main component of rock asphalt is bitumen, which enables it to substitute part of the binder used in asphalt mixtures. On the other hand, the negative low-temperature performance of RA modified asphalt impeded its application in cold regions. The object of this paper is to improve the low-temperature performance of RA modified asphalt by compound modified with styrene-butadiene rubber (SBR). The 70-penetration grade binder and the RA modified asphalt with 15% RA by weight were applied as the base binder. Five types of RA-SBR modified asphalt were prepared, and the content of SBR was 2%, 4%, 5%, 6% and 8% by weight of BRA modified binder. The Fourier transform infrared spectroscopy (FTIR) tests were utilized to illustrate the reasons for the poor low-temperature performance of BRA modified asphalt and reveal the compound modification mechanism of BRA-SBR modified asphalt. The Brookfield viscosity test, dynamic shear rheometer test, and bending beam rheometer test were adopted to reveal the variation patterns of rheological behavior and low-temperature performance with mass contents of SBR. The test results indicated that the worse of low-temperature performance was caused by the increase of asphaltene content and the stress concentration due to ash in RA modified asphalt. And the compound modification is a physical process. The addition of SBR has improved the low-temperature performance of RA modified asphalt dramatically. And based on the rheological behaviors and low-temperature performance of RA-SBR compound modified asphalt, the optimum content of SBR was determined, which is about 4%~5%.

## 1. Introduction

With the steadily growing axle loads and traffic volume, neat asphalt would fail to meet the requirements of durable pavement, unless it was well modified [1–3]. For example, SBS modified asphalt is the most popular modified asphalt, with both good performance of high- and low-temperature [4–7]. However, the production of most modifier and modified asphalt is complex and costly, resulting in an increase in fuel consumption and polluting gases [8–11]. Moreover, the dissolution of most modifiers with asphalt is not qualified enough, which disperses states of modifier in asphalt, segregation [12–15]. Therefore, most researchers have been committed to the development of economical and effective modifier.

Rock asphalt is a natural material, which is produced by impregnation of petroleum or oil into rocks such as limestone followed by the combined action of heat, pressure, oxidation, and bacteria over millions of years [16–18]. Obviously, the two predominant constituents of rock asphalt are asphaltene and mineral fillers, which are combined stably and guaranteed its good solubility in asphalt [19, 20]. Rock asphalt has some advantages in terms of saving base asphalt, having lower cost, and being used easily during asphalt

production without shearing, which reduced the resource consumption and polluting gases emission during pavements construction. One type of rock asphalt is Buton rock asphalt with a large number of reserves, which is widely used as a preferred modifier for asphalt in road engineering.

Buton rock asphalt is produced on the island of Buton, Indonesia, Southeast Asia. The asphaltene content of BRA is about 20%, which could substitute part of asphalt binder used in asphalt mixture [21]. Previous research by other researchers has shown that Buton rock asphalt could act as a physical modifier to enhance honeycomb structure of the binder [22]. Multiple types of research and engineering also had proved that the addition of Buton rock asphalt could improve the performance of asphalt and asphalt mixtures, such as high-temperature performance, antiaging properties, antifatigue performance, and antisliding performance [23–25].

On the other hand, the low-temperature performances of BRA modified asphalt were unfavorable in comparison to the base binder [26]. So, some other additives were adopted by individuals as compound modifiers to modify the base binder accompanied by BRA to improve all kinds of performances. Two kinds of modifiers—styrene-butadiene rubber (SBR) and nano-$CaCO_3$—were selected as the compound modifiers in Lv's research to improve the low-temperature performances of BRA modified asphalt [27]. The results indicated that thermal crack resistance of BRA modified asphalt was improved dramatically with the addition of both SBR and nano-$CaCO_3$, and the effects of SBR were better. Ren et al. investigated the effects of SBR on the properties of gilsonite modified asphalt and found that the compatibility and high- and low-temperature performance of gilsonite/SBR modified asphalt containing 30 wt% gilsonite realized the balance when the mixing content of SBR was about 7.5 wt% [28]. Cai et al. used nanosilica, rock asphalt, and SBS to compose modified asphalt and found that nanosilica/rock asphalt/SBS modified asphalt mixture had higher temperature stability, low-temperature cracking resistance, moisture susceptibility, and durability than single modified asphalt [29]. In a word, the compound modification could keep the balance of high- and low-temperature performance of asphalt. SBR is supposed to be a preferable compound modifier of BRA modified asphalt, as it has advantages of lower cost and better cracking resistance. As mentioned above, there had been some researchers focusing on the mechanism for the better performance of BRA modified asphalt, but little existing research reveals the internal cause for the drop of low-temperature performance of BRA modified asphalt. Despite these significant research advancements in improving the low-temperature of BRA modified asphalt, rare research compares the changes of the components and microstructures of asphalt before and after modification.

In addition, the mechanisms of the variation of its performance could be revealed to verify the modification. Therefore, in this paper, SBR was employed to improve the low-temperature performance of BRA modified asphalt. The Fourier transform infrared spectroscopy (FTIR) tests were implemented to reveal the modification mechanism by determining the changes of the components of asphalt before and after modification. The Brookfield viscosity test, dynamic shear rheometer test, and bending beam rheometer were adopted to reveal the variation patterns of rheological behavior and low-temperature performance with mass contents of SBR, with which the optimum content of SBR could be obtained for the high-performance BRA-SBR modified asphalt.

## 2. Objectives

The main objectives of this research are as follows:

(1) To improve the low-temperature performance of BRA modified asphalt by compound modified with styrene-butadiene rubber (SBR).

(2) To reveal the modification mechanism of asphalt compound modified by BRA and SBR by changes of the components and functional groups of asphalt before and after modification.

(3) To analyze the effects of SBR on the road performances of BRA modified asphalt and determine the optimum content of SBR based on the variation patterns of mechanic parameters with the SBR content.

## 3. Materials and Preparation

*3.1. Asphalt Binder.* The asphalt binder of 70-penetration grade adopted in this research was produced in Wuhan province in China. Its specific technical properties were tested according to the Chinese Technical Specification for Construction of Highway Asphalt Pavements (JTG F40-2004), and the test results are in agreement with the requirement of standard specification and are presented in Table 1.

*3.2. Buton Rock Asphalt.* Buton rock asphalt used in this study was produced in Southeast Asia on the island of Buton, Indonesia. The asphaltene content of BRA is about 20%, which could substitute part of the asphalt binder used in asphalt mixture. Moreover, Buton rock asphalt also takes advantage of compatibility with asphalt, improving the antiaging and durability of asphalt, and nonwax. The specific technical properties were tested according to the Chinese Standard Test Methods of Bituminous and Bituminous Mixtures for Highway Engineering (JTG E20-2011), and test results are presented in Table 2. The test results showed that Buton rock asphalt meets all technical requirements in specifications.

*3.3. Styrene-Butadiene Rubber.* Styrene-butadiene rubber is a kind of synthetic rubber that has been proved to be an effective modifier for the low-temperature performance of asphalt. In this research, the SBR employed as a compound modifier was SBR 1502 rubber, which is specially produced for modifying asphalt by a company of Tianjin city in China. Its specific technical properties were tested according to the

Table 1: Technical properties of asphalt binder of 70-penetration grade.

| Property | Units | Test results | Technical requirements | Specification |
|---|---|---|---|---|
| Penetration (25°C, 100 g. 5 s) | 0.1 mm | 68.2 | 60–80 | JTG E20 T0604 |
| Penetration index | / | -0.743 | - 1.5~+1.0 | |
| Softening point (R&B) | °C | 49.1 | ≥46 | JTG E20 T0606 |
| Ductility at 15°C | cm | >100 | >100 | JTG E20 T0605 |
| After TFOT (163°C, 85 min) | | | | |
| Mass loss | % | 0.15 | ≤±0.8 | JTG E20 T0609 |
| Residual penetration rate (25°C) | % | 64 | ≥61 | JTG E20 T0604 |
| Residual ductility (15°C) | cm | 8.1 | ≥6 | JTG E20 T0605 |

Table 2: Technical properties of Buton rock asphalt.

| Property | Test result | Technical requirements | Specification |
|---|---|---|---|
| Solubility in trichloroethylene (%) | 25.8 | > 25 | JTG E20 T0607 |
| Content of impurities such as soil (%) | 0.8 | < 1 | JTG E42 T0333 |
| Moisture content (%) | 0.5 | < 1 | JTG E42 T0332 |
| Ash content (%) | 74.1 | 65–75 | JTG E20 T0735 |
| Ash content difference in the same batch of samples (%) | 0.4 | ≤1 | JTG E20 T0735 |
| Ash content difference in the different batch of samples (%) | 0.8 | ≤5 | JTG E20 T0735 |
| Density (g/cm$^3$) | 1.75 | > 1.6 | JTG E42 T0328 |

Chinese Standard of Rubber, styrene-butadiene-rubber (SBR) 1520 (GB12824), and the test results were presented in Table 3. Each indicator meets the Chinese specification.

*3.4. Preparation of Modified Asphalt.* Based on the previous research (reference), Buton rock asphalt could improve the high-temperature performance, durability, and moisture sensitivity of asphalt. The BRA modified asphalt would peak at the climax of comprehensive performance when the weight content of BRA was 15%. Therefore, in this study, the content of the BRA was 15%, and five different weight contents of SBR were 0%, 2%, 4%, 5%, 6%, and 8%. The asphalt binder of 70-penetration grade and BRA modified asphalt were applied as control samples.

The high-speed shear emulsifying machine was employed to mixing the base asphalt binder, BRA, and SBR to prepare BRA-SBR modified asphalt. The preparation procedure referred to Chinese Standard Test Methods of Bituminous and Bituminous Mixtures for Highway Engineering (JTG E20-2011), details presented in Figure 1.

(1) Heat the base binder stored in the metal cup by the oven to the temperature of 150°C, and keep the temperature steady for an hour.

(2) Take out of the base binder from the oven, and put it on an electronic furnace to keep the temperature of the binder at a range of 160–170°C, which is monitored by a thermometer inserted in the binder.

(3) Mix the base binder at the rotation rate of 1000 rpm, during which the weighted SBR was added into the base binder in several times. Then, the rotation speed is adjusted to 3000 rpm after all SBR added into the binder, and keep mixing for 20 min.

(4) Add the weighted BRA, and mix for half an hour.

## 4. Experiment Plan

*4.1. Characteristic of Morphology and Microstructures.* Fourier-transform infrared spectroscopy (FT/IR) can be applied to get the material structure and functional group of the solid, liquid, and gas according to its infrared absorbance spectrum [30]. In this study, the experimental equipment was BRUKER TENSOR II Fourier transform infrared spectrometer made by a German company. The scanning range recorded in this study was from 400 cm$^{-1}$ to 4000 cm$^{-1}$ wavenumber range with averaging 16 scans at a resolution of 4 cm$^{-1}$. The scanning range was decided by the molecular structure of asphalt, shown in Table 4. The main wavenumber of the asphaltic material was presented in Table 4.

During the FT/IR test, the equipment shines a beam containing the infrared frequency of light at once and measures how much of that beam is absorbed by the sample. This process is repeated many times. Afterwards, computer processing is required to turn the raw data (interferogram) into the desired result (light absorption for each wavenumber). By analyzing the absorbance of infrared in a certain region, the existence and intensity of specific functional groups can be identified. In this study, the BRUKER TENSOR II Fourier transform infrared spectrometer was adopted to assess the chemical changes of base binder treated with BRA, SBR, or BRA-SBR.

*4.2. Characteristic of Rheological Performances at Different Temperatures.* The rheological performance at different temperatures is usually thought to be a sensitive evaluation method to evaluate the temperature sensitivity and high-temperature performance. In this study, the Brookfield viscosity test and dynamic shear rheometer test were adopted to characterize the rheological performances of the asphalt at different temperatures. The Brookfield viscosity test was conducted under four experimental temperatures,

Table 3: Technical properties of SBR 1502.

| Property | Test result | Technical requirement | Specification |
|---|---|---|---|
| Content of butadiene (%) | 70 | 68–71 | GB12824-91 |
| Mooney viscosity | 52 | 50–53 | GB12824-91 |
| Fineness with the mesh number of 10 (%) | 100 | Mesh number of 10 or 20 | GB12824-91 |
| Styrene content (%) | 23.5 | 23.5 | GB12824-91 |
| Volatilization (%) | 0.2 | ≤0.8 | GB12824-91 |
| Ash content (%) | 7.5 | ≤8 | GB12824-91 |
| Tensile strength | 26.5 | ≥26 | GB-8655-88 |
| Elongation at break (%) | 540 | ≥500 | GB-8655-88 |
| Soap content (%) | 0.15 | ≤0.5 | GB12824-91 |
| Content of organic acid (%) | 6.3 | 6.3 | GB12824-91 |

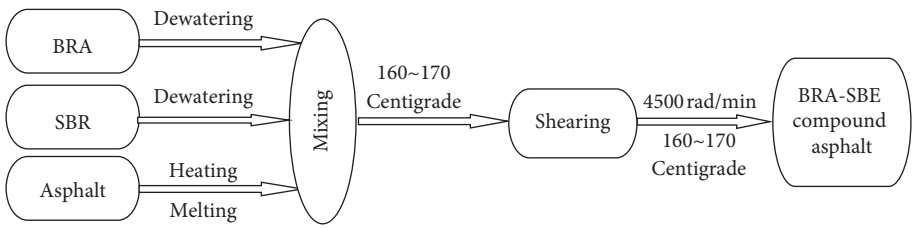


Figure 1: Production process of BRA-SBR compound modified asphalt.

Table 4: Assignations of the Main Bonds of FT/IR Spectra in the main compounds of asphalt.

| Peak items | Main wavenumber ($cm^{-1}$) | Vibrations |
|---|---|---|
| Saturated hydrocarbon | 1475–700, 1375–1380, 1400, 720 | C-H, C-C, C-CH3, H-C-H, -CH2-, |
| Aromatic hydrocarbon | 3030, 1600–1500, 1500–1480, 1610–1500, 1650–1600, 1525–1450, 2000–1670 | C-H, C=C |
| Carboxyl compound | 1725, 1690, 2820, 2720, 1700–1670, 1690–1600, 3550, 3200–2500, 1700–1680, 920, 1860–1750, 1740, 1700, 1300–1050, 1210–1160 | C=O, O-H, C-O-C |
| Hydroxy compound | 2700–2500 | -COOH |
| Nitrogen-containing compound | 3050, 1690–1650, 1640–1600, 1400, 1680–1655, 1550–1530, 1300, 620 | C-H, C-N, O=C-N |
| Sulfur-containing compound | 2992–2955, 2897–2869, 1090, 2590–2560, 1065–1030, 520–430 | S-C, ArSH, S=O, S-S |

i.e., 135, 145, 165, and 175°C, with a rotation rate of 10 r/min. The viscosity in different temperatures can be used to evaluate the temperature sensitivity and simulate the workability of the asphalt used in asphalt mixtures application for different seasons. Furthermore, the rheological behaviors of asphalt were evaluated by dynamic shear rheology (DSR) test. The Smart Pave Dynamic Shear Rheometer (DSR) was employed to investigate the performance of these three types of asphalt, e.g., rutting resistance. It is well known that rutting and stripping are the common distresses in asphalt pavements. The rutting indicator, $G*/\sin(\delta)$, of the asphalt was examined according to the Chinese Standard Test Methods of Bituminous and Bituminous Mixtures for Highway Engineering (JTG E20-2011). The initial test temperature was 40°C, at which the complex shear moduli $G*$ and phase angle $\delta$ were measured. And then, the test temperature increased by 6°C each time, until the rutting indicator was less than 1 kPa.

*4.3. Low-Temperature Performance Tests.* The bending beam rheometer (BBR) creep test is usually thought to be the effective evaluation method to evaluate the low-temperature performance of asphalt according to the specification of Superpave. Therefore, BBR was employed to evaluate the low-temperature performance of these three types of asphalt in this study. According to the Chinese Standard Test Methods of Bituminous and Bituminous Mixtures for Highway Engineering (JTG E20-2011), the stress-controlled procedure was conducted to obtain the creep stiffness $S(t)$ and parameter $m$ of the asphalt. The creep tests of the asphalt were carried out under different test temperatures, i.e., −6°C, −12°C and −18°C by TE-BBR as shown in Figure 1. The size of the asphalt specimen test by TE-BBR was 101.6 mm × 12.7 mm × 6.4 mm, as Figure 2 showed. The loads and deformation in the testing process are automatically collected by the computer data acquisition system.

## 5. Results and Discussions

*5.1. Fourier-Transform Infrared Spectroscopy Test.* The base asphalt, BRA modified asphalt, and BRA-SBR compound modified asphalt were analyzed through the FTIR test. The infrared spectra of these three types of asphalt are shown in Figure 3.

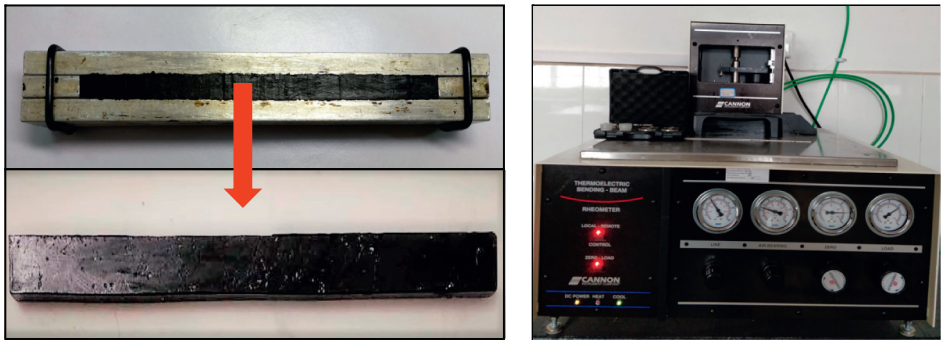

(a) (b)

Figure 2: Thermoelectric bending beam rheometer and specimen.

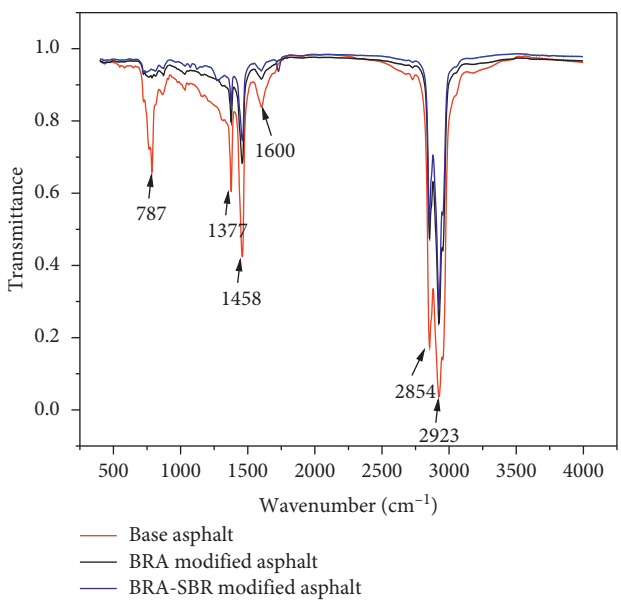


Figure 3: Infrared spectra of three types of asphalt.

FTIR methodology can detect molecular vibrations. From the infrared spectra, the material information on chemical bonding and material structure can be obtained. As can be seen from Figure 3, it is obvious that the infrared spectra of base asphalt differed from the BRA modified asphalt and BRA-SBR compound modified asphalt. Many peaks were smaller after modification, and no new peaks were generated. This denoted that the content of some compounds was decreased, and the modification was a physical reaction. The peak at 787 cm$^{-1}$ decreased dramatically, and this peak was the extrinsic bending vibrations of C-H in Alkene. The peak at 1377 cm$^{-1}$, the peak at 1458 cm$^{-1}$ 1, and the peak at 1600 cm$^{-1}$ were the C=C ring stretch from aromatic compounds.

*5.2. Brookfield Viscosity Test.* Usually, the series of viscosity tests are designed to determine the mixing and compaction temperature for asphalt mixtures. On the other hand, the various properties of viscosity with temperature have thought to be an effective method to evaluate the temperature sensitivity of asphalt. The Brookfield viscosity of BRA-SBR modified asphalt with different contents of SBR was measured under four selected test temperatures in this study. The test results are presented in Figure 4.

As can be seen in Figure 3, the addition of SBR had an obvious effect on the viscosity of BRA-SBR modified asphalt. In a certain threshold of SBR content and the selected test temperatures, the viscosity varied with the content of SBR in three stages. First, the viscosity declined slightly but obviously, when the BSR content increased from 0% to 4%. Then, the decreasing rate increased when the BSR content increased from 4% to 6%, and the valley values occurred when the SBR content was 6%. After the content of SBR exceeded 6%, the changing trend of viscosity altered and increased with the increase of SBR content. When the content of SBR exceeded 6%, it was becoming difficult for SBR to diffuse in asphalt uniformly, which contributes to the increase of the viscosity of BRA-SBR modified asphalt.

Meanwhile, it was also observed that when the test temperature became higher, the rate in which viscosity decreased with SBR content was visibly smaller. The viscosity of BRA-SBR modified asphalt with 6% SBR, where the viscosity was at the valley value and was about 0.077 Pa·s smaller than that of asphalt with 2% SBR at the test temperature of 135°C, while at the temperature of 175°C, it was 0.027 Pa·s.

The viscosity-temperature index (VTS) was adopted to evaluate the temperature sensitivity of asphalt, and the greater the VTS, the worse the temperature sensitivity. Viscosity-temperature curve and index were obtained by regression and fitting, which guarantee the precision of VTS while comparing with other methods. The Brookfield viscosity test results were fitted with test temperature by equation (1), and the fitting results could be found in Figure 5 and Table 5.

It is observed from Table 5 that the VTS of BRA-SBR modified asphalt changed with the addition of SBR. The VTS increased with the increase of SBR contents before the SBR content exceeded 6%, after which the VTS decreased but still larger than that of BRA modified asphalt. It indicated that the addition of SBR aggravated the temperature sensitivity and the high-temperature stability of BRA modified asphalt. But the temperature sensitivity and the high-temperature

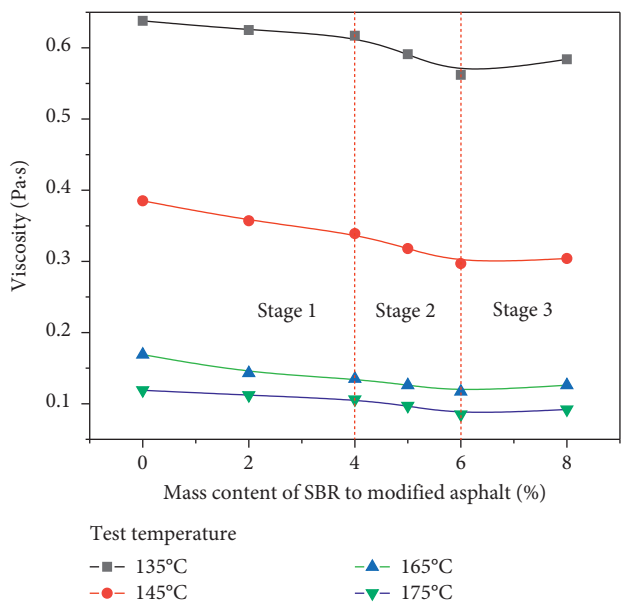


Figure 4: Variation patterns of brookfield viscosity with SBR contents.

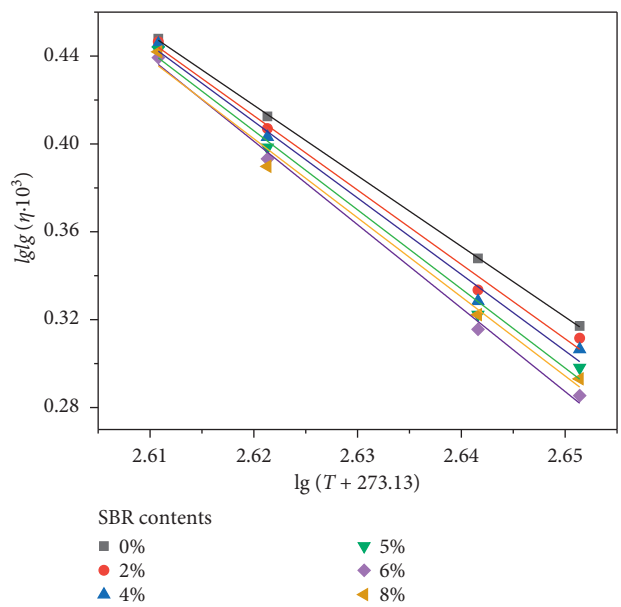


Figure 5: Viscosity-temperature curves of BRA-SBR modified asphalt with different SBR contents.

stability of BRA-SBR modified asphalt were still better than those of base asphalt and even than SBS modified asphalt according to previous researches.

*5.3. Dynamic Shear Rheology Test.* As shown in the Brookfield viscosity test results, the addition of SBR has a significant influence on the temperature stability of BRA modified asphalt. In order to reveal the effects of SBR on the viscoelastic properties and the antirutting performance, the dynamic shear rheology (DSR) test was conducted for the BRA-SBR modified asphalt with different SBR contents. The test results were presented in Figure 6 and Figure 7.

As can be seen in Figure 6, the phase angle of all the asphalt increased with the increase of test temperatures. The phase angle has usually been thought as an indicator to reflect the viscoelastic properties, and the greater phase angle means greater viscous portion. Under the same test temperature, the phase angle increased with the content of SBR, which implied that the addition of SBR improved the elasticity properties of asphalt.

On the other hand, the rutting indicators were calculated to reveal the influences of SBR on the BRA modified asphalt. The higher value of rutting indicators indicates a better high-temperature performance. Figure 6 displayed the $G*/\sin(\delta)$ of BRA-SBR modified asphalt with different contents of SBR. It could be observed that the $G*/\sin(\delta)$ of all the asphalt declined with the increase of test temperatures and decreased slowly after 64°C. Meanwhile, at the same test temperature, the $G*/\sin(\delta)$ increased with the increase of the SBR content. It suggested that the resistance to rutting was reduced with the rise of temperature but improved with the addition of SBR.

The distress of asphalt pavement like rutting usually occurred in summer when the temperature of pavement was about 60°C. The test temperatures of DSR were

Table 5: The fitting results of the viscosity-temperature curve for BRA-SBR modified asphalt.

| Parameters | SBR content (%) | | | | | |
|---|---|---|---|---|---|---|
| | 0 | 2 | 4 | 5 | 6 | 8 |
| $M$ | 3.21 | 3.39 | 3.48 | 3.60 | 3.80 | 3.61 |
| $N$ | 8.84 | 9.28 | 9.53 | 9.84 | 10.35 | 10.25 |
| $R^2$ | 0.97 | 0.94 | 0.96 | 0.92 | 0.95 | 0.94 |

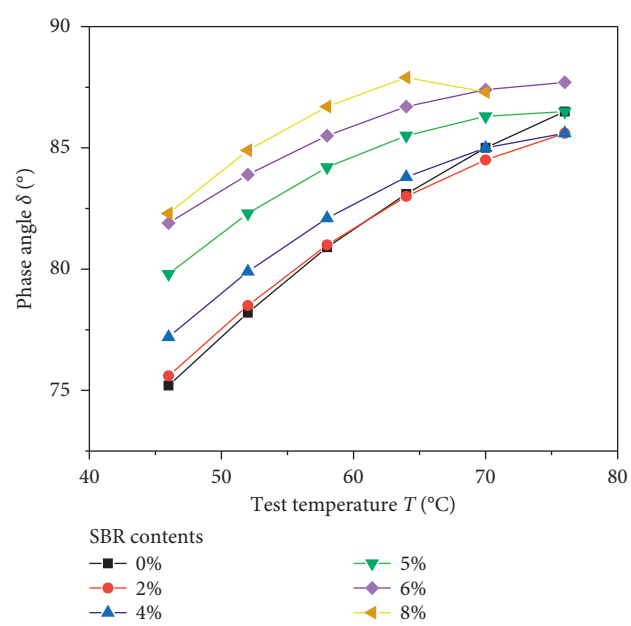


Figure 6: The variation patterns of phase angle and test temperatures.

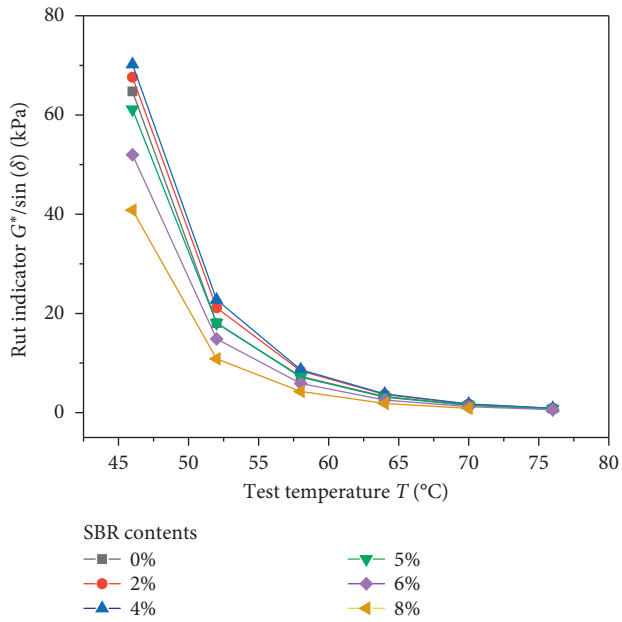


Figure 7: The variation patterns of rutting indicators and test temperatures.

approximately similar to the temperature of the pavement in summer. So, it has been thought that the variation pattern of $G^*/\sin\delta$ during this range of temperature was more suitable to evaluate the temperature stability of asphalt used in road engineering than penetration or Brookfield viscosity. According to reference [30], the $G^*/\sin\delta$ was fitted by equation (1) in double natural logarithmic coordinates, and the fitting results were presented in Figure 8 and Table 6.

$$\lg\lg\left(\eta \times 10^3\right) = n - m\lg(T + 273.13). \quad (1)$$

As can be seen in Figure 8, the slope of the curve quantified by the parameter $a$ in equation (1) could reflect the change rate of $G^*/\sin\delta$ with test temperature. So, the parameter could be adopted as an index to evaluate the temperature sensitivity of asphalt. It is obviously observed from Table 6 that the change rate became down with the increase of SBR content, which meant that the temperature stability of BRA-SBR modified asphalt improved with the content of SBR.

*5.4. Bending Beam Rheometer (BBR) Creep Test.* According to the specification of Superpave, the low-temperature performance of asphalt binder is qualified when its creep stiffness is less than 300 MPa, and the $m$-value is larger than 0.3. The bending beam rheometer creep test results of BRA modified asphalt modified with different content of SBR were presented in Table 7.

Based on the results, it could be found that the addition of SBR has a significant influence on the low-temperature performance of BRA modified asphalt. The creep stiffness $S_t$ decreased with the content of SBR dramatically. Under the SBR content of 2%, 4%, 5%, 6%, and 8%, the creep stiffness of BRA modified asphalt decreased about 14.5%, 27.7%, 43.0%, 48.6%, and 53.4%, respectively. As to the creep rate, the $m$-value increased with the content of SBR obviously. Under the SBR content of 2%, 4%, 5%, 6%, and 8%, and the $m$-value of BRA modified asphalt increased about 8.6%, 14.3%, 21.9%, 28.9%, and 35.9%, respectively.

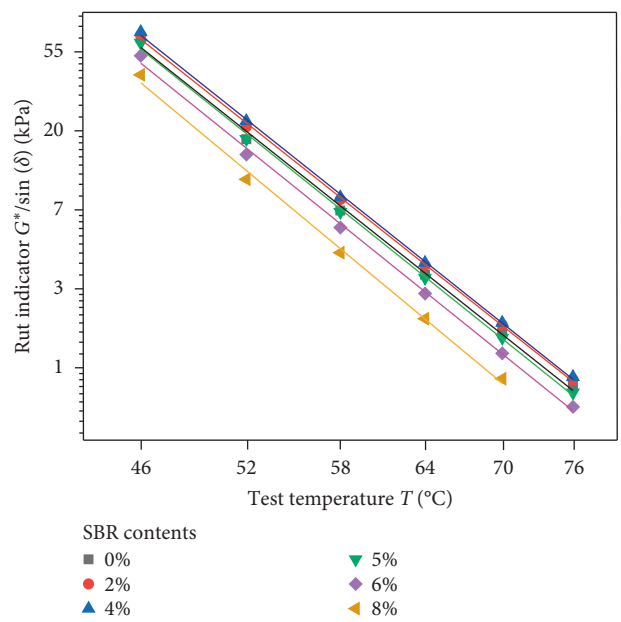


Figure 8: The variation patterns of rutting indicators and test temperatures.

Table 6: Fitting results of $G*/\sin(\delta)$ with test temperature.

| Parameters | SBR content (%) | | | | | |
|---|---|---|---|---|---|---|
| | 0 | 2 | 4 | 5 | 6 | 8 |
| $a$ | −8.65 | −8.63 | −8.68 | −8.74 | −8.77 | −9.06 |
| $b$ | 37.19 | 37.21 | 37.42 | 37.48 | 37.42 | 38.30 |
| $R^2$ | 0.98 | 0.97 | 0.99 | 0.99 | 0.98 | 0.96 |

Table 7: BBR test results of BRA-SBR compound modified asphalt.

| Content of SBR (%) | | 0 | 2 | 4 | 5 | 6 | 8 |
|---|---|---|---|---|---|---|---|
| S (MPa) | −6°C | 248 | 214 | 181 | 143 | 129 | 117 |
| | −12°C | 523 | 437 | 377 | 298 | 266 | 248 |
| | −18°C | — | — | — | 631 | 582 | 524 |
| M | −6°C | 0.301 | 0.327 | 0.344 | | 0.388 | 0.409 |
| | −12°C | 0.253 | 0.265 | 0.290 | 0.327 | 0.333 | 0.346 |
| | −18°C | — | — | — | 0.263 | 0.271 | 0.289 |
| S/M (MP-1) | −6°C | 0.001209 | 0.001535 | 0.001911 | 0.002585 | 0.003031 | 0.003526 |
| | −12°C | 0.000485 | 0.000608 | 0.000771 | 0.001101 | 0.001257 | 0.001401 |
| | −18°C | — | — | — | 0.000417 | 0.000466 | 0.000552 |

## 6. Conclusions

Waste rubber caused many environment problems nowadays, and waste rubber is mainly generated from waste tires and rubber track in the athletic field. In this paper, styrene-butadiene rubber (SBR), the main component of rubber, is introduced as a modifier to improve the low-temperature performance of BRA modified asphalt. Five types of BRA-SBR modified asphalt were prepared, and the content of SBR was 2%, 4%, 5%, 6%, and 8% by weight of BRA modified binder. The modification mechanism was revealed by Fourier transform infrared spectroscopy (FTIR) tests. And the road performance, including high and low-temperature performance, was evaluated by Brookfield viscosity test, dynamic shear rheometer test, and bending beam rheometer test. Some conclusions could be drawn from this study as follows.

(1) According to the results of FTIR test, there was no new functional group generated, only reduction of some functional group, which meant that the modification of BRA and SBR to asphalt is a physic modification.

(2) The change rate of $G*/\sin\delta$ with test temperature could be adopted as an index to evaluate the temperature sensitivity of asphalt, and the temperature stability of BRA-SBR modified asphalt improved with the content of SBR.

(3) SBR has an apparent influence on the low-temperature performance of BRA modified asphalt when the content was within a certain range. Based on the high- and low-temperature performance, the content of SBR was recommended to be about 4%–5%.

## Data Availability

All data generated or analyzed during this study are included in this published article.

## Conflicts of Interest

The authors declare no conflicts of interest.

## Authors' Contributions

Conceptualization was done by Xiangming Deng and Hui Huang. Experiment was done by Hui Huang, Bin Wuang, and Jie Chen. Data curation was performed by Xiangming Deng, Hui Huang, and Jie Chen. Formal analysis was performed by Xiangming Deng, Hui Huang, and Jie Chen. Funding acquisition was done by Hui Huang. Methodology was done by Xiangming Deng and Hui Huang. Project administration was performed by Xiangming Deng and Hui Huang. Resources were provided by Xiangming Deng and Hui Huang. Validation was done by Hui Huang. The original draft was written by Xiangming Deng and Hui Huang.Reviewing and editing were performed by Xiangming Deng, Hui Huang, Bin Wuang, and Jie Chen.

## Acknowledgments

This study was supported by Guangxi Key Science and Technology Project (Nos. AA18242032, AB20297030, and AB19245019) and Science and Technology Project of Guangxi Housing and Urban Construction Department (2018-2-2).

## References

[1] S. Lv, C. Liu, D. Chen, J. Zheng, Z. You, and L. You, "Normalization of fatigue characteristics for asphalt mixtures under different stress states," *Construction and Building Materials*, vol. 177, pp. 33–42, 2018.

[2] E. Cicek, "The effects of different types of fibres and geotextiles for pavement design," *Road Materials and Pavement Design*, vol. 20, no. 4, pp. 793–814, 2019.

[3] C. C. Liu, S. T. Lv, X. H. Peng, J. L. Zheng, and M. Yu, "Analysis and comparison of different impacts of aging and loading frequency on fatigue characterization of asphalt concrete," *Journal of Materials in Civil Engineering*, vol. 32, no. 9, Article ID 04020240, 2020.

[4] D. Zhang, Z. Chen, H. Zhang, and C. Wei, "Rheological and anti-aging performance of SBS modified asphalt binders with different multi-dimensional nanomaterials," *Construction and Building Materials*, vol. 188, pp. 409–416, 2018.

[5] R. He, S. H. Wu, X. F. Wang, Z. J. Wang, and H. X. Chen, "Temperature sensitivity characteristics of SBS/CRP-Modified bitumen after different aging processes," *Materials*, vol. 11, no. 11, p. 2136.

[6] T. Nian, P. Li, X. Wei, P. Wang, H. Li, and R. Guo, "The effect of freeze-thaw cycles on durability properties of SBS-modified bitumen," *Construction and Building Materials*, vol. 187, pp. 77–88, 2018.

[7] Z. L. Li, X. Xu, J. Y. Yu, and S. P. Wu, "Assessment on physical and rheological properties of aged SBS modified bitumen

containing rejuvenating systems of isocyanate and Epoxy substances," *Materials*, vol. 12, no. 4, p. 618.

[8] B. Li, Y. J. Cui, X. Liu, H. L. Li, and X. M. Li, "Effect of material composition on nano-adhesive characteristics of styrene-butadiene-styrene copolymer-modified bitumen using atomic force microscope technology," *International Journal of Adhesion and Adhesives*, vol. 89, pp. 168–173, 2019.

[9] M. Saltan, S. Terzi, and S. Karahancer, "Mechanical behavior of bitumen and hot-mix asphalt modified with zinc oxide nanoparticle," *Journal of Materials in Civil Engineering*, vol. 31, no. 3, Article ID 04018399, 2019.

[10] D. Zheng, Z.-D. Qian, P. Li, and L.-B. Wang, "Performance evaluation of high-elasticity asphalt mixture containing inorganic nano-titanium dioxide for applications in high altitude regions," *Construction and Building Materials*, vol. 199, pp. 594–600, 2019.

[11] Y. Gong, H. Bi, Z. Tian, and G. Tan, "Pavement performance investigation of nano-TiO2/CaCO3 and basalt fiber composite modified asphalt mixture under freeze–thaw cycles," *Applied Sciences*, vol. 8, no. 12, p. 2581, 2018.

[12] S. Eskandarsefat, G. Dondi, and C. Sangiorgi, "Recycled and rubberized SMA modified mixtures: a comparison between polymer modified bitumen and modified fibres," *Construction and Building Materials*, vol. 202, pp. 681–691, 2019.

[13] A. Behnood and M. Modiri Gharehveran, "Morphology, rheology, and physical properties of polymer-modified asphalt binders," *European Polymer Journal*, vol. 112, pp. 766–791, 2019.

[14] A. Diab, M. Enieb, and D. Singh, "Influence of aging on properties of polymer-modified asphalt," *Construction and Building Materials*, vol. 196, pp. 54–65, 2019.

[15] G. Cuciniello, P. Leandri, S. Filippi, D. Lo Presti, M. Losa, and G. Airey, "Effect of ageing on the morphology and creep and recovery of polymer-modified bitumens," *Materials and Structures*, vol. 51, no. 5, p. 136, 2018.

[16] I. Widyatmoko and R. Elliott, "Characteristics of elastomeric and plastomeric binders in contact with natural asphalts," *Constrution and Building Material*, vol. 22, no. 3, pp. 239–249, 2005.

[17] M. Yilmaz and M. E. Çeloğlu, "Effects of SBS and different natural asphalts on the properties of bituminous binders and mixtures," *Construction and Building Materials*, vol. 44, pp. 533–540, 2013.

[18] Z. F. Lu, Z. Y. He, Q. Yu, and G. Huang, "Influence of rock asphalt modified bitumen on asphalt rheological property," *Journal of ChongQingJiaoTong University (Natural Science)*, vol. 28, pp. 543–547, 2009.

[19] A. Sassan and T. Nader, "Proposals for modification of Iranian bitumen to meet the climatic requirements of Iran," *Constrution and Building Material*, vol. 23, no. 6, pp. 2141–2150, 2009.

[20] M. Ameri, A. Mansourian, S. S. Ashani, and G. Yadollahi, "Technical study on the Iranian gilsonite as an additive for modification of asphalt binders used in pavement construction," *Construction and Building Materials*, vol. 25, no. 3, pp. 1379–1387, 2011.

[21] J. Jin, Y. Gao, Y. Wu et al., "Rheological and adhesion properties of nano-organic palygorskite and linear SBS on the composite modified asphalt," *Powder Technology*, vol. 377, pp. 212–221, 2021.

[22] Y. F. Li, J. Chen, J. Yan, and M. Guo, "Influence of buton rock asphalt on the physical and mechanical properties of asphalt binder and asphalt mixture," *Advances in Materials Science and Engineering*, vol. 2018, Article ID 2107512, 7 pages, 2018.

[23] S. Liu, W. Cao, X. Li, Z. Li, and C. Sun, "Principle analysis of mix design and performance evaluation on Superpave mixture modified with Buton rock asphalt," *Construction and Building Materials*, vol. 176, pp. 549–555, 2018.

[24] S. P. Hadiwardoyo, E. S. Sinaga, and H. Fikri, "The influence of Buton asphalt additive on skid resistance based on penetration index and temperature," *Construction and Building Materials*, vol. 42, pp. 5–10, 2013.

[25] G. L. Zou and C. Wu, "Evaluation of rheological properties and field applications of Buton rock asphalt," *Journal of Testing and Evaluation*, vol. 43, no. 5, Article ID 20130205, 2015.

[26] R. Li, P. Karki, P. Hao, and A. Bhasin, "Rheological and low temperature properties of asphalt composites containing rock asphalts," *Construction and Building Materials*, vol. 96, pp. 47–54, 2015.

[27] C. C. Liu, S. T. Lv, D. Z. Jin, and F. T. Qu, "Laboratory investigation for the road performance of asphalt mixtures modified by rock asphalt/styrene butadiene rubber," *Journal of Materials in Civil Engineering*, vol. 33, no. 3, Article ID 04020504, 2021.

[28] S. Ren, M. Liang, W. Fan et al., "Investigating the effects of SBR on the properties of gilsonite modified asphalt," *Construction and Building Materials*, vol. 190, pp. 1103–1116, 2018.

[29] L. Cai, X. Shi, and J. Xue, "Laboratory evaluation of composed modified asphalt binder and mixture containing nano-silica/rock asphalt/SBS," *Construction and Building Materials*, vol. 172, pp. 204–211, 2018.

[30] H. Wei, J. Li, F. Wang, J. Zheng, Y. Tao, and Y. Zhang, "Numerical investigation on fracture Evolution of asphalt mixture compared with acoustic emission," *International Journal of Pavement Engineering*, pp. 1–11, 2021.

Hindawi
Advances in Civil Engineering
Volume 2021, Article ID 6610534, 11 pages
https://doi.org/10.1155/2021/6610534

*Research Article*

# Experimental-Numerical Study of Indexation of Scenic Road Vertical Alignment in China

**Ronghua Wang**,[1] **Xingliang Liu**,[2] **and Zhe Yuan**[3]

[1]*College of Architecture and Civil Engineering, Beijing University of Technology, Beijing 100124, China*
[2]*College of Traffic & Transportation, Chongqing Jiaotong University, Chongqing 400074, China*
[3]*Jinan Urban and Rural Transportation Bureau, Jinan 250014, China*

Correspondence should be addressed to Xingliang Liu; xingliang1125@outlook.com

Received 19 October 2020; Accepted 3 March 2021; Published 22 March 2021

Academic Editor: Zhanping You



The vertical alignment design method of road in scenic spots does not evolve enough along the vehicle's rapid variation. Values of the maximum longitudinal slope (MLS) and longest slope length (LSL) applicable to scenic roads used by the environmental-friendly vehicle (EFV) are not provided. To compensate for this shortage, a multibody vehicle dynamic model in uphill traving is built, providing the static equilibrium state and dynamic balancing process of a typical vehicle. MLS and LSL values in scenic roads are obtained based on this model through numerical simulation, considering typical EFV, maximum velocity loss (MVL), and ideal velocity loss (IVL). Field experiments for verifying the results are also carried out in Huashan Mountain, Cuihua Mountain National Park, and Taiping Forest Park, using two EFV types. MLS and LSL values in scenic roads applicable to EFV obtained in this research vary from 7.8% to 10.2% and 200 to 955 m, respectively, and both are larger than the corresponding values in current criteria. According to verification results, relative errors of climbing velocity vary from 0.0104 to 0.0205, showing the dynamic model's accuracy and further proving the practicality of MLS and LSL values obtained. The results obtained in this research lay a foundation for establishing the scenic-road vertical alignment design method.

## 1. Introduction

In early 1900s, the first steam-powered carriage entered Yosemite National Park in U.S. Since then, automobiles have become the major method adopted by travelers to experience landscape resources in scenic spots. The reasonable and environmental-friendly roadway alignment design would promote this experience. The vertical alignment design is an essential part of the roadway alignment design. And, the vehicle's dynamic performance determines the technical index values of vertical alignment. The scenic road vertical alignment design method largely relies on contemporary typical vehicle's dynamic characters [1]. However, an environmentally friendly vehicle (EFV) with electric- or ethanol-powered engine has been introduced in scenic spots in China in recent years, and private vehicles cannot enter in the scenic spot for environment protection. The dynamic performance of EFV is lower than that of the oil-powered vehicle for the lower power of EFV, which would influence the maximum longitudinal gradient and the length of the longitudinal slope. On account of smaller pollutant emissions from EFV compared with oil-powered vehicles during the driving of EFV in the scenic spot, it can be beneficial for the sustainable development for scenic spot management. Therefore, providing a scenic road vertical alignment design method applicable to EFV is important and promising.

In past several decades, series studies related to scenic road or scenic spot traffic have been conducted, which concentrated on recreational routes' choices [2], tourism forecasting [3, 4], emissions and noise [4, 5], wilderness retaining [6, 7], alignment design [8, 9], etc., using both field research and simulation. However, the vertical alignment design method of roads in scenic spots did not evolve enough with vehicle's rapid variation. There are still lack of the

maximum longitudinal slope (MLS) value and longest slope length (LSL) value applicable to scenic roads used by EFV.

In order to compensate abovementioned shortages and promote the scenic road design method, this study focuses on vertical alignment based on the EFV dynamic character, providing some basis to scenic road design practices. Indices of MLS and LSL in scenic road representing vertical alignment are chosen as objectives in this study. Scenic spots and typical vehicle types selected in this research are selected in China, and the results obtained are also expected to be used in domestic conditions Indicators of MLS and LSL used in ordinary rural roads in current China design criteria are shown in Table 1 [10, 11].

Data from Table 1 are obtained based on the typical heavy vehicle on current ordinary rural roads in China. However, EFV used on scenic road reflects different dynamic characters. It is necessary to reconsider these indicators based on typical EFV. Moreover, indicators used in current scenic roads are usually directly chosen from the grey area in Table 1. But in practice, the longitudinal slope in scenic roads is sometimes larger than 10%, exceeding the boundary of current criteria. In that, to obtain appropriate MLS and LSL in scenic roads used by EFV, a dynamic model of the multibody vehicle considering the complex and real uphill travel environment is built. Based on this model, MLS and LSL in scenic roads are calculated using numerical simulation incorporating typical EFV determined by field studies. In addition, to prove the practicality of calculated MLS and LSL, field experiments are carried out to verify the multibody vehicle model.

Table 1: MLS and LSL used in current rural road design criteria in China.

| Operation velocity (km/h) | 120 | 100 | 80 | 60 | 40 | 30 | 20 |
|---|---|---|---|---|---|---|---|
| MLS (%) | 3 | 4 | 5 | 6 | 7 | 8 | 9 |
| Longitudinal slope (%) | LSL (m) | | | | | | |
| 3 | 900 | 100 | 1100 | 1200 | — | — | — |
| 4 | 700 | 800 | 900 | 1000 | 1100 | 1100 | 1200 |
| 5 | — | 600 | 700 | 800 | 900 | 900 | 1000 |
| 6 | — | — | 500 | 600 | 700 | 700 | 800 |
| 7 | — | — | — | — | 500 | 500 | 600 |
| 8 | — | — | — | — | 300 | 300 | 400 |
| 9 | — | — | — | — | — | 200 | 300 |
| 10 | — | — | — | — | — | — | 200 |

## 2. Literature Review

The related works of scenic road or scenic spot traffic could be divided into four aspects, which are travel traffic analysis, ecological road construction method, tourism transport economy problems, and scenic road geometric design. In travel traffic analysis, approaches focused on tourists or recreational travelers' routes choices draw some attention [2, 12]. Further, empirical and simulated data were analyzed using quantitative and qualitative methods to forecast tourists [3, 5], and models focusing on traffic capacity of roads in scenic spots and protected lands were also investigated [13, 14]. In the second aspect of the ecological road construction method, it was stated that, with an extension of the scenic road network and increase of travel traffic volume, harmful effects including traffic accidents, emissions, and noise will be imposed on local residents, flora, and fauna [4, 7, 15, 16]. Therefore, public concerns on scenic road construction and maintaining have existed for several decades, by claiming a retaining of road-less wilderness [6, 17]. The third aspect of tourism transport economy problems mainly derived from explosive growth of visitors' popularity. This is a problem governed by management departments of scenic spots [18, 19], and their objective is to gain a balance between scenic road charge and travelers' acceptance. Therefore, road toll strategies and travelers' demand models were widely studied [9, 20, 21].

In the fourth aspect of the scenic road geometric design method, which is also the subject of this paper, the most important and classical works are "The Highway Capacity Manual (HCM)" [22] and "A Policy on Geometric Design of Highways and Streets" [8]. These two guidelines provided the principle of the road alignment design, which was as "grades or straight vertical segments are designed to be steep enough to allow for longitudinal drainage, but not so steep as to pose a danger to vehicles through inadvertent excessive speed at downhill segments (and, conversely, difficulty of climbing steep uphill segments that pose safety risks where there are inadequate passing opportunities)." Unfortunately, there is little standard or guideline to guide the geometric design of roads in the scenic spot in China. The most frequently used method of designing the alignment of scenic roads is under the Technical Standard of Highway Engineering [23] and Design Specification for Highway Alignment [10]. The designing method in these materials must give the consideration of multiple vehicle types, such as medium-sized vehicles with loading capacity between 7 tons and 20 tons, or large vehicles with loading capacity over 20 tons. These types of vehicles are forbidden to entering in the scenic spot.

Following this principle, many related studies have been carried out. Some studies paid their attentions on methods of ensuring consistent roadway alignment to meet the drivers' demand [24, 25]. Some studies focused on the sight distance constrained by vertical curvature, which consequently determined the operating speed [26]. Furthermore, models or equations estimating operation velocity were also developed in many works [27–29]. In "Green Book" by AASHTO [8], contents related to scenic roads were stated. However, this statement is insufficient for practical works, and abovementioned studies merely concerned scenic roads whose design basis and indices were mainly directly adopted from those used in ordinary rural roads.

To study vertical alignment in scenic roads, the relationship between vertical grade and slope length should be specified. Typical vehicles travelling uphill with the specific weight-to-power ratio tend to lose operation velocity to some extent. The velocity reduction is restricted by some certain requirements, for instance, safety, affection on traffic flow, and traffic efficiency [8, 23, 30–33]. It is concluded from these studies that the dynamic model of the typical vehicle is a prerequisite of the vertical alignment design. In ordinary rural roads, heavy vehicles are always selected. However, as mentioned previously, electric or ethanol-consuming EFV is widely used in scenic roads, which reflects

different dynamic characters. Therefore, a model representing EFV dynamic characters is needed in this research.

Traditionally, the vehicle is simulated as a point mass in AASHTO Green Book [8], whose motion is examined independently in vertical and lateral directions. Following this classical model, compensations were made in several aspects, including the bicycle model used for simulating the vehicle by an axle in the steady state cornering [34], a transient formulation of the bicycle model used in cases of variable steering inputs [11], and the sophisticated multibody vehicle model (CarSim and TruckSim) used for high-reliability vehicle stability prediction in automotive industry [35–37]. According to related research studies, a multibody vehicle model considering the complex and real uphill travel environment will be developed in this research, which is used to assess the EFV motion problem.

## 3. Multibody Vehicle Model in Uphill

MLS and LSL are basically determined by dynamic characteristics of the vehicle when climbing a slope. When the vehicle starts to climb up at a specific initial velocity, it begins to decelerate due to the resistance brought by the slope. According to actual driving experience, the output driving force will increase at this moment if the output power remained unchanged. At a time point, the vehicle will reach a mechanical equilibrium condition, and it will be operated at a lower stable velocity. During the process described above, the vehicle will travel a specific length, on which MLS and LSL determined will largely depend. To study MLS and LSL based on dynamic performance of typical vehicles driven on roads in scenic spots, the static equilibrium state and dynamic balancing process should be studied as the basis of this paper.

*3.1. Static Equilibrium State of the Typical Vehicle.* As depicted in the previous part, the vehicle will operate at a relatively lower stable velocity in the static equilibrium state. The purpose of this part is to find out the stable velocity when climbing a slope with specific gradient and initial climbing velocity. The static force condition of a typical vehicle on a slope, according to classical mechanics theory, is shown in Figure 1. In this figure, $M$ (kg) represents the total mass of the vehicle, $F(N)$ represents the driving force, $R_a(N)$ represents the air resistance, $R_r(N)$ represents the rolling resistance, $R_g(N)$ represents the slope resistance, and $\alpha(^\circ)$ stands for the elevation angle of the slope.

According to automotive dynamics theory and the analysis shown above, the effective driving force $F_t$ and the maximum driving force $F_{\max}$ could be calculated by using the following equation:

$$F_t = 3600\left(\frac{P_e}{V}\right)\eta_T, \qquad F_{\max} = 9.8066M_{ta}\mu. \tag{1}$$

In equation (1), $P_e$ (kW) stands for engine power, $V$ (km/$h$) stands for operation velocity, and $\eta_T$ stands for transmission efficiency which can be found in reference [38];

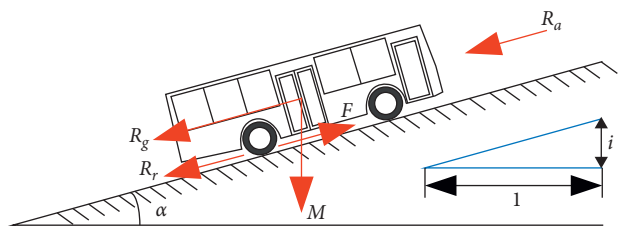


Figure 1: The static force condition of an EFV on a slope.

In equation (1), $M_{ta}$ (kg) stands for total weight acting on the drive shaft and $\mu$ stands for the road friction coefficient, which can be found in reference [39].

As depicted in Figure 1, resistance forces $R_a$, $R_r$, and $R_g$ should also be considered. Based on related aerodynamic research studies and experiments [39], the air resistance $R_a$ could be calculated using the following equation:

$$R_a = \frac{C_d C_h}{21.15}AV^2, \qquad C_h = 1 - \xi H. \tag{2}$$

In equation (2), $A$ (m$^2$) stands for the frontal area of the vehicle, $C_d$ stands for the air resistance coefficient which is related to the vehicle type and can be found in reference [39], and the parameter $C_h$ represents the altitude factor which could be calculated by altitude $H$ (m), and in the plain area, $C_h = 1$. Taking rolling resistance $R_r$ into consideration, the types of tire, road surface conditions, and operation velocity are deciding factors. It could be calculated by the following equation:

$$R_r = 9.8006C_r(c_1 + c_2V)\left(\frac{M}{1000}\right). \tag{3}$$

In equation (3), $C_r$ refers to the rolling factor, which is related to road surface conditions and the parameters $c_1$ and $c_2$ refer to the rolling friction coefficient, which is related to the tire pattern. The values of the three parameters mentioned above could be found in reference [39]. According to classical mechanics theory, the slope resistance $R_g$ could be obtained using the following equation:

$$R_g = 9.8006M\sin\alpha = 9.8006Mi. \tag{4}$$

According to the static equilibrium state mentioned above, the driving force of the velocity equals to the joint force of resistance forces $R_a$, $R_r$, and $R_g$, and we have the following equation:

$$\begin{cases} P_e = F_iV_i = aV^3 + bV^2 + cV, \\ a = \dfrac{C_dC_hA}{77400\eta_T}, \\ b = \dfrac{C_rc_2M}{367308\eta_T}, \\ c = \left(\dfrac{C_rc_1M}{367308\eta_T}\right) + \left(\dfrac{Mi}{367.3\eta_T}\right). \end{cases} \tag{5}$$

From equation (5), when a typical vehicle is climbing a slope, the stable velocity under the static equilibrium state is

determined by output power $P_e$ (which could be represented by initial velocity $V_i$ and gradient $i$). However, the process of reaching this static equilibrium state could not be described using abovementioned analysis, and MLS and LSL are still unknown.

*3.2. Dynamic Balancing Process of the Typical Vehicle.* When a typical vehicle is climbing a slope with constant output power, LSL is defined as the travel distance of this vehicle when it reaches a static equilibrium state, as introduced in the previous part. In this dynamic process, the real-time acceleration $a(t_i)$ of the typical vehicle at time point $t_i$ could be calculated using the following equation:

$$a(t_i) = \frac{(F(t_i) - R(t_i))}{M}. \tag{6}$$

The real-time motion state of the typical vehicle could be expressed in the following equation:

$$\begin{aligned} \frac{d[V(t_i)]}{dt} &= a(t_i), \\ \frac{d[X(t_i)]}{dt} &= V(t_i), \\ V(t_i) &= V(t_{i-1}) + a(t_{i-1})\Delta t, \\ X(t_i) &= X(t_{i-1}) + V(t_{i-1})\Delta t, \\ t_i - t_{i-1} &= \Delta t \cong 0. \end{aligned} \tag{7}$$

It is known that output power $P_e$ is the product depending on driving force $F_i$ and real-time velocity $V_t$. When $P_e$ remains constant, it is necessary to discuss the initial driving force $F_i$ and the initial velocity $V_i$ because they will determine the motion state of the typical vehicle in this dynamic balancing process. At initial time point $t_i$, the typical vehicle begins to climb the slope with specific gradient $i$. Assuming $F_i > R_a + R_r + R_g$, due to the constant $P_e$, the travel velocity will increase, while the driving force will fall down. In the end of this dynamic process $t_e$, driving force $F_e$ will be equal to the sum of $R_a$, $R_r$, and $R_g$, and the typical vehicle will stop its acceleration. The process of this condition is depicted using the blue line in Figure 2. In another circumstance $F_i < R_a + R_r + R_g$, it is easy to know that the travel velocity will decrease, while the driving force will rise and finally get to the static equilibrium state. The process of this condition is depicted using the red line in Figure 2.

## 4. Numerical Simulation of EFV Climbing Velocity

As depicted in Section 1, the dynamic performance of EFV in scenic spots differs from it of ordinary vehicles. Therefore, numerical simulation of EFV climbing velocity based on the multibody vehicle model is carried out, considering the typical EFV type obtained from field research. From Figure 2, the fundamental of determining LSL on a certain slope with specific initial velocity is provided. In practical

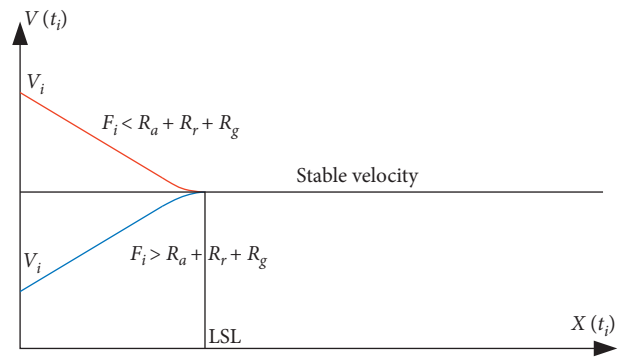


Figure 2: Schematic diagram of the dynamic motion process.

application, the phenomenon depicted by the blue line is rarely found because in most cases, the driver will maintain a relatively higher velocity in the flat area. If the situation expressed by the blue line happened, there is still no need to deal with it because it will not negatively affect the driver and traveler. Therefore, in this research, the situation of $F_i < R_a + R_r + R_g$ is analyzed.

However, the circumstance of the red line in Figure 2 could be interpreted as an extreme situation, which means the driver and the traveler will not show any dissatisfaction and intervention, and this is obviously unreasonable. In reality, large velocity loss in the slope section always causes serious safety risk. Therefore, the concept of maximum velocity loss (MVL) is defined in related road design criteria, which equals to 50% of designed velocity (DV) [39]. Furthermore, as the road in scenic spots, the satisfaction and comfort of the travelers should also be considered. For the most important reason, slope sections can be commonly seen in scenic roads. If MVL in slope sections is too large, it will further reduce the travelers' transmission efficiency and causes tourist backlog. Thus, another concept of ideal velocity loss (IVL) is defined based on above description and a lot of studies, including Cuihua Mountain National Park, Taiping Forest Park, and Huashan Mountain National Park. According to the results of field studies, the value of IVL is determined as 10 km/h.

The purpose of numerical simulation is to find the theoretical values of LSL in slopes with the specific gradient using the dynamic model provided in Section 3. The indices of MVL and IVL mentioned above were used as two principles to determine LSL. As depicted in Section 3, several parameters related to EFV should be chosen before calculation. According to the results of field studies, the parameters of the typical EFV type were obtained (Jinlong XMQ6801G type), with $M/P_e = 87$ kg/kW and $P_e = 132$ kW. Combining the operation velocity in abovementioned scenic roads, initial climbing velocity was chosen, as shown in Table 2, and 4%–11% was chosen as the slope gradient according to field research.

From Section 3, it is found that the stable velocity could be directly calculated using equation (5) after the parameters related to the vehicle are determined. However, the value of LSL could not be calculated using equation (7). To model the process of climbing a slope, iterative calculation was adopted in numerical simulation, and a simulation program was

Table 2: Initial climbing velocity in numerical simulation.

| Initial climbing velocity (km/h) | 60 | 50 | 40 | 30 |
|---|---|---|---|---|
| MVL (km/h) | 30 | 25 | 20 | 15 |
| IVL (km/h) | 10 | 10 | 10 | 10 |

developed based on Visual Basic. The framework of this program is shown in Figure 3, and it outputs the simulation results expressed by a two-dimensional image, the horizontal axis represents the length EFV traveled, and the vertical axis represents the operation velocity. The results of numerical simulation are shown in Figure 4.

Before analyzing the results given above, the method of defining LSL should be provided. As depicted in the previous part, MVL and IVL are principles of defining LSL. The parameter of IVL could be expressed as a loose boundary in Figure 4, shown as a red dotted line in the upper position of the figures. Under the condition of specific initial velocity (understood as operation velocity) and specific slope gradient, if the stable velocity remained larger than the value determined by IVL, then it could be described as the slope will not affect the travelers' experience; further, it will definitely satisfy the safety criteria MVL. The index of MVL could be seen as the restricted boundary of climbing a slope with specific gradient and initial velocity because the velocity drops too fast in this condition which affects the operation safety. In Figure 4, it is depicted as a red dotted line in the lower position of the figures. If the stable velocity exceeds this boundary, the slope will not satisfy the safety criteria in this condition, and not to mention the travelers' experience criteria IVL. The line in the top position (60 km/h-4%, 50 km/h-5%, 40 km/h-6%, and 30 km/h-6%) in each figure in Figure 4 does not reach the loose boundary in above-mentioned contents. According to the description, there is no need to determine the LSLs using these lines. Besides, the line in the bottom position (60 km/h-8%, 50 km/h-9%, 40 km/h-10%, and 30 km/h-11%) in each figure in Figure 4 exceeds the restricted boundary depicted in the previous part. It is known that these four conditions should not exist in the real scenic road design because they break the safety criteria. Apart from the eight lines mentioned above, the left are all situated between the boundaries based on MVL and IVL. Using IVL as the principle of determining LSL by considering the feeling of the travelers, the intersections of the curves and the upper boundaries are read as the theoretical values of LSLs (expressed as Theo. in the table), given in Table 3. Further, if the stable velocity of a specific slope equals to the lower boundary, then the maximum longitudinal slope (MLS) could be obtained using equation (5), as shown in Table 3. Besides, the LSLs used in previous road design criteria are provided as comparisons (expressed as Used in the table).

## 5. Model Verification

The data shown in Table 3 were obtained based on the theoretical model provided in Section 2. Though the detailed information of the vehicle and the road were considered in this model, the accuracy of the model still should be verified because the real climbing condition could not be completely and precisely simulated. Therefore, model verification is provided in this part based on the experiments in real scenic road sections.

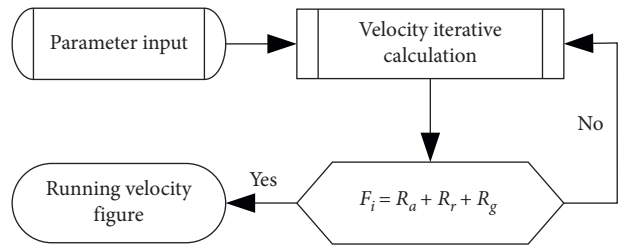


Figure 3: The framework of the simulation program.

*5.1. The Field Experiments.* As depicted in Section 3, the theoretical results were obtained based on the typical large-passenger EFV type Jinlong XMQ6801G, shown in Figure 5(a), and this vehicle type has a large market penetration rate in scenic spots. Therefore, the field experiments will be carried out using this vehicle type. In addition, to further validate the accuracy and the practicality of the model, the small passenger EFV type Wuling WLQ2110 ($M/P_e = 57$ kg/kW, $P_e = 28.5$ kW) used in Huashan Mountain was adopted in this field experiment, carrying water bags to increase load, seen in Figure 5(b). Besides, from the analysis in the previous part, some vehicle operation conditions could be concluded.

(i) A flat road section should be provided before climbing the slope, which will guarantee the EFV a stable initial velocity

(ii) The EFV should maintain a stable output power, and the driver should keep a specific gear position (third gear in this experiment) when climbing the slope

(iii) The EFV used in this experiment should be in the full-load status to keep the same condition used in numerical simulation

(iv) The slope should have an enough length to collect available and stable data

(v) The slope gradient could not be completely continuous and stable, but there should not be a large gradient change in a single chosen slope

Following these operation conditions, nine scenic road slope sections were chosen in three scenic spots, which were Huashan Mountain, Cuihua Mountain National Park, and Taiping Forest Park. The detailed information is provided in Table 4.

The OES noncontact photoelectric velocity sensor, including silicon photocell, optical system, and computer, was used to collect the climbing real-time velocity, as shown in Figure 5(c). The resolution for collecting running velocity, distance, time, and deceleration is 0.1 km/h, 1 mm, 1 ms, and 0.1 m/s$^2$, respectively. And, the accuracy of the four indicators above is 0.5%, 0.2%, 0.1%, and 1%, separately. The

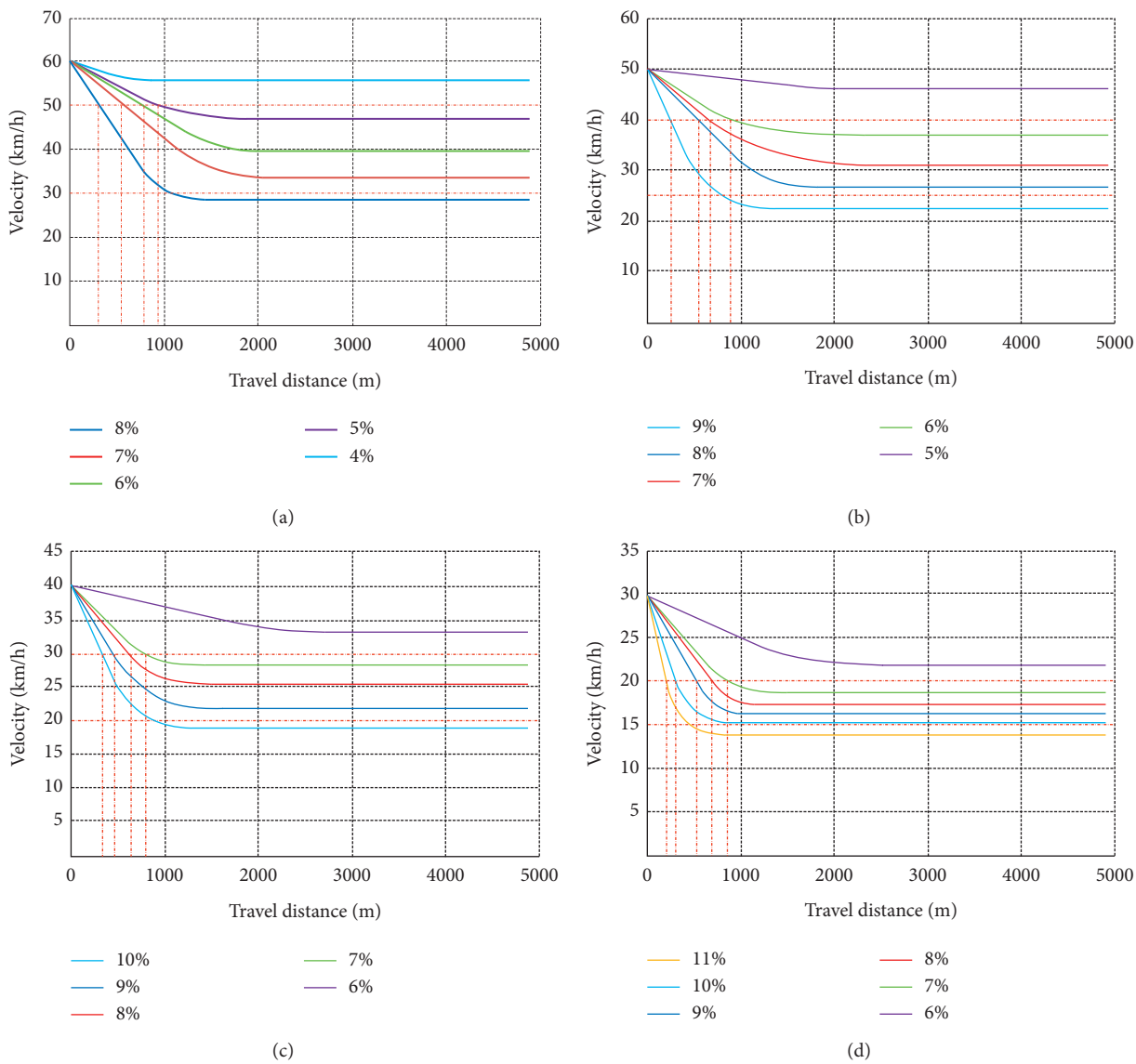


Figure 4: The results of numerical simulation. (a) Simulation results of initial velocity of 60 km/h. (b) Simulation results of initial velocity of 50 km/h. (c) Simulation results of initial velocity of 40 km/h. (d) Simulation results of initial velocity of 30 km/h.

Table 3: The theoretical values of LSLs.

| Operation velocity (km/h) | | 60 | | 50 | | 40 | | 30 | |
|---|---|---|---|---|---|---|---|---|---|
| MLS (%) | | 7.8 | | 8.4 | | 9.7 | | 10.2 | |
| LSL (m) | | Theo. | Used | Theo. | Used | Theo. | Used | Theo. | Used |
| Slope gradient (%) | 5 | 955 | 800 | — | — | — | 900 | — | 900 |
| | 6 | 720 | 600 | 843 | — | — | 700 | — | 700 |
| | 7 | 512 | — | 639 | — | 825 | 500 | 960 | 500 |
| | 8 | — | — | 433 | — | 573 | 300 | 730 | 300 |
| | 9 | — | — | — | — | 427 | — | 505 | 200 |
| | 10 | — | — | — | — | — | — | 296 | — |
| | 11 | — | — | — | — | — | — | — | — |

drivers participating in this experiment are all EFV full-time drivers, and they were alcohol, coffee, and tea forbidden for 72 hours before the experiment. In the experiment, the driver was required to enter the specific slope with stable velocity shown in Table 3, following the second principle given above. Each climbing test was repeated for three times

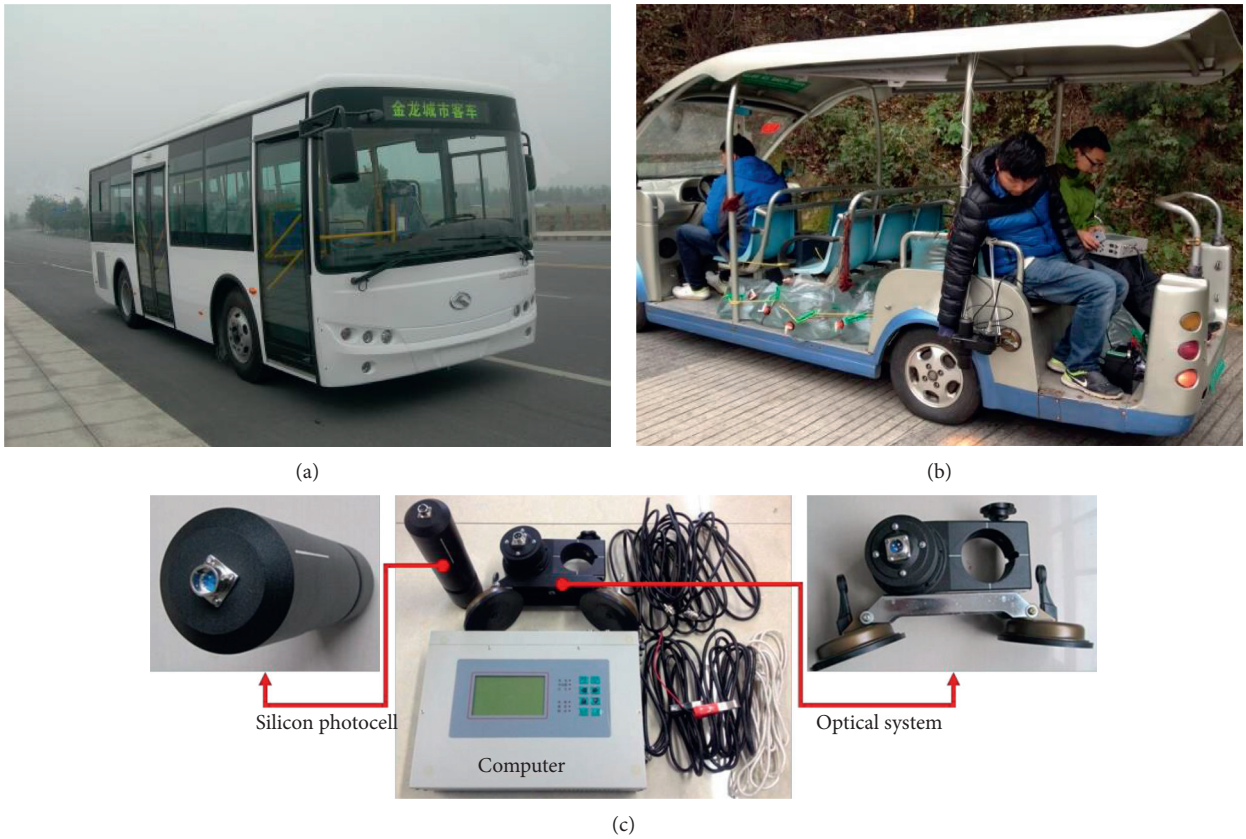


Figure 5: Equipment used in this experiment. (a) Jinlong XMQ6801G. (b) Wuling WLQ2110. (c) Photoelectric velocity sensor.

Table 4: The detailed information of chosen slopes.

| Number | Slope gradient (%) | Slope length (m) | Operation velocity (km/h) | Location | EFV type |
|---|---|---|---|---|---|
| 1 | 8.6 | 105 | 40 | | |
| 2 | 9.6 | 205 | 30 | Huashan Mountain | Jinlong XMQ6801G |
| 3 | 10.0 | 160 | 30 | | |
| 4 | 6.5 | 210 | 60 | | |
| 5 | 8.0 | 163 | 50 | Taiping Forest Park | Jinlong XMQ6801G |
| 6 | 7.5 | 165 | 50 | | |
| 7 | 13.0 | 119 | 30 | | |
| 8 | 14.8 | 145 | 30 | Cuihua Mountain National Park | Wuling WLQ2110 |
| 9 | 16.0 | 120 | 30 | | |

to obtain enough and reliable data, which comprised a single test group. In one climbing test, the real-time data were output meter by meter, and they were used to verify the theoretical model.

*5.2. The Model Verification.* As depicted in Section 4, field experiments were carried out in nine slope sections using two EFV types, and each climbing test was repeated for three times. To verify the mechanical model in Section 3, theoretical climbing velocities were calculated using the program in Section 4, and actual climbing velocities were obtained by averaging the values in three tests abovementioned. The results were shown in Figure 6. In these figures, the red straight lines stand for theoretical values, and the curved parts seen in Figure 4 were not depicted because the slope length was not long enough. Further, the blue polylines represent the actual velocities collected in the field experiment. Seen from these figures directly, actual velocities are distributed nearby the theoretical values, and their overall trends appeared the same. In Figures 6(a)–6(f), the accuracy of the mechanical model based on EFV Jinlong XMQ6801G was proved. In Figures 6(g)–6(i), the model using EFV Wuling WLQ2110 was also proved to be accurate. The relative errors between theoretical values and collected values were shown in Table 5.

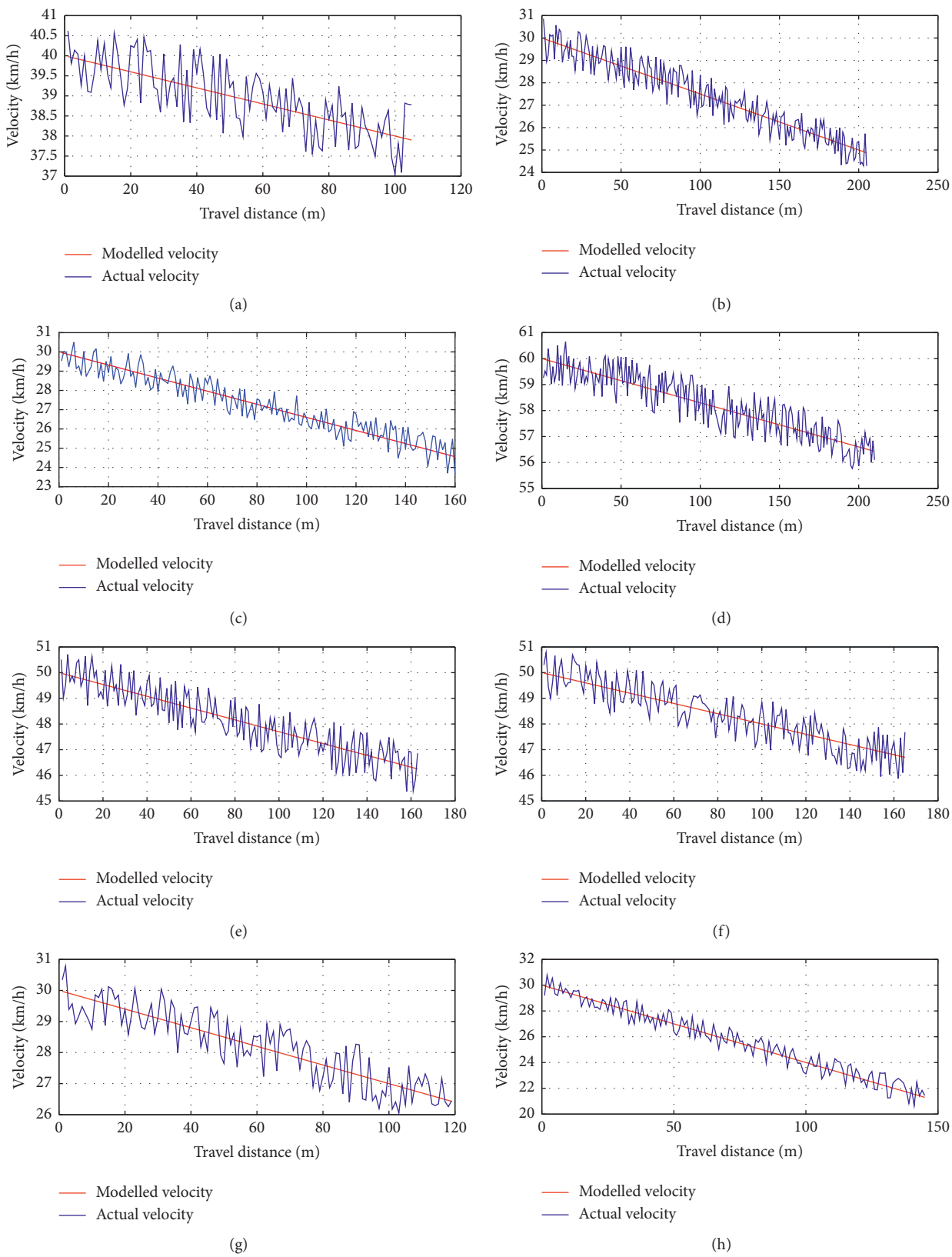


Figure 6: Continued.

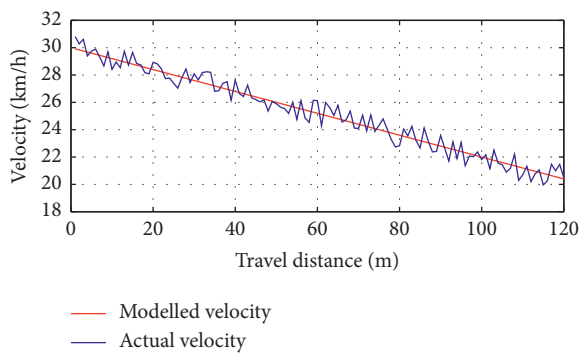


(i)

Figure 6: The results of model validation. (a) Slope 1. (b) Slope 2. (c) Slope 3. (d) Slope 4. (e) Slope 5. (f) Slope 6. (g) Slope 7. (h) Slope 8. (i) Slope 9.

Table 5: The relative errors between theoretical values and collected values.

| Slope number | Relative errors | EFV type |
|---|---|---|
| 1 | 0.0143 | |
| 2 | 0.0184 | Jinlong XMQ6801G |
| 3 | 0.0202 | |
| 4 | 0.0090 | |
| 5 | 0.0108 | Jinlong XMQ6801G |
| 6 | 0.0104 | |
| 7 | 0.0187 | |
| 8 | 0.0201 | Wuling WLQ2110 |
| 9 | 0.0205 | |

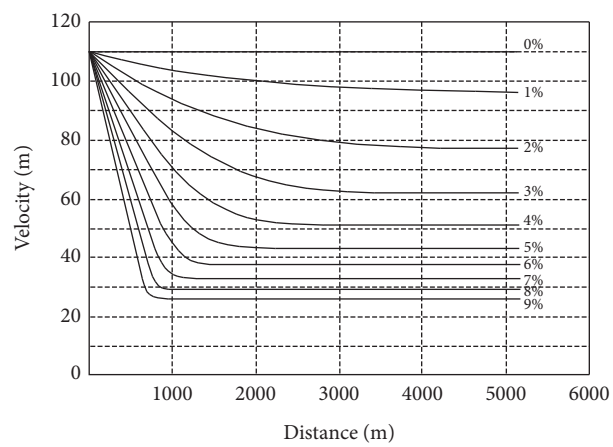


Figure 7: Velocity variation curves of uphill travelling under different longitudinal gradients in AASHTO Green Book [8].

## 6. Discussion

As shown in Figure 6, relative errors of the typical vehicle Jinlong XMQ6801G using the multibody vehicle model varied from 0.0090–0.0184, and relative errors of the typical vehicle Wuling WLQ2110 varied from 0.0187–0.0205. In summary, the vehicle dynamic model showed basically the same accuracy in simulating different typical vehicle's dynamic characters. With high accuracy of the dynamic model, curves obtained in Figure 4 could be directly used in practice under different principles. Here, it provides a comparison between curves in Figure 4 and related ones from AASHTO Green Book [8], as shown in Figure 7.

As shown in Figure 7, the curve results of AASHTO display the same trend compared to results in this article, which proves the practicality of the dynamic model. However, a large gap apparently exists. The typical vehicle adopted in AASHTO Green Book has the specific weight-to-power ratio of 120 kg/kW, but EFVs used in this study have the weight-to-power ratio of 87 kg/kW and 57 kg/kW. The longitudinal slope in this research varies from 4%–11%, and the longitudinal slope in Figure 7 varies from 0%–9%. Moreover, uphill travelling velocity loss in Figure 7 is much larger than that in Figure 4. Taking the instance of 9% grade as an example, velocity loss in Figure 7 is more than 80 km/h, but the largest velocity loss in Figure 4 is about 28 km/h, owing to special dynamic characters of EFV. Besides, situations depicted in AASHTO Green Book are somehow simpler, involving two initial velocities, 110 km/h and 70 km/h. Situations depicted in Figure 4 are more detailed, involving four initial velocities, 60 km/h, 50 km/h, 40 km/h, and 30 km/h. In conclusion, the results in this article are more practical in the domestic scenic road design.

In Table 3, MLSs and LSLs obtained using the dynamic model are compared with those in current criteria, as shown in Table 1. When operation velocities are 60 km/h, 40 km/h, and 30 km/h, MLSs used in current criteria are 6%, 7%, and 8%, respectively, and MLSs obtained in Table 3 are 7.8%, 9.7%, and 10.2%, respectively, obviously larger than current criteria values. Besides, operation velocity of 50 km/h is not provided in current criteria. Considering the values of LSLs in Table 3 and Table 1, it could be seen that, values in this article are larger than those in current criteria. This could be also contributed to the superior characters of modern EFV. Integrating the large gap and scenic road environment, data in Table 3 are practical.

## 7. Conclusions

In this research, MLS and LSL values applicable to scenic roads using EFV are provided. The multibody vehicle model

in uphill was established, providing the static equilibrium state and dynamic balancing process of the typical vehicle. Based on this model, MLS and LSL values in scenic roads were obtained using numerical simulation, considering typical EFV, MVL representing travel safety, and IVL representing travel efficiency. MLS values in scenic roads using EFV obtained in this research vary from 7.8%–10.2%, which are larger than current criteria values. LSL values obtained vary from 200–955 m, which are also larger than current criteria values. To prove the accuracy of the dynamic model, also the practicality of MLS and LSL values, field experiments were carried out in Huashan Mountain, Cuihua Mountain National Park, and Taiping Forest Park, using two EFV types. According to the verification results, the relative errors of climbing velocity vary from 0.0104–0.0205, showing the dynamic model's accuracy.

Almost all of scenic spots are under the sealed management, and private passenger vehicles are forbidden to run in the scenic spots in China. Roads' alignment design in the scenic spots must consider the characteristics of the vehicles running in the scenic spots and environment protection. There was little guideline for MLS and LSL values applicable to scenic roads using EFV. The results could make up this shortage. Furthermore, the MLS and LSL values used for EFV are larger than current criteria values (6%–8% of MLS and 200 = 900 m of LSL) used for the typical vehicles running on the highways or freeways. The total length of the scenic roads can be shortened, and the cut and fill volumes can be decreased, which will be beneficial for the natural landscape through making the route alignment fitting the terrain much better and reducing damage to the environment. The planners and designers can use the MLS and LSL values to design the vertical alignment of the roads in scenic spots.

This research can lay a foundation for establishing the vertical alignment design for the roads in scenic spots. In the future, the technical indices and values of horizontal alignments should be studied through simulation and field experiments applicable for EFV. Furthermore, the coordination design of horizontal and vertical alignment should be proposed in order to perfect the geometric design for the roads in scenic spots.

## Data Availability

The data used to support the findings of this study are available from the corresponding author upon request.

## Conflicts of Interest

The authors declare that there are no conflicts of interest regarding the publication of this paper.

## Acknowledgments

This research was funded by the National Key R&D Program of China (Grant nos. 2018YFB1600302 and 2018YFB1600300) and partly supported by the Science Foundation Project of Chongqing Jiaotong University (Grant no. 20JDKJC-B001).

## References

[1] L. W. Green, *Yosemite: The Park and its Resources: Historical Resource Study*, National Park Service, Washington, DC, USA, 1987.

[2] H. H. Hochmair, *Towards a Classification of Route Selection Criteria for Route Planning Tools*, pp. 481–492, Springer, Berlin, Germany, 2004.

[3] S. F. Witt and C. A. Witt, "Forecasting tourism demand: a review of empirical research," *International Journal of Forecasting*, vol. 11, no. 3, pp. 447–475, 1995.

[4] F. C. Jaarsma and F. Van Langevelde, "The motor vehicle and the environment: balancing between accessibility and habitat fragmentation," in *Proceedings of the 29th ISATA, Dedicated Conference on the Motor Vehicle and the Environment*, pp. 299–306, Florence, Italy, February 1996.

[5] W.-C. Hong, "Traffic flow forecasting by seasonal SVR with chaotic simulated annealing algorithm," *Neurocomputing*, vol. 74, no. 12-13, pp. 2096–2107, 2011.

[6] T. Williams, "The unkindest cuts," *Audubon*, vol. 100, no. 1, pp. 24–31, 1998.

[7] F. C. Jaarsma, "Rural low-traffic roads (LTRs): the challenge for improvement of traffic safety for all road users," in *Proceedings of the 27th ISATA, Dedicated Conference on Road and Vehicle Safety*, Aachen, Germany, November 1994.

[8] American Association of State Highway and Transportation Officials, *A Policy on Geometric Design of Highway and Streets*, AASHTO, Washington, DC, USA, 2018.

[9] J. M. Dargay and M. B. F. Hanly, *Elasticities. Interim Report to the Department of the Environment Transport and the Regions*, ESRC Transport Studies Unit, London, UK, 1999.

[10] CCCC First Highway Consultants Co., Ltd., *Design Specification for Highway alignment*, China Communications Publishing & Media Management Co., Ltd., Beijing, China, 2017.

[11] H. B. Pacejka, *Tire and Vehicle Dynamics*, Society of Automotive Engineers. Inc., London, UK, 2006.

[12] J. Zhang, H. Kawasaki, and Y. Kawai, "A tourist route search system based on web information and the visibility of scenic sights," in *Proceedings of the IEEE 2008 Second International Symposium on Universal Communication*, pp. 154–161, Osaka, Japan, December 2008.

[13] R. E. Manning, *Studies in Outdoor Recreation: Search and Research for Satisfaction*, Oregon State University Press, Corvallis, OR, USA, 2nd edition, 1999.

[14] R. E. Manning, *Parks and Carrying Capacity: Commons without Tragedy*, Island Press, Washington, DC, USA, 2007.

[15] C. F. Jaarsma, "Approaches for the planning of rural road networks according to sustainable land use planning," *Landscape and Urban Planning*, vol. 39, no. 1, pp. 47–54, 1997.

[16] T. Tang, Y. Guo, X. Zhou, S. Labi, and S. Zhu, "Understanding electric bike riders' intention to violate traffic rules and accident proneness in China," *Travel Behaviour and Society*, vol. 23, pp. 25–38, 2021.

[17] D. N. Cole and P. B. Landres, "Threats to wilderness ecosystems: impacts and research needs," *Ecological Applications*, vol. 6, no. 1, pp. 168–184, 1996.

[18] Countryside Commission, *Visitors to National Parks Summary of the 1994 Survey Findings: Technical Report*, Countryside Commission, Cheltenham, UK, 1996.

[19] Yorkshire Dales National Park, *The 1994 National Parks Visitor Survey, Key Findings*, Yorkshire Dales National Park, Bainbridge, UK, 1996.

[20] T. J. Steiner and A. L. Bristow, "Road pricing in national parks: a case study in the Yorkshire Dales National Park," *Transport Policy*, vol. 7, no. 2, pp. 93–103, 2000.

[21] P. B. Goodwin, "A review of new demand elasticities with special reference to short and long run effects of price change," *Journal of Transport Economics and Policy*, vol. 26, no. 2, pp. 155–169, 1992.

[22] Transportation Research Board, *Highway Capacity Manual*, TRB, Washington, DC, USA, 5th edition, 2010.

[23] CCCC First Highway Consultants Co., Ltd., *Technical Standard of Highway Engineering*, China Communications Publishing & Media Management Co., Ltd., Beijing, China, 2014.

[24] G. Kanellaidis and S. Vardaki, "Highway geometric design from the perspective of recent safety developments," *Journal of Transportation Engineering*, vol. 137, no. 12, pp. 841–844, 2011.

[25] S. Jung, K. Wang, C. Oh, and J. Chang, "Development of highway safety policies by discriminating freeway curve alignment features," *KSCE Journal of Civil Engineering*, vol. 22, no. 4, pp. 1418–1426, 2018.

[26] D. B. Fambro, K. Fitzpatrick, and C. W. Russell, "Operating speed on crest vertical curves with limited stopping sight distance," *Transportation Research Record: Journal of the Transportation Research Board*, vol. 1701, no. 1, pp. 25–31, 2000.

[27] D. R. Jessen, K. S. Schurr, P. T. McCoy, G. Pesti, and R. R. Huff, "Operating speed prediction on crest vertical curves of rural two-lane highways in Nebraska," *Transportation Research Record: Journal of the Transportation Research Board*, vol. 1751, no. 1, pp. 67–75, 2001.

[28] H. Gong and N. Stamatiadis, "Operating speed prediction models for horizontal curves on rural four-lane highways," *Transportation Research Record: Journal of the Transportation Research Board*, vol. 2075, no. 1, pp. 1–7, 2008.

[29] J. Tang, F. Liu, W. Zhang, R. Ke, and Y. Zou, "Lane-changes prediction based on adaptive fuzzy neural network," *Expert Systems with Applications*, vol. 91, pp. 452–463, 2018.

[30] R. Archilla and J. Morrall, "Traffic characteristics on two-lane highway downgrades," *Transportation Research Part A: Policy and Practice*, vol. 30, no. 2, pp. 119–133, 1996.

[31] C. M. Morris and E. T. Donnell, "Passenger car and truck operating speed models on multilane highways with combinations of horizontal curves and steep grades," *Journal of Transportation Engineering*, vol. 140, no. 11, 2014.

[32] L. Wang, J.-C. Cheng, and Y.-L. Zhang, "Reliability-based specification on critical length of highway sections with near-maximum grade," *KSCE Journal of Civil Engineering*, vol. 22, no. 4, pp. 1406–1417, 2018.

[33] Y. Guo, Y. Li, P. C. Anastasopoulos, S. Peeta, and J. Lu, "China's millennial car travelers' mode shift responses under congestion pricing and reward policies: a case study in Beijing," *Travel Behaviour and Society*, vol. 23, pp. 86–99, 2021.

[34] M. Kontaratos, B. Psarianos, and A. Yiotis, "Minimum horizontal curve radius as a function of grade incurred by vehicle motion in driving mode," *Transportation Research Record: Journal of the Transportation Research Board*, vol. 1445, no. 1, pp. 86–93, 1994.

[35] T.-H. Chang, "Effect of vehicles' suspension on highway horizontal curve design," *Journal of Transportation Engineering*, vol. 127, no. 1, pp. 89–91, 2001.

[36] S. Mavromatis and B. Psarianos, "Analytical model to determine the influence of horizontal alignment of two-axle heavy vehicles on upgrades," *Journal of Transportation Engineering*, vol. 129, no. 6, pp. 583–589, 2003.

[37] T. Varunjikar, *Design of Horizontal Curves with Downgrades Using Loworder Vehicle Dynamics Models*, Master of Science Thesis, The Pennsylvania State University, University Park, PA, USA, 2011.

[38] T. Watanada, *The Highway Design and Maintenance Standard Model, V.1: Description of the HDM-III Model*, The Johns Hopkins University Press, Baltimore, MA, USA, 1987.

[39] J. W. Fitch, *Motor Truck Engineering Handbook*, Society of Automotive Engineers, Warrendale, PA, USA, 1993.

Hindawi
Advances in Civil Engineering
Volume 2021, Article ID 6658299, 12 pages
https://doi.org/10.1155/2021/6658299

*Research Article*

# Invulnerability Simulation of Urban Agglomeration Passenger Transport Network under Incomplete Information Attack Strategy

**Chengbing Li,[1,2] Zhicheng Yang,[3] and Yuan Zhu[1,2]**

[1]*Transportation Institute, Inner Mongolia University, Hohhot 010021, China*
[2]*Inner Mongolia Engineering Research Center for Urban Transportation Data Science and Applications, Hohhot 010021, China*
[3]*School of Traffic and Transportation, Beijing Jiaotong University, Beijing 100044, China*

Correspondence should be addressed to Yuan Zhu; zhuyuan@imu.edu.cn

Received 12 October 2020; Revised 13 February 2021; Accepted 2 March 2021; Published 18 March 2021

Academic Editor: Hui Yao



This paper explores the invulnerability of urban agglomeration transportation network under the incomplete information attack strategy. This approach employed the site mapping method to construct the urban agglomeration composite transportation network model, and the network is weighted based on the actual passenger flow. Then the nodes are defined according to the overload conditions. In addition, based on the capacity-load model, the cascading failure model of the urban agglomeration passenger transport network is constructed, and the incomplete information attack strategy and network invulnerability measure index are determined. Finally, the case of Hu-Bao-E-Yu urban agglomeration is simulated to quantify the effects of attack strategies with varied information level, node load factors, and capacity weight and distance weight of the residual connected edge. The results reveal that the network crash speed is positively related to the information span of the attacker unless the information span exceeds 0.9 or accuracy exceeds 0.6. When the information span is low, the information accuracy $\delta$ has a critical impact on the network crash speed. Moreover, in the presence of attack, high or low values of node load factor are conducive to the improvement of network invulnerability. As a scale-free network, urban agglomeration transportation network shows strong robustness to random attacks and exhibits vulnerability to deliberate attacks. The capacity weight value $\alpha$ and distance weight value $\beta$ of residual connected edge have different effects on the network invulnerability under different information span strategies.

## 1. Introduction

In the process of urbanization, urban agglomeration gradually replaced single city as the basic unit of global competition and division of labor [1]. The multimodal transportation network provides movement for the people and cargoes among cities in the urban agglomeration. Meanwhile, the increasingly complex transportation network is also facing the threats of passenger flow surge, natural disasters, terrorist attacks, etc. Once a component in the urban agglomeration is malfunctioning, the passengers and cargoes have to disperse into the surrounding components, affecting their operations, and then deteriorate the whole urban agglomeration transportation network. Therefore, it is crucial to improve the resilience of urban agglomeration transportation network under sudden disasters and deliberate attacks, particularly the cascading failure phenomenon of urban agglomeration transportation network.

Various research studies have been added to the literature works regarding the cascading failure of complex network. Luo and Zhang proposed a cascade failure model based on local priority redistribution rules with the consideration of the difficulty in implementing traditional shortest path routing under load distribution strategy in reality [2]. Ren et al. defined a random failure model in which the failure probability of each unit is related to the overload degree [3]. Plietzsch et al. defined a new cascading

failure model to observe the recovery power of electricity grid system under cascading failures by adjusting global and local redundancy [4]. Yin et al. analyzed the influence of node capacity by establishing a cascading failure model of scale-free network based on node degree [5]. Similarly, there are some research flows focusing on the capacity and load distribution [6–10].

On the other hand, the research to explore the impact of different attack strategies on the cascading failure process was widely carried out. Wang et al. analyzed the influence of two attack strategies on the robustness of cascading failures when the nodes are attacked in increasing or decreasing order in terms of the connectivity degree [11]. Based on the traditional capacity-load model, the cascading failure scenario of the weighted bus network was constructed by Zhang et al. and the simulation results under three attack strategies proved the effectiveness of the cascade failure model [12]. In view of the lack of research on multinode attack strategy under the condition of incomplete information, Chaoqi et al. proposed three attack strategies with information of different levels, and the impacts are simulated and analyzed. The results showed different advantages of strategies under three conditions [13]. According to the characteristics of equipment support network, Tian and Zhang introduce information precision parameters and intelligence span parameters to construct a general attack strategy model of equipment support network under incomplete information. Simulation results revealed that the existence of a threshold of information degree and the impact of the attack reach the maximum level when the threshold is attained [14].

In addition, some scholars jumped out of the system of the single isolated network and turned their attention to a complex system. Chen et al. studied cascading failure of coupled networks [15]. Cai et al. established an interdependence model between power system and dispatching data network to analyze the complex influence of cascading faults [16]. Hong et al. studied the performance of interdependent network under random attacks [17]. In the transportation field, Wu et al. studied the cascading failure of the weighted transportation network in urban transportation [18], which tried to establish the dynamic relationship between cascading failures and large scale of complex traffic flows. Yan et al. constructed a complicated network based on the original traffic flow to study its dynamic characteristics [19]. Additional research focused on the invulnerability change of urban transit networks causing by cascading failure [20–22], especially on rail transit networks [23].

The abovementioned research on cascading failure is mostly from the perspective of topological data on large network and the impact of network structures and load distribution strategies. However, the research on the transportation network cascading failure is mostly based on single mode in urban area, with little mention of the interaction of multimodal traffic in an urban agglomeration. Recently, with the acceleration of regional integration, the study of urban agglomerations is becoming an emerging field of urban research [24]. In addition, network attacks are mainly divided into two categories, namely, deliberate and random attacks. Since the attacker may neither understand all information nor know nothing on the network, it is difficult to quantify the threat merely based on single attack. Therefore, this paper constructs a cascading failure model of agglomeration transportation network under the incomplete information attack strategy (the strategy to select target nodes and attack when network information is only partially known) based on the impact of information span, node load factor, and load distribution mechanism.

The contents of this paper are structured as follows. Section 2 constructs a weighted transportation network model on the actual traffic flow using the existing research methodologies [24, 25]. Section 3 introduces incomplete information attack strategy, load factor, residual capacity weight of connected edge, and spatial distance weight index to establish the cascading failure model of an urban agglomeration and proposes the measurement indicator of invulnerability. Section 4 simulates and analyzes the model based on the investigation data of Hu-Bao-E-Yu urban agglomeration. The approach is summarized in Section 5.

## 2. The Weighted Transportation Network Model of Urban Agglomeration

In the previous research of agglomeration transportation network proposed by the author of this paper, road mapping methods are used to construct the topological graph of transportation network with multiple modes, which is based on the features of wide geographical range and large coverage area. In the approach, the stations of various transportation modes are regarded as the nodes and the interconnected edges. To study the characteristics of the composite transportation network in urban agglomeration, the adjacent stations are merged into one node and different transportation networks of various transportation modes are composed [24, 25]. Based on the previous research, transportation network model is constructed using the composite concept. Firstly, the subnetwork of single transportation mode is constructed, respectively. Then the adjacent stations of different transportation modes in urban agglomeration are merged into one node to implement the passenger flow between different transportation modes. The weight of the new node is the sum of the merged nodes, and the set of neighbor nodes came from all the adjacent nodes from the original subnetwork. Due to the wide geographical area of urban agglomeration, it should be noticed that the sites with close distance often exist within the same city. The distance between these sites can be obtained through GIS technology, and the sites within 20 minutes range by walking or transit are merged into a composite node.

Based on the analysis above, the following assumptions are made for the composite network considering the realistic characteristics of urban agglomeration transportation network:

Hypothesis 1: the urban agglomeration transportation network is an undirected network, which means the traffic from one node to another also used the same link to return, and the traffic flow is approximately the same.

Hypothesis 2: the passenger flow between any two stations in the urban agglomeration transportation network remains unchanged for a certain period.

Hypothesis 3: the stations are merged when passenger's transfer time between connected stations is short, and the merged node is denoted as a composite node. In addition, $V'$ represents the set of nodes to be merged, and $V''$ is the set of composite nodes.

Hypothesis 4: if there are multiple edges connecting two nodes, they are regarded as one edge named composite edge. $E'$ represents the set of edges to be merged, and $E''$ is the set of composite edges.

The composite transportation network model of urban agglomeration is denoted by $G(V, E, W, H)$, where $V$ means the set of network nodes, $V = \cup_{s=1}^{q} V_s \backslash V' \cup V'' = \{v_1, v_2, \ldots, v_i, \ldots, v_n\}$. $V_s$ represents the node set of the $s$th subnetwork, $V'$ denotes the set of nodes to be merged, $V''$ is the set of composite nodes, $q$ is the number of subnets, and $n$ is the number of nodes of the composite network in urban agglomeration. $E$ represents the set of edges corresponding to $V$, $E = \cup_{s=1}^{q} E_s \backslash E' \cup E'' = (e_{ij})_{n\times n}$. $E_s$ denotes the edge set of the $s$th subnet, $E'$ represents the set of edges to be merged, and $E''$ is the set of composite edges. When $v_i R v_j$, it means node $v_i$ is connected with $v_j$, and $e_{ij} = 1$. When $v_i \overline{R} v_j$, it means node $v_i$ is not connected with $v_j$, and $e_{ij} = 0$. $W = (w_{ij})_{n\times n}$ denotes edge weight matrix of transportation network in urban agglomeration, where $w_{ij}$ is the weight of edge $ij$. $H = \{h_1, h_2, \ldots, h_i, \ldots, h_n\}$ denotes node matrix of transportation network, where $h_i$ is the weight of node $i$.

This paper uses the actual passenger flow data of urban agglomeration transportation network to measure the edge weight, that is, the maximum daily passenger volume between these edges. Based on the number of maximum daily passenger aggregation in station, the maximum daily passenger volume of the node is corrected and used as the node weight. For the composite edge, the weight is the sum of combined edges weight of each subnet. For the composite node, the weight is the sum of merged nodes weights of each subnet.

## 3. The Invulnerability Analyses of Urban Agglomeration Transportation Network under Cascading Failure

*3.1. The Cascading Failure Analysis of Urban Agglomeration Transportation Network.* In reality, when a node or an edge of the network malfunctions due to an attack or natural disaster, the original load of the network is allocated to its adjacent nodes or edges according to certain rules. The reallocation may result in malfunctions of other nodes or links, and such chain reactions are called cascading failures. In the urban agglomeration transportation network, the failures of composite nodes and edges connecting multiple subnets will cause not only load redistribution of its own subnet but also the load change of some other subnets combined with it and eventually lead to the cascading failure of the entire composite transportation network in urban agglomeration.

The cascading failure model of the urban agglomeration transportation network is built based on the improved capacity-load model. The procedure is as follows:

Step 1: in urban agglomeration transportation network, assume that the capacity of node $i$ is $C_i$, so $C_i = h_i$. $L_i$ represents the initial load of node $i$ with $\tau \times C_i = L_i$, and $\tau$ is node load factor with $0 \le \tau \le 1$. Similarly, the capacity of edge $ij$ is $C_{ij}$, and $C_{ij} = w_{ij}$. $L_{ij}$ denotes the initial load of edge $ij$. $\mu \times C_{ij} = L_{ij}$, and $\mu$ is edge load factor with $0 \le \mu \le 1$.

Step 2: under the incomplete information, the target node $i$ is attacked.

Step 3: after node $i$ fails, the node and its connected edge are deleted, and its load is redistributed to the adjacent nodes. The load distribution model is constructed by considering the distance and residual capacity of connected edges based on the attractiveness between lines caused by different redundant capabilities of connected edges and the spatial distance between connected and failed nodes. $\alpha$ is defined as the redundant capability weight of connected edge, $\beta$ is spatial distance weight. When $\alpha + \beta = 1$, the failed node $i$ distributes the load to the connected node, as shown in the following equation:

$$L_j(t+1) = L_j(t) + \left( \alpha \frac{C_{ij} - L_{ij}}{\sum_{j\in\Pi}\left(C_{ij} - L_{ij}\right)} + \beta \frac{d_{ij}}{\sum_{j\in\Pi} d_{ij}} \right) L_i(t), \tag{1}$$

where $L_j(t)$ is the load of node $j$ at time $t$., $C_{ij}$ represents the capacity of edge $ij$, $L_{ij}$ denotes the load of edge $ij$, $d_{ij}$ is the distance of edge $ij$, and $\Pi$ represents the node set adjacent to node $i$.

Step 4: update the network load and determine the overloaded node. According to the difference between nodes load and capacity, the nodes are divided into three states: normal, pause, and failure, as shown in the following equation:

$$\text{If} \begin{cases} L_i < C_i \longrightarrow \text{normal} \\ L_i \ge C_i, \text{rand} > p_i \longrightarrow \text{pause} \\ L_i \ge C_i, \text{rand} \le p_i \longrightarrow \text{failure} \end{cases}, \tag{2}$$

where rand is the random number between 0 and 1 and $p_i = (L_i - C_i/C_i)$ is the failure probability of node $i$.

Step 5: identification of cascading failure occurrence. If there is a pause or failure node in the network, the cascade fails and goes to Step 6. Otherwise, there is no cascading failure, goes to Step 7.

Step 6: the redistribution of the load. For the failed node, redistribute load according to equation (1), and delete the node and its connected edges. For the pause node, only the excessive load is evacuated. The load distribution formula for the pause node $i$ is as follows:

$$L_j(t+1) = L_j(t) + \left(\alpha \frac{C_{ij} - L_{ij}}{\sum_{j\in\Pi}\left(C_{ij} - L_{ij}\right)} + \beta \frac{d_{ij}}{\sum_{j\in\Pi} d_{ij}}\right) \times \left(L_i(t) - C_i(t)\right). \tag{3}$$

Go to Step 4.

Step 7: the judgment of attack end. If all the nodes in the network fail, the network is paralyzed, then the simulation ends, and the output is the invulnerability measure index (that is, to modify the relative scale of the largest connected subgraph; this index will be used to describe the degree of damage of the current network relative to the original network, and the change of the network's survivability can be determined by observing the change of this index). Otherwise, if the network nodes are not completely failed, go to Step 2 for the next round of attack.

The algorithm of this approach is presented in Figure 1.

*3.2. Incomplete Information Strategy.* Most of the existing research on complex network invulnerability used the random or deliberate strategy to investigate the network invulnerability. However, in urban agglomeration transportation network, due to the significant network coverage and the operation distance, the situation may become extremely uncertain. It is impossible for terrorists to know nothing or everything about the nodes and edges information of the transportation network. So, the selection of attack targets considers neither random attacks nor deliberate attacks. To describe the attacks on nodes in real network, this paper uses the incomplete information attack strategy to conduct the network attack.

The information index $(\lambda, \delta)$ is used to describe the degree of information acquisition of the network. The information span parameter $\lambda \in [0, 1]$ represents the level of understanding of the entire network. Assuming that there are $N$ nodes in the network, if $\lambda N$ nodes with known information, deliberate attack strategy will be taken to attack these nodes, and $(1-\lambda)N$ nodes with unknown information will be attacked by random attack strategy. It can be seen that when the parameter $\lambda$ is higher, we know more about the network. The information accuracy parameter $\delta \in [0, 1)$ represents the acquisition of important node information. All nodes in urban agglomeration transportation network $G$ are sorted in the descending order according to their weight, the sequence group $R = \{r_1, r_2, \ldots, r_i, \ldots, r_n\}$ is obtained, and the number of node $v_i$ is $r_i$. $\nabla_i$ is defined as the information acquisition status of node $v_i$; when $\nabla_i = 1$, the weight of node $v_i$ is certain; when $\nabla_i = 0$, the weight is unknown. Considering that the understanding of node information is often incomplete, so $\nabla \in [0, 1]$.

Here, the auxiliary variable $\pi_i$ of the node $v_i$ is introduced as follows:

$$\pi_i = r_i^{-(\delta/1-\delta)}. \tag{4}$$

Thus, the determination of known information nodes can be regarded as an unequal probability sampling problem. The probability of node $v_i$ is $\nabla_i$, as shown in the following equation:

$$\nabla_i = \frac{\pi_i}{\sum_{i=1}^{N}\pi_i} = \frac{r_i^{-(\delta/1-\delta)}}{\sum_{i=1}^{N} r_i^{-(\delta/1-\delta)}}. \tag{5}$$

Obviously, under the larger $\delta$ value, the node with larger weight will be selected easier. When $\nabla_i = (1/N)$, we randomly obtain the node information. When $\delta$ tends to 1, if $r_i = 1$, then $\nabla_i = 1$; if $r_i \neq 1$, then $\nabla_i = 0$, and the node with the highest weight is selected preferentially.

In conclusion, the method of unequal probability sampling is used to sequentially determine the set of known information nodes. Then, the set of known information nodes is attacked by deliberate strategy, and unknown information nodes are attacked by random strategy until the network is paralyzed.

*3.3. Invulnerability Measure Indicator.* Aiming at the features of wide area and large differences of passenger flow among nodes in urban agglomeration, this paper improves the traditional invulnerability measure indicator (the ratio of the number of effective nodes in the maximum connected subgraph before and after the attack), and the ratio of the sum of effective nodes load in the maximum connected subgraph before and after network attack is used as the new invulnerability measure indicator called the relative scale of the maximum connected subgraph, as shown in the following equation:

$$S = \frac{\sum_{i=1}^{N'} L_i}{\sum_{i=1}^{N} L_i}, \tag{6}$$

where $N'$ represents the number of nodes in the maximum connected subgraph after the network is attacked, $N$ denotes the number of network nodes without attack, and $L_i$ represents the load of node $i$ in the maximum connected subgraph. When the network is not attacked, the relative scale of the maximum connected subgraph is 1, and the network is in a fully connected state.

## 4. The Case Study

*4.1. The Transportation Network Model Construction of Hu-Bao-E-Yu Urban Agglomeration.* To demonstrate the impact of our model to an urban agglomeration network, the Hu-Bao-E-Yu urban agglomeration is taken as an example to simulate and analyze the abovementioned invulnerability model. Hu-Bao-E-Yu urban agglomeration is located in the inland area of northwestern China. The operation of large-scale passenger and cargo flow is mainly carried out through the railway and road transportation networks. Because of the limitation of the natural environment, there is no water transportation in Hu-Bao-E-Yu urban agglomeration. There are only three airports, which bear a small proportion of passengers and freight. Therefore, this paper takes all the bus

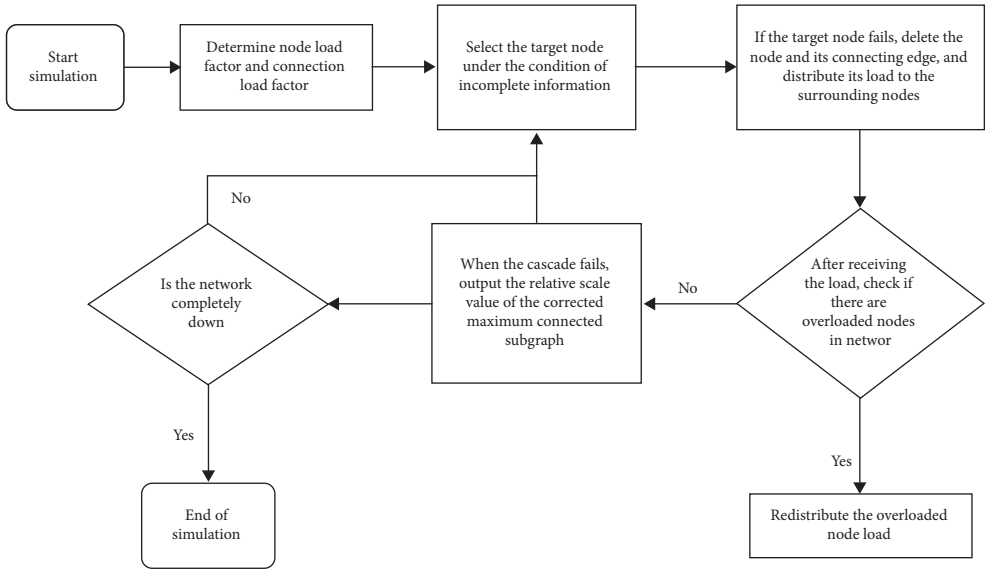


Figure 1: Algorithm flowchart.

stations and railway stations of Hu-Bao-E-Yu urban agglomeration as the nodes and the traffic lines as connected edges to construct the road transportation subnet $G_1$ and rail transportation subnet $G_2$. In this case, the road transportation subnet nodes $|V_1| = 263$, connected edges $|E_1| = 761$, and rail transportation nodes $|V_2| = 40$, connected edges $|E_2| = 164$. Furthermore, as mentioned above, the nodes where the passenger can transfer within 20 minutes are merged into a composite node [25]. And the composite transportation network model of urban agglomeration is constructed by combining road and rail transportation subnetworks. For the composite network, if there are multiple edges between two nodes, they are merged to be a composite edge. Here, nodes to be merged $|V'| = 36$, composite nodes $|V''| = 17$, and the composite transportation network nodes $V = V_1 \cup V_2 \cup V'' \backslash V'$, $|V| = 284$. The edges to be merged $|E'| = 104$, composite edges $|E''| = 57$, and the composite transportation connected edges $E = E_1 \cup E_2 \cup E'' \backslash E'$, $|E| = 878$. The composite nodes are shown in Table 1, and the transportation network topological graph of Hu-Bao-E-Yu urban agglomeration is shown in Figure 2.

Based on the transportation network model of Hu-Bao-E-Yu urban agglomeration, the distance between the stations is obtained through GIS, and the actual transportation data are obtained through the Inner Mongolia Transportation Administration, the Shaanxi Provincial Communications Department of Transportation Administration, and train stations. The initial node weight and connected edge weight are derived through the maximum daily passenger volume of nodes and edges. Further, the node weight is corrected by the value of the maximum daily passenger gathered on the station, and the capacity of each node is equal to the maximum daily passenger gathered on the station.

*4.2. The Network Invulnerability Simulation under Incomplete Information Attack.* In this paper, the impact of different attack strategies on the invulnerability of urban agglomeration transportation network is studied and simulated with MATLAB, which means that the values of information span parameter $\lambda$ or information accuracy $\delta$ are changed on the basis of fixed parameters $\tau = 0.6$, $\mu = 0.6$, the connected edge residual capacity weight $\alpha = 0.5$, and the spatial distance weight $\beta = 0.5$. To substantiate the analysis, 50 nodes in the network are attacked, and the changes in the relative scale of the corrected maximum connected subgraph are captured. The simulation results are shown in Figure 3.

As shown in Figure 3, when the number of attacks increases, the relative scale of the corrected maximum connected subgraph decreases. It can be seen from Figures 3(a) and 3(b) that when the information accuracy is unchanged, the network crash speed (the degree to which the network's survivability measurement index drops for each attack on a node) increases with the information span. In particular, when the value of the information span $\lambda$ reaches 0.9, continuous attack on 50 nodes can cause the global crash, and the relative scale of the corrected maximum connected subgraph becomes 0. When the information accuracy changes from $\delta = 0$ to $\delta = 0.2$, the acceleration speed of network collapse under different information span is different. According to Figures 3(a)–3(f), it is found that when the information span $\lambda$ reaches 0.9, the network completely collapses after attacking 50 nodes, and the variation of the relative scale of the corrected maximum connected subgraph does almost not change with the change of the information accuracy value $\delta$. This indicates that the attack strategy of the network has been optimal at this time. That is, the attack sequence of the node is almost certain, and at this point, the attack is almost a deliberate attack, under which the impact

Table 1: Composite nodes.

| Normal node | Transportation network type | Composite node | Passenger's transfer time (min) |
|---|---|---|---|
| Hohhot coach station<br>Passenger western station<br>Hohhot railway station | Road transportation network<br>Railway transportation network | Hohhot coach station-passenger western station-railway station | 5 |
| Yulin car passenger station<br>Passenger south station<br>Yulin railway station | Road transportation network<br>Railway transportation network | Yulin car passenger station-passenger south station-railway station | 10 |
| Ordos bus station<br>Ordos railway station | Road transportation network<br>Railway transportation network | Ordos bus station-railway station | 8 |
| Dalad Banner bus station<br>Dalad Banner railway station | Road transportation network<br>Railway transportation network | Dalad Banner bus station-railway station | 6 |
| Chasuqi bus station<br>Chasuqi railway station | Road transportation network<br>Railway transportation network | Chasuqi bus station-railway station | 3 |
| Baotou coach station<br>Baotou east railway station | Road transportation network<br>Railway transportation network | Baotou coach station-east railway station | 8 |
| Suide bus station<br>Suide railway station | Road transportation network<br>Railway transportation network | Suide bus station-railway station | 15 |
| Dongsheng bus station<br>Dongsheng railway station | Road transportation network<br>Railway transportation network | Dongsheng bus station-railway station | 11 |
| Shenmu bus station<br>Shenmu railway station | Road transportation network<br>Railway transportation network | Shenmu bus station-railway station | 13 |
| Qingjian bus station<br>Qingjian railway station | Road transportation network<br>Railway transportation network | Qingjian bus station-railway station | 3 |
| Jinjie bus station<br>Jinjie railway station | Road transportation network<br>Railway transportation network | Jinjie bus station-railway station | 10 |
| Mizhi bus station<br>Mizhi railway station | Road transportation network<br>Railway transportation network | Mizhi bus station-railway station | 5 |
| Wubao bus station<br>Wubao railway station | Road transportation network<br>Railway transportation network | Wubao bus station-railway station | 14 |

Table 1: Continued.

| Normal node | Transportation network type | Composite node | Passenger's transfer time (min) |
|---|---|---|---|
| Dingbian bus station | Road transportation network | Dingbian bus station-railway station | 15 |
| Dingbian railway station | Railway transportation network | | |
| Jingbian bus station | Road transportation network | Jingbian bus station-railway station | 13 |
| Jingbian railway station | Railway transportation network | | |
| Zizhou bus station | Road transportation network | Zizhou bus station-railway station | 14 |
| Zizhou railway station | Railway transportation network | | |
| Fugu bus station | Road transportation network | Fugu bus station-railway station | 8 |
| Fugu railway station | Railway transportation network | | |

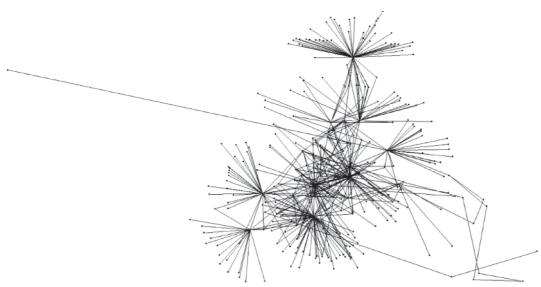

Figure 2: The topological graph of the road-railway composite transportation network of Hu-Bao-E-Yu urban agglomeration.

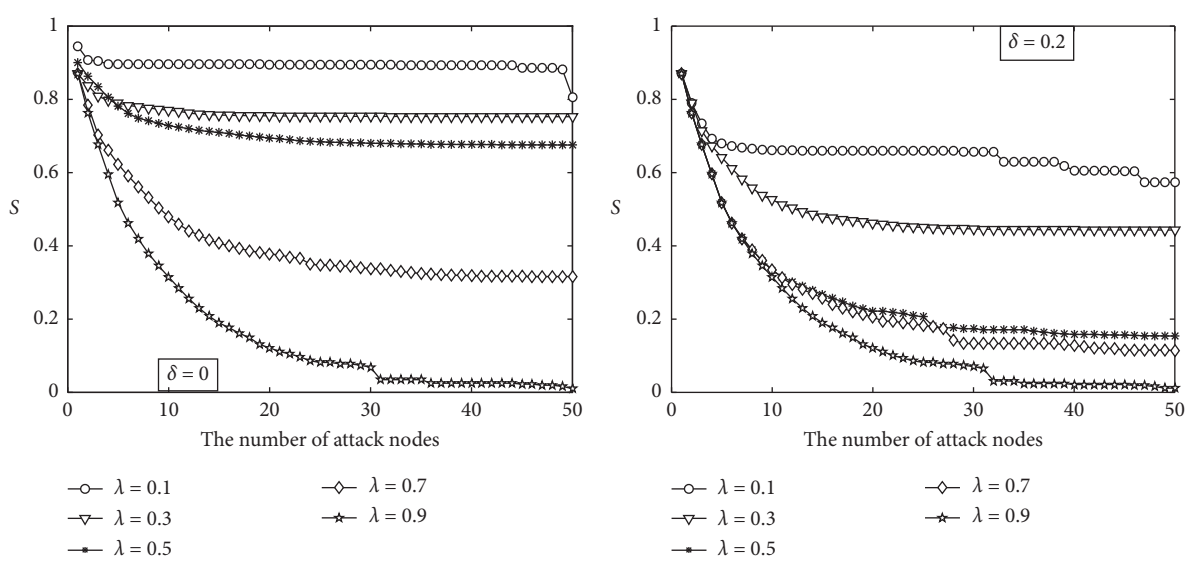


(a) (b)

Figure 3: Continued.

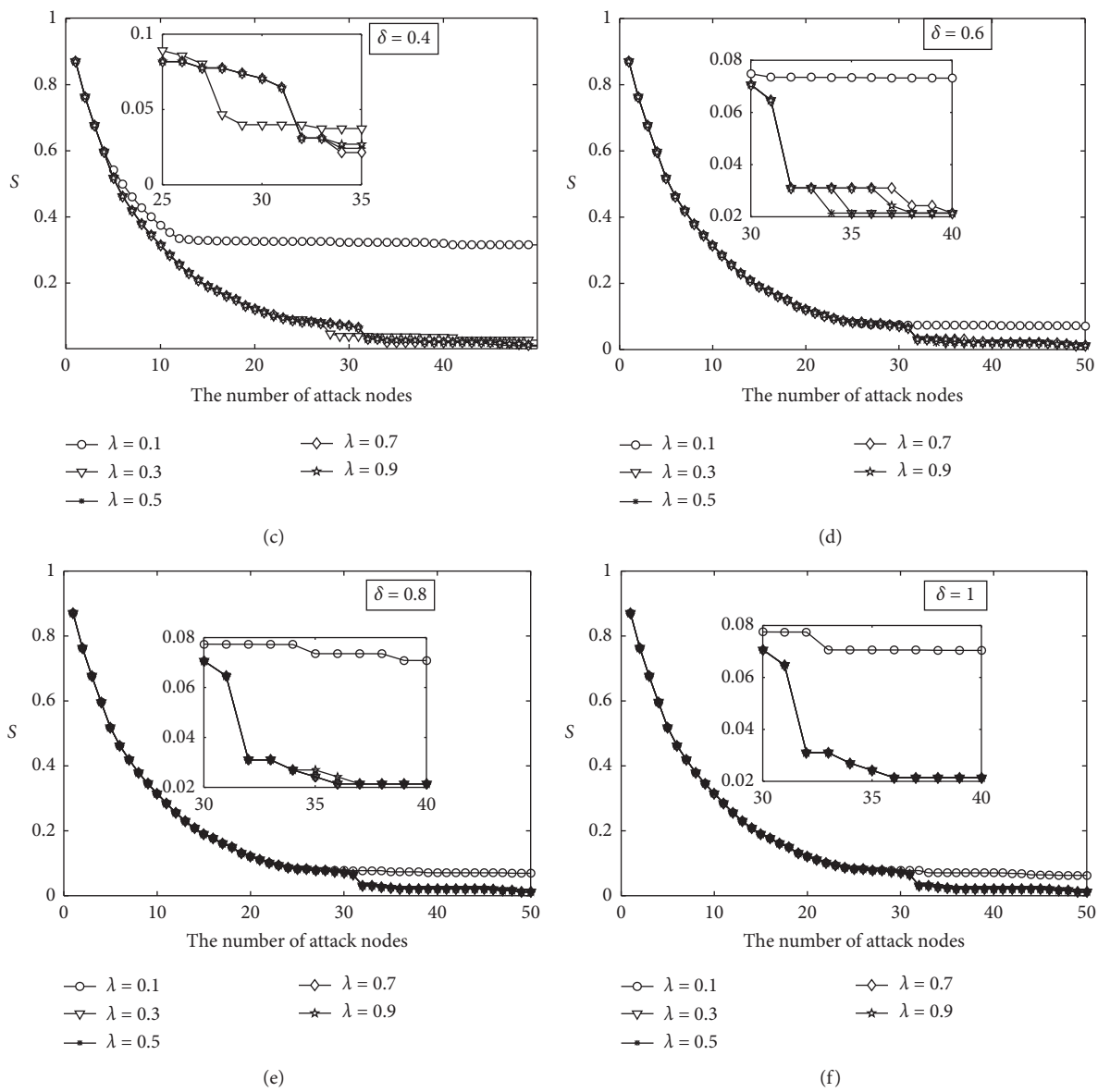


Figure 3: The simulation result of network invulnerability under different information conditions.

of the cascade failure is maximized. This shows that the impact of cascading failure will reach the maximum if the attack information span is 0.9. Therefore, the attacker does not need to obtain all the network information, but only needs to obtain the information that exceeded 0.9 to maximize the effect of the network attack. In addition, observing from Figures 3(d)–3(f), when $\lambda = 0.1$ and $\delta = 0.6$, no matter how the value of information accuracy $\delta$ changes, and the relative scale of the corrected maximum connected subgraph changes very little after the number of attack nodes reaching 30. This indicates that when the attacker obtains a small range of information, there is a threshold of the information accuracy. When the value is below the threshold, the network invulnerability does not change significantly.

*4.3. Influence Analysis of Node Load Factor on the Network Invulnerability under Incomplete Information Attack.* Under incomplete information attack, the influence of node load factor on network invulnerability is studied with the connected edge load factor $\mu = 0.6$, the residual capacity weight $\alpha = 0.5$, and spatial distance weight $\beta = 0.5$. Meanwhile, considering that information accuracy and information span are similar to each other in terms of their effects on invulnerability change, the information accuracy parameter is set to $\delta = 0.2$. The network invulnerability in different information span is observed by uniformly increasing the node load factor. The relative scale of the corrected maximum connected subgraph changes with the number of attack nodes, as shown in Figure 4.

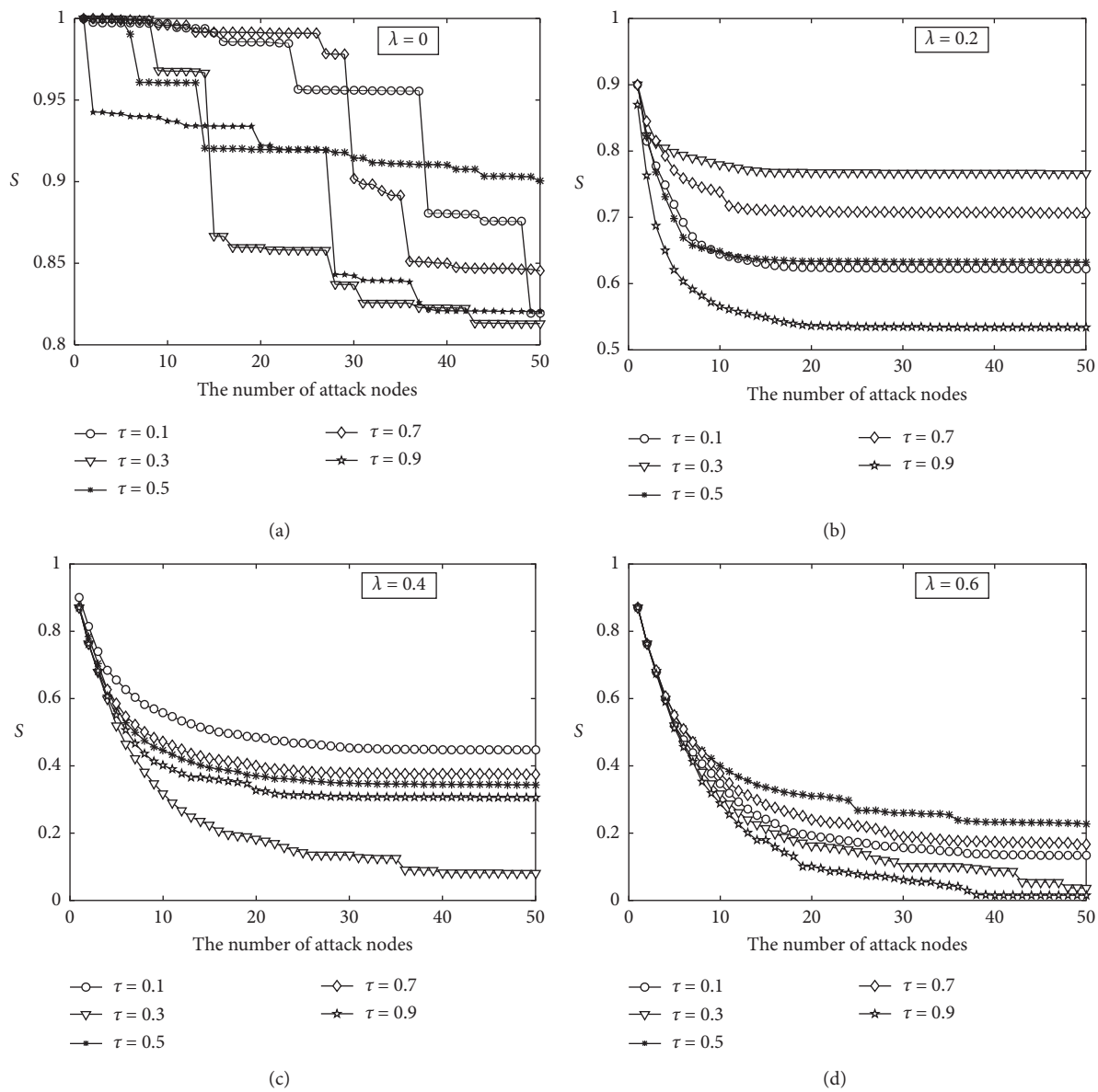


Figure 4: The simulation result of node load factor on urban agglomeration transportation invulnerability under different information conditions.

It can be seen from Figure 4(a) that when the information span parameter $\lambda = 0$, the attacker's access to network information is 0, which means that the attack sequence of the node is extremely irregular, and at this point, the attack is almost a random attack. Because the urban agglomeration transportation network has a wide geographical range and large coverage area and distinct capacity among stations, the relative scale of the corrected maximum connected subgraph is different. The network invulnerability is significantly influenced by a small number of important nodes. Once these stations are destroyed, the overall connectivity of the transportation network in urban agglomeration will be greatly affected. In addition, by comparing the scenarios, the urban agglomeration transportation network as a scale-free network shows strong robustness to random attacks but exhibits vulnerability to deliberate attacks. Comparing Figures 4(b)–4(d), we find that, under different information access degrees, the change of the relative scale of the corrected maximum connected subgraph shows different characteristics for distinct node load factors. Here, when $\lambda = 0.2$, the load factor $\tau = 0.3$ shows the strongest invulnerability. However, when the value of $\lambda$ increases to 0.4 and the load factor $\tau = 0.3$, the network becomes highly vulnerable. No matter what the information span is, the network shows poor invulnerability to the load factor when $\tau = 0.9$. This indicates that the impact of the load factor on the network invulnerability is greatly affected by the attacker's access degree of information. If the redundant capacity of the station in the network is higher with a lower load factor, the invulnerability is not necessarily better.

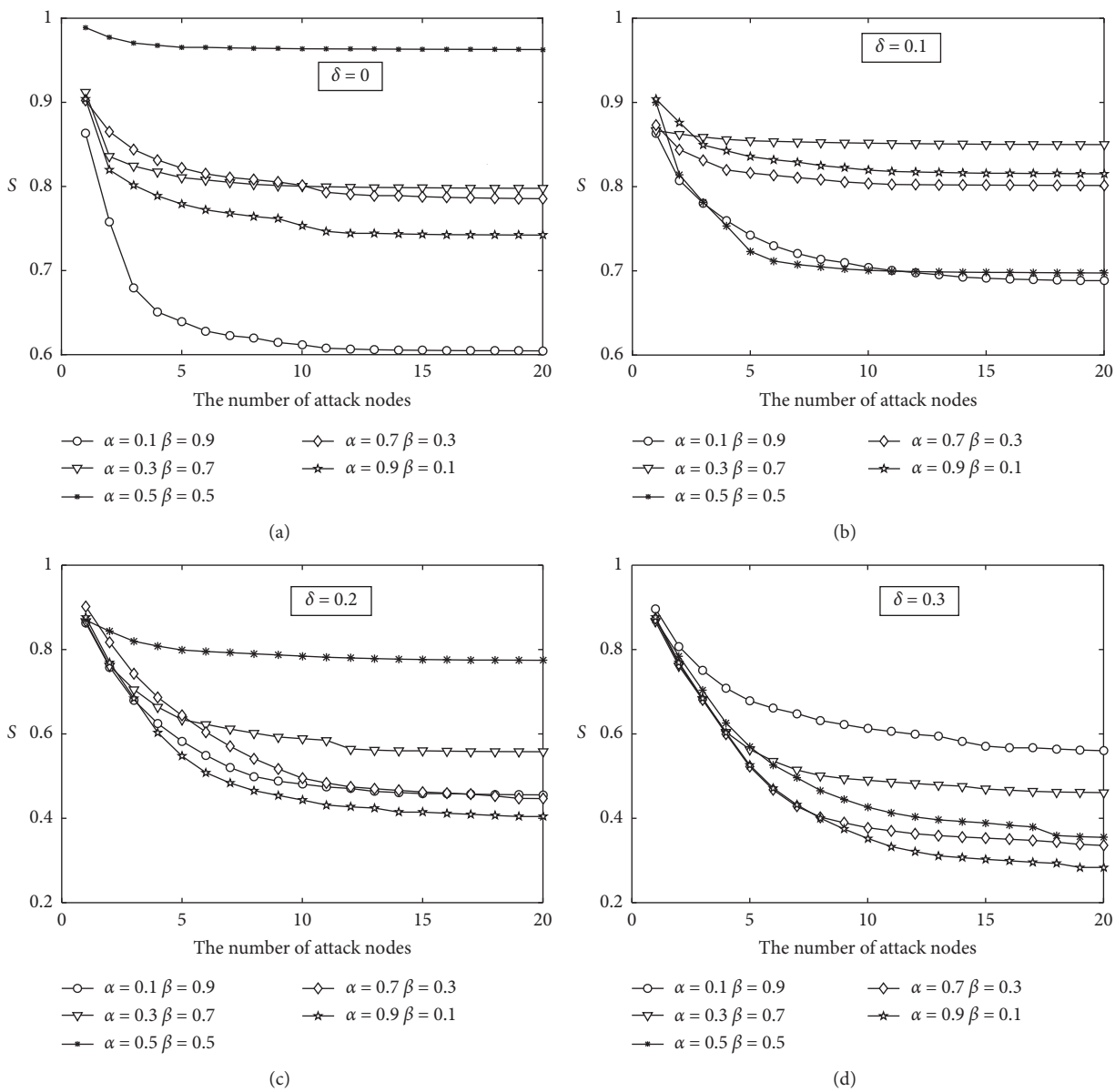


Figure 5: The simulation result of load distribution strategy on urban agglomeration transportation invulnerability under different information conditions.

*4.4. Influence Analysis of Load Distribution Strategy on Network Invulnerability.* By adjusting the values of residual capacity and spatial distance weights, this paper studies the effects of different load distribution strategies on network invulnerability during cascading failure. The node and connected edge load factor are set to $\tau = 0.6$ and $\mu = 0.6$, and the information span parameter is set to $\lambda = 0.2$; the effects of different load distribution strategies ($\alpha = 0.1$, $\beta = 0.9$; $\alpha = 0.3$, $\beta = 0.7$; $\alpha = 0.5$, $\beta = 0.5$; $\alpha = 0.7$, $\beta = 0.3$; $\alpha = 0.9$, $\beta = 0.1$) on network invulnerability under different information accuracies are shown in Figure 5.

As can be seen from Figure 5, under different information accuracies, the impact of load distribution strategies on the network invulnerability presents varied characteristics. According to Figures 5(a) and 5(c), when $\delta = 0$, 0.2, $\alpha = 0.5$, $\beta = 0.5$, the network invulnerability is optimal. But the network invulnerability is poor when $\alpha = 0.1$, $\beta = 0.9$ and $\alpha = 0.9$, $\beta = 0.1$. In other words, the more balanced weight of the spatial distance and the connected edge residual capacity is, the stronger the network invulnerability will be. According to Figure 5(d), when $\delta = 0.3$, the network invulnerability increases with the load distribution weighting the spatial distance weight.

As can be seen from the above, the methodology aims at the passenger evacuation for failed nodes in the urban agglomeration transportation network. When the attacker knows little about the network information, the evacuation strategy will reduce the impact of the cascading failures and make better invulnerability of transportation by considering the impact of the residual capacity and the spatial distance.

Moreover, when the attacker knows more about the network information, the evacuation strategy based on the distance of adjacent station will reduce the impact of the cascading failure and make better invulnerability of transportation.

## 5. Conclusions

This paper proposes the cascading failure model of the urban agglomeration passenger transport network based on the improved capacity-load model. A simulation scenario on the invulnerability of Hu-Bao-E-Yu urban agglomeration transportation network under incomplete information attack is built based on different node load factors and load distribution mechanisms. The research conclusions are as follows:

(1) The attack information span has a threshold 0.9, and the degree of information accuracy has a threshold 0.6. Once one of the thresholds is exceeded, maximum damage to the network can be achieved. Therefore, the attacker does not need to obtain all the information of the network, and the obtained information only needs to exceed a certain value to achieve the best attack effect.

(2) Under the influence of attackers' access information of the network, the site redundant capacity will be too high or too low, which will reduce the invulnerability of urban agglomeration transportation network. Therefore, larger station scale may not be beneficial to the improvement of invulnerability.

(3) Due to the large gap of different sites, the transportation network shows strong robustness to random attacks and vulnerability to deliberate attacks. A few key sites play a decisive role in the normal operation of the urban agglomeration transportation network.

(4) The impact of different load distribution strategies on network invulnerability is also different with the situation of the attackers' access network information. Therefore, to reduce the impact of cascading failure and improve the resilience of urban agglomeration transportation network, strategies with different weights of factors are considered to deal with various types of attackers.

The research in this article helps to further reveal the cascading failure mechanism of the urban agglomeration transportation network in reality. The article explores how different factors can resist the destruction of the urban agglomeration passenger transportation network when the attacker fails to fully grasp the network information to attack the network. The research results show that a small number of key sites have a decisive effect on whether the urban agglomeration traffic network can maintain good resilience. This reminds the urban agglomeration traffic management personnel to identify those more important sites that need daily special maintenance. In addition, when an accident causes some stations in the transportation network to fail, managers should formulate passenger flow evacuation strategies under different conditions to ensure the minimal impact on the network.

This paper constructs a passenger transportation network model for urban agglomerations based on complex networks. Then the survivability of the network is analyzed. In the process of constructing the network model, the composite method adopted and referred to the actual traffic network. However, there are not entirely the same in terms of dynamic characteristics. More specifically, in a composite network, the load of the network node is relatively fixed, while it is always changing in the realistic network. At the same time, in the process of cascade failure simulation, the evacuation of passengers cannot be carried out simultaneously due to the influence of time. In addition, the existing research mainly focuses on the dynamic simulation of the invulnerability characteristics of the urban agglomeration traffic network, and the related research on optimization and repair has not been carried out in depth, so further research will focus on the above issues.

## Data Availability

The tabular data used to support the findings of this study are included within the article.

## Conflicts of Interest

The authors declare that they have no conflicts of interest.

## Acknowledgments

The work presented in this paper was partially funded by the Special Fund of National Natural Science Foundation of China (Grant no. 71940010), General Fund of Natural Science of Inner Mongolia (Grant no. 2019MS05083), Research Program of Science and Technology at Universities of Inner Mongolia Autonomous Region (Grant no. NJZY19013), and the Young Scientists Fund of Natural Science of Inner Mongolia (Grant no. 2019BS07002).

## References

[1] J. He, C. Li, Y. Yu, Y. Liu, and J. Huang, "Measuring urban spatial interaction in Wuhan urban agglomeration, Central China: a spatially explicit approach," *Sustainable Cities and Society*, vol. 32, pp. 569–583, 2017.

[2] X. S. Luo and B. Zhang, "Analysis of cascading failure in complex power networks under the load local preferential redistribution rule," *Physica A: Statistical Mechanics and its Applications*, vol. 391, no. 8, pp. 2771–2777, 2012.

[3] W. Ren, J. Wu, X. Zhang, R. Lai, and L. Chen, "A stochastic model of cascading failure dynamics in communication networks," *IEEE Transactions on Circuits and Systems II: Express Briefs*, vol. 65, no. 5, pp. 632–636, 2018.

[4] A. Plietzsch, P. Schultz, J. Heitzig, and J. Kurths, "Local vs. global redundancy-trade-offs between resilience against cascading failures and frequency stability," *The European Physical Journal Special Topics*, vol. 225, no. 3, pp. 551–568, 2016.

[5] R.-R. Yin, B. Liu, H.-R. Liu, and Y.-Q. Li, "Research on invulnerability of the random scale-free network against

cascading failure," *Physica A: Statistical Mechanics and its Applications*, vol. 444, pp. 458–465, 2016.

[6] H. J. Sun, H. Zhao, and J. J. Wu, "A robust matching model of capacity to defense cascading failure on complex networks," *Physica A: Statistical Mechanics and its Applications*, vol. 387, no. 25, pp. 6431–6435, 2008.

[7] J. Lehmann and J. Bernasconi, "Stochastic load-redistribution model for cascading failure propagation," *Physical Review E*, vol. 81, no. 3, Article ID 031129, 2010.

[8] W. X. Wang and G. Chen, "Universal robustness characteristic of weighted networks against cascading failure," *Physical Review E*, vol. 77, no. 2, Article ID 026101, 2008.

[9] H.-P. Ren, J. Song, R. Yang, M. S. Baptista, and C. Grebogi, "Cascade failure analysis of power grid using new load distribution law and node removal rule," *Physica A: Statistical Mechanics and its Applications*, vol. 442, pp. 239–251, 2016.

[10] M. Du, X. Jiang, L. Cheng et al., "Robust evaluation for transportation network capacity under demand uncertainty," *Journal of Advanced Transportation*, vol. 2017, Article ID 9814909, 11 pages, 2017.

[11] J. Wang, L. Rong, L. Zhang, and Z. Zhang, "Attack vulnerability of scale-free networks due to cascading failures," *Physica A: Statistical Mechanics and its Applications*, vol. 387, no. 26, pp. 6671–6678, 2008.

[12] L. Zhang, B.-b. Fu, and Y.-x. Li, "Cascading failure of urban weighted public transit network under single station happening emergency," *Procedia engineering*, vol. 137, pp. 259–266, 2016.

[13] F. Chaoqi, W. Ying, W. Xiaoyang, and G. Yangjun, "Multi-node attack strategy of complex networks due to cascading breakdown," *Chaos, Solitons & Fractals*, vol. 106, pp. 61–66, 2018.

[14] X. G. Tian and C. M. Zhang, "Survivability model of equipment support network based on incomplete information," *System Engineering-Theory & Practice*, vol. 37, no. 3, pp. 790–798, 2017.

[15] Z. Chen, W.-B. Du, X.-B. Cao, and X.-L. Zhou, "Cascading failure of interdependent networks with different coupling preference under targeted attack," *Chaos, Solitons & Fractals*, vol. 80, pp. 7–12, 2015.

[16] Y. Cai, Y. Cao, Y. Li, T. Huang, and B. Zhou, "Cascading failure analysis considering interaction between power grids and communication networks," *IEEE Transactions on Smart Grid*, vol. 7, no. 1, pp. 530–538, 2016.

[17] S. Hong, B. Wang, X. Ma, J. Wang, and T. Zhao, "Failure cascade in interdependent network with traffic loads," *Journal of Physics A: Mathematical and Theoretical*, vol. 48, no. 48, p. 485101, 2015.

[18] J. J. Wu, H. J. Sun, and Z. Y. Gao, "Cascading failures on weighted urban traffic equilibrium networks," *Physica A: Statistical Mechanics and its Applications*, vol. 386, no. 1, pp. 407–413, 2007.

[19] Y. Yan, S. Zhang, J. Tang, and X. Wang, "Understanding characteristics in multivariate traffic flow time series from complex network structure," *Physica A: Statistical Mechanics and its Applications*, vol. 477, pp. 149–160, 2017.

[20] O. Cats and E. Jenelius, "Planning for the unexpected: the value of reserve capacity for public transport network robustness," *Transportation Research Part A: Policy and Practice*, vol. 81, pp. 47–61, 2015.

[21] E. Rodríguez-Núñez and J. C. García-Palomares, "Measuring the vulnerability of public transport networks," *Journal of transport geography*, vol. 35, pp. 50–63, 2014.

[22] E. Jenelius and O. Cats, "The value of new public transport links for network robustness and redundancy," *Transportmetrica A: Transport Science*, vol. 11, no. 9, pp. 819–835, 2015.

[23] A. De-Los-Santos, G. Laporte, J. A. Mesa, and F. Perea, "Evaluating passenger robustness in a rail transit network," *Transportation Research Part C: Emerging Technologies*, vol. 20, no. 1, pp. 34–46, 2012.

[24] C. B. Li, L. Wei, and Y. C. Hao, "Research on characteristics of city agglomeration compound traffic network," *Journal of System Simulation*, vol. 28, no. 12, pp. 2958–2965, 2016.

[25] C. B. Li, L. Wei, F. X. Li et al., "Study on vulnerability of city agglomeration compound traffic network based on attack strategy," *Journal of Highway and Transportation Research and Development*, vol. 34, no. 3, pp. 101–109, 2017.

Hindawi
Advances in Civil Engineering
Volume 2021, Article ID 6624579, 11 pages
https://doi.org/10.1155/2021/6624579

*Research Article*

# Bayesian Network-Based Knowledge Graph Inference for Highway Transportation Safety Risks

**Luo Wenhui, Cai Fengtian, Wu Chuna, and Meng Xingkai**

*Research Institute of Highway Ministry of Transport, Beijing 100088, China*

Correspondence should be addressed to Luo Wenhui; 815345591@163.com

Received 16 October 2020; Revised 20 January 2021; Accepted 18 February 2021; Published 5 March 2021

Academic Editor: Songtao Lv



Accurate inference of knowledge about highway transportation safety risks forms a crucial aspect of building a knowledge graph. Based on the data related to highway transportation accidents, this study has developed a Bayesian network model. The initial identification of the network nodes is through expert scoring. The network structure is then constructed by utilizing the prior expert knowledge and K2 greedy search algorithm. Later, the network parameters are trained via the expectation-maximization (EM) algorithm. Finally, knowledge about highway transportation safety risks is inferred using the junction tree algorithm. A comparison is made between the trained conditional and actual probabilities during the network parameter training to verify the validity of the proposed model that accords with expert experience, thereby proving the model validity. Further, its main "causal chain" is inferred to be an improper emergency response-human failure-accident occurrence, where the probability of driver failure is 82%, and the probability of accident occurrence is 68% by taking "a certain road traffic accident" as an example. There is consistency between the inference results and the actual accident sequence that suggests the effectiveness of the proposed knowledge inference method.

## 1. Introduction

Knowledge graphs that contain abundant knowledge from various areas have become a hot topic across various research fields, with the rapid explosion of network information. As a reliable source of all-round information and underlying support, they have performed remarkably in the safety risk management realms, such as medicine and finance [1, 2]. An important area of mass casualty monitoring has always been highway transportation. The top priority of safe highway transportation is safety risk management, and, for this, building a complete knowledge graph of highway transportation safety risk management is necessary for achieving risk control. Crucial to the completion and expansion of knowledge graphs, the knowledge inference technique—among key techniques of building knowledge graphs, such as knowledge extraction, fusion, and inference—deduces new knowledge or identifies errors in a knowledge graph by using certain methods based on the existing knowledge in the graph. The ultimate aim for highway transportation safety risk management is to predict the risks faced in transportation in advance that can be understood as a risk inference problem in knowledge graphs. Extensive research achievements concerning knowledge inference have been made to date:

(1) Inferences based on logical rules: The logical rule-based reasoning process divides knowledge into rules and facts. There are forward, backward, and bidirectional reasoning approaches to inference methods. The Markov logic network (MLN), where the common inference tasks include the maximum posterior probability estimation and the conditional probability reasoning, is a particularly fruitful model. Chen et al. [3] applied the MLN to risk management in response to information security issues. First, they constructed an infrastructure dependency network by the expert method that was then converted into an MLN for the calculation of node weights via a learning algorithm. The proposed model's

innovativeness is in the introduction of new network threat factors and the calculation of their possible impacts on the entire system. Yang et al. [4] proposed an MLN-based method for joint sentiment analysis of sentences to address the inadequate utilization of contextual information with the existing knowledge inference methods, as well as the cross-domain connection problem of sentence information, in the context of knowledge graph inference. They found through experimentation that MLN-based knowledge inference achieved rather desirable results. Liu et al. [5] put forward an ensemble learning-based MLN model, as well as its learning algorithm, in response to the difficulty of MLN in inferring large-scale data, respecting the modification and improvement of MLN models. They conducted a knowledge extraction experiment in Google's large-scale corpus using this method. As experiments proved, their method had higher precision and recall than the pipelining approach.

(2) Bayesian network-based inference models: Bayesian inference is a process of calculating posterior probability, based on conditional and prior probabilities. Relating to risk management, Lu et al. [6] proposed a Bayesian network-based model for flood risk inference aiming at the problem of flood risk misreporting. Here, expert scoring identified the Bayesian network, and parameter learning was performed with the Monte Carlo model. These helped in analyzing the changes in flood risk under one- and two-factor uncertainties. The Bayesian network built by them allowed bidirectional reasoning and probability distribution inference of arbitrary nodes. Experiments proved that their model was practically applicable to the risk assessment and control in reservoirs. Based on a qualitative weighted Bayesian network, Yin et al. [7] put forward a human factor inference model for coalmine accidents in order to address the analytical deficiency of human factors in coal mine accident analysis. The Bayesian network, based on typical accident cases, was constructed using the Human Factors Analysis and Classification System (HFACS) model, and the weight magnitudes between network nodes were obtained by the expert method. The mutual logical relationships between the human factors were reflected rather accurately by their model. With a view to combing the evolution process of such events, Xia et al. [8] proposed a dynamic Bayesian network-based unconventional scenario inference model for sudden disaster events. They constructed a dynamic Bayesian network with nodes such as the scenario condition, handling goals, handling measures, and intrinsic variables. The prior probabilities were designated for root nodes, while for variables without parent nodes, the expert method was employed to determine conditional probabilities. In the end, inference of accident scenario evolution was executed by introducing the "July 16 Oil Depot Explosion and Fire" that yielded correct inference results. Seyed Hassani et al. [9] developed a Bayesian network related to inference on knowledge graphs by taking into consideration some hidden or ignored information in complex social networks. They identified the nodes of the Bayesian network, such as comments, avatar information, ensemble photos, or interactive information, and using the collected data, trained its parameters. The effectiveness of their algorithm was tested on Facebook that found the model is highly accurate in finding information between users. Rajabi and Ataie-Ashtiani [10] proposed a fuzzy Bayesian inference method, in terms of model modification and improvement, to address the unavailability of parameter training data in conventional Bayesian inference. The method fused the information provided by experts with the Bayesian network model. They also developed an algorithm for solving the model. Computational results were compared with the Markov Chain Monte Carlo- (MCMC-) based algorithm that proved the effectiveness of their model and algorithm.

(3) Machine learning-based models: Xie et al. [11] proposed a model that targeted the knowledge completion issue with knowledge graphs based on bag-of-words and convolutional neural network, where the bag-of-words model was used for the vector representation of texts, and the convolutional neural network was responsible for classifying and inferring word relationships. They confirmed the validity of their model through experimentation. A novel convolution-based model was proposed by Annervaz et al. [12] that extracted relevant prior knowledge from the graphs via an attention mechanism. Experiments on public datasets demonstrated that their method was effective in enhancing the performance of deep learning models. Godin et al. [13] developed a ternary reward framework to cope with the incorrect answering problem in the existing reinforcement learning-based question answering systems that established a new evaluation criterion by setting different rewards for wrong answers and no answers, thereby achieving better evaluation of model effectiveness. All of the above—completion, fast retrieval, and answering problems related to knowledge graphs—can be understood as the scenario applications of knowledge inference.

(4) Hybrid models: Jiang et al. [14] developed a method for representing knowledge based on weighted knowledge graphs that was then combined with the probabilistic graphical model to establish a medical diagnosis knowledge network. A path sorting algorithm-based random walk model was proposed by Liu et al. [15] that performed knowledge inference on the semantics of sentences regarding the inverse relationship from object to subject. An exhaustive

search was avoided by introducing a random sampling mechanism, and the effectiveness of their knowledge inference model was experimentally verified.

The advantage of logical rule-based reasoning is the intuitive inference procedure that can reflect prior knowledge, and its disadvantage is the difficulty in obtaining rules that lead to error accumulation. The advantage of deep learning-based inference models is a powerful reasoning capability, while their disadvantages are insufficient interpretability and data limitations. Predicting the probability of accident occurrence and estimating the "causal chain" are the foremost tasks of knowledge graph inference for highway transportation safety risks. On the other hand, we consider the task of inferring a knowledge graph about highway transportation safety risks from the Bayesian networking perspective, given the limited data collected in this study. Expert scoring identifies the nodes of the Bayesian network. The node parameters are learned via the EM algorithm, and knowledge about highway transportation safety risks is inferred with the junction tree model.

The contributions of this paper include the following:

(1) A knowledge inference framework for road transportation risks is proposed, and annotated datasets are provided for the research field.

(2) During the identification of network nodes, a network architecture identification method based on expert scoring combined with the K2 algorithm is proposed that ensures the incorporation of expert knowledge about road transportation risks by the network architecture.

(3) Based on the Bayesian network created in this paper, the probability distributions of accident occurrence are inferred under multiple factors, including the driver, vehicle, road, environment, and management.

The remainder of this paper is organized as follows:

Section 2 puts forward a model framework for risk knowledge inference, Section 3 builds a Bayesian network-based knowledge inference model for road transportation risks, Section 4 infers knowledge about road transportation risks, and Section 5 concludes the study.

## 2. Creation of Risk Knowledge Inference Model

The Bayesian network may be summarized as a probabilistic inference network that is based on the Bayesian formula, where the nodes represent the random variables, and the directed edges between nodes represent the internode causality. Each node has a probability distribution. Assuming a given Bayesian network $G(S, P)$ consists of two parts, with $S$ being a directed acyclic graph containing all nodes and $P$ being a collection of conditional probability distribution tables. Construction of Bayesian network for inferring highway transportation safety risk knowledge comprises four steps, namely, (i) the network node identification, (ii) the network architecture identification, (iii) the determination of node conditional probabilities, and (iv) the inference of safety risk knowledge for highway transportation. Overall, the modeling procedure incorporates the expert method and machine learning. Figure 1 presents the model framework proposed in this study.

*2.1. Network Node Identification.* At this stage, expert scoring identifies the network nodes. Prior expert knowledge is collected according to five categories of "drivers, vehicles, roads, environment, and management," thereby constructing a matrix for node information acquisition as shown in the following expression:

$$E_f = \left(e_{ij}\right)_{m\times n}, \tag{1}$$

where $e_{ij}\,(0 \le e_{ij} \le 1)$ denotes the confidence that the $i$th expert has, regarding the causality between the $j$th risk and the $f$th category, $i \in [1, n]$, $j \in [1, m]$, $f \in [1, 5]$. Matrix $E_f$ is traversed, and if $e_{ij} \ge a$, it indicates that the $j$th risk and the $f$th category are casually correlated.

*2.2. Network Architecture Identification.* The network architecture identification is divided into two steps, given the limited amount and quality of training data in this study, namely, the expert method based network architecture and the network architecture modification by data-based learning. For network architecture learning, the greedy search and conditional restriction algorithms are generally used, of which the methods based on greedy space search are adapted to minimum data size. K2 algorithm optimizes the search capability on the basis of ordinary greedy search by deleting the redundant edges. Hence, for network architecture learning, this study adopts the K2 algorithm, whose core idea is to find a network structure with high score functions. The K2 scoring method is described in the following formula[16]:

$$F\left(\frac{D}{G}\right) = \prod_{i=1}^{n} \prod_{j=1}^{q_i} \frac{(r_i - 1)!}{\left(N_{ij} + r_i - 1\right)} \prod_{k=1}^{r_i} N_{ijk}!, \tag{2}$$

where $G$ represents the Bayesian network architecture, $D$ stands for the training dataset, $i$ denotes the $i$th node, $n$ denotes the number of nodes, $j$ denotes the $j$th parent node of the current node, $q_i$ is the number of parent nodes of the current node, $k$ represents the $k$th value of the current node, $r_i$ represents the number of possible values of the current node, and $N_{ijk}$ denotes the number of examples in the training dataset $D$ that corresponds to the $k$th value of current node and the $j$th value of parent node, $N_{ij} = \sum_{k=1}^{r_i} N_{ijk}$.

For the K2 algorithm, its pseudocode is as in Algorithm 1 [16].

*2.3. Network Parameter Learning.* During network parameter learning, commonly used algorithms include the maximum likelihood estimation (MLE) and the Bayesian estimation and expectation-maximization (EM) algorithms, of which the MLE algorithm is generally suitable for scenarios with large data size. When the sample size is small and

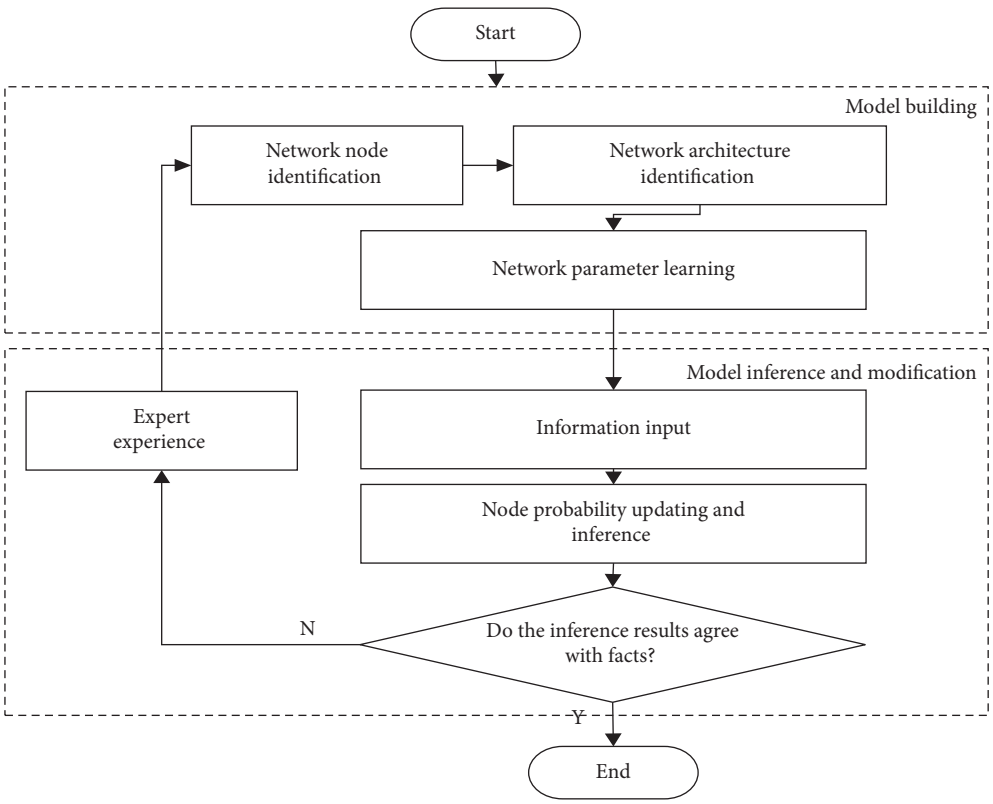


Figure 1: Flow chart of safety risk knowledge inference for highway transportation.

Input: training data $D$, node sequence $\rho$, positive integer $u$ ($u$ denotes the number of parent nodes)
Output: $G$
*for* $i = 1$ *to* $n$ *do*
  $\mathrm{pa}(V_i) = \varnothing$
  $F_{\mathrm{old}} = f_{\mathrm{CH}}((V_i, \mathrm{pa}(V_i)), D)$
  *start* = *true*
  *while start (true) and* $|\mathrm{pa}(V_i)| < u$ *do*
  $Z \leftarrow \mathrm{pred}(V_i) \backslash \mathrm{pa}(V)$, $f_{\mathrm{CH}}((V_i, \mathrm{pa}(V_i) \cup \{Z\})D)$ it reaches the maximum node
    $F_{\mathrm{new}} = f_{\mathrm{CH}}((V_i, \mathrm{pa}(V_i) \cup \{Z\})D)$
    if $F_{\mathrm{new}} > F_{\mathrm{old}}$ then $F_{\mathrm{old}} = F_{\mathrm{new}}$
      $\mathrm{pa}(V_i) = \mathrm{pa}(V_i) \cup \{Z\}$
    *else Start* = *false*
  *end*
*end*
where $\mathrm{pred}(V_i)$ represents the nodes before $V_i$ and $\mathrm{pa}(V_i)$ is a collection of parent nodes.

Algorithm 1

the prior probability is hardly attainable, the use of the EM algorithm yields a good learning effect. Hence, this study adopts the EM algorithm to learn network parameters. Its algorithmic procedure can be divided into E-step and M-step (see Algorithm 2) [17].

*2.4. Network Inference.* Network inference is the ultimate objective of this study. All joint probability distributions for nodes are obtained through the network parameter learning stage. The probability (result) distributions for a set of query variables at the network inference stage are computed under exact values given for a set of evidence variables (causes).

Among common algorithms for network inference, such as junction tree and variable elimination, the former is adopted herein for network inference, owing to its easy-to-understand and accurate inference advantages. The junction tree algorithm is divided into four phases:

(1) In the initial phase, the built Bayesian network is modularized, and the parent nodes of each node are connected with undirected edges

Input: observation variable $Y$, hidden variable $Z$, joint distribution $P(Y, Z|\theta)$, conditional probability distribution $P(Z|Y, \theta)$.
Output: model parameter $\theta$
(1) Assignment of the initial values for the model parameter;
(2) E-step: $\theta_i$ is the value of the model parameter after the $i$th iteration, the calculated function of expectation on $i+1$ th iteration, $Q(\theta, \theta_i) = E_{Z\sim P(Z|Y,\theta_i)}[\log P(Y, Z|\theta)] = \sum_Z P(Z|Y, \theta_i) \log P(Y, Z|\theta)$
(3) M-step: find $Q(\theta, \theta_i)$ that maximizes $\theta$, determine the estimated value $\theta_{i+1}$ of the $i+1$ th iteration.
(4) Repeat steps 2-3 until model converges.

Algorithm 2

(2) The Bayesian network is converted into an undirected graph, where each arrow is replaced by an edge
(3) The graph is triangulated, and an edge is added to the variables in the same loop
(4) The triangulated graph is converted into a clustering tree, where each node represents factors in the variable subset

## 3. Bayesian Network-Based Knowledge Inference Model for Highway Transportation Safety Risks

The purpose of safety risk knowledge inference for road transportation is to achieve the "prior" control of unsafe risk factors. However, these risk factors have strong uncertainties, while Bayesian networks have provided preferable solutions to complex and uncertain problems [16]. Hence, following this idea, a Bayesian network-based knowledge inference model for road transportation risks, with which the inference problems of safety risk knowledge for road transportation are solved, has been proposed in this paper.

*3.1. Network Node Identification.* Since the focus of this research is on solving the problem of risk knowledge inference, our team has listed a total of 28 risk sources involving "drivers, vehicles, roads [18, 19], environment, and management" based on the description of safety risks in the accident reports over the years that have been accomplished by taking specific risks as the network nodes. We developed a quantitative questionnaire and distributed it among ten experts within the field. When $e_{ij} \geq 0.7$, a causality is considered to exist between risk and category. A risk has been chosen as an effective node if more than six experts confirmed its causality with the category. By employing expert scoring, the network nodes for road transportation risk knowledge have been constructed according to formula (1) as detailed in Table 1 that was done by selecting a total of 26 observable nodes and 5 virtual nodes.

*3.2. Network Architecture Identification.* A combination of the K2 algorithm and expert scoring has been used to identify the Bayesian network architecture. Initially, with the aid of GeNIe 2.0 software, learning of network structure was completed based on the database using the K2 algorithm. Figure 2 displays the learned network architecture. Afterward, modification of the network structure was performed based on expert experience. Figure 3 illustrates the finalized network architecture.

As is clear from Figure 2, the network architecture presents a strong progressive causal relationship that was divided into three layers vertically. The relationship between nodes is clear, and there are no connecting lines between unrelated factors. The nodes are divided into two parts, including observable nodes and virtual nodes. The observable nodes are the nodes with actual data description, while the virtual nodes are the nodes added for the integrity of the network.

As is clear from Figure 3, the hierarchy of the network is not obvious, because through the learning of the algorithm, the implicit relationship between the nodes is further revealed, and the overall structure of the network satisfies the requirement of the cognition.

*3.3. Network Parameter Learning.* Learning of various network parameters was accomplished via the EM algorithm in GeNIe 2.0. The learning process can be summarized into five steps:

(1) Assignment of initial values for various root nodes.
(2) Establishment of correspondences between node names and IDs.
(3) Import of datasets.
(4) Matching of data with network nodes.
(5) Parameter learning. The learning results are listed in Table 2, where N implies normal and F implies failure.

Table 2 clearly shows that, under identical conditions, improper emergency response and traffic violations exhibit the highest posterior probabilities among the driver factors, followed by fatigue driving, distracted driving, and drunk driving, while inexperienced driving shows the lowest posterior probability. These results are in line with expert experience and perception.

## 4. Inference of Safety Risk Knowledge for Highway Transportation

Using the junction tree algorithm, Bayesian network inference is implemented on highway transportation safety risks. According to the Bayesian network architecture,

Table 1: Bayesian network nodes for road transportation risk knowledge.

| Final state | Risk category | Primary risk sources |
|---|---|---|
| A accident | V vehicle | V1 braking system; V2 steering system; V3 light signal system; V4 tires; V5 overload or unbalanced load |
| | D driver | D1 drunk driving; D2 fatigue driving; D3 distracted driving; D4 traffic violations; D5 improper emergency response; D6 inexperienced driving |
| | R road | R1 roadsides; R2 bridge and tunnel; R3 alignment; R4 intersections; R5 pavements; R6 signs and markings; R7 sight distance; R8 safety protection facilities |
| | E environment | E1 interference from traffic accidents; E2 severe weather; E3 natural disasters; E4 night lighting |
| | M management | M1 dynamic monitoring; M2 regulations; M3 private contracting |

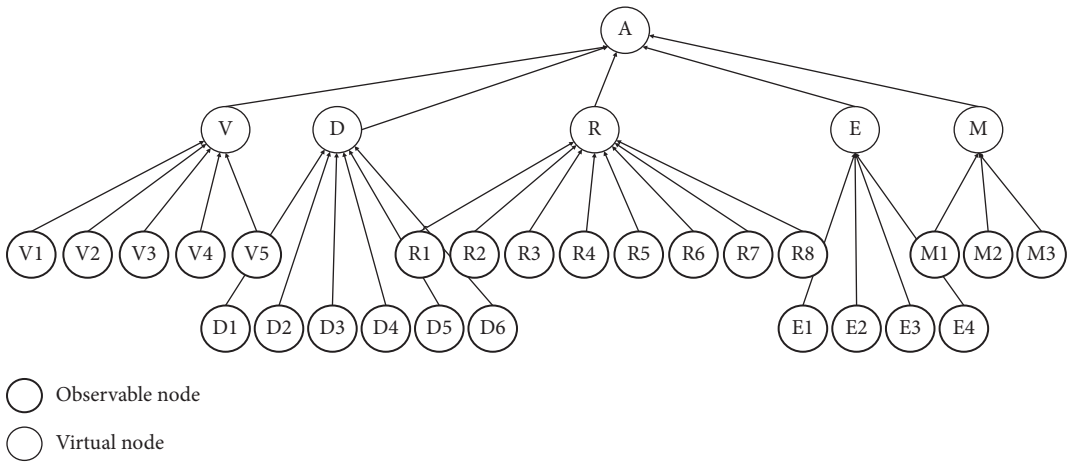


Figure 2: Bayesian network topology for highway transportation accidents.

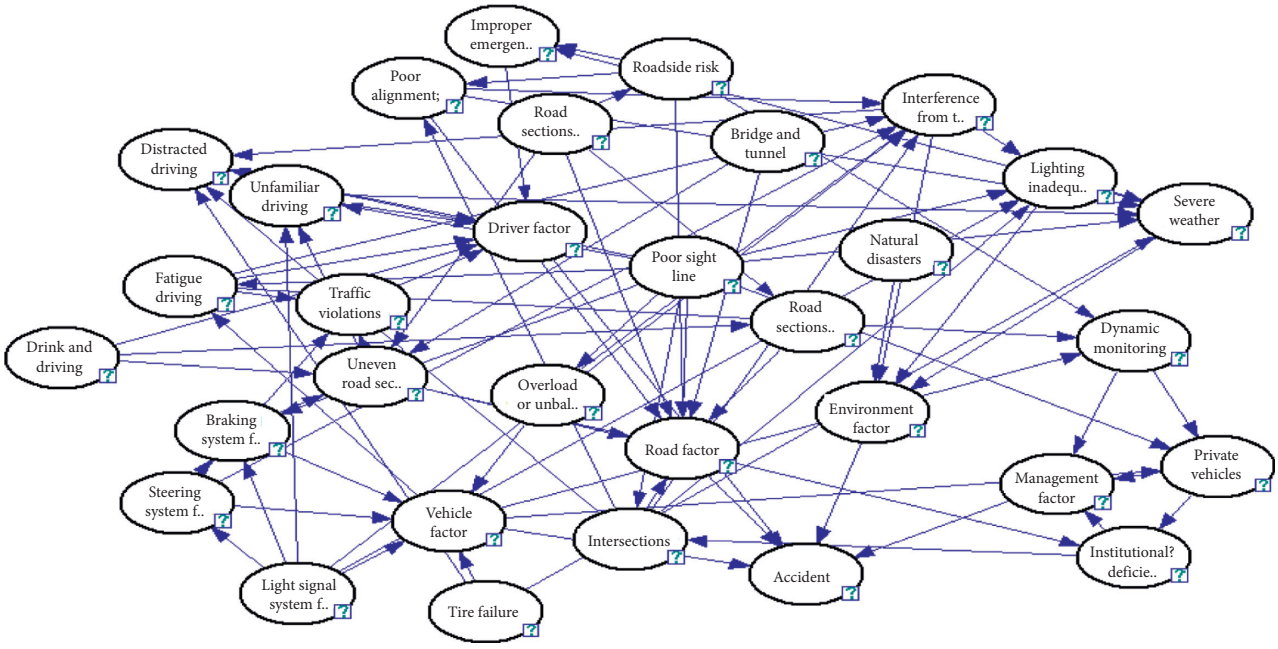


Figure 3: Final optimized network architecture.

Table 2: Driver parameter learning results.

| Risk | | Status | | | | | | |
|---|---|---|---|---|---|---|---|---|
| Drink and driving | | N | N | N | N | N | N | F |
| Fatigue driving | | N | N | N | N | N | F | N |
| Distracted driving | | N | N | N | N | F | N | N |
| Traffic violated | | N | N | N | F | N | N | N |
| Improper emergency response | | N | N | F | N | N | N | N |
| Unfamiliar driving | | N | F | N | N | N | N | N |
| Driver factors | N | 0.899 | 0.8125 | 0.3053 | 0.339638 | 0.558 | 0.506 | 0.5666 |
| | F | 0.101 | 0.1875 | 0.6946 | 0.66036 | 0.441 | 0.493 | 0.4333 |

impact analysis is carried out keeping in mind the following aspects:

(1) Effects of the driver, vehicle, road, environment, and management factors on the occurrence of accidents.

(2) Effects of drunk driving, fatigued driving, distracted driving, traffic violations, improper emergency response, and inexperienced driving on the driver risks.

(3) Effects of the braking system, steering system, light signal system, tires, truck overload, and unbalanced load on the vehicle risks.

(4) Effects of roadsides, bridges and tunnels, alignment, intersections, pavements, signs and markings, sight distance, and safety protection facilities on the road risks.

(5) Effects of traffic accidents, severe weather, natural disasters, and night lighting on the traffic environment risks.

(6) Effects of dynamic monitoring, regulations, and private contracting on the management risks.

*4.1. Data Description and Model Evaluation.* Our team collected 600 reports on road transportation accidents from the safety management websites that occurred between 2012 and 2019. These accident reports have been sorted into three categories. The risk factors of each accident are marked either as 0 or as 1, where 1 indicates that the assessed risk is an accident-causing factor, and 0 indicates that the assessed risk is not an accident-causing factor. The model evaluation criteria are as follows:

(a) Accordance with expert experience and knowledge of the analysis of the effects of relevant factors on accident occurrence.

(b) Conformance to the accident state description of the accident reports in the case analysis.

### 4.2. Inference Analysis of Relevant Influencing Factors

*4.2.1. Effects of Relevant Factors on the Occurrence of Accidents.* The probability distributions of accident occurrence, based on the built Bayesian network model for highway transportation safety risks and the inference results, are depicted in Figure 4 under human, vehicle, road, environment, and management factors.

From Figure 4(a), it is clear that, among the causes of accidents, the accident probability is the highest for the driver factors, with an inferential probability of 0.899, followed by the management factors, with an inferential probability of 0.485. In contrast, road factors constitute the least probable factors, primarily because they are indirect causes in general. According to Figure 4(b), the probability of accidents resulting from the failure of drivers, vehicles, and management is quite high, while that caused by the failure of environmental and road factors is rather low.

*4.2.2. Effects of Relevant Factors on the Driver Risks.* Figure 5 illustrates the influences of drunk driving, fatigue driving, distracted driving, traffic violations, improper emergency response, and inexperienced driving on the driver risks.

From Figure 5, it is clear that, regarding driver factors, the failure probabilities attributed to improper emergency response and traffic violations are comparatively higher at 0.694 and 0.660, respectively. In comparison, the failure probability caused by inexperienced driving is lower. The occurrence frequencies are the highest among causes of accidents for speeding, illegal lane changing, illegal overtaking, illegal parking, and illegal emergency lane parking, all of which can be classified as forms of a traffic violation. The probability of an accident is generally high in case of improper emergency response. The probability of accidents caused by inexperienced driving is rather low because of the strict management of drivers by road transportation companies.

*4.2.3. Effects of Relevant Factors on the Vehicle Risks.* The impacts of the braking system, steering system, light signal system, tires truck overload, and unbalanced load on the vehicle risks are illustrated in Figure 6.

As shown in Figure 6, the failure probabilities attributable to the braking system and tires are the highest among all vehicle factors—0.885 and 0.888, respectively. Braking system faults generally refer to braking failure or poor braking caused by improper operation, wear of parts, or inadequate vehicle clearance, while tire faults often refer to the severe wear or blowout of tires. The lowest failure probability is attributable to light signal system faults

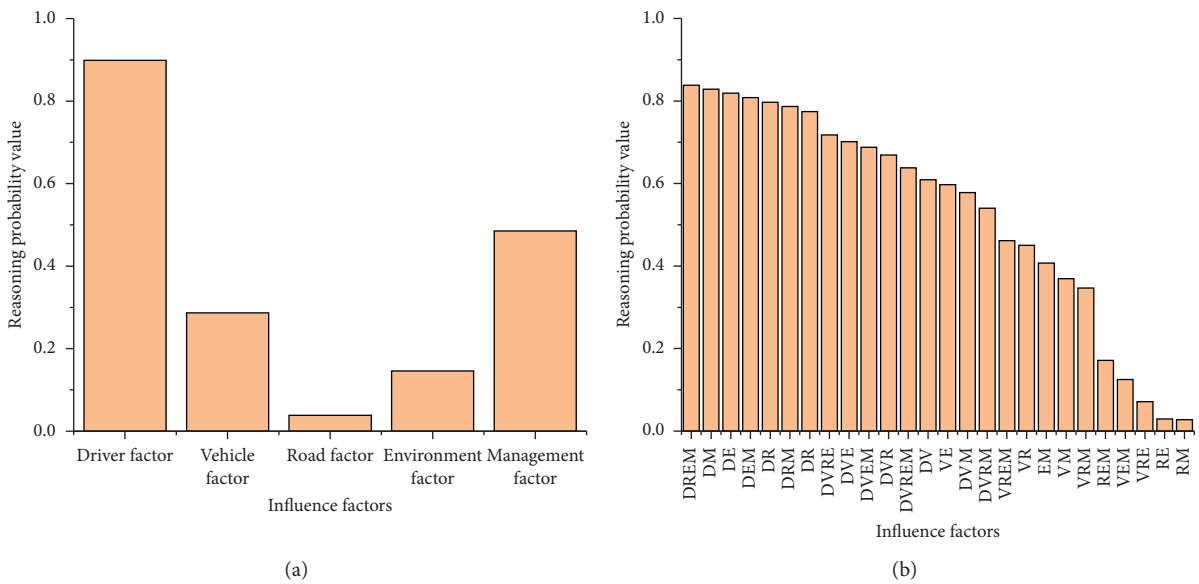


Figure 4: Effects of relevant factors on the occurrence of accidents.

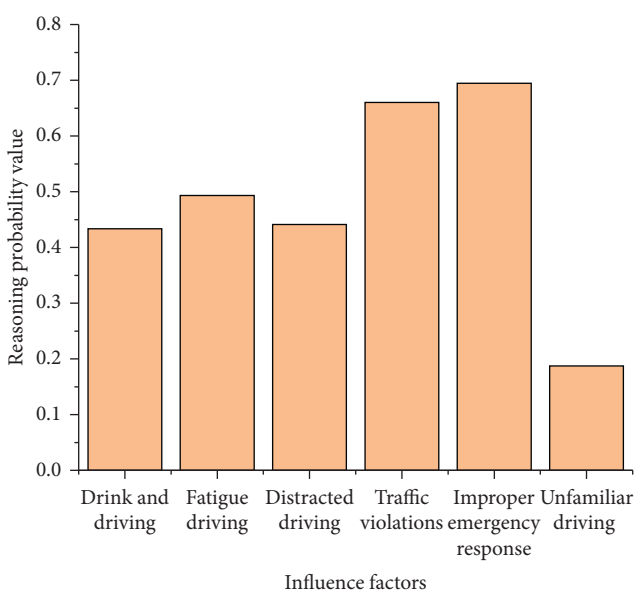


Figure 5: Effects of relevant driver factors.

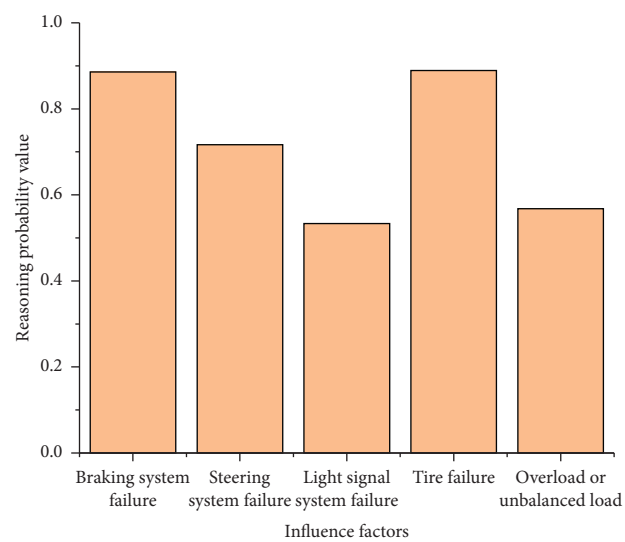


Figure 6: Effects of relevant factors on the vehicle risks.

because accidents can often be avoided in this case as long as the drivers take appropriate emergency measures.

*4.2.4. Effects of Relevant Factors on the Road Risks.* In Figure 7, the influences of roadsides, bridges and tunnels, alignment, intersections, pavements, signs and markings, sight distance, and safety protection facilities on the road risks are detailed.

From Figure 7, it is clear that the failure probabilities attributable to pavement and alignment problems are the highest among all road factors—valued at 0.852 and 0.782, respectively. Pavement problems generally refer to slippery surfaces, potholes, and so forth, while alignment problems include sharp bends, steep slopes, and long descents. As these are rather common causes of accidents, the relevant probabilities are also high. In contrast, sight distance is the least likely cause among all road factors because such problems generally involve roadside obstructions or intersections, whose probabilities are rather low according to accident statistics.

*4.2.5. Effects of Relevant Factors on Management Failures.* Figure 8 presents how dynamic monitoring, regulations, and private contracting affect the management risks.

According to Figure 8, the probability of management problems caused by improper dynamic monitoring is the highest at 0.699. At present, information about fatigued driving, distracted driving, speeding, vehicle trajectories, and so forth can be tracked and forewarned by the dynamic

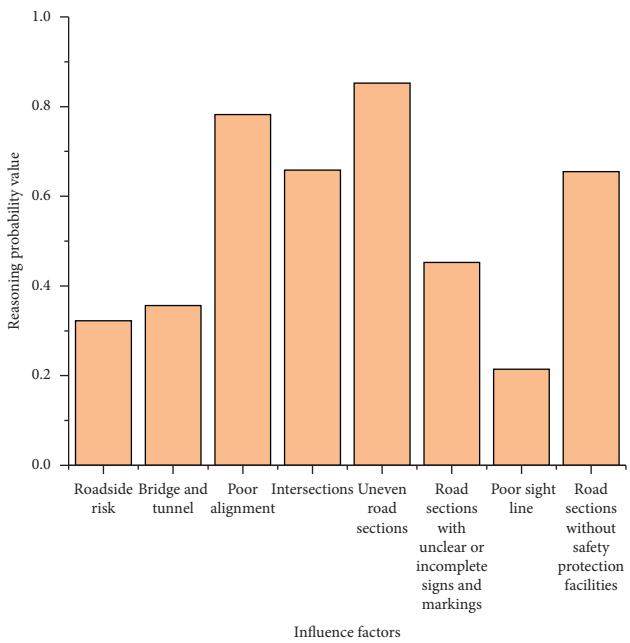


Figure 7: Effects of relevant factors on the road risks.

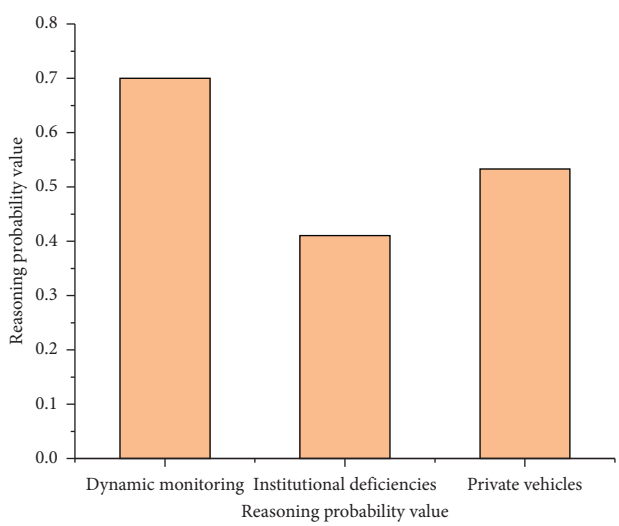


Figure 8: Effects of relevant factors on management failures.

monitoring system for road transport vehicles. A substantial number of accidents can be avoided by the proper functioning of the vehicle monitoring system. In contrast, the occurrence of an accident is generally attributed to the improper functioning of the dynamic monitoring system. Regulations are the least likely factors causing management failures. Overall, regulatory problems include driving management and inadequate vehicle management that is indirectly responsible for the causes of accidents in general.

*4.2.6. Effects of Relevant Factors on the Traffic Environment.* Figure 9 illustrates how traffic accidents, severe weather, natural disasters, and night lighting affect the traffic environment.

From the figure, it is clear that the failure probability attributable to severe weather is the highest among all environmental factors, which is at 0.666. Severe weather mainly refers to conditions such as heavy rain, fog, snow, or wind warnings, which are the most common causes of traffic environment failures. Meanwhile, given the relatively low incidence of natural disasters, the probability of environmental failures resulting from them is the lowest.

All the above analysis results accord with expert experience and knowledge, suggesting the effectiveness of the created model.

*4.3. Case-Based Analysis.* Introducing "a certain major road traffic accident" helps in carrying out an empirical analysis of knowledge inference. On February 20, 2019, at 19:07 h, an ordinary passenger bus collided with the sidewall of a tunnel on the 2441 km + 100 m section of the G65 Baotou–Maoming Expressway (within a tunnel in Hezuo Village, Lingui District, Guilin), which caused 4 deaths, 3 serious injuries, 16 minor injuries, and severe vehicle damage. The causes of this major road traffic accident were analyzed as follows:

(1) Driver factors: after the bus entered the tunnel, the driver oversped, ignoring the signs and markings. In response to the deceleration of the preceding vehicle, the driver applied emergency brakes, which was an improper emergency response, thereby losing control of his vehicle.

(2) Vehicle factor: during steering, the bus suddenly went out of control, so the possibility of vehicle failure cannot be ruled out.

(3) Environment factor: there was a heavy shower at the time of the accident that made the road surface slippery.

(4) Management factors: due to the long-term, nonlocal, out-of-scope operation of the tourist bus, its dynamic vehicle monitoring terminal had been offline.

Based on the above description, the node elements for this accident are detailed in Table 3.

Based on the Bayesian network built in Figure 3, the nodes relating to accident occurrence are mapped into a Bayesian network, followed by knowledge inference in GeNIe 2.0. As shown in Figure 10, the probabilities are updated for each node.

Figure 10 clearly shows that the foremost cause of this accident was the human failure attributed to improper emergency response and traffic violations, whose probability was 82%; the second important cause was the vehicle failure

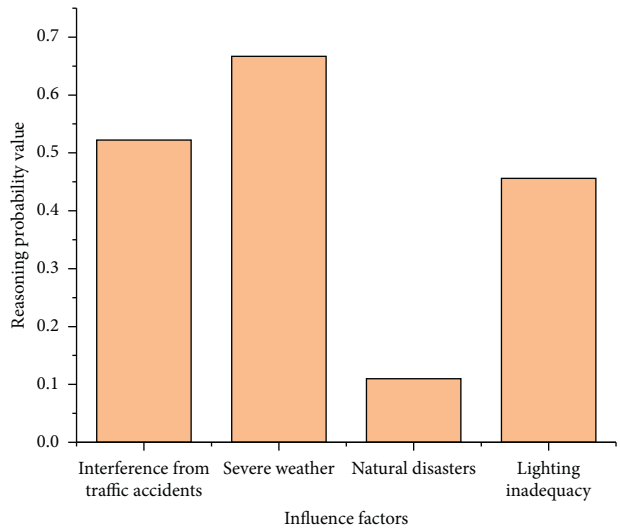


Figure 9: Effects of relevant factors on the environmental risks.

Table 3: Bayesian network nodes for the accident.

| Risk factor | Network node |
|---|---|
| Driver | Improper emergency response<br>Traffic violation |
| Vehicle | Vehicle fault |
| Road | Pavement<br>Bridge and tunnel |
| Environment | Severe weather |
| Management | Dynamic monitoring<br>Private contracting |

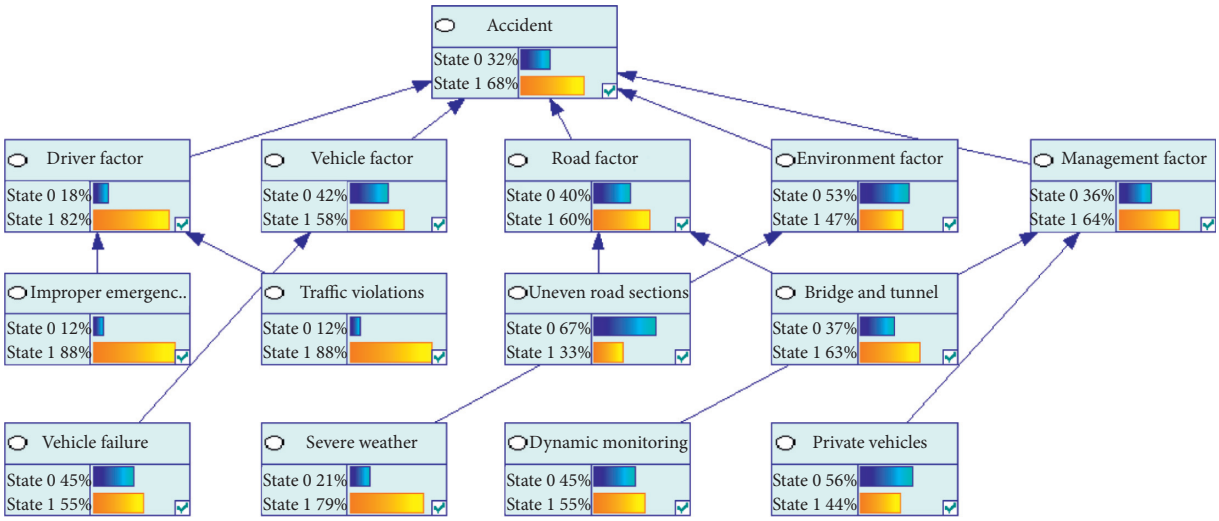


Figure 10: Probability updates and inference diagram of the accident.

attributable to vehicle fault, with a probability of 58%; besides, the probability of traffic environment problems resulting from severe weather that was 47%; and the probability of management failure resulting from inadequate dynamic monitoring and private contracting was 68%. Ultimately, the probability of occurrence of the accident was 0.68, which is rather high. These descriptions conform to the actual accident inference process that proves the feasibility of the proposed method.

## 5. Conclusions

Highway transportation safety risks involve multiple factors, such as driver, vehicle, road, environment, and management. According to the results of the Bayesian network inference, the primary cause of accidents is driver-related. Meanwhile, management factors are nonnegligible as well. The foremost human factors are improper emergency responses and traffic violations, of which improper emergency responses are often ignored by drivers or managers. Additionally, the foremost vehicle factor is faulty vehicles, which is attributed to the failure of the braking system or tires. Severe weather serves as the foremost factor for traffic environment. Interference from existing accidents is another factor that is often ignored by drivers or managers.

By using the Bayesian network for inference of knowledge graphs oriented to highway transportation safety risks, the rule acquisition problem with rule-based reasoning, as well as the limitations in data size and quality can be avoided. With powerful reasoning, the above method can preferably be integrated with the transportation safety risk knowledge graphs to achieve flexible inference of accident probability in the dynamic risk coupling scenarios. In the next phase, in view of the dynamic nature of such knowledge graphs, we will probe deeper into the collaborative fusion between the Bayesian network-based knowledge inference and the dynamic knowledge graphs.

## Data Availability

The data are available through contacting the authorvia e-mail: 815345591@163.com; hyperlink (https://pan.baidu.com/s/1Y9d3zGtXtowCmWKHrQ678g).

## Conflicts of Interest

The authors declare that they have no conflicts of interest.

## Acknowledgments

This work was supported by the Special Fund 2019-C507 of Science and Technology Innovation of Research Institute of Highway Ministry of Transport, and the Special Fund Project of Basic Research Expenses of Central Public Welfare Research Institutes 2020-9066.

## References

[1] T. Yu, J. Li, Q. Yu et al., "Knowledge graph for TCM health preservation: design, construction, and applications," *Artificial Intelligence in Medicine*, vol. 77, pp. 48–52, 2017.

[2] B. Ribeiro, N. Chen, and A. Kovacec, "Shaping graph pattern mining for financial risk," *Neurocomputing*, vol. 326-327, pp. 123–131, 2019.

[3] Y. Chen, Y. D. Wang, J. D. Wang et al., "Method for information system risk management based on Markov logic networks," *Computer Engineering and Applications*, vol. 52, no. 18, pp. 104–110, 2016.

[4] L. G. Yang, S. P. Tang, and J. Zhu, "A Markov logic network based sentence sentimental analysis method," *Transactions of Beijing Institute of Technology*, vol. 33, no. 6, pp. 600–604, 2013.

[5] Y. Liu, C. Ouyang, and J. Li, "Ensemble method to joint inference for knowledge extraction," *Expert Systems with Applications*, vol. 83, pp. 114–121, 2017.

[6] Q. Lu, P.-a. Zhong, B. Xu et al., "Risk analysis for reservoir flood control operation considering two-dimensional uncertainties based on Bayesian network," *Journal of Hydrology*, vol. 589, Article ID 125353, 2020.

[7] D. L. Yin, Z. B. Chen, J. C. Zeng et al., "Human factors inference of safety accidents in coal mine based on qualitative Bayesian network with weight," *Journal of WUT (Information & Management Engineering)*, vol. 39, no. 1, pp. 514–518, 2017.

[8] D. Y. Xia, X. M. Qian, and Z. P. Duan, "Scenario deduction model of unconventional emergency based on dynamic Bayesian network," *Journal of Northeastern University (Natural Science)*, vol. 36, no. 6, pp. 897–902, 2015.

[9] A. Seyed Hassani, M. S. Haghighi, and A. Khonsari, "Bayesian inference of private social network links using prior information and propagated data," *Journal of Parallel and Distributed Computing*, vol. 125, pp. 72–80, 2019.

[10] M. M. Rajabi and B. Ataie-Ashtiani, "Efficient fuzzy Bayesian inference algorithms for incorporating expert knowledge in parameter estimation," *Journal of Hydrology*, vol. 536, pp. 255–272, 2016.

[11] R. Xie, Z. Liu, J. Jia et al., "Representation learning of knowledge graphs with entity descriptions," in *Proceedings of the 30th AAAI Conference on Artificial Intelligence*, Phoenix, AZ, USA, 2016.

[12] K. M. Annervaz, S. B. R. Chowdhury, and A. Dukkipati, "Learning beyond datasets: knowledge graph augmented neural networks for natural language processing," 2018, https://arxiv.org/abs/1802.05930.

[13] F. Godin, A. Kumar, and A. Mittal, "Using ternary rewards to reason over knowledge graphs with deep reinforcement learning," 2019, https://arxiv.org/abs/1902.10236.

[14] J. Jiang, X. Li, C. Zhao, Y. Guan, and Q. Yu, "Learning and inference in knowledge-based probabilistic model for medical diagnosis," *Knowledge-Based Systems*, vol. 138, pp. 58–68, 2017.

[15] Q. Liu, M. H. Han, L. Y. Jiang et al., "Two-tier random walk based relational inference algorithm," *Chinese Journal of Computers*, vol. 40, no. 6, pp. 1275–1290, 2017.

[16] G. F. Cooper and E. Herskovits, "A Bayesian method for the induction of probabilistic networks from data," *Machine Learning*, vol. 9, no. 4, pp. 309–347, 1992.

[17] S. L. Lauritzen, *The EM Algorithm for Graphical Association Models with Missing Data*, Elsevier Science Publishers, Amsterdam, Netherlands, 1995.

[18] C. Liu, S. Lv, X. Peng et al., "Analysis and comparison of different impacts of aging and loading frequency on fatigue characterization of asphalt concrete," *Journal of Materials in Civil Engineering*, vol. 32, no. 9, Article ID 04020240, 2020.

[19] C. Liu, S. Lv, D. Jin et al., "Laboratory investigation for the road performance of asphalt mixtures modified by rock asphalt-styrene butadiene rubber," *Journal of Materials in Civil Engineering*, vol. 33, no. 3, Article ID 04020504, 2021.

Hindawi
Advances in Civil Engineering
Volume 2021, Article ID 6676807, 16 pages
https://doi.org/10.1155/2021/6676807

*Research Article*

# Cognitive Distraction State Recognition of Drivers at a Nonsignalized Intersection in a Mixed Traffic Environment

**Qiang Hua**,[1] **Lisheng Jin**,[1,2] **Yuying Jiang**,[3] **Ming Gao**,[4] **and Baicang Guo**[1]

[1]*Transportation College, Jilin University, Changchun 130022, China*
[2]*School of Vehicle and Energy, Yanshan University, Qinhuangdao 066004, China*
[3]*Department of Ophthalmology, China-Japan Union Hospital, Jilin University, Changchun 130022, China*
[4]*Laboratory of Automotive Safety and Energy, Department of Automotive Engineering, Tsinghua University, Beijing 100084, China*

Correspondence should be addressed to Yuying Jiang; jiangyy@jlu.edu.cn

Received 17 October 2020; Revised 21 January 2021; Accepted 23 February 2021; Published 4 March 2021

Academic Editor: Songtao Lv



Distracted driving has become a growing traffic safety concern. With advances in autonomous driving and connected vehicle technology, a mixture of various types of intelligent vehicles will become normal in the near future, while more factors that may cause driver cognitive distraction are emerging. However, there are rarely studies on distracted driving in mixed traffic environments. To fill this gap, we conducted a natural driving experiment with three representative events at a nonsignalized intersection in a mixed traffic environment and proposed a novel method of identifying cognitive distraction based on bidirectional long short-term memory (Bi-LSTM) with attention mechanism. Forty participants were recruited for each event, who completed three different cognitive distraction experiments induced by three different secondary tasks in contrast with a normal driving process when passing a nonsignalized intersection. Related driving performance and eye movement data were collected to train and test the Bi-LSTM with attention mechanism model. Compared with the support vector machine (SVM) model, its recognition accuracy rate is 94.33%, which is 3.83% higher than that of the SVM in the total event, which has reasonable applicability for distraction recognition in a mixed traffic environment. Potential applications of this model include distraction alarm and autonomous driving assistance systems, which could avoid road traffic accidents.

## 1. Introduction

Distracted driving has become a dominant cause of traffic accidents [1]. In the United States, 3450 people died of distracted driving in 2016 [2]. Another survey based on 1,367 drivers found that serious accidents caused by distracted driving account for 14% to 33% of traffic accidents [3]. Generally, distracted driving refers to the allocation of attention resources from driving to secondary tasks, causing the driver's remaining attention resources to be unable to guarantee the minimum attention demand required by the current driving environment, leading to a decline in driving performance capabilities [4]. When identifying whether a driver is in a distracted state, not only the driver's current behavioral characteristic status but also the complexity of the traffic environment must be considered. With the application of intelligent network technology and advanced control algorithms in the automobile field [5], all types of intelligent vehicles are developing rapidly, and mixed traffic is bound to become normal, where manual driving vehicles (MVs), connected manual vehicles (CMVs) [6], automated vehicles (AVs) [7], and connected automated vehicles (CAVs) will simultaneously share the road. The complex traffic environment creates many incentives for distracted driving. Therefore, it is extremely crucial to study distracted driving considering mixed traffic environments [8]. The National Highway Traffic Safety Administration roughly divides distraction into visual distraction [9], operational distraction [10], and cognitive distraction [11]. Visual distraction, such as distracted visual attention during driving while focusing

on things not related to the driving area, can weaken driving safety, and visual distraction changes as the amount of time that the gaze point leaves the road ahead increases. Operational distraction refers to actions during driving that are not related to driving and have a detrimental effect on normal driving, such as smoking and manipulating the display while driving. Operational distraction changes as operational complexity increases.

Cognitive distraction means that the driver shifts his cognitive attention to secondary tasks that are not related to the driving task. Unlike visual distraction and operational distraction, when cognitive distraction occurs, the driver's eyes remain on the road ahead, and thus, this type of distraction is more concealed, such as daydreaming and hands-free cellphone conversation. Cognitive distraction changes with an increase in the cognitive load required for different secondary driving tasks. The driving information including the external driving information and in-vehicle driving information in a mixed traffic environment is more abundant than that in a traditional traffic environment, as a mixed traffic environment is particularly complicated [12], which is more likely to lead to cognitive distraction than a traditional traffic environment. The negative effects of cognitive distraction on driving in a mixed traffic environment are also more serious than those in a traditional traffic environment. Thus, detecting cognitive distraction is of paramount importance.

Approximately 18.1% of accidents each year are caused by distractions at traditional traffic environment intersections [13, 14]; however, traffic conditions are more complicated at a mixed traffic environment intersection. More attention is required from the driver in this environment than in other traffic environments [15], with a short stay and limited access to outside driving information. If cognitive distraction occurs, it will have a greater adverse impact on driving safety, increasing the probability of accidents. However, we found few studies on cognitive distraction in mixed traffic environments, especially at a nonsignalized intersection in a mixed traffic environment. The researchers [16] adopted a support vector machine (SVM) as a data mining method using driver eye movement data and driving performance data to develop a method for detecting cognitive distraction in real time [17]. The results showed that the SVM model can detect driver distraction with an average accuracy of 81.1%, which is better than that of a traditional logistic regression model [18]. A previous study [19] collected driving performance and driver eye movement data and applied a genetic selection algorithm with SVM-recursive feature elimination (SVM-RFE) to rank alternative indicators of driver distraction and obtain the order of importance for 29 candidate indicators. A driver distraction recognition model that is based on AdaBoost-genetic algorithm (GA)-backpropagation (BP) was established; using the driver distraction recognition model with the best feature index to identify a driver's state, the model's recognition accuracy rate was 95.09%, which indicated that the model could accurately identify the distraction state of a driver. A method for detecting driver cognitive distraction at stop-controlled intersections was proposed [20]. The method uses the SVM-RFE algorithm to extract the optimal features from features constructed with driving performance and eye movement. After feature extraction, the SVM classifier is trained and cross-validated. The results showed that the SVM classifier based on the fusion of driving performance features and eye movement features achieved the best accuracy rate of 95.8% for stop-controlled intersections. The study [21] built an efficient model for detecting driver distraction and recognizing the type of distraction. Based on the active sensor Kinect and computer vision tools, the AdaBoost classifier and hidden Markov model were used to merge relevant information that is used for assessing driver inattention, and qualitative and quantitative results showed strong and accurate detection and recognition capacity. The researchers [22] proposed a real-time method for detecting a driver's cognitive and visual distraction using lateral driving performance measures, and radial basis probabilistic neural networks (RBPNNs) were adopted to construct classification models. As a result, the RBPNN model using the standard deviation of the lane position and steering wheel reversal rate could be an effective distraction detector with easy-to-obtain and inexpensive inputs. All of the above studies were based on traditional traffic scenarios and did not involve mixed traffic scenarios.

To fill this gap, this study proposes a method based on bidirectional long short-term memory (Bi-LSTM) with attention mechanism [23] to identify driver cognitive distraction at a nonsignalized intersection in a mixed traffic environment [24]. However, limited by actual conditions, complex mixed traffic scenarios cannot be completely reproduced. This paper studies cognitive distraction in three typical situations that occur at a nonsignalized intersection in a mixed traffic environment. These three situations are defined as three different events. In each event, the ego vehicle is the only vehicle that drives in the longitudinal lane, which is a CMV driven by the participant. The types of vehicles that approach from the lateral lane are different in each event; if a connected vehicle is approaching from the lateral lane, the ego vehicle will communicate with it to obtain the driving information of the lateral vehicle and eventually meet it at the intersection. In the driving process of each event, three different secondary tasks are arranged independently in turn, and if the participant of the ego vehicle is assigned a secondary task, this is considered to be distracted driving, while no assigned task is considered to be normal driving. To create the real effect of cognitive distraction in driving experiments, this study arranges a method in which a specific secondary task must be completed within a specified time to cause distracted driving. There are three types of secondary tasks (one-back task, two-back task, and clock task), each of which is easy to implement and requires different cognitive strengths. These tasks can be randomly arranged and repeated multiple times. The resulting distraction is appropriate.

Multiple real vehicle experiments are performed to collect driving performance data for distracted driving at nonsignalized intersections in mixed traffic environments, such as vehicle longitudinal and lateral control data as well as eye movement data from an eye tracker; the driver's

physiological state information is collected by a BIOPAC physiological recorder. Then, all of the data are subjected to fusion and preprocessing [25], and the optimal feature selection method based on the gray rough set theory is used to extract the optimal feature subset. Ten evaluation feature indices were extracted from 27 candidate feature indices and ranked based on the fuzzy analytic hierarchy process (FAHP). Different combinations of evaluation features were input into the Bi-LSTM with attention mechanism model to obtain the optimal number of feature combinations. Compared to the SVM model, the results show that the Bi-LSTM with attention mechanism model can reliably recognize the distracted driving behaviors of the participants with the best accuracy rate of 94.33% in the total event, which is 3.83% higher than that of SVM in the total event, and thus, it is suitable for distraction recognition in a mixed traffic environment. The findings of this study can be applied to distracted driving alarms for autonomous driving assistance systems.

## 2. Experimental System and Methods

*2.1. Participants.* This study was approved by the Ethics Committee of the China-Japan Union Hospital of Jilin University. A total of 40 drivers who were in satisfactory physical condition, had normal vision, and held legal C1 driver's licenses were recruited for the study. The recruited drivers included 20 males and 20 females, and their occupations included students and faculty members of Jilin University and urban office workers. Informed consent was obtained from the participants before the data collection stage of the study. The drivers were 21–57 years old, with a mean age of 29 years old and a standard deviation of 7.40 years. The driving experience of the participants ranged from 1 to 20 years, and the average length of driving experience was 5 years and the standard deviation was 3.46. The average total driving mileage was 39.2 thousand kilometers and the standard deviation was 14.6. None of the participants exhibited any adverse effects, such as drug effects, fatigued driving, or drunk driving, during the test. Table 1 shows the group personal statistics.

*2.2. Experimental Equipment.* The equipment utilized in the driving experiment includes connected vehicles, VAG-COM Diagnostic System (VCDS) equipment, a BIOPAC physiological recorder, and the Tobii Pro Glasses 2 eye tracker, as shown in Figure 1. The connected vehicles could communicate with each other in real time, which allows the driving information of other connected vehicles, such as the current speed of a vehicle, the distance from the vehicle, and the distance from the vehicle to the intersection, to be obtained. The participant's driving performance data are directly collected by VCDS equipment, and the driving performance data are output in the CSV format.

The participant's physiological state information is collected by a BIOPAC physiological recorder. In this experiment, electroencephalography (EEG) 100C amplifiers, 2 LEAD110 shielded wires, 2 LEAD100 unshielded wires, and 4 disposable patch electrodes were used to collect EEG signals, and the corresponding AcqKnowledge 4.2 physiological signal processing software was utilized to preprocess the original physiological signal data and extract the valid data.

The Tobii Pro Glasses 2 eye tracker has a sampling rate of 50 Hz and four eye-tracking cameras, which can obtain a driver's blink frequency, fixation direction, saccade frequency, degree of eyelid opening, and other information [26]. Additionally, the tracker can obtain the information of the road ahead and visually present the driver's fixation point and fixation track in a scene by superimposition with the video of the driver information acquisition system. Eye-tracking data acquired by Tobii Pro Glasses 2 can be synchronized with a wide range of physiological data, including EEG [27], EMG, motion detection, breathing, and heart rate.

*2.3. Experimental Design.* A nonsignalized mixed traffic environment intersection is designed in this paper. The location is on the Nanling Campus of Jilin University, and the road is a two-way two-lane road. Participants were asked to drive CMVs in the longitudinal lane, which is the only vehicle that drives in the longitudinal lane. In the lateral lane, there are MVs, CMVs, AVs, and CAVs, and the maximum speed does not exceed 50 km/h. The appearance of vehicles in lateral lanes was triggered when the ego vehicle passed 150 m before the center of the intersection, and connected vehicles could communicate with the ego vehicle. Information was reported to the participant in the ego vehicle in the form of voice reminders, and the content was the speed and location of the vehicle in the lateral lane. Since the types of vehicles that approach from the lateral lane are different, this paper divides the scenarios into three different types of events, as shown below:

(i) Event 1: the first vehicle approaching from the right side of the lateral lane is an MV, and the second vehicle is an AV; there is no communication between the lateral vehicle and the ego vehicle in the longitudinal lane

(ii) Event 2: the first vehicle approaching from the right side of the lateral lane is a CMV, and the second vehicle is an MV; there is communication between the CMV in the lateral lane and the ego vehicle in the longitudinal lane

(iii) Event 3: the first vehicle approaching from the right side of the lateral lane is a CMV, and the second vehicle is a CAV; there is communication between the two vehicles in the lateral lane and the ego vehicle in the longitudinal lane

The time headway between two vehicles in the lateral lane is randomized from 1 s to 3 s. All vehicles in the lateral lane are driven by professionals. When the ego vehicle is 150 m before the center of the intersection, the appearance of vehicles in the lateral lane and the secondary tasks are triggered. Eventually, the ego vehicle in the longitudinal lane meets the vehicles in the lateral lane at the intersection and then drives away from the intersection.

Table 1: Main effect test table.

| Gender | Sample size | Mean age (years) | Average mileage (thousand km) | SD of mileage (thousand km) |
|---|---|---|---|---|
| Male | 20 | 30 | 45.7 | 17.8 |
| Female | 20 | 28 | 32.7 | 13.4 |


Figure 1: Vehicles and information collection equipment.

The process of intersection crossing is extracted from 150 m before the ego vehicle crosses the stop line of the intersection to 20 m after the center of the intersection in each event [28], and each event contains normal driving and driving with three different secondary tasks, respectively.

Driving with the secondary tasks is considered distracted driving, and driving without the secondary tasks is considered normal driving. All the durations of the secondary tasks exceeded the time of the extracted event data, which ensures that distracted driving covered the entire target event. The above measures were repeated to extract data under each representative important event, and the number of normal driving instances collected for each event was the same as the number of every secondary task driving instance collected in each event.

A 15-minute test drive and secondary task training were conducted with participants before the formal experiment to ensure that the participants were familiar with the entire experimental process. The experimental scenario is shown in Figure 2. There are three nonsignalized intersections that cross the longitudinal lane, each participant was required to drive the experimental road six times to encounter 18 intersections under each driving situation, and four driving situations (one-back, two-back, clock tasks, and normal driving) were involved in each event for the 40 participants. Therefore, a total of 2880 sets of data were collected from all participants in each event, and 1800 sets of data were selected from the 2880 sets of data, including 720 sets for normal driving and 1080 sets for distracted driving. The total event is the sum of the three events and includes 720 sets for normal driving and 1080 sets for distracted driving (240 sets of normal driving data and 360 sets of distracted driving data were selected from each event).

*2.4. Cognitive Distraction Generation.* When the ego vehicle was 150 m before the center of the intersection, a test assistant in the ego vehicle arranged secondary tasks for the participants, and these tasks were divided into three types of secondary tasks [29]: one-back, two-back [30], and clock tasks. These chosen surrogate secondary tasks consumed the drivers' cognition and easily distracted them, and they were also easy to implement. The correspondingly scheduled secondary tasks required the participants to answer questions. All of the durations of the question-and-answer process exceeded the time of the extracted event data; there was an interval of 2 s between two questions. If the participant could not answer, they proceeded to the next question; the details of the secondary tasks are as follows:

(i) One-back task: the assistant says a number, and participants say the preceding number of the number given by the assistant. There is no need to answer the first question (the value ranges from 0 to 9).

(ii) Two-back task: the assistant says a number, and participants say the preceding two numbers of the number given by the assistant. There is no need to answer the first two questions (the value ranges from 0 to 9).

(iii) Clock task: the assistant says a random time for participants to determine whether the angle between the hour and minute hands is an acute angle (1 : 00–12 : 59).

If a problem was encountered during an experiment, the participants restarted the actual driving to ensure the validity of the experimental data. During the experiment, except for the secondary task set in this experiment, no other human factors interfered with participants to ensure the validity of the data, and the time of each experiment was generally consistent, between 8–11 am and 2–5 pm. The secondary tasks are shown in Figure 3.

*2.5. Cognitive Load Assessment.* The value of the EEG index R $(\theta+\beta)$ was applied to evaluate the cognitive load [31]. During an experiment, the participant wore a BIOPAC physiological recorder, which consisted of many modules. The EEG module can collect the driver's EEG signals, export collected data information in CSV format, import the original EEG data into MATLAB for noise reduction, and then extract the EEG indicator R $(\theta+\beta)$ value [32]. SPSS is used to statistically analyze the EEG index R $(\theta+\beta)$ values in different secondary tasks. The purpose of analyzing the EEG index R $(\theta+\beta)$ values in different secondary tasks is to verify that each secondary task increased the cognitive load of the participant [33] and then caused a driving distraction, which verifies the feasibility of the designed secondary tasks, and that the cognitive load level required for each secondary task

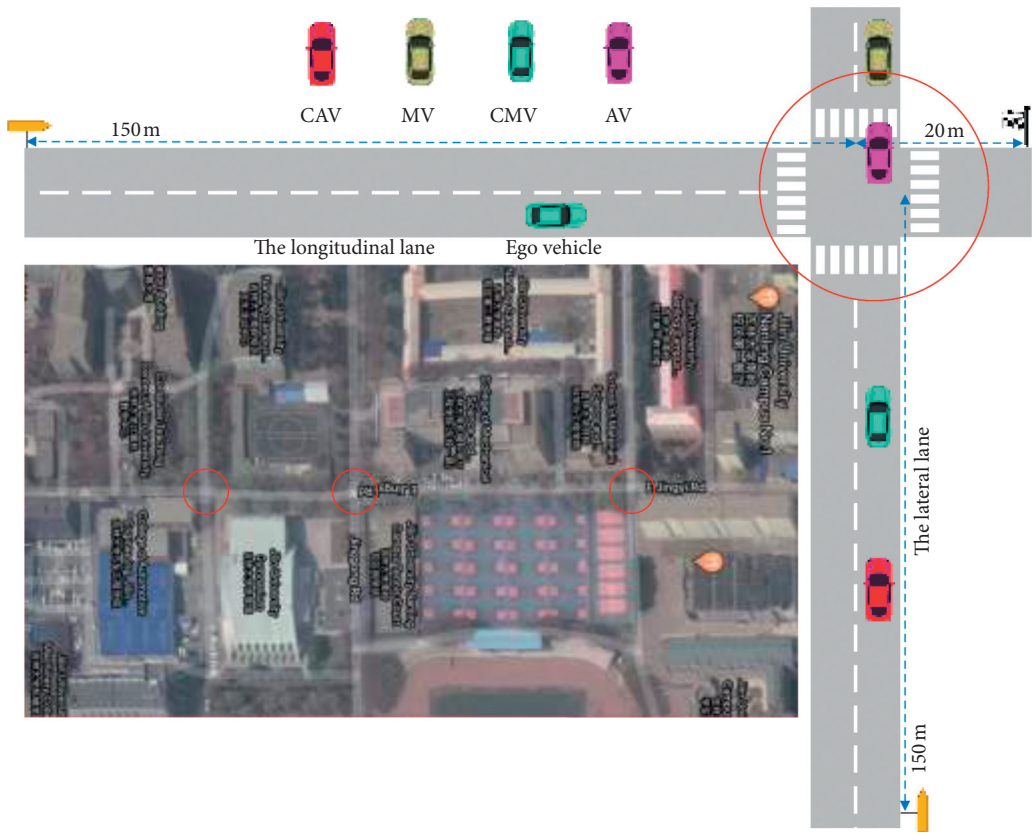


Figure 2: Illustration of experimental scenario.

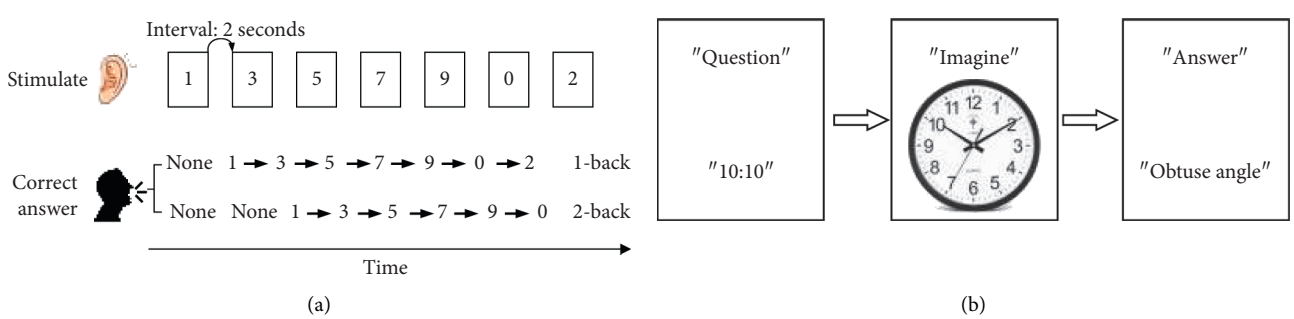


Figure 3: Illustration of the cognitive secondary tasks. (a) N-back task. (b) Clock task.

was different. This approach also verified the feasibility of research on distracted driving under different levels of secondary tasks. The EEG index extraction process is shown in Figure 4.

*2.6. Data Description.* Data collection was performed according to the experimental design process, that is, data were collected for the entire process of participants driving the vehicle 150 m before the intersection stop line to 20 m after the center of the intersection. Basic characteristics that were collected include the driving performance features and eye movement features, which provided a basis for calculating the average, variance, and correlation analysis of various parameters. To extract the most important features for cognitive distraction detection, the candidate feature set was divided into two categories.

*2.6.1. Driving Performance-Related Features.* Driving performance-related features were calculated based on driving performance features, including lateral control performance features and longitudinal control performance features. The corresponding driving performance-related features are shown in Table 2.

*2.6.2. Eye Movement Features.* The eye movement data were collected in real time through the Tobii Pro Glasses 2 eye

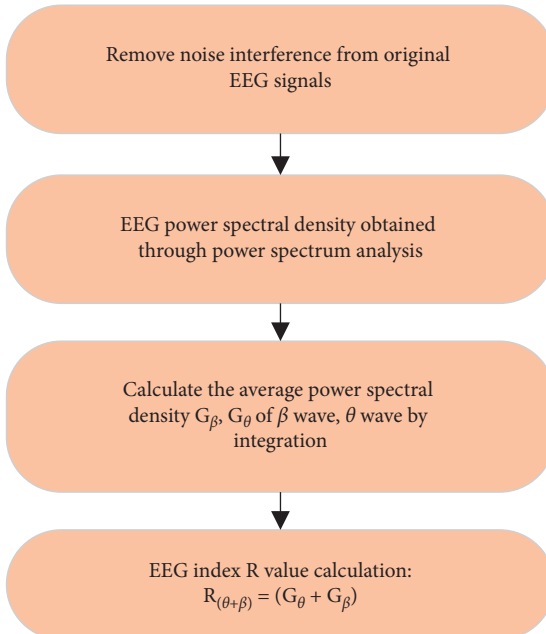


Figure 4: EEG index extraction process.

Table 2: Driving performance-related features.

| Dependent variable | Variable description | Unit |
|---|---|---|
| Min_Dec | Minimum deceleration | $m/s^2$ |
| SWA_SD | Standard deviation of steering wheel angle | ° |
| Accelerator pedal $H_b$ | Accelerator pedal opening | cm |
| SWA_Mean | Mean steering wheel angle | ° |
| Distance $H_p$ | Distance from vehicle to intersection | m |
| SP_SD | Standard deviation of speed | m/s |
| SP_Mean | Mean speed | m/s |
| LA_Mean | Mean lateral acceleration | $m/s^2$ |
| Braking position $H_p$ | Brake pedal opening | cm |
| SE_Mean | Mean steering entropy, which measures the smoothness of steering control without turning behavior to quantify the workload imposed on drivers | — |

tracker worn by participants. The eye data collection time was synchronized with the driving performance data collection time. The corresponding eye movement features are shown in Table 3.

### 2.7. Feature Screening and Model Construction

*2.7.1. Screening the Optimal Features Based on Gray Rough Set Theory.* Rough set theory and gray system theory are both effective mathematical theories for dealing with uncertainty problems. Gray clustering is used to replace the equivalent relationship in rough set theory to form gray rough set theory. This theory can deal with uncertain information from different aspects. To obtain a scientific and reasonable evaluation index system of optimal features, gray rough set theory is used to screen feature evaluation indices [34]. Using gray cluster analysis theory and rough set theory, 10 evaluation feature indices were screened from 27 candidate feature indices [35, 36]. The corresponding candidate features are shown in Tables 2 and 3.

*2.7.2. Weight Calculation of the Optimal Features Using the FAHP.* Since 10 evaluation feature indices were selected, a streamlined optimal feature evaluation index system was built. On this basis, the FAHP [37] was used to determine the weight values of the optimal feature evaluation index, and the extracted optimal feature evaluation index was sorted. It is provided in Tables 4 and 5. This approach lays a

Table 3: Eye movement features.

| Feature | Variable description | Unit |
|---|---|---|
| Blink F | Blink frequency | Hz |
| Fixation P_SD | Standard deviation of fixation point position in the horizontal direction | ° |
| Saccade F | Saccade frequency | Hz |
| SacAmp_Mean | Mean saccade amplitude | ° |
| Blink T_Mean | Mean blink time | ms |
| Blink T_SD | Standard deviation of blink time | ms |
| Fixation T_Mean | Mean fixation time | ms |
| Fixation T_SD | Standard deviation of fixation time | ms |
| Pupil_SD | Standard deviation of pupil diameter | mm |
| Pupil_Mean | Mean pupil diameter | mm |
| SacAmp_SD | Standard deviation of saccade amplitude | ° |
| SacPSP_Mean | Mean saccade peak speed | °/s |
| SacPSP_SD | Standard deviation of saccade peak speed | °/s |
| SacSP_Mean | Mean saccade speed | °/s |
| SacSP_SD | Standard deviation of saccade speed | °/s |
| SaccadeT_Mean | Mean of saccade time | ms |
| SaccadeT_SD | Standard deviation of saccade time | ms |

Table 4: Feature-level division.

| First-level feature indices | Weights | Secondary-level feature indices | Weights |
|---|---|---|---|
| Eye movement features | 0.631 | Blink F | 0.301 |
| | | Fixation P_SD | 0.286 |
| | | Saccade F | 0.175 |
| | | SacAmp_Mean | 0.162 |
| | | Pupil_Mean | 0.157 |
| | | Pupil_SD | 0.143 |
| | | Blink T_SD | 0.126 |
| Driving performance-related features | 0.502 | SP_Mean | 0.347 |
| | | SWA_SD | 0.262 |
| | | SE_Mean | 0.165 |

Table 5: Optimal feature index ranking.

| Rank | Optimal feature index | Variable description |
|---|---|---|
| 1 | SP_Mean | Mean speed |
| 2 | Blink F | Blink frequency |
| 3 | Fixation P_SD | Standard deviation of fixation point position in the horizontal direction |
| 4 | SWA_SD | Standard deviation of steering wheel angle |
| 5 | Saccade F | Saccade frequency |
| 6 | SE_Mean | Mean steering entropy |
| 7 | SacAmp_Mean | Mean saccade amplitude |
| 8 | Pupil_Mean | Mean pupil diameter |
| 9 | Pupil_SD | Standard deviation of pupil diameter |
| 10 | Blink T_SD | Standard deviation of blink time |

foundation for the next step in understanding the influence of the different numbers of optimal features on the recognition model.

*2.7.3. LSTM Network.* LSTM is a recurrent neural network (RNN), which achieves the same satisfactory performance as the standard RNN when processing times series data. However, compared to the standard RNN, LSTM can remember important features or moments in long-term historical time series data, which introduce forget gate to prevent gradient explosion and gradient vanish. The standard LSTM consists of three parts: input gate $\mathbf{i_t}$, output gate $\mathbf{o_t}$, and forget gate $\mathbf{f_t}$. The calculation results can be output via a series of calculations in the hidden state inside the cell, where $\sigma$ represents a logistic sigmoid function, $\mathbf{W_f}, \mathbf{W_i}, \mathbf{W_o}, \mathbf{W_c}$ represents the cyclic weight, and $\mathbf{b_f}, \mathbf{b_i}, \mathbf{b_o}, \mathbf{b_c}$ represents the corresponding bias. The internal calculation process of the LSTM cell is as follows.

The first step is to select the information that will be discarded in the nerve cell through a sigmoid layer of the forgetting gate. The gate will draw the input $\mathbf{x_t}$ of the current layer and the output $\mathbf{h_{t-1}}$ of the hidden layer from its upper layer and then output a value between 0 and 1 to the cell state $\mathbf{C_{t-1}}$. The formula is provided as follows:

$$\mathbf{f_t} = \boldsymbol{\sigma}\left(\mathbf{w_f}\left[\mathbf{h_{t-1}}, \mathbf{x_t}\right] + \mathbf{b_f}\right). \tag{1}$$

The second step is to determine what new information is stored in the cell state, which is composed of two parts. First, a sigmoid layer of the input gate determines what information should be updated. A tan*h* layer creates the new candidate state $\widetilde{\mathbf{C}}_\mathbf{t}$, which is employed to update the next state, as shown in the following formula:

$$\begin{aligned} \mathbf{i_t} &= \boldsymbol{\sigma}\left(\mathbf{W_i}\left[\mathbf{h_{t-1}}, \mathbf{x_t}\right] + \mathbf{b_i}\right), \\ \widetilde{\mathbf{C}}_\mathbf{t} &= \tan\mathbf{h}\left(\mathbf{W_c}\left[\mathbf{h_{t-1}}, \mathbf{x_t}\right] + \mathbf{b_c}\right). \end{aligned} \tag{2}$$

The third step is to update the old cell state $\mathbf{C_{t-1}}$ to the new cell state $\mathbf{C_t}$. First, $\mathbf{C_{t-1}}$ and $\mathbf{f_t}$ are multiplied to discard unimportant information, and second, $\mathbf{i_t} * \widetilde{\mathbf{C}}_\mathbf{t}$ is added to generate the new state $\mathbf{C_t}$ of the nerve cell, as illustrated in the following formula:

$$\mathbf{C_t} = \mathbf{f_t} * \mathbf{C_{t-1}} + \mathbf{i_t} * \widetilde{\mathbf{C}}_\mathbf{t}. \tag{3}$$

Last, the output value is determined based on the cell state $\mathbf{C_t}$. First, a sigmoid layer of the output gate is used to determine what important information should be output. Second, tan*h* is employed to process the cell state $\mathbf{C_t}$, and the result is multiplied by the output of $\mathbf{o_t}$ to obtain the last output $\mathbf{h_t}$. This process is shown as follows:

$$\begin{aligned} \mathbf{o_t} &= \boldsymbol{\sigma}\left(\mathbf{W_o}\left[\mathbf{h_{t-1}}, \mathbf{x_t}\right] + \mathbf{b_o}\right), \\ \mathbf{h_t} &= \mathbf{o_t} * \tan\mathbf{h}\left(\mathbf{C_t}\right). \end{aligned} \tag{4}$$

*2.7.4. Bi-LSTM Model with Attention Mechanism.* Bi-LSTM is composed of forward LSTM and backward LSTM. The hidden layer state $\mathbf{h_t}$ at time $\boldsymbol{t}$ is derived from the weighted sum of the forward hidden layer states $\overrightarrow{\mathbf{h}}_\mathbf{t}$; the backward hidden layer states $\overleftarrow{\mathbf{h}}_\mathbf{t}$, $\mathbf{U_t}$, and $\mathbf{V_t}$ are the corresponding weights; and $\mathbf{b_t}$ represents the bias of the hidden layer state at time $\boldsymbol{t}$. The relationship among the distraction features can be learned more comprehensively to further improve the recognition accuracy. Applying an attention mechanism in the Bi-LSTM framework enables more attention to be paid to the specific input feature sequence, which eliminates redundant features due to the attention weight of features and captures the key feature information. Thus, the validity and accuracy of the recognition model are improved. The Bi-LSTM framework-introduced attention mechanism is illustrated in Figure 5.

The details of the attention mechanism are provided as follows:

$$\begin{aligned} \overrightarrow{\mathbf{h}}_\mathbf{t} &= \mathrm{LSTM}\left(\mathbf{x_t}, \overrightarrow{\mathbf{h}}_\mathbf{t-1}\right), \\ \overleftarrow{\mathbf{h}}_\mathbf{t} &= \mathrm{LSTM}\left(\mathbf{x_t}, \overleftarrow{\mathbf{h}}_\mathbf{t-1}\right), \\ \mathbf{h_t} &= \mathbf{U_t}\overrightarrow{\mathbf{h}}_\mathbf{t} + \mathbf{V_t}\overleftarrow{\mathbf{h}}_\mathbf{t}, \\ \mathbf{e_t} &= \mathbf{F}\left(\mathbf{h_t}\right), \\ \mathbf{W_t} &= \frac{\mathbf{exp}\left(\mathbf{e_t}\right)}{\sum_{\mathbf{i=1}}^{\mathbf{n}} \mathbf{exp}\left(\mathbf{e_i}\right)}, \\ \mathbf{a} &= \sum_{\mathbf{i=1}}^{\mathbf{n}} \mathbf{exp}\left(\mathbf{W_t h_t}\right), \\ \mathbf{y_j} &= \mathrm{softmax}\left(\mathbf{aW_j} + \mathbf{b_j}\right), \end{aligned} \tag{5}$$

where $\mathbf{F}$ is a learning function, which is used to calculate the weight $\mathbf{W_t}$ of the output vector $\mathbf{h_t}$ of the LSTM layer at time $\boldsymbol{t}$, and the final feature representation vector $\mathbf{a}$ is obtained by weighting. Finally, the recognition result of cognitive distraction is transmitted through the softmax layer. $\mathbf{W_j}$ and $\mathbf{b_j}$ are the weight coefficient matrix and the corresponding bias in the output layer, respectively.

*2.7.5. Model Construction and Identification Process.* Cognitive distraction state recognition can be regarded as a time series modeling and prediction problem. Feature indices are extracted through the continuous data flow of time series in cognitive distraction and normal driving. Model inputs are the eigenmatrix, which consists of evaluation feature index vectors, and the eigenvectors are composed of the time series of each evaluation feature index 0-T s.

The identification process of the distraction state recognition model of drivers based on Bi-LSTM with attention mechanism at a nonsignalized intersection in a mixed traffic scenario is described as follows:

(i) Use the "leave one out method" [38] to divide the test set and training set of the model. During each training, select the current single sample as the test set and the remaining samples as the training set to ensure that the training set includes normal driving and distracted driving states in each event.

(ii) To avoid the influence of different unit cell dimensions between different parameters and eliminate the differences between the indices, the min-max normalization method is used to normalize the sample data:

$$\mathbf{x}' = \frac{\left(\mathbf{x} - \mathbf{x}_{\min}\right)}{\left(\mathbf{x}_{\max} - \mathbf{x}_{\min}\right)}, \tag{6}$$

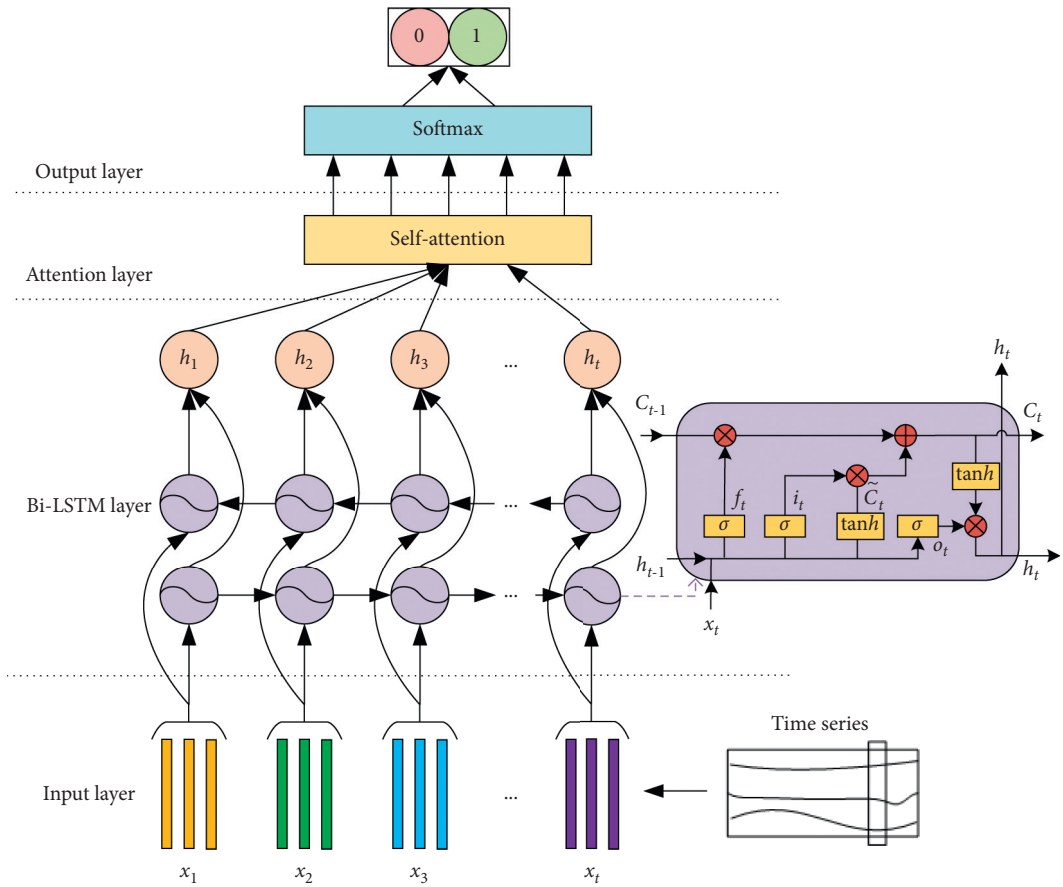


Figure 5: Bi-LSTM framework with the attention mechanism.

where $\mathbf{x}'$ is the normalized value, $\mathbf{x}$ is the original value of the sample, $\mathbf{x}_{\min}$ is the minimum value of the sample, and $\mathbf{x}_{\max}$ is the maximum value of the sample.

(iii) The first $n$ (4–10) feature index vectors in Table 5 are selected as the input eigenmatrix for driver distraction recognition in each event, which are input into the model to obtain the performance of driver distraction recognition models with a different number of feature indices.

(iv) The expert experience method is applied to set the parameter of the Bi-LSTM, employing the default parameter setting to run the algorithm, where the number of hidden units is 100, the initial learning rate is 0.1, the dropout rate is 0.5, and the max number of epochs is 60. After repeated experiments on the validation set, the loss tends to be stable, and the optimal adjustment parameters are obtained. An Adam optimizer is adopted in the network, with a learning rate of 0.01 and an attenuation of 0.9. The number of hidden units per layer is 128; the max number of epochs is 90, and the dropout rate is 0.4.

(v) Model performance evaluation: for the test set data, accuracy, precision, recall, and $\mathbf{F}_1$values were utilized to evaluate the model performance, which are introduced as follows:

$$P = \frac{\mathrm{TP}}{\mathrm{TP} + \mathrm{FP}},$$
$$R = \frac{\mathrm{TP}}{\mathrm{TP} + \mathrm{FN}},$$
$$A = \frac{\mathrm{TP} + \mathrm{TN}}{\mathrm{TP} + \mathrm{FN} + \mathrm{FP} + \mathrm{TN}}, \tag{7}$$
$$F_1 = \frac{2\mathrm{TP}}{2\mathrm{TP} + \mathrm{FN} + \mathrm{FP}},$$

where TP is the number of instances labeled 1 that are predicted to be 1, FN is the number of instances labeled 1 that are predicted to be 0, FP is the number of instances labeled 0 that are predicted to be 1, and TN is the number of instances labeled 0 that are predicted to be 0. 1 = distracted driving, 0 = normal driving. $P$ indicates the proportion of positive examples judged to be true. $R$ is the ratio of positive examples identified as true to the total positive examples in the classifier. $A$ is the ratio of the number of instances correctly classified to the total

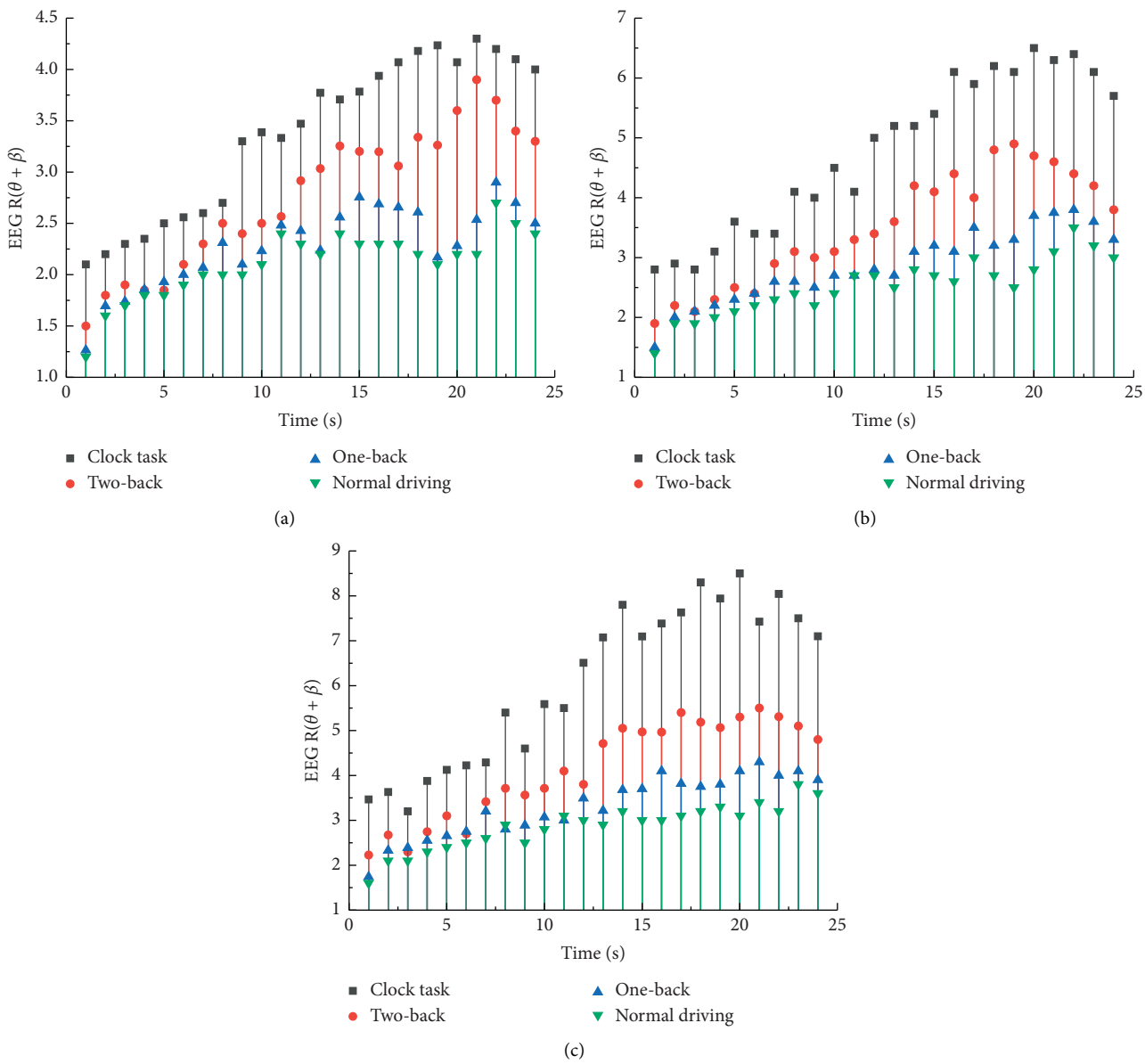


Figure 6: EEG index R $(\theta+\beta)$ values of the three events in different secondary tasks, (a) participant's cognitive load graph for event one, (b) participant's cognitive load graph for event two, and (c) participant's cognitive load graph for event three.

number of instances.·$F_1$ is the harmonic average of $P$ and $R$ .

*2.7.6. Description of the SVM Method.* The SVM was first proposed by Cortes and Vapnik in 1995 [39], which has many unique advantages in solving small sample, nonlinear, and high-dimensional pattern recognition. SVMs are based on a statistical learning technique and can be used for pattern classification and inference of nonlinear relationships between variables. This method has been successfully applied in the field of recognition and detection [40].

The labeled binary class data $\mathbf{B_t} = \{(\mathbf{x}_1^T, \mathbf{x}_2^T, \ldots, \mathbf{x}_i^T, \mathbf{y_i})\}$ is the input eigenmatrix, where $\mathbf{x_i}$ is the eigenvector, which is composed of the first $n$ (4–10) features in Table 5, $T$ is the time series length of 0-Ts, and $\mathbf{y_i}$ is a class indicator with a value of either 0 or 1. In this paper, the radial basis function (RBF) kernel function is selected via many tests, and the optimal parameter was determined, where $C = 16.57$ and gamma = 53.61.

## 3. Results

The EEG signals of the driver were collected by a BIOPAC physiological recorder, and the EEG index R $(\theta+\beta)$ values that represented the cognitive load were extracted. SPSS software was employed to statistically analyze the EEG index R $(\theta+\beta)$ values of the collected data. Cognitive load graphs of one participant in the three events are shown in Figure 6.

It can be seen that when the secondary tasks were added, the cognitive load required by the participants increased accordingly. The higher the EEG index R $(\theta+\beta)$ value is, the

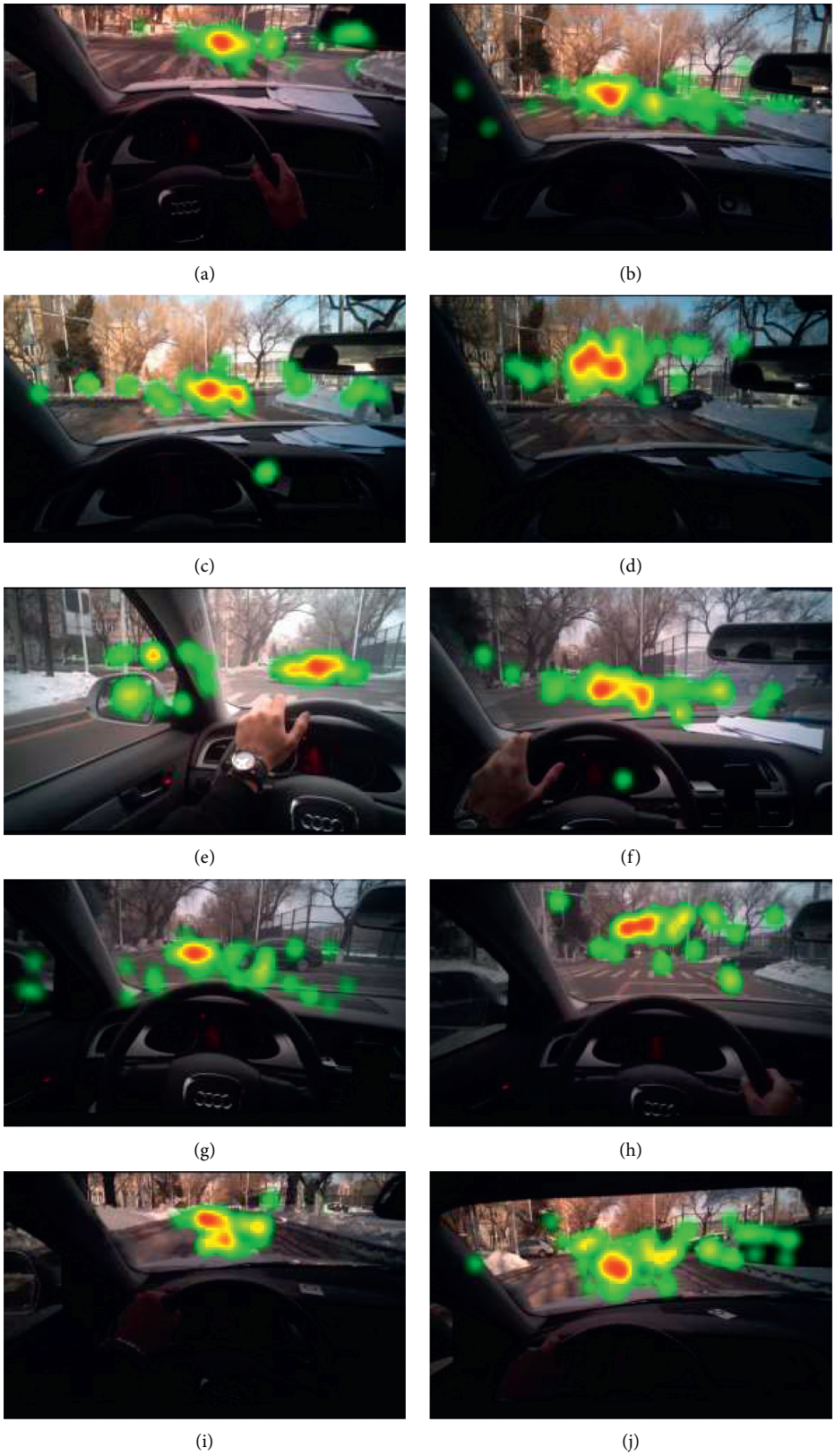


Figure 7: Continued.

(k) (l)

Figure 7: Distribution of the hot spots in the area of interest of the participant: (a) normal driving in event one, (b) distracted driving (one-back) in event one, (c) distracted driving (two-back) in event one, (d) distracted driving (clock task) in event one, (e) normal driving in event two, (f) distracted driving (one-back) in event two, (g) distracted driving (two-back) in event two, (h) distracted driving (clock task) in event two, (i) normal driving in event three, (j) distracted driving (one-back) in event three, (k) distracted driving (two-back) in event three, and (l) distracted driving (clock task) in event three.

higher the corresponding participant's cognitive load is. Figure 6 also shows that each secondary task increased the cognitive load of the participant to be higher than the cognitive load required in normal driving conditions; this situation will cause distracted driving. This also verifies the rationality of considering secondary tasks [41]. The EEG index R $(\theta+\beta)$ value of event three was higher than that of event one and event two for the same secondary task, which indicates that the cognitive load required for the participant to drive in event three was higher than the cognitive load required for the participant to drive in event one and event two because the scenario of event three is more complex than that of the remaining two events, which produces a higher cognitive load. When the clock task was conducted in each event, the participant experienced the greatest cognitive load. The two-back task was second, and the one-back task corresponded to the smallest cognitive load, indicating that the clock task was the most difficult, requiring a larger cognitive load. In addition, the cognitive load in all tasks has an increasing trend with the passage of time, and it begins to decrease after reaching its peak. This occurred because as the experimental vehicle approached the nonsignalized intersection, the driving environment became more complicated, and the required cognitive load significantly increased. When vehicles leave the intersection, the traffic environment becomes simple, and the cognitive load required is reduced.

Figure 7 shows the distribution of the hot spots in the areas of interest of the participants during normal driving and distracted driving. In the corresponding events, under normal driving conditions in each event, the participant's fixation points were concentrated on the vehicle approaching from the lateral lane of the intersection. When one-back and two-back tasks were employed, the participant's fixation points were scattered. However, most of the fixation points were concentrated on the front driving area, and the participant's fixation points were mostly concentrated directly above the front driving area when the clock task was employed. We argue that when the participant has a large cognitive load required to think about the question of the clock task, the participant looks above the front driving area and can no longer allocate his attention to the driving area of the intersection.

*3.1. Selected Feature Indices.* The weight values of the optimal features are shown in Table 4. The weight values of the eye movement features were greater than the weight values of the driving performance-related features in the first-level evaluation indices, indicating that the eye movement feature indices better reflected the distracted driving state than the driving performance-related feature indices.

The weight value of the SP_Mean index was 0.347 in the second-level evaluation indices, which indicates that SP_Mean was the most important evaluation index among all evaluation indices. The ranking of second-level evaluation indices was obtained according to the weight values. The ranking of optimal feature indices is shown in Table 5.

*3.2. Model Analysis Results.* Tables 6–9 present the results of distracted driver recognition based on the Bi-LSTM with attention mechanism. As shown in Table 6, as the number of input features increases, the distraction recognition accuracy rate continues to increase. When the first 8 feature indices were input in the total event, the recognition accuracy rate was the highest, with a value of 94.33%, and the precision value was 96.57%, the recall was 93.88%, and the $F_1$ value was 95.21%. When the number of input feature indices exceeded eight, the recognition accuracy decreased and tended to stabilize. For distraction recognition in event one, the recognition accuracy rate continued to increase as the number of feature indices increased. When the first 8 feature indices were input, the recognition accuracy rate was the highest, with a value of 89.16%, and the precision value was 93.25%, the recall was 88.33%, and the $F_1$ value was 91.71%. When more than 8 features were input, the recognition accuracy also tended to be stable.

It is not obvious from the results that the more the feature indices there are, the better the recognition effect. The optimal number of input feature indices for distraction recognition was 7 in event two and event three, and the recognition accuracies were 93% and 96.16%, respectively. The optimal number of input features in each event also varied, and event three was the most complicated scenario among the three events. Event two was second, but the optimal distraction recognition accuracy of event three was

Table 6: Model performance with different indicators in total event.

| Number of features | Accuracy (%) | Precision (%) | Recall (%) | $F_1$ (%) | Event |
|---|---|---|---|---|---|
| 4 | 87.66 | 92.30 | 86.66 | 89.39 | |
| 5 | 89.50 | 93.54 | 88.61 | 91.01 | |
| 6 | 91.83 | 95.07 | 91.11 | 92.63 | |
| 7 | 92.33 | 95.37 | 91.66 | 93.48 | Total event |
| 8 | 94.33 | 96.57 | 93.88 | 95.21 | |
| 9 | 93.50 | 95.92 | 93.05 | 94.49 | |
| 10 | 91.16 | 94.49 | 90.55 | 92.48 | |

Table 7: Model performance with different indicators in event one.

| Number of features | Accuracy (%) | Precision (%) | Recall (%) | $F_1$ (%) | Event |
|---|---|---|---|---|---|
| 4 | 83.66 | 89.45 | 82.50 | 85.83 | |
| 5 | 85.33 | 90.70 | 84.16 | 87.31 | |
| 6 | 86.50 | 91.39 | 85.55 | 88.37 | |
| 7 | 88.83 | 92.96 | 88.05 | 90.44 | Event one |
| 8 | 89.16 | 93.25 | 88.33 | 91.71 | |
| 9 | 88.83 | 92.86 | 88.05 | 90.44 | |
| 10 | 87.16 | 91.98 | 86.11 | 88.95 | |

Table 8: Model performance with different indicators in event two.

| Number of features | Accuracy (%) | Precision (%) | Recall (%) | $F_1$ (%) | Event |
|---|---|---|---|---|---|
| 4 | 87.43 | 92.11 | 86.45 | 89.39 | |
| 5 | 89.33 | 93.27 | 88.61 | 90.88 | |
| 6 | 91.38 | 94.50 | 90.83 | 93.04 | |
| 7 | 93 | 95.68 | 92.50 | 94.06 | Event two |
| 8 | 92.50 | 95.38 | 91.94 | 93.63 | |
| 9 | 91.16 | 94.49 | 90.55 | 92.48 | |
| 10 | 88.66 | 92.94 | 87.77 | 90.28 | |

Table 9: Model performance with different indicators in event three.

| Number of features | Accuracy (%) | Precision (%) | Recall (%) | $F_1$ (%) | Event |
|---|---|---|---|---|---|
| 4 | 89.66 | 93.56 | 88.85 | 91.16 | |
| 5 | 91.16 | 94.49 | 90.55 | 92.48 | |
| 6 | 93.66 | 96.26 | 93.05 | 94.63 | |
| 7 | 96.16 | 97.26 | 95.83 | 96.77 | Event three |
| 8 | 94.16 | 96.03 | 93.82 | 95.09 | |
| 9 | 92.50 | 95.38 | 91.94 | 93.63 | |
| 10 | 90.33 | 94.15 | 89.44 | 91.73 | |

the highest, indicating that the algorithm is applicable to scenarios with high complexity. Tables 6–9 also show that different numbers of input features produced different recognition accuracies for distracted driving in the same event. If too many optimal features are input, the accuracy of distraction recognition will tend to decline. Therefore, the number of input feature indices has a certain influence on distracted driver recognition.

*3.3. Comparison with the SVM in the Total Event.* The SVM algorithm was used for model accuracy comparison in the total event. Table 10 shows that the Bi-LSTM model with attention mechanism outperformed the SVM. The recognition accuracy rate of the Bi-LSTM model is 94.33%, and the $F_1$ value is 95.21%, which are higher than the recognition accuracy rates of SVM, whose recognition accuracy rate is 90.5% and $F_1$ value is 91.91%. Figure 8 shows the receiver operating characteristic (ROC) curve of the two recognition models for the total event. The two curves display satisfactory results, which illustrates that while both models have acceptable recognition performance, the Bi-LSTM model is better than the SVM algorithm. The optimal number (8) of the input feature indices, which are the top eight features in the optimal feature index ranking, as shown in Table 5, is the same for the two models. From these results, which illustrate

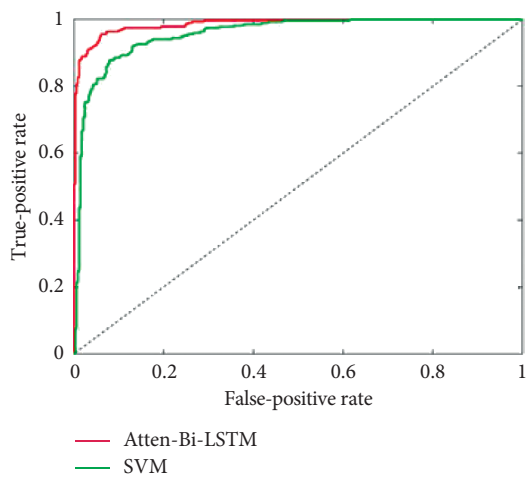


Figure 8: ROC curves of the identification by the two models in the total event.

Table 10: Comparison of distracted driving behavior recognition results of different algorithms.

| Optimal number of features | Accuracy (%) | Precision (%) | Recall (%) | $F_1$ (%) | Type of model | Event |
|---|---|---|---|---|---|---|
| 8 | 94.33 | 96.57 | 93.88 | 95.21 | Atten-Bi-LSTM | Total event |
| 8 | 90.5 | 93.91 | 90 | 91.91 | SVM | |

that the Bi-LSTM model was more accurate than the SVM model for distracted driving, we can draw a conclusion that the Bi-LSTM model has a reasonable effect on distraction recognition in mixed traffic environments.

## 4. Discussion

Mixed traffic environments will be more complicated as more factors that induce driver cognitive distraction are introduced. To explore a driver cognitive distraction recognition method in a mixed traffic environment, this paper presents a method for identifying cognitive distraction based on Bi-LSTM with attention mechanism at a nonsignalized intersection in a mixed traffic environment, using the combinations of the optimal feature indices as inputs to the classifier.

The optimal feature screening method based on the gray rough set theory was used to extract the optimal feature indices from driving performance-related features and eye movement features. Twenty-seven candidate indices were reduced to 10, a scientific and reasonable evaluation index system of optimal features was established, and the FAHP was used to determine the weight values of the feature evaluation indices and rank the feature indices. The weight value of the eye movement features was the greatest in the first-level evaluation indices, and there was a large difference in the distribution of the hot spots in the area of interest of the participant during normal driving and distracted driving in event 1, event 2, and event 3. Figure 7 shows that the fixation points are relatively concentrated during normal driving, while the fixation points are relatively divergent during distracted driving. The results indicate that the eye movement index plays a crucial role in distraction recognition in mixed traffic environments.

The cognitive load required by participants for driving with secondary tasks is greater than the cognitive load required for normal driving, and this finding verifies the rationality of considering secondary tasks. Observing the cognitive load of the participant with the same secondary task in these three events, Figure 6 shows that the cognitive load required by the participant in event 3 was the highest, which indicates that the more complex the scenario is, the greater the driving load required for the participant, and a complex scenario more easily causes distracted driving. When the participants were given different secondary tasks in each event, the cognitive load required for the clock task was higher than those for the two-back and one-back tasks, and this result indicates that the clock task is the most difficult and the most likely to cause cognitive distraction. As shown in Tables 6–9, the recognition accuracy rate varies with the number of optimal feature combinations. After the best number of optimal feature combinations is reached, the recognition accuracy rate gradually decreases and tends to be stable. The driving scenario of event 3 is the most complicated, and the driving scenario of event 2 is the second most complicated. However, the best recognition accuracies of event three and event two were generally higher than that of event one. The recognition accuracies of event three and event two were 96.16% and 93%, respectively. We can conclude that the driving scenario and the number of input features have considerable impacts on the recognition accuracy of the algorithm.

Compared with the traditional SVM algorithm model, the recognition accuracy of the Bi-LSTM model with

attention mechanism in the total event reached 94.33%, which is a high accuracy of distraction recognition. This result is 3.83% higher than that of the SVM model. The model proposed in this paper indicates reasonable applicability for distraction recognition in mixed traffic environments, which can be applied in an autonomous driving assistance system. It is of practical significance for the driver to effectively avoid road traffic accidents and improve driving efficiency in mixed traffic environments.

Limitations of this study are as follows:

(i) The Bi-LSTM model with attention mechanism discussed in this paper does not perform real-time recognition

(ii) There is a certain gap between the created mixed traffic environment and a real mixed traffic environment

## 5. Conclusion

This paper proposes a method based on Bi-LSTM with attention mechanism to identify the cognitive distraction state of a driver. An on-road experiment was implemented at a nonsignalized mixed traffic environment intersection, in which the driver's physiological state information, driving performance data, and eye movement data were collected. The algorithm uses the optimal feature combinations of driving performance-related features and eye movement features as inputs to identify distracted driving, and the algorithm is compared with the traditional SVM model. The following conclusions can be summarized as follows: (1) The weight value of the eye movement features is greater than the weight value of the driving performance-related features in the first-level evaluation indices. This result indicates that the eye movement features are very useful for identifying cognitive distraction in mixed traffic environments. (2) The cognitive load required for drivers in mixed traffic scenarios is higher than that required in traditional traffic scenarios, and the higher is the likelihood of distracted driving. (3) The cognitive distraction state recognition of drivers based on Bi-LSTM with attention mechanism provided more advantages in mixed traffic environments, which is 3.83% higher than the SVM model in the total event. This model provides a foundation for intelligent in-vehicle devices to detect driver distraction, which can reduce the number of accidents caused by distracted driving.

In this study, the cognitive distraction recognition model does not perform real-time recognition; therefore, future research can improve this model and transform it into a real-time recognition model.

## Data Availability

The data used to support the findings of this study are available from the corresponding author upon request.

## Conflicts of Interest

The authors declare that they have no conflicts of interest.

## Authors' Contributions

Qiang Hua wrote the main manuscript text. Lisheng Jin established the experimental platform and provided financial support. Yuying Jiang conducted the experiments. Ming Gao and Baicang Guo improved the manuscript.

## Acknowledgments

This work was supported by the National Key R&D Program of China under Grant 2018YFB1600501, the National Natural Science Foundation of China (nos. U19A2069 and 52072333); the National 13th Five-Year Plan's Science and Technology Project of the Education Department of Jilin Province (JJKH20200988KJ), the Natural Science Foundation of Hebei Province (no. E2020203092), and Hebei Provincial Key Research Projects (no. 20310801D). The contributions of specific colleagues, institutions, or agencies that aided the efforts of the authors are acknowledged.

## References

[1] D. Omid, R. Vikas, and T. Mojtaba, "Wearable driver distraction identification on-the-road via continuous decomposition of galvanic skin responses," *Sensors*, vol. 18, no. 2, pp. 503–518, 2018.

[2] National Highway Traffic Safety Administration, *Distracted Driving*, https://www.nhtsa.gov/risky-driving/distracted-driving, 2017.

[3] S. P. Mcevoy, M. R. Stevenson, and M. Woodward, "The prevalence of, and factors associated with, serious crashes involving a distracting activity," *Accident Analysis & Prevention*, vol. 39, no. 3, pp. 475–482, 2007.

[4] G. Li, W. Lai, X. Sui et al., "Influence of traffic congestion on driver behavior in post-congestion driving," *Accident Analysis & Prevention*, vol. 141, p. 1055508, 2020.

[5] J. Pérez, F. Seco, V. Milanés, A. Jiménez, J. C. Díaz, and T. De Pedro, "An RFID-based intelligent vehicle speed controller using active traffic signals," *Sensors*, vol. 10, no. 6, pp. 5872–5887, 2010.

[6] C. B. Néstor, A. S. Raúl, M. E. Pedro, A.-V. José, E.-B. Arthur, and M. C. Aldo, "Traffic congestion detection system through connected vehicles and big data," *Sensors*, vol. 16, no. 5, pp. 599–625, 2016.

[7] D. Isele, R. Rahimi, A. Cosgun, K. Subramanian, and K. Fujimura, "Navigating occluded intersections with autonomous vehicles using deep reinforcement learning," in *Proceedings of the International Conference on Robotics and Automation*, pp. 2034–2039, Brisbane, Australia, May 2018.

[8] B. K. Pathivada and V. Perumal, "Analyzing dilemma driver behavior at signalized intersection under mixed traffic conditions," *Transportation Research Part F: Traffic Psychology and Behaviour*, vol. 60, pp. 111–120, 2019.

[9] Y. Liang and J. D. Lee, "Combining cognitive and visual distraction: less than the sum of its parts," *Accident Analysis and Prevention*, vol. 42, no. 3, pp. 881–890, 2010.

[10] L. Li, B. Zhong, C. J. Hutmacher et al., "Detection of driver manual distraction via image-based hand and ear recognition," *Accident; Analysis and Prevention*, vol. 137, 2020.

[11] T. C. Ojsteršek and D. Topolšek, "Influence of drivers' visual and cognitive attention on their perception of changes in the traffic environment," *European Transport Research Review*, vol. 11, no. 1, pp. 1–9, 2019.

[12] A. Olia, S. Razavi, B. Abdulhai, and H. Abdelgawad, "Traffic capacity implications of automated vehicles mixed with regular vehicles," *Journal of Intelligent Transportation Systems*, vol. 22, no. 3, pp. 244–262, 2018.

[13] J. Wang, R. Kinipling, and M. Goodman, "The role of driver inattention in crashes: new statistics from the 1995 crash worthiness data system (CDS)," in *Proceedings of the 40th Annual Proceedings: Association for the Advancement of Automotive Medicine*, pp. 377–392, Vancouver, Canada, October 1996.

[14] P. Choudhary and N. R. Velaga, "Gap acceptance behavior at unsignalized intersections: effects of using a phone and a music player while driving," *Traffic Injury Prevention*, vol. 20, no. 4, pp. 372–377, 2019.

[15] G. Li, Y. Wang, F. Zhu et al., "Drivers' visual scanning behavior at signalized and unsignalized intersections: a naturalistic driving study in China," *Journal of Safety Research*, vol. 71, pp. 219–229, 2019.

[16] Y. Liang, M. L. Reyes, and J. D. Lee, "Real-time detection of driver cognitive distraction using support vector machines," *IEEE Transactions on Intelligent Transportation Systems*, vol. 8, no. 2, pp. 340–350, 2007.

[17] M. Atiquzzaman, Y. Qi, and R. Fries, "Real-time detection of drivers' texting and eating behavior based on vehicle dynamics," *Transportation Research Part F: Traffic Psychology and Behaviour*, vol. 58, no. 10, pp. 594–604, 2018.

[18] D. W. Hosmer and S. Lemesbow, "Goodness of fit tests for the multiple logistic regression model," *Communications in Statistics - Theory and Methods*, vol. 9, no. 10, pp. 1043–1069, 1980.

[19] H. Zhang, D. L. Qian, and C. F. Shao, "Discrimination of driver distraction in simulated driving environment," *Journal of China Highway and Transport*, vol. 31, no. 4, pp. 43–51, 2018.

[20] Y. Liao, S. E. Li, W. Wang, Y. Wang, G. Li, and B. Cheng, "Detection of driver cognitive distraction: a comparison study of stop-controlled intersection and speed-limited highway," *IEEE Transactions on Intelligent Transportation Systems*, vol. 17, no. 6, pp. 1628–1637, 2016.

[21] C. Craye and F. Karray, "Driver distraction detection and recognition using RGB-D sensor," *Computer Science*, http://arxiv.org/abs/1502.00250, 2015.

[22] J. Son and M. Park, "Detection of cognitive and visual distraction using radial basis probabilistic neural networks," *International Journal of Automotive Technology*, vol. 19, no. 5, pp. 935–940, 2018.

[23] H. Zhang, Y. Liu, C. Wang, R. Fu, Q. Sun, and Z. Li, "Research on a pedestrian crossing intention recognition model based on natural observation data," *Sensors*, vol. 20, no. 6, pp. 1776–1797, 2020.

[24] W. Wang, S. Yang, Y. Jiang, S. Zhang, and W. Deng, "What contributes to driving behavior prediction at unsignalized intersections?," *Transportation Research Part C: Emerging Technologies*, vol. 108, pp. 100–114, 2019.

[25] J. Wu and H. Xu, "Driver behavior analysis for right-turn drivers at signalized intersections using shrp 2 naturalistic driving study data," *Journal of Safety Research*, vol. 63, pp. 177–185, 2017.

[26] C. Cabrall, N. Janssen, J. Goncalves, A. Morando, M. Sassman, and J. D Winter, "Eye-based driver state monitor of distraction, drowsiness, and cognitive load for transitions of control in automated driving," in *Proceedings of the 2016 IEEE International Conference on Systems, Man, and Cybernetics*, pp. 1981-1982, Budapest, Hungary, October 2016.

[27] S. W. Savage, D. D. Potter, and B. W. Tatler, "Does preoccupation impair hazard perception? a simultaneous EEG and Eye Tracking study," *Transportation Research Part F: Traffic Psychology and Behaviour*, vol. 17, no. 2, pp. 52–62, 2013.

[28] Y. Liao, S. E. Li, W. Wang, Y. Wang, G. Li, and B. Cheng, "The impact of driver cognitive distraction on vehicle performance at stop-controlled intersections," in *Proceedings of the 2015 IEEE Intelligent Vehicles Symposium (IV)*, pp. 946–951, Seoul, Korea (South), June 2015.

[29] D. L. Strayer and F. A. Drews, "Cell-Phone-induced driver distraction," *Current Directions in Psychological Science*, vol. 16, no. 3, pp. 128–131, 2007.

[30] M. J. Kane, A. R. A. Conway, T. K. Miura, and G. J. H. Colflesh, "Working memory, attention control, and the N-back task: a question of construct validity," *Journal of Experimental Psychology: Learning, Memory, and Cognition*, vol. 33, no. 3, pp. 615–622, 2007.

[31] V. Alizadeh and O. R. Dehzangi, "The impact of secondary tasks on drivers during naturalistic driving: analysis of EEG dynamics," in *Proceedings of the IEEE 19th International Conference on Intelligent Transportation Systems (ITSC)*, pp. 2493–2499, Rio de Janeiro, Brazil, November 2016.

[32] Y. L. Pei, Y. Q. Jin, and H. F. Chen, "Experimental study on EEG characteristics of driving fatigue in different ages," *Journal of China Highway and Transport*, vol. 31, no. 4, pp. 59–65, 2018.

[33] J. Lee, B. D. Sawyer, B. Mehler et al., "Linking the detection response task and the attend algorithm through assessment of human–machine interface workload," *Transportation research record: Journal of the Transportation Research Board*, vol. 2663, pp. 82–89, 2017.

[34] L. S. Jin, B. C. Guo, X. Y. Jiang, F. Wang, X. Xie, and M. Gao, "Study on the impact degrees of several driving behaviors when driving while performing secondary tasks," *IEEE Access*, vol. 6, p. 1, 2018.

[35] J. Li, Z. Q. Yue, and S. C. Wong, "Performance evaluation of signalized urban intersections under mixed traffic conditions by gray system theory," *Journal of Transportation Engineering*, vol. 130, no. 1, pp. 113–121, 2004.

[36] F. R. Wang, B. C. Guo, L. S. Jin, L. L. Gao, and X. Y. Yue, "Selection of safe evaluation indexes and weight calculation for secondary task driving," *Journal of Jilin University (Engineering and Technology Edition)*, vol. 47, no. 6, pp. 1710–1715, 2017.

[37] Z. Wu, "The application of FAHP in decisions of pavement maintenance," in *Proccedings of the 3rd International Conference on Energy Materials and Environment Engineering*, pp. 1755–1315, Bristol, England, April 2017.

[38] G. C. Cawley and N. L. C. Talbot, "Efficient leave-one-out cross-validation of kernel Fisher discriminant classifiers," *Pattern Recognition*, vol. 36, no. 11, pp. 2585–2592, 2003.

[39] C. Cortes and V. Vapnik, "Support-vector networks," *Machine Learning*, vol. 20, no. 3, pp. 273–297, 1995.

[40] C. C. Chang and C.-J. Lin, "Libsvm: a library for support vector machines," *ACM Transactions on Intelligent Systems & Technology*, vol. 2, no. 3, p. 27, 2011.

[41] J. Engström, G. Markkula, T. Victor, and N. Merat, "Effects of cognitive load on driving performance: the cognitive control hypothesis," *Human Factors: The Journal of the Human Factors and Ergonomics Society*, vol. 59, no. 5, pp. 734–764, 2017.

Hindawi
Advances in Civil Engineering
Volume 2021, Article ID 8816965, 13 pages
https://doi.org/10.1155/2021/8816965

*Research Article*

# Flexible Bus Route Optimization Scheduling Model

**Ji-yang Sun,[1] Yan-yan Chen ,[2] Jian-ling Huang,[3] Pan-yi Wei ,[1] and Cheng-cheng Song[1]**

[1]*Beijing Key Laboratory of Traffic Engineering, Beijing University of Technology, Beijing 100124, China*
[2]*Center of Cooperative Innovation for Beijing Metropolitan Transportation, Beijing 100124, China*
[3]*Beijing Transportation Information Center, Beijing 100161, China*

Correspondence should be addressed to Pan-yi Wei; weipanyi@foxmail.com

Received 28 June 2020; Revised 7 December 2020; Accepted 28 January 2021; Published 27 February 2021

Academic Editor: Shazim Memon



A flexible bus route optimization scheduling model that considers the dynamic changes of passenger demand is proposed to address the large difference in demand for flexible bus passengers and real-time variability. This model uses the heuristic algorithm based on gravity model to determine the following: passenger booking; vehicle passenger capacity; team known conditions such as size, according to the dynamic changes of passenger demand for real-time iterative update shuttle travel time; vehicle operating costs (vehicle); and time cost for passengers (passengers waiting time for the vehicle, actual time of arrival, and the difference between expected and actual times of arrival) before minimization as the target. Finally, the practicabilities of the model and algorithm are verified by an example. Analysis results show that for 102 travel demands of 15 randomly generated demand points, completing all services requires 17–21 vehicles with average travel time of 24.59 minutes each. The solution time of 100 groups of data is within 25 seconds and the average calculation time is 12.04 seconds. Under the premise of real-time adjustment of connection planning time, this optimization model can thus better meet the dynamic demand of passengers compared with the current scenario. The model effectively reduces the planning path error, shortens the travel distance and passenger travel time, and achieves better results than the flexible bus scheduling model that ignores changes of connection travel time.

## 1. Introduction

How to realize optimal scheduling is the main problem faced by urban public transport operation and management. A good bus scheduling system can quickly optimize and adjust the line operation plan according to the travel needs of passengers. In addition, this system can improve the line service rate, reduce running time, and reduce travel time cost of passengers [1–3]. The traditional bus route optimization method is mainly designed based on experience, long-term observation, or IC card data statistical analysis. The objective is to extend, shorten, add, or delete certain lines, adjusting to the optimization and priority that meet the passenger demand of large passenger flow site. This method is mainly suitable for fixed-line bus route optimization with long cycle adjustment [4–7]. The emergence of flexible buses provides the possibility for dynamic optimization and adjustment of routes [7–10]. Vincent et al. [11] proposed a mixed-integer linear programming model and a variable neighborhood search to deal with the flexible vehicle and crew scheduling problem, by solving the problem that urban bus transport agencies have to assign their resources (vehicles and drivers) to cover timetables generated at the tactical level. Giorgio et al. [12] explored the potential contribution that the public transport agency can make to the emerging mobility as a service (MaaS) paradigm through the integration of regular collective transport services with complementary flexible transport schemes and other forms of shared-use transport. Nourbakhsh and Ouyang [13] presented an alternative flexible-route transit system in which each bus is allowed to travel across a predetermined area to serve passengers, analyzed the agency and user cost components of this proposed system in idealized square cities, and sought the optimum network layout, service area of each bus, and bus

headway, to minimize the total system cost. Mulley and John [14] presented a viewpoint through their research that well-implemented FTS has the potential to revitalise bus-based public transport services which are traditionally based on fixed networks with variable geographical coverage and levels of service. Jenny et al. [15] designed a multicommodity network flow programming model and obtained exact routing solutions using Lagrangian relaxation and a dynamic programming algorithm. Quadrifoglio and Dessouky [16] established the mixed-integer programming equation of system route optimization through analysis of key parameters of the flexible bus system. They likewise conducted simulation verification analysis on the system route design and scheduling problems to correct the model parameters [17]. Fu et al. [18] used super network to simultaneously simulate user activities and travel behaviors and then established a bus route selection model according to user travel behavior characteristics. Koffman [19] proposed an intelligent scheduling algorithm for urban public transport based on multiobjective demands. Tsubouchi [20] used the minimum spanning tree to find the optimal bus path. Xiong [21] developed an optimization method of community bus-subway connection route considering potential demand. Qian-fei et al. [22, 23] established a hyperpath bus transport path adjustment model by deducing the expected waiting time of passengers and the probable number of passengers on the route. Pan [24] proposed a flexible bus route optimization and scheduling method based on long reservation. Guo [25] offered a customized bus route optimization selection method based on demand response. These studies are all flexible bus route optimization algorithms established according to passengers' reservation needs. However, the preconditions are that passengers make advance appointments or assume that passenger needs are known, that is, the methods are all based on "static demands." However, travel often requires short or instant reservation according to passenger needs. Flexible buses need to calculate the change of vehicle connection travel time caused by changes according to the "dynamic demand" of passengers. And these buses need to adjust routes to achieve dynamic optimization. In addition, the flexible bus connection modes in almost all the research studies mentioned above are in form of "many-to-one," that is, multiple flexible stations corresponding to one target station. The case of multiple flexible sites corresponding to multiple target sites (the "many-to-many" pattern) has rarely been studied.

With such consideration, the present study proposes a flexible bus route optimization scheduling method based on passenger dynamic demand and the "many-to-many" pattern. This method considers dynamic changes of passenger demand and the resulting changes of vehicle connection travel time. A flexible bus route optimization scheduling model is constructed on the basis of the known passenger carrying capacity and vehicle fleet size. Then, the connection trip time is updated in real time according to the dynamic variation characteristics of passenger demand and considering the time cost of vehicle operation and passenger travel.

## 2. Problem Description and Modeling

*2.1. Problem Description.* A flexible bus is a demand-based transportation system that can gather individual passengers' travel needs and provide personalized transportation services. Under the "dynamic real-time" demand mode, which is the focus of this study, the flexible bus system has high requirements on algorithm and operation cost control. The following assumptions, parameter selection, and modeling are carried out to establish a reasonable and appropriate model. Several factors such as passenger demand and operating cost are likewise considered.

*2.2. Model Assumptions.* The following assumptions are proposed, with (1) and (2) as dynamic hypotheses and (3)–(6) as static hypotheses:

(1) Passenger reservation demand changes dynamically at each station.

(2) The travel time between stations is dynamic.

(3) Location of each site is known.

(4) After booking, the time for each passenger to arrive at the target station is known.

(5) The service time for passengers to board the train is constant.

(6) The passenger-carrying capacity of the transfer vehicle is known.

*2.3. Model Parameters.* Table 1 shows the definition and description of the input and decision variables in the model.

*2.4. Model Presentation.* The coordination scheduling optimization model can be expressed as the following nonlinear programming model.

$$\min\left[\sum_{i\in H\cup D}\sum_{j\in H\cup D}\sum_{k\in K} c_{ij}Y_{ijk} + \sum_{r\in R} a_r + \sum_{r\in R}\sum_{k\in K}\sum_{t}\left(X_{rkt}T_t - e_r\right)\right]. \tag{1}$$

Equation (1) is the objective equation, which includes the minimization of the sum of three factors: (1) travel time of all vehicles to reduce operating costs; (2) sum of waiting time of all passengers in each station; and (3) sum of waiting time of all passengers in the target station. The latter two are determined to reduce the passenger time cost.

$$\sum_{j\in H\cup D}\sum_{k\in K} Y_{ijk} \geq 1, \quad \forall i \in H, \tag{2}$$

$$\sum_{j\in H\cup D}\sum_{k\in K} Y_{ijk} \leq V, \quad \forall i \in H. \tag{3}$$

Constraints (2) and (3) indicate that for each demand point, at least one vehicle service and at most $V$ vehicle service are available.

Table 1: Model parameter.

| Variable | Definitions and descriptions | Parameter type |
|---|---|---|
| $H$ | Passenger demand station set | Set of integers |
| $D$ | Target station set | Set of integers |
| $K$ | Shuttle operation vehicle set | Set of integers |
| $R$ | Passenger demand set | Set of integers |
| $N$ | Total passenger demand, $N \geq 0$ | Parameters |
| $V$ | Shuttle fleet size, $V \geq 0$ | Parameters |
| $M$ | A large constant | Constant |
| $T_t$ | The $t$th departure time of the target station | Decision variables |
| $d_r$ | Target stations $d$ of passenger demands $r$ | Decision variables |
| $p_r$ | Pickup station$p$ for passenger demand $r$ | Decision variables |
| $T_r$ | The starting time of the target station for passenger demand $r$ | Decision variables |
| $c_{ij}$ | The travelling time between station $i$ and station $j$ | Decision variables |
| $Q_k$ | The capacity of shuttle bus $k$, $Q_K \geq 0$ | Decision variables |
| $X_{rkt}$ | If shuttle bus $k$connects demand $r$to the target station at time $t$, $X_{rkt} = 1$; otherwise, $X_{rkt} = 0$ | Decision variables |
| $Y_{ijk}$ | If shuttle bus $k$selects the link$(i, j)$ as driving path, $Y_{ijk} = 1$; otherwise, $Y_{ijk} = 0$ | Decision variables |
| $a_r$ | The time when the shuttle bus reaches the demand point where the demand $r$ is located | Decision variables |
| $a_s$ | Travel time of the shuttle bus to reach the required point | Decision variables |
| $e_r$ | Time of passenger demand $r$reaches target station | Decision variables |
| $U_{ik}$ | Auxiliary variable is used to ensure that there is no loop in the driving path of the connecting vehicle $K$; $i$ indicates the shuttle bus passing through the station; if shuttle bus $k$ leaves station $i$, $U_{ik} = 0$; if shuttle bus $k$ arrives station $i$, $U_{ik} = 1$ | Auxiliary variable |

$$\sum_{i \in H} \sum_{k \in K} Y_{ijk} \leq V, \quad \forall j \in D. \tag{4}$$

Constraint (4) means that at most $V$ vehicles participate in the operation.

$$\sum_{j \in H \cup D} Y_{ijk} - \sum_{p \in H} Y_{pik} \geq 0, \quad \forall i \in H, k \in K. \tag{5}$$

Constraint (5) indicates that in addition to the first demand point of each vehicle service, the number of vehicles entering should be equal to that leaving to serve the other demand points.

$$U_{ik} - U_{jk} + |H| \times Y_{ijk} \leq |H| - 1, \quad \forall i, j \in H \cup D, k \in K. \tag{6}$$

Constraint (6) avoids loops in the vehicle path.

$$\sum_{i \in H} \sum_{j \in D} Y_{ijk} \geq 1, \quad \forall k \in K, \tag{7}$$

$$\sum_{i \in H} \sum_{j \in D} Y_{ijk} \leq 0, \quad \forall k \in K. \tag{8}$$

Constraints (7) and (8) ensure that each vehicle delivers passengers to their final destination.

$$\sum_{r \in R} \sum_{t \in T} X_{rkt} \leq Q_k, \quad \forall k \in K. \tag{9}$$

Constraint (9) ensures that the capacity of each feeder vehicle does not exceed its rated capacity to ensure the service level.

$$\sum_{k \in K} \sum_{t \in T} X_{rkt} = 1, \quad \forall r \in R. \tag{10}$$

Constraint (10) means that any requirement can only be served by one vehicle.

$$\sum_{m \in T/\{t\}} X_{skm} - (1 - X_{rkt})M \leq 0, \quad \forall r, s \in R, \forall k \in K, \forall t \in T. \tag{11}$$

Constraint (11) indicates that a transfer vehicle can only connect passengers at one departure time of a target station.

$$\sum_{r \in R} \sum_{k \in K} \sum_{t \in T} X_{rkt} = N. \tag{12}$$

Constraint (12) guarantees that all demand served is equal to the known reservation demand.

$$a_r + c_{p_r p_s} - a_s + Y_{p_r p_s k} M \le M, \quad \forall r, s \in R, \forall k \in K, \tag{13}$$

$$a_s - a_r - c_{p_r p_s} + Y_{p_r p_s k} M \le M, \quad \forall r, s \in R, \forall k \in K. \tag{14}$$

Constraints (13) and (14) indicate that if two stations are successively served by a transfer vehicle, then the arrival time of demand in the latter station is equal to the sum of the arrival time of demand in the previous demand point and the travel time between the two demand points.

$$a_r + c_{p_r j} - a_s + Y_{p_r p_s k} M \le M, \quad \forall r \in R, \forall k \in K, \forall j \in D, \tag{15}$$

$$a_s - a_r - c_{p_r j} + Y_{p_r p_s k} M \le M, \quad \forall r \in R, \forall k \in K, \forall j \in D. \tag{16}$$

Constraints (15) and (16) indicate that the time for the passenger to reach the target station at the last demand station of the connecting vehicle is equal to the sum of the travel time of the vehicle to reach the demand point and the travel time between the two demand points.

$$e_r \le \sum_{k \in K} \sum_{t \in T} X_{rkt} T_t, \quad \forall r \in R. \tag{17}$$

Constraint (17) ensures that the vehicle arrives at the target station no later than the departure time of the target station.

## 3. Model Solution

The flexible bus route optimization scheduling problem for multiobjective stations is a typical NP-hard problem. As the problem scale expands, the computation likewise increases exponentially. Therefore, this kind of problem is usually solved by heuristic algorithm that can guarantee calculation speed and accuracy. Inspired by the law of universal gravitation, the present study proposes a heuristic algorithm that first generates the initial solution on the basis of the gravitation model. Then, the route is separately improved by the inter-route and intra-route optimization algorithm to obtain the final route. Figure 1 is the overall flow of the heuristic algorithm based on the gravity model and is the overall description of the following steps 1 to 4.

*3.1. Passenger Travel Reservation and Demand Distribution.* First, the passenger travel reservation and demand allocation are completed according to the following steps.

Step 1: passengers make travel reservations according to their travel needs. Each passenger transmits his/her departure station, target station, expected arrival time, and other information to the travel reservation platform. Considering their dynamic changing characteristics, passenger demand on reservation platforms and travel time between connecting vehicle stations are updated every five minutes.

Step 2: travel reservation platform clusters all passengers according to the target station and expected arrival time of each passenger according to the principle that the actual arrival time is not later than the expected arrival time of passengers.

Step 3: results are generated according to the path in Sections 2.2 and 2.3. The arrival time of the transfer vehicle at each demand point is preliminarily estimated on the basis of several factors, including the expected arrival time of the transfer vehicle, average driving speed, position of the passenger demand point, and number of passengers at each demand point.

Step 4: the preliminarily estimated time of the connecting vehicle arriving at each demand point is sent to the passengers of the corresponding demand point. Passenger can choose whether to take the bus or wait for the connecting vehicle according to the rationality of its arrival time.

*3.2. Generating Initial Vehicle Path Solution on the Basis of the Gravity Model.* The path search problem is transformed into the iterative problem of the site selection chain, which is most attractive to the current site based on the gravity model algorithm. The gravity between the two sites is defined as follows.

$$F_{ij} = \frac{N_i N_j}{c_{ij}^2}, \tag{18}$$

where $N_i$ is the number of passengers at station $i$ and $c_{ij}$ is the travel time between station $i$ and station $j$. The higher value of $F_{ij}$ means that the two stations have more passengers and less travel cost, thus needing priority service. Therefore, station $j$ should be set as the next station of station $I$.

Given the rated vehicle carrying capacity, the steps of the gravity model algorithm to generate the initial path solution are as follows.

Step 1: determine the vehicle starting point. Initial $k = 1$. Randomly select one station with passenger boarding requirements as the starting point of vehicle $k$.

Step 2: determine if similar passengers are not serviced. If so, proceed to Step 3. Otherwise, proceed to Step 5.

Step 3: search for the next site. The most attractive station $X$ is that between the current station and that in the boarding station with similar passengers. Station $X$ is then added to the route selection chain, and the number of passengers is calculated after the vehicle arrives at the station, and the time to arrive at the target site after joining station $X$.

Step 4: determine whether the vehicle route is reasonable after joining station $X$. If the number of passengers served by the current vehicle does not exceed the on-board capacity $Qk$ and the time to reach the target station does not exceed the time required by passengers, then station $X$ shall be taken as a new starting point. Thus, Step 5 is skipped. Otherwise, proceed to Step 5.

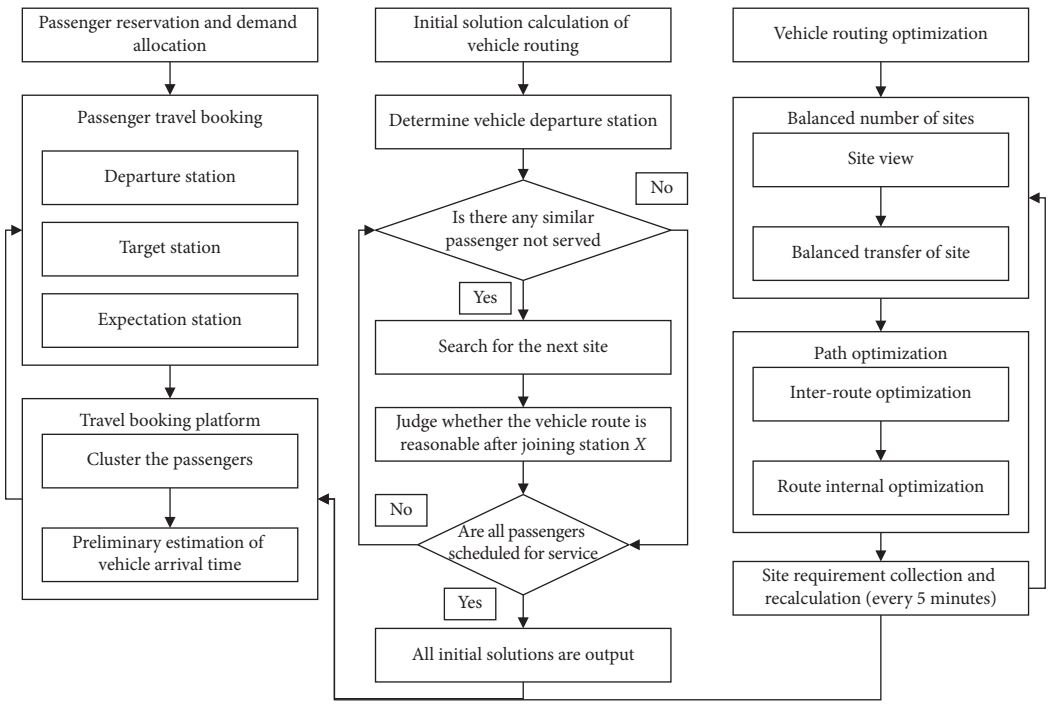


Figure 1: Flexible bus route optimization scheduling process responding to dynamic demand.

Step 5: determine if all classes of passengers are served. If several passengers are not scheduled, then the next car should be dispatched, $k = k + 1$ and go back to Step 1. Otherwise, all current initial paths are output, and the initial vehicle path solution generation algorithm based on the gravity model is completed.

*3.3. Vehicle Routing Optimization Based on Station Equilibrium and Exchange.* This section introduces the route optimization algorithm between and within routes to further improve the route quality and passenger service level. Notably, Steps 1 and 2 of the algorithm belong to inter-vehicle path optimization. During their execution, multiple feasible route solutions may be searched. If only the current optimal set of solutions is saved during the search and Step 3 is performed, the final route result may not be optimal. Therefore, the proposed algorithm saves all feasible solution groups found in Steps 1and 2, and Step 3 is performed for each feasible solution group. Moreover, the objective function of all route solution groups is comprehensively evaluated so as to find the final optimal solution.

Step 1: first, the number of stations between the vehicles serving the target site and taking the same time to reach the target site is equalized. Service stations are checked for any imbalance in this number. If found, then on the premise of meeting the requirements of vehicle capacity and time to reach the target site, several vehicle routes that need to pass through more sites are transferred to the vehicle routes that need to pass through fewer sites. Thus, reasonable site sequence is arranged.

Step 2: the path between vehicles that serve the target site and those that need the same amount of time to reach the target site is optimized. The main application between the two routes is the exchange of two sites and search for better routes. In the process of exchange optimization, vehicle capacity and time to reach the target site are guaranteed.

Step 3: route of each car is internally optimized. The order of the two stops is exchanged mainly within the same vehicle route to evaluate whether the objective function value is reduced. If so, then site order is exchanged. Otherwise, this exchange is abandoned. After a certain number of attempts, the algorithm is terminated and the final route result is output.

Step 4: considering the dynamic variation characteristics of passenger demand and the variation characteristics of travel time between stations, the requirements of each station are collected and recalculated every five minutes, and Steps 1–3 above are repeated.

After the above four steps, the objective function of the route scheduling model can be optimized on the premise of ensuring that passengers arrive at the target station according to the expected time. The entire service time can be reduced and the route of each vehicle is more reasonable than before. In addition, the running cost of vehicles and waiting time of passengers can be reduced while service quality and efficiency can be improved.

## 4. Case Analysis

Huilongguan District of Beijing is a densely populated area of commuters, with large travel demand during peak hours, and the travel time of travelers with different work nature

Table 2: Constant variables in the case.

| Variable | Variable name | Number of variables | Unit |
|---|---|---|---|
| $H$ | Number of demand points | 15 | Unit |
| $D$ | Number of target stations | 3 | Unit |
| $Q$ | Vehicle rated passenger capacity | 7 | Person |
| $V$ | Fleet size/vehicle | 18 | Car |
| $W$ | Expected arrival time/minute | 30/40/50 | Minute |
| $F$ | Passenger arrival and boarding time/minute | 0.5 | Minute |

Table 3: The quantity demanded at the initial moment.

| Passenger number | Departure station | Target station | Expected arrival time/minute |
|---|---|---|---|
| *(a) Passenger demand with target station 1* | | | |
| 1 | 1 | 1 | 30 |
| 2 | 1 | 1 | 50 |
| 3 | 1 | 1 | 50 |
| 4 | 2 | 1 | 30 |
| 5 | 2 | 1 | 50 |
| 6 | 3 | 1 | 30 |
| 7 | 3 | 1 | 40 |
| 8 | 4 | 1 | 30 |
| 9 | 5 | 1 | 30 |
| 10 | 5 | 1 | 40 |
| 11 | 5 | 1 | 50 |
| 12 | 5 | 1 | 50 |
| 13 | 6 | 1 | 30 |
| 14 | 6 | 1 | 40 |
| 15 | 7 | 1 | 30 |
| 16 | 7 | 1 | 50 |
| 17 | 7 | 1 | 50 |
| 18 | 8 | 1 | 30 |
| 19 | 8 | 1 | 40 |
| 20 | 9 | 1 | 40 |
| 21 | 10 | 1 | 40 |
| 22 | 10 | 1 | 50 |
| 23 | 11 | 1 | 40 |
| 24 | 11 | 1 | 50 |
| 25 | 12 | 1 | 30 |
| 26 | 12 | 1 | 50 |
| 27 | 13 | 1 | 30 |
| 28 | 14 | 1 | 40 |
| 29 | 14 | 1 | 40 |
| 30 | 15 | 1 | 40 |
| *(b) Passenger demand with target station 2* | | | |
| 31 | 1 | 2 | 30 |
| 32 | 1 | 2 | 50 |
| 33 | 2 | 2 | 30 |
| 34 | 2 | 2 | 50 |
| 35 | 3 | 2 | 30 |
| 36 | 3 | 2 | 40 |
| 37 | 3 | 2 | 50 |
| 38 | 4 | 2 | 30 |
| 39 | 5 | 2 | 30 |
| 40 | 5 | 2 | 40 |
| 41 | 5 | 2 | 50 |
| 42 | 6 | 2 | 30 |
| 43 | 6 | 2 | 40 |
| 44 | 6 | 2 | 50 |
| 45 | 7 | 2 | 30 |
| 46 | 7 | 2 | 50 |

Table 3: Continued.

| Passenger number | Departure station | Target station | Expected arrival time/minute |
|---|---|---|---|
| 47 | 8 | 2 | 30 |
| 48 | 8 | 2 | 40 |
| 49 | 8 | 2 | 50 |
| 50 | 9 | 2 | 40 |
| 51 | 10 | 2 | 40 |
| 52 | 10 | 2 | 50 |
| 53 | 11 | 2 | 40 |
| 54 | 12 | 2 | 30 |
| 55 | 12 | 2 | 50 |
| 56 | 12 | 2 | 50 |
| 57 | 13 | 2 | 30 |
| 58 | 14 | 2 | 40 |
| 59 | 15 | 2 | 40 |
| 60 | 15 | 2 | 40 |
| *(c) Passenger demand with target station 3* | | | |
| 61 | 1 | 3 | 30 |
| 62 | 1 | 3 | 50 |
| 63 | 1 | 3 | 50 |
| 64 | 2 | 3 | 30 |
| 65 | 2 | 3 | 50 |
| 66 | 3 | 3 | 30 |
| 67 | 3 | 3 | 40 |
| 68 | 4 | 3 | 30 |
| 69 | 5 | 3 | 30 |
| 70 | 5 | 3 | 40 |
| 71 | 5 | 3 | 50 |
| 72 | 5 | 3 | 50 |
| 73 | 6 | 3 | 30 |
| 74 | 6 | 3 | 40 |
| 75 | 7 | 3 | 30 |
| 76 | 7 | 3 | 50 |
| 77 | 8 | 3 | 30 |
| 78 | 8 | 3 | 40 |
| 79 | 8 | 3 | 50 |
| 80 | 9 | 3 | 40 |
| 21 | 10 | 1 | 40 |
| 22 | 10 | 1 | 50 |
| 23 | 11 | 1 | 40 |
| 24 | 11 | 1 | 50 |
| 25 | 12 | 1 | 30 |
| 26 | 12 | 1 | 50 |
| 27 | 13 | 1 | 30 |
| 28 | 14 | 1 | 40 |
| 29 | 14 | 1 | 40 |
| 30 | 15 | 1 | 40 |

and commuting distance varies greatly. Therefore, it is suitable to be used as a case study of demand responsive flexible public transport model. In order to facilitate the model analysis, this paper abstracts the Huilongguan regional public transport network and retains the network topology.

A small network is used as case solution to verify the accuracy and applicability of the above model. Table 2 shows the input parameter of the constant variable of a small network, whereas Table 3 shows the passenger demand of each station at the initial moment. Table 4 shows the travel time matrix between stations at the initial time, where $H$ is the demand point and $D$ is the target station.

Using the heuristic algorithm proposed in this paper to solve the numerical case of demand at the initial moment obtains the service path of each vehicle, number of passengers served, and objective function corresponding to each path, as shown in Table 5.

Then, with the dynamic change of passenger demand and travel time between stations, the above path planning

Table 4: Case network travel time matrix at the initial moment.

| | $H1$ | $H2$ | $H3$ | $H4$ | $H5$ | $H6$ | $H7$ | $H8$ | $H9$ | $H10$ | $H11$ | $H12$ | $H13$ | $H14$ | $H15$ | $D1$ | $D2$ | $D3$ |
|---|---|---|---|---|---|---|---|---|---|---|---|---|---|---|---|---|---|---|
| $H1$ | 0 | 3 | 6 | 5 | 4 | 5 | 8 | 6 | 9 | 9 | 6 | 3 | 3 | 4 | 8 | 3 | 9 | 9 |
| $H2$ | 7 | 0 | 6 | 9 | 8 | 3 | 5 | 5 | 4 | 7 | 9 | 3 | 3 | 3 | 6 | 3 | 8 | 7 |
| $H3$ | 9 | 6 | 0 | 6 | 5 | 8 | 8 | 8 | 3 | 7 | 9 | 4 | 5 | 5 | 5 | 9 | 7 | 9 |
| $H4$ | 4 | 7 | 6 | 0 | 9 | 7 | 8 | 5 | 5 | 7 | 7 | 4 | 5 | 6 | 8 | 9 | 5 | 6 |
| $H5$ | 5 | 3 | 8 | 8 | 0 | 5 | 7 | 9 | 5 | 6 | 3 | 8 | 6 | 5 | 8 | 9 | 6 | 5 |
| $H6$ | 8 | 3 | 5 | 9 | 5 | 0 | 5 | 4 | 5 | 9 | 9 | 8 | 7 | 8 | 6 | 9 | 8 | 3 |
| $H7$ | 9 | 8 | 4 | 5 | 6 | 8 | 0 | 3 | 4 | 8 | 6 | 8 | 8 | 8 | 5 | 6 | 7 | 6 |
| $H8$ | 5 | 5 | 5 | 7 | 5 | 6 | 6 | 0 | 6 | 4 | 4 | 9 | 5 | 8 | 5 | 8 | 5 | 6 |
| $H9$ | 3 | 5 | 8 | 5 | 4 | 5 | 5 | 6 | 0 | 7 | 3 | 6 | 8 | 3 | 3 | 6 | 8 | 3 |
| $H10$ | 5 | 9 | 9 | 5 | 9 | 4 | 5 | 5 | 5 | 0 | 9 | 9 | 4 | 3 | 5 | 6 | 8 | 7 |
| $H11$ | 5 | 3 | 7 | 6 | 6 | 7 | 8 | 3 | 3 | 4 | 0 | 7 | 4 | 9 | 6 | 3 | 7 | 9 |
| $H12$ | 5 | 3 | 9 | 9 | 6 | 6 | 7 | 7 | 9 | 5 | 9 | 0 | 7 | 3 | 5 | 5 | 5 | 4 |
| $H13$ | 7 | 5 | 7 | 9 | 7 | 8 | 7 | 5 | 3 | 7 | 5 | 7 | 0 | 5 | 5 | 6 | 5 | 5 |
| $H14$ | 9 | 5 | 6 | 5 | 6 | 4 | 8 | 5 | 8 | 9 | 5 | 9 | 9 | 0 | 6 | 8 | 8 | 9 |
| $H15$ | 6 | 9 | 6 | 4 | 8 | 8 | 3 | 4 | 5 | 3 | 4 | 5 | 9 | 4 | 0 | 7 | 9 | 6 |

Table 5: Vehicle service path results for the initial moment.

| Passenger number | Vehicle path | Number of passengers served | Expected arrival time/ minute | The target function value corresponding to the path |
|---|---|---|---|---|
| 1 | 5-2-3-12-4-$D_1$ | 1-1-1-1-1 | 30 | 83 |
| 2 | 13-1-7-8-6-$D_1$ | 1-1-1-1-1 | 30 | 92 |
| 3 | 14-3-11-15-10-$D_1$ | 2-1-1-1-1 | 40 | 123 |
| 4 | 8-5-6-9-$D_1$ | 1-1-1-1 | 40 | 109 |
| 5 | 1-2-10-$D_1$ | 2-1-1 | 50 | 156 |
| 6 | 7-11-12-5-$D_1$ | 2-1-1-2 | 50 | 216 |
| 7 | 5-13-6-3-12-7-$D_2$ | 1-1-1-1-1-1 | 30 | 102 |
| 8 | 4-1-8-2-$D_2$ | 1-1-1-1 | 30 | 72 |
| 9 | 6-15-3-9-11-$D_2$ | 1-2-1-1-1 | 40 | 130 |
| 10 | 8-14-10-5-$D_2$ | 1-1-1-1 | 40 | 111 |
| 11 | 7-2-6-1-3-$D_2$ | 1-1-1-1-1 | 50 | 163 |
| 12 | 12-8-10-5-$D_2$ | 2-1-1-1 | 50 | 180 |
| 13 | 5-2-12-7-3-$D_3$ | 1-1-1-1-1 | 30 | 85 |
| 14 | 4-8-6-1-13-$D_3$ | 1-1-1-1-1 | 30 | 86 |
| 15 | 15-10-6-9-14-$D_3$ | 2-1-1-1-1 | 40 | 135 |
| 16 | 3-8-11-5-$D_3$ | 1-1-1-1 | 40 | 113 |
| 17 | 8-10-2-$D_3$ | 1-1-1 | 50 | 125 |
| 18 | 12-5-7-1-$D_3$ | 2-2-1-2 | 50 | 235 |

*Note*. The vehicle path in the table above is represented by the number sequence of the passenger demand points passed by. For example, 5-2-3-12-4-$D1$ indicates that the vehicle passes through the passenger demand points numbered 5, 2, 3, 12, and 4 in turn and finally arrives at the target station numbered $D1$. "Number of passengers served" corresponds to "vehicle path." For example, in the data in row 5, "vehicle path" is 1-2-10-$D1$, and number of passengers served is 2-1-1, which means that the number of passengers served at the passenger demand point with No. 1 is 2, and the number of passengers served at the passenger demand point Nos. 2 and 10 is 1.

results do not meet the current passenger demand and real situation. Thus, new path planning was needed. At this point, the reservation platform updates the travel time between the new passenger demand and the connecting vehicle station after the first five minutes of the summary. Table 6 shows the quantity demanded within the first five minutes after the initial moment. Table 7 shows the case network travel time matrix at the first five minutes. Table 8 shows the vehicle service path results for the first five minutes.

Then, such platforms are solved again using the method described in Section 2.2. Figure 2 shows the schematic diagram of vehicle routing results.

According to the calculation results in Table 8, Figure 2 shows the network topology of some vehicle driving paths. As Table 8 has a lot of contents, three groups of routes are

Table 6: The quantity demanded within the first 5 minutes.

| Passenger number | Departure station | Target station | Expected arrival time/minute |
|---|---|---|---|
| *(a) Passenger demand with target station 1* | | | |
| 1 | 1 | 1 | 30 |
| 2 | 1 | 1 | 50 |
| 3 | 1 | 1 | 50 |
| 4 | 2 | 1 | 30 |
| 5 | 2 | 1 | 50 |
| 6 | 3 | 1 | 30 |
| 7 | 3 | 1 | 40 |
| 8 | 4 | 1 | 30 |
| 9 | 5 | 1 | 30 |
| 10 | 5 | 1 | 30 |
| 11 | 5 | 1 | 30 |
| 12 | 5 | 1 | 30 |
| 13 | 5 | 1 | 40 |
| 14 | 5 | 1 | 50 |
| 15 | 5 | 1 | 50 |
| 16 | 6 | 1 | 30 |
| 17 | 6 | 1 | 40 |
| 18 | 7 | 1 | 30 |
| 19 | 7 | 1 | 50 |
| 20 | 7 | 1 | 50 |
| 21 | 8 | 1 | 30 |
| 22 | 8 | 1 | 40 |
| 23 | 9 | 1 | 40 |
| 24 | 10 | 1 | 40 |
| 25 | 10 | 1 | 50 |
| 26 | 11 | 1 | 40 |
| 27 | 11 | 1 | 50 |
| 28 | 12 | 1 | 30 |
| 29 | 12 | 1 | 50 |
| 30 | 13 | 1 | 30 |
| 31 | 14 | 1 | 40 |
| 32 | 14 | 1 | 40 |
| 33 | 15 | 1 | 40 |
| 34 | 15 | 1 | 50 |
| *(b) Passenger demand with target station 2* | | | |
| 35 | 1 | 2 | 30 |
| 36 | 1 | 2 | 50 |
| 37 | 2 | 2 | 30 |
| 38 | 2 | 2 | 50 |
| 39 | 2 | 2 | 50 |
| 40 | 3 | 2 | 30 |
| 41 | 3 | 2 | 40 |
| 42 | 3 | 2 | 50 |
| 43 | 4 | 2 | 30 |
| 44 | 5 | 2 | 30 |
| 45 | 5 | 2 | 40 |
| 46 | 5 | 2 | 50 |
| 47 | 6 | 2 | 30 |
| 48 | 6 | 2 | 40 |
| 49 | 6 | 2 | 50 |
| 50 | 7 | 2 | 30 |
| 51 | 7 | 2 | 50 |
| 52 | 8 | 2 | 30 |
| 53 | 8 | 2 | 40 |
| 54 | 8 | 2 | 50 |
| 55 | 9 | 2 | 40 |
| 56 | 10 | 2 | 40 |
| 57 | 10 | 2 | 40 |
| 58 | 10 | 2 | 50 |

Table 6: Continued.

| Passenger number | Departure station | Target station | Expected arrival time/minute |
|---|---|---|---|
| 59 | 11 | 2 | 40 |
| 60 | 12 | 2 | 30 |
| 61 | 12 | 2 | 50 |
| 62 | 12 | 2 | 50 |
| 63 | 13 | 2 | 30 |
| 64 | 14 | 2 | 40 |
| 65 | 15 | 2 | 40 |
| 66 | 15 | 2 | 40 |
| 67 | 1 | 3 | 30 |
| 68 | 1 | 3 | 30 |
| *(c) Passenger demand with target station 3* | | | |
| 69 | 1 | 3 | 50 |
| 70 | 1 | 3 | 50 |
| 71 | 2 | 3 | 30 |
| 72 | 2 | 3 | 40 |
| 73 | 2 | 3 | 50 |
| 74 | 3 | 3 | 30 |
| 75 | 3 | 3 | 40 |
| 76 | 3 | 3 | 50 |
| 77 | 4 | 3 | 30 |
| 78 | 5 | 3 | 30 |
| 79 | 5 | 3 | 40 |
| 80 | 5 | 3 | 50 |
| 81 | 5 | 3 | 50 |
| 82 | 6 | 3 | 30 |
| 83 | 6 | 3 | 40 |
| 84 | 7 | 3 | 30 |
| 85 | 7 | 3 | 50 |
| 86 | 8 | 3 | 30 |
| 87 | 8 | 3 | 40 |
| 88 | 8 | 3 | 50 |
| 89 | 9 | 3 | 40 |
| 90 | 10 | 3 | 40 |
| 91 | 10 | 3 | 50 |
| 92 | 11 | 3 | 40 |
| 93 | 12 | 3 | 30 |
| 94 | 12 | 3 | 50 |
| 95 | 12 | 3 | 50 |
| 96 | 13 | 3 | 30 |
| 97 | 13 | 3 | 30 |
| 98 | 14 | 3 | 40 |
| 99 | 15 | 3 | 40 |
| 100 | 15 | 3 | 40 |
| 101 | 15 | 3 | 40 |
| 102 | 15 | 3 | 40 |

selected and displayed according to the passenger destination; with $D_1$ as the destination, we show the path 5-2-3-12-4-$D_1$; with $D_2$ as the destination, we show the paths 5-13-6-3-12-7-$D_2$; with $D_3$ as the destination, we show the path 8-10-2-$D_3$.

A total of 102 travel demands of 15 randomly generated demand points in 100 groups are tested by the model. The objective is to further verify the algorithm's reliability, with the existing constant variables and the travel time matrix table of the case network unchanged. Figures 3–5 show the test results. Under the given conditions, all the 102 travel demands are completed, the number of vehicles required is 17–21, and the total travel time of 84% vehicles is 552–624 minutes (as shown in Figure 3). Moreover, the average travel time of each vehicle is 24.59 minutes, indicating that the travel time of vehicles solved by the heuristic algorithm is

Table 7: Case network travel time matrix at the first 5 minutes.

| | $H_1$ | $H_2$ | $H_3$ | $H_4$ | $H_5$ | $H_6$ | $H_7$ | $H_8$ | $H_9$ | $H_{10}$ | $H_{11}$ | $H_{12}$ | $H_{13}$ | $H_{14}$ | $H_{15}$ | $D_1$ | $D_2$ | $D_3$ |
|---|---|---|---|---|---|---|---|---|---|---|---|---|---|---|---|---|---|---|
| $H_1$ | 0 | 7 | 8 | 9 | 5 | 7 | 7 | 4 | 9 | 6 | 4 | 3 | 7 | 6 | 5 | 5 | 3 | 3 |
| $H_2$ | 6 | 0 | 3 | 5 | 4 | 9 | 7 | 9 | 3 | 4 | 4 | 3 | 8 | 3 | 7 | 9 | 7 | 9 |
| $H_3$ | 6 | 8 | 0 | 7 | 5 | 4 | 3 | 5 | 8 | 5 | 4 | 8 | 3 | 7 | 8 | 6 | 5 | 3 |
| $H_4$ | 9 | 5 | 7 | 0 | 9 | 3 | 6 | 5 | 5 | 6 | 3 | 8 | 8 | 5 | 5 | 8 | 9 | 4 |
| $H_5$ | 8 | 5 | 8 | 8 | 0 | 6 | 9 | 8 | 9 | 7 | 3 | 3 | 7 | 4 | 6 | 6 | 4 | 3 |
| $H_6$ | 5 | 3 | 4 | 9 | 5 | 0 | 5 | 6 | 6 | 4 | 9 | 5 | 7 | 8 | 9 | 8 | 4 | 7 |
| $H_7$ | 7 | 8 | 4 | 5 | 7 | 8 | 0 | 9 | 5 | 7 | 7 | 8 | 7 | 4 | 5 | 8 | 8 | 3 |
| $H_8$ | 7 | 5 | 6 | 5 | 5 | 5 | 8 | 0 | 3 | 6 | 5 | 4 | 6 | 6 | 5 | 4 | 5 | 8 |
| $H_9$ | 9 | 6 | 5 | 7 | 8 | 8 | 3 | 4 | 0 | 7 | 3 | 4 | 7 | 4 | 5 | 3 | 3 | 3 |
| $H_{10}$ | 9 | 3 | 9 | 5 | 8 | 6 | 5 | 3 | 6 | 0 | 7 | 4 | 6 | 9 | 8 | 6 | 8 | 6 |
| $H_{11}$ | 9 | 8 | 4 | 3 | 9 | 9 | 6 | 5 | 7 | 5 | 0 | 3 | 3 | 7 | 3 | 9 | 5 | 7 |
| $H_{12}$ | 7 | 3 | 3 | 4 | 9 | 4 | 9 | 9 | 7 | 6 | 3 | 0 | 3 | 9 | 9 | 3 | 9 | 9 |
| $H_{13}$ | 7 | 3 | 5 | 6 | 7 | 4 | 7 | 8 | 3 | 8 | 7 | 8 | 0 | 3 | 7 | 6 | 3 | 5 |
| $H_{14}$ | 4 | 8 | 6 | 5 | 7 | 7 | 6 | 8 | 5 | 9 | 7 | 8 | 9 | 0 | 4 | 6 | 5 | 8 |
| $H_{15}$ | 6 | 3 | 9 | 4 | 8 | 4 | 9 | 6 | 7 | 6 | 3 | 3 | 9 | 6 | 0 | 7 | 6 | 5 |

Table 8: Vehicle service path results for the first 5 minutes.

| Passenger number | Vehicle path | Number of passengers served | Expected arrival time/minute | The target function value corresponding to the path |
|---|---|---|---|---|
| 1 | 5-2-3-12-4-$D_1$ | 2-1-1-1-1 | 30 | 84 |
| 2 | 13-1-7-8-6-5-$D_1$ | 1-1-1-1-1-2 | 30 | 132 |
| 3 | 14-3-11-15-10-$D_1$ | 2-1-1-1-1 | 40 | 123 |
| 4 | 8-5-6-9-$D_1$ | 1-1-1-1 | 40 | 109 |
| 5 | 1-2-10-$D_1$ | 2-1-1 | 50 | 156 |
| 6 | 7-11-15-12-5-$D_1$ | 2-1-1-1-2 | 50 | 259 |
| 7 | 5-13-6-3-12-7-$D_2$ | 1-1-1-1-1-1 | 30 | 102 |
| 8 | 4-1-8-2-$D_2$ | 1-1-1-1 | 30 | 72 |
| 9 | 6-15-3-9-11-$D_2$ | 1-2-1-1-1 | 40 | 130 |
| 10 | 8-14-10-5-10-$D_2$ | 1-1-1-1-1 | 40 | 131 |
| 11 | 7-2-6-1-3-$D_2$ | 1-1-1-1-1 | 50 | 163 |
| 12 | 12-8-10-5-2-$D_2$ | 2-1-1-1-1 | 50 | 191 |
| 13 | 5-2-12-7-3-$D_3$ | 1-1-1-1-1 | 30 | 85 |
| 14 | 4-8-6-1-13-1-$D_3$ | 1-1-1-1-1-1 | 30 | 95 |
| 15 | 15-10-6-9-14-$D_3$ | 2-1-1-1-1 | 40 | 135 |
| 16 | 3-8-15-11-5-13-2-$D_3$ | 1-1-2-1-1-1-1 | 40 | 175 |
| 17 | 8-10-2-$D_3$ | 1-1-1 | 50 | 125 |
| 18 | 12-5-7-1-3-$D_3$ | 2-2-1-2-1 | 50 | 288 |

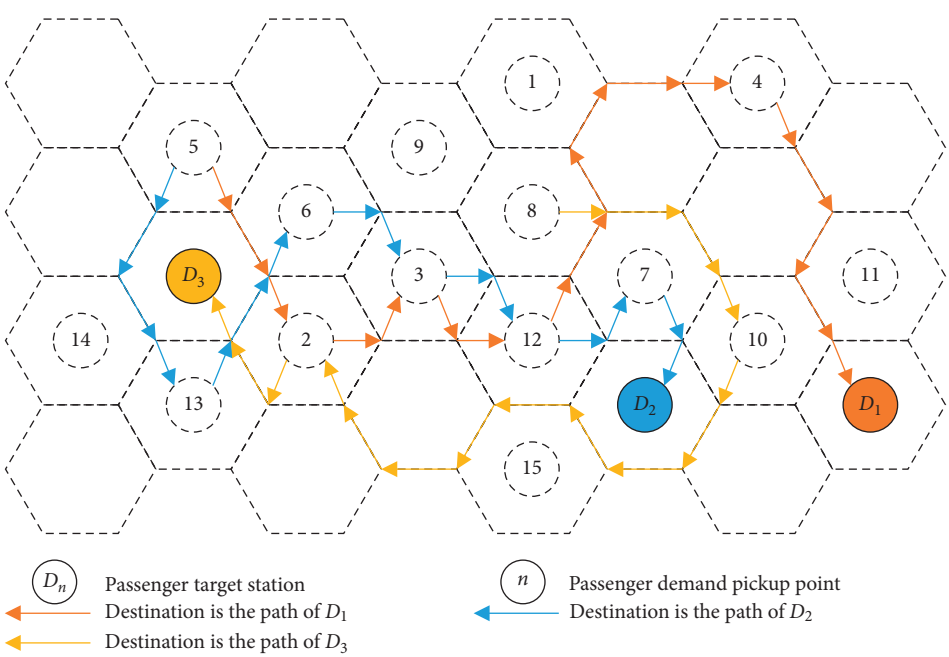


Figure 2: The schematic diagram of vehicle routing results.

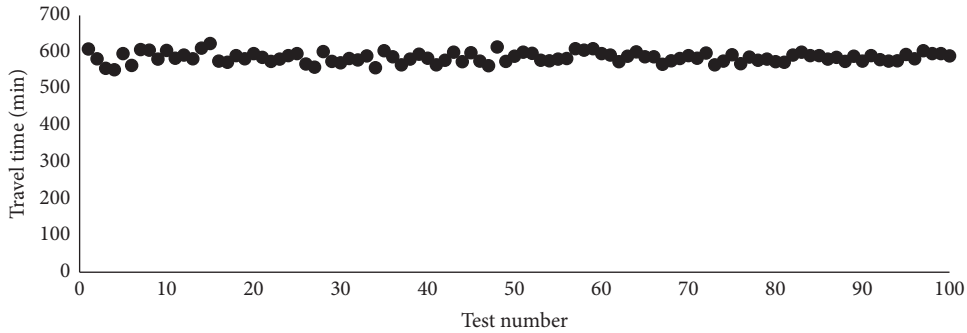


Figure 3: Vehicle routing results.

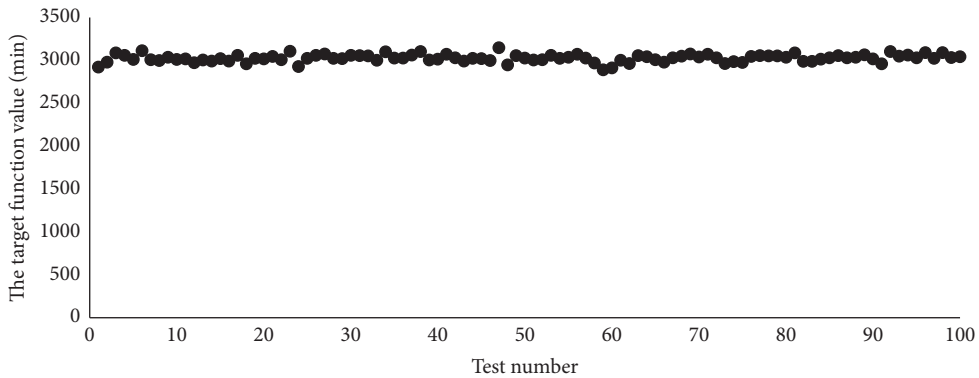


Figure 4: Total objective function result distribution.

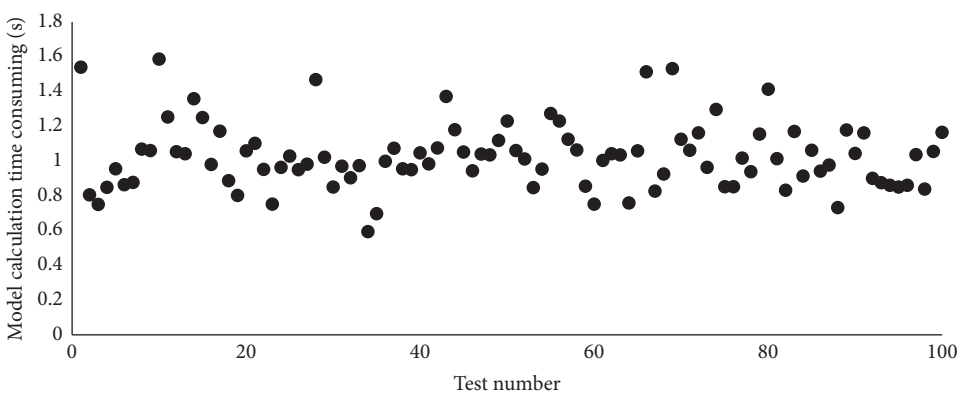


Figure 5: The time distribution of the model is calculated.

relatively stable. Although the demand distribution is highly uncertain, stable and reliable results are still generated due to the high robustness of the model and algorithm. The total objective function value remains mostly concentrated between 2888 and 3146 under the influence of demand changes (as shown in Figure 4). At the same time, the solution time of all 100 groups of data is less than 1.6 seconds, and the calculation time is 1.03 seconds on average (as shown in Figure 5). Thus, the algorithm proposed in this study is applicable to the actual system and the vehicle path optimization and collaborative scheduling can be completed within the limited time window of reservation and service provision.

## 5. Conclusion

This study investigates the flexible bus route optimization scheduling problem. The proposed model is dynamically constructed on the basis of passenger needs and "many-to-many" flexible bus system (i.e., multiple flexible stations corresponding to multiple target sites). Moreover, the routes are considered according to the dynamic changes of passenger demand and real-time updated shuttle travel time. The routes are established to maximize passenger services, minimize travel time for all passengers, and minimize operating time for all vehicles. The example shows that the flexible bus route optimization scheduling model in

response to dynamic demand can give more reasonable route optimization scheme and optimize passenger travel and vehicle operation cost compared with the model which ignores the change of passenger demand and takes the connection travel time as a fixed value.

In addition, we select more parameters in modeling and consider more factors, such as passenger demand, operating cost, etc., to make our solution to be nearer to the reality of the flexible bus system. At the same time, we focus on the actual travel demand for flexible bus scheduling in Huilongguan District of Beijing and establish the flexible bus scheduling model for multiple flexible stations and multiple target sites, which has more practicability than the "many-to-one" (i.e., multiple flexible stations corresponding to one target site) scheduling model.

For future research, we will select more areas to use our proposed flexible bus route optimization scheduling method, and then we will continually evaluate the effectiveness of the model for urban public transport operation and management and optimize the model and parameters.

## Data Availability

The data used to support the findings of this study are available from the corresponding author upon request, and the reader can use MATLAB for verification.

## Conflicts of Interest

The authors declare that they have no conflicts of interest.

## References


[1] M. Flusberg, "An innovative public transportation system for a small city: the Merrill, Wisconsin, case study," *Transportation Research Record*, vol. 606, pp. 54–59, 1976.

[2] Y. Lei, P.-q. Lin, and K.-b. Yao, "The network scheduling model and its solution algorithm of internet customized shuttle bus," *Journal of Transportation Systems Engineering and Information Technology*, vol. 17, no. 1, pp. 157–163, 2017.

[3] L. Yun, Y.-s. Jiang, and X.-m. Song, "Introduction of mobility allowance shuttle transit system (MAST) and the summary of its research progress," *Journal of Transportation Engineering and Information*, vol. 7, no. 4, pp. 79–83, 2009.

[4] Y. Shen and H.-f. Guan, "Study on demand responsive transport system and implementation issues," *Traffic & Transportation*, vol. 12, pp. 75–78, 2010.

[5] C. Peng and N. Yu, "Optimal design of demand adaptive paired-line hybrid transit: case of radial route structure," *Transporation Research Part E: Logistics & Transportation Review*, vol. 110, pp. 71–89, 2018.

[6] G. Chen, *Locating Flexible Feeder Bus Stations to Connect Urban Railway Systems*, Shandong University, Shandong, China, 2015.

[7] C. Avishai, "Integrated smart feeder/shuttle transit service: simulation of new routing strategies," *Journal of Advanced Transportation*, vol. 47, pp. 595–618, 2013.

[8] S.-l Pan, J. Yu, X.-l Lu, and N. Zou, "Review of flexible transit service," *Urban Transport of China*, vol. 2, pp. 62–68, 2014.

[9] A. Pratelli and F. Schoen, "A mathematical programming model for the bus deviation route problem," *Journal of the Operational Research Society*, vol. 52, no. 5, pp. 494–502, 2001.

[10] Y.-w Lei, P.-q Lin, and K.-b Yao, "The network scheduling model and its solution algorithm of internet customized shuttle bus," *Journal of Transportation Systems Engineering and Information Technology*, vol. 17, no. 1, pp. 157–163, 2017.

[11] B. Vincent, J. I.-R Omar, and Á. R.-S Yasmin, "Vehicle and Crew scheduling for flexible bus transportation systems," *Transportation Research Part B: Methodological*, vol. 112, pp. 216–229, 2018.

[12] A. Giorgio, D. N. John, and B. Marco, "Enabling intermodal urban transport through complementary services: from flexible mobility services to the shared use mobility agency: workshop 4. developing intermodal transport systems," *Research in Transportation Economics*, vol. 59, pp. 179–184, 2016.

[13] S. M. Nourbakhsh and Y. Ouyang, "A structured flexible transit system for low demand areas," *Transportation Research Part B: Methodological*, vol. 1, no. 46, pp. 204–216, 2012.

[14] C. Mulley and D. N John, "Flexible transport services: a new market opportunity for public transport," *Research in Transportation Economics*, vol. 1, no. 25, pp. 39–45, 2009.

[15] B. Jenny and D. N. John, "A case study of flexible solutions to transport demand in a deregulated environment," *Journal of Transport Geography*, vol. 4, no. 15, pp. 262–273, 2007.

[16] L. Quadrifoglio and M. Dessouky, "Insertion heuristic for scheduling mobility allowance shuttle transit (MAST) services: sensitivity to service area," *Computer-Aided Systems in Public Transport*, Springer Series: Lecture Notes in Economics and Mathematical Systems, Berlin, Germany, 2007.

[17] L. Quadrifoglio and M. Dessouky, "Sensitivity analyses over the service area for mobility allowance shuttle transit (MAST) services," *Computer-Aided Systems in Public Transport*, pp. 419–432, Springer Series: Lecture Notes in Economics and Mathematical Systems, Berlin, Germany, 2008.

[18] X. Fu, Y. Gu, and Z. Liu, "Scheduling activity and travel patterns in multi-modal transit networks with customized bus services," *Journal of Transportation Systems Engineering and Information Technology*, vol. 19, no. 4, pp. 20–27, 2019.

[19] D. Koffman, *Operational Experiences with Flexible Transit Services: A Synthesis of Transit Practice*, Transportation Research Board, Washington DC, USA, 2015.

[20] K. Tsubouchi, "Adapted scheduling algorithm for on-demand bus system," *International Journal of Intelligent Transportation Systems Research*, vol. 10, no. 2, pp. 82–92, 2013.

[21] J. Xiong, *Optimal Microcirculation System of Community Shuttle Linked with Metro Service*, Beijing Jiaotong University, Beijing, China, 2015.

[22] Q.-f. Li, P. Chen, and Y. Nie, "Finding optimal hyperpaths in large transit networks with realistic headway distributions," *European Journal of Operational Research*, vol. 240, no. 1, pp. 98–108, 2015.

[23] P. Chen and Y. Nie, "Optimal transit routing with partial online information," *Transportation Research Part B: Methodological*, vol. 72, pp. 40–58, 2015.

[24] S. Pan, *The Design Theory and Methodologdy of Flesaxible Microcirculation Transit System Oriented on the Transfer Station*, Shandong University, Shandong, China, 2015.

[25] X. Guo, *Research of Real-Time Custom Bus System Based on Demand Response*, Beijing Jiaotong University, Beijing, China, 2016.

Hindawi
Advances in Civil Engineering
Volume 2021, Article ID 6647766, 9 pages
https://doi.org/10.1155/2021/6647766

*Research Article*

# Study on Cracking Resistance of Basalt Fiber-Reinforced Microbond Asphalt Macadam

**Xin Yan,[1] Ronghua Ying,[1] Jian Jin,[1] and Yuntai Zhang[2]**

[1]*School of Traffic & Transportation Engineering, Changsha University of Science & Technology, Changsha 410114, China*
[2]*School of Civil Engineering, Central South University, Changsha 410075, China*

Correspondence should be addressed to Yuntai Zhang; zhangyuntai@csu.edu.cn

Received 18 November 2020; Revised 25 November 2020; Accepted 21 January 2021; Published 23 February 2021

Academic Editor: Arnaud Perrot



The aim of the present study was to explore the effect of basalt fibers on the cracking resistance of microbond asphalt macadam and reduce the occurrence of cracks in asphalt pavements with semirigid base. To this end, compressive resilient modulus tests, rutting tests, and semicircular bending tests were conducted on microbond asphalt macadam with different fiber contents, and the change trends of the compressive resilient modulus, dynamic stability, and flexibility index (FI) with fiber content were revealed. According to the results of this study, the addition of basalt fibers affected the compressive resilient modulus, dynamic stability, and FI of microbond asphalt macadam significantly. With the increase of fiber content, the compressive resilient modulus, dynamic stability, and FI presented a uniform trend of increasing first and decreasing afterwards. When the fiber content was 0.4%, various indices reached their maximum values, suggesting that the cracking resistance of the basalt fiber-reinforced microbond asphalt macadam was optimal under this content. This study is of great significance for the application and promotion of basalt fiber-reinforced microbond asphalt macadam.

## 1. Introduction

The development of China's highways mainly began in the mid-1980s. The economy has developed rapidly in recent years, highways have developed to a certain scale. Up to now, China's highway mileage has reached 150,000 kilometers. Semirigid base materials are applied on most high-grade highways in China, due to their high rigidity, strength, and diffusion-induced stress [1–3]. However, cracks of different sizes emerge in the early service period of pavements, the size and number of which tend to grow gradually with the increase of service time, resulting in the deterioration of the pavement status [4]. This is due to the fact that the dry- and temperature-shrinkage characteristics of the materials make the semirigid base susceptible to cracking under the combined actions of temperature, load, and other external factors. Gradually, cracks extend to the surface course, forming reflection cracks and damaging the integrity of the pavement structures [5]. Consequently, reflection cracks and their effects are notoriously tricky problems that cannot be ignored in the design and construction of semirigid base asphalt pavements. Currently, the solution of the reflection crack problem in semirigid base asphalt pavements constitutes a research hotspot in the field of road engineering [6–9].

To prevent the occurrence of cracks in asphalt pavements, related studies have been conducted by scholars both at home and abroad [10–13]. Some scholars paved an intermediate course of grading macadam between the subbase and surface courses, aiming to inhibit the occurrence of cracks and prolong the service life of semirigid base asphalt pavements. However, grading macadam has some apparent defects. First, due to the absence of cementing materials, it has low strength and weak load resistance and is vulnerable to rutting, permanent deformation, net-shaped cracks, and other damage. Second, it is very loose and poses difficulties to rolling in construction. In order to improve the strength and load resistance of grading macadam material, a kind of microbond asphalt macadam is proposed as an antireflection material. It has better construction performance and the modulus of grading macadam is increased to enhance its load

resistance and antireflection capability. Li et al. [14] added a small number of asphalt cementing materials into the grading macadam, used microbond asphalt macadam with a certain thickness as the intermediate course of the pavement structure, and gave due consideration to the lower surface course. As a result, both the strength and load resistance of the grading macadam were improved, and the occurrence of cracks was inhibited to some extent. Wang et al. [15] studied the microbonding bituminous macadam material transition of semirigid base asphalt pavement, the aggregate gradation type influence on microbonding bituminous macadam material performance, and drawing the conclusion, and the grading macadam at the grass-roots level on the G-A-5 material gradation value in the scope of the antirutting performance is better than that of using AM grading of antirutting performance of the value of the material. Its cracking resistance is also better than that of the materials with AM grading. However, those methods presented also some problems. It was found that when consideration was given to the lower surface course in the use of existing microbond asphalt macadam materials, rutting and other defects would occur, seriously hindering the application and promotion of microbond asphalt macadam. This means that it is necessary to further enhance the cracking resistance of microbond macadam materials. This is where basalt fibers come into play since they are characterized by high tensile strength and resistance to low and high temperatures and corrosion [16–19]. Wang et al. [20] investigated the effect of basalt fibers on the properties of asphalt concrete. They found that adding basalt fibers could significantly improve the high-temperature deformation resistance and cracking resistance of the asphalt concrete and that the optimal performance was achieved under a fiber content of 0.5%. So far, existing domestic studies have mainly focused on the effect of basalt fibers on the properties of asphalt concrete but rarely touch upon basalt fiber-modified microbond asphalt macadam. To answer the question whether basalt fibers can improve the cracking resistance of microbond asphalt macadam, further research is required [21].

In view of the above problems and the performance defects of existing microbond asphalt macadam materials, this study designed a novel basalt fiber-reinforced microbond asphalt macadam material. By taking this novel material as the research object, compressive resilient modulus tests, rutting tests, and semicircular bending tests under different fiber contents were conducted to reveal the change trends of its modulus, high-temperature deformation resistance, and cracking resistance. The crack resistance of the intermediate layer of basalt fiber microbonded asphalt gravel is evaluated. The results of this study provide some reference for the anticracking design of basalt fiber-reinforced microbond asphalt macadam and a method to solve the reflection crack of semirigid base pavement.

## 2. Raw Material Selection

In this study, grade-A 70# paving asphalt developed by PetroChina was used. The coarse and fine aggregates were limestones produced by Yangjiaqiao Macadam Court. The fibers, which were 12 mm in length, were basalt fibers manufactured by Changsha Fibers Hi-tech Co., Ltd. (Figure 1). Relevant technical properties of the raw materials used are presented in Tables 1–4 .

According to Tables 1–4, the technical properties of all materials conform to the requirements of relevant codes and can be used for related performance tests on basalt fiber-reinforced microbond asphalt macadam.

## 3. Mix Design and Specimen Preparation

*3.1. Gradation Selection.* The gradation type selected in this study was the gradation median of the gradation range of G-A-5 grading macadam for the upper base, which is recommended in the Specifications for Design of Highway Asphalt Pavement (JTG D50-2017) [22] (Table 5).

*3.2. Determination of Minimum and Maximum Asphalt Content.* To ensure that the material could reach a certain strength without becoming loose due to a low asphalt content, specimens were molded using asphalt contents of 1.5%, 2.0%, and 2.5%. It was observed that, under an asphalt content of 2.0%, the specimens were well molded with only a little aggregate shedding, while, under an asphalt content of 2.5%, the specimens were fully molded. However, due to the strong subjectivity of the coating test, the results can only serve as a reference. Cold-patch mixture cohesiveness tests were employed according to the Technical Specification for Construction of Highway Asphalt Pavements (JTG F40-2004) to evaluate the cohesiveness of the fiber-reinforced asphalt mixtures [23]. On the basis of the asphalt contents of 2.0% and 2.5%, specimens were molded using six different asphalt contents (2.1%, 2.2%, 2.3%, 2.4%, 2.5%, and 2.6%), followed by the cohesiveness test. The minimum asphalt contents corresponding to the specimens with fiber contents of 0%, 0.2%, 0.4%, and 0.6% were 2.2%, 2.3%, 2.4%, and 2.5%, respectively. The specific test results are shown in Figure 2:

To ensure adequate aggregate coating, drain-down tests were carried out to determine the maximum asphalt content, and mixtures were prepared under five different asphalt contents (2.8%, 3.0%, 3.2%, 3.4%, and 3.6%). Referring to the practice of Germany and Japan [24], enamel basins were used in the tests. In the drain-down tests, the mass loss rate of 0.5% corresponded to the maximum asphalt content [25]. As it can be seen by the test results in Figure 3, the maximum asphalt contents of the mixtures with fiber contents of 0%, 0.2%, 0.4%, and 0.6% were 3.2%, 3.3%, 3.4%, and 3.4%, respectively.

*3.3. Determination of Optimal Asphalt Content.* It has been shown [26] that the Marshall test cannot be employed for the determination of the optimal asphalt content of microbond asphalt macadam, mainly due to the low content, unstable fluidity, and irregularity of the asphalt. In this case, indices can be designed with reference to the composition of the grading macadam, in order to determine the optimal asphalt

Figure 1: Basalt fibers.

Table 1: Technical indices of asphalt.

| Test item | Unit | Test result | Code requirement | Test method |
|---|---|---|---|---|
| Penetration (25°C, 5s, 100 g) | 0.1 mm | 74 | 60~80 | T0604 |
| Penetration index, PI | — | 0.034 | −1.5~1.0 | T0604 |
| Softening point | °C | 52.3 | ≥45 | T0606 |
| Ductility at 15°C | cm | 127 | ≥100 | T0605 |
| Flash point | °C | 300 | ≥260 | T0611 |
| Solubility | % | 98.8 | ≥99.5 | T0607 |
| Relative density | — | 1.036 | — | T0603 |

Table 2: Physical and mechanical indices of coarse aggregates with different particle sizes.

| Number | Test item | Standard value | Test results of coarse aggregates | | | | Test method |
|---|---|---|---|---|---|---|---|
| | | | 15~25 mm | 10~15 mm | 5~10 mm | 3~5 mm | |
| 1 | Crushing strength (%) | ≤26 | — | 15.8 | — | — | T0316 |
| 2 | Apparent relative gravity (g/cm$^3$) | ≥2.5 | 2.742 | 2.721 | 2.734 | 2.752 | T0304 |
| 3 | Bulk volume density (g/cm$^3$) | Measured | 2.673 | 2.724 | 2.687 | 2.636 | T0304 |
| 4 | Water absorption rate (%) | ≤3.0 | 2.02 | 2.08 | 2.31 | 2.42 | T0310 |
| 5 | Los Angeles abrasion value (%) | ≤28 | 11 | 13.3 | 14.3 | — | T0320 |
| 6 | Asphalt adhesion grade | ≥4 | 4 | — | — | — | T0616 |

Table 3: Physical and mechanical indices of fine aggregate (0~3 mm).

| Number | Test item | Technical requirement | Test results of fine aggregate | Test method |
|---|---|---|---|---|
| 1 | Apparent density (g/cm$^3$) | ≥2.5 | 2.731 | T0328 |
| 2 | Sand equivalent (%) | ≥50 | 59 | T0340 |
| 3 | Mud equivalent (%) | ≤4 | 2.1 | T0349 |

Table 4: Performance indices and test results of basalt fibers.

| Test item | Technical requirement | Measured value |
|---|---|---|
| Breaking strength (MPa) | ≥1,500 | 2325 |
| Elongation at break (%) | ≤3.1 | 2.58 |
| Oil absorption rate (%) | ≥50 | 51.1 |
| Combustible content (%) | 0.1~1.0 | 0.5 |
| Water content (%) | ≤0.2 | 0.08 |
| Heat resistance-break strength retention (%) | ≥85 | 92 |

The heat resistance is defined as the break strength retention after 4 h of continuous heating in an oven at 250°C.

Table 5: Gradation range of G-A-5 grading macadam for the upper base.

| Sieve mesh (mm) | Passing percentage (%) | | | | | | | | | | | |
|---|---|---|---|---|---|---|---|---|---|---|---|---|
| | 26.5 | 19 | 16 | 13.2 | 9.5 | 4.75 | 2.36 | 1.18 | 0.6 | 0.3 | 0.15 | 0.075 |
| Upper limit | 100 | 100 | 89 | 79 | 63 | 40 | 28 | 20 | 14 | 10 | 7 | 5 |
| Lower limit | 100 | 95 | 82 | 70 | 53 | 30 | 19 | 12 | 8 | 5 | 3 | 2 |
| Gradation median | 100 | 97.5 | 85.5 | 74.5 | 58 | 35 | 23.5 | 16 | 11 | 7.5 | 5 | 3.5 |

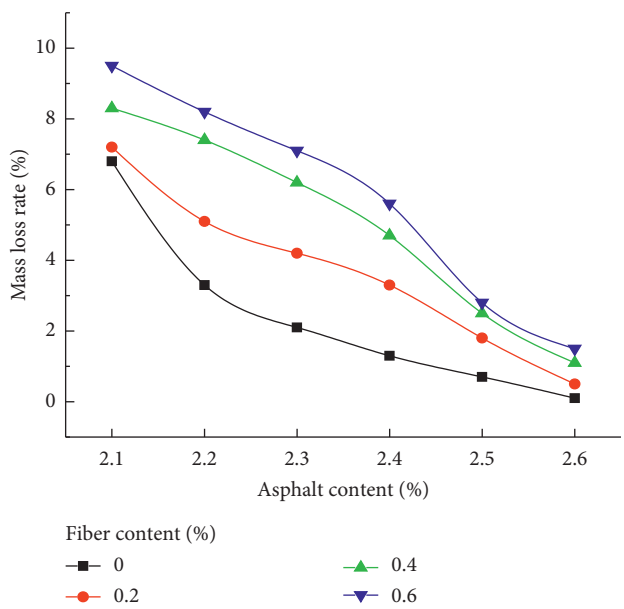


Figure 2: Mass loss rate.

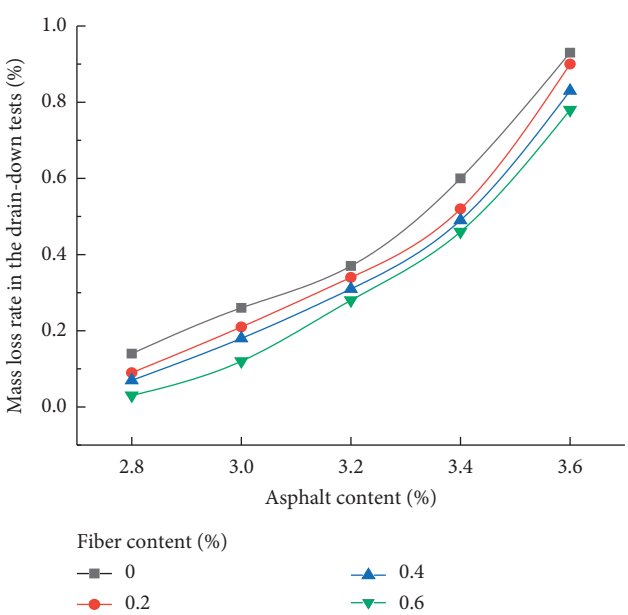


Figure 3: Mass loss rate in the drain-down tests.

content of microbond asphalt macadam using bearing ratio tests. The California bearing ratio (CBR) index can reflect the ability of basalt fiber-reinforced microbond asphalt macadam as the intermediate course material to withstand deformation. When CBR reaches its peak value, the corresponding asphalt content can be adopted as the optimal asphalt content [27].

*3.3.1. Void Percentage.* The compactness of a material is affected by a variety of factors. In this study, research was conducted from the perspective of material factors, and the wax sealing method was introduced to investigate the changing effects of the asphalt and fiber contents on the void percentage of the microbond asphalt macadam [28]. The specific test results are shown in Figure 4.

According to Figure 4, given the fiber content, the void percentage of the specimen would gradually decrease with the increase of the asphalt content and vary within the range of 9%–18%. The above results meet the technical requirements for microbond asphalt macadam stipulated in the specifications.

*3.3.2. Bearing Ratio Test.* The bearing ratios were determined using the uniaxial penetration method described in the Standard Test Methods of Bitumen and Bituminous Mixtures for Highway Engineering (T0713-2017). The specimens, which were standard Marshall Specimens, were molded according to the typical compacting method. The testing instrument was a pressing machine.

Change trends of the specimen CBR under different fiber and asphalt contents. The test results are summarized in Table 6 and Figure 5:

For the microbond asphalt macadam specimens prepared with four different fiber contents, given the fiber content, the CBR increased first and then decreased with increasing asphalt content. In all these cases, peaks emerged and their change trends were roughly the same. The asphalt content corresponding to the CBR peak was determined as the optimal asphalt content. The results are summarized in Table 7.

*3.4. Specimen Preparation.* In this study, the cracking resistance of microbond asphalt macadam with four different fiber contents (0, 0.2%, 0.4%, and 0.6%, calculated by mass) was investigated according to relevant test codes and specifications. Molding was performed at around 160°C. The cylindrical specimens used in the compressive resilient modulus tests were 100 mm in diameter and height, and they were obtained through static molding. Four parallel specimens were prepared. The specimens used in the rutting tests were 100 mm × 100 mm × 50 mm in size (length × width × height). They were molded using the wheel rolling method and prepared with three parallel specimens. The semicircular

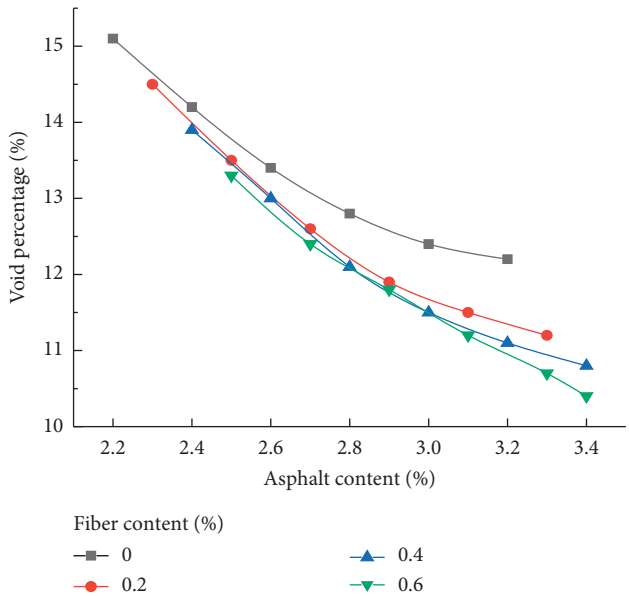


Figure 4: Void percentage.

Table 6: CBR values of specimens with different fiber contents.

| | | | | | | | |
|---|---|---|---|---|---|---|---|
| 0% basalt fiber content | Asphalt content (%) | 2.2% | 2.4% | 2.6% | 2.8% | 3.0% | 3.2% |
| | CBR (%) | 182 | 189 | 202 | 195 | 187 | 179 |
| 0.2% basalt fiber content | Asphalt content (%) | 2.3% | 2.5% | 2.7% | 2.9% | 3.1% | 3.3% |
| | CBR (%) | 191 | 200 | 212 | 208 | 196 | 186 |
| 0.4% basalt fiber content | Asphalt content (%) | 2.4% | 2.6% | 2.8% | 3.0% | 3.2% | 3.4% |
| | CBR (%) | 202 | 225 | 233 | 228 | 216 | 209 |
| 0.6% basalt fiber content | Asphalt content (%) | 2.5% | 2.7% | 2.9% | 3.1% | 3.3% | 3.4% |
| | CBR (%) | 197 | 209 | 219 | 212 | 201 | 195 |

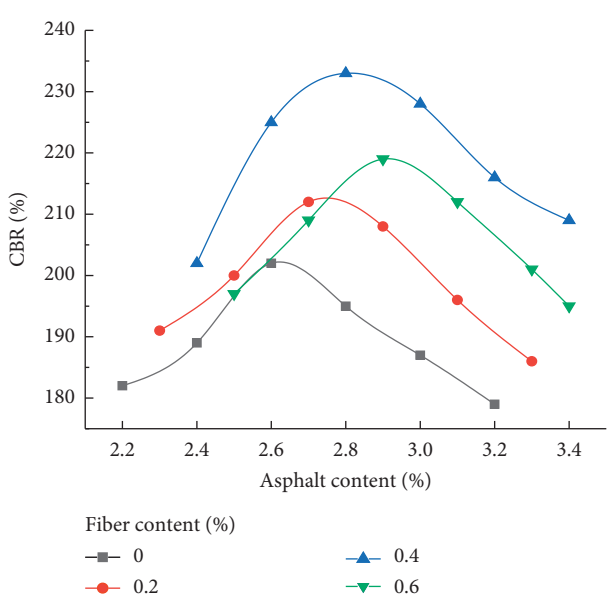


Figure 5: Relationship between CBR and fiber content.

Table 7: Optimal asphalt content of microbond asphalt macadam for different fiber contents.

| Fiber content (%) | 0 | 0.2 | 0.4 | 0.6 |
|---|---|---|---|---|
| Optimal asphalt content (%) | 2.6 | 2.7 | 2.8 | 2.9 |

specimens used in the semicircular bending tests were 101.6 mm in diameter and 50 mm in height. They were designed with a 1.5 cm kerf at the bottom, molded according to the typical compacting method, and prepared with three parallel specimens.

## 4. Pavement Performance Test on Microbond Asphalt Macadam

As the intermediate course, basalt fiber-reinforced microbond asphalt macadam must have adequate strength and modulus of elasticity and sound high-temperature stability and cracking resistance [29]. Thus, it is necessary to verify its pavement performance and propose an evaluation method.

*4.1. Compressive Resilient Modulus Test.* In this study, the uniaxial compression test method described in the Standard Test Methods of Bitumen and Bituminous Mixtures for Highway Engineering (JTGE20-2011) was adopted. A Mechanical Testing and Simulation was used to perform the compressive resilient modulus tests at a loading rate of 2 mm/min at 20°C. Before testing, the specimens were placed in a thermostatic water bath (20°C) for heat preservation for no less than 2.5 h; during heat preservation, a minimum spacing of 10 mm between specimens was maintained. A cylindrical specimen was randomly selected to measure the compressive stress at specimen failure. The compressive strength of the basalt fiber-reinforced microbond asphalt macadam specimen can be calculated according to the following equation:

$$R_c = \frac{4P}{\pi d^2}, \tag{1}$$

where $R_c$ is compressive strength of the specimen (MPa); $P$ is maximum load at specimen failure (N); and $d$ is specimen diameter (mm).

The $q_i$–$\Delta_{Li}$ curve is plotted and intersects with the axes, thus producing the correction origin. The fifth-level load and the corresponding $\Delta_L$ are obtained from the curve based on the origin coordinates. The compressive resilient modulus is calculated according to the following equation:

$$q_i = \frac{4P_i}{\pi d^2}, \tag{2}$$

$$E = \frac{q_s \times h}{\Delta L_S}, \tag{3}$$

where $q_i$ is pressure under applied load $P_i$, MPa; $P_i$ is load applied on the specimen, $N$; $E$ is compressive resilient modulus, MPa; $q_s$ is pressure under the fifth-level load (0.5 P), MPa; $h$ is axis height of the specimen; and $\Delta_{Ls}$ is rebound

deformation corrected by the origin under the fifth-level load (0.5 P).

*4.2. High-Temperature Rutting Test.* Rutting tests are most commonly used for evaluating the high-temperature stability of asphalt mixtures [30]. As required by related test specifications, the test temperature was set at 60°C, the reciprocating wheel pressure rate at 42 ± 1 times/min, and the wheel pressure at 0.7 ± 0.05 MPa. A rutting test machine was used, and the dynamic stability of the specimens was calculated using 45 min and 60 min rutting deformation values calculated according to the following equation:

$$DS = \frac{(t_2 - t_1) \times N}{d_2 - d_1} \times C_1 \times C_2, \quad (4)$$

where $DS$ is dynamic stability, time/mm; $d_1$ is deformation of the basalt fiber-reinforced microbond asphalt macadam specimen at rutting test time $t_1$, mm; $d_2$ is deformation of the basalt fiber-reinforced microbond asphalt macadam specimen at rutting test time $t_2$, mm; $C_1$, $C_2$ are test coefficients (based on the specimen preparation process for this test, $C_1 = C_2 = 1.0$); and $N$ is reciprocating rolling rate, usually set as 42 times/min.

*4.3. Cracking Test.* Semicircular bending tests are often used to evaluate the cracking resistance of asphalt mixtures [31]. In this study, the tests were conducted using a universal testing machine at a loading rate of 50 mm/min at 25°C until specimen failure. The work required to fracture the specimen completely (work of fracture $W_f$) can be determined from the area enclosed by the curve segment and the axes. The ratio of the work of fracture $W_f$ to the specimen ligament area denotes the fracture energy $G_f$, as shown by the following equations:

$$G_f = \frac{W_f}{\text{Area}_{lig}} \times 10^6. \quad (5)$$

$$\text{area}_{\text{lig}} = \text{length of tough zone} \times \text{t}, \quad (6)$$

where $G_f$ is fracture energy ($J/m^2$); $W_f$ is work of fracture ($J$); $\text{Area}_{\text{lig}}$ is area of tough zone ($mm^2$); and $t$ is specimen thickness (mm).

Studies have demonstrated that the postpeak slope |m| and the flexibility index (FI) can reflect the anticrack propagation performance of asphalt mixtures. |m| refers to the postpeak point at 75% of the peak load and is closer to the knee of the curve [11], as shown by the following equation:

$$FI = \frac{G_f}{|m|} \times A, \quad (7)$$

where FI is the flexibility index; $|m|$ is the absolute value of postpeak slope (kN/mm); and A is unit conversion, equal to 0.01.

## 5. Test Results and Analysis

*5.1. Relationship between Compressive Resilient Modulus and Fiber Content.* Molded specimens were tested using the uniaxial compression test method according to related test specifications. The uniaxial compression test results of microbond asphalt macadam specimens with different fiber contents are listed in Table 8.

As can be seen in Figure 6, when the fiber content increased within the range of 0–0.4%, the compressive resilient modulus of the material increased as well. When the fiber content was 0.4%, the compressive resilient modulus reached its peak value. When the fiber content exceeded 0.4%, the compressive resilient modulus decreased to some extent. This is attributed to that a suitable fiber content in microbond asphalt macadam plays bridging and reinforcing roles and timely transmits and disperses loads, thus making the stress applied to the basalt fiber-reinforced microbond asphalt macadam more uniform. Above the threshold of 0.4%, the distribution of fibers becomes less uniform, making the basalt fiber-reinforced microbond asphalt macadam prone to balling and resulting in a lower compressive resilient modulus.

*5.2. Effect of Fiber Content on High-Temperature Stability.* The tests were conducted according to the rutting test method described in the literature. The test results are listed in Table 9.

By analyzing the above rutting test results in Figure 7, the following can be found.

The dynamic stability of the specimens increased first and then decreased with increasing fiber content. Compared to an ordinary microbond asphalt macadam specimen, the dynamic stability of specimens with basalt fiber contents of 0.2%, 0.4%, and 0.6% increased by 14.8%, 26.7%, and 25.3%, respectively. This suggests that the addition of basalt fibers improved the high-temperature stability of microbond asphalt macadam, while the peak dynamic stability and optimal high-temperature stability was achieved when the fiber content was 0.4%.

*5.3. Cracking Test.* The cracking tests were carried out according to the semicircular bending test method described in the literature. The test results are listed in Table 10.

Effect of fiber content on the crack propagation performance of microbond asphalt macadam.

According to the comparison between Table 10 and Figures 8 and 9 , when the fiber content fell within the range of 0~0.4%, the work of fracture Wf and fracture energy Gf of the specimens were both positively correlated with fiber content. When the fiber content was 0.4%, both the work of fracture Wf and fracture energy Gf exhibited a peak and were increased by 29.7% compared to those of an ordinary microbond asphalt macadam. When the fiber content was further increased, the work of fracture Wf and fracture

Table 8: Uniaxial compression test results.

| Fiber content (%) | $E_c$ (MPa) | $E_c$ (MPa) |
|---|---|---|
| 0 | 335, 334, 331, 340 | 335 |
| 0.2 | 401, 404, 398, 413 | 404 |
| 0.4 | 491, 495, 499, 499 | 496 |
| 0.6 | 472, 475, 483, 474 | 476 |

$E_c$ is the compressive resilient modulus and $E_c$ is the mean compressive resilient modulus.

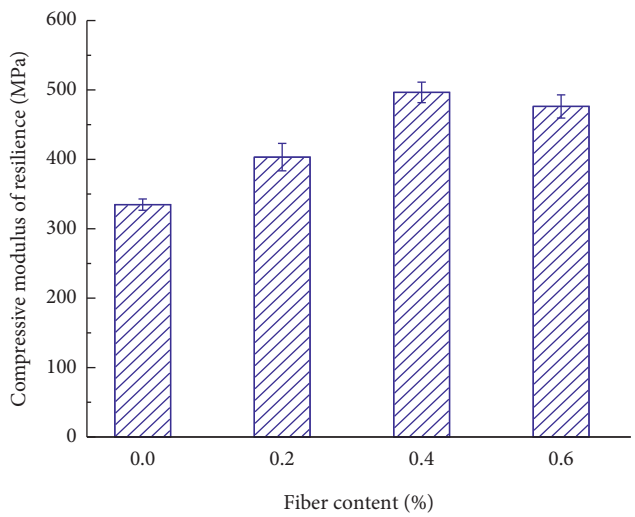


Figure 6: Relationship between compressive resilient modulus and fiber content.

Table 9: Rutting test results on microbond asphalt macadam specimens with different basalt fiber contents.

| Fiber content (%) | Optimal asphalt content (%) | $DS$ (time/min) | $\overline{DS}$ (time/min) |
|---|---|---|---|
| 0 | 2.7 | 2,061, 2,072, 2,053 | 2,062 |
| 0.2 | 2.8 | 2,378, 2,371, 2,355 | 2,368 |
| 0.4 | 2.9 | 2,611, 2,623, 2,602 | 2,612 |
| 0.6 | 3.0 | 2,576, 2,583, 2,593 | 2,584 |

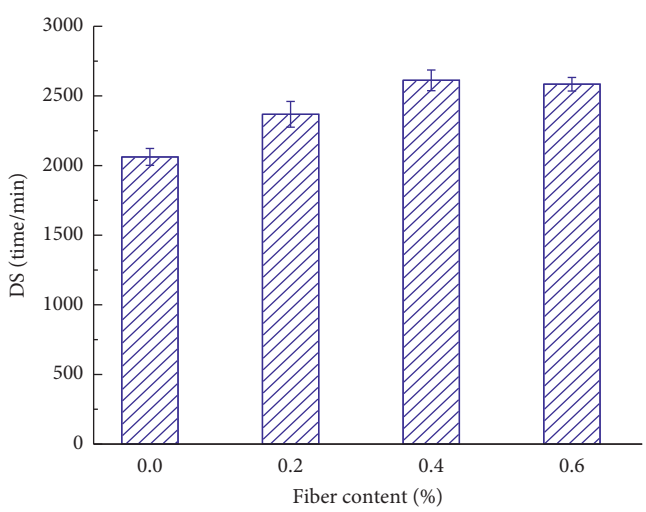


Figure 7: Effect of fiber content on dynamic stability.

Table 10: Semicircular bending test results of microbond asphalt macadam with different fiber contents.

| Fiber content (%) | $W_f$ ($j$) | $G_f$ ($j/m^2$) | $\lvert m \rvert$ | FI |
|---|---|---|---|---|
| 0 | 7.75, 7.48, 7.89 | 4,428.57, 4,274.29, 4,508.57 | 1.145, 1.152, 1.149 | 38.68, 37.10, 39.24 |
| 0.2 | 8.93, 9.22, 9.37 | 5,102.86, 5,268.57, 5,354.28 | 1.022, 1.016, 1.014 | 49.93, 51.85, 52.80 |
| 0.4 | 10.35, 10.13, 10.55 | 5,914.29, 5,788.57, 6,028.57 | 0.938, 0.943, 0.936 | 63.05, 61.39, 64.40 |
| 0.6 | 9.59, 9.63, 9.55 | 5,480.00, 5,502.86, 5,457.14 | 0.977, 0.975, 0.981 | 56.09, 56.44, 55.63 |

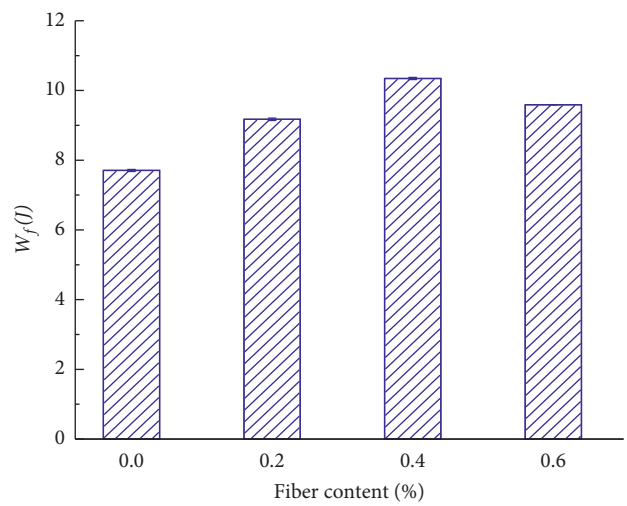


Figure 8: Work of fracture $W_f$ versus fiber content.

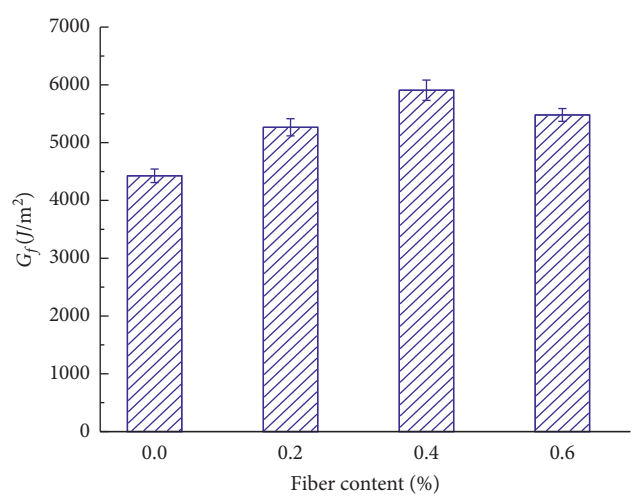


Figure 9: Fracture energy $G_f$ versus fiber content.

energy Gf decreased, suggesting that more work would be required to fracture the specimen with a fiber content of 0.4%. Table 10, Figure 10, and Figure 11 revealed that the

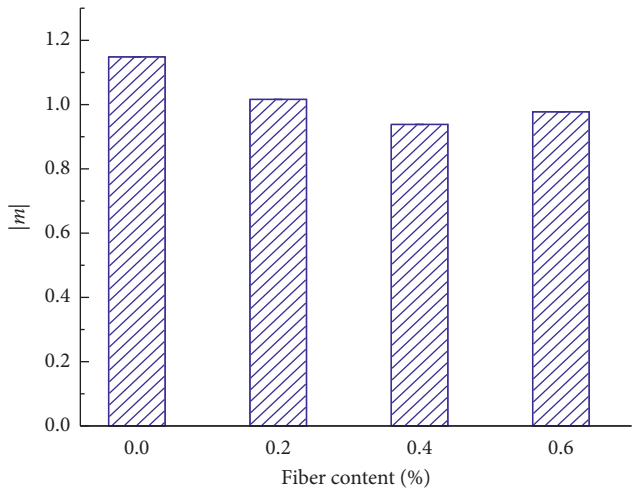


Figure 10: Slope versus fiber content.

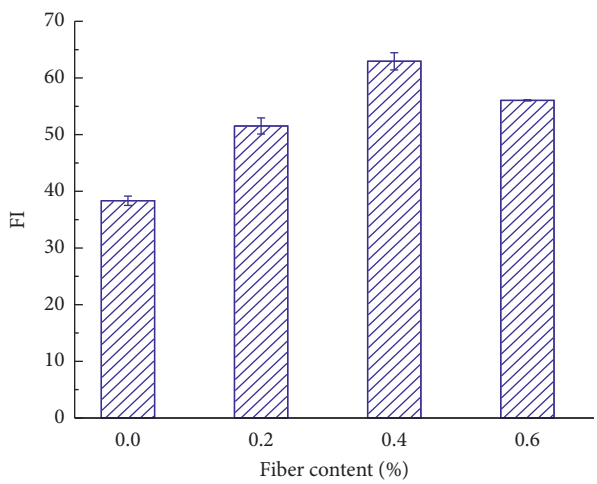


Figure 11: FI versus fiber content.

specimen postpeak slope |m| reached its minimum value when the fiber content was 0.4% and that the specimen FI also reached its maximum value when the fiber content was 0.4%; an improvement of 57.1% compared to those of an ordinary microbond asphalt macadam. This suggested that the fiber content of 0.4% was the most effective in slowing crack propagation; that is, it provided a microbond asphalt macadam with optimal cracking resistance.

## 6. Conclusions

This study mainly investigated the high-temperature stability and cracking resistance of basalt fiber-reinforced microbond asphalt macadam and analyzed the effects of fiber content on the compressive resilient modulus, dynamic stability, and flexibility index (FI). The conclusions are drawn as follows:

(1) The compressive resilient modulus, high-temperature rutting resistance, and cracking resistance of basalt fiber-reinforced microbond asphalt macadam were significantly affected by the basalt fiber content. In particular, they increased first and then decreased with increasing fiber content. This was mainly due to the fact that, under a high fiber content, the uniform distribution of the fibers was compromised, making the structure prone to agglomeration phenomena such as balling. As a result, the compressive resilient modulus, dynamic stability, and flexibility index (FI) presented a decreasing trend.

(2) The optimal fiber content for basalt fiber-reinforced microbond asphalt macadam was 0.4%. Compared to an ordinary microbond asphalt macadam, the cracking resistance of the basalt fiber-reinforced microbond asphalt macadam exhibited an improvement of 57.1%.

(3) In addition, while this study investigated the effect of fiber content on compressive resilient modulus, high-temperature stability, and cracking resistance, it did not take into account the effect of the gradation type of mineral aggregates on their cracking resistance. Considering the highly significant effects of gradation type on compressive resilient modulus, high-temperature stability, and cracking resistance, in future research, it will be necessary to optimize the design of gradation for the sake of improving the cracking resistance

## Data Availability

The data used to support the findings of this study are included within the article.

## Conflicts of Interest

The authors declare that they have no conflicts of interest.

## Authors' Contributions

Yan Xin and Ying Ronghua contributed equally to this paper.

## Acknowledgments

The work was financially supported by the Innovation-Driven Plan in Central South University (2020zzts159).

## References

[1] B. Peng, L. G. Li, and G. K. Yin, "Low cement dosage stabilized crushed stone gradation composition design and performance research," *Highway*, vol. 6, pp. 33–36, 2018.

[2] Y. Zhang, L. Jiang, W. Zhou, Y. Feng, Z. Tan, and X. Chai, "Study of bridge-subgrade longitudinal constraint range for high-speed railway simply-supported beam bridge with CRTSII ballastless track under earthquake excitation," *Construction and Building Materials*, vol. 241, Article ID 118026, 2020.

[3] L. Z. Jiang and Y. T. Zhang, "Simplified calculation modeling method of multi-span bridges on high-speed railways under

earthquake condition," *Bulletin of Earthquake Engineering*, vol. 18, no. 2, 2020.

[4] H. P. Li, F. Wang, and C. Li, "Analysis and research on the influence of basalt fiber on the performance of asphalt mixture," *China & Foreign Highway*, vol. 18, pp. 22–33, 2016.

[5] Z. Y. Yao and Y. J. Zhang, "Performance analysis of basalt fiber asphalt stabilized macadam," *Journal of Shandong University: Engineering Edition*, vol. 4, pp. 69–74, 2018.

[6] B. Peng, W. Gong, and X. G. Meng, "A study on gradation design method of micro asphalt gravel middle layer mixtures," *Journal of Wuhan University of Technology (Transportation Science&Engineering)*, vol. 25, pp. 259–263, 2018.

[7] L. Wang and Z. G. Liu, "Cracking cause and treatment measure of semi-rigid base asphalt pavement," *Journal of China&Foreign Highway*, vol. 5, pp. 84–86, 2020.

[8] J. G. Wei, Q. L. Fu, and J. D. Xu, "Effect of asphalt binder on pavement performance of asphalt macadam," *Journal of Highway and Transportation Research and Development*, vol. 11, pp. 1–8, 2014.

[9] D. Li, "Research on mechanical characteristics and design method of graded crushed stone material," *China and Foreign Highway*, vol. 19, pp. 102–106, 2017.

[10] B. Huang, X. Shu, and Y. Tang, "Comparison of semi-circular bending and indirect tensile strength tests for HMA mixtures," *Advances in Pavement Engineering*, vol. 81, pp. 1–12, 2019.

[11] C. Xia, S. Lv, M. B. Cabrera, X. Wang, C. Zhang, and L. You, "Unified characterizing fatigue performance of rubberized asphalt mixtures subjected to different loading modes," *Journal of Cleaner Production*, vol. 279, 2021.

[12] M. SheikllZadeh and S. Mahdi Hejazi, "Fiber-reinforced asphalt- concrete- a review," *Construction and Building Materials*, vol. 21, pp. 871–877, 2010.

[13] C. Liu, S. Lv, D. Jin, and F. Qu, "Laboratory investigation for the road performance of asphalt mixtures modified by rock asphalt/styrene butadiene rubber," *Journal Of Materials In Civil Engineering*, vol. 10, 2020.

[14] K. F. Li, *Research on the Design Method of Micro-asphalt Macadam Mix Ratio*, Chang'an University, Xi'an, China, 2014.

[15] F. Y. Wang, "Research on the design method of micro-asphalt macadam mix ratio," *China and Foreign Highway*, vol. 3, pp. 3–10, 2014.

[16] J. Han, X. F. Yu, and D. H. Zhou, "Study on the preparation technology and performance of basalt fiber reinforced high-viscosity asphalt mixture," *China and Foreign Highway*, vol. 58, pp. 217–220, 2015.

[17] X. J. Liu, "Research on the road performance of basalt fiber asphalt mixture," *China and Foreign Highway*, vol. 11, pp. 74–76, 2015.

[18] X. Qin, A. Q. Shen, and Y. C. Guo, "Experimental study on the performance of basalt fiber asphalt mortar," *Journal of Building Materials*, vol. 17, no. 4, 2016.

[19] H. Lu and X. N. Zhang, "application of mineral fiber asphalt mixture in long steep slope sections," *China and Foreign Highway*, vol. 25, pp. 84–86, 2017.

[20] Y. Y. Wang, "Research on the performance and design method of graded crushed stone base course," Master's Degree thesis, Southeast University, Nanjing, China, 2020.

[21] Z. G. Zhou, Y. Zeng, and X. K. Sun, "Research on mechanical properties of asphalt pavement cement modified graded gravel," *Transportation Science and Engineering*, vol. 35, pp. 84–86, 2012.

[22] B. Peng and S. J. Cao, "Study on the composition design and performance of a new type of asphalt-poor macadam," *Journal of Dalian University of Technology*, vol. 6, pp. 609–614, 2017.

[23] People's Communications Press, *The Ministry of Transport of the People's Republic of China. Code for Design of Highway Asphalt Pavement: JTG D50—2017*, People's Communications Press, Beijing, China, 2017.

[24] B. Y. Yu, M. J. Zhang, and T. W. Li, "Analysis of the micro bonding graded gravel asphalt pavement structure," *Journal of Shenyang Jianzhu University (Natural Science)*, vol. 42, no. 1, pp. 852–860, 2013.

[25] Z. J. Zhang, "Mitigation strategies for reflection cracking in rehabilitated pavements-A synthesis," *International Journal of Pavement Research and Technology*, vol. 5, pp. 284–286, 2016.

[26] J. Zhou, X. L. Wang, C. Y. Zheng, and X. C. Bao, "comparison of design methods of micro-bonded asphalt macadam mix ratio," *Journal of Wuhan University of Technology*, vol. 36, pp. 68–70, 2017.

[27] D. G. Sun, L. Peng, and F. J. Ni, "Re-search&application of inverted bituminous pave-ment structure in secondary road," *Communica-tions Standardization*, vol. 131, pp. 59–62, 2018.

[28] K. F. Liu, "Research on road performance of fiber asphalt mortar and asphalt mixture," *Journal of Chongqing Jiaotong University (Natural Science Edition)*, vol. 98, pp. 407–410, 2019.

[29] Q. Zheng, "Basalt fiber:perfect choice ofSMA and OGFC pavement," *Chin Highway*, vol. 65, pp. 5–8, 2018.

[30] P. Li, Z. Wu, and K. Ma, "Cracking resistant of asphalt mixture at the low temperature based on the SCB test," *Journal of Wuhan University of Technology:Transportation Science and Engineering*, vol. 66, pp. 238–241, 2019.

[31] S. Amarasiri, M. Gunaratne, and S. Sarkar, "Modeling of crack depths in digital images of concrete pavements using optical reflection properties," *Journal of Transportation Engineering*, vol. 38, pp. 489–499, 2020.

Hindawi
Advances in Civil Engineering
Volume 2021, Article ID 6619137, 10 pages
https://doi.org/10.1155/2021/6619137

*Research Article*

# A Car-Following Model Based on Safety Margin considering ADAS and Driving Experience

**Yugang Wang** [1,2] **and Nengchao Lyu** [1,2]

[1] *Intelligent Transportation Systems Research Center, Wuhan University of Technology, Wuhan 430063, China*
[2] *National Engineering Research Center for Water Transport Safety, Wuhan 430063, China*

Correspondence should be addressed to Nengchao Lyu; lnc@whut.edu.cn

Received 16 October 2020; Revised 29 January 2021; Accepted 8 February 2021; Published 19 February 2021

Academic Editor: Hui Yao



Existing studies had shown that advanced driver assistance systems (ADAS) and driver individual characteristics can significantly affect driving behavior. Therefore, it is necessary to consider these factors when building the car-following model. In this study, we established a car-following model based on risk homeostasis theory, which uses safety margin (SM) as the risk level quantization parameter. Firstly, three-way Analysis of Variance (ANOVA) was used to analyze the influencing factors of car-following behavior. The results showed that ADAS and driving experience have a significant effect on the drivers' car-following behavior. Then, according to these two significant factors, the car-following model was established. The statistical method was used to calibrate the parameter reaction response $\tau$. Other four parameters ($SM_{DL}$, $SM_{DH}$, $\alpha_1$, and $\alpha_2$) were calibrated using a classical genetic algorithm, and the effects of ADAS and driving experience in these four parameters were analyzed using $T$-test. Finally, the proposed model was compared with the GHR model, and the result showed that the proposed model has a smaller Root Mean Square Error (RMSE) than the GHR model. The proposed model is a method of simulating different driving behaviors that are affected by ADAS and individual characteristics. Considering more driver individual characteristics, such as driving style, is the future research goal.

## 1. Introduction

With the increasing number of vehicles, societies have been faced with significant challenges to congestion and traffic crashes. A recent report from World Health Organization [1] indicated that, annually, 1.24 million people die due to traffic crashes. Human factors are the most important cause of traffic accidents, and driver behavior plays a leading role in safe driving. Car-following behavior is one of the most common and important behaviors in the driving process, and it is closely related to traffic safety. Researchers have been studying the car-following process for more than half a century and have established a number of car-following models that focus on traffic flow theory, control algorithms, or driver psychology and physiology. These car-following models are important to ADAS, especially the ACC system [2, 3], and are considered to be key assessment tools for transportation systems [4, 5]. The existing car-following model mainly includes the CA model (collision avoidance model), which is based on maintaining a safe braking distance, and the GM model (stimulus-response model), which is based on a stimulus-response mechanism. The CA model calculates the specific theoretical safety following distance combined with vehicle braking performance and driver response time by using Newton's law of motion [6]. The GM model uses the relative speed between the leading and host vehicle as the stimulus standard, uses the host vehicle's acceleration and deceleration as the reaction situation, and introduces the sensitivity as the adjustment coefficient to study the relationship between the parameters in the car-following process [7]. These evaluation models effectively simulate the car-following behavior and determine how the car-following occurs in the actual scenario, but the reasons for the vehicles to follow each other in some way are not

discussed in depth. Hamdar et al. explained car-following behaviors based on the prospect theory and proposed a car-following model by evaluating the gains and losses while driving [8]. Wilde's risk homeostasis theory (RHT), another risk-taking theory, is also helpful in explaining car-following behaviors [9]. A car-following model based on risk perception, which is RHT and stimulus-response mechanism, helps understand car-following mechanisms and facilitate the simulation of car-following behaviors that differ depending on varied individual characteristics, which have different levels of acceptable risk [10].

To improve drivers' attention and perceptual ability, various Advanced Driver Assistance Systems (ADAS) were developed to provide drivers with correct preaccident human errors. ADAS are designed to complement driver capabilities for perception, cognition, action selection, and action implementation in a dynamic environment [11, 12]. For the influence of ADAS on driving behavior, many scholars have carried out research from different aspects. Blaschke et al. [13] tested the effectiveness of ADAS through Field Operational Tests (FOT) and found that the driver can more accurately estimate the distance to the leading vehicle after using ADAS and can maintain a safer time headway (THW) while driving. Saito et al. [11] conducted a simulated driving experiment to test the performance of ADAS through drivers awakening status and lane keeping performance. The results show that ADAS helps reduce traffic accidents, which is related to fatigue driving. Birrell et al. [14] tested ADAS through FOT. In their tests, after using ADAS, the driver's fuel efficiency increased by 4.1%, and the average THW increased to 2.3 seconds. Adell et al. [15] studied the effects of ADAS on the safety distance and safe speed of drivers through FOT. The results showed that both positive and negative effects existed. Lyu et al. [16] studied the effect of driving experience on the effectiveness of ADAS through FOT. The results showed that ADAS had a positive impact on skilled drivers and unskilled drivers, especially for unskilled drivers, in the following vehicle scenario. But in the braking scenario, ADAS had a positive impact on unskilled drivers but a negative impact on skilled drivers. Lyu et al. [17] evaluated the effectiveness of ADAS in improving driver's risk perception in near-crash events using a novel metric from risk homeostasis theory. The results show that ADAS has a positive impact on the low-risk group and moderate-risk group for all drivers, but a negative impact on the high-risk group for skilled drivers. These studies show that ADAS can significantly affect the driver's acceptable risk level, so it is necessary to consider the impact of ADAS when establishing a car-following model.

In addition, driver characteristics can significantly affect the effectiveness of ADAS, such as gender [18] and driving experience [19]. Existing studies had shown that driving experience has an impact on driving performance. Rich driving experience can make the excellent driving performance, which is related to the driver's learning process and experience [20]. Compared with skilled drivers, unskilled drivers take up more attention resources and cause higher workload [21], and the accident risk is 2–4 times higher [22]. In addition, gender is one of the most commonly measured variables in driving behavior researches, and it has been identified as a key demographic variable that affects driving performance [23]. Therefore, the driver characteristics should also be considered when establishing a car-following model.

This article analyzes which driver characteristics can significantly affect the driver's car-following behavior firstly. Then, we establish the car-following model based on significant influencing factors.

## 2. Database and Preparation

*2.1. Field Operational Tests Design.* Driving simulator [11] and Field Operational Tests [14] approaches were employed to study the influences of ADAS to driver behavior. With the development of intelligent vehicles and the application of vehicle sensors, it is becoming a trend to evaluate the effect of ADAS with Field Operational Tests. Hence, an instrumented vehicle, which is equipped with ADAS, was developed to carry out Field Operational Tests on a variety of roads in Wuhan, China.

44 participants (24 males, 20 females) were recruited in these Field Operational Tests. Their age ranged from 22 to 55 years old (mean = 32.2; SD = 8.2). On average, they had 6.9 years of driving experience, ranging from 2 to 18 years. It should be noted that, in China, many people obtain their driver's license but do not obtain actual driving experience. In order to avoid interfering with the credibility of the experiment, this research used a driver's total driving mileage rather than his/her driving license age as an indicator of proficiency. In terms of driving mileage, participants drove an average of 110,000 kilometers, ranging from 400 to 400,000 kilometers. In this study, drivers with a total driving range of more than 40,000 kilometers were defined as skilled drivers, while those with less than 40,000 kilometers were defined as unskilled drivers. There were 22 skilled drivers and 22 unskilled drivers in the recruited participants.

An instrumented vehicle has been developed to collect complete coverage of data on drivers' behavior, vehicle kinematics, and vehicle surroundings. The main equipment of the instrumented vehicle is shown in Figure 1. Mobileye was used to obtain headway and lane position, as well as to alert forward collision and lane departure. One video camera was used to collect vehicle surroundings video information. The INS system was used to obtain the vehicle's three-axis acceleration, latitude, and longitude. Lidar was used to obtain the forward target information (distance, velocity, relative velocity, etc.). The CAN bus was used to obtain vehicle data such as vehicle speed, accelerator pedal information, brake pedal information, and steering wheel angle. All data was synchronized with the master time that was transmitted by the monitoring software every 0.1 s.

*2.2. Extraction of the Car-following Data.* Based on LiDAR and CAN bus data, the car-following segments were extracted. Table 1 summarized the rules used to extract the car-following segments from existing studies.

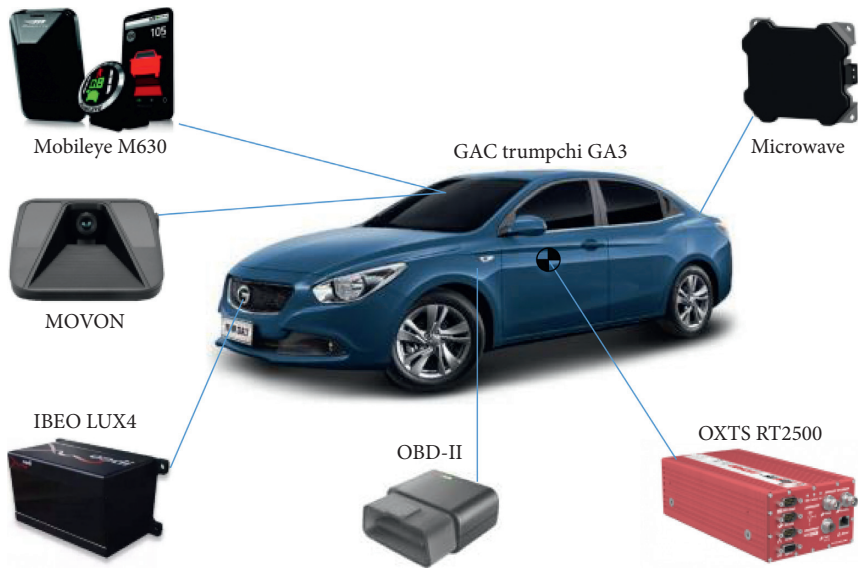


Figure 1: Equipment of instrumented vehicle.

Table 1: Summary of car-following event extraction criteria in the existing literature.

| | Absolute lateral distance (m) | Host vehicle speed (km/h) | Longitudinal distance (m) | Relative velocity (m/s$^2$) | Segment duration (s) |
|---|---|---|---|---|---|
| Leblanc et al. [24] | | >40 | | <2.0 | >15 |
| Chong et al. [25] | <1.9 | >20 | <120 | | >30 |
| Ervin et al. [26] | | >40 | | <2.0 | |
| Wang et al. [27] | <2.5 | >18 | >7 and <120 | <2.5 | >15 |

The key to the extraction of car-following segments is the setting of the threshold values. Due to the differences in traffic environment and driving behaviors between domestic and foreign, the threshold value in the literature could only be used as a reference, and it needs to be revised according to the data of these FOTs. According to the distribution range of each parameter in the FOTs data and the threshold values in the existing literature, the threshold values of the various car-following extraction rules in this study are determined as follows:

(1) Absolute lateral distance is <2.5 m, which ensures that the target vehicle is in the same lane as the experimental vehicle.

(2) The longitudinal distance is <120 m, and the host vehicle speed is >20 km/h. These two rules can eliminate traffic flow conditions of congestion and free flow, and the congestion is excluded when the host vehicle speed >20 km/h. The distance between two vehicles in free flow is too large, in which case the leading vehicle cannot restrict the driving behavior of the host vehicle, so a longitudinal distance <120 m is required.

(3) The absolute value of longitudinal relative velocity is <2.5 m/s$^2$, and the absolute value of relative velocity is small enough to ensure that the vehicle is in a stable car-following state.

(4) The segment duration should be more than 30 seconds to ensure the stability of the car-following status.

According to the above four extracting thresholds, 354 car-following segments were extracted from FOTs.

*2.3. Risk Perception Quantification Index.* We need a risk level quantitative parameter to describe the driver's risk perception changes in the car-following process. Commonly used risk level quantization parameters are Time Headway (THW) and Time to Collision (TTC). But THW and TTC have limitations as traditional indicators of risk quantification. THW retains only the vehicle speed information and does not consider the impact on relative speed, while TTC retains only the relative speed information and does not take into account the impact of the vehicle speed. Additionally, the expected means of THW and TTC are quite different between drivers with different characteristics [28] Therefore, there is a need for an indicator that is consistent between drivers with different characteristics to evaluate the effectiveness of ADAS. This indicator should take into account the impact of speed and relative speed. The safety margin proposed by the risk homeostasis theory (RHT) [29] is a suitable indicator. Nilsson [30] suggested that "everything in the driver's visual field that could be an obstacle or a threat is surrounded by zones, that is,

safety margins." In the driver's control system, the safety margin (SM) is defined as the threshold that protects the driver from danger [17]. The SM is independent of the actual driving situation. In accordance with that definition, the SM should have the following features: (a) it should be a monotonic function of the objective risk level; (b) drivers should have a fixed acceptable SM to guide their behaviors; and (c) an acceptable SM varies depending on the driver's characteristics; however, a certain type of driver (such as a highly skilled driver) should have a similar acceptable SM.

According to the barking process of the car-following task, the risk level can be defined as [31]

$$\xi(\tau,t)=\frac{V_1(t)\cdot\tau+\left([V_1(t)]^2/2a_1(t)\right)-\left([V_2(t)]^2/2a_2(t)\right)}{D_1(t)}. \tag{1}$$

In the above formula, $V_1(t)$ is the host vehicle's speed. $V_2(t)$ is the lead vehicle's speed. $a_1(t)$ is the car-following's acceleration; $a_2(t)$ is the lead vehicle's acceleration; $D_1(t)$ is the relative spacing between the two vehicles. $\tau$ is the reaction time, which consisted of the driver's reaction time $\tau_1$ and the braking system's reaction time $\tau_2$. This formula shows that when one vehicle was following another, the lead vehicle emergency brake could be applied until its speed dropped to zero. The driver of the car-following could observe the brake light signal of the lead vehicle and respond quickly. The distance the car-following passes is expressed as $V_1(t)\cdot\tau+([V_1(t)]^2/2a_1(t))$, and the distance the lead vehicle passes is expressed as $[V_2(t)]^2/2a_2(t)$. In this case, the quantitative objective driving risk level can be expressed as the difference between the distance and the relative spacing at time $t$. In this study, the formula was changed based on elements of driver and vehicle system factors:

$$\xi(\tau,t)=\xi(\tau_2,t)+\frac{V_1(t)\cdot\tau_1}{D_1(t)}. \tag{2}$$

Basing driving simulator on that definition, traffic safety can be ensured when $\xi(\tau,t)\le 1$. It is important to note that, in a real-world scenario, it is possible that $\xi(\tau,t)>1$; however, no accident will occur in some circumstances. This is because the absolute value of the acceleration of the car-following is greater than that of the lead vehicle. However, if the lead vehicle brakes by the maximum deceleration at this time, a rear-end crash will still occur even if the car-following brakes at the maximum deceleration.

Therefore, under ideal conditions,

$$\frac{V_1(t)\cdot\tau_1}{D_1(t)}\le 1-\xi(\tau_2,t). \tag{3}$$

From here, the SM can be defined as

$$\mathrm{SM}(t)=1-\xi(\tau_2,t). \tag{4}$$

According to previous research, the limit value of the acceleration of the vehicle is 0.3 G–0.75 G [32]. Combining the FOTs on the actual road, deceleration in the calculation of risk was set as

$$a_1(t)=a_2(t)=7.0\,\mathrm{m/s^2}. \tag{5}$$

Braking system response time is usually between 0.10 and 0.30 s. During emergency situations, a driver may quickly and strongly apply the brakes. Thus, $\tau_2$ was set as 0.15 s.

Therefore, the SM can be calculated by the following formula:

$$\mathrm{SM}(t)=1-\xi(0.15,t)=1-\frac{0.15*V_1(t)+\left([V_1(t)]^2/14\right)-\left([V_2(t)]^2/14\right)}{D_1(t)}. \tag{6}$$

According to the definition, the smaller the SM is, the higher the objective risk level is, which means that the risk of rear-end is higher. In the next section, each car-following segment will calculate the mean value of SM. Based on the ANOVA of the mean value of SM, the significant influencing factors to driver's car-following behavior can be obtained.

*2.4. Factors Affecting Car-Following Behavior.* Before the analysis of variance, judging by box figure, there is no abnormal data value, and after Shapiro-Wilk test, all groups of $\mathrm{SM_{mean}}$ are of normal distribution ($P>0.05$). Furthermore, $P$ value of Levene homogeneity test of variance is 0.130, which is greater than 0.05, and it is believed that the dependent variables in each classification have equal variance. According to the above test, the data obey normal distribution, have no abnormal value, and have equal variance, so the three-way ANOVA can be analyzed.

The results of three-way ANOVA are shown in Table 2.

The results of three-way ANOVA showed that ADAS, gender, and driving experience did not have the interaction between three factors on the $\mathrm{SM_{mean}}$, $F$ (2, 129) = 0.454, $P$ = 0.636. In the interaction between two factors, the influence of ADAS* gender on the dependent variable was not statistically significant, $F$ (1, 129) = 0.824, $P$ = 0.193; the influence of ADAS*driving experience on the dependent variable was statistically significant, $F$ (1, 129) = 0.001, $P$ = 11.841; the influence of gender*driving experience on the dependent variable was not statistically significant, $F$ (1, 129) = 0.505, $P$ = 0.688. In the main effect, ADAS has no main effect on the dependent variable, $F$ (1, 129) = 0.017, $P$ = 0.896; the gender has no main effect on the dependent

Table 2: Three-way ANOVA results for $SM_{mean}$.

| Source | Type III sum of squares | df | Mean square | $F$ | Sig |
|---|---|---|---|---|---|
| ADAS | 0.000 | 1 | 0.000 | 0.017 | 0.896 |
| Gender | 0.075 | 1 | 0.037 | 2.538 | 0.085 |
| Driving experience | 0.016 | 1 | 0.016 | 4.159 | **0.043*** |
| ADAS*gender | 0.002 | 1 | 0.001 | 0.193 | 0.824 |
| ADAS*driving experience | 0.046 | 1 | 0.046 | 11.841 | **0.001**** |
| Gender*driving experience | 0.005 | 1 | 0.003 | 0.688 | 0.505 |
| ADAS* gender * driving experience | 0.004 | 2 | 0.002 | 0.454 | 0.636 |

***Sig. < 0.001, **sig. < 0.01, and *sig. < 0.05.

variable, $F$ (1, 129) = 2.538, $P$ = 0.085; the driving experience has a main effect on the dependent variable, $F$ (1, 129) = 4.159, $P$ = 0.043.

The results of ANOVA showed that only driving experience can significantly affect the driver's car-following behavior, but in the interaction between two factors, the influence of ADAS*driving experience on the dependent variable was statistically significant. Therefore, the effect of ADAS on the car-following behavior cannot be ignored. The subsequent model will take into account the factors of ADAS and driving experience.

## 3. Car-Following Model Based on Risk Perception

*3.1. Model Assumptions.* When the driver follows another vehicle, he will adjust the relative spacing to ensure an acceptable level of risk. That is, the driver of the following vehicle responds to the difference between the perceived safety margin (perceived risk level) and the desirable safety margin (DSM), as the driver of the following vehicle decides to accelerate (perceived safety margin is greater than DSM), decelerate (perceived safety margin is less than DSM), or maintain a constant speed (perceived safety margin is within DSM) [10]. Since the proposed model is based on the difference between the driver's DSM and the perceived safety margin, it is called the DSM model.

The DSM model for car-following is described as follows:

$$a_n(t+\tau) = f\left(\mathrm{SM}(t) - \mathrm{SM}_D\right) = \begin{cases} \alpha_1\left(\mathrm{SM}(t) - \mathrm{SM}_{\mathrm{DH}}\right), & \mathrm{SM}(t) > \mathrm{SM}_{\mathrm{DH}}, \\ \alpha_2\left(\mathrm{SM}(t) - \mathrm{SM}_{\mathrm{DL}}\right), & \mathrm{SM}(t) < \mathrm{SM}_{\mathrm{DL}}, \\ 0, & \text{else}, \end{cases} \tag{7}$$

where $a_n(t)$ is the acceleration of a following car at time $t$. $\mathrm{SM}_{\mathrm{DH}}$ is the upper limit of the DSM, and $\mathrm{SM}_{\mathrm{DL}}$ denotes the lower limit of the DSM. The goal of our modeling is to describe natural driving, and DSM may change due to psychological factors. However, in the simulation used to analyze the main factors affecting the automatic tracking process, the random factors can be ignored, so in the specific traffic environment, for the same type of driver, $\mathrm{SM}_{\mathrm{DH}}$ and $\mathrm{SM}_{\mathrm{DL}}$ can be constant values. $\alpha_1$ and $\alpha_2$ are the sensitivity factors for acceleration and deceleration, where $\alpha_1 > 0$, $\alpha_2 > 0$.

According to previous research, the limit value of the acceleration of the vehicle is 0.3 G–0.75 G [30], so the maximum deceleration is set as 7.0 m/s$^2$. If $a_n(t) < -7.0$ m/s$^2$, then $a_n(t) = -7.0$ m/s$^2$. Maximum favorite acceleration is set as 3.0 m/s$^2$. If $a_n(t) > 3.0$ m/s$^2$, then $a_n(t) = 3.0$ m/s$^2$.

Because of the simulated time interval, the result of calculated speed may be negative when the speed is close to zero in numerically updated process. Thus, the minimum speed of the following car is set as $V(t) = 0.0$ m/s, if $V_n(t) < 0.0$ m/s, $V_n(t) = 0.0$ m/s.

*3.2. Model Calibration.* According to the car-following model, a total of five parameters need to be calibrated: response time $\tau$, DSM lower limit $\mathrm{SM}_{\mathrm{DL}}$, DSM upper limit $\mathrm{SM}_{\mathrm{DH}}$, acceleration sensitivity coefficient $\alpha_1$, and deceleration sensitivity coefficient $\alpha_2$.

The response time is the reaction time of the following vehicle. According to the existing research, the reaction time in the car-following process can be determined by comparing the relative speed curve and the acceleration curve of following vehicle [33]. According to the theory of the stimulus-response model [34], the acceleration of the following vehicle is determined by the relative speed of the two vehicles; that is, the relative speed change (stimulus) will cause a corresponding change (reaction) of the following vehicle's acceleration after a certain time delay, and this delay is the car-following reaction time.

From the extracted 354 car-following events, the reaction time of each pair of stimulus-response points was extracted, and the mean value was calculated according to whether or not to use ADAS and driving experience, respectively. When ADAS is off, the average response time of

unskilled drivers is 1.5 s, and the average response time of skilled drivers is 1.3 s. This is because, without the support of ADAS, unskilled drivers need to take more attention resources and cause higher workload when handling driving tasks, so the response time is slower than that of skilled drivers. After exposure to ADAS, the average response time of unskilled drivers is 1.0 s, and the average response time of skilled drivers is 0.9 s. After exposure to ADAS, the response time of skilled drivers and unskilled drivers will be shortened, and the change of unskilled drivers is more obvious. This phenomenon indicates that ADAS has more influence on skilled drivers than unskilled drivers, consistent with the existing research [35].

The remaining four parameters, DSM lower limit $SM_{DL}$, DSM upper limit $SM_{DH}$, acceleration sensitivity coefficient $\alpha_1$, and deceleration sensitivity coefficient $\alpha_2$, cannot be directly derived using statistical methods; therefore, we denote them as a vector, $\mathbf{V} = (SM_{DL}, SM_{DH}, \alpha_1, \alpha_2)$. The target of calibration is to obtain a vector $\mathbf{V}$, which can minimize the difference between measured and simulated trajectories.

The genetic algorithm is a nonlinear optimization algorithm that simulates biological evolution and has been widely used to solve complex nonlinear optimization problems. It is also used to calibrate the vehicle model [10]. Therefore, we used the genetic algorithm to calibrate the parameter vector $\mathbf{V}$ of the car-following model. With the relative distance, the following vehicle speed and the following vehicle acceleration are common indicators used to evaluate the car-following model, so, we defined the difference parameter $F$ as the fitness function of the genetic algorithm based on these three parameters. The difference parameter $F$ is calculated as follows:

$$dF(t) = \frac{\left(|v_s(t) - v_r(t)|/v_r(t)\right) + \left(\left|d_s(t) - d_r(t)\right|/d_r(t)\right) + \left(\left|a_s(t) - a_r(t)\right|/a_r(t)\right)}{3},$$
$$F = \frac{1}{N}\sum_{t=1}^{N} dF(t), \tag{8}$$

where $v_s(t)$ represents the simulated speed of the following vehicle at time $t$, $v_r(t)$ represents the real speed of the following vehicle at time $t$, $d_s(t)$ represents the simulated relative spacing at time $t$, and $d_r(t)$ represents the real relative spacing at time $t$; $a_s(t)$ represents the simulated acceleration of the following vehicle at time $t$; $a_r(t)$ represents the real acceleration of the following vehicle at time $t$; $N$ represents the sampling points number during this car-following event. The genetic algorithm is used to find a vector $p$ to minimize the fitness function $F$.

According to the definition of fitness function, one parameter vector $\mathbf{V}$ can be obtained in one car-following event. Therefore, in the extracted 354 car-following events, 354 parameter vectors $\mathbf{V}$ can be obtained, of which unskilled drivers with ADAS OFF have 85 cases, skilled drivers with ADAS OFF have 93 cases, unskilled drivers with ADAS ON have 86 cases, and skilled drivers with ADAS ON have 90 cases. In the next section, these four parameters of the parameter vector $\mathbf{V}$ will carry out $t$-test, respectively.

As shown in Table 3, the test result of $SM_{DL}$ shows that there is a statistically significant difference between the $SM_{DL}$ of skilled drivers and unskilled drivers during naturalistic driving (ADAS OFF). The $SM_{DL}$ of unskilled drivers is significantly affected by the ADAS, and the $SM_{DL}$ of skilled drivers is also significantly affected by the ADAS, which indicates that ADAS can significantly affect the drivers' $SM_{DL}$. In terms of mean value, the $SM_{DL}$ of skilled driver rose from 0.718 to 0.756 after exposure to ADAS, and the $SM_{DL}$ of unskilled driver rose from 0.740 to 0.752 after exposure to ADAS, indicating that, in terms of $SM_{DL}$, ADAS has a greater impact on skilled drivers than unskilled drivers.

As shown in Table 4, the test result of $SM_{DH}$ shows that there is a statistically significant difference between the $SM_{DH}$ of skilled drivers and unskilled drivers during naturalistic driving. After exposure to ADAS, there is also a statistically significant difference between the $SM_{DH}$ of skilled drivers and unskilled drivers. This shows that skilled drivers have higher $SM_{DH}$ than unskilled drivers, and ADAS has no significant effect on $SM_{DH}$ to both skilled drivers and unskilled drivers.

As shown in Table 5, the test result of $\alpha_1$ shows that there is a significant statistical difference between $\alpha_1$ of skilled drivers and unskilled drivers during naturalistic driving. After exposure to ADAS, there is also a statistically significant difference between the $\alpha_1$ of skilled drivers and unskilled drivers. Unskilled drivers have more rapid acceleration due to insufficient control of the throttle, so the average value of $\alpha_1$ is greater than skilled drivers. In terms of $\alpha_1$, ADAS has no significant effect on skilled drivers and unskilled drivers.

As shown in Table 6, the test results of $\alpha_2$ show that there is a significant statistical difference between $\alpha_2$ of skilled drivers and unskilled drivers during naturalistic driving. The $\alpha_2$ of unskilled drivers was significantly affected by the ADAS. Unskilled drivers have more sharp decelerations than skilled drivers because of lack of perceived ability, so the $\alpha_2$ is greater than that of skilled drivers during naturalistic driving. After exposure to ADAS, the $\alpha_2$ of unskilled drivers fall to the same level as skilled drivers'. It is worth

Table 3: $T$-test result of $SM_{DL}$.

| | | ADAS OFF | | ADAS ON | |
|---|---|---|---|---|---|
| | | Skilled drivers | Unskilled drivers | Skilled drivers | Unskilled drivers |
| ADAS OFF | Skilled drivers (mean value: 0.718) | — | **0.026*** | **0.035*** | — |
| | Unskilled drivers (mean value: 0.740) | **0.026*** | — | — | **0.002**** |
| ADAS ON | Skilled drivers (mean value: 0.756) | **0.035*** | — | — | 0.561 |
| | Unskilled drivers (mean value: 0.752) | — | **0.002**** | 0.561 | — |

***Sig. < 0.001, **sig. < 0.01, and *sig. < 0.05.

Table 4: $T$-test result of $SM_{DH}$.

| | | ADAS OFF | | ADAS ON | |
|---|---|---|---|---|---|
| | | Skilled drivers | Unskilled drivers | Skilled drivers | Unskilled drivers |
| ADAS OFF | Skilled drivers (mean value: 0.718) | — | **0.015*** | 0.125 | — |
| | Unskilled drivers (mean value: 0.740) | **0.015*** | — | — | 0.224 |
| ADAS ON | Skilled drivers (mean value: 0.756) | 0.125 | — | — | **0.024*** |
| | Unskilled drivers (mean value: 0.752) | — | 0.224 | **0.024*** | — |

***Sig. < 0.001, **sig. < 0.01, and *sig. < 0.05.

Table 5: $T$-test result of $\alpha_1$.

| | | ADAS OFF | | ADAS ON | |
|---|---|---|---|---|---|
| | | Skilled drivers | Unskilled drivers | Skilled drivers | Unskilled drivers |
| ADAS OFF | Skilled drivers (mean value: 0.926) | — | **0.017*** | 0.235 | — |
| | Unskilled drivers (mean value: 0.974) | **0.017*** | — | — | 0.314 |
| ADAS ON | Skilled drivers (mean value: 0.929) | 0.235 | — | — | **0.033*** |
| | Unskilled drivers (mean value: 0.976) | — | 0.314 | **0.033*** | — |

***Sig. < 0.001, **sig. < 0.01, and *sig. < 0.05.

Table 6: $T$-test result of $\alpha_2$.

| | | ADAS OFF | | ADAS ON | |
|---|---|---|---|---|---|
| | | Skilled drivers | Unskilled drivers | Skilled drivers | Unskilled drivers |
| ADAS OFF | Skilled drivers (mean value: 12.021) | — | **0.044*** | 0.235 | — |
| | Unskilled drivers (mean value: 12.884) | **0.044*** | — | — | **0.045*** |
| ADAS ON | Skilled drivers (mean value: 12.075) | 0.235 | — | — | 0.033 |
| | Unskilled drivers (mean value: 12.126) | — | **0.045*** | 0.033 | — |

***Sig. < 0.001, **sig. < 0.01, and *sig. < 0.05.

noting that ADAS has no significant effect on skilled drivers in terms of $\alpha_2$.

In order to reduce the influence of sampling error on the model, the parameters that have insignificant $T$ test results adopt overall mean. The parameters that have significant $T$ test results adopt mean of each part. The parameter vector is as follows: skilled driver under ADAS OFF $\mathbf{V_1} = (1.3, 0.718, 0.927, 6.446, 12.072)$, unskilled driver under ADAS OFF $\mathbf{V_2} = (1.5, 0.740, 0.975, 6.860, 12.884)$, skilled driver under ADAS ON $\mathbf{V_3} = (0.9, 0.754, 0.927, 6.446, 12.072)$, and unskilled driver under ADAS ON $\mathbf{V_4} = (1.0, 0.754, 0.975, 6.860, 12.072)$.

*3.3. Model Validation.* In this section, the proposed model is validated in real car-following events data and then compared with the Gazis Herman Rothery (GHR) model. GHR model is an effective car-following model by producing lower percentile errors for speed and acceleration predictions. The GHR model is formulated as follows [36]:

$$a_n(t) = c v_n^m(t) \frac{v(t-\tau)}{x^l(t-\tau)}, \tag{9}$$

where $a_n(t)$ is the acceleration of vehicle $n$ (following vehicle) implemented at time $t$, $V_n(t)$ is the speed of the following vehicle, $\Delta x$ and $\Delta v$ refer to the relative distance and speed between the following vehicle and the $(n+1)$ vehicle (leading vehicle), $\tau$ is the driver reaction time, and $m$, $l$, and $c$ represent the constants.

Four typical types of car-following data (2 (ADAS) $*$ 2 (driving experience)) were randomly selected from the database. The simulation results of the proposed model and the GHR model were shown in Figure 2. The Root Mean Square Error (RMSE) was shown in Table 7. From the RMSE

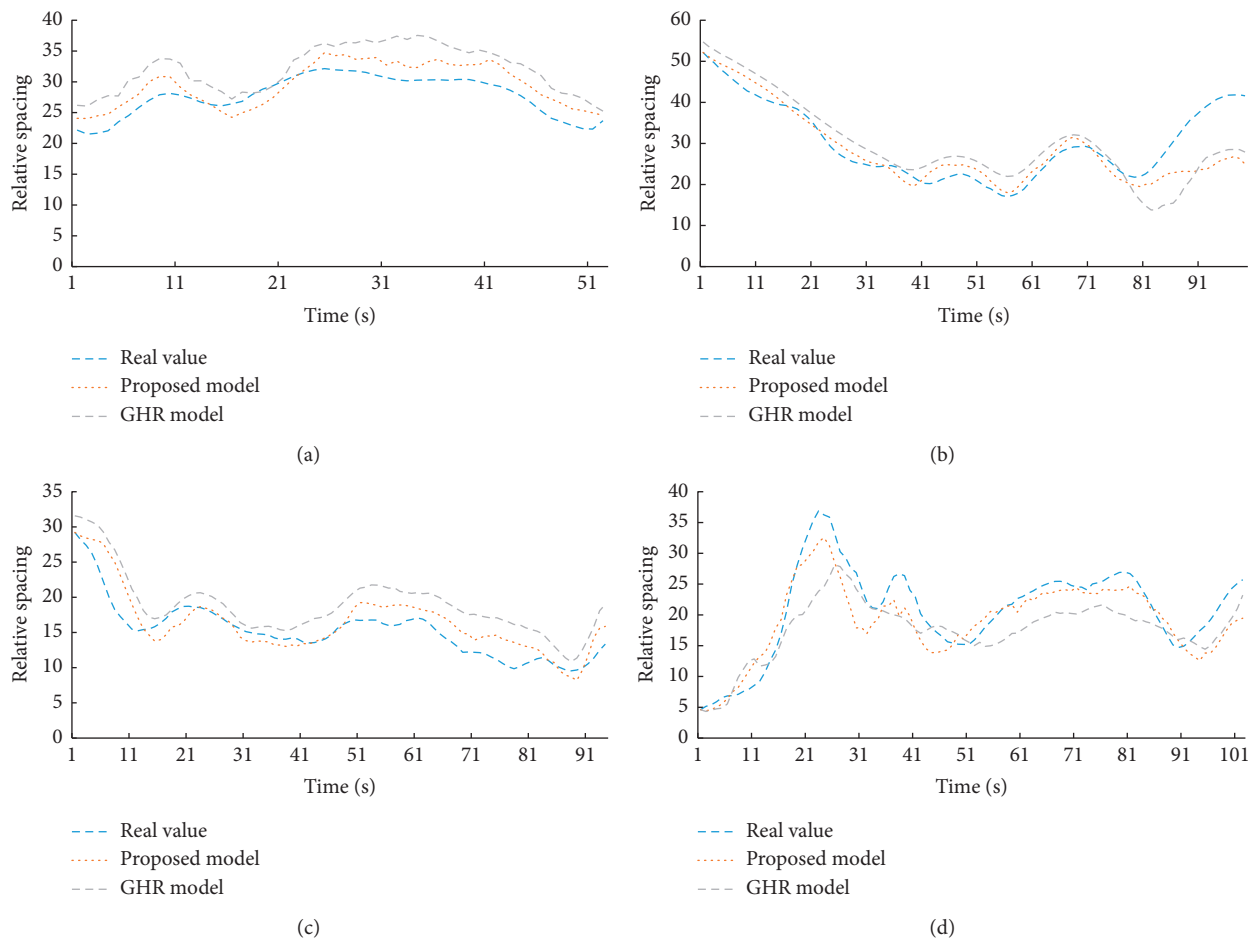


Figure 2: Simulation results of proposed model and GHR model. (a) Skilled driver under ADAS OFF. (b) Unskilled driver under ADAS OFF. (c) Skilled driver under ADAS ON. (d) Unskilled driver under ADAS ON.

Table 7: RMSE of the proposed model and the GHR model.

| | ADAS OFF | | ADAS ON | |
|---|---|---|---|---|
| | Unskilled driver | Skilled driver | Unskilled driver | Skilled driver |
| Proposed model | 5.61 | 2.39 | 3.26 | 2.29 |
| GHR mode | 6.68 | 4.68 | 4.72 | 4.08 |

of the simulation results, it can be seen that the proposed model is better than the GHR model.

## 4. Conclusion

In this study, a total of 354 car-following events were extracted from 87 times of FOTs. Based on these data, we established a car-following model using SM as the risk level quantization parameter based on risk homeostasis theory. Firstly, three-way ANOVA was used to analyze the three independent variables (ADAS, driving experience, and gender). The results showed that ADAS and driving experience have a significant effect on the drivers' car-following behavior. Then, according to these two significant factors, the car-following model was established. In the calibration process of the five model parameters ($\tau$, $SM_{DL}$, $SM_{DH}$, $\alpha_1$, and $\alpha_2$), the statistical method was used to calibrate the first parameter reaction response $\tau$. The remaining four parameters were calibrated using a classical genetic algorithm, and the effects of ADAS and driving experience on these four parameters were analyzed using $T$-test. Finally, the proposed model was compared with the GHR model, which was adopted by most ACC systems. The result showed that the proposed model has smaller RMSE than the GHR model. The proposed model is a method for simulating different driving behaviors that are affected by ADAS and individual

characteristics. Considering more driver individual characteristics, such as driving style, is the future researches goal.

## Data Availability

The data used to support the findings of this study are available from the corresponding author upon request.

## Conflicts of Interest

The authors declare no conflicts of interest.

## Acknowledgments

This research was funded by the National Nature Science Foundation of China (Nos. 51775396 andNo. 52072290), Hubei Province Science Fund for Distinguished Young Scholars (No. 2020CFA081), and the Fundamental Research Funds for the Central Universities (No. 191044003, No. 2020-YB-028).

## References

[1] World Health Organization, *Global Status Report on Road Safety 2017*, World Health Organization, Geneva, Switzerland, 2017.

[2] J. Mar and H.-T. Lin, "A car-following collision prevention control device based on the cascaded fuzzy inference system," *Fuzzy Sets and Systems*, vol. 150, no. 3, pp. 457–473, 2005.

[3] J. Wang, L. Zhang, D. Zhang, and K. Li, "An adaptive longitudinal driving assistance system based on driver characteristics," *IEEE Transactions on Intelligent Transportation Systems*, vol. 14, no. 1, pp. 1–12, 2013.

[4] S. Panwai and H. Dia, "Comparative evaluation of microscopic car-following behavior," *IEEE Transactions on Intelligent Transportation Systems*, vol. 6, no. 3, pp. 314–325, 2005.

[5] C. Wang and B. Coifman, "The effect of lane-change maneuvers on a simplified car-following theory," *IEEE Transactions on Intelligent Transportation Systems*, vol. 9, no. 3, pp. 523–535, 2008.

[6] E. Kometani and T. Sasaki, "Dynamic behavior of traffic with a nonlinear spacing-speed relationship," in *Proceedings of the Symposium on Theory of Traffic Flow, Research Laboratories, General Motors*, pp. 105–119, New York, NY, USA, 1959.

[7] R. E. Chandler, R. Herman, and E. W. Montroll, "Traffic dynamics: studies in car following," *Operations Research*, vol. 6, no. 2, pp. 165–184, 1958.

[8] S. H. Hamdar, M. Treiber, H. S. Mahmassani, and A. Kesting, "Modeling driver behavior as sequential risk-taking task," *Transportation Research Record: Journal of the Transportation Research Board*, vol. 2088, no. 1, pp. 208–217, 2008.

[9] G. J. S. Wilde, "The theory of risk homeostasis: implications for safety and Health," *Risk Analysis*, vol. 2, no. 4, pp. 209–225, 1982.

[10] G. Lu, B. Cheng, Y. Wang, and Q. Lin, "A car-following model based on quantified homeostatic risk perception," *Mathematical Problems in Engineering*, vol. 2013, Article ID 408756, 13 pages, 2013.

[11] Y. Saito, M. Itoh, and T. Inagaki, "Driver assistance system with a dual control scheme: effectiveness of identifying driver drowsiness and preventing lane departure accidents," *IEEE Transactions on Human-Machine Systems*, vol. 46, no. 5, pp. 1–12, 2016.

[12] J. Son, M. Park, and B. B. Park, "The effect of age, gender and roadway environment on the acceptance and effectiveness of advanced driver assistance systems," *Transportation Research Part F: Traffic Psychology and Behaviour*, vol. 31, pp. 12–24, 2015.

[13] C. Blaschke, F. Breyer, B. Färber, J. Freyer, and R. Limbacher, "Driver distraction based lane-keeping assistance," *Transportation Research Part F: Traffic Psychology and Behaviour*, vol. 12, no. 4, pp. 288–299, 2009.

[14] S. A. Birrell, M. Fowkes, and P. A. Jennings, "Effect of using an in-vehicle smart driving aid on real-world driver performance," *IEEE Transactions on Intelligent Transportation Systems*, vol. 15, no. 4, pp. 1801–1810, 2014.

[15] E. Adell, A. Várhelyi, and M. D. Fontana, "The effects of a driver assistance system for safe speed and safe distance-a real-life field study," *Transportation Research Part C: Emerging Technologies*, vol. 19, no. 1, pp. 145–155, 2011.

[16] N. Lyu, Z. Duan, L. Xie, and C. Wu, "Driving experience on the effectiveness of advanced driving assistant systems," in *Proceedings of the 2017 4th International Conference on Transportation Information and Safety (ICTIS)*, pp. 987–992, Banff, Canada, August 2017.

[17] N. Lyu, Z. Duan, C. Ma, and C. Wu, "Safety margins - a novel approach from risk homeostasis theory for evaluating the impact of advanced driver assistance systems on driving behavior in near-crash events," *Journal of Intelligent Transportation Systems*, vol. 25, no. 1, pp. 93–106, 2021.

[18] N. Lyu, C. Deng, L. Xie, C. Wu, and Z. Duan, "A field operational test in China: exploring the effect of an advanced driver assistance system on driving performance and braking behavior," *Transportation Research Part F: Traffic Psychology and Behavior*, vol. 65. , 2018 In press.

[19] N. Lyu, Z. Duan, and C. Wu, "The impact of driving experience on advanced driving assistant systems," *Journal of Transportation Systems Engineering and Information Technology*, vol. 17, no. 6, pp. 48–55, 2017.

[20] I. Engströme, N. P. Gregersen, K. Hernetkoski, E. Keskinen, and A. Nyberg, *Jeunes Conducteurs Novices, Education & Formation du Conducteur. Etude bibliographique. Rapport VTI 491A*, Université de Turku, Turku, Finland, 2003.

[21] G. Underwood, P. Chapman, N. Brocklehurst, J. Underwood, and D. Crundall, "Visual attention while driving: sequences of eye fixations made by experienced and novice drivers," *Ergonomics*, vol. 46, no. 6, pp. 629–646, 2003.

[22] L. L. D. Stasi, V. Álvarez-Valbuena, J. J. Cañas, A. Maldonado, A. Catena, and A. Antolí, "Risk behavior and mental workload: multimodal assessment techniques applied to motorbike riding simulation," *Transportation Research Part F: Traffic Psychology and Behavior*, vol. 12, no. 5, pp. 361–370, 2009.

[23] C. Maag, D. Muhlbacher, and H.-P. Mark, "Studying effects of advanced driver assistance systems (ADAS) on individual and group level using multi-driver simulation," *IEEE Intelligent Transportation Systems Magazine*, vol. 4, no. 3, pp. 45–54, 2012.

[24] D. J. Leblanc, S. Bao, J. R. Sayer, and S. Bogard, "Longitudinal driving behavior with integrated crash-warning system," *Transportation Research Record: Journal of the Transportation Research Board*, vol. 2365, no. 1, pp. 17–21, 2013.

[25] L. Chong, M. M. Abbas, A. Medina Flintsch, and B. Higgs, "A rule-based neural network approach to model driver naturalistic behavior in traffic," *Transportation Research Part C: Emerging Technologies*, vol. 32, no. 4, pp. 207–223, 2013.

[26] R. Ervin, J. Sayer, D. Leblanc, S. Bogard, and M. Mefford, *Automotive Collision Avoidance System Field Operational Test*

*Report*, University of Michigan Ann Arbor Transportation Research Institute, Ann Arbor, MI, USA, 2005.

[27] X. Wang, M. Zhu, and Y. Xing, "Impacts of collision warning system on car following behavior based on naturalistic driving data," *Journal of Tongji University (Natural Science)*, vol. 44, no. 7, pp. 1045–1051, 2016.

[28] G. Lu, B. Cheng, Q. Lin, and Y. Wang, "Quantitative indicator of homeostatic risk perception in car following," *Safety Science*, vol. 50, no. 9, pp. 1898–1905, 2012.

[29] G. J. S. Wilde, "Critical issues in risk homeostasis theory," *Risk Analysis*, vol. 2, no. 4, pp. 249–258, 2010.

[30] R. Nilsson, *Safety Margins in the Driver. The Faculty of Social Sciences*, Uppsala University, Uppsala, Sweden, 2001.

[31] X. Zhang, G. Lu, and B. Cheng, "Parameters calibration for car-following model based desired safety margin," *International Conference on Optoelectronics and Image Processing (ICOIP)*, vol. 2, pp. 97–100, 2010.

[32] T. L. Brown, J. D. Lee, and D. V. Mcgehee, "Human performance models and rear-end collision avoidance algorithms," *Human Factors: The Journal of the Human Factors and Ergonomics Society*, vol. 43, no. 3, pp. 462–482, 2001.

[33] G. S. Gurusinghe, T. Nakatsuji, Y. Azuta, P. Ranjitkar, and Y. Tanaboriboon, "Multiple car-following data with real-time kinematic global positioning system," *Transportation Research Record: Journal of the Transportation Research Board*, vol. 1802, no. 1, pp. 166–180, 2002.

[34] H. Ozaki, "Reaction and anticipation in the car-following behavior," *Transportation and Traffic Theory*, vol. 49, no. 6, pp. 2302–2306, 1993.

[35] N. Lyu, Z. Duan, and C. Wu, *Evaluated the Effectiveness of Advanced Driving Assistant Systems in Near-Crash Events Based on Safety Margin*, in *Proceedings of the 97st Transportation Research Board Annual Meeting*, Washington, DC, USA, 2018.

[36] M. Brackstone and M. McDonald, "Car-following: a historical review," *Transportation Research Part F: Traffic Psychology and Behaviour*, vol. 2, no. 4, pp. 181–196, 1999.

Hindawi
Advances in Civil Engineering
Volume 2021, Article ID 8818771, 12 pages
https://doi.org/10.1155/2021/8818771

*Research Article*

# Reducing Compressibility of the Expansive Soil by Microbiological-Induced Calcium Carbonate Precipitation

**Xiaobing Li,[1] Chunshun Zhang,[2] Hongbin Xiao,[1] Weichang Jiang,[1] Junfeng Qian,[1,3] and Zixiang Li[1]**

[1]*Institute of Geotechnical Engineering, Central South University of Forestry and Technology, Changsha 410004, China*
[2]*Department of Civil Engineering, Monash University, Clayton, VIC 3800, Australia*
[3]*Technology R&D Center, Hubei Road & Bridge Group Co., Wuhan 430056, China*

Correspondence should be addressed to Chunshun Zhang; ivan.zhang@monash.edu and Hongbin Xiao; t20090169@csuft.edu.cn

Received 12 August 2020; Accepted 19 January 2021; Published 10 February 2021

Academic Editor: Songtao Lv



Most of the research studies on the improvement of expansive soils are focused on reducing their expansive properties; however, there are few studies on the impact of the soil compressibility after the improvement. In this paper, through indoor high-pressure consolidation tests, the recent microbial-induced calcium carbonate precipitation (MICP) technology is studied to improve the compression characteristics of the expansive soil. The significant effect of different microbial concentrations (achieved by different number of treatments) on the compression deformation is revealed with the hyperbolic function that involves two parameters with clear physical meanings. In particular, after 6 times of treatment with the microbial solution, the compression characteristics of the expansive soil reach the best improvement effect; continuing to increase the number of microbial treatments is, otherwise, not conducive to improving the soil compression performance. Also, a dramatical increase of the structural strength of the microbial-treated expansive soil is presented and investigated. Moreover, we performed a scanning electron microscope (SEM) experiment and confirmed the existence of crystals due to mineralization. This study shows that MICP is an effective and environmentally friendly means of reducing the compressibility of the expansive soil.

## 1. Introduction

Expansive soil is a special kind of catastrophic clay and is widely distributed in the world. In order to use land resources rationally, it is usually necessary to improve the poor engineering characteristics of the soil so that the expansive soil can be used to fill the embankment or the subgrade of a building.

One way is to add a certain amount of inorganic materials such as lime, cement, or fly ash for chemical and physical improvement of the expansive soil [1, 2]. For example, Phanikumar and Nagaraju [3] proposed a comparative study of an expansive clay using fly ash and rice husk ash. The test results showed that liquid limit, plasticity index, and free swell index decreased significantly with increasing fly ash and rice husk ash contents. However, coefficient of permeability increased with additive content. Bian et al. [4] studied the physical and mechanical characteristics of lime-modified expansive soil through experimental research and found that, as the ash content increases, the cohesion, internal friction angle, and CBR value of the expansive soil increase; after that, they proposed that the CBR and direct shear strength of 7-day cured lime soil could be adopted to determine the best ash content. Voottipruex and Jamsawang [5] analyzed the swelling and strength characteristics of the expansive soil using cement and fly ash, and then they concluded that the swelling percentage can predict the swelling and strength characteristics of the soil. Though these are useful findings, there are some limitations, such as the uniform mixture of lime and expansive soil is difficult to achieve, long period, high construction cost, and environmental pollution due to the mixing process. Therefore, it is necessary to find a new, environmentally friendly, and more applicable alternative method for improving the expansive soil.

Alternatively, microbially induced carbonate precipitation (MICP) technology is an emerging technology that has developed rapidly in recent years and has been widely used in many fields. This new technology has also been used in geotechnical engineering and gradually formed a new microbial geotechnical technology with great significance in soil mechanics and engineering applications [6–14]. The mechanism of MICP technology is to catalyze the hydrolysis of urea through urease generated during microbial metabolism; this process generates ammonia and carbon dioxide that are dissolved in water in an alkaline environment to generate ammonium and carbonate ions; once these carbonate ions meet sufficient calcium ions, calcium carbonate precipitates with gelling effect are generated. This calcium carbonate precipitation can not only fill the pores between the soil particles but also form glue on the surface of the soil particles to make the soil particles adhere to each other. When calcium carbonate precipitates and solidifies, a relatively high-strength calcium carbonate crystals are formed, which improve many engineering properties of the soil [15–17]. The chemical reaction process of calcium carbonate precipitation induced by microorganisms can be simplified as shown in the following:

$$\begin{gathered} CO(NH_2)_2 + H_2O \longrightarrow CO_2 + 2NH_3 \\ 2NH_3 + 2H_2O \leftrightarrow 2NH_4^+ + 2OH^- \\ CO_2 + OH^- \longrightarrow HCO_3^- \\ Ca^{2+} + OH^- + HCO_3^- \longrightarrow CaCO_3 + H_2O \end{gathered} \tag{1}$$

Whiffin [18] used *Bacillus pasteurii* to induce calcium carbonate to precipitate and cement sand particles, thereby improving the shear strength of the sand; also, the solidification effect of *Bacillus pasteurii* and urease-producing strains isolated from the soil was compared; thereafter, the effects of calcium ion concentration and grouting methods on the strength of microbially reinforced sand were studied. His experimental results showed that the uniaxial compressive strength of the sand sample treated by *Bacillus pasteurii* was as high as 5.8 MPa. Sharaky et al. [19] found that *Sporosarcina pasteurii* plays an important role in the sand biocementation process, and the research results showed that the compressive strength of sandy soil increased due to the precipitation of calcium carbonate by the bacterial activity. Through experimental research, Liu et al. [20] systematically analyzed the strength characteristics of MICP-reinforced sand and proposed a unified strength theory for the reinforcement of calcareous sand. Based on MICP technology, Khaleghi and Rowshanzamir [21] had a comparison study on sandy soil using single and mixed cultures. The research results verified that the mechanical and physical properties of sandy soil with both single and mixed media improved through the MICP, especially the outcome of the mixed medium was much better than that of the single medium. Wang et al. [22] used different treatment cycles of MICP technology to improve the wind erosion resistance of the sand; it showed that the density and wind erosion resistance of the sand increase with the number of treatments, so using MICP technology could reduce and prevent the increase of desertification. Liu [23] analyzed the dynamic characteristics of calcareous sand and its cementation mechanism based on the MICP technology and concluded that, after the MICP treatment, the dynamic strength and resistance to deformation of calcareous sand were improved to a certain extent. Canakci et al. [24] used MICP technology to improve organic soil. The test results indicated that the bacterial treatment increased shear strength and reduced compressibility of the organic soil.

The above application of MICP technology in domestic and international geotechnical engineering has made some preliminary research advances [25–28]. However, the results of the above studies are intended to improve the strength of sandy soils [29–32], and there is little research on the effect of MICP on improving the compressibility of clay, especially expansive soil. Considering the increase in engineering demand in expansive soil areas, this requires a new environmentally friendly and economical method to improve expansive soil. Therefore, we try to apply the emerging MICP technology to study its effect and mechanism on the improvement of expansive soil, focusing on soil compressibility. Through laboratory consolidation tests, the compression characteristics and deformation laws of the expansive soil before and after the MICP improvement are compared and studied.

## 2. Soil Samples and Testing Scheme

*2.1. Preparation of Soil Samples.* The test soil material was taken from the expansive soil excavated from the ring road engineering in Nanning, Guangxi. According to the code, Test Methods of Soils for Highway Engineering (JTGE 40-2019), the measured basic physical properties and chemical composition of the soil are shown in Tables 1 and 2, respectively.

According to the free expansion rate in Table 1 and the classification as specified in the code JTGE 40-2019, it can be determined that the soil samples used in the tests are medium expansive soils. The microorganism used in our experimental study is *Bacillus pasteurii* with strain number ATCC11859, which was purchased through the China National General Microbial Species Collection Management Center (CGMCC). It has high-yielding urease and is widely used *Bacillus*, which is harmless to humans and the environment.

During the test, the first step was to quickly propagate and cultivate *Bacillus pasteurii*: the bacteria were taken from the refrigerator, cells were activated, and the culture solution was inoculated on a sterile operation platform. The culture medium used in the test was mainly composed of nutrients such as urea, casein peptone, soy peptone, and sodium chloride. Then, the inoculated culture solution was cultured on a shaker for 48 hours, and then the concentration of the bacterial solution was measured using a spectrophotometer. The concentration of the bacterial solution is usually expressed by the absorbance OD600 value, and it can be used for the test when it is greater than 1.0 [33–36].

The bacterial solution and cementation solution (mixed solution of calcium chloride and urea) were added into the

Table 1: Physical properties of the expansive soil.

| Soil source | Natural density (g/cm$^2$) | Max dry density (g/cm$^2$) | Relative gravity $G_s$ | Liquid limit (%) | Plastic limit (%) | Plastic index (%) | Optimum moisture content (%) | Free swelling rate (%) |
|---|---|---|---|---|---|---|---|---|
| Nanning | 1.94 | 1.88 | 2.70 | 60.8 | 22.4 | 38.4 | 16.2 | 61.3 |

Table 2: Chemical composition of the expansive soil.

| $Si^{4+}$ (%) | $Al^{3+}$ (%) | $Fe^{3+}$ (%) | $K^{+}$ (%) | $Mg^{2+}$ (%) | $Ca^{2+}$ (%) | $Ti^{4+}$ (%) | $Cu^{2+}$ (%) | $S^{2+}$ (%) | $Mn^{2+}$ (%) |
|---|---|---|---|---|---|---|---|---|---|
| 23.5 | 57.6 | 8.9 | 4.2 | 2.3 | 1.6 | 0.9 | 0.7 | 0.2 | 0.1 |

soil sample at a volume ratio of 1 : 1. The concentration of the cementation solution was determined to be 0.2 M [37]. The concentration of the bacterial solution and cementation solution used in this experiment was found to be the optimum concentration and beneficial to the generation of microorganism mineralization. We collectively refer to bacterial solution and cement solution as treatment solution. During this test, we perform multiple processing on the expansive soil using treatment solution, which can ensure the cumulative concentration of the treatment solution is sufficient and the soil sample is in a plastic state. And the soil samples were subjected to 0, 2, 4, 6, and 8 treatments, respectively. All soil samples after curing and drying are tested with the optimum moisture content [38–41]. All soil samples are 61.8 mm in diameter and 20 mm in height to meet the requirement of the consolidation test.

*2.2. Testing Scheme.* The consolidation instrument used in the test is a GDG-4S Triplex high-pressure consolidation testing apparatus. Consolidation tests were performed according to code JTGE 40-2019.

First, 1 kPa pressure was applied, and prepressed to ensure that all parts of the consolidation instrument were in close contact. Then, the preload was removed, and the first load was quickly applied. After the first-level load was stabilized for 24 hours, the next-level load was applied, and the total load was divided into eight levels. The load of each level was 12.5 kPa, 25 kPa, 50 kPa, 100 kPa, 200 kPa, 300 kPa, 400 kPa, and 800 kPa. During the loading process, the consolidated specimens were wrapped around with a damp cloth to prevent evaporation of water in the soil sample during the long-term loading.

## 3. Test Results and Analysis

*3.1. Variation of the Compression Curve.* According to the test results, the *e-p* curves of the expansive soil after microbial improvement (the number of treatments is represented by *x*, which is 2, 4, 6, and 8, respectively) and the untreated expansive soil, as shown in Figure 1.

It can be found from Figure 1 that the initial porosity ratios of the expansive soil samples subjected to different number of times of microorganism treatment are slightly different from those of the untreated microorganism. This is because the amounts of calcium carbonate precipitated in the soil particles after different number of times of microbial treatment are different, so the bulk densities of the soil samples changed slightly, although the initial water content of each soil sample is the same.

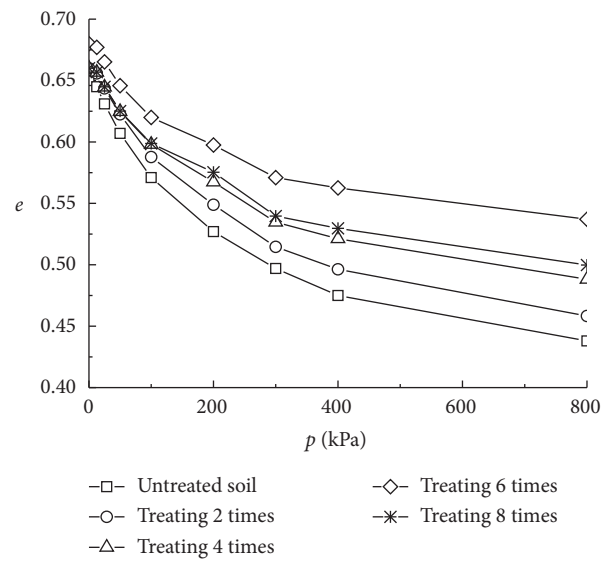


Figure 1: *e-p* curves of the expansive soil.

It can also be found from Figure 1 that the porosity ratios of the expansive soil treated with different number of times of microorganisms decrease with the increase of the consolidation pressure. That is to say, the expansive soil has undergone compression deformation under different consolidation pressures. On the contrary, with the increase of the consolidation pressure, the *e-p* curves of the expansive soil samples with different number of times of microbial treatment decrease significantly at different rates. Except for the soil samples after 8 times of treatment, the *e-p* curves of other soil samples become smoother with the increasing number of treatments, that is, the compression coefficient becomes smaller, and the compression modulus becomes larger. This law shows that the compression characteristics of the expansive soil have been improved to varying degrees after microbial treatment; particularly, when the number of treatments is less than six, the more the number of treatments is, the more obvious the compression characteristics improve. Note that when the number of soil modifications reached 8 times, the compression characteristics of the soil samples became significantly worse. This is because during the test, after each microbial treatment, the soil samples were

air-dried and crushed, which affected the mesostructure of soil particles, resulting in increasing fine particles, some of which might not be sufficiently cemented by the calcium carbonate precipitates. Therefore, in order to ensure the improvement effect of the expansive soil, it is necessary to avoid excessive crushing of the soil sample during the test. In addition, as the number of soil modifications increases, the precipitation efficiency of calcium carbonate between soil particles may decrease [42]. Therefore, we do need to control the number of soil modifications.

When the consolidation pressure is 0 to 400 kPa, after the microorganism treatment of 0, 2, 4, 6, and 8 times, the corresponding reduction ratios of the porosity ratio are 17.5%, 16.4%, 13.9%, 11.7%, and 13.0%, respectively; when the consolidation pressure is further increased from 400 kPa to 800 kPa, the corresponding porosity ratios are further reduced to 3.8%, 3.7%, 3.3%, 2.6%, and 3.0% for the 5 times of treatment. These reductions in porosity ratios under increasing the consolidation pressure are listed in Table 3.

It can be seen from Table 3 that, on the one hand, regardless of whether the expansive soil is processed by the MICP technology, the overall compression characteristics of the soil remain unchanged: at the initial compression stage, the slope of the *e-p* curve is larger, and the amount of soil compression is larger, reflecting the large decrease in soil porosity ratios at low compression levels; when the vertical pressure exceeds 400 kPa, the *e-p* curve tends to be gentle, and the amount of compression of the soil body gradually decreases, reflecting the decrease in the reduction of the porosity ratio of the soil body. This is because when the soil is compressed, the soil particles will rearrange and become densely packed with each other, and also, water and gas in the soil are squeezed out of the pores of the soil. All these contribute to the soil compactness, so the movement of the soil particles becomes more and more difficult, resulting in smaller and smaller compression deformation.

On the other hand, under the same consolidation pressure, the reductions of porosity ratios of the microbially modified expansive soil samples are less than those of the untreated soil sample. As the number of microbial treatments increases, the change of the porosity ratio of the soil decreases first. After the treatment for 6 times, the change of the porosity ratio is the smallest. This evidently confirms the effect of using microorganisms to improve the compressibility of the expansive soil that is related to the number of treatments. In our study, the compressibility of the expansive soil obtained the best improvement after 6 microbial treatments.

*3.2. Variation of the Index of Compressibility.* According to the test results, the relationships between the coefficient of compressibility, $a_{1\text{-}2}$, $a_{1\text{-}2}$ is the compression coefficient of consolidation pressure between 100 kPa and 200 kPa, the compression modulus $E_s$, and the final compression amount $S_f$ of the microbially modified expansive soil are shown in Figures 2 and 3, respectively.

It can be seen from Figure 2 that, after 6 times of microbial solution treatment, the coefficient of compressibility, $a_{1\text{-}2}$, of the expansive soil decreased from 0.44 MPa$^{-1}$ to 0.22 MPa$^{-1}$, and its compression modulus increased from 3.74 MPa to 7.48 MPa; the final compression of the soil sample was reduced from 2.57 mm to 1.70 mm. Both the compression coefficient and the final compression amount of the expansive soil decrease first and then increase with the increase in the number of microbial treatments; the compression coefficient and the final compression amount of the unimproved plain expansive soil are the largest. After 6 times of microbial treatment, both reached the minimum. The expansion modulus of the expansive soil increased first and then decreased with the increase of the number of microbial treatments. The untreated expansive soil has the smallest compression modulus. After 6 times of microbial

Table 3: Reduction of the void ratio.

| $p$ (kPa) | $x$ (times) | | | | |
|---|---|---|---|---|---|
| | 0 (%) | 2 (%) | 4 (%) | 6 (%) | 8 (%) |
| 0–400 | 17.5 | 16.4 | 13.9 | 11.7 | 13.0 |
| 400–800 | 3.8 | 3.7 | 3.3 | 2.6 | 3.0 |

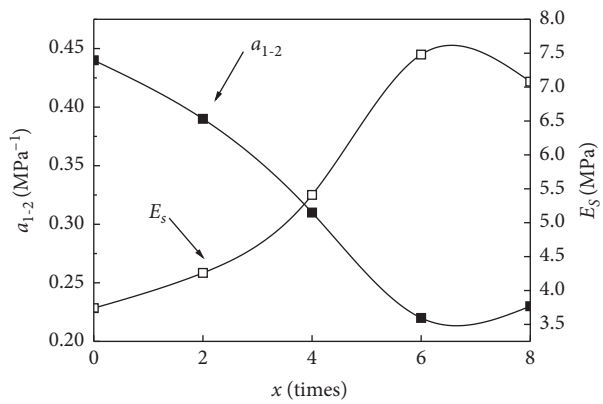


Figure 2: Relation between $a_{1\text{-}2}$ or $E_s$ and $x$.

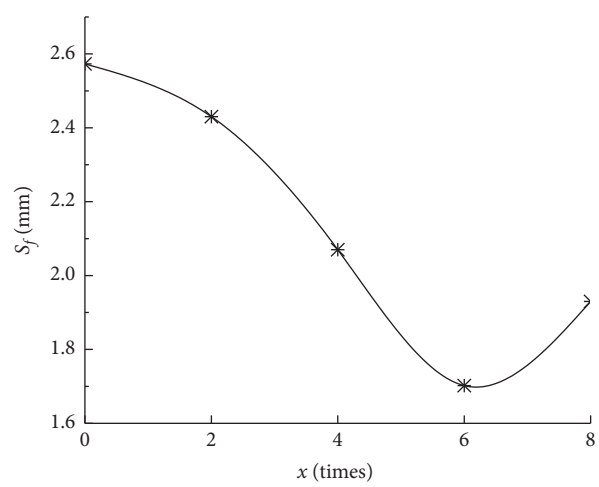


Figure 3: Relation between $S_f$ and $x$.

treatment, the expansive soil has the highest compression modulus.

In practical engineering, the compression coefficient $a_{1\text{-}2}$ is usually used to judge the compressibility of the soil.

(1) For $a_{1\text{-}2} \leq 0.1\,\text{MPa}^{-1}$, it is a lowly compressible soil

(2) For $0.1\,\text{MPa}^{-1} \leq a_{1\text{-}2} \leq 0.5\,\text{MPa}^{-1}$, it is a moderately compressible soil

(3) For $a_{1\text{-}2} \geq 0.5\,\text{MPa}^{-1}$, it is a highly compressible soil

From the above range, it can be known that the untreated expansive soil with $a_{1\text{-}2} = 0.44\,\text{MPa}^{-1}$ is a medium-high compressive soil. After the microbial treatment for 6 times, $a_{1\text{-}2} = 0.22\,\text{MPa}^{-1}$, which is a moderately compressible soil. Therefore, the above results show that the compression characteristics of the expansive soil can be significantly improved by using the MICP technology. The reason is associated with the increase of calcium carbonate precipitation induced by microorganisms. The generation of microorganisms has been confirmed. Through the scanning electron microscope (SEM), as shown in Section 4, a thin layer of calcite covering soil particles was observed. This finding is consistent with that of Islam [43]. Calcium carbonate precipitates not only cement the surface of the soil particles but also fill the pores between the soil particles so that the fine soil particles may form aggregates, serving as an additional skeleton to resist external loads. Therefore, the compression characteristics of the expansive soil are improved, and the amount of compressive deformation is reduced.

On the contrary, the improvement effect of the expansive soil is related to the number of microbial treatments. When the microbial treatment reaches 6 times, the treatment effect reaches the best. When the number of treatments reaches 8 times, the coefficient of compressibility of the expansive soil sample becomes larger, which indicates that when the number of times of treatment with treatment solution is not the more, the better. As the number of treatments increases, the number of times that the expansive soil is crushed (following the processing requirement) also increases, resulting in an increase in fine particles in the soil that might not be sufficiently wrapped by the calcium carbonate precipitates, and thereby a larger coefficient of compressibility. Moreover, as the processing number of times increases, the precipitation efficiency of calcium carbonate between soil particles may reduce. Therefore, in order to achieve the best improvement effect, not only excessive crushing should be avoided but also there is a need to reasonably control the processing number of times during the test.

By processing the test data, the change curves between the coefficient of compressibility, $a$, the compression coefficients at consolidation pressures of 12.5–50 kPa, 50–100 kPa, 100–200 kPa, 200–400 kPa, and 400–800 kPa, and the consolidation pressure, $p$, of the expansive soil after different number of times of microbial treatment were obtained, as shown in Figure 4. For convenience, the consolidation pressures of the expansive soil in the figure are represented by the midpoints of 12.5–50 kPa, 50–100 kPa, 100–200 kPa, 200–400 kPa, and 400–800 kPa, respectively.

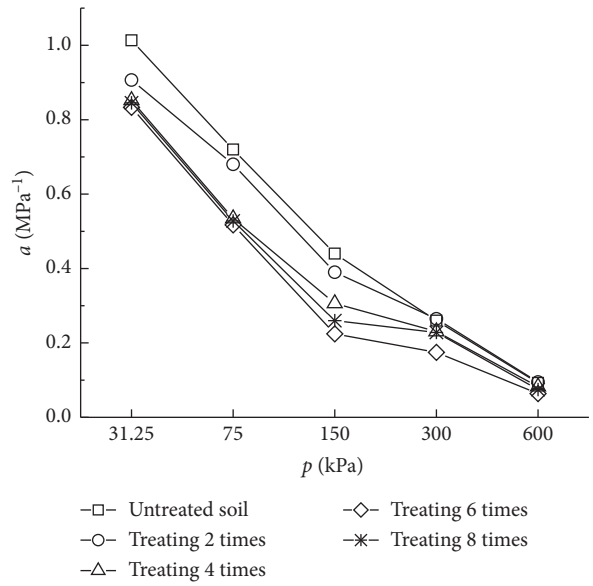


Figure 4: Relations between $a$ and $p$.

From Figure 4, it can be found that, under the same consolidation pressure, the coefficients of compressibility of the expansive soil samples after microbial improvement are all smaller than those of the untreated soil sample. Also, the slopes of the curve of the microbially treated soil samples are more or less similar to those of the untreated sample at low consolidation pressure, say less than 75 kPa; as the consolidation pressure increases, say over 150 kPa, the slopes of the curves of the microbially treated soil samples are then significantly reduced compared to those of the untreated soil sample. The above findings show that, as the consolidation pressure increases, the microbially treated soil samples become more and more difficult to be compressed due to the improvement of the MICP effect and also the increasing consolidation pressure. As a comparison, when it exceeds 150 kPa to 600 kPa, the coefficient of compressibility of the untreated soil samples decreases dramatically, which indicates that the soil samples still undergo considerable compression deformation within this high-pressure range.

*3.3. Variation of Vertical Strain and Consolidation Pressure.* After the expansive soil samples were treated with microorganisms for a different number of times, the changes of the soil vertical strains with the increase of consolidation pressures are shown in Figure 5.

It can be known from Figure 5 that (1) in all soil samples, whether or not being improved, their vertical strains increase with the increase of the consolidation pressures; however, increase rates of the vertical strains gradually slow down, so the increase in the consolidation deformation gradually decreases; (2) under the same consolidation pressure, the vertical strain of the soil samples after microbial improvement is significantly lower than that of the unimproved soil samples; (3) at the same consolidation pressure, the number of microbial treatments increased to the sixth, and the vertical strains of the soil samples reduce to be minimum; continuous

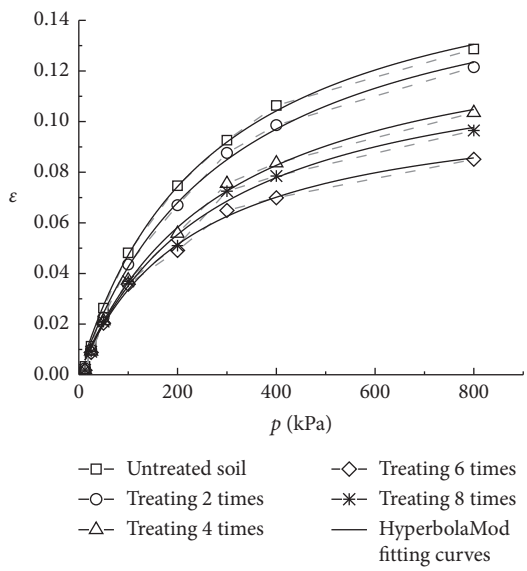


Figure 5: Relations between $\varepsilon$ and $p$.

improvement of soil samples, say the 8th time, results in the strain to rebound considerably.

The above three aspects can be explained as follows: on the one hand, as the consolidation pressure increases, the soil particles are rearranged and gradually compacted, and the soil coefficient of compressibility decreases, so the incremental amount of compression decreases; on the other hand, the generated calcium carbonate precipitates in the microbially treated expansive soil samples are cemented on the surface of the soil particles or filled in the pores of the soil, which provides additional skeleton strength to the soil, so the compressive strength of the soil is increased, resulting in a decrease in the incremental vertical strain of the soil. The changes between the vertical strains and the consolidation pressures shown in Figure 5 adequately show that the compression characteristics of the expansive soil after microbial improvement have been significantly improved.

By observing the curve of the vertical strain and consolidation pressure in Figure 5, the hyperbolic function can be used for fitting. The relationship between the vertical strain and the consolidation pressure before and after the improvement of the expansive soil can be obtained:

$$\varepsilon = \frac{p}{a + bp}, \tag{2}$$

where $\varepsilon$ indicates the vertical strain under consolidation pressure, $p$, and $a$ and $b$ are fitting parameters as listed in Table 4.

From equation (2), it is straightforward to obtain the inverse of the pressure-dependent instantaneous elastic modulus, $1/E_t$:

$$\frac{1}{E_t} = \frac{d\varepsilon}{dp} = \frac{a}{(a + bp)^2}. \tag{3}$$

From equations (2) and (3), the physical meanings of the parameters $a$ and $b$ are clear:

(1) $1/a$ indicates the initial slope of the strain to the consolidation pressure:

$$\frac{1}{E_0} = \frac{1}{a}. \tag{4}$$

In another word, $a$ itself means the initial elastic modulus, $E_0$.

(2) $1/b$ represents the asymptotic strain when $p$ increases to infinity:

$$\varepsilon_{ult} = \frac{1}{b}. \tag{5}$$

Also, from equation (2), the consolidation pressure can be expressed as a function of the vertical strain:

$$p = \frac{a\varepsilon}{1 - b\varepsilon}. \tag{6}$$

Substitute equation (6) into (3) to obtain

$$\frac{1}{E_t} = \frac{(1 - b\varepsilon)^2}{a}. \tag{7}$$

Therefore, the relationship between the vertical strain of microbially modified expansive soil and the consolidation pressure can also be expressed in the incremental form as follows:

$$d\varepsilon = \frac{(1 - b\varepsilon)^2}{a} dp. \tag{8}$$

Also, from Table 4, it is found that the coefficient $a$ gradually increases with the increase in the number of microbial treatments, while $b$ increases till the 6th treatment and then decreases at the 8th treatment.

*3.4. Preconsolidation Pressure of Microbially Modified Expansive Soil.* As another critical soil index, preconsolidation pressure normally reflects the stress history of the soil. The pressure is normally determined by Casagrande's empirical method. Nevertheless, it is challenging to determine the point of minimum radius of curvature, so as to follow Casagrande's empirical method.

Alternatively, we adopt $\ln(1 + e) - \lg p$, the double logarithm method, i.e., the compression curve of the expansive soil is represented by double straight lines, and the intersection of the two straight lines is considered to be the preconsolidation pressure $p_c$. The double logarithm method was first proposed by Butterfield [44]. Afterwards, Onitsuka et al. [45] and Hong and Onitsuka [46] validated the method through a large number of experiments. It can be seen from Figure 6 that the bilogarithmic characteristic of each compression curve is significant, in line with the bilinear

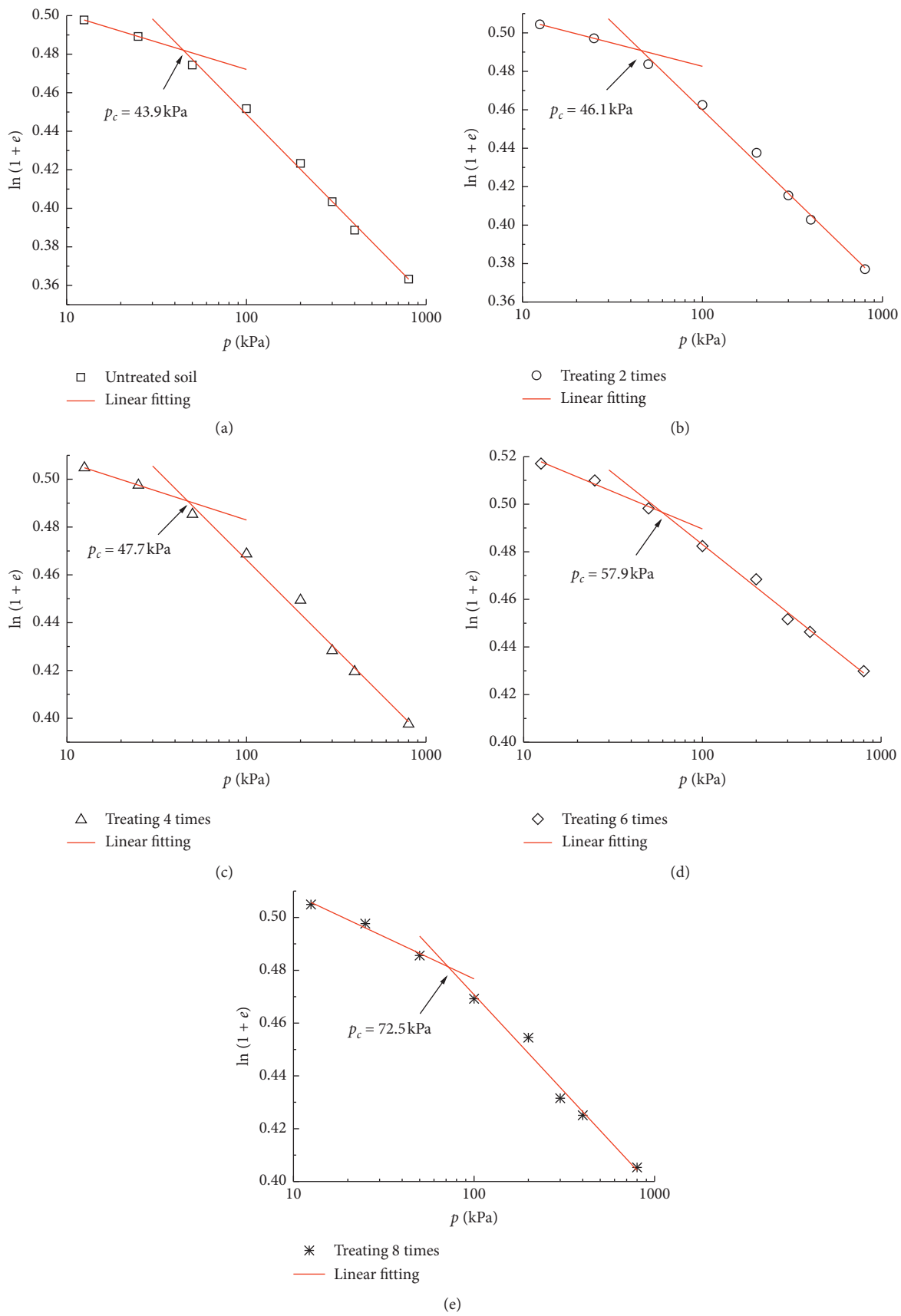


Figure 6: compression curve (ln (1+e) - lgp) of microbially-treated expansive soil samples.

Table 4: Fitting parameters.

| Soil samples | $a$ | $b$ | $R^2$ |
|---|---|---|---|
| Untreated soil | 1543.202 | 5.735 | 0.997 |
| Treating 2 times | 1761.237 | 5.902 | 0.996 |
| Treating 4 times | 2035.680 | 7.000 | 0.996 |
| Treating 6 times | 2069.820 | 9.086 | 0.993 |
| Treating 8 times | 2087.056 | 7.628 | 0.992 |

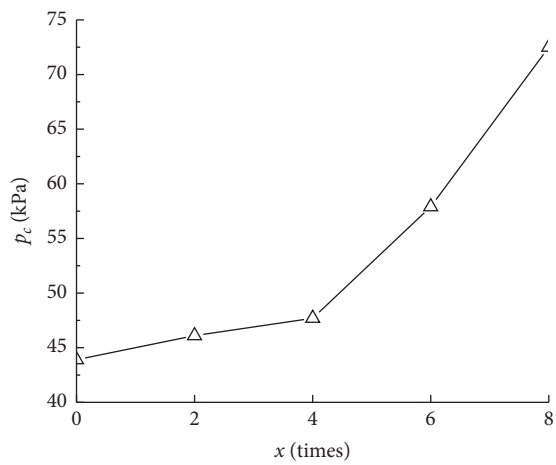


Figure 7: Relationship between $pc$ and times of treatment, $x$.

rule, and the inflection point ($p_c$) value of each curve can be straightforwardly identified.

As shown in Figure 7, it is obvious that the $p_c$ values of the expansive soil improved by microorganisms are higher than those of the unimproved; the $p_c$ value of the expansive soil increases with the number of treatments; particularly, a dramatical increase is found after 4 times of microbial treatment. This phenomenon shows that the microbial treatment has a significant effect on the increase of $p_c$ in the expansive soil. However, it should be noted that the change of the inflection point $p_c$ shown in Figures 6 and 7 is obviously not the "real" preconsolidation pressure, but a reflection of the structural strength.

The increase of the structural strength can be illustrated as follows: the microorganisms which entered the pores of the soil were mineralized to generate calcium carbonate precipitates that were found to be mainly calcite crystals [36]. These crystals were generated in irregular particles on the surface and gaps of the soil particles, wrapping up and tightly connecting the soil particles. As a result, the contact area between the soil particles is increased and the connection capacity between the soil particles is enhanced, which cause more integrated and denser internal structure of the soil. Therefore, the structural strength of the soil is largely improved.

Furthermore, in Figures 6(a)–6(e), by fitting lines of the compression curves after $p_c$, the slopes correspond to the (post-$p_c$) normal compression lines. These slopes are obtained under the double logarithmic coordinates of Figure 6, similar to the compression index in the $e$-$p$ curve, hence reflecting the soil compression characteristics. The results of each slope are shown in Figure 8. It can be seen that (1) when the consolidation pressure reaches the inflection point, the slope of the compression curve of the expansive soil modified by microorganisms is less than that of the unmodified soil; (2) the slope of the normal compression curve decreases first and then increases with the increase of the number of treatments; in particular, the slope is the smallest when the microorganisms are treated 6 times.

The above two findings, again, show that the compression properties of the expansive soil after microbial treatment have been improved. Nevertheless, excessive treatment (such as the eight treatments in our study) is not conducive to improving the compression performance of the expansive soil when the compressive stress is higher than $p_c$. The reason is that too many treatments mean excessive grinding of the soil samples, which may severely disrupt some cementation of the soil and produce a large amount of microparticles to small particles, minimizing the amount of medium to large particles. In addition, excessive treatments of the soil may result in a decrease in the precipitation efficiency of calcium carbonate between soil particles. This leads to significant changes of the structure of the particles and pores of the expansive soil. Such changes in the internal structure of the soil are very complicated and need further observation of the development of calcite crystals.

## 4. Microstructural Analysis

Through using the scanning electron microscope (SEM), the microstructure characteristics of the soil sample under the appropriate magnification were observed, as shown in

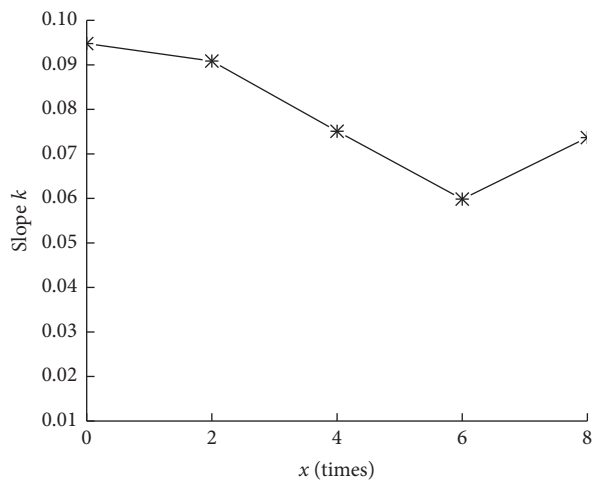


Figure 8: Relationship between the slope of the compression curve and $x$.

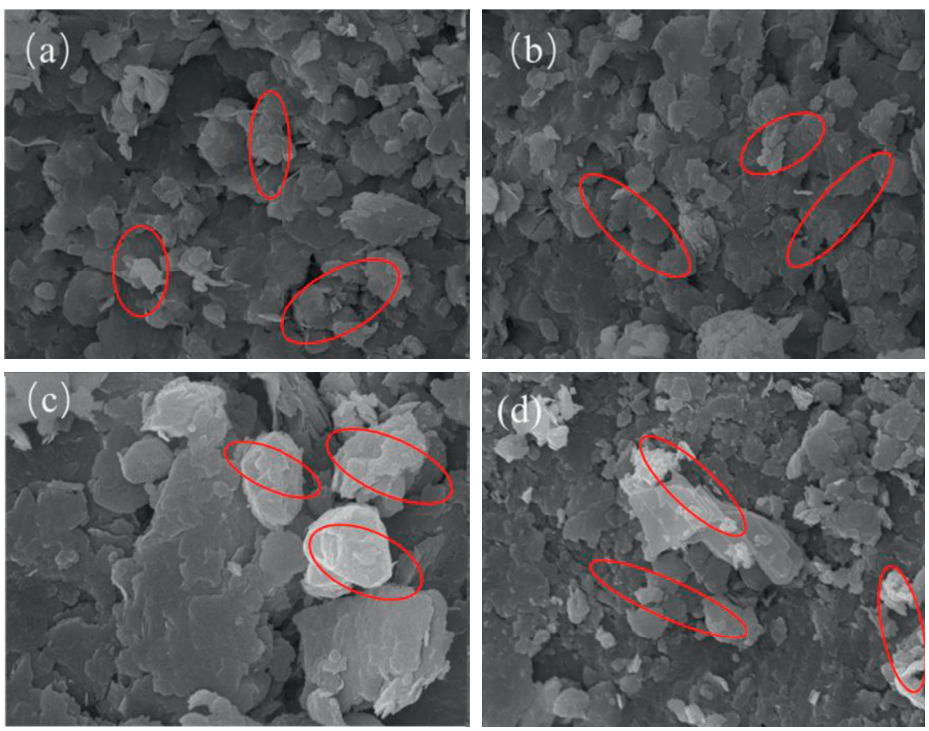


Figure 9: SEM micrographs of (a) 2 times, (b) 4 times, (c) 6 times, and (d) 8 times. Some crystals are marked with circles.

Figure 9. As can be seen from the figure, a number of irregularly shaped, angular crystals are distributed around the soil particles. These crystals are calcium carbonate precipitates produced by microbial mineralization. They wrap on the surface of soil particles, cement the soil particles, and improve the stability of the soil particles. This helps to understand the mechanism of the improved compressibility and structural strength of the expansive soil. By further observing Figures 9(a)–9(d), it is found that the degree of crystal development and morphology and cementation effect vary with the number of treatments. This shows that different treatment times have an impact on the mineralization of microorganisms. However, only based on the current preliminary SEM results, the relationship between treatment times and mineralization is not significant enough. Therefore, future work needs to be continued from a microscopic perspective to further observe the shape of the crystal and the effect of the interaction between the crystal and the soil particles.

## 5. Mechanism Analysis of Microbial Improvement of Compression Characteristics of the Expansive Soil

*5.1. Filling Effect.* In the process of calcium carbonate precipitation induced by the microorganisms, some crystalline and

noncrystalline inorganic compound precipitates are produced, and their main component is calcium carbonate colloid. The microbial process that produces these colloids, followed by colloidal crystallization and solidification, is also called microbial mineralization. From our study, this mineralization process in the expansive soil can be efficiently completed using *Bacillus pasteurii*. After the mineral compounds are mineralized, they precipitate in the pores between the soil particles so that a large amount of pores are filled, which results in a decrease in soil porosity and an increase in soil compactness.

*5.2. Cementing Effect.* In the process of MICP, calcium carbonate colloids are precipitated on the surface of the soil particles as shown in Figure 9. The soil particles are cemented with each other, and they are firmly connected to each other. In this process, on the one hand, because the microorganisms enter the soil pores and undergo mineralization, the fine particles (such as colloidal particles and clay particles) in the soil are consolidated with each other to form aggregates and become coarse particles (such as silt and sand). As a result, the content of colloidal and clay particles in the soil decreases, the content of silt and sand particles increases, and the particle grading of the expansive soil changes. On the other hand, due to the cementation of the soil particles, the connection between the soil particles is enhanced. Therefore, the structural strength of the soil is improved, and the ability of the soil to resist external deformation is significantly improved.

## 6. Conclusions

Most of the current research studies focus on reducing the expansive properties of the expansive soil; however, after the improvement of the soil, the research on how the compressibility of the expansive soil will affect is rare. In this paper, through the experimental study of the compression characteristics of the improved expansive soil by MICP technology, the effects of different microbial contents (via the number of treatments) on the compression characteristics of the expansive soil were investigated, and the microstructure of mineralization was analyzed. The main conclusions obtained in this paper are as follows:

(1) It is feasible to improve the compression characteristics of the expansive soil based on the MICP technology by adopting a suitable treatment method. After the microbial improvement, the coefficient of compressibility of the expansive soil was significantly reduced, and the soil compressibility changed from high to low level. Among them, in our study, the compressibility improvement effect was the best at 6 times of microbial treatment.

(2) After microbial improvement, the relationship between the soil vertical strain and consolidation pressure can be simply and accurately represented by a hyperbolic function that is controlled by two physically meaningful parameters $a$ and $b$.

(3) As the numbers of treatment increase, the preconsolidation pressure (here reflecting the structural strength of the expansive soil) increases significantly. This increase in soil strength is closely related to changes in the internal structure of the soil body.

(4) We observe the existence of crystals between soil particles by SEM test and validate the microbial mineralization based on MICP.

In practice, the expansive soil treated by MICP might also be used with other granular soils [47] and mixtures [48, 49] to improve the performance of embankments, which is worthy of further study.

## Data Availability

The data that support the plots within this paper and other findings of this study are available from the corresponding author upon reasonable request.

## Conflicts of Interest

The authors declare that they have no conflicts of interest.

## Acknowledgments

The work described in this paper was supported by a grant from the National Natural Science Foundation of China (Project no. 50978097).

## References

[1] J. James and P. K. Pandian, "Plasticity, swell-shrink, and microstructure of phosphogypsum admixed lime stabilized expansive soil," *Advances in Civil Engineering*, vol. 2016, Article ID 9798456, 10 pages, 2016.

[2] Y. Liu, Y. Su, A. Namdar, G. Zhou, Y. She, and Q. Yang, "Utilization of cementitious material from residual rice husk ash and lime in stabilization of expansive soil," *Advances in Civil Engineering*, vol. 2019, Article ID 5205276, 17 pages, 2019.

[3] B. R. Phanikumar and T. V. Nagaraju, "Effect of fly ash and rice husk ash on index and engineering properties of expansive clays," *Geotechnical and Geological Engineering*, vol. 36, no. 6, pp. 3425–3436, 2018.

[4] J. M. Bian, L. Jiang, and B. T. Wang, "Strength test of expansive soil improved by lime," *Journal of Chang'an University*, vol. 33, pp. 38–43, 2013.

[5] P. Voottipruex and P. Jamsawang, "Characteristics of expansive soils improved with cement and fly ash in northern Thailand," *Geomechanics and Engineering*, vol. 6, no. 5, pp. 437–453, 2014.

[6] W. Deng and Y. Wang, "Investigating the factors affecting the properties of coral sand treated with microbially induced calcite precipitation," *Advances in Civil Engineering*, vol. 2018, Article ID 9590653, 6 pages, 2018.

[7] R. Gui, Y.-X. Pan, D.-X. Ding, Y. Liu, and Z.-J. Zhang, "Experimental study on the fine-grained uranium tailings reinforced by MICP," *Advances in Civil Engineering*, vol. 2018, Article ID 2928985, 10 pages, 2018.

[8] J. K. Mitchell and J. C. Santamarina, "Biological considerations in geotechnical engineering," *Journal of Geotechnical*

*and Geoenvironmental Engineering*, vol. 131, no. 10, pp. 1222–1233, 2005.

[9] W. De Muynck, N. De Belie, and W. Verstraete, "Microbial carbonate precipitation in construction materials: a review," *Ecological Engineering*, vol. 36, no. 2, pp. 118–136, 2010.

[10] M. Umar, K. A. Kassim, and K. T. Ping Chiet, "Biological process of soil improvement in civil engineering: a review," *Journal of Rock Mechanics and Geotechnical Engineering*, vol. 8, no. 5, pp. 767–774, 2016.

[11] J. T. DeJong, K. Soga, E. Kavazanjian et al., "Biogeochemical processes and geotechnical applications: progress, opportunities and challenges," *Géotechnique*, vol. 63, no. 4, pp. 287–301, 2013.

[12] X. Sun, L. Miao, T. Tong, and C. Wang, "Improvement of microbial-induced calcium carbonate precipitation technology for sand solidification," *Journal of Materials in Civil Engineering*, vol. 30, Article ID 4018301, 2018.

[13] C. Dupraz, R. P. Reid, O. Braissant, A. W. Decho, R. S. Norman, and P. T. Visscher, "Processes of carbonate precipitation in modern microbial mats," *Earth-Science Reviews*, vol. 96, no. 3, pp. 141–162, 2009.

[14] J. T. DeJong, M. B. Fritzges, and K. Nüsslein, "Microbially induced cementation to control sand response to undrained shear," *Journal of Geotechnical and Geoenvironmental Engineering*, vol. 132, no. 11, pp. 1381–1392, 2006.

[15] M. G. Gomez, C. M. R. Graddy, J. T. DeJong, and D. C. Nelson, "Biogeochemical changes during bio-cementation mediated by stimulated and augmented ureolytic microorganisms," *Scientific Reports*, vol. 9, Article ID 11517, 2019.

[16] D. Gat, M. Tsesarsky, D. Shamir, and Z. Ronen, "Accelerated microbial-induced CaCO," *Biogeosciences*, vol. 11, pp. 2561–2569, 2014.

[17] V. Achal and X. L. Pan, "Characterization of urease and carbonic anhydrase producing bacteria and their role in calcite precipitation," *Current Microbiology*, vol. 62, pp. 894–902, 2011.

[18] V. S. Whiffin, *Microbial $CaCO_3$ Precipitation for the Production of Biocement*, Murdoch University, Perth, Australia, 2004.

[19] A. M. Sharaky, N. S. Mohamed, M. E. Elmashad, and N. M. Shredah, "Application of microbial biocementation to improve the physico-mechanical properties of sandy soil," *Construction and Building Materials*, vol. 190, pp. 861–869, 2018.

[20] L. Liu, H. Liu, A. W. Stuedlein, T. M. Evans, and Y. Xiao, "Strength, stiffness, and microstructure characteristics of biocemented calcareous sand," *Canadian Geotechnical Journal*, vol. 56, pp. 1502–1513, 2019.

[21] M. Khaleghi and M. Rowshanzamir, "Biologic improvement of a sandy soil using single and mixed cultures: a comparison study," *Soil & Tillage Research*, vol. 186, pp. 112–119, 2019.

[22] Z. Wang, N. Zhang, J. Ding, C. Lu, and Y. Jin, "Experimental study on wind erosion resistance and strength of sands treated with microbial-induced calcium carbonate precipitation," *Advances in Materials Science and Engineering*, vol. 2018, Article ID 3463298, 10 pages, 2018.

[23] H. L. Liu, "Experimental study on dynamic characteristics of MICP cemented sand," *Chinese Journal of Geotechnical Engineering*, vol. 40, pp. 38–45, 2018.

[24] H. Canakci, W. Sidik, and I. H. Halil, "Effect of bacterial calcium carbonate precipitation on compressibility and shear strength of organic soil," *Soils Found*, vol. 55, pp. 1211–1221, 2015.

[25] V. Ivanov and J. Chu, "Applications of microorganisms to geotechnical engineering for bioclogging and biocementation of soil in situ," *Reviews in Environmental Science and Biotechnology*, vol. 7, pp. 139–153, 2008.

[26] J. Do, "Debonding of microbially induced carbonate precipitation-stabilized sand by shearing and erosion," *International Journal of Geo-Engineering*, vol. 17, pp. 429–438, 2019.

[27] J. F. Tang, "Development of microbially induced calcium carbonate precipitation technology in soil improvement," *International Journal of Advanced Research and Technology*, vol. 2, pp. 26–29, 2016.

[28] Y.-M. Kwon, I. Chang, M. Lee, and G.-C. Cho, "Geotechnical engineering behavior of biopolymer-treated soft marine soil," *International Journal of Geo-Engineering*, vol. 17, pp. 453–464, 2019.

[29] A. Almajed, H. K. Tirkolaei, E. Kavazanjian, and N. Hamdan, "Enzyme induced biocementated sand with high strength at low carbonate content," *Scientific Reports*, vol. 9, p. 1135, 2019.

[30] M. Burbank, "Geotechnical tests of sands following bio-induced calcite precipitation catalyzed by indigenous bacteria," *Journal of Geotechnical & Geoenvironmental Engineering*, vol. 139, pp. 928–936, 2013.

[31] A. Gurbuz, Y. D. Sari, Z. N. Yuksekdag, and B. Cinar, "Cementation in a matrix of loose sandy soil using biological treatment method," *African Journal of Biotechnology*, vol. 10, pp. 7432–7440, 2011.

[32] A. Mahawish, A. Bouazza, and W. P. Gates, "Improvement of coarse sand engineering properties by microbially induced calcite precipitation," *Geomicrobiology*, vol. 35, pp. 887–897, 2018.

[33] B. C. Martinez, "Experimental optimization of microbial-lnduced carbonate precipitation for soil improvement," *Journal of Geotechnical & Geoenvironmental Engineering*, vol. 139, pp. 587–598, 2013.

[34] H. A. Keykha, A. Asadi, B. B. K. Huat, and S. Kawasaki, "Laboratory conditions for maximal calcium carbonate precipitation induced by *Sporosarcina pasteurii* and *Sporosarcina aquimarina* bacteria," *Environmental Geotechnics*, vol. 6, pp. 1–20, 2018.

[35] G. D. O. Okwadha and J. Li, "Optimum conditions for microbial carbonate precipitation," *Chemosphere*, vol. 81, pp. 1143–1148, 2010.

[36] A. A. Qabany, K. Soga, and C. Santamarina, "Factors affecting efficiency of microbially induced calcite precipitation," *Journal of Geotechnical & Geoenvironmental Engineering*, vol. 138, pp. 992–1001, 2012.

[37] V. Achal and X. Pan, "Influence of calcium sources on microbially induced calcium carbonate precipitation by Bacillus sp. CR2," *Biotechnology and Applied Biochemistry*, vol. 173, pp. 307–317, 2014.

[38] M. P. Harkes, L. A. Van Paassen, J. L. Booster, V. S. Whiffin, and M. C. Van Loos-Drecht, "Fixation and distribution of bacterial activity in sand to induce carbonate precipitation for ground reinforcement," *Ecological Engineering*, vol. 36, pp. 112–117, 2010.

[39] J. F. Qian, Y. S. Yao, J. Li, H. B. Xiao, and S. P. Luo, "Resilient properties of soil-rock mixture materials: preliminary investigation of the effect of composition and structure," *Materials*, vol. 13, no. 7, p. 1658, 2020.

[40] C. Xia, S. Lv, M. B. Cabera, X. Wang, C. Zhang, and L. You, "Unified characterizing fatigue performance of rubberized asphalt mixtures subjected to different loading modes," *Journal of Cleaner Production*, vol. 249, 2020.

[41] C. Lin, S. Lv, D. J, and F. Qu, "Laboratory investigation for the road performance of asphalt mixtures modified by rock asphalt/styrene butadiene rubber," *Journal of Materials in Civil Engineering*, vol. 33, 2021.

[42] P. Anbu, C.-H. Kang, Y.-J. Shin, and J.-S. So, *Formations of Calcium Carbonate Minerals by Bacteria and its Multiple Applications*, Springer International Publishing, New York City, NY, USA, 2016.

[43] T. Islam, *Studying the Applicability of Biostimulated Calcite Precipitation in Stabilizing Expansive Soils*, Boise State University, Boise, ID, USA, 2018.

[44] R. Butterfield, "A natural compression law for soils (anadvance on e-logp)," *Geotechnique*, vol. 29, pp. 469–480, 1979.

[45] K. Onitsuka, Z. Hong, Y. Hara, and S. Yoshitake, "Interpretation of oedometer test data for natural clays," *Soils Found.*vol. 35, pp. 61–70, 1995.

[46] Z. Hong and K. Onitsuka, "A method of correcting yield stress and compression index of ariake clays for sample disturbance," *Soils and Foundations*, vol. 38, pp. 211–222, 1998.

[47] Y. Yao, J. Ni, and J. Li, "Stress-dependent water retention of granite residual soil and its implications for ground settlement," *Computers and Geotechnics*, vol. 129, Article ID 103835, 2021.

[48] C. Liu, S. Lv, D. Jin, and F. Qu, "Laboratory investigation for the road performance of asphalt mixtures modified by rock asphalt/styrene butadiene rubber," *Journal of Materials in Civil Engineering*, vol. 33, 2020.

[49] S. Zhang, Y. Ronald, S. Pak, and J. Zhang, "Vertical time-harmonic coupling vibration of an impermeable, rigid, circular plate resting on a finite, poroelastic soil layer," *Acta Geotechnica*, vol. 2, pp. 1–25, 2020.

Hindawi
Advances in Civil Engineering
Volume 2021, Article ID 6687674, 13 pages
https://doi.org/10.1155/2021/6687674

*Research Article*

# Analysis on the Influencing Factors of Driving Behaviours Based on Theory of Planned Behaviour

**Lisheng Jin**,[1] **Baicang Guo**,[1,2] **Yuying Jiang**,[3] **and Qiang Hua**[2]

[1]*School of Vehicle and Energy, Yanshan University, Qinhuangdao 066004, China*
[2]*Transportation College, Jilin University, Changchun 130022, China*
[3]*Department of Ophthalmology, China-Japan Union Hospital, Jilin University, Changchun 130022, China*

Correspondence should be addressed to Baicang Guo; guobaicang@126.com

Received 9 October 2020; Revised 6 December 2020; Accepted 10 December 2020; Published 29 January 2021

Academic Editor: Hui Yao



Driving behaviour is a complex and multidisciplinary research domain, and bad driving behaviours that threaten the safety of road users should be refrained. In order to better educate, manage, and restrain driver's behaviours, from the perspective of human factors and psychology, the present study deconstructed driving behaviours based on theory of planned behaviour (TPB) into five categories: mistakes (Mis), lapses and slips (LaS), violations (Vio), driving experience (Exp), and safety attitude and awareness (SAA). According to today's practical traffic rules and conditions in China, a driving behaviour questionnaire was built as an analysing tool and the survey data were collected in accordance with the demographic of Chinese drivers. Furthermore, a driving behaviour analysis model contains the aforementioned categories was established by using the structural equation model (SEM). Through the path analysis results among latent variables and manifested variables, it was found that Exp has an impact on Vio and LaS, and better SAA can inhibit Vio and Mis. In conclusion, the prime aim of improving road traffic safety is to reduce Vio by means of educating and improving the drivers' Exp and SAA. Moreover, drivers' LaS and Mis are transition processes which should be corrected timely and prevented from continuing to evolve into Vio.

## 1. Introduction

The economic development of contemporary China has increased the number of private vehicles. As shown in Figure 1, the growth trend of drivers is fierce; by December 2019, there are 435 million motor vehicle drivers and 397 million car drivers in China. The problems caused by the rapid population growth of drivers are the increasing difficulty of traffic management and incidence of traffic accidents. Driving safety has always been a common concern for researchers and the public. Statistics have shown that approximately 1.25 million people worldwide and approximately 100,000 people in China die due to road traffic accidents each year [1–3]. The research results on the causes of road traffic accidents showed that people are the key factors leading to traffic accidents, and drivers, as the operators of vehicles, are one of the most crucial causes of road traffic accidents. Consequently, before the era of fully automatic driving, it is necessary to analyse the driver's influencing factors and take differential corrective measures for bad behaviours. Moreover, it also provides help for the study of humanoid behaviours of autonomous driving.

In the field of driving experience and driving behaviours, on-road experience plays an important role to strengthen hazard mitigation skills [4–6] and also helps to alleviate the tendency of distracted driving behaviour [7]. Experienced drivers show reduced crash risks in comparison to novice drivers [8], which means driving experience helps to allocate attention resources effectively to identify potential hazards [9]. Lacking maturity and driving experience increases the risk of traffic accidents for novice drivers [10]. Pnina et al. [11] found that although there are a lot of driving practices during the learning period, the probability of making mistakes in early license holding period is still high. Lack of driving experience is related to the driver's insufficient ability to monitor potential road hazards, which can lead to rear end, fatigue driving, drunk driving, or other behaviours

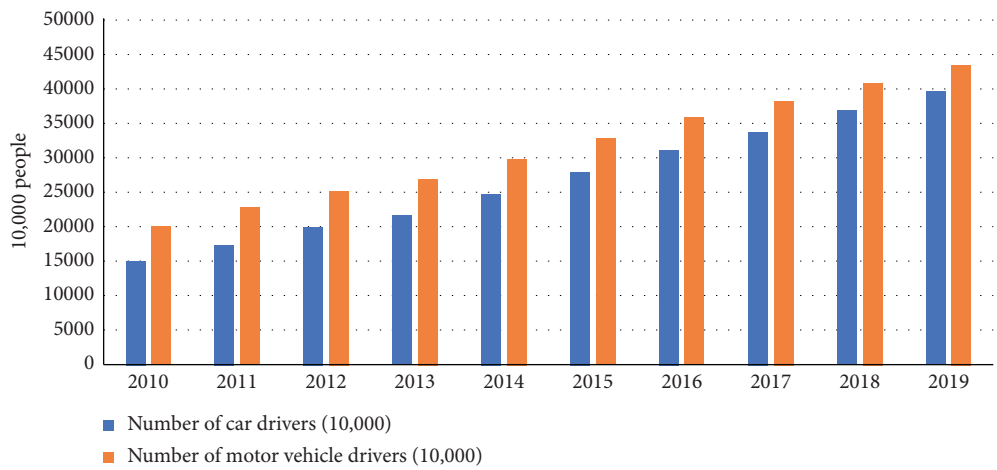


Figure 1: Driver growth trend in China in the past 10 years (data source: National Bureau of Statistics, 2019, China).

[12]. When dealing with incidents on road, experienced drivers exhibited more proactive actions than novices [13]; moreover, experienced drivers are better than novices in situational perception [14]. In conclusion, lack of driving experience is a safety threat to drivers, passengers, and other road users. Driving experience has a strong correlation with driver's psychology (self-confidence, attitude, and awareness), emergency response ability, peripheral monitoring ability, etc.

In the domain of psychology and driving behaviours and in the aspect of driver's psychology on driving behaviour, many research studies have shown that Theory of Planned Behaviour (TPB) can be used to explain driving behaviours (e.g., Przepiorka et al. [15]; Waddell and Wiener [16]; and Walsh et al. [17]). One of the basic TPB hypothetical models is to use intention to predict behaviours, whilst intentions result from an individual's attitude towards the behaviour, subjective norms, and perceived behavioural control (PBC) over the behaviour. Attitude is the positive or negative evaluation of the behaviour [18]. Subjective norms refer to the constraints that individuals feel about whether to execute a particular behaviour. PBC is the perceived level of control that one has over engaging in or refraining from engaging in this behaviour [19]. Furthermore, factors such as emotional driving and sensation seeking can lead to dangerous driving behaviours. Novice drivers have a high risk of distraction when travelling with young passengers, which Siebe [20] believes is due to a lack of confidence in vehicle control.

With respect to human factor research, driving behaviour questionnaire (DBQ) is one of the most widely used tools to measure self-reported driving style and investigate the relationship between driving behaviour and accident participation [21]. Based on the theoretical classification of abnormal behaviours, Qu et al. [22] divided driving behaviours into three types: slips and lapses, mistakes, and deliberate violations [22, 23]. In the follow-up research on DBQ, scholars confirmed the rationality of the three-factor structure of DBQ in their own research studies and proved that DBQ is relatively reliable over time [24–26]. Rimmö et al. [27] utilized three-factor structure (aggressive violations, ordinary violations, and errors) compare driving behaviours across six countries, and they found that the importance of driver characteristics and behaviours in predicting traffic accidents varies from country to country.

Therefore, in practical application research, scholars in different countries will consider the local traffic conditions, cultural habits, and other actual conditions and make corresponding deletion, supplement, and adjustment of DBQ according to their research purposes. Bener et al. [21] and Mesken et al. [28], respectively, investigated Qatar and the United Arab Emirates with their own DBQ and, respectively, analysed the relationship among several driving behaviours and traffic accidents by the Driver Positive Behaviour Scale (DPBS) and Driver Aggression Indicators Scale (DAIS). Cordazzo et al. [29] included more driving behaviour samples based on the previous version of DBQ and conducted research on driving behaviours such as targeting inattention, distraction, and aggressive driving. Lajunen et al. [30] studied the applicability of Manchester DBQ in three countries: Finland, the United Kingdom, and the Netherlands. Their conclusion shows that although the classification methods of the DBQ factor structure in these three countries are not exactly the same, the original DBQ structure is still applicable to these three countries. In China, after resulting the questionnaire on some Chinese people in Beijing and Chengde, Jing Shi et al. [31] divided the violations into emotional violations, risky violations, and self-willed violations, and the errors included inexperience errors and distraction errors.

According to the abovementioned literature studies, it can be found that scholars have extensive and lasting interest in studying driving behaviour (types, causes, and impact on traffic safety) by exploring the psychology and driving experience of drivers. This paper studies from the following aspects:

(1) From the illation of TPB, for laying a foundation for questionnaire analysis, we deduce the influencing mechanism of driving behaviours and deconstruct the influencing factors of driving behaviours into latent variables and manifest variables.

(2) By referencing and adapting proper items from Manchester Driver Behaviour Questionnaire [22], Dula Dangerous Driving Index [32], and Chinese Driving Questionnaire [33], additionally we put forward some items with Chinese characteristics. After that, a Chinese driving behaviour questionnaire with good reliability and validity is proposed.

(3) A driving behaviour analysis model based on SEM is established by matching items as manifest variables to latent variables. After model calculation, the path analysis results are utilized to show the main factors that influence the driving behaviours.

## 2. Materials and Methods

### *2.1. Driving Behaviour Questionnaire*

*2.1.1. Driving Behaviours and Its Influencing Factors.* The present study mainly focuses on Chinese drivers' psychology and driving experience and explores the mechanism of their influence on driving behaviours. At first, a self-reported questionnaire was designed and produced as the observation variable of the subsequent SEM model. The contents of the questionnaire are mainly divided into three types of driving behaviour (lapses and slips, mistakes, and violations) and three types of influencing factors (driving experience, rules and regulations, and psychology).

(1) Driving behaviours

The present study chose 3 typical driving behaviours (violations, lapse and slips, and mistakes) which are quoted directly or revised from classical previous studies [22, 24, 32]; meanwhile, the revised ones are modified in line with the actual traffic situation in China. For example, (1) the radical driving style of motorcycles for delivery who are usually cut-in recklessly or stop suddenly is easy to cause road chaos and give challenges to drivers' driving skills, temper, mental states, etc. (2) Although the traffic laws and penalties have been strengthened in the past few years, the Yield Here to Pedestrians in China is just in its infancy, the phenomenon of the Chinese crossing the road (gathering several people to cross the road and ignore the traffic lights) usually forces drivers to give the way even on green lights, and the drivers' emotion and mood may be changed in a negative or aggressive direction. (3) Due to different transportation facilities in different countries, some items, such as pelican crossing light (variable 37 in DBQ [22]), are inapplicable in China. In addition, inspired by the mechanism of driving behaviour research studies about Chinese drivers [34–38]), the other items were proposed based on authors' empirical views of actual road conditions, driving habits, traffic rules and regulations, etc. in China.

(a) Slips, lapses, and mistakes

Errors (slips, lapses, and mistakes) may be accounted for by reference to the information-processing characteristics of the individual. Reason et al. [22] defined that the failure of planned actions to achieve their intended consequences can involve two psychologically distinct kinds of "straying": the unwitting deviation of action from intention (slips and lapses) and the departure of planned actions from some satisfactory paths towards a desired goal (mistakes).

Therefore, the difference between error and slips or lapses is as follows: slips and lapses are undesirable results of involuntary actions and behaviours without thinking and decision-making, while error is caused by conscious deviation from rules or safety practices, mainly from the attitude and/or psychology of drivers [38, 39]. Norman [40] expressed it as follows: "if the intention is not appropriate, this is a mistake. If the action is not what was intended, this is a slip."

Unintentional violations often result from the driver's unintentional decisions, and the causes of unintentional violations are mostly misjudgement or error [41, 42]. For this reason, in this study, some unintentional violations are classified as errors or lapses and slips.

(b) Violations

Violations require explanation in terms of social and motivational factors [22]. This kind of behaviour of drivers will cause safety threats to other users on the road and have a negative impact on traffic safety. The reasons for the generation of violations are mainly divided into sense seeking and motion, egoism et al. [43]. Considering the influence of driver's mood, driving style, and characteristics on driving safety, the present study classifies violation driving behaviours into three categories: aggressive driving behaviour, emotional driving behaviour, and egoism driving behaviour. It is worth mentioning that the common unique road conditions in China are taken into consideration when formulating items, for example, (1) groups of takeout two-wheelers do not drive in a standard way, which is easy to cause road chaos or irritate drivers. (2) The phenomenon of the Chinese crossing scene (gathering enough people to cross the road and ignore the traffic lights) puts forward higher requirements for driver's courtesy to pedestrians and emotional adjustment.

(2) Influencing factors

(a) Driving experience

Since it is a vague and abstract concept, it is necessary to make a definition of the driving experience: rich driving experience means that the driver can play a positive role in maintaining and promoting traffic safety, which shows that they have good driving skills (driving stably, efficiently, and safely) and active solutions to road problems, as well as better emotional management and self-control ability. This paper proposes the hypothesis that experience has

variable influence on driving behaviours. Variables used to observe driving experience include emergency handling, vehicle condition control and monitoring, etc.

(b) Rules and regulations

Rules and regulations can affect driving behaviours from two perspectives: the first is that there are external constraints on drivers. Studies have found that human behaviour is not entirely voluntary, but under control [1, 44]. This paper holds that road rules and regulations, to some extent, are the factors to regulate and control the behaviour of drivers, and all drivers are supposed to be within the scope of this control. The driver's compliance with the rules and regulations limits some of his/her driving behaviours.

On the other hand, the existence of rules and regulations makes drivers have subjective internal locus of control [36, 45, 46]. People with high internal locus of control may have a more positive attitude towards maintaining traffic safety.

(c) Psychology

Attitude is a behavioural belief which has been shown approximately 50 percent of variance in intentions and approximately 30 percent in overall behaviour [1, 2]. Studies have tested the relevancy of attitude as a significant predictor and found it to be the significant [47–49]. Therefore, the driver's attitude plays a certain role in promoting or guiding the behaviour and the quality of the behaviour. On the other side, self-confidence and psychology are the important factors that influence drivers' intention and intervene their behaviour [45, 50, 51]. Moreover, as a daily activity, driving behaviour is influenced by various stressors [12, 52, 53], for example, when there are family or friends in the car, if the driver feels nervous, it may increase the probability of errors. The abovementioned points are in line with TPB: behaviour attitude, subjective norm, and perceptual behaviour control are the three main variables that determine behaviour intention. Thus, the psychology of this paper includes self-confidence, attitude, and awareness.

*2.1.2. Questionnaire Contents.* The questionnaire is mainly divided into two parts, the first part is the demographic characteristics of the subjects and the second part is the main body of the questionnaire:

(1) Demographic characteristics of the subjects: the proportion of gender and age of the investigated population should conform to the distribution of demographic characteristics of Chinese drivers, so that the sample can accurately and reasonably reflect the overall representativeness. The questionnaire needs to collect the information of the subjects including gender, age, and years of license.

(2) Main survey: the second part of the questionnaire is all of the rest items, the original is Chinese, and the English version is translated by two doctoral students majoring in transportation engineering. Details are provided in Supplementary Materials.

### 2.2. Measures

*2.2.1. Procedure.* All participants were informed that their information would be strictly confidential and would be used only for research. The questionnaires took approximately 6 minutes to complete. Participants received ¥8 compensation when they finished the questionnaire.

The questionnaire was designed using 5-point Likert scales [31]. Subjects were asked to rate how often they committed the behaviours described in the items. The options ranged from 0 to 5 as follows: 0, never; 1, hardly ever; 2, occasionally; 3, often; 4, frequently; and 5, nearly all the time.

*2.2.2. Subjects.* In the opinions of Rigdon et al. [54] and Tabachnick et al. [54], a sample larger than 200 can be considered as a medium-sized sample; to pursue stable SEM analysis results, it is better to have a sample larger than 200. If the number of samples is less than 150, the model estimation will be unstable, and the statistical testing strength of the model will be very low [56–59].

Referencing to the demographic characteristics of Chinese drivers, questionnaires are randomly distributed throughout China with conditions (controlling gender, age, etc.) through an online platform. The subjects under investigation have a Chinese-approved driving license. The questionnaires were successfully issued and recovered twice. After sorting out and eliminating invalid questionnaires, the effective questionnaires actually recovered for the first and second times were 262 and 528, respectively. The demographic data of the subjects are shown in Table 1.

### 2.3. Data Analysis

*2.3.1. Reliability Test.* In the research domain of human factors, many things cannot be measured directly and the questionnaires are often chosen as solutions by researchers. However, whether these items can achieve the purpose of research requires further analysis through statistical measure. Consequently, Cronbach's $\alpha$ is often used to measure the level of observational consistency of different items in the same dimension (especially when using the Likert scale [60]). The larger the value of $\alpha$, the stronger the internal consistency. The consistency level corresponding to each level of Cronbach's $\alpha$ is shown in Table 2.

After testing the reliability of the whole and part of the first questionnaire, we found that the overall reliability is excellent (68 items, Cronbach's $\alpha = 0.95$), but three parts (emergency response, rules and regulations, and psychology) are poor/unacceptable Table (see 3), which means the internal consistency is not ideal and the structure is supposed to be modified.

Table 1: Demographic characteristics of survey subjects.

| Demographic characteristics | | First survey | | Second survey | | Percentage of total Chinese driver population in 2019 |
|---|---|---|---|---|---|---|
| | | Quantity | Percentage | Quantity | Percentage | |
| *Gender* | Male | 170 | 65% | 348 | 66% | 70%* |
| | Female | 92 | 35% | 180 | 34% | 30%* |
| *Age* | 18~25 | 101 | 39% | 148 | 28% | — |
| | 26~35 | 83 | 32% | 201 | 38% | 34.12%* |
| | 36~50 | 73 | 28% | 174 | 33% | 38.88%* |
| | >60 | 5 | 2% | 5 | 1% | 2.9%* |
| *Years of license* | 0~1 | 30 | 11% | 48 | 9% | 7.94%** |
| | 1~3 | 74 | 28% | 211 | 40% | — |
| | 3~9 | 72 | 27% | 174 | 33% | — |
| | >10 | 37 | 14% | 95 | 18% | — |
| *Sample size* | | 262 | | 528 | | |

*Data source: Road Traffic Safety Research Centre of the Ministry of Public Security. **Data source: China Transportation Association Driving School Federation.

Table 2: Internal consistency level corresponding to Cronbach's $\alpha$.

| Cronbach's $\alpha$ | Internal consistency |
|---|---|
| $0.9 \le \alpha$ | Excellent |
| $0.8 \le \alpha < 0.9$ | Good |
| $0.7 \le \alpha < 0.8$ | Acceptable |
| $0.6 \le \alpha < 0.7$ | Questionable |
| $0.5 \le \alpha < 0.6$ | Poor |
| $\alpha < 0.5$ | Unacceptable |

Considering the number of observation variables contained in each latent variable is not more than 15, which is beneficial to improve the goodness-of-fit of SEM, the total number of items has reached 59 after several exploratory adjustments and deletion. According to the actual content of the items, emergency response, rules and regulations, and psychology are separated, reorganized, and replaced by safety awareness and attitude.

Finally, the deconstruction way of latent variable which meets the reliability standard is obtained. Cronbach's $\alpha$ of all latent variables is greater than 0.7 (see Table 4), and Cronbach's $\alpha$ of the whole items is 0.946. It shows that the overall reliability of the current questionnaire is good and the data are reliable [61].

*2.3.2. Validity Test.* In this paper, the KMO and Bartlett spherical test was conducted on the sample data and the maximum variance method was used to rotate the factors. Previous literature studies hold when the value is KMO test coefficient larger than 0.8, and the results could have better worth and practicability. From Table 5, the KMO statistic result indicates that the data structure of this study is good and performs internal correlation. The statistical significance probability of Bartlett's spherical test ($P < 0.001$) indicates that the validity of factor analysis data is good.

Table 3: Reliability test of initial latent variables.

| Latent variables | Items | Quantity | Cronbach's $\alpha$ | Reliability |
|---|---|---|---|---|
| Lapse and slips | L1 ~ L18 | 18 | 0.886 | Good |
| Mistakes | M1 ~ M9 | 9 | 0.859 | Good |
| Violations | D1 ~ D18 | 18 | 0.881 | Good |
| Experience | H1 ~ H11 | 11 | 0.885 | Good |
| Emergency response | E1 ~ E3 | 3 | 0.602 | Poor |
| Rules and regulations | R1 ~ R4 | 4 | 0.556 | Unacceptable |
| Psychology | P1 ~ P5 | 5 | 0.541 | Unacceptable |

### 2.4. Driving Behaviour Analysis Model Based on SEM

*2.4.1. Hypothetical Structural Model.* The proposed primary hypothetical model is shown in Figure 2. According to the relevant criteria of the TPB, the comprehensive analysis of the factors affecting the driver's behaviour is carried out. Furthermore, each driving behaviour module and influencing factor module are proposed, and the logical relationship of each module is expressed in the form of paths:

(1) According to TPB, learning from the outside world (knowledge, ideas, etc.) will indirectly/directly affect behaviour attitude, subjective norms, and perceptual behaviour control and ultimately affect intention and behaviour. Therefore, driving experience is an important factor influencing driver's behaviour. In the hypothesis model, the Exp includes emergency response, bad driving habits, peripheral monitoring (front, rear, left, and right), etc.

(2) In TPB, behaviour attitude, subjective norm, and perceptual behaviour control are the three main variables that determine behaviour intention. Therefore, SAA in this model includes observation variables such as safety awareness, subjective attitude, and traffic norm awareness.

Table 4: Test results of adjusted latent variable reliability.

| Latent variables | Abbr. | Items | Quantity | Cronbach's $\alpha$ | Reliability |
|---|---|---|---|---|---|
| Lapse and slips | LaS | L8 ~ L18, M2 | 12 | 0.855 | Good |
| Mistakes | Mis | M1, M3 ~ M9, D3, D9, R2, L6 | 12 | 0.868 | Good |
| Violations | Vio | D1, D4, D5, D7, D8, D11 ~ D18, R1 | 14 | 0.921 | Excellent |
| Experience | Exp | H1, H2, H7 ~ H11, E1 ~ E3 | 10 | 0.887 | Good |
| Safety attitudes and awareness | SAA | P1 ~ P5, D2, D10, H4, H5, R3, L3 | 11 | 0.728 | Acceptable |

Table 5: KMO and Bartlett's test.

| | | |
|---|---|---|
| Kaiser–Meyer–Olkin measure of sampling adequacy | | 0.912 |
| Bartlett's test of sphericity | Approx. chi-square | 9310.063 |
| | df | 1711 |
| | Sig. | 0.000 |

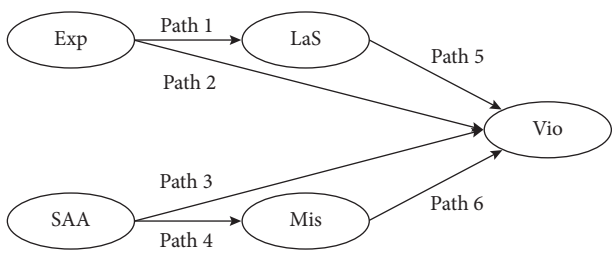


Figure 2: A hypothesis conceptual model of driving behaviours.

(3) Although Mis and LaS are usually unintentional violations, they may still threaten the safety of pedestrians and other road users; thus, they are used as intermediary effect in the structural model.

(4) According to Ajzen et al. [1], involuntary fully controlled behaviour is not only affected by the behaviour intention but also subject to the actual control conditions such as the subject's personal capabilities and experience. In the case of sufficient actual control conditions, behavioural intention directly determines the behaviour [62]. In the hypothesis model, SAA is the "behavioural intention," which includes driver's psychology, attitude, awareness, etc. Driver's driving experience is the constraint condition, and SAA and Exp are independent and mutually restricted to each other. Therefore, the Path 1 to Path 4 is proposed.

(5) Mis is mainly determined by the driver's awareness or psychology and is not directly related to the driving experience. Furthermore, LaS is not the result of the decision made by the driver, so it is not related to SAA.

*2.4.2. SEM Test.* SEM is a validated analysis model in the field of advanced statistics. It is a statistical method for analysing the relationship between variables based on the covariance matrix. It contains two secondary models: structural model and measurement model [61]. The structural model reflects the relationship between latent variables; the measurement model describes how latent variables are measured or conceptualized by the corresponding manifest indicators. Due to SEM can handle multiple manifest indicators and latent variables at the same time, it is often used to analyse concepts that are difficult to measure directly in social sciences and natural sciences.

This paper proposes manifest indicators for driving experience, psychology, etc., uses the SEM to analyse the influencing mechanism of various factors on driving behaviours, and then obtains the direct and indirect effects between each variable. The specific method is as follows: using data from the second batch of questionnaires (528 samples), the initial structural equation analysis model for driving behaviour research was constructed in AMOS 22.0. The maximum likelihood estimation method is used to estimate the parameters in the model, and the results are shown in Figure 3.

The companion probability P of critical ratio (C.R.) value was used to test the significance of the model's path coefficients. The path coefficients and its significance of the hypothetical model are listed in Table 6. The chi-square value of the initial model fit is 9738.043 ($P < 0.001$), and degree of freedom is 1646. Comparing with the recommended value in Table 7, the commonly used fitting index values, CFI and IFI, meet the requirements. However, RMSEA, $\chi^2$/DF, GFI, AGFI, NFI, and TLI do not meet the standard, and further structural model adjustment is needed to improve the goodness-of-fit.

According to the calculation results of the significant path coefficients in Table 8, the estimated normalized path coefficients of H7, H11, P1, and P4 are not significant. H7 and H11 were originally classified in the experience category because they examined the driver's ability to prevent risks; after analysing the items' content, these two items can try to be classified in SAA. Moreover, P1 and P4 were initially classified in the SAA because of their relationship with the driver's mental state and thoughts; from a practical point of view, the degree of driving experience will have a decisive effect on these two items. Therefore, P1 and P4 are recategorized into Exp. In addition, R3 more reflects the driver's psychological state, so it is classified in SAA.

## 3. Results

*3.1. Driving Behaviour Analysis Model.* Based on the above analysis and adjustment scheme, the revised structural equation model is obtained as shown in Figure 4. All the estimated values of path coefficient in the revised model are significant at the level of 0.01, indicating that the model has good significance, the model is credible at 95% confidence, and the model modification meets the standard.

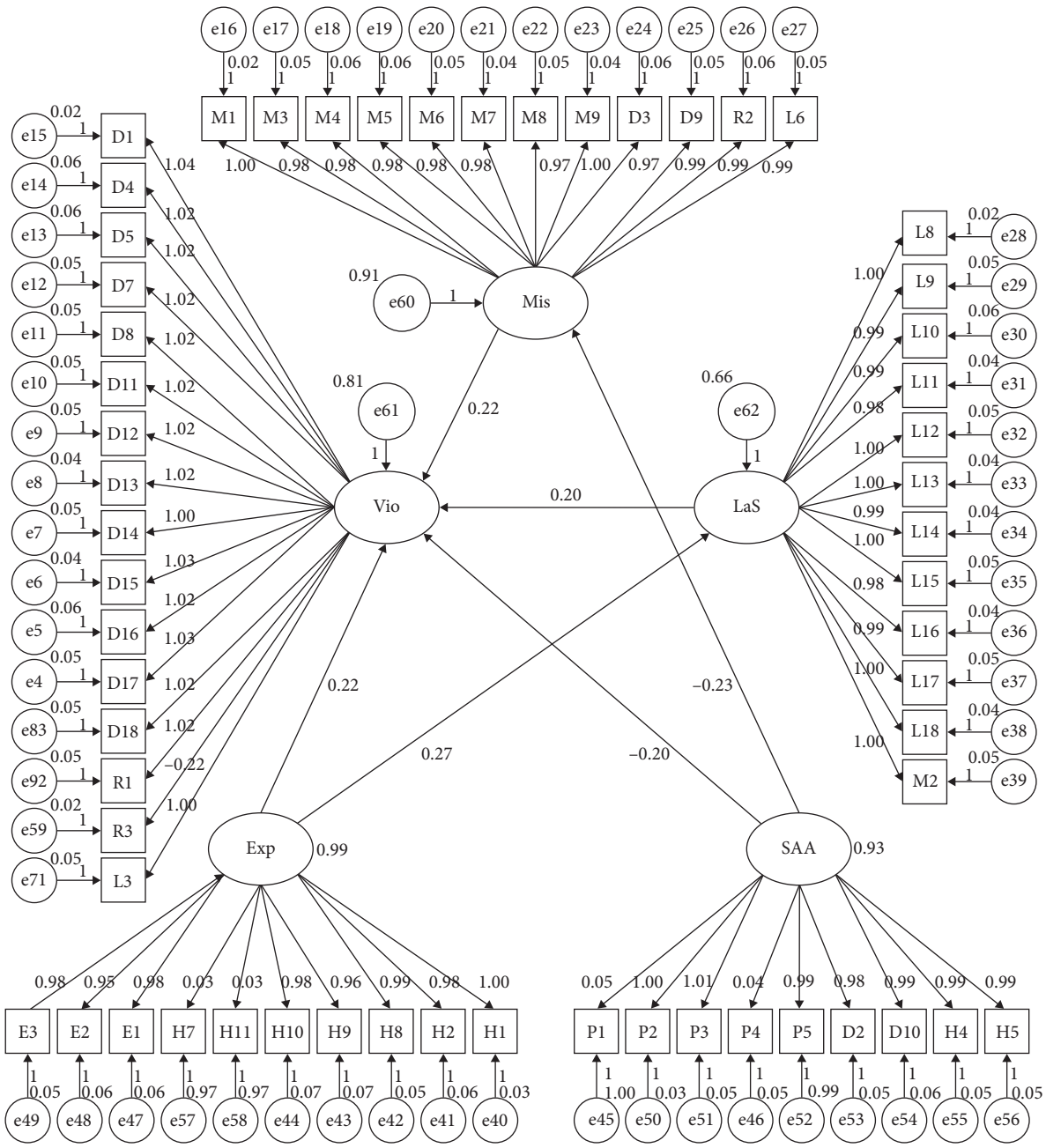


Figure 3: Results of the hypothetical structural model.

By comparing the goodness-of-fit values of the model before and after the modification (see Table 7), $\chi^2$/DF decreased from 5.697 to 2.392, and the fitting indexes were better than before the correction. The values of GFI, CFI, NFI, and IFI all reached the standard value, which means the driving behaviour analysis model has a good fit. The structure of final driving behaviour questionnaire is shown in Table 6. The manifested variables in each category can provide reference for measuring driving behaviour, driver's psychology, driving experience, and other factors that are difficult to measure directly.

*3.2. Analysis and Calculation Based on Path Coefficients.* By sorting out the path values, latent variables, and observation variables in Figure 4, the evaluation indexes of driving behaviour and its influencing factors are extracted. The structure diagram is shown in Figure 5. The results are as follows:

(1) The total influencing coefficient of Exp on Vio is 0.29 (direct impact coefficient is 0.23, and indirect impact coefficient is $0.27 * 0.21 \approx 0.06$). The direct influencing coefficient of Exp on LaS is 0.27, so it can be seen that the lack of driving experience can promote

Table 6: Structure of final driving behaviour questionnaire.

| Categories | Concise generalization | Items |
|---|---|---|
| *Lapse and slips* | Distracted driving | L9, L10 |
| | Vehicle condition control and monitoring | L11, L16, L18 |
| | Perception of road environment | L12, L15 |
| | The choice of correct driving lane | L13, L14 |
| | Blind area monitoring | L17, L18, M2 |
| *Violations* | Aggressive driving behaviour | D4, D5, D7, D8, D14, D16, D18, R1 |
| | Emotional driving behaviour | D1, D11, D12, D13, D15, D17 |
| | Egoism behaviour | L3 |
| *Mistakes* | Wrong identification of traffic signs | M1 |
| | Wrong lane selection | M3, M7, M8, D3 |
| | Distracted driving | M4 |
| | Illegal driving | M5, D9, L6 |
| | Distance misjudgement | M6, M9, R2 |
| *Experience* | Vehicle condition control and monitoring | H1, H2, |
| | Vehicle peripheral monitoring | H8, H9, H10 |
| | Driving confidence | P1 |
| | Experienced cautious driving style | P4, E3 |
| | Emergency handling | E1, E2 |
| *Safety awareness and attitude* | Attitude to ADAS | P2 |
| | Attitude to other drivers | P3, P5 |
| | Attitude to pedestrians | D2 |
| | Bad driving behaviours | H4, H5 |
| | Attitude to traffic regulations | D10, R3 |
| | Self-safety awareness | H7 |
| | Safety awareness to others | H11 |

Table 7: Comparison of the goodness-of-fit values between the hypothetical model and the modified model.

| Fit indices | Recommended value | Before revision | After revision |
|---|---|---|---|
| $\chi^2$/DF | 1 ~ 3 | 5.697 | 2.392 |
| GFI | ≥0.9 | 0.706 | 0.849 |
| AGFI | ≥0.8 | 0.684 | 0.838 |
| CFI | ≥0.9 | 0.902 | 0.971 |
| NFI | ≥0.9 | 0.884 | 0.951 |
| IFI | ≥0.9 | 0.903 | 0.971 |
| TLI | ≥0.9 | 0.899 | 0.970 |
| RMSEA | ≤0.08 | 0.094 | 0.051 |

Table 8: Path coefficients of the hypothetical structural model.

| Path | Estimate | C.R. | *P* | Path | Estimate | C.R. | *P* | Path | Estimate | C.R. | *P* |
|---|---|---|---|---|---|---|---|---|---|---|---|
| LaS←Exp | 0.27 | 7.534 | *** | M1←Mis | 1 | — | — | L18←LaS | 1 | 74.819 | *** |
| Mis←SAA | −0.23 | −5.284 | *** | M3←Mis | 0.977 | 82.261 | *** | M2←LaS | 0.999 | 70.054 | *** |
| Vio←Mis | 0.222 | 5.348 | *** | M4←Mis | 0.979 | 78.667 | *** | H1←Exp | 1 | — | — |
| Vio←LaS | 0.205 | 4.202 | *** | M5←Mis | 0.978 | 79.83 | *** | H2←Exp | 0.977 | 73.308 | *** |
| Vio←SAA | -0.2 | −4.735 | *** | M6←Mis | 0.983 | 82.447 | *** | H7←Exp | 0.028 | 0.639 | 0.523 |
| Vio←Exp | 0.221 | 5.265 | *** | M7←Mis | 0.981 | 87.988 | *** | H8←Exp | 0.988 | 79.909 | *** |
| L3←Vio | 1 | — | - | M8←Mis | 0.974 | 83.402 | *** | H9←Exp | 0.964 | 68.949 | *** |
| R1←Vio | 1.023 | 73.71 | *** | M9←Mis | 1.001 | 88.661 | *** | H10←Exp | 0.984 | 72.016 | *** |
| D18←Vio | 1.021 | 72.601 | *** | D3←Mis | 0.974 | 77.81 | *** | H11←Exp | 0.029 | 0.663 | 0.507 |
| D17←Vio | 1.027 | 72.885 | *** | D9←Mis | 0.986 | 83.606 | *** | E1←Exp | 0.98 | 74.487 | *** |
| D16←Vio | 1.017 | 68.226 | *** | R2←Mis | 0.986 | 80.271 | *** | E2←Exp | 0.952 | 72.162 | *** |
| D15←Vio | 1.027 | 74.666 | *** | L6←Mis | 0.985 | 85.305 | *** | E3←Exp | 0.978 | 77.372 | *** |
| D14←Vio | 1.003 | 70.161 | *** | L8←LaS | 1 | — | — | P1←SAA | 0.046 | 1.022 | 0.307 |
| D13←Vio | 1.024 | 75.156 | *** | L9←LaS | 0.986 | 69.682 | *** | P2←SAA | 1 | — | — |

Table 8: Continued.

| Path | Estimate | C.R. | *P* | Path | Estimate | C.R. | *P* | Path | Estimate | C.R. | *P* |
|---|---|---|---|---|---|---|---|---|---|---|---|
| D12←Vio | 1.015 | 72.633 | *** | L10←LaS | 0.986 | 68.049 | *** | P3←SAA | 1.013 | 80.123 | *** |
| D11←Vio | 1.018 | 72.713 | *** | L11←LaS | 0.977 | 74.258 | *** | P4←SAA | 0.039 | 0.87 | 0.384 |
| R3←Vio | −0.224 | −5.402 | *** | L12←LaS | 1.003 | 73.931 | *** | P5←SAA | 0.994 | 81.872 | *** |
| D8←Vio | 1.021 | 71.747 | *** | L13←LaS | 0.999 | 77.335 | *** | D2←SAA | 0.982 | 76.561 | *** |
| D7←Vio | 1.016 | 73.164 | *** | L14←LaS | 0.994 | 78.108 | *** | D10←SAA | 0.989 | 75.543 | *** |
| D5←Vio | 1.018 | 68.899 | *** | L15←LaS | 1.003 | 70.004 | *** | H4←SAA | 0.995 | 81.042 | *** |
| D4←Vio | 1.02 | 70.28 | *** | L16←LaS | 0.984 | 74.61 | *** | H5←SAA | 0.994 | 79.244 | *** |
| D1←Vio | 1.041 | 87.044 | *** | L17←LaS | 0.994 | 70.609 | *** | | | | |

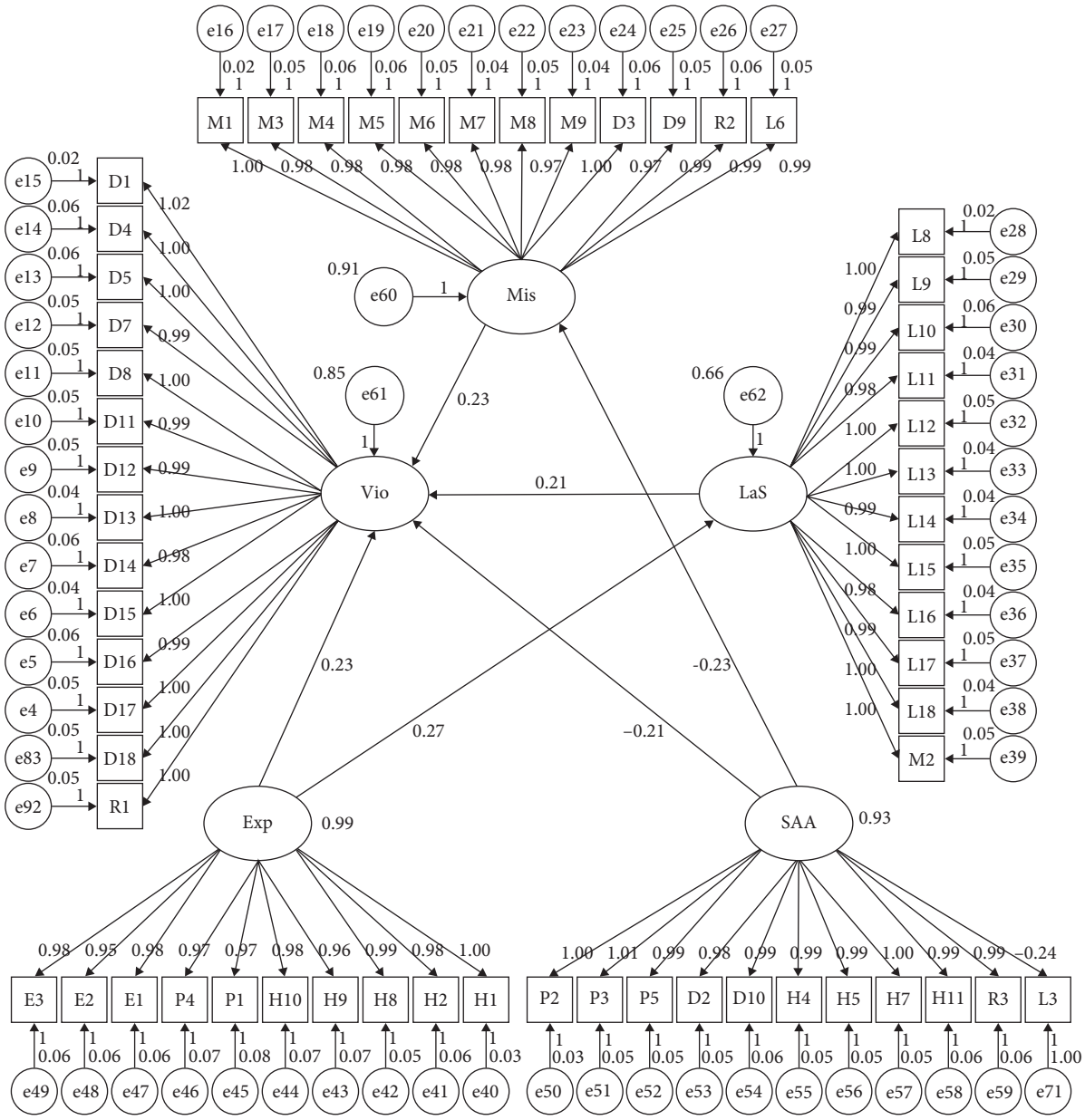


Figure 4: Driving behaviour analysis model.

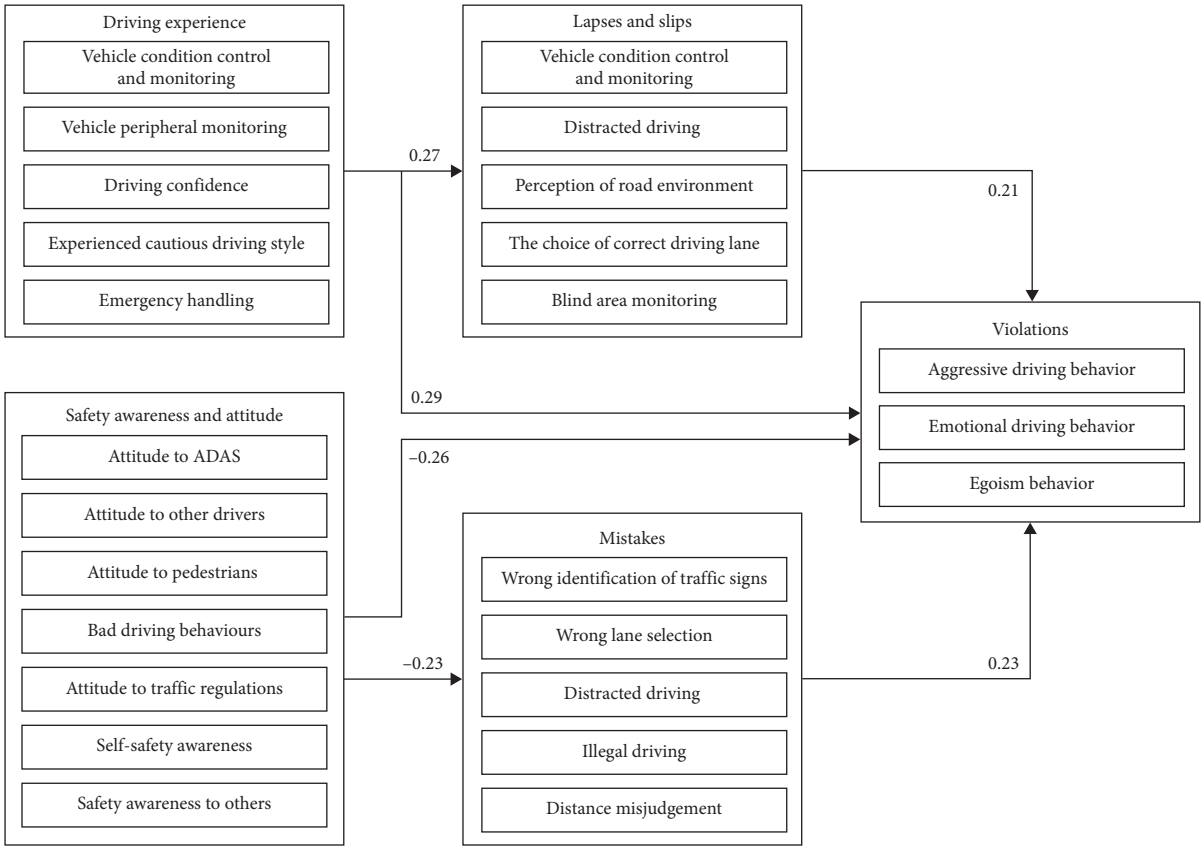


Figure 5: Schematic diagram of driving behaviour and its influencing factors.

the violation behaviours and the lapses and slips behaviours.

(2) The total influencing coefficient of SAA on Vio is −0.26 (direct impact coefficient is -0.21, and indirect impact coefficient is $-0.23 * 0.23 \approx 0.05$). The direct influencing coefficient of SAA on Mis is −0.23. It is shown that good safety attitude and awareness can inhibit the violation behaviours and the mistake behaviours, especially the violation behaviours.

(3) In addition to driving experience, safety attitude, and awareness, violations are also influenced by mistakes, lapses, and slips. The influencing coefficients of Mis and LaS on Vio are 0.23 and 0.21, respectively. It shows that there is a chance that error driving behaviour will be transformed into violation driving behaviours.

## 4. Discussion

*4.1. Summaries and Conclusions.* Latent factors such as driving experience, psychology, and attitude are important elements affecting driving behaviour; however, it is difficult to quantify their influencing mechanism by means of direct instruments. The self-report survey method is a commonly used and effective method to solve this kind of problems. In this paper, based on the results of previous related research studies, we developed a refined version of a 59-item Chinese driving behaviour questionnaire. The results confirmed that the structure of the questionnaire has good construct validity and that it is a useful scale to measure the self-reported driving behaviours in China. Moreover, after the deconstruction of driving behaviour and its influencing factors by TPB, the hypothesis structural equation model was built, tested, and improved into a well-organized version. Taking the path direction and the path value as the direction and degree of action among latent variables, combining with the actual item contents, the influencing mechanism among driving behaviours and its influencing factors was analysed. Finally, we reached the following conclusions:

(1) The influence coefficients of Exp on Vio and LaS are 0.29 and 0.27, respectively, indicating that driving experience has an impact on violations, lapses, and slips. Combining the contents of the items, with the goal of reducing violations and lapses and slips, it should be improved from the following aspects: vehicle peripheral monitoring (H8, H9, and H10), vehicle condition control and monitoring (H1 and H2), experienced cautious driving style (P4 and E3), emergency handling (E1 and E2), and driving confidence (P1).

(2) The influencing coefficients of SAA on Vio and Mis are −0.26 and −0.23, respectively, indicating that good safety awareness and attitude can inhibit violations and mistakes. Combined with the actual content of manifested variables, it is necessary to

improve and correct the driver's psychology, attitude, and awareness to reduce the violational driving behaviours and bad driving behaviours. And it should be improved from the following aspects: attitude to other drivers (P3 and P5) and pedestrians (D2), attitude to traffic regulations (D10 and R3), bad driving behaviours (H4 and H5), self-safety awareness (H7), attitude to ADAS (P2), and safety awareness to others (H11).

(3) LaS and Mis, respectively, are intermediary effect behaviours between Exp and Vio, SAA, and Vio. Which means although LaS and Mis are the actual behaviours behaved by drivers, they are not exactly the terminal from the plan to the behaviour; in some cases, they will be converted to Vio. Based on (1) and (2), the prime aim of improving road traffic safety is to reduce Vio; the main measures of which are to educate and correct the drivers' Exp and SAA. Furthermore, drivers' LaS and Mis are buffering and transition processes, which should be corrected timely and prevented from continuing to develop into Vio.

To sum up, the Chinese driving behaviour questionnaire designed in this paper can be used to study and measure the driving behaviour, driving psychology and driving experience. The results of the study also have certain practical application and theoretical support reference value for improving road traffic safety, reducing the threat of drivers to road users, and training and educating drivers.

*4.2. Limitations and Prospects.* This paper aims to improve road traffic safety from the perspective of improving and reducing bad driving behaviours and can also provide reference for the training program of driving schools. The advantages of the current study are based on the demographic characteristics of Chinese drivers, and this makes the conclusions close to the actual situation as much as possible. However, due to not all drivers know enough about themselves or are unwilling to confess their real situation, for other reasons, the questionnaire may be affected by the driver's subjective errors. We believe that using the present analysis results and real vehicle driving tests to verify each other could better solve this problem. Before coming to fully autonomous driving stage, it is necessary to explore better ways to educate and restrain drivers scientifically and improve traffic safety.

## Data Availability

The data used to support the result of this study are available from the corresponding author upon request.

## Conflicts of Interest

The authors declare that there are no conflicts of interest regarding the publication of this paper.

## Acknowledgments

This work was supported by the National Natural Science Foundation of China (52072333), Natural Science Foundation of Hebei Province (E2020203092), Hebei Provincial Key Research Projects (no. 20310801D), National Natural Science Foundation of China (no. U19A2069), National Key Research and Development Program of China (2018YFB1600501), and the First Batch of 2020 MOE Industry-University Collaborative Education Program (program no.202001SJ05, Kingfar-CES "Human Factors and Ergonomics Program").

## Supplementary Materials

Supplementary Materials (Chinese driving behaviour questionnaire) are provided as an attached document along with the article. (*Supplementary Materials*)

## References

[1] China Road Traffic Accidents Statistics, *Traffic Administration Bureau of the Ministry of Public Security of PRC*, China Road Traffic Accidents Statistics, Beijing, China, 2013.

[2] L. Melton, B. Guo, Y. Jiang, F. Wang, X. Xie, and M. Gao, "Study on the impact degrees of several driving behaviors when driving while performing secondary tasks," *IEEE Access*, vol. 6, pp. 65772–65782, 2018.

[3] T. L. Milfont and R. Fischer, "Testing measurement invariance across groups: applications in cross-cultural research," *International Journal of Psychological Research*, vol. 3, no. 1, pp. 111–130, 2010.

[4] D. R. Mayhew, H. M. Simpson, and A. Pak, "Changes in collision rates among novice drivers during the first months of driving," *Accident Analysis & Prevention*, vol. 35, no. 5, pp. 683–691, 2003.

[5] J. Kroenung and A. Eckhardt, "The attitude cube-a three-dimensional model of situational factors in is adoption and their impact on the attitude-behavior relationship," *Information & Management*, vol. 52, no. 6, pp. 611–627, 2015.

[6] K. T. Hua and Z. J. Cheng, "Application and analytical strategies of structural equation modelling," *Exploration of Psychology*, vol. 19, no. 69, pp. 54–59, 1999.

[7] J. Reason, A. Manstead, S. Stradling et al., "Errors and violations on the roads: a real distinction?" *Ergonomics*, vol. 33, no. 10-11, pp. 1315–1332, 1990.

[8] L. M. Martinussen, L. Hakamies-Blomqvist, M. Møller, T. Özkan, and T. Lajunen, "Age, gender, mileage and the DBQ: the validity of the driver behavior questionnaire in different driver groups," *Accident Analysis & Prevention*, vol. 52, pp. 228–236, 2013.

[9] D. Lauro, R. Zhang, and X. Qu, "The role of personality traits and driving experience in self-reported risky driving behaviors and accident risk among Chinese drivers," *Accident Analysis & Prevention*, vol. 99, pp. 228–235, 2017.

[10] B. Guo, L. Jin, D. Sun, J. Shi, and F. Wang, "Establishment of the characteristic evaluation index system of secondary task driving and analyzing its importance," *Transportation Research Part F: Traffic Psychology and Behaviour*, vol. 64, pp. 308–317, 2019.

[11] T. Özkan, T. Lajunen, J. E. Chliaoutakis, D. Parker, and H. Summala, "Cross-cultural differences in driving

behaviours: a comparison of six countries," *Transportation Research Part F: Traffic Psychology and Behaviour*, vol. 9, no. 3, pp. 227–242, 2006.

[12] A. E. Curry, K. B. Metzger, A. F. Williams, and B. C. Tefft, "Comparison of older and younger novice driver crash rates: informing the need for extended graduated driver licensing restrictions," *Accident Analysis & Prevention*, vol. 108, pp. 66–73, 2017.

[13] M. Van Gelderen, M. Brand, M. Van Praag, W. Bodewes, E. Poutsma, and A. Van Gils, "Explaining entrepreneurial intentions by means of the theory of planned behaviour," *Career Development International*, vol. 13, no. 6, pp. 538–559, 2008.

[14] Y.-H. Huang, W. Zhang, M. Roetting, and D. Melton, "Experiences from dual-country drivers: driving safely in China and the us," *Safety Science*, vol. 44, no. 9, pp. 785–795, 2006.

[15] M. Fishbein and I. Ajzen, "Belief, attitude, intention, and behavior: an introduction to theory and research," *Contemporary Sociology*, vol. 6, no. 2, 1977.

[16] M. Tenenhaus, V. E. Vinzi, Y.-M. Chatelin, and C. Lauro, "Pls path modeling," *Computational Statistics & Data Analysis*, vol. 48, no. 1, pp. 159–205, 2005.

[17] E. Yadegaridehkordi, M. H. Nizam Bin Md Nasir, N. Fazmidar Binti Mohd Noor, L. Shuib, and N. Badie, "Predicting the adoption of cloud-based technology using fuzzy analytic hierarchy process and structural equation modelling approaches," *Applied Soft Computing*, vol. 66, pp. 77–89, 2018.

[18] C. Siebe, "Distracted driving and risk of road crashes among novice and experienced drivers," *The Journal of Emergency Medicine*, vol. 46, no. 4, pp. 54–59, 2014.

[19] A. Dinis, A. Do Paço, J. Ferreira, M. Raposo, and R. Gouveia Rodrigues, "Psychological characteristics and entrepreneurial intentions among secondary students," *Education + Training*, vol. 55, no. 8/9, pp. 763–780, 2013.

[20] C. Schlaegel and M. Koenig, "Determinants of entrepreneurial intent: a meta-analytic test and integration of competing models," *Entrepreneurship Theory and Practice*, vol. 38, no. 2, pp. 291–332, 2014.

[21] WHO, *Global Status Report on Road Safety 2015*, World Health Organization, Geneva, Switzerland, 2015.

[22] W. Qu, Y. Ge, C. Jiang, F. Du, and K. Zhang, "The Dula dangerous driving index in China: an investigation of reliability and validity," *Accident Analysis & Prevention*, vol. 64, pp. 62–68, 2014.

[23] P. Stahl, B. Donmez, and G. A. Jamieson, "Eye glances towards conflict-relevant cues: the roles of anticipatory competence and driver experience," *Accident Analysis & Prevention*, vol. 132, pp. P105–P255, 2019.

[24] J. Shi, Y. Bai, X. Ying, and P. Atchley, "Aberrant driving behaviors: a study of drivers in beijing," *Accident Analysis & Prevention*, vol. 42, no. 4, pp. 1031–1040, 2010.

[25] J. J. M. Ferreira, M. L. Raposo, R. Gouveia Rodrigues, A. Dinis, and A. Do Paço, "A model of entrepreneurial intention," *Journal of Small Business and Enterprise Development*, vol. 19, no. 3, pp. 424–440, 2012.

[26] Y. Gürol and N. Atsan, "Entrepreneurial characteristics amongst university students," *Education + Training*, vol. 48, no. 1, pp. 25–38, 2006.

[27] P.-A. Rimmö, "Aberrant driving behaviour: homogeneity of a four-factor structure in samples differing in age and gender," *Ergonomics*, vol. 45, no. 8, pp. 569–582, 2002.

[28] D. Chliaoutakis, J. T. Reason, A. S. R. Manstead, and S. G. Stradling, "Driving errors, driving violations and accident involvement," *Ergonomics*, vol. 38, no. 5, pp. 1036–1048, 1995.

[29] D. P. Upahita, Y. D. Wong, and K. M. Lum, "Effect of driving experience and driving inactivity on young driver''s hazard mitigation skills," *Transportation Research Part F: Traffic Psychology and Behaviour*, vol. 59, pp. 286–297, 2018.

[30] A. Bener, T. Özkan, and T. Lajunen, "The driver behaviour questionnaire in Arab gulf countries: Qatar and United Arab Emirates," *Accident Analysis & Prevention*, vol. 40, no. 4, pp. 1411–1417, 2008.

[31] B. González-Iglesias, J. A. Gómez-Fraguela, and M. Á. Luengo-Martín, "Driving anger and traffic violations: gender differences," *Transportation Research Part F: Traffic Psychology and Behaviour*, vol. 15, no. 4, pp. 404–412, 2012.

[32] K. Stradling, A. Raineri, V. Beanland, J. Bell, and M. Borzycki, "Expert drivers are better than non-expert drivers at rejecting unimportant information in static driving scenes," *Transportation Research Part F: Traffic Psychology and Behaviour*, vol. 59, no. A, pp. 389–400, 2018.

[33] M. Naushad, "A study on the antecedents of entrepreneurial intentions among Saudi students," *Entrepreneurship and Sustainability Issues*, vol. 5, no. 3, pp. 600–617, 2018.

[34] B. Scott Parker, T. De Regt, C. Jones, and J. Caldwell, "The situation awareness of young drivers, middle-aged drivers, and older drivers: same but different?" *Case Studies on Transport Policy*, vol. 8, no. 1, pp. 206–214, 2018.

[35] X. Wang and X. Xu, "Assessing the relationship between self-reported driving behaviors and driver risk using a naturalistic driving study," *Accident Analysis & Prevention*, vol. 128, pp. 8–16, 2019.

[36] A. Rauch and M. Frese, "Let''s put the person back into entrepreneurship research: a meta-analysis on the relationship between business owners'' personality traits, business creation, and success," *European Journal of Work and Organizational Psychology*, vol. 16, no. 4, pp. 353–385, 2007.

[37] B. G. Tabachnick and L. S. Fidell, "Using multivariate statistics," *Journal of Clinical Psychopharmacology*, vol. 2, no. 6, 2007.

[38] L. P. Waddell and K. K. K. Wiener, "What's driving illegal mobile phone use? Psychosocial influences on drivers' intentions to use hand-held mobile phones," *Transportation Research Part F: Traffic Psychology and Behaviour*, vol. 22, pp. 1–11, 2014.

[39] W. Qu, Q. Zhang, W. Zhao, K. Zhang, and Y. Ge, "Validation of the driver stress inventory in China: relationship with dangerous driving behaviors," *Accident Analysis & Prevention*, vol. 87, pp. 50–58, 2016.

[40] C.-Q. Xie and D. Parker, "A social psychological approach to driving violations in two Chinese cities," *Transportation Research Part F: Traffic Psychology and Behaviour*, vol. 5, no. 4, pp. 293–308, 2002.

[41] W. Du, W. Zhang, and Y. Ge, "The moderating effect of delay discounting between sensation seeking and risky driving behavior," *Safety Science*, vol. 123, Article ID 104558, 2020.

[42] W. Minglong, *Structural Equation Model: Operation and Application of AMOS (2nd edtion)*, Chongqing university press, Chongqing, China, 2019.

[43] D. Norman, "Position paper on human error," *NATO Advanced Research Workshop on Human Error*, Beilagio, Italy, 1983.

[44] I. Ajzen and M. Fishbein, "Attitudes and the attitude-behavior relation: reasoned and automatic processes," *European Review of Social Psychology*, vol. 11, no. 1, pp. 1–33, 2000.

[45] G. Pnina, P. E. Johnathon, C. Zhu et al., "Crash risk and risky driving behaviour among adolescents during learner and independent driving periods," *Journal of Adolescent Health*, vol. 63, no. 5, pp. 568–574, 2018.
[46] L. Chandrasekaran, A. Crookes, and T. C. Lansdown, "Driver situation awareness-investigating the effect of passenger experience," *Transportation Research Part F: Traffic Psychology and Behaviour*, vol. 61, pp. 152–162, 2019.
[47] S. Nasip, S. R. Amirul, S. L. Sondoh Jr., and G. H. Tanakinjal, "Psychological characteristics and entrepreneurial intention," *Education + Training*, vol. 59, no. 7/8, p. 825, 2017.
[48] E. Gulian, G. Matthews, A. I. Glendon, D. R. Davies, and L. M. Debney, "Dimensions of driver stress," *Ergonomics*, vol. 32, no. 6, pp. 585–602, 1989.
[49] R. O. Mueller and O. Ralph, "Structural equation modeling: back to basics," *Structural Equation Modeling: A Multidisciplinary Journal*, vol. 4, no. 4, pp. 353–369, 1997.
[50] S. F. Niu, Y. J. Liu, L. Wang, and H. Q. Li, "Effects of different intervention methods on novice drivers' speeding," *Sustainability*, vol. 11, 2019.
[51] C. S. Dula and M. E. Ballard, "Development and evaluation of a measure of dangerous, aggressive, negative emotional, and risky Driving1," *Journal of Applied Social Psychology*, vol. 33, no. 2, pp. 263–282, 2003.
[52] A. M. Przepiorka, A. P. Błachnio, and M. J. M. Sullman, "Factors influencing intentions to text while driving among Polish drivers," *Transportation Research Part F: Traffic Psychology and Behaviour*, vol. 55, pp. 306–313, 2018.
[53] S. Matus, L. Sramkova, and R. Risser, "The manchester driver behaviour questionnaire: self-reports of aberrant behaviour among Czech drivers," *European Transport Research Review*, vol. 6, no. 4, pp. 493–502, 2014.
[54] I. Ajzen, "The theory of planned behavior," *Organizational Behavior and Human Decision Processes*, vol. 50, no. 2, pp. 179–211, 1991.
[55] R. Summala, "A technique for the measurement of attitudes," *Archieves of Psychology*, vol. 22, pp. 1–55, 1932.
[56] S. P. Walsh, K. M. White, M. K. Hyde, and B. Watson, "Dialling and driving: factors influencing intentions to use a mobile phone while driving," *Accident Analysis & Prevention*, vol. 40, no. 6, pp. 1893–1900, 2008.
[57] J. Mesken, T. Lajunen, and H. Summala, "Interpersonal violations, speeding violations and their relation to accident involvement in Finland," *Ergonomics*, vol. 45, no. 7, pp. 469–483, 2002.
[58] S. T. D. Cordazzo, C. T. Scialfa, and R. J. Ross, "Modernization of the driver behaviour questionnaire," *Accident Analysis & Prevention*, vol. 87, pp. 83–91, 2016.
[59] G. Sta, "Global status report on road safety," *Injury Prevention*, vol. 15, no. 4, p. 286, 2015.
[60] E. E. Rigdon and E. Edward, "A necessary and sufficient identification rule for structural models estimated in practice," *Multivariate Behavioral Research*, vol. 30, no. 3, pp. 359–383, 1995.
[61] P.-A. Rimmö and L. Åberg, "On the distinction between violations and errors: sensation seeking associations," *Transportation Research Part F: Traffic Psychology and Behaviour*, vol. 2, no. 3, pp. 151–166, 1999.
[62] T. Lajunen, D. Parker, and H. Summala, "The manchester driver behaviour questionnaire: a cross-cultural study," *Accident Analysis & Prevention*, vol. 36, no. 2, pp. 231–238, 2004.

Hindawi
Advances in Civil Engineering
Volume 2021, Article ID 6657017, 14 pages
https://doi.org/10.1155/2021/6657017

*Research Article*

# Modeling and Simulation of Departure Passenger's Behavior Based on an Improved Social Force Approach: A Case Study on an Airport Terminal in China

**Yaping Zhang,[1] Jialin Li,[1] Dexuan Kong,[1] Xiaoqing Xing,[2] Qian Luo,[3,4] and Jian Mao[4]**

[1]*School of Transportation Science and Engineering, Harbin Institute of Technology, Harbin 150090, China*
[2]*School of Aeronautical Engineering, Civil Aviation Flight University of China, Guanghan 618307, China*
[3]*The Second Research Institute of CAAC, Chengdu 610041, China*
[4]*Chengdu Civil Aviation Information Technology Co. Ltd., Chengdu 611430, China*

Correspondence should be addressed to Yaping Zhang; zxlt0905@163.com

Received 23 October 2020; Revised 31 December 2020; Accepted 9 January 2021; Published 28 January 2021

Academic Editor: Hui Yao



The unprecedented growth of passenger throughput in large airport terminals highlights the importance of analyzing passengers' movement to achieve airport terminal's elaborate management. Based on the theory of original social force model, video data from a departure hall of a large airport terminal in China were analyzed to summarize passengers' path planning characteristics. Then, a double-level model was established to describe passengers' path planning behaviors. At the decision level of the proposed model, the avoiding force model including common avoiding force and additional horizontal avoiding force was established on the basis of setting time and space limitations for taking avoiding action and was used to describe passengers' path planning in close-range space. At the tactical level of the proposed model, the route and node choice models were established to describe passengers' path planning in long-range space. In the route choice model, a distribution of intermediate destination areas was proposed, with detouring distance, pedestrian density, speed difference, and pedestrian distribution considered in choosing an intermediate destination area. In the node choice model, the walking distance, the quantity of people waiting, and luggage were considered in choosing a check-in counter or security check channel. The main parameters of the proposed model were confirmed according to video data. Simulation results show that the proposed model can simulate departure passengers' path planning behaviors at an acceptable accuracy level.

## 1. Introduction

With the growth of passenger throughput, more airport terminals lack sufficient infrastructures to offer passengers efficient service. At the same time, huge passenger throughput may cause congestion in some parts of an airport terminal and lead to potential risk of security assurance [1, 2]. An important way to solve these problems is to dispatch and use the existing terminal facilities efficiently to organize the passengers sensibly.

An airport terminal is a complex infrastructure composed of many subsystems, such as check-in, security check, waiting in the airport lounge, and boarding [3]. Passengers are the main service targets of all these segments. Thus, analyzing passengers' traffic behaviors is the basis for improving the terminal's internal facility planning, resource allocation, and passenger organization. Among all the segments mentioned above, many departure passengers are accompanied by relatives and friends before security check, making pedestrians' traffic behaviors in the departure hall more complex than other regions in the terminal. Therefore, focusing on departure passengers' traffic behaviors before security check is significant to provide a decision-making basis for improving airport terminal's internal facility planning, resource allocation, and passenger organization. To describe departure passengers' path planning behaviors, we chose the social force model [4] as the basic theory given its previous application to describe pedestrian's microscopic traffic behaviors in several different scenes.

Analyzing passengers' microscopic traffic behaviors is the key to realizing airport terminal's elaborate management of facility planning and passenger organization needs [5, 6]. Additionally, in the departure hall before entering the security check area, departure passengers' avoiding, route, and node choice behaviors are different from those shown in other walking scenes due to the special layouts. Thus, this study analyzed passengers' characteristic microscopic traffic behaviors in a departure hall based on a video of a large airport terminal in China. Then, a double-level model was established to describe passengers' path planning behaviors for the first time. At the decision level, by defining passengers' avoiding time and space limitations, the close-range avoiding behavior can be described quantificationally. At the tactical level, passengers' long-range route and node choice behaviors were modeled. Finally, the simulation results were compared with video data to prove the proposed model's accuracy.

The structure of this paper is as follows. Section 1 briefly introduces the research background. Section 2 presents the literature review. Section 3 introduces the original social force model's theory. Section 4 describes our analysis of the departure passenger's avoiding behavior in the departure hall and the design of the avoiding social force model as the decision-level path planning model. Section 5 details our analysis of departure passenger's route and service facility choice behaviors in the departure hall and the establishment of the route and node choice social force model as the tactical-level planning model. Section 6 confirms the proposed model's parameters according to video data and then compares the simulation results with video data to prove the proposed model's effectiveness. Section 7 concludes the research findings and proposes further research suggestions.

## 2. Literature Review

Modeling and simulating the motion of passengers in a terminal departure hall is a valid approach. The models on pedestrian dynamics can be categorized as macroscopic and microscopic. Compared with the macroscopic models, which study the movement characteristics of the pedestrian flow, the microscopic models focus on the movement of each pedestrian and have been much more widely used in the pedestrian traffic research field. The most common microscopic simulation models include the cellular automata model [7] and the social force model [4]. In the automata model, pedestrians are assumed to be homogeneous [8], consequently ignoring pedestrian heterogeneity and preference. However, the social force model is a successful approach in the field of crowd dynamics [9, 10], in which the agents having personalized characteristics form a complex crowd dynamic system. The social force model in the form of various forces can not only simulate pedestrian's microscopic movement but also describe the relationship between group behaviors. The simulation results largely fit the actual observation results and thus mainly explain why the social force model is chosen as the research method in this study.

In 1998, the social force model was first proposed by Dirk Helbing [4], which indicates that a pedestrian's movement is determined by three kinds of social force, namely, self-driven, psychological repulsive, and attractive forces. Helbing et al. improved the model by considering physical force (friction and stress) in subsequent research [11, 12]. Since then, more researchers pay attention to pedestrian's microscopic behaviors on the basis of the social force model. Their related studies can be divided into two categories: one only focuses on pedestrian's decision-level behaviors and improves the theory of each social force; the other adds a tactical-level route and the destination choice model in which the original social force model was not mentioned before.

Pedestrian's avoiding behavior is the main focus of research in path planning's decision level. The original social force model's psychological repulsive force could not show a pedestrian's voluntary avoiding behavior; thus, further research improved social avoiding force's form and mechanism [13–15]. For example, Wang et al. [16] proposed that pedestrians adjust their desired speed considering the position of exits, obstacles, and other pedestrians to facilitate their discovery of the quickest path to destination. Additionally, Xiao et al. [17] and Qu et al. [18] employed the Voronoi diagram to calculate the detour route of an agent. Based on the avoiding force's prediction mechanism, pedestrians decide how to avoid conflicting objects by considering their relative positions when collision happens [19–21]. To sum up, the recent research about the social force model (shown in Table 1) puts emphasis on the pedestrian collision avoidance and the shortest detour route, to name a few.

Path planning's tactical level includes pedestrians' route and node choice behaviors. For pedestrians' route choice behaviors, researchers tend to consider more factors which affect pedestrians' choices. Walking time [22] and route length [23] are utilized as the evaluation indexes of the shortest path. Two major factors affect the route choice: (a) environmental and (b) personal factors. The most influential environmental factors are distances from destination [24], congestion degree [25], speed difference [26], and exit's width [27, 28]. Apart from environmental factors, personal factors can also affect exit choice. The most influential personal factor is the familiarity of the decision-maker with the route [29]. Furthermore, physical ability (depending on the age or health), habits, and sociopsychological characteristics (e.g., direct or indirect risk perception, cultural background or training, and past experience) can affect route choice. The research on pedestrians' node choice behavior showed a similar trend with route choice. For example, Zheng et al. [30] established the metro station's exit choice model regarding distance, pedestrian density, and width of exit.

The research mentioned above was mainly applied in the outdoors and metro or railway stations and cannot be used to study pedestrian flow at airport terminal. In fact, the terminal departure hall and the above scenarios have common characteristics (e.g., the avoiding, route, and node selection behaviors). Thus, the studies can be extended to explore the pedestrian flow in the terminal departure hall. This research will propose a revised social force model

Table 1: Comparison of current research about the social force model.

| | Basic model | Repulsive force revision | Pedestrian collision avoidance | Detour |
|---|---|---|---|---|
| Helbing [4] | √ | | | |
| Helbing [11, 12] | √ | √ | | |
| Wang [16] | √ | | √ | |
| Xiao [17] | √ | | | √ |
| Jia [14] | √ | √ | | √ |
| Qu [18] | √ | | | √ |
| Yamamoto [15] | √ | | √ | |

according to the motion characteristic of the pedestrians and companions in the terminal departure hall.

## 3. Social Force Model

The original social force model proposed by Helbing [4,11,12] indicates that pedestrians move according to three different kinds of social forces, namely, self-driven, psychological repulsive, and physical forces. A pedestrian's movement is calculated by Newton's second law considering the three kinds of social forces: self-driven force $\vec{f}_i^0$, demonstrating the expectation of pedestrian $i$ arriving at the destination, and "interaction forces" $\vec{f}_{ij}$ and $\vec{f}_{iw}$ from other pedestrians $j$ and walls $w$, respectively. The corresponding equations are given by

$$m_i \frac{\mathrm{d}\vec{V}_i}{\mathrm{d}t} = \vec{f}_i^0 + \sum_{j(j\neq i)} \vec{f}_{ij} + \sum_w \vec{f}_{iw}, \quad \vec{f}_i^0 = m_i \frac{V_i^0 \vec{e}_i(t) - \vec{V}_i(t)}{\tau_i}, \tag{1}$$

where $m_i$ is the mass of pedestrian $i$, $\vec{V}_i$ is pedestrian $i$'s velocity at time $t$, $V_i^0$ is the value of pedestrian $i$'s desired velocity, and $\vec{e}_i(t)$ is the unit vector of pedestrian $i$'s desired velocity pointing from pedestrian $i$'s position to his/her destination.

$\vec{f}_{ij}$ is the resultant force of psychological repulsive and physical forces from pedestrians $j$ to $i$, which can be calculated as follows:

$$\begin{aligned}\vec{f}_{ij} &= A_i \exp\left[\frac{r_{ij} - d_{ij}}{B_i}\right]\vec{n}_{ij} + kg\left(r_{ij} - d_{ij}\right)\vec{n}_{ij} \\ &\quad + Kg\left(r_{ij} - d_{ij}\right)\Delta V_{ji}^t \vec{t}_{ij},\end{aligned} \tag{2}$$

where $A_i$ is the strength parameter and $B_i$ is the range parameter. $r_{ij}$ is the sum of pedestrian $i$'s radius $r_i$ and pedestrian $j$'s radius $r_j$, and $d_{ij}$ is the distance between pedestrians $i$ and $j$. $\vec{n}_{ij}$ is the unit vector pointing from pedestrians $j$ to $i$. $k$ and $K$ are the strength parameters of friction and press, respectively; $\vec{t}_{ij}$ is the unit vector of the relative motion's direction; and $\Delta V_{ji}^t = (\vec{V}_j - \vec{V}_i) \cdot \vec{t}_{ij}$ is the tangential speed difference between pedestrians $i$ and $j$. $g(x)$ is a piecewise function which can be calculated as follows:

$$g(x) = \begin{cases} 0, & d_{ij} > r_{ij}, \\ x, & d_{ij} \leq r_{ij}. \end{cases} \tag{3}$$

The resultant force $\vec{f}_{iw}$ including wall $w$ to pedestrian $i$'s psychological repulsive and physical forces has a similar form to the resultant force from pedestrians $j$ to $i$, which is given by

$$\begin{aligned}\vec{f}_{iw} &= A_i \exp\left[\frac{r_i - d_{iw}}{B_i}\right]\vec{n}_{iw} + kg\left(r_i - d_{iw}\right)\vec{n}_{iw} \\ &\quad + Kg\left(r_i - d_{iw}\right)\left(\vec{V}_i^t \cdot \vec{t}_{iw}\right)\vec{t}_{iw}.\end{aligned} \tag{4}$$

Figure 1 illustrates the interpretation of the social force model.

## 4. Departure Passengers' Decision-Level Path Planning Model

Pedestrians' decision-level traffic behaviors determine their walking direction and speed in a close range around themselves. For departure passengers, avoiding other pedestrians and obstacles in a close range is their decision-level path planning behavior. In this paper, close-range area refers to the small area around the passenger, where pedestrian avoiding behavior occurs, defined as a semicircular area with a radius of 1.5 m centered on the passenger. Here, the avoiding behavior includes not only avoiding collision with opposite pedestrians but also overtaking low-speed pedestrians walking ahead. This section first summarizes departure passengers' avoiding behavior according to video data from a large airport terminal in China. Then, it establishes departure passengers' avoiding social force model on the basis of the characteristics of their avoiding behavior.

*4.1. Departure Passenger Avoiding Behavior's Characteristics.* In this part, we collect a 15 min (starting at 6 a.m.) video on March 21, 2018, from the surveillance camera installed on the east side of island C of a departure hall in a large airport terminal in China, to analyze and summarize passengers' avoiding behavior. The video includes check-in area, queuing area before security check, and common walking area in the departure hall, with over 500 passengers involved in it. According to the analysis of the video data, we summarize passengers' avoiding behavior characteristics as follows:

(1) Passengers only avoid other pedestrians or obstacles in a close range.

(2) Passengers only avoid other pedestrians or obstacles within their visual field.

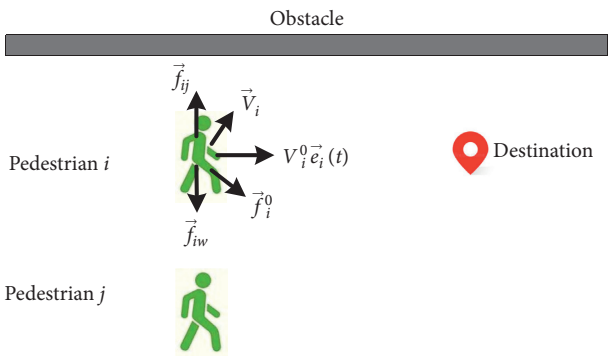


Figure 1: Diagram of the social force model.

(3) Passengers' avoiding action has different priorities; the sooner a potential conflict happens, the earlier they will take avoiding action.

(4) Passengers have the ability to anticipate potential collisions. They forecast their future positions and potential conflict objects. Then, they change their speed accordingly instead of merely keeping a distance from their conflict objects' real-time location.

(5) Each passenger has a smallest personal demand space just a little larger than the space he/she occupies on the ground. The area of this space differs from person to person, but nearly all the passengers avoid others because they do not want others to enter their personal space.

According to the avoiding characteristics mentioned above, we first provide the time and space limitations of taking avoiding action and then establish departure passengers' avoiding social force model.

*4.2. Time and Space Limitations of Taking Avoiding Action.* Given that passengers only avoid other pedestrians or obstacles in their visual field and are not far from themselves, we combine sight and distance to describe the space limitation of avoiding.

As shown in Figure 2, a passenger can possibly take avoiding action in such a sector area. In the sector area, the middle circle $P_i$ is passenger $i$. Defining that the space occupied by passenger $i$ is a circle area, the smallest personal demand space should be a circle area just a little larger than the area occupied by passenger $i$. Therefore, we use the concentric circle larger than passenger $i$ to describe his/her smallest personal demand space, with its radius represented by $r_i^0$. The angle of this sector is 180°, which represents a passenger's range of vision. $l_i^0$ is the radius of the sector, which limits that a passenger will not avoid other objects farther than this distance to himself/herself. To summarize, a departure passenger's space limitation of taking avoiding behavior can be represented as follows:

$$P_i^0 = \left\{P_j | d_{ij} \le l_i^0, \varphi_{ij} \in \left[-\frac{\pi}{2}, \frac{\pi}{2}\right]\right\}, \tag{5}$$

where $P_i^0$ is the set of other pedestrians and obstacles that will be possibly avoided by passenger $i$ according to the space limitation and $P_j$ represents pedestrian or obstacle $j$.

Based on the space limitation, we then confirm the time limitation of taking avoiding action. Given that passengers have the ability to anticipate potential collisions, we forecast their positions while in conflict by the following equation:

$$\left\| \left(\vec{x}_j + \vec{V}_j t\right) - \left(\vec{x}_i + \vec{V}_i t\right) \right\| = r_i^0 + r_j, \tag{6}$$

where $\vec{x}_i$ and $\vec{x}_j$ are the real-time locations of passengers $i$ and $j$, respectively, and $t$ is the time interval from the current moment to the time when potential collision happens.

Equation (6) indicates that if passengers $i$ and $j$ maintain their motion at the current moment, they will conflict with each other after time $t$. Here, passengers $i$ and $j$ conflicting with each other equals passenger $i$'s smallest personal space boundary tangents to the circle occupied by passenger $j$. In equation (6), $t$ is the unknown value, and the minimum positive root of equation (6) is the time interval to potential conflict. If equation (6) has no positive root, conflict will not happen; thus, passenger $i$ does not have to avoid. In addition, the smaller the $t$ is, the sooner the passenger $i$ will have to take avoiding action.

In summary, passenger $i$ will take avoiding action only if the time and space limitation are both qualified. Moreover, passenger $i$ will first avoid passenger $j$ with the smallest time interval to potential conflict.

*4.3. Avoiding Social Force Model.* According to departure passengers' avoiding behavior characteristics mentioned in Section 4.1, passengers forecast future positions of themselves and potential conflict objects and change their speed accordingly. Thus, the direction of avoiding force should be from passenger $j$'s centroid to passenger $i$'s centroid at the potential conflict place. Moreover, the closer passenger $i$ is to his/her position while conflicting with passenger $j$, the stronger the avoiding force will be. Therefore, the avoiding social force can be measured as follows:

$$\vec{f}_i^{soc} = A_i \exp\left(\frac{-d_{ij}'}{B_i}\right)\vec{n}_{ij}', \tag{7}$$

where $d_{ij}'$ is the distance from passenger $i$'s real-time location to his/her location when conflict happens and $\vec{n}_{ij}'$ is the unit vector pointing from passenger $j$'s centroid to passenger $i$'s centroid at the potential conflict place.

Figures 3(a) and 3(b) show the differences between the original social force model's repulsive force and the avoiding force model proposed in this paper. As shown in Figure 3(a), the original social repulsive force points from pedestrian $j$ to pedestrian $i$, making pedestrian $i$ take action to move away from $j$. By contrast, in Figure 3(b), our avoiding force model lets passenger $i$ walk faster to arrive at the potential conflict point earlier than $j$ to avoid conflicting with passenger $j$, and this action fits the true behavior of passengers in the departure hall.

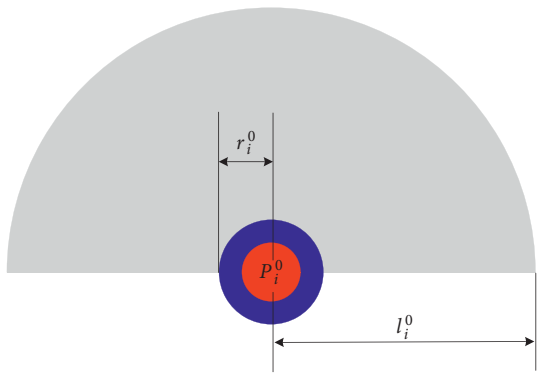


Figure 2: Space limitation of taking avoiding action.

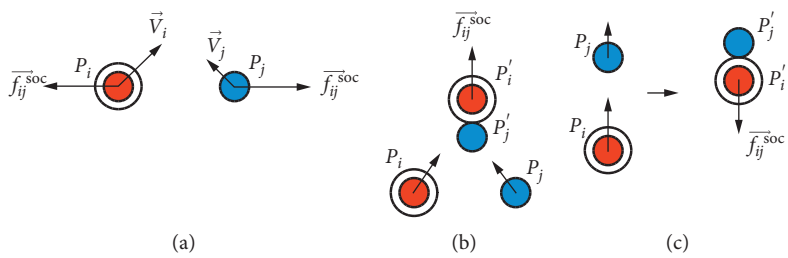


Figure 3: Comparison of avoiding force and original psychological repulsive force.

Figure 3(c) shows a possible condition in which the avoiding force points to the opposite direction of passenger $i$'s velocity vector. According to observations from the departure hall's video, a passenger will change his/her walking direction rather than merely decelerating. In such circumstances, we add a horizontal avoiding force to passenger $i$ to describe his/her flexible detouring behavior. The bigger the passenger $i$ and $j$'s velocity difference on $i$'s horizontal direction, the easier for passenger $i$ to detour; thus, the horizontal avoiding force should be smaller. Therefore, the accessional horizontal avoiding force can be calculated as follows:

$$\vec{f}_i^{\text{avo}} = -\frac{C_i}{\vec{V}_j \cdot \sin\langle \vec{V}_i, \vec{V}_j \rangle}, \tag{8}$$

where $C_i$ is the strength parameter of the accessional horizontal avoiding force and $\vec{V}_i, \vec{V}_j$ is the angle between passengers $i$ and $j$'s walking direction.

In summary, a passenger avoids his/her first conflicting object under the common avoiding force calculated by equation (7). If the common avoiding force is opposite to his/her walking direction, the accessional horizontal avoiding force calculated by equation (8) also exists.

## 5. Departure Passengers' Tactical-Level Path Planning Model

Pedestrians' tactical-level traffic behaviors determine their walking direction and speed in a long range in their walking scene. For departure passengers, the long-range area can be the entire terminal departure hall, and their tactical-level path planning behavior includes route and node choices (including check-in counters and security check channels). In our model, passengers' tactical-level model determines their self-driven force by changing their temporary walking direction. This section first summarizes departure passengers' route and node choice characteristics according to video data mentioned in Section 3 and then establishes departure passengers' tactical-level route choice model.

*5.1. Departure Passengers' Route and Node Choice Characteristics.* Combining on-the-spot study and analysis of video data, we summarize passengers' route and node choice characteristics as follows:

(1) Each passenger has a final destination in the departure hall, but their trajectories are not always direct to the destination. Instead, they often change their walking direction and approach the final destination gradually.

(2) The factors that passengers consider while changing their walking direction include distance, pedestrian density, and speed difference. Passengers seemingly tend to reduce detour distance to achieve efficiency. They also tend to walk through areas where pedestrian density is low and speed difference is small to walk comfortably.

(3) The nodes that passengers have to choose in the departure hall are service facilities including manual check-in counters, self-service check-in facilities, and

security check channels. These facilities are usually distributed in line. Accordingly, passengers choose one from the same kind of facilities when entering relevant service segments.

(4) When choosing a manual check-in counter or security check channel, a passenger typically considers his/her distance to the facility and the number of passengers waiting for service in each queue. While walking to the queuing area, they cannot always know the number of people in the queue because people at the end of the queue may cover their front people. In such a circumstance, passengers tend to estimate the number of people waiting in the queue by observing the distribution of people and luggage at the end of the queue.

(5) Passengers waiting before a self-service check-in facility often distribute themselves similar to a sector: The first passenger using the facility occupies the sector's vertex, while other waiting passengers behind him/her stand on his/her left or right and attempt to forecast when they can use the facility.

Among all the characteristics mentioned above, the first and second characters are related to route choice behaviors, and the rest are about passengers' node choice. Based on these characteristics, we establish route and node choice models, respectively, in Sections 5.2 and 5.3.

*5.2. Departure Passengers' Route Choice Model.* To describe passengers changing walking direction, we first set a series of intermediate destination areas and then model passengers' temporary desired speed direction to simulate passengers' gradual path planning behavior until they reach their final destination.

As shown in Figure 4, considering passengers' visual field and average horizontal and vertical displacement, we distribute the walking area of the departure hall into a series of identical rectangles. Using $l_i^{\text{sight}}$ to represent the distance between passenger $i$'s regard point and his/her real-time location when making long-range tactical decision, we define the length of the rectangle's long side as half of $l_i^{\text{sight}}$, and the length of the rectangle's short side is adjusted according to passengers' average horizontal displacement. In this circumstance, when passenger $i$ arrives at the lower boundary of a rectangle, he/she begins to choose one of the rectangles whose lower boundaries are collinear with the upper boundary of the rectangle he/she is standing on.

According to passengers' route choice characteristics mentioned in Section 4.1, passengers tend to reduce detouring distance. Thus, the sum of the distance from passenger $i$'s location to an intermediate destination area and the distance from the same intermediate destination area to passenger $i$'s final destination should be as small as possible. At the same time, passenger $i$ tends to choose an intermediate destination area with low pedestrian density and small speed difference between him/her and others. Furthermore, other pedestrians' distribution in an intermediate destination area also affects passenger $i$'s choice. If pedestrians in an intermediate destination area are not close to its lower boundary, passenger $i$ is more likely to choose this area. On the basis of these analyses, we use a cost function to measure the cost if passenger $i$ chooses intermediate destination area $j$:

$$U_j = \left(\frac{\omega_1 l_1 + \omega_2 l_2}{d_{i-des}}\right)^{k_3} + \left(\frac{\sum_a \left\|\vec{V}_a - \vec{V}_i\right\|}{\left\|\vec{V}_i\right\|}\right)^{k_4} \times \left(\frac{n}{S_j}\right)^{k_5} \times \left(1 - \frac{S_j'}{S_j}\right)^{k_6}, \quad (9)$$

where $l_1$ and $l_2$ are the distances from passenger $i$'s location to an intermediate destination area's lower boundary midpoint and the distance from the same intermediate destination area's lower boundary midpoint to passenger $i$'s final destination, respectively. $\omega_1$ and $\omega_2$ are the weights of $l_1$ and $l_2$, respectively, which are used to guarantee that passenger $i$ will not keep being farther from his/her final destination when making temporary route choices (if passenger $i$'s route choice draws him/her away from the final destination, $\omega_1$ will decrease and $\omega_2$ will increase). $n$ is the number of pedestrians in the intermediate destination area $j$, $S_j$ is the area of walking space in intermediate destination area $j$, and $S_j'$ is the area of the rectangle formed by passenger $i$'s nearest pedestrian and the lower boundary of intermediate destination area $j$. $k_3$ to $k_6$ are the impact degree parameters of detouring distance, speed difference, pedestrian density, and pedestrian distribution, respectively.

Among the intermediate destination areas on the same horizontal line, passenger $i$ will choose the one with the smallest cost function value as his/her temporary destination area. On the basis of this choice, passenger $i$'s desired speed vector should be pointing from $i$'s real-time location to the midpoint of $i$'s nearest passable gap in the chosen rectangle given that pedestrians always tend to adjust their motion as slightly as possible.

*5.3. Departure Passengers' Node Choice Model.* Departure passengers' node choice can be seen as a kind of special route choice. Therefore, passengers' node choice shares the same trigger mechanism with route choice behavior. In the departure hall, the nodes that passengers must choose are the service facilities including manual check-in counters, self-service check-in facilities, and security check channels. Considering that passengers typically choose one from the same kind of service facilities which are located in line, we discuss passengers' choices of each kind of service facility, respectively.

When choosing a manual check-in counter, a passenger usually considers the distance he/she has to walk to reach the counter as well as the expected waiting time. For a certain counter, waiting time depends on the quantity of passengers and their luggage in the queue, because both printing boarding pass and checking luggage need time. However, clearly counting the number of people and bags is difficult for passengers out of the queue. In such a circumstance, passengers estimate the total number of people and the amount of luggage in the queue through the distribution of people and luggage at the tail of the queue. Therefore, we use a cost function to measure the cost if passenger $i$ chooses manual check-in counter $j$:

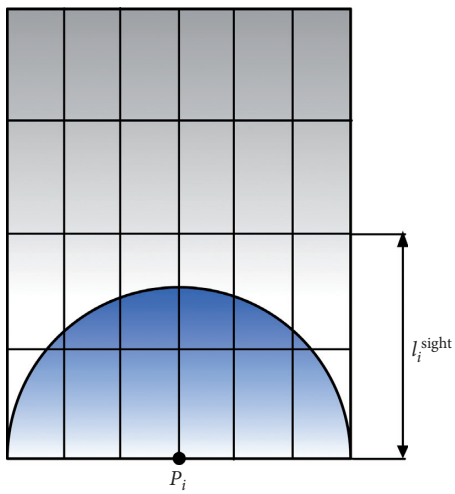


Figure 4: Distribution of intermediate destination areas.

$$U_j = \left(\frac{d_{ij}}{d_{ij}^{\min}}\right)^{k_7} + \left[\frac{Q_j^{\text{length}}}{Q_{\text{res}}} \cdot \left(\omega_3 N_j^P + \omega_4 N_j^L\right)\right]^{k_8}, \quad (10)$$

where $d_{ij}$ is the distance from passenger $i$ to manual check-in counter $j$; $d_{ij}^{\min}$ is the distance between passenger $i$ and his/her nearest manual check-in counter. $Q_i^{\text{lenght}}$ is the length of queue before counter $j$ and $Q_{\text{res}}$ is the length of dividing strip in check-in area. $N_j^P$ and $N_j^L$ represent the density of people and luggage at the tail of the queue before counter $j$, respectively. $\omega_3$ and $\omega_4$ are the weights of $N_j^P$ and $N_j^L$, respectively, and their ratio is equal to the ratio of printing boarding pass for a passenger's time consumption and checking a piece of luggage's time consumption. $k_7$ and $k_8$ are the impact degree parameters of distance and the quantity of waiting passengers and their bags, respectively.

When choosing a self-service check-in facility, passengers also consider the distance to reach the facility and the number of waiting passengers before each facility. An obvious difference with manual check-in counter is that people who use self-service check-in facility have no luggage to check. Thus, the time consumption of checking luggage is not a concern. Moreover, passengers waiting before a self-service check-in facility are often distributed similar to a sector as mentioned in Section 4.1. Accordingly, we use the area of this sector to estimate the number of waiting passengers because counting waiting people clearly at once is difficult for approaching passengers. Following these analyses, we use a cost function to measure the cost if passenger $i$ chooses self-service check-in facility $j$:

$$U_j = \left(\frac{d_{ij}}{d_{ij}^{\min}}\right)^{k_9} \times \left(\frac{S_j^{\text{occ}}}{S^{\text{one}}}\right)^{k_{10}}, \quad (11)$$

where $S_j^{\text{occ}}$ is the area of the sector occupied by waiting passengers before self-service check-in facility $j$; $S^{\text{one}}$ is the area of the space occupied by the first passenger using the self-service check-in facility. $k_9$ and $k_{10}$ are the impact degree parameters of distance and the number of waiting passengers.

When choosing a security check channel, the factors considered by passengers are the same as those of manual check-in counter. Therefore, we use equation (10) to measure the cost if passenger $i$ chooses security check channel $j$.

Above all, passenger $i$ will choose a service facility with the smallest cost value among all service facilities of the same kind in line.

## 6. Model Simulation and Verification

In this section, we first propose our parameter settings and then compare the simulation results of the proposed model with relevant video data to show its effectiveness in simulating departure passengers' path planning behaviors.

*6.1. Parameter Settings.* We simulated video data mentioned in Section 3 and also considered previous work to confirm the value of the proposed model's main parameters. Table 2 provides each parameter's symbol, description, and value.

*6.2. Simulation and Verification of Passengers' Avoiding and Route Choice Behavior.* To simulate passengers' avoiding and route choice behavior, we use a common walking area in the departure hall of a large airport terminal in China as the walking scene. As shown in Figure 5, the common walking area is cut out from the surveillance video. The dashed areas in this figure represent obstacles: The smaller one on the top of the figure is a billboard, and the bigger one in the middle of the figure is a parterre. The upper right corner is part of check-in counters' dividing strips.

To record passengers' location conveniently, we establish a plane Cartesian coordinate system on the scene. According to Figure 5, we set the lower left quarter as the origin of the coordinate system, and the lower boundary and left boundary are the $x$- and $y$-axes, respectively. Based on these settings, each point in the scene can be represented by 2D coordinates. According to the video data, we define the long side of the intermediate destination as equal to 2.5 m and the short side as equal to 1.5 m. Thus, the walking scene can be divided into $7 \times 3$ suppositional rectangles.

As examples, trajectories of thirteen passengers in this area were used to simulate passengers' movement, and each passenger was given a number according to his/her entrance order. To show the effects of each part of the route choice cost function, we discuss the motion of three passengers (passengers 1, 6, and 13) who are amply affected by different factors and briefly summarize the results of the rest.

Passenger 1 entered the walking scene from the right of the billboard, with his trajectory nearly straight at the beginning. Then, he detoured a handcart which stands to the right of the parterre, with its ordinate equal to 4.25 and the maximum distance to the right boundary of the parterre equal to 0.5 m. After detouring, he slowly approached the parterre's right boundary and finally sat down at the boundary where ordinate is equal to 2.387 m.

Table 2: Parameter settings.

| Symbol | Description | Value |
|---|---|---|
| $\tau_i$ | Time consumption of changing velocity | 0.5 s |
| $l_i^0$ | Radius of avoiding behavior's space limitation | 1.5 m |
| $A_i$ | Strength parameter of avoiding force | 200N |
| $B_i$ | Range parameter of avoiding force | 1.5 m |
| $C_i$ | Strength parameter of horizontal avoiding force | 40N |
| $k_1$ | Strength parameter of press | $1.2 \times 10^5$ kg·s$^{-2}$ |
| $k_2$ | Strength parameter of friction | $2.4 \times 10^5$ kg m$^{-1}$·s$^{-1}$ |
| $k_3$ | Impact degree parameter of distance in route choice | 2 |
| $k_4$ | Impact degree parameter of speed difference in route choice | 1 |
| $k_5$ | Impact degree parameter of density in route choice | 2 |
| $k_6$ | Impact degree parameter of distribution in route choice | 1 |
| $k_7$ | Impact degree parameter of distance in node choice | 1 |
| $k_8$ | Impact degree parameter of waiting people in node choice | 1 |

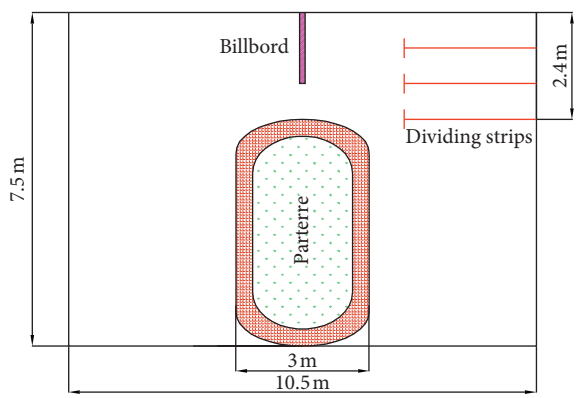


Figure 5: Common walking area used for simulation.

Figure 6 shows the comparison between the real trajectory and the emulational trajectory of passenger 1. The red line represents the real trajectory extracted from the video by Tracker, while the blue line represents the trajectory simulated by the proposed model (the places of abscissa and ordinate are exchanged to observe the trajectories conveniently). Qualitatively comparing the two trajectories, we can find that their overall trends are similar, and the places on $y$-axis when maximum abscissa appears are also adjacent, which indicated that the proposed model can simulate the passenger's moving trend. Quantificationally analyzing the two trajectories, we find that when passenger 1 was entering the second row of intermediate destination areas, the coordinates of emulational trajectory were (7.0027, 5.1045), while the corresponding abscissa of real trajectory was 6.85, which had an aberration smaller than half of passenger 1's radius with emulational coordinates. The emulational trajectory's maximum abscissa appeared at (7.7971, 4.2255). Compared with the real trajectory's maximum abscissa points (7.990, 4.395), their ordinate aberration when maximum abscissa appeared was about 0.17 m, which is also smaller than half of passenger 1's radius. When closely approaching the right boundary of the parterre, the rake ratios of real and emulational trajectory were 2.29 and 1.87, respectively. In addition, the end points of real and emulational trajectory were (6.801, 2.387) and (6.7945, 2.3807), respectively, with an aberration smaller than 1 cm. These results indicated that the proposed model can accurately simulate the process of approaching the destination.

Passenger 6's motion was similar to passenger 1, but an obvious difference was that when passenger 6 was entering the second row of intermediate destination areas, four walking passengers occupied the intermediate destination area which had the smallest detouring distance for passenger 6. By contrast, when passenger 1 began to choose intermediate destination areas on the second row, no passenger was blocking his way.

Figure 7 shows the comparison between the real trajectory and the emulational trajectory of passenger 6. The red line represents the real trajectory extracted from the video by Tracker, while the blue line represents the trajectory simulated by the proposed model (the places of abscissa and ordinate are exchanged to observe the trajectories conveniently). Qualitatively comparing the two trajectories, we can find that the first half of the two trajectories is not superimposed but shows a similar trend. Maximum abscissa appeared at a similar place, and the values of maximum abscissa are also similar. The two trajectories' latter half shows an accordant trend when approaching the destination. Thus, the proposed model can simulate the passenger's moving trend. Quantificationally analyzing the two trajectories, we find that when ordinate approached 5 m (which indicated that passenger 6 was entering the second row of intermediate destination areas), the coordinates of real trajectory were (7.4669, 5.0029), and emulational trajectories were (7.1712, 5.0534), which indicated that passenger 6 chose the intermediate destination area closest to the parterre's right boundary both in reality and in simulation. Both real trajectory and emulational trajectory's maximum abscissa appeared when ordinate was between 4.2 and 4.3 m, with their coordinates equal to (8.267, 4.256) and (8.2792, 4.2735), respectively, and the distance between these two coordinates was only 0.02 m. Moreover, passenger 6's emulational maximum abscissa appeared at a similar vertical position to passenger 1, which indicates that the proposed model can simulate passenger's close-range direction change after choosing an intermediate destination area. The only difference from real trajectory was that when the ordinate

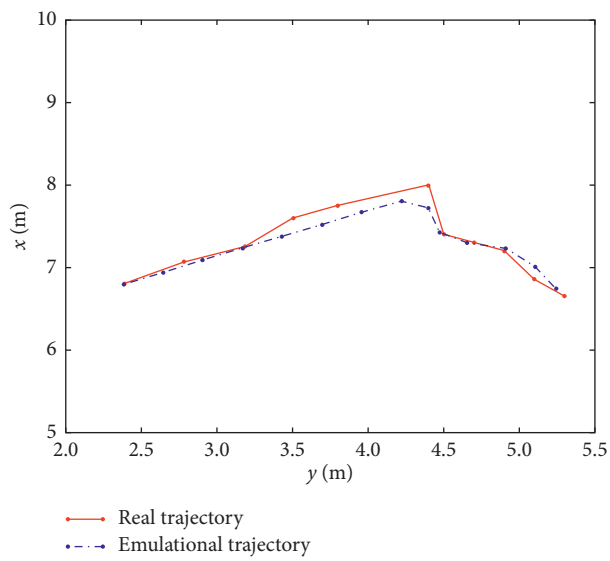


Figure 6: Comparison of passenger 1's real and emulational trajectory.

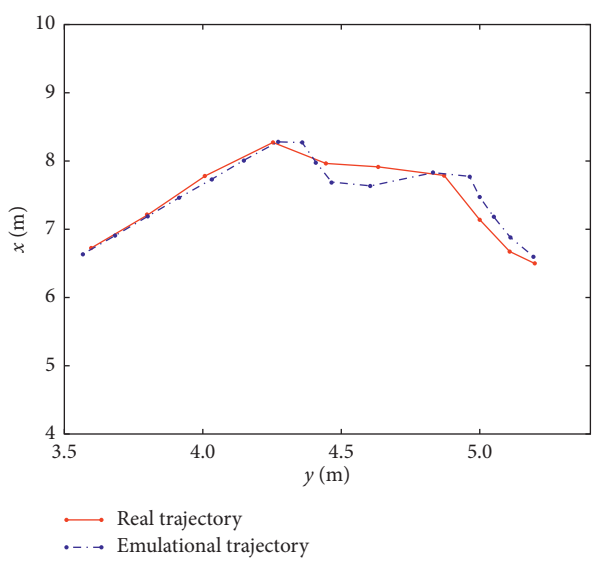


Figure 7: Comparison of passenger 6's real and emulational trajectory.

was between 4.4098 and 4.6048 m, emulational trajectory's abscissa decreased at nearly 0.2 m compared to the last point before it. This finding is due to the deviation of passenger 6's self-driven force and avoiding force. When passenger 6 was not very close to the parterre, avoiding force did not exceed the self-driven force, thereby explaining the appearance of such phenomenon which was different from reality.

Passenger 13 started his motion in the middle of the billboard and the parterre and then walked to the parterre's right side and detoured six static passengers who were standing in the two second-row intermediate destination areas closest to the parterre's right side, before finally approaching slowly the parterre's right side.

Figure 8 shows the comparison between the real trajectory and the emulational trajectory of passenger 13. The red line represents the real trajectory extracted from the video by Tracker, while the blue line represents the trajectory simulated by the proposed model (the places of abscissa and ordinate are exchanged to observe the trajectories conveniently). Qualitatively comparing the two trajectories, we can find that the two trajectories showed similar overall trend and maximum abscissa. In the horizontal movement part, two trajectories accord with each other well; in the vertical movement part, emulational trajectory seems to be closer to the parterre's right side than the real trajectory. Qualitatively comparing the two trajectories, we can find that emulational trajectory's maximum abscissa appeared at (9.2840, 5.2656). Under the same ordinate, real trajectory's relevant abscissa was 9.296 m. The deviation of these two abscissae was only 0.012 m, which shows that the proposed

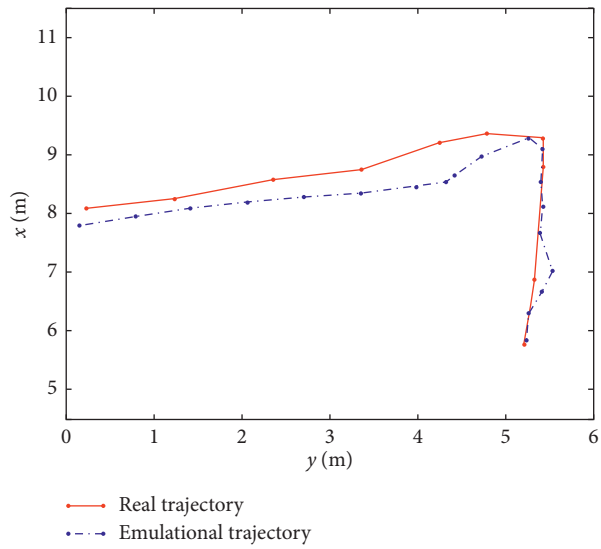


Figure 8: Comparison of passenger 13's real and emulational trajectory.

model can accurately simulate passengers' maximum horizontal displacement when making route choices and avoiding others. After detouring the static passengers, the distance between the real and emulational trajectories was around 1.0 m. This finding holds because, in reality, passenger 13 nearly kept walking straight after detouring and suddenly changed his walking direction at the end of his motion. By contrast, the proposed model's simulation results slowly moved close to his destination. Therefore, this deviation appears due to passenger 13's personal walking habits.

Comparing the movement trends of passengers 1, 6, and 13, we can find that all of them moved under self-driven and avoiding forces. When passenger 1 began to choose an intermediate destination area on the second row, none of these areas was occupied by other pedestrians. Thus, he only needed to be concerned about the handcart to the right of the parterre and made small horizontal movement. When passenger 6 began to choose an intermediate destination area on the second row, the area which had the shortest detouring distance for passenger 6 was occupied by four moving pedestrians. Fortunately, the speed differences between passenger 6 and the four moving pedestrians were quite small, thereby preventing them from blocking passenger 6 if he chose this area. Thus, passenger 6's route choice and avoiding behaviors were similar to those of passenger 1. When passenger 13 began to choose an intermediate destination area on the second row, the two intermediate destination areas with the shortest detouring distances were both occupied by static pedestrians, which made it difficult for passenger 13 to walk through them to reduce walking distance. Thus, passenger 13 showed large horizontal movement under self-driven and avoiding forces.

Furthermore, the other ten passengers' deviations between real and simulation trajectories were all smaller than the radius of their occupied space on the ground, indicating that the proposed model can simulate passengers' avoiding and route choice behaviors at an acceptable accuracy level.

*6.3. Simulation and Verification of Passengers' Node Choice Behavior.* In this section, we simulate passengers' node choice behavior in the queuing area before security check channels. As shown in Figure 9, the simulation scene is also cut out from the surveillance video of a large airport terminal in China. Passengers enter this area from the lower left quarter, and walking through the dashed area is not possible. While shooting this video, three security check channels were in use. From top to bottom, we number these channels from No. 1 to No. 3. To record passengers' location conveniently, we establish a plane Cartesian coordinate system on the scene. According to Figure 9, we set the lower left quarter as the origin of the coordinate system, and the lower boundary and left boundary are the $x$- and $y$-axes, respectively.

The video showed fourteen passengers arriving at this queuing area at the same time. To record their node choices clearly, we number them from No. 1 to No. 14 according to their order of entering the simulation scene. Each passenger's suitcase number is recorded in Table 3. At the same time, Table 4 shows each queue's original information.

Among the fourteen passengers, passengers 2 to 5 were a group of people led by passenger 2, and all of them followed passenger 2's choice. Other eleven passengers independently chose security check channels. Based on this circumstance, Table 4 presents the node choice comparison of reality and simulation results.

According to the results in Table 5, after all these passengers made their node choices, the numbers of passengers who chose channels 1 to 3 were five, four, and five, respectively; and these results are all the same in reality and simulation. Comparing each passenger's node choice, we can find that only passengers 11 and 13's emulational choices did not match their real choices. Therefore, the proposed model can simulate passengers' node choices at an acceptable accuracy level.

Discussing the reason why such simulation results appeared, we find that after passengers 1 and 2 chose channel

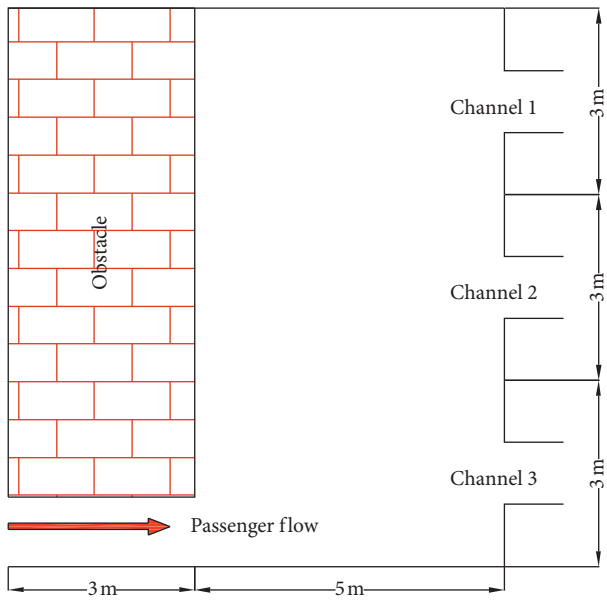


Figure 9: Queuing area before security check used for simulation.

Table 3: Collection of passengers' suitcase numbers.

| Passenger number | Suitcase number |
|---|---|
| 1 | 1 |
| 2 | 1 |
| 3 | 1 |
| 4 | 1 |
| 5 | 1 |
| 6 | 0 |
| 7 | 0 |
| 8 | 0 |
| 9 | 0 |
| 10 | 0 |
| 11 | 1 |
| 12 | 1 |
| 13 | 1 |
| 14 | 2 |

Table 4: Original information of each queue.

| Channel number | Queue length (m) | Pedestrian density at the tail of the queue (person/m$^2$) | Suitcase density at the tail of the queue (item/m$^2$) |
|---|---|---|---|
| Channel 1 | 0.4 | 1 | 1 |
| Channel 2 | 0.8 | 2 | 2 |
| Channel 3 | 0 | 0 | 0 |

3 because it was close to them with not many waiting people, passengers 3 to 5 followed their leader and made the waiting people number of channel 3 exceed those of the other two channels. The following passenger, 6, chose channel 1 because it had the least waiting people at that moment. Considering that passenger 6 was not carrying a suitcase, passengers 7 and 8 still thought that they would not have to wait for a long time before channel 1. Accordingly, these two people also chose channel 1. At this moment, the number of waiting people before channel 1 exceeded that of channel 2; consequently, passengers 9 and 10 chose channel 2. Given that passengers 9 and 10 had no luggage, channel 2 could still attract passenger 11. When passenger 12 began to make a node choice, channel 1 had the least waiting people and suitcases; thus, passenger 12 chose channel 1. For passenger 13, waiting people and suitcases before each channel were nearly the same. Thus, passenger 13 chose channel 1 because it was closest to him. After passengers 12 and 13 chose

Table 5: Comparison of passengers' choices in reality and simulation.

| Passenger number | Channel number choice in reality | Channel number choice in simulation |
|---|---|---|
| 1 | 3 | 3 |
| 2 | 3 | 3 |
| 3 | 3 | 3 |
| 4 | 3 | 3 |
| 5 | 3 | 3 |
| 6 | 1 | 1 |
| 7 | 1 | 1 |
| 8 | 1 | 1 |
| 9 | 2 | 2 |
| 10 | 2 | 2 |
| 11 | 1 | 2 |
| 12 | 1 | 1 |
| 13 | 2 | 1 |
| 14 | 2 | 2 |

channel 1, passenger 14 chose channel 2 because it was the closest channel to him with not many people waiting in it.

## 7. Conclusions

The original social force model lacks the description of pedestrians' tactical traffic behaviors, and passengers in airport terminal's departure hall have their special traffic behavior characteristics. In this paper, we first analyzed passengers' traffic behaviors in a departure hall according to video data from a large airport terminal in China and then established a double-level path planning model of departure passengers. In the proposed model, passengers' decision-level path planning behaviors are described by passengers' avoiding social force model, and passengers' tactical-level path planning behaviors are described by passengers' route and node choice models. Passengers' avoiding force model uses common avoiding force and additional horizontal avoiding force to describe how they change their velocity and walking direction in close range. Passengers' route and node choice models use cost functions to determine the direction of their desired speed to change their self-driven force and describe their walking direction changes in the long range. Simulation results show that the proposed model can simulate passengers' path planning behaviors at an acceptable accuracy level in both common walking space and service facility choosing area of a departure hall. Based on such detailed description of departure passengers' path planning behavior, airport terminal's internal layout can be better planned. Simulation results of passengers' trajectories can also help the managers in airport terminal determine the region where conflicts and walking direction changes are frequent to prepare adequate service and security management resource in time and achieve grid-based elaborate management.

The findings of this study can help the airport management department obtain a better grasp of the rules of passenger movement and aggregation in the terminal. The social force model of departure passengers proposed in this study can be applied to all aspects of terminal operation management:

(1) Terminal facility planning: the main flow direction of passengers walking in the departure hall can be attained through the analysis using the route choice model. Moreover, the main flow direction of passengers between different origins and destinations can be used to evaluate the rationality of internal planning of departure halls.

(2) Passenger safety management: the entire departure hall is divided into smaller areas. Under the joint action of self-driven and avoidance forces, passengers' trajectories are simulated by the proposed double-level model. The change in passenger's movement path in each area and the number and degree of conflicts with other passengers can be calculated [31, 32]. The area with large fluctuations and frequent conflicts is the area where local passenger safety management must be strengthened.

(3) Service resource allocation: the allocation evaluation of check-in counters in the departure hall of a terminal is realized by the service node choice model of departure passengers.

Further research can be started in these regions: (1) extending surveillance video's collecting area to analyze passengers' desired velocity change in different parts of the departure hall; (2) extending passenger traffic behavior model from 2D to 3D world to model passengers' reactions to information boards set in different parts of the departure hall.

## Data Availability

The raw/processed data required to reproduce these findings, such as surveillance videos, cannot be shared at this time as the data also form a part of an ongoing study. All figures and tables of this article can be shared.

## Conflicts of Interest

The authors declare that they have no conflicts of interest.

## Authors' Contributions

Y.Z. and J.L. participated in conceptualization; X.X. contributed to data curation; Y.Z., J.L., and D.K. carried out formal analysis; Y.Z. was responsible for funding acquisition and wrote the original draft; J.L. and D.K. were involved in methodology and validation; Y.Z. and Q.L. helped with project administration; X.X., Q.L., and J.M. were responsible for resources; and Y.Z., J.L., D.K., X.X., and Q.L. reviewed and edited the paper. All authors have read and agreed to the published version of the manuscript.

## Acknowledgments

This research was supported by the Key Research and Development Program of Sichuan Province of China (grant no. 2019YFG0050), the Science and Technology Cooperation Research and Development Project of Sichuan Provincial Academy and University (grant no. 2019YFSY0024), and the Guangxi Natural Science Foundation (grant no. AD19245021).

## References

[1] H. Xie and Y. Gao, *Simulation Based Estimation Approach for Departure Passenger Flow at Airport Terminal*Institute of Electrical and Electronics Engineers Inc., Hangzhou, Zhejiang, China, 2015.

[2] X. Liu, L. Li, X. Liu et al., "Field investigation on characteristics of passenger flow in a Chinese hub airport terminal," *Building and Environment*, vol. 133, pp. 51–61, 2018.

[3] P. Di Mascio, L. Moretti, and M. Piacitelli, "Airport landside sustainable capacity and level of service of terminal functional subsystems," *Sustainability*, vol. 12, no. 21, p. 8784, 2020.

[4] P. M. Dirk Helbing, "Social force model for pedestrian dynamics," *Physical Review E*, vol. 5, pp. 4282–4286, 1998.

[5] Y. Geng, J. Yu, B. Lin, Z. Wang, and Y. Huang, "Impact of individual IEQ factors on passengers' overall satisfaction in Chinese airport terminals," *Building and Environment*, vol. 112, pp. 241–249, 2017.

[6] M. Eshtaiwi, I. Badi, A. Abdulshahed, and T. E. Erkan, "Determination of key performance indicators for measuring airport success: a case study in Libya," *Journal of Air Transport Management*, vol. 68, pp. 28–34, 2018.

[7] V. J. Blue, M. J. Embrechts, and J. L. Adler, *Cellular Automata Modeling of Pedestrian Movements*IEEE, New York, NY, USA, 1997.

[8] P. Zhang, X. X. Jian, S. C. Wong, and K. Choi, "Potential field cellular automata model for pedestrian flow," *Phys Rev E Stat Nonlin Soft Matter Phys*, vol. 85, p. 21119, 2012.

[9] X. Zheng, T. Zhong, and M. Liu, "Modeling crowd evacuation of a building based on seven methodological approaches," *Building and Environment*, vol. 44, no. 3, pp. 437–445, 2009.

[10] H. Vermuyten, J. Beliën, L. De Boeck, G. Reniers, and T. Wauters, "A review of optimisation models for pedestrian evacuation and design problems," *Safety Science*, vol. 87, pp. 167–178, 2016.

[11] D. Helbing, I. Farkas, and T. Vicsek, "Simulating dynamical features of escape panic," *Nature*, vol. 407, no. 6803, pp. 487–490, 2000.

[12] D. Helbing, I. J. Farkas, P. Molnar, and T. Vicsek, "Simulation of pedestrian crowds in normal and evacuation situations," Edited by M. Schreckenberg and S. D. Sharma, Eds., pp. 21–58, 2002.

[13] Z. Yuan, H. Jia, L. Zhang, and L. Bian, "Simulation of pedestrian behavior in the collision-avoidance process considering their moving preferences," *Discrete Dynamics in Nature and Society*, vol. 2017, Article ID 3678268, 11 pages, 2017.

[14] X. Jia, H. Yue, X. Tian, and H. Yin, "Simulation of pedestrian flow with evading and surpassing behavior in a walking passageway," *Simulation*, vol. 93, no. 12, pp. 1013–1035, 2017.

[15] H. Yamamoto, D. Yanagisawa, C. Feliciani, and K. Nishinari, "Body-rotation behavior of pedestrians for collision avoidance in passing and cross flow," *Transportation Research Part B: Methodological*, vol. 122, pp. 486–510, 2019.

[16] Q. Wang, Y. Chen, H. Dong, M. Zhou, and B. Ning, "A new collision avoidance model for pedestrian dynamics," *Chinese Phys B*, vol. 24, 2015.

[17] Y. Xiao, Z. Gao, Y. Qu, and X. Li, "A pedestrian flow model considering the impact of local density: Voronoi diagram based heuristics approach," *Transportation Research Part C: Emerging Technologies*, vol. 68, pp. 566–580, 2016.

[18] Y. Qu, Y. Xiao, J. Wu, T. Tang, and Z. Gao, "Modeling detour behavior of pedestrian dynamics under different conditions," *Physica A: Statistical Mechanics and its Applications*, vol. 492, pp. 1153–1167, 2018.

[19] I. Karamouzas, P. Heil, P. van Beek, and M. H. Overmars, "A predictive collision avoidance model for pedestrian simulation," in *Lecture Notes in Computer Science*, A. Egges, R. Geraerts, and M. Overmars, Eds., vol. 5884, pp. 41–52, Springer, Berlin, Germany, 2009.

[20] N. Cao, L. Zhao, Z. Qu, Y. Chen, Q. Bai, and X. Deng, "Social force model considering Bi-direction pedestrian slipstreaming behavior," *Jilin Daxue Xuebao (Gongxueban)/Journal of Jilin University (Engineering and Technology Edition)*, vol. 49, pp. 688–694, 2019.

[21] Y. Gao, T. Chen, P. B. Luh, and H. Zhang, "Modified social force model based on predictive collision avoidance considering degree of competitiveness," *Fire Technology*, vol. 53, no. 1, pp. 331–351, 2017.

[22] T. Kretz, A. Grosse, S. Hengst, L. Kautzsch, A. Pohlmann, and P. Vortisch, "Quickest paths in simulations of pedestrians," *Advances in Complex Systems*, vol. 14, no. 5, pp. 733–759, 2011.

[23] B. R. Werberich, C. O. Pretto, and H. B. B. Cybis, "Pedestrian route choice model based on friction forces," *Simulation*, vol. 90, no. 10, pp. 1177–1187, 2014.

[24] Z. Zhang and L. Jia, "Direction-decision learning based pedestrian flow behavior investigation," *IEEE Access*, vol. 8, no. 8, pp. 15027–15038, 2020.

[25] N. Cao, Z. Qu, Y. Chen, L. Zhao, X. Song, and Q. Bai, "Destination and route choice models for bidirectional pedestrian flow based on the social force model," *Iet Intell Transp Sy*, vol. 11, pp. 537–545, 2017.

[26] N. Cao, Y. Chen, Z. Qu, L. Zhao, Q. Bai, and Q. Yang, "Pedestrian route choice model based on social force model," *Zhejiang Daxue Xuebao (Gongxue Ban)/Journal of Zhejiang University (Engineering Science)*, vol. 52, pp. 352–357, 2018.

[27] Y. Han, H. Liu, and P. Moore, "Extended route choice model based on available evacuation route set and its application in crowd evacuation simulation," *Simulation Modelling Practice and Theory*, vol. 75, pp. 1–16, 2017.

[28] Y. Han and H. Liu, "Research on route choice model based on evacuation route set and its application in crowd evacuation simulation," *Jisuanji Xuebao/Chinese Journal of Computers*, vol. 41, pp. 2653–2669, 2018.

[29] R. Lovreglio, A. Fonzone, and L. dell'Olio, "A mixed logit model for predicting exit choice during building evacuations," *Transportation Research Part A: Policy and Practice*, vol. 92, pp. 59–75, 2016.

[30] X. Zheng, H.-y. Li, L.-y. Meng, X.-y. Xu, and X. Chen, "Improved social force model based on exit selection for microscopic pedestrian simulation in subway station," *Journal of Central South University*, vol. 22, no. 11, pp. 4490–4497, 2015.

[31] C. Fu, T. Sayed, and L. Zheng, "Multivariate bayesian hierarchical modeling of the non-stationary traffic conflict extremes for crash estimation," *Analytic Methods in Accident Research*, vol. 28, Article ID 100135, 2020.

[32] C. Fu and T. Sayed, "Multivariate Bayesian hierarchical Gaussian copula modeling of the non-stationary traffic conflict extremes for crash estimation," *Analytic Methods in Accident Research*, 2020.

Hindawi
Advances in Civil Engineering
Volume 2021, Article ID 8867091, 11 pages
https://doi.org/10.1155/2021/8867091

*Research Article*

# Intelligent Vehicle Automatic Stop-and-Go Task Based on Humanized Learning Control Model

**Tianjun Sun,[1,2] Zhenhai Gao,[1,2] Fei Gao,[2] Tianyao Zhang,[2] Di Ji,[3] and Siyan Chen[1,2]**

[1]*College of Automotive Engineering, Jilin University, Changchun 130012, China*
[2]*State Key Laboratory of Automotive Simulation and Control, Jilin University, Changchun 130012, China*
[3]*College of Communication Engineering, Jilin University, Changchun 130012, China*

Correspondence should be addressed to Siyan Chen; chensiyan@jlu.edu.cn

Received 29 September 2020; Revised 12 November 2020; Accepted 6 January 2021; Published 18 January 2021

Academic Editor: Songtao Lv



The automatic stop-and-go task of intelligent vehicles can make the adaptive cruise control system achieve a full-speed range. However, the conventional design methods mostly focus on functional safety, without considering drivers' behaviors, thereby leading to a poor driving experience. To improve the situation, a humanized learning control model is used instead of mechanical switching logic. Therefore, first, the common characteristics of human drivers with different driving styles are found by analyzing real drivers' experiments. Then, the vehicle automatic starting function is designed based on iterative learning control with the fast Fourier transform for acceleration fitting. Next, the vehicle automatic braking function is designed based on dynamic time to collision. Finally, the simulation of the stop-and-go scenario is shown in CARSIM, and the real vehicle test is performed under the urban overpass driving condition. Results show that the proposed model can improve the humanization in the vehicle stop-and-go task.

## 1. Introduction

With the high pace of modern life, the increasing number of citizens will cause traffic congestion. Although conventional adaptive cruise control (ACC) systems can provide partial drive assistance, such systems could still be improved. On the one hand, most ACC systems may not cover the full-speed range [1]. On the other hand, the current automatic stop-and-go control methods of vehicles do not consider drivers' behavior [2].

Research on stop-and-go tasks is presently one of the most important topics in the field of ACC systems. One of the reasons is that the conventional ACC will frequently withdraw from the system when the velocity is less than 30 km/h. Moreover, the velocity is very low to enable cruise control (CC) function [3]. Furthermore, the current control methods mostly focus on functional safety. However, the poor driving experience will be increasingly evident when drivers' behaviors are not considered. For instance, some drivers used to have a violent start, such as a sense of push the back, but the control logic may limit the acceleration by considering safety and comfort. The other drivers used to make a double brake when a vehicle in front suddenly slows down, but the control logic may provide a great deceleration such that the host vehicle can stop by only braking once. Therefore, when the driver is aware of the relative motion of the vehicle in the field of view, the driver will make a series of habitual actions to catch up with the target vehicle and keep a safe distance. Thus, these actions reflect the real drivers' driving behaviors in car following, but the existing decision-making algorithms or control methods are compliant with the established rules.

The challenges of the research comprehensively regard drivers' behavior characteristics, vehicle's dynamic characteristics, safety, and humanization in vehicle automatic control. Moreover, in this study, an automatic stop-and-go control method is designed by analyzing the real drivers' starting and braking behaviors based on an intelligent vehicle platform, as shown in Figure 1.

According to previous studies, the conventional control methods for vehicle stop-and-go scenario can be

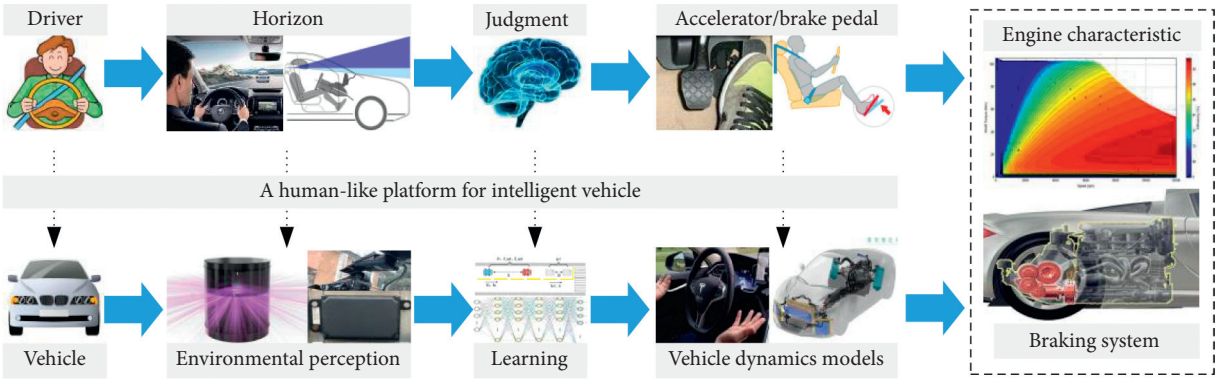


Figure 1: A human-like platform for intelligence vehicle.

summarized as model-based control. For example, Junchen [4] established a car-following model based on drivers' behavior and dynamic vehicle characteristics. However, model-based control methods are usually regarded as complicated and hard-to-debug systems. In the above methods, while also considering safety, the calculation of time to collision (TTC) plays an important role in the process of braking. As a quintessential example, Jahandideh et al. [5] found that pedestrians prefer to cross the road at the intersection point at the average TTC of approximately 6.2 s, and 54% of men and 39% of women face TTC risk for less than 3 s. Zhenhai and Wu [6, 7] established models based on TTC for warning and braking time prediction on the basis of drivers' habitual braking and braking force characteristics. However, the conventional TTC algorithm cannot meet the change of acceleration. Compared with the conventional methods, some new trends toward learning control exist. For example, Lu et al. [8] designed a learning module based on neural reinforcement learning before the PID control. This model can learn from human drivers online based on the on-board sensing information and realize human-like longitudinal speed control by learning from the demonstration paradigm. Xing et al. [9] provided a personalized leading vehicle trajectory prediction method based on joint time series modeling. This method can generate three different driving styles for the leading vehicle through the JTSM algorithm and achieve better results. Lv et al. [10, 11] proposed a CPS-based framework for codesign optimization of an automated electric vehicle with different driving styles, which used unsupervised machine learning to develop the driving style recognition algorithm.

By analyzing the above results, this study finds that conventional methods are applicable, but humanization is not considered due to its inherent logic strategies. Therefore, based on previous studies, we propose a humanized vehicle automatic stop-and-go control method based on the iterative learning (IL) algorithm and the dynamic time to collision (DTTC) model. This study aims to develop a humanized learning control model based on IL and DTTC while focusing on the stop-and-go task for autonomous driving. The main contributions of this study are as follows: (1) the drivers' control behavior characteristics are extracted through the real vehicle tests with different types of drivers. (2) An automatic drive control method based on the IL algorithm is proposed to learn the driver behavior and realize the human-like control. Based on the IL algorithm, complex dynamic calculations are not required, and the control method can be learned directly from the acceleration curve equation. (3) An automatic brake control method based on the DTTC model is proposed in this study to learn the driver behavior and realize the human-like control. Based on the DTTC model, on the one hand, the safety of the braking process is improved by the consideration of dynamic deceleration; on the other hand, different types of braking can be learned directly from the real vehicle tests. (4) Automatic stop-and-go control is implemented by combining the automatic drive control and automatic brake control methods. The validity and feasibility of the proposed method are verified through simulation and real tests.

The remainder of this paper is organized as follows: the second part is "extraction of drivers' control behavior characteristics." The third part is the "learning model for vehicle automatic starting control." The fourth part is the "learning model for vehicle automatic braking control." The fifth part is "simulation and experimental tests." The sixth part is "results and comparative analysis." The final part is "conclusions and future work."

## 2. Extraction of Drivers' Control Behavior Characteristics

The three types of typical drivers are examined based on the previous classification to obtain the common characteristics of different drivers with evident driving styles [12–14]. In this study, we choose three types, namely, aggressive driver, normal driver, and steady driver. Many factors causing different characteristics should be neglected because this part aims to find the humanized common characteristics of human drivers compared with the conventional model-based design. Therefore, we assume that the target vehicle stops at the stop line 200 m away from the host vehicle. Then, the host vehicle starts to catch up with the target vehicle through acceleration or deceleration control over a period of

time. Finally, the host vehicle will stop behind the target vehicle. Figure 2 shows the experimental scenario.

As shown in Figure 3, we conduct further analysis of vehicle velocity and acceleration in the stop-and-go scenario. In the case of low speed, the vehicle stop-and-go characteristics controlled by different drivers have some similarities. One similarity is that the trend of the acceleration curve will increase along with the velocity and then gradually reduce to half of the peak value. From a practical point of view, the drivers in the experiment with different start characteristics usually choose to step down the accelerator pedal. Then, they slowly release the accelerator pedal in the process of starting. The other similarity is the time of braking. Although different drivers have varying braking decelerations, a humanized braking method is reflected in a reasonable double brake. Moreover, the trend of acceleration change is highly similar to the same velocity adjustment, and the trend of deceleration with a large increase or decrease can be classified as a double brake.

## 3. Learning Model for Vehicle Automatic Starting Control

When the vehicle deals with repetitive tasks in an actual environment, people expect to use a certain amount of human manipulation samples to match the automatic control system with the behavior of the drivers. To imitate human learning abilities and their self-regulation function, the IL algorithm can improve the control target through iterative correction, which is suitable for controlled objects with repetitive motion properties. The IL algorithm can realize the control of strong coupled nonlinear dynamic systems with high uncertainty in a limited time. Moreover, this algorithm does not depend on precise mathematical models [15, 16]. Therefore, IL has been widely used in automation controls, such as industrial robots, digital control machines, and machine manufacturing.

However, in the practical environment, the driving styles of drivers are better described through behaviors but hard to describe through theoretical analysis. Therefore, in humanized features' extraction, we will transform the practical problem into a function approximation problem based on experimental data. Thus, the first step is to design a function to make it as close as possible to the trend of the acceleration curve.

According to previous studies, two methods are usually used for solving function approximation problems, namely, interpolation and fitting. If the experimental data are discrete, then the interpolation is suitable. When considering the continuity of the acceleration curve, the fitting is suitable instead. The three main methods of fitting that are used widely are algebraic polynomials, rational fractional functions, and triangular polynomials. Typical samples for the fitting methods above are polynomial fitting, Gaussian fitting, and fast Fourier transform (FFT). Moreover, we construct a function similar to the trend of the acceleration curve in the experiment, which will increase along with the velocity and then gradually reduce to half of the peak value. If we choose the polynomial power function for fitting, then estimating the error is difficult although easy to operate, and the amount of calculation is small. When the sampling points are rare, the fitting effect is poor, as shown in Figure 4(a). Otherwise, if we choose the Gaussian function for fitting, then the positioning accuracy for edge detection of data will be low, and the fitting will be sensitive to noise although calculating the integral is convenient, as shown in Figure 4(b).

Figure 4 shows that underfitting occurs in polynomial fitting, and overfitting occurs in Gaussian fitting. From the results above, these two methods for acceleration curve fitting can meet the approximation standard, but each has shortcomings. Therefore, FFT fitting is made by analyzing polynomial and Gaussian fitting methods to better reflect the humanization of acceleration in the vehicle stop-and-go scenario. FFT is not a change of discrete Fourier transform (DFT) but is a fast algorithm which can reduce the number of DFT operations. Among them, any periodic function can be converted into the sum of several trigonometric functions by dividing the periodic function to be converted $f(t)$ into a trigonometric function of innumerable sin and cos, as shown in the following equation:

$$\begin{aligned} f(t) = \frac{1}{T}\int_{t_0}^{t_0+T} f(t)dt + \left[\frac{2}{T}\int_{t_0}^{t_0+T} f(t)\sin(\omega t)dt\,\sin(\omega t) + \frac{2}{T}\int_{t_0}^{t_0+T} f(t)\cos(\omega t)dt\,\cos(\omega t)\right]+,\ldots, \\ + \left[\frac{2}{T}\int_{t_0}^{t_0+T} f(t)\sin(n\omega t)dt\,\sin(n\omega t) + \frac{2}{T}\int_{t_0}^{t_0+T} f(t)\cos(n\omega t)dt\,\cos(n\omega t)\right]+,\ldots \end{aligned} \tag{1}$$

Furthermore, we use the toolbox of MATLAB to conduct the acceleration fitting based on FFT to the experimental data for vehicle starting, and Figure 5 shows the result.

The FFT fitting curve on level 4 can effectively express the fluctuation trend of the experimental data through comparative analysis. If we regard the FFT fitting curve on level 4 as the target acceleration that the system needs to follow, then the second step would be the vehicle automatic starting based on the IL algorithm.

Owing to the influence of several factors, such as external air resistance, road friction resistance, and internal transmission, the longitudinal acceleration of the vehicle and the torque of the engine have a nonlinear relationship. Furthermore, the control principle of the automatic vehicle start control algorithm is based on the engine torque control to track the target acceleration. Hence, to express the nonlinear relationship, this study uses the PD-type close-loop IL

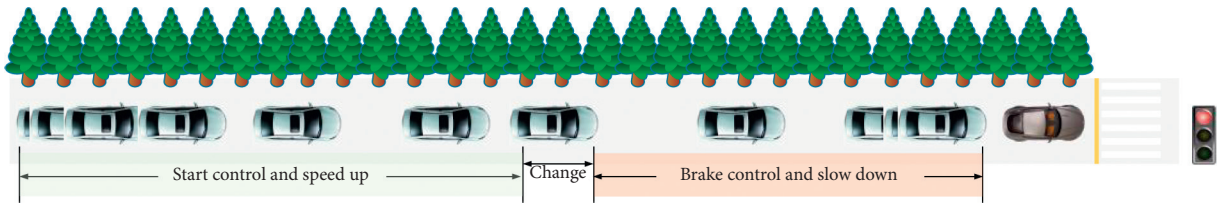


Figure 2: The experimental scenario.

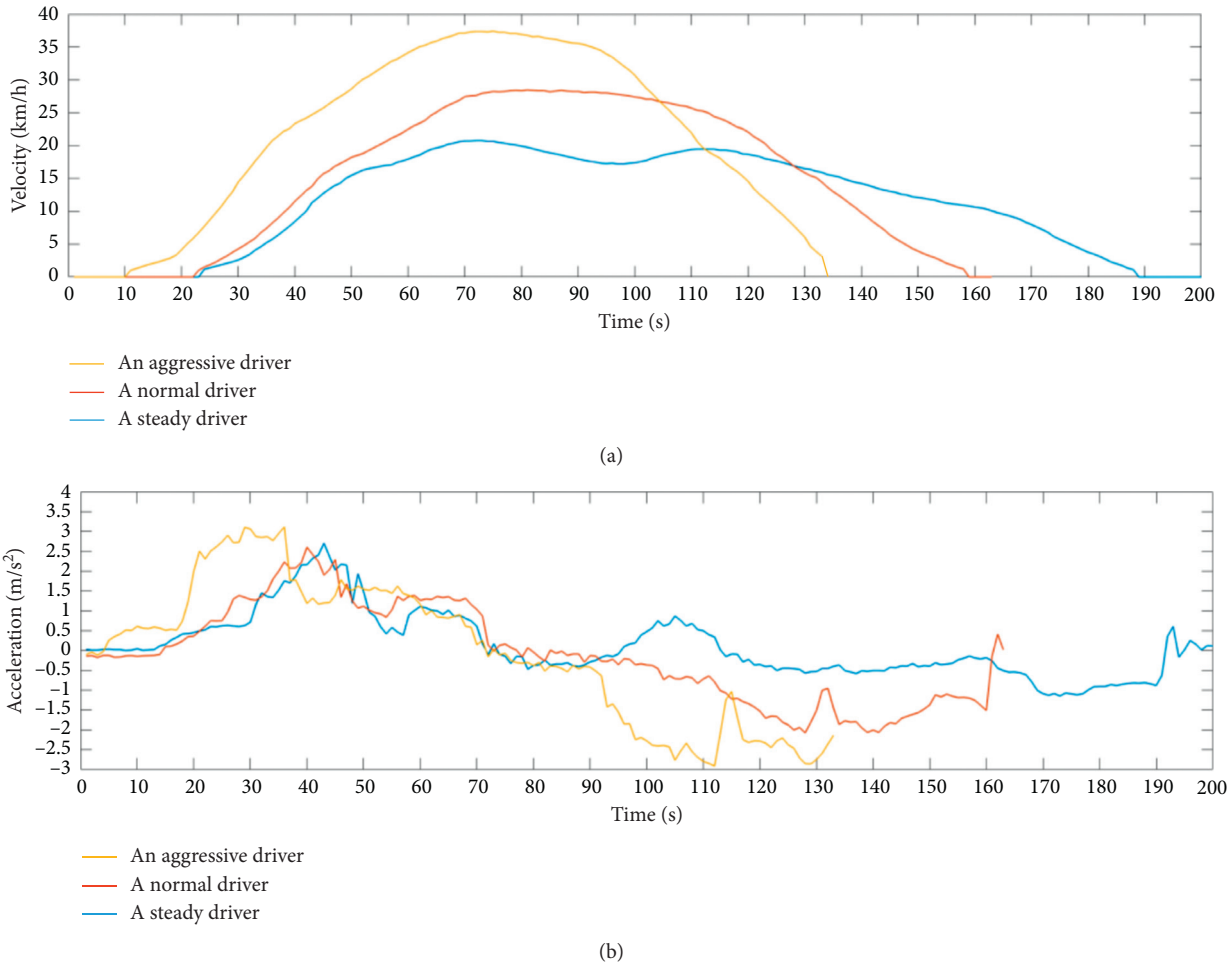


Figure 3: The experimental results for three drivers in the vehicle stop-and-go scenario.

control method to convert the engine torque control problem into an engine throttle opening problem. The IL algorithm can be described as shown in the following equation:

$$\begin{cases} p_k(t) &= p_{k-1}(t) + L_p e_k(t) + L_d e_k(t), \\ e_k(t) &= a_{\text{expected}}(t) - a_{\text{real}}(t), \end{cases} \tag{2}$$

where $p_k(t)$ represents the throttle percentage, $a_{\text{expecred}}(t)$ represents the expected acceleration, $a_{\text{real}}(t)$ represents the real acceleration, $L_p$ and $L_d$ represent the learning gain factors, and $e_k(t)$ represents the error.

As mentioned before, in this study, a typical fitting function is extracted from the experimental test data to be used as the target acceleration for tracking the target of IL control, as shown in Figures 6 and 7.

In Figure 6, the error gradually decreases with the increase of the iteration number, and when the iteration reaches the eighth time, the error is close to 0. Therefore, in Figure 7, the acceleration following the curve from the first iteration to the eighth iteration and the throttle change curve is provided. Figure 7(a) shows that with the increase of iteration time, the actual acceleration of the vehicle draws closer to the target acceleration and converges to the expected trajectory. In addition, Figure 7(b) shows that with the increase of the number of iterations, the control quantity gradually converges to the expected control quantity and converges to the expected trajectory.

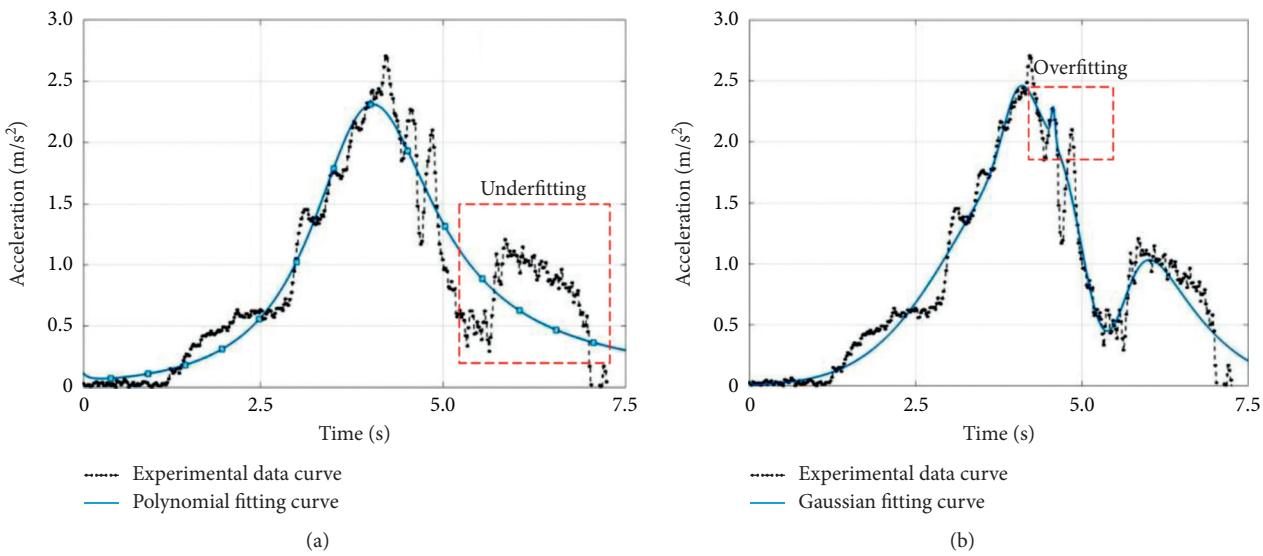


Figure 4: Acceleration fitting based on different fitting methods. (a) Polynomial fitting. (b) Gaussian fitting.

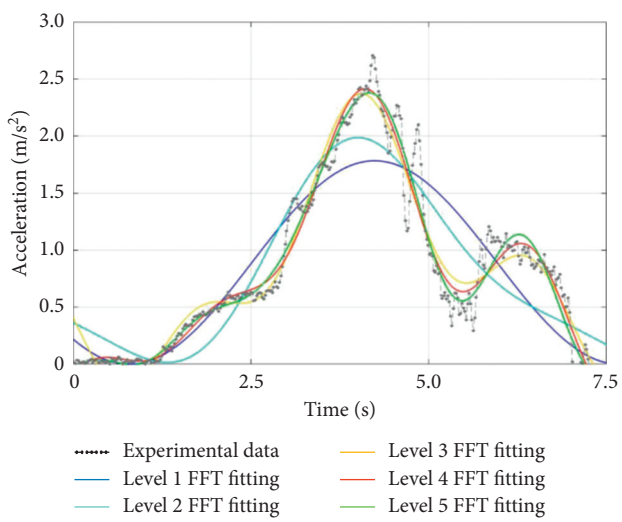


Figure 5: Acceleration fitting based on multiple FFT method.

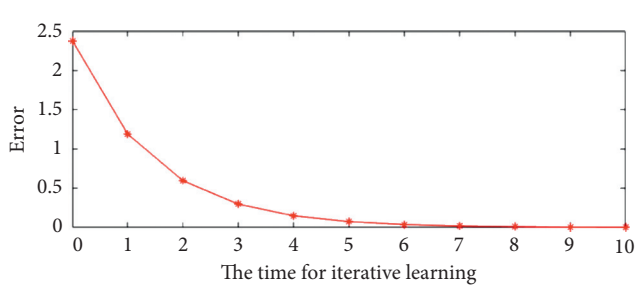


Figure 6: The error varies with the time for iteration learning.

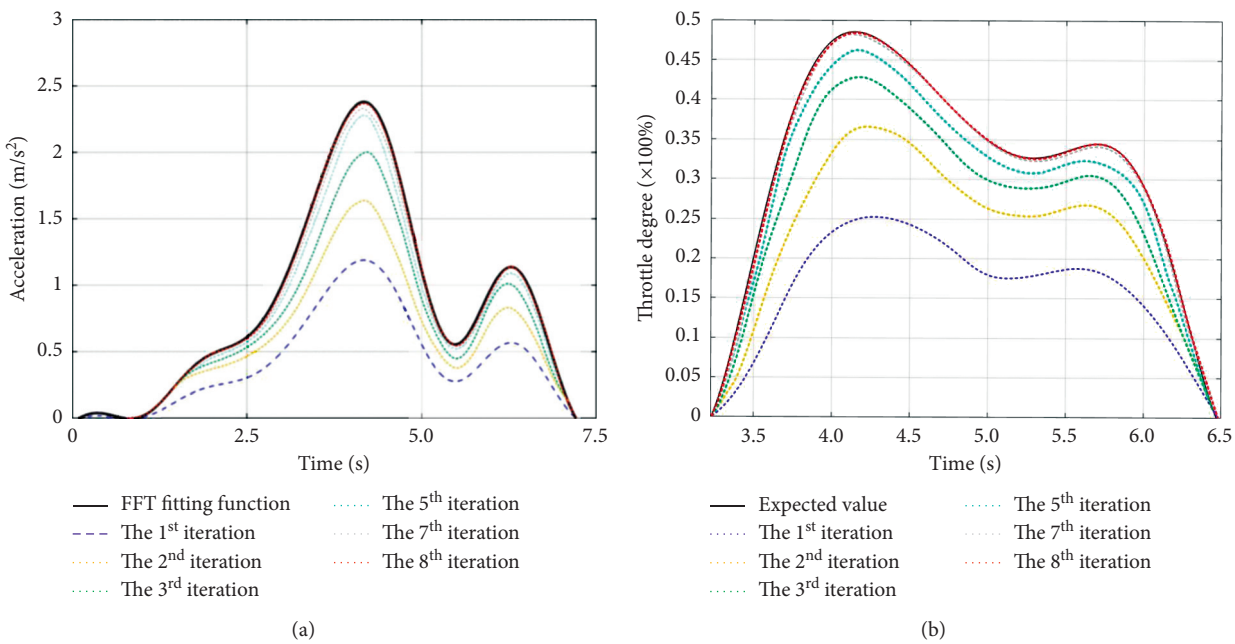


Figure 7: The results of the vehicle automatically start based on the IL control method. (a) Acceleration following with multiple iterations. (b) Throttle change with acceleration following.

## 4. Learning Model for Vehicle Automatic Braking Control

The vehicle automatic braking control is an active method to apply braking force through the electronic stability program before the collision happens. Safety should be prioritized to ensure that the host vehicle can slow down when the target vehicle decelerates or suddenly brakes when car following, which is different from the starting control. According to previous studies [17–19], the cause of the collision is related to different drivers' braking time, braking behavior, and braking force. The design of the conventional vehicle automatic braking control method only considers the rigid body kinematics characteristics and collision theory. Therefore, the driver and the passenger will feel an evident sense of frustration and tension due to the lack of understanding of the driver's braking characteristics.

At present, classification judgment is a popular method widely used in the vehicle longitudinal automatic braking control. This method is based on the comprehensive information of vehicle and traffic conditions. As the danger comes, the vehicle will slow down through active intervention. However, in this study, we aim to consider the uncertainty of the target vehicle and propose an anthropomorphic automatic braking control method based on the DTTC model. Thus, through the analysis of Figure 3, the humanized design problem is transformed into the interpretation of brake commonality.

As previously mentioned, the basic requirement of the vehicle automatic braking control is to achieve driving safety. The conventional calculation method for TTC is shown in the following equation:

$$\mathrm{TTC} = \frac{D_{\mathrm{rel}}}{V_{\mathrm{rel}}}, \tag{3}$$

where $D_{\mathrm{rel}}$ and $V_{\mathrm{rel}}$ represent the relative distance and velocity between the vehicles, respectively. However, this definition of TTC does not consider the speed change of the ego vehicle and target vehicle during acceleration and deceleration. Therefore, as shown in Figure 8, DTTC is a definition of a collision which considers the host vehicle's velocity $v_{\mathrm{ego}}$ and deceleration $a_{\mathrm{ego}}$ and the target vehicle's velocity $v_{\mathrm{tar}}$ and deceleration $a_{\mathrm{tar}}$.

Based on the kinematic relation of the vehicle, the value of DTTC can be obtained as shown in the following equation:

$$\begin{aligned} D_{\mathrm{ego}} &= V_{\mathrm{ego}}t + \frac{1}{2}a_{\mathrm{ego}}t^2, \\ D_{\mathrm{tar}} &= V_{\mathrm{tar}}t + \frac{1}{2}a_{\mathrm{tar}}t^2, \\ D_{\mathrm{ego}} &= D_{\mathrm{rel}} + D_{\mathrm{tar}}, \\ V_{\mathrm{rel}}t &+ \frac{1}{2}a_{\mathrm{tar}}t^2 + D_{\mathrm{rel}} = 0. \end{aligned} \tag{4}$$

Moreover, through the further discussion on $v_{\mathrm{rel}}$ and $a_{\mathrm{rel}}$, the DTTC can be described as shown in the following equation:

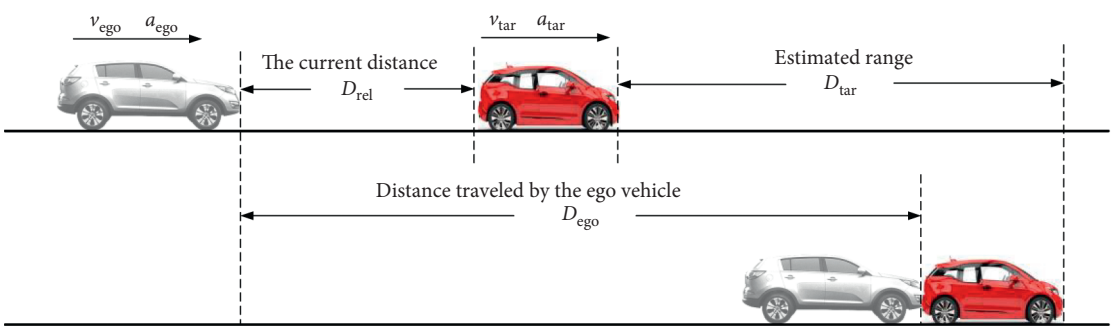


Figure 8: The condition of the DTTC process.

$$\mathrm{DTTC} = \begin{cases} \infty, & V_{rel} < 0 \text{ and } a_{rel} < 0, \\ \dfrac{(-V_{rel}) - \sqrt{V_{rel}^2 - (2a_{rel}D_{rel})}}{a_{rel}}, & V_{rel} < 0 \text{ or } a_{rel} < 0. \end{cases} \tag{5}$$

An ideal braking model based on the minimum safe distance should be considered to make the deceleration process of vehicle automatic braking control reflect the characteristics of the driver's behavior. In Figure 8, on the one hand, the ideal braking model provides an expected deceleration in the process of slowing down, which can be defined as $a_{req}$ represents the deceleration avoiding a collision. On the other hand, the host vehicle should maintain a minimum safe distance from the target vehicle after braking, which can be defined as $D^*$, as shown in Figure 9. Furthermore, the following equation provides the calculation of $a_{req}$:where $D_{rel}$ represents the current distance, $D_{tar}$ represents the estimated distance, and $D_{ego}$ represents the distance the host vehicle traveled.

$$D_{ego} = V_{ego}t + \frac{1}{2}a_{req}t^2,$$

$$D_{ego} + D^* = D_{rel} + D_{tar},$$

$$a_{req} = \begin{cases} 0, & V_{rel} > 0 \text{ and } a_{tar} > 0, \\ \dfrac{V_{ego}^2}{\left(V_{tar}^2/a_{tar}\right) - 2^*\left(D_{rel} - D^*\right)}, & V_{rel} > 0 \text{ and } a_{tar} < 0,\ V_{rel} < 0 \text{ and } a_{tar} < 0 \text{ and } t_{ego} > t_{tar}, \\ a_{tar} - \dfrac{V_{rel}^2}{2^*\left(D_{rel} - D^*\right)}, & V_{rel} < 0 \text{ and } a_{tar} > 0,\ V_{rel} < 0 \text{ and } a_{tar} < 0 \text{ and } t_{ego} < t_{tar}, \end{cases} \tag{6}$$

## 5. Simulation and Experimental Tests

A simulation test based on CARSIM and a real vehicle test under the urban overpass driving condition are provided to verify the validity and feasibility of the proposed method. In this part, we first establish a vehicle longitudinal automatic control model in MATLAB/SIMULINK. This model contains car, sensor, decision-making, and execution modules, as shown in Figure 10.

The car module is connected to CARSIM, which provides some vehicle, environmental, and road parameters. The sensor module is connected between CARSIM and SIMULINK, which provides information for the host and target vehicles. The decision-making module is designed on MATLAB/SIMULINK, which provides the key strategies and important logics for the vehicle autonomous stop-and-go task. The execution module is a computational relationship between vehicle dynamics and the braking system. Then, we conducted a simulation test for the vehicle autonomous stop-and-go scenario through CARSIM/SIMULINK, as shown in Figures 11 and 12.

To further verify the proposed method, a real vehicle test is conducted. The experimental vehicle is HAVAL H7 equipped with a millimeter wave radar and dSPACE AutoBox. The former is used to obtain the information of the target vehicle, whereas the latter is used to obtain the information of the host vehicle. Moreover, we download the control algorithm to dSPACE AutoBox instead of the original controller of the vehicle. Therefore, a real vehicle test is performed under the urban overpass driving condition, as shown in Figures 13 and 14.

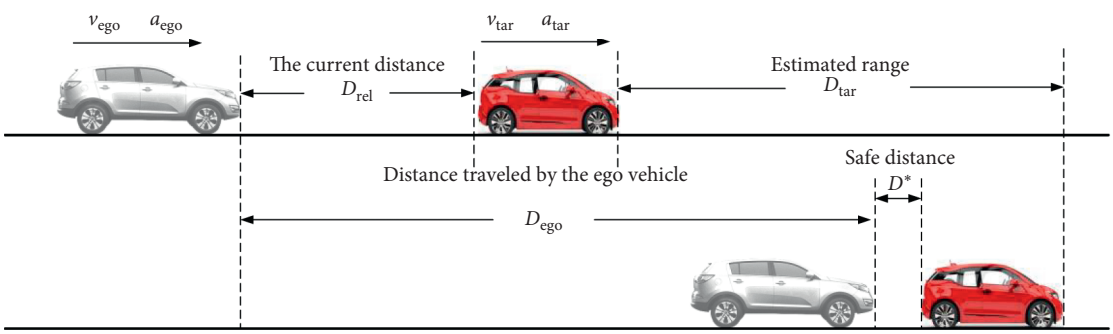


Figure 9: The ideal braking model based on DTTC.

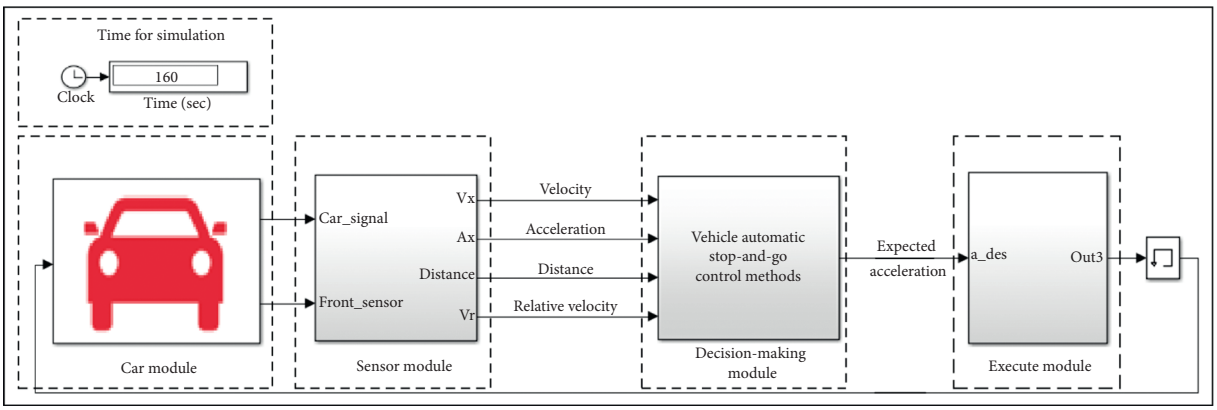


Figure 10: The vehicle longitudinal automatic control model based on MATLAB/SIMULINK.


Figure 11: The vehicle autonomous stop-and-go task in CARSIM.

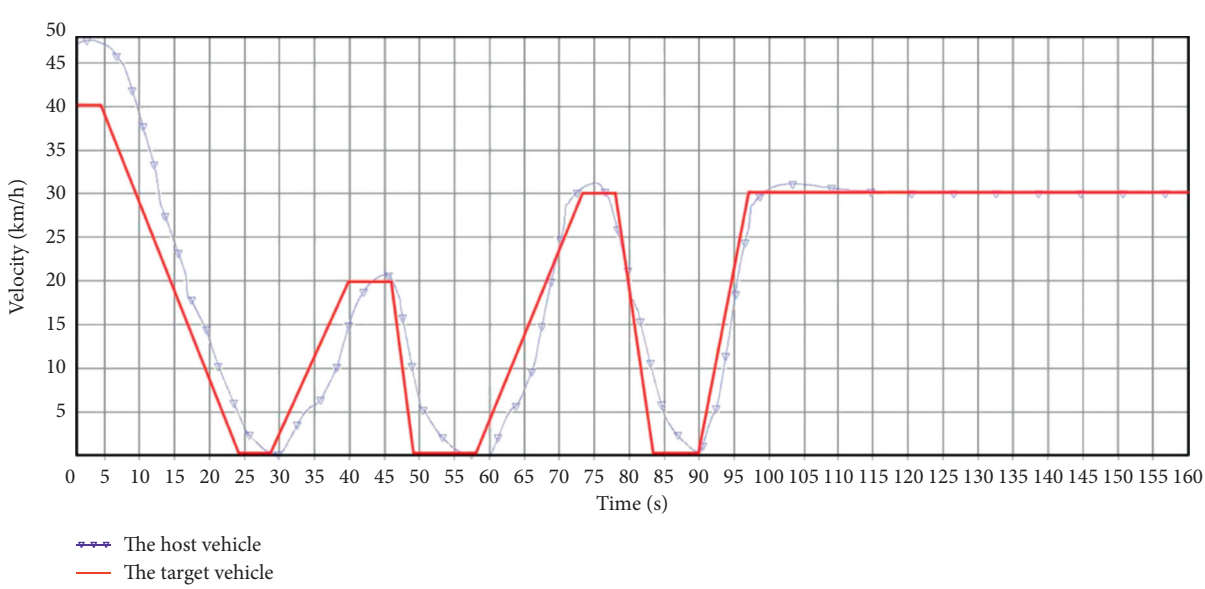


(a)

Figure 12: Continued.

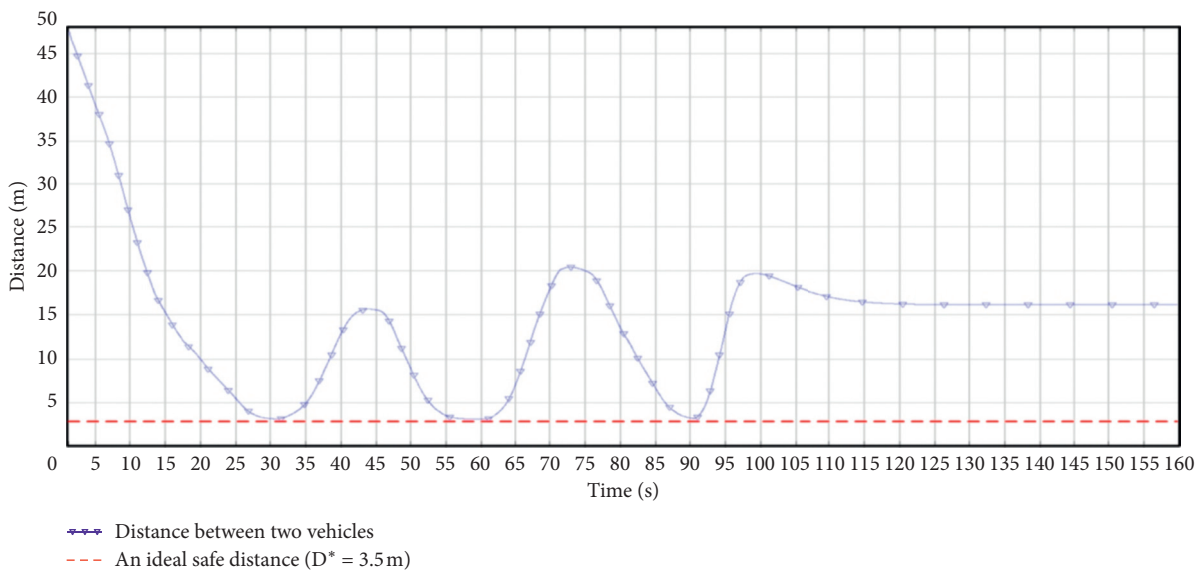


(b)

Figure 12: The simulation results for vehicle automatic stop-and-go control. (a) The simulation results for velocity in vehicle stop-and-go scenario. (b) The simulation results for distance in vehicle stop-and-go scenario.

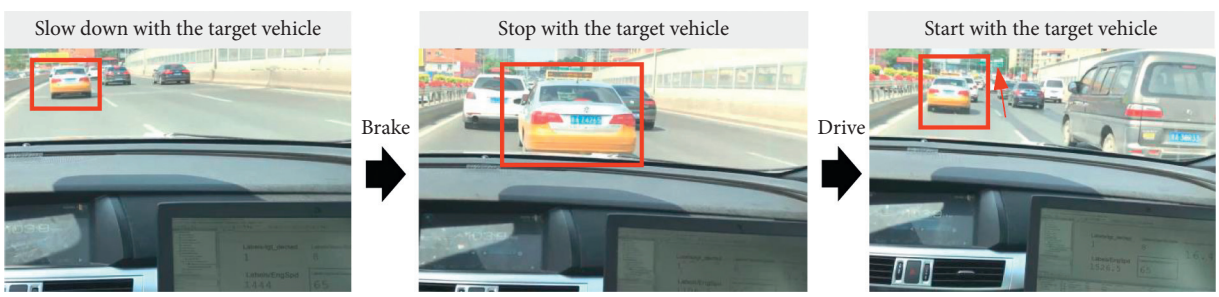


Figure 13: The real vehicle automatic stop-and-go task under the urban overpass driving condition.

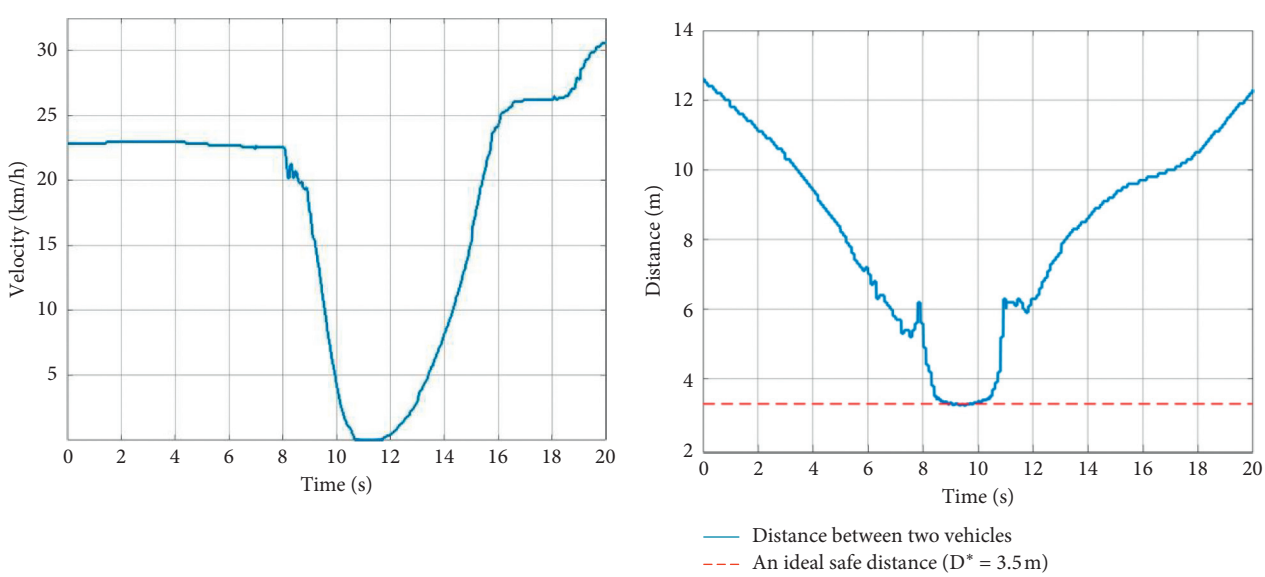


(a) (b)

Figure 14: The real vehicle automatic stop-and-go task under the urban overpass driving condition. (a) The host vehicle's velocity. (b) The distance between two vehicles.

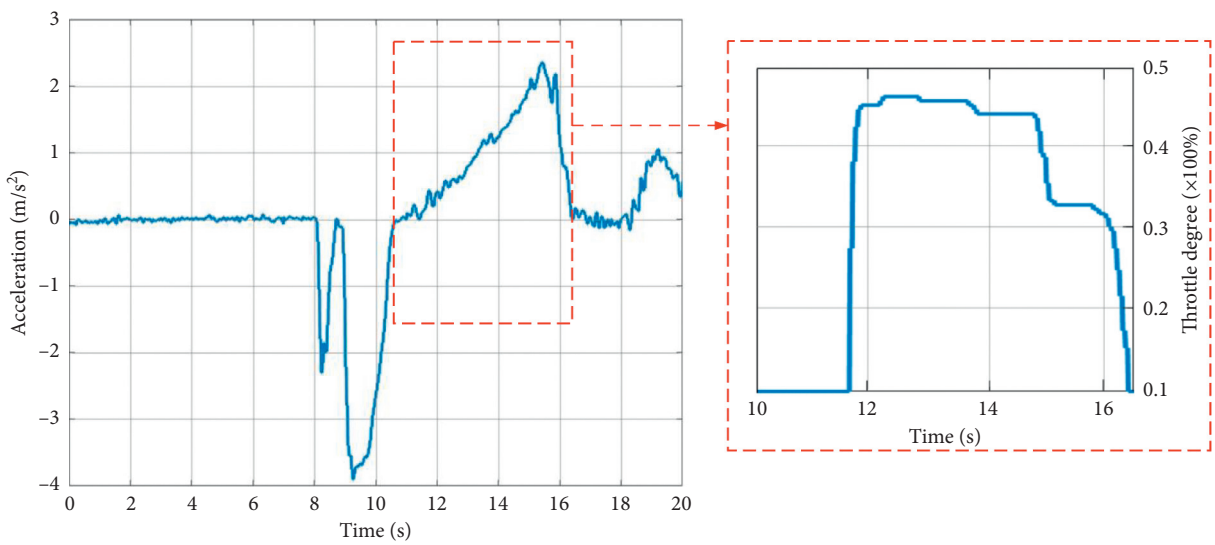


Figure 15: The acceleration and throttle degree for the real vehicle experimental test.

## 6. Results and Comparative Analysis

During the simulation, as shown in Figure 12, the driving condition is set to realize the vehicle's frequent stop-and-go task. The results show that the host vehicle can catch up with the target vehicle and keep an ideal distance when car following. Moreover, as shown in Figure 14, the experimental condition is random under urban overpass. The results show that the host vehicle can achieve an autonomous stop-and-go control based on the proposed method when the target vehicle is accelerating or decelerating. However, to further illustrate humanization, a comparative analysis is conducted, as shown in Figure 15.

The trend of acceleration is similar to the trend in Figure 7(a). Moreover, the trend of throttle degree is also similar to the trend in Figure 7(b). Therefore, on the one hand, the sense of starting in the real vehicle's experimental test will be similar to the real drivers. On the other hand, with the evident change in double deceleration, the behavior of braking will also be similar to the real drivers. Furthermore, the ideal distance in the simulation is similar to the test, and, then, the effectiveness of the proposed method is verified on the premise of ensuring safety.

## 7. Conclusions and Future Work

In this article, we propose an automatic stop-and-go control method based on a learning model for vehicles. First, the real drivers' starting and braking behaviors are obtained through the real vehicle's experimental test. The results show that the common characteristics of human drivers with different driving styles are their humanized acceleration and deceleration. Then, according to the variation trend of acceleration, the vehicle automatic starting control strategy is designed based on FFT and the IL algorithm. Next, based on the DTTC model, the vehicle automatic braking control strategy is designed by further analyzing the common humanized characteristics. Finally, the validity and feasibility are proved through the simulation and real vehicle tests. Furthermore, compared with the initial experiment, the method proposed can provide automatic stop-and-go control in car-following and improve the sense of humanity in the vehicle stop-and-go task.

However, the humanized learning control method has still some limitations: (1) considering the limited sample size, the humanization of the algorithm is slightly inadequate. (2) A switch logic should be designed between drive and brake controls. (3) The proposed method does not consider some extreme conditions, such as emergency braking behavior.

Future work can increase the sample size of the learning model. In addition, the switch strategy can be improved to solve the fluctuation problem, and some extreme conditions may be tested in the simulation.

## Data Availability

The data used in the paper are obtained through actual experiments, rather than using the established experimental data. Among them, some data or curves were derived from previous research results, which have been presented at a conference in 2019 Chinese Automation Congress (CAC); https://ieeexplore.ieee.org/document/8996633).

## Disclosure

This study is a continuation of the previous work , which has been presented at a conference in 2019 Chinese Automation Congress (CAC; https://ieeexplore.ieee.org/document/8996633).

## Conflicts of Interest

The authors declare no potential conflicts of interest with respect to the research, authorship, and/or publication of this article.

## Acknowledgments

This work was supported by National Science Foundation of China (Grants 51775236, 51675224, and U1564214), National Key Research and Development Program (Grant 2017YFB0102600), and Science and Technology Development Project of Jilin province (20200501012GX). The authors gratefully acknowledge Zhenhai Gao, Fei Gao, Tianyao Zhang Ji Di, and Siyan Chen of Jilin University for their helpful discussion.

## References

[1] Z. Li, *Research on Full Speed Adaptive Cruise Control System of Pire Electric Vehicle*, Harbin Institute of Technology, Harbin, China, 2017.

[2] L. Yishi, Z. Zhe, W. Liqiang, and H. Zongqi, "Design of vehicle full-speed adaptive cruise control with stop and go," *Machinery Design and Manufacture*, vol. 5, pp. 174–177, 2017.

[3] V. Paul, N. Karl, and A. Bartono, *Stop and Go Cruise Control*, FISITA World Automatic Congress, Seoul, Korea, 2000.

[4] J. Junchen, "Improved analysis of the car-following model based on ACC system," *Science, Technology and Engineering*, vol. 11, no. 26, pp. 6396–6400, 2011.

[5] Z. Jahandideh, B. Mirbaha, and A. A. Rassafi, "Modelling the risk intensity of crossing Pedestrians in intersections based on selected critical time to collision: a case study of Qazvin city," *Transportation Research Board 96th Annual Meeting*, vol. 1, 2017.

[6] G. Zhenhai, "Vehicle virtual following collision avoidance driver braking time model," *Journal of Jilin University (Engineering Edition)*, vol. 44, no. 5, pp. 1233–1239, 2014.

[7] T. Wu, *"A Study on Forward Collision Prevention System Considering the Characteristics of the Driver's Collision Avoidance Behavior*, Jilin University, Changchun, China, 2014.

[8] C. Lu, J. Gong, C. Lv, X. Chen, D. Cao, and Y. Chen, "A personalized behavior learning system for human-like longitudinal speed control of autonomous vehicles," *Sensors (Basel, Switzerland)*, vol. 19, no. 17, pp. 3671–3690, 2019.

[9] Y. Xing, C. Lv, and D. Cao, "Personalized vehicle trajectory prediction based on joint time series modeling for connected vehicles," *IEEE Transactions on Vehicular Technology*, vol. 69, no. 2, pp. 1341–1352, 2019.

[10] Y. Xing, C. Lv, H. Wang et al., "Driver lane change intention inference for intelligent vehicles: framework, survey, and challenges," *IEEE Transactions on Vehicular Technology*, vol. 68, no. 5, pp. 4377–4390, 2019.

[11] C. Lv, X. Hu, A. Sangiovanni-Vincentelli, Y. Li, C. M. Martinez, and D. Cao, "Driving-style-based codesign optimization of an automated electric vehicle: a cyber-physical system approach," *IEEE Transactions on Industrial Electronics*, vol. 66, pp. 2965–2975, 2018.

[12] N. Kuge, T. Yamamura, O. Shimoyama, and A. Liu, "A driver behavior recognition method based on a driver model framework," *SAE Technical Paper*, vol. 109, no. 6, pp. 469–476, 2000.

[13] M. Quintero, J. Lopez, and A. C. C. Pinilla, "Driver behavior classification model based on an intelligent driving diagnosis system," in *Proceedings of the 2012 15th International IEEE Conference on Intelligent Transportation Systems*, pp. 894–899, Anchorage, Alaska, USA, September 2012.

[14] G. Zhenhai, S. Tianjun, and H. Lei, "A multi-mode control strategy for EV based on typical situation," *SAE Technical Paper*, vol. 1, pp. 1–8, 2017.

[15] H.-S. Ahn, Y. Chen, and K. L. Moore, "Iterative learning control: brief survey and categorization," *IEEE Transactions on Systems, Man and Cybernetics, Part C (Applications and Reviews)*, vol. 37, no. 6, pp. 1099–1121, 2007.

[16] R. Chi, D. Wang, Z. Hou, and S. Jin, "Data-driven optimal terminal iterative learning control," *Journal of Process Control*, vol. 22, no. 10, pp. 2026–2037, 2012.

[17] M. M. Minderhoud and P. H. L. Bovy, "Extended time-to-collision measures for road traffic safety assessment," *Accident Analysis & Prevention*, vol. 33, no. 1, pp. 89–97, 2001.

[18] W. Wachenfeld, P. Junietz, R. Wenzel, and H. Winner, "The worst-time-to-collision metric for situation identification," in *Proceedings of the Intelligent Vehicles Symposium (IVS)*, pp. 356–362, Gotenburg, Sweden, September 2016.

[19] L. Zhang, H. Ding, J. Shi et al., "An adaptive backstepping sliding mode controller to improve vehicle maneuverability and stability via torque vectoring control," *IEEE Transactions on Vehicular Technology*, vol. 69, no. 3, pp. 2598–2612, 2020.

Hindawi
Advances in Civil Engineering
Volume 2021, Article ID 6685900, 11 pages
https://doi.org/10.1155/2021/6685900

*Research Article*

# Prognostics and Health Management System for Electric Vehicles with a Hierarchy Fusion Framework: Concepts, Architectures, and Methods

**Cheng Wang,[1,2,3] Tongtong Ji,[3] Feng Mao,[3] Zhenpo Wang,[1] and Zhiheng Li[3]**

[1]*National Engineering Laboratory for Electric Vehicles, School of Mechanical Engineering, Beijing Institute of Technology, Beijing 100081, China*
[2]*Beijing CATARC Science and Technology Co., Ltd., Beijing 100070, China*
[3]*Tsinghua Shenzhen International Graduate School, Tsinghua University, Shenzhen 518055, China*

Correspondence should be addressed to Tongtong Ji; jtt18@mails.tsinghua.edu.cn

Received 30 October 2020; Revised 22 December 2020; Accepted 2 January 2021; Published 15 January 2021

Academic Editor: Hui Yao



The prognostics and health management (PHM) of electric vehicles is an important guarantee for their safety and long-term development. At present, there are few studies researching about life cycle PHM system of electric vehicles. In this paper, we first summarize the research progress and key methods of PHM. Then, we propose a three-level PHM system with a hierarchy fusion architecture for electric vehicles based on the structure, data source of them. In the PHM system, we introduce a database consisting of the factory data, real-time data, and detection data. The electric vehicle's factory parameters are used for determining the life curve of the electric vehicle and its components, the real-time data are used for predicting the remaining useful lifetime (RUL) of the electric vehicle and its components, and the detection data are used for fault diagnosis. This health management database is established to help make condition-based maintenance decisions for electric vehicles. In this way, a complete electric vehicle PHM system is formed, which can realize the whole-life-cycle life prediction and fault diagnosis of electric vehicles.

## 1. Introduction

The development of new-energy-related technologies and the advancement of environmental awareness have promoted the rise of new energy vehicle [1, 2], and electric vehicle is one of the important branches. Electric vehicles have become the development trend in the automotive field since their energy-saving nature.

Compared with traditional automobiles, electric vehicles are different in electric drive and control systems due to different energy consumption types. Meanwhile, the fault and accident types of electric vehicles are also different from traditional vehicles. In terms of the fault type, electric vehicles may fail in the battery system (such as inconsistency of cells and degradation of battery), while traditional vehicles may fail in their fuel engine (such as the failure of the cooling system). In terms of the accident type, fire accidents are more likely to occur in electric vehicles than traditional ones. In recent years, many electric vehicle accidents have occurred in different countries. Take China as an example; 59 accidents such as fire accidents occurred in electric vehicles in China between 2016 and 2018. The causes of the accidents are related to many factors of the battery system such as battery aging and overcharging. The health management mode of traditional fuel vehicles cannot be directly used. Therefore, it is urgent to establish a prognostics and health management (PHM) system specifically for the essential characteristics of electric vehicles, comprehensively monitor the health state of electric vehicles, and improve the safety level of electric vehicles. The contribution of this study is that we show a comprehensive PHM system for electric vehicles.

This paper summarizes the research progress of health management and the demand of electric vehicle health management and then proposes a comprehensive three-level

PHM system with a hierarchy fusion architecture for electric vehicles. The remainder of this paper is organized as follows. Section 2 introduces the content of PHM. Section 3 describes the architectures and key methods of the PHM method. Section 4 proposes a three-level PHM system with a hierarchy fusion architecture for electric vehicles. Finally, we conclude the work of this paper.

## 2. Prognostics and Health Management

*2.1. What Is PHM?* The content of PHM includes two aspects, namely, prognostics and health management. Prognostics is to predict the future status based on the current and historical status of the system, including the health state, remaining useful lifetime, and faults of the system and components. Health management is to make decisions on maintenance based on fault prediction information, maintenance resources, and application requirements. Prognostics is the core aspect of health management. PHM systems usually have functions such as fault detection, fault isolation, fault diagnosis, fault prediction, health management, and life tracking. For complex equipment and systems, PHM can achieve comprehensive diagnosis and fault prediction at different levels.

In the 20th century, the US military first proposed the concept of health management. Health management aims to monitor equipment working conditions, predict its remaining useful lifetime, potential failures, and health issues, and provide repair and maintenance recommendations. Advanced sensor technology, data transmission technology, and data processing technology are often used as the technical methods. In recent years, health management technology has received extensive attention, research, and application and has now developed into prognostics and health management technology [3–5]. Lee [6] proposed a "5S"-based health management system and process for the mechanical system. Brahimi et al. [7] summarized the health management system of railway infrastructure. Pecht [8] analyzed the health management and technical methods of electronic systems. Johnson et al. [9] described the health management system and application of the space system. In addition to military field, health management technology plays an important role in the mechanical system [6, 10], battery health management system [11, 12], aerospace [13], and other fields. For example, the PHM technology is widely used in the aircraft system in the UK, the US, and Canada, as well as other complex engineering equipment such as automobiles. Vehicle health management (VHM) system has been utilized to realize the automated decisions in the last decades. For instance, the OnStar system of General Motors company sets a good example for the use of VHM. This system is capable of prognostics and information transmission from subsystem to a central processing system. This centralized architecture and data processing technology can be applied to the electric vehicle PHM system design.

*2.2. Why PHM for Electric Vehicles?* The market of electric vehicles has been expanding a lot for the last decade and the number of electric vehicles is increasing sharply. The monitoring of the safety level and identifying of possible faults about the vehicle in use are of great significance. Electric vehicle is a complex system composed of the battery system, motor system, and electronic control system, and the safety performance is closely related to each system. However, nowadays the health management is mainly concentrated on battery systems [14–16]. A mature electric vehicle health management system framework has not yet been formed. Therefore, it is necessary to establish a health management system for electric vehicles, which will directly affect the long-term development of electric vehicles. The PHM system has been successfully applied to some complex system such as the aircraft system. And, it has advantages over the whole-life cycle health management. Therefore, introducing the idea of PHM to the electric vehicle field is a promising idea.

## 3. PHM Architectures and Key Methods

In this section, we will give an overview about the PHM architectures, especially three different classifications. Next, two important technologies used in the PHM system will be introduced, namely, the life prediction and fault diagnosis. Fault diagnosis is used to realize the prognosis, and life prediction is an import branch of health management. Thus, we mainly carry on the elaboration in these two aspects.

*3.1. PHM Architectures.* PHM architectures are divided into three categories: centralized architecture, distributed architecture, and hierarchy fusion architecture. In the centralized PHM architecture, the information is processed within a central management controller which integrates the function of information collection, transformation, and processing. In a distributed architecture, each subsystem can realize the information processing process and then achieve the function of fault diagnosis and prediction. After the processing of the subsystem, the health status of the subsystem can be directly transmitted to the integrated display and control unit. The hierarchical fusion architecture combines the centralized and distributed architecture. Each subsystem has basic PHM functions, while the higher-level system has more powerful integration capability. And the high-level system can comprehensively process and control all diagnosis and prediction results.

*3.2. Life Prediction Methods.* There exist three kinds of methods to make the life prediction: physical model-based method, data-driven method, and fusion method.

The physical model-based method establishes a physical failure model to investigate the internal cause of the system failure and then predicts the remaining useful lifetime (RUL) of the system [17]. Son et al. [18] proposed a RUL prediction method based on the gamma process. A nonstationary gamma process model was used to establish a system degradation model to predict the RUL. Wang [19] proposed a second-order remaining life prediction model based on semirandom, semilinear, and non-Gaussian filtering techniques based on degradation data. Lin [20] studied the two-

stage modelling method of failure based on Bayesian change point estimation, mainly considering the existence of change points in the system failure rate function. Yuan and Yuo [21] also considered the existence of change points in the failure rate function. The physical model-based method can accurately predict the remaining life of the equipment, but it is often difficult to obtain the model parameters. Meanwhile, it is difficult to establish a physical model for the failure of complex systems.

Data-driven methods can overcome those aforementioned difficulties. These kinds of methods use system detection data to establish the state models of the characteristic index and the remaining life of the system. Data-driven methods include neural networks, support vector machines, Bayesian networks, and stochastic processes. Wang and Vachtsevanos [22] realized the life prediction of the automobile-bearing system through the dynamic wavelet neural network model. You et al. [23] proposed a method for predicting the real-time state of electric vehicle power batteries based on neural network models and proved the accuracy of the method through battery tests. Khelif et al. [24] used support vector machines to build a model between the remaining life and sensor parameters. In addition, according to different degradation models, researchers have also established RUL prediction methods based on the Gamma process [25] and Wiener process [26, 27]. Data-driven methods require large-scale and high-quality datasets. At the same time, the algorithm needs to make a balance between the accuracy and complexity so that the efficiency of the algorithm is acceptable.

The fusion method combines the advantages of the physical model-based method and the data-driven method. Liao Kottig [28] proposed a hybrid method combining a data-driven method and a physical model method. The validity of the method was proved by the prediction of the remaining life of the lithium battery. The fusion method can combine the advantages of the first two methods, but the algorithm is more complicated.

*3.3. Fault Diagnosis Methods.* A fault is a deviation from expectations of the parameters or states in a normally operating system. Fault diagnosis technologies mainly include model-based fault diagnosis and data-based fault diagnosis.

The model-based method compares the model output information with the actual monitoring information of the system to determine whether the system has failed. Common methods include observer-based methods [29, 30] and parameter identification-based methods [31]. Observer-based methods are flexible and easy to apply, such as Kalman filter (EKF) [32], adaptive EKF (AEKF) [33], sliding model observer (SMO) [34], or proportional integral observer (PIO) [30]. The parameter identification-based methods detect abnormalities through online parameter estimation to diagnose faults. However, the application of model-based method is limited since it is difficult to obtain an accurate system model for a complex system.

The data-based method analyzes and diagnoses based on a large amount of historical data without the need for accurate system models and signal types. The main methods include neural networks, decision trees, and support vector machines. Yam realized the prediction of system failure through the regression neural network model [35]. Wang chose a fuzzy neural network model to predict and determine system failures [36]. Qiu et al. proposed a fault recognition algorithm based on Hidden Markov for fault sign recognition at an early stage [37]. Goebel compared the performance of three data analysis methods, i.e., neural network, decision tree, and support vector machine in fault prediction [38]. Skormi et al. realized prediction of the fault development process based on clustering algorithm [39].

The rise of electric vehicles in recent years has accumulated a small volume of fault data. And, the methods based on big data are not applicable due to the small-scale sample data. There are some studies dealing with the fault diagnosis of small-scale data. Vachtsevanos [40] calculated the probability density of fault by statistical methods such as Bayes. Weibull [41] used the Weibull distribution to expand the sample data. The application of Monte Carlo and Bayesian methods [42] to obtain the probability density of faults is often used.

In summary, the PHM method is mainly oriented to fault prediction and fault diagnosis. There are some differences in the methods and application requirements in different fields. For the PHM for electric vehicles, we should not only focus on battery system health management but also establish a complete PHM system for the entire vehicle.

## 4. PHM System for Electric Vehicles

*4.1. PHM System.* PHM system for electric vehicle mainly concerns with the following two problems: prognostics and health management. First health management deals with the life prediction and evaluation for electric vehicle and its components. And, prognostics deals with the fault diagnosis and prediction.

Three kinds of PHM architectures are described before, and now we will introduce a three-level PHM system with a hierarchy fusion architecture for electric vehicles considering the vehicle structure, data source, and health management requirements of them. The PHM system is shown in Figure 1.

The detailed composition of the database is shown in Figure 2. There are four sources of data in this database, namely, the electronic control system, motor system, battery system, and electric vehicle. For each component, factory data, detection data, and real-time data are included to provide a comprehensive view about the vehicle. According to different stages of data source in the health management database, the PHM system is divided into three levels:

> Level 1 deals with the life prediction of electric vehicles at the factory stage. In this level, the lifetime of electric vehicles and its subsystems and components are predicted. The main product is the life curves of electric vehicle, battery system, motor system, electronic control system, and components.

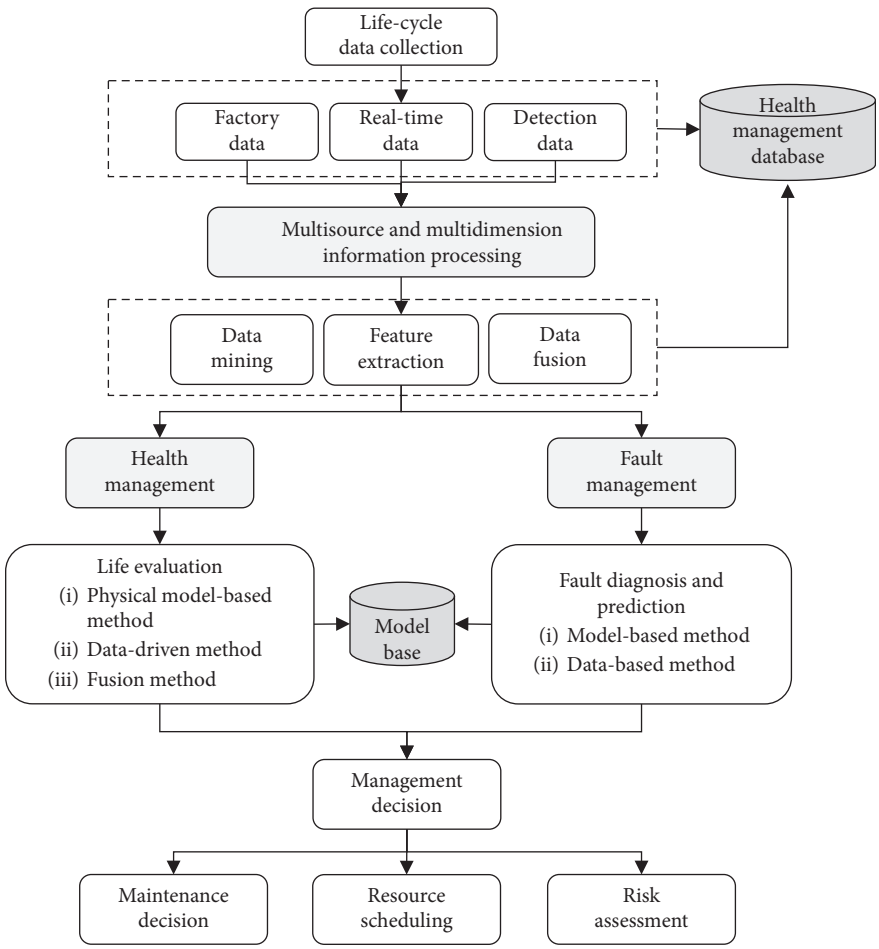


Figure 1: PHM system for electric vehicles.

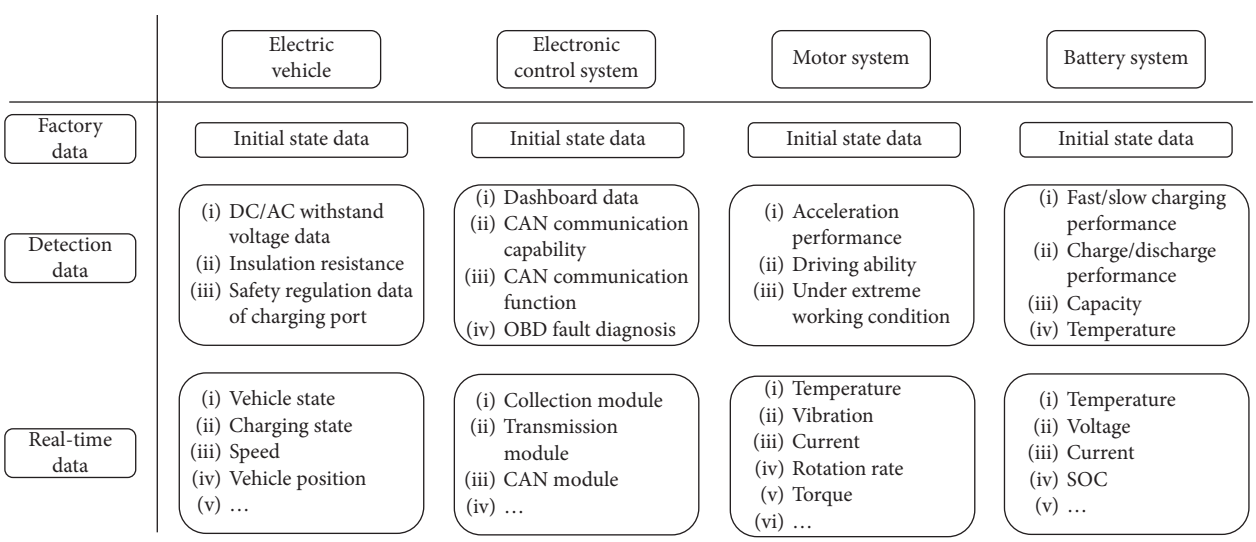


Figure 2: Composition of health management database.

Level 2 deals with the real-time remaining useful lifetime prediction of electric vehicles. In this level, the remaining useful lifetime is predicted through the real-time operation data of electric vehicle to realize the real-time monitoring and evaluation of electric vehicle's state.

Level 3 deals with the fault diagnosis of electric vehicle detection process. In this level, we detect the faults of the electric vehicle and diagnose the faulty system or components.

The main functions of the electric vehicle PHM system include information collection, fault detection, fault diagnosis, fault prediction, and health management. The details of each function are listed as follows.

(1) Information collection: integrate the factory parameters, test data, and real-time driving data of electric vehicles to form a health management database
(2) Fault detection: determine the performance degradation state of battery, motor, and electronic control system, such as normal state, performance degradation state, or a function failure state
(3) Fault diagnosis: determine the fault system or parts to be repaired
(4) Fault prediction: predict the time when the battery, motor, and electronic control system will fail
(5) Health management: make condition-based maintenance decision on battery, motor, electronic control system, and parts according to the information of fault detection, fault diagnosis, and fault prediction

Next, we will introduce the key methods of the PHM system for electric vehicles. Firstly, we will elaborate the life prediction at factory stage and real-time life prediction of electric vehicle in use (postfactory stage). The life prediction at the factory stage is a necessary input for the real-time life prediction, which provides information for health management. Secondly, we will show the fault diagnosis of electric vehicle.

## 5. Life Prediction of Electric Vehicles at Factory Stage

The key components of a vehicle will have permanent damage during long-time driving, and its fatigue life has always been the focus of vehicle safety. The life of the components of electric vehicles and the life of battery, motor, and electronic control systems are closely related. For example, the individual battery cells in the battery system constitute the entire battery pack. And the battery system, the motor system, and the electronic control system interact with each other to form the entire vehicle. Thus, the life of electric vehicle is closely related to its components and subsystems. Through the method of nonlinear and linear fusion, the life curve can be obtained from the component to the entire vehicle. Therefore, the life prediction of the electric vehicle at the factory stage includes the life curve of single components, the life curve of the subsystem, and the life curve of the entire vehicle.

*5.1. Life Curve of Single Component.* The life of electric vehicle components changes with time and shows nonlinear characteristics. So, the traditional regression algorithm is difficult to predict the life accurately. Taking the battery system as an example, its life prediction methods mainly includes physical model-based method, data-driven method, and fusion method. And, the algorithm based on data-driven has good adaptability, among which the BP neural network is used the most widely. Through the error backpropagation algorithm, the model parameters can be self-updated and the training data can be fitted. The model structure is shown in Figure 3.

Here, we take the battery system as an example. Assume that the parameters of the component are the number of charge and discharge, discharge voltage, and temperature, which is noted as vector $[x_1, x_2, x_3]$. Using this vector as the input data of the neural network, through multiple hidden layers and delinearized softmax layers, the feature of the part can be extracted and the corresponding component life can be predicted.

The model can also be applied to life prediction of other components such as motor bearings. By collecting the vibration data of the motor bearing, transforming it to the frequency domain for feature analysis, and extracting indicators related to bearing performance degradation through PCA (Principal Component Analysis), we can obtain the input data. Taking these indicators as the input and the predicted life of the motor bearing as the output, the model is established.

*5.2. Life Curve of Subsystem.* Electric vehicle is a complex mechanical and electronic system. The life curve of a single component cannot accurately reflect the performance and life of the module or system, not to mention the entire vehicle. The life of the multicomponent system usually depends on the components with the shortest life. Linear and nonlinear fusion of each component life curves can obtain the life curve of the corresponding module or system.

*5.2.1. Life Curve of Subsystems Based on Linear Fusion.* The life of each component is given in different weights according to its importance. The system life prediction model can be obtained by the linear weighting method :

$$T = \sum_{i=1}^{n} \omega_i \cdot t_i, \tag{1}$$

where $T$ represent the life of system, $n$ indicates the number of components that make up the system, $t_i$ is the life of component $i$, and $\omega_i$ is the weight of component $i$.

This method can be applied to the life prediction of the battery, motor, and electronic control system. Taking battery pack as an example, the life of single battery is predicted by particle filter and data-driven algorithm. Then, the life of the whole battery pack is obtained by weighting the life of all single batteries, in which the weight of each single battery is the same.

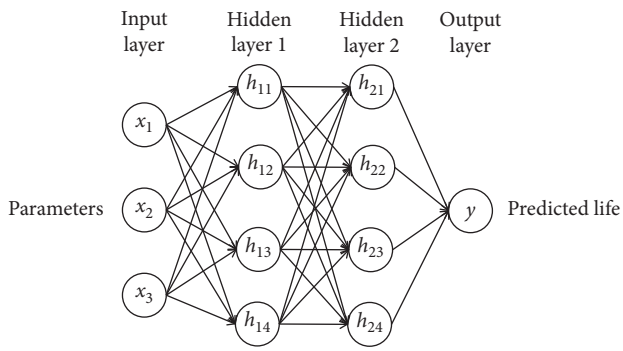


Figure 3: The structure of the neural network.

The linear weighting method is simple to realize, but the results of prediction is not good. Due to the nonlinear characteristics of electrical components and complex driving conditions, the linear model with the same weight assigned to subsystem cannot be directly applied to different conditions. Aiming at this problem, the weight is adjusted dynamically to improve the applicability of the model.

*5.2.2. Life Curve of Systems Based on Nonlinear Fusion.* The commonly used methods are the waterfall fusion method and feature fusion method. The waterfall fusion method is suitable for modules with strong correlation between various components. This method connects each component in series. The life of the previous component will affect the next component. It is progressively connected in series to finally obtain the life of the entire module. The feature fusion method is a statistical-based method. It collects the life curve and parameters of the same module in multiple samples and digs the statistical rules to obtain the life curve of this module.

This method can be applied to the life prediction of batteries, motors, and electronic control systems. Take the motor system as an example. The system includes bearings, insulation, DC bus capacitors, IGBT (insulated gate bipolar transistor), and other electronic components. The series model is shown in Figure 4. The life of the whole system is composed of all components in series, not a simple linear combination.

*5.3. Life Curve of the Entire Electric Vehicle.* The relationship between the battery, motor, and electronic control systems of an electric vehicle is shown in Figure 5. The battery system provides power. The motor system drives the vehicle. The electronic control system sends commands to the motor controller to control the motor according to the accelerator pedal and brake pedal signal input by the driver.

The life of the entire vehicle is related to the life of the three subsystems: battery system, motor system, and electronic control system. It can be determined by statistical analysis methods, simulation methods, and data-driven methods.

Statistical analysis methods mainly include series system, parallel system, and series-parallel system reliability analysis. Cheng et al. and Dong et al. [43, 44] studied the reliability analysis and life estimation of a two-component series system. Gu [45] studied the parameter estimation problem of series systems subject to discrete binary geometric distribution. Dong [46] studied the reliability equivalent factor of series systems under the gamma distribution. Zhang and Chang and Sadegh [47, 48] discussed the estimation of the remaining useful lifetime of parallel systems with independent and different distributed structures. Li et al. [49] studied the random comparison of the life of series-parallel systems for a series-parallel system composed of $N$ components with random numbers and $N$ components with nonrandom numbers.

In terms of simulation methods, the Monte Carlo method is widely used for reliability analysis due to its robustness and ability to solve complex failure area problems [50]. However, it is inefficient to solve the problem of large number of random variables and small probability. In addition, the Monte Carlo method cannot calculate the multiple failure function combination equation.

Data-driven methods mainly include support vector machines, neural networks, and fuzzy logic. Data-driven methods require a large amount of data to support them. Data acquisition and data quality are particularly important in this method.

## 6. Real-Time Life Prediction of Electric Vehicles in Use

The remaining useful lifetime of electric vehicles can be predicted using the real-time electric vehicle data, which can be used to monitor and evaluate the status of the electric vehicle. The remaining useful lifetime is defined as the time interval from the current moment to the predicted failure according to the current operating conditions [51, 52], also known as the remaining life. A typical life curve is shown in Figure 6, which can be divided into three stages. The first stage is the early failure period, in which the fault shows a tendency of degradation. This stage can be found through detection data. The second stage is the effective life period. There is no early failure of the system. In this stage, the vehicle will stay in a normal working condition. The third stage is the loss failure period, in which the system is under the process of degradation to failure. There is an abnormal time point at the end of the second stage, which is generally called a symptom point.

*6.1. Real-Time Operating Data Collection of Electric Vehicles.* Real-time operating data is divided into three categories: battery, motor, and electronic control system.

(1) Data acquisition of the battery system.

Battery system is the power source of the vehicle, and it provides the energy to drive the vehicle. The battery system collects the basic attributes and real-time status of the battery including the number of

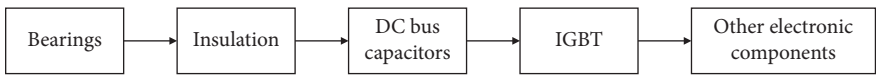


Figure 4: Series model of the motor system.

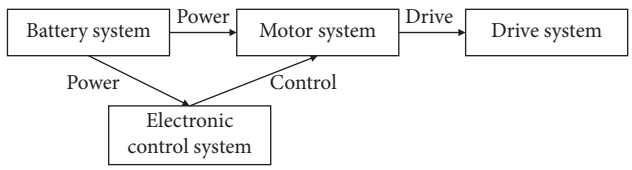


Figure 5: Relationships among the subsystems of the electric vehicle.

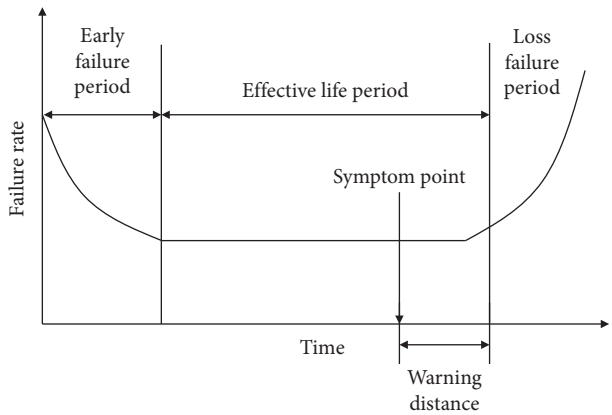


Figure 6: Life prediction model.

battery packs, the number of single batteries, the voltage value of the single battery, the battery pack temperature, the state of charge and discharge, the total voltage, the total current, the State of Charge (SOC), the insulation resistance, and the battery failure. The battery pack is also called a battery box, and each battery box contains a fixed number of single batteries.

(2) Data acquisition of the motor system

The motor system is mainly composed of a high-voltage motor that provides torque for the vehicle. In other words, it gives the force to drive the vehicle. The motor system mainly collects information such as the number, temperature, and speed of the driving motors.

(3) Data acquisition of the electronic control system

Although batteries and motors are indispensable, the electronic control system is much more complex. It plays a central role in energy vehicles, and its main function is to collect all kinds of signals from accelerator, brake pedal, steering wheel, and so on and send out corresponding instructions according to the information. The data collected from the electronic system including the output from steering control, power drive control, braking control, CAN management control, and vehicle status monitoring display. For example, vehicle speed gear position, accelerator pedal position, brake pedal position, and air-conditioner temperature. The electronic control system is a core part of the electric vehicles.

*6.2. Prediction of the Remaining Life of Electric Vehicles under Real-Time Operation.* By using various data collected from systems, various algorithms, and intelligent models (such as physical models, neural networks, data fusion, fuzzy logic, and expert systems), the state of the system of electric vehicle is monitored, predicted, and managed. The system is always under monitoring so that the faults can be predicted before this system fails. Meanwhile, a series of maintenance advice is condition-based maintenance. The flowchart is shown in Figure 7.

There are many parameters of the real-time data collected by electric vehicles, so feature extraction is necessary. Feature extraction is to select important indicators as input to the prediction model. Common feature extraction methods can be classified into three categories: filtering, wrapper, and embedding [53]. The filtering method performs feature extraction on the data first, and then filtered features are used to train the model. The main idea of feature extraction is to assign weights to the features in each dimension and then rank them according to the weight. The main methods are the Pearson correlation coefficient method and mutual information coefficient method. Wrapper method directly integrates feature extraction and

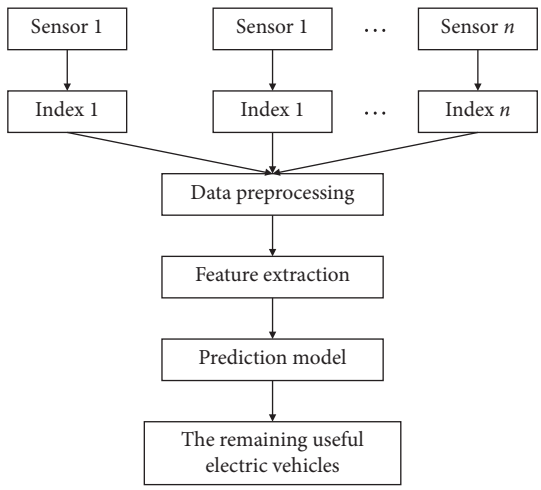


Figure 7: Flowchart of electric vehicle life prediction based on detection data.

model training and uses the performance of the model as an evaluation criterion for the feature subset, such as GA algorithm. The embedding algorithm includes a feature extraction process, in which the feature extraction is performed by itself during the training of the learner, such as a decision tree and a random forest.

After the extraction of important indicators, the remaining useful lifetime of electric vehicles can be predicted through inference algorithms and intelligent models. Refer to the life prediction method in the previous section "Life Prediction Methods," and the remaining useful lifetime prediction methods of the system are divided into physical model methods and data-driven methods [54].

The support vector regression-particle filter is used to predict the remaining useful life of battery [55], and many other machine learning methods are used as well such as neural networks. For each subsystem and component, the prediction models and methods overlapped in many ways except the difference in input data. As for the vehicle remaining useful life prediction, like we introduced before, it needs a model to integrate the information from subsystems to get a final result.

## 7. Fault Diagnosis of Electric Vehicle Detection Process

When an electric vehicle malfunction occurs, detection is required to determine the malfunctioning system or component for repair and maintenance. As introduced in Section 3.3, fault diagnosis methods can be divided into model-based fault diagnosis and data-based fault diagnosis. In the early stage of the establishment of the electric vehicle fault database, fault diagnosis based on big data is difficult to implement, and the prediction will have a low accuracy rate. A method based on small sample data is needed to achieve the fault diagnosis at this stage. After the accumulation of data, big data analytical methods can be used to find out the fault pattern.

*7.1. Fault Diagnosis Based on Quantitative Model.* By establishing a mathematical model and comparing the residuals between the model output and the standard output, we can diagnose the occurrence of faults and the corresponding fault types. Residual generation method can be divided into parameter estimation, state estimation, and synchronization state parameter estimation. Parameter estimation includes methods such as least squares and boundary parameter analysis. Common methods for state estimation include fault detection methods based on Kalman filtering, interval observers, and set theory.

Taking the battery system as an example, the common indicators of the single cell are temperature and voltage. Parameter estimation is the simplest way to identify the temperature and voltage anomaly of single cell. Existing standards require electric vehicles to record and upload the information of minimum single voltage, the maximum cell voltage, the minimum cell temperature, and the maximum cell temperature. Through parameter estimation methods, a quantitative model can be established to perform temperature and voltage consistency analysis and fault detection on the battery.

*7.2. Fault Diagnosis Based on Small Sample Data.* At present, there are two ways to solve the problem of small-scale sample data analysis: (1) expand the sample data by random algorithms, and then analyze them by traditional data analysis methods; (2) use Bootstrap method, Bayes method, Monte Carlo method, and other analysis methods suitable for small-scale data. However, each method has its limitations. The Bootstrap method neutron sample has a large impact on the estimated parameters, and it is easy to generate parameter faults, causing inaccuracies in the estimation [56]. The accuracy of the Monte Carlo method depends on the mathematical model of the parent. The Bayesian method [57] is more suitable for processing small sample data. When the number of samples is small, the probability of failure can be better estimated, but its prior probability will greatly affect the posterior result. Support vector machine algorithm is also a commonly used machine learning method. It supports fault diagnosis under small sample data and is suitable for fault diagnosis of battery systems.

Next, an instance of fault identification will be given. Taking a motor system as an example, we first combine the

Weibull fault distribution model with the Bayesian method to obtain the fault probability density of components and then analyze the probability and category of fault occurrence. The steps are as follows:

(1) Fit the Weibull distribution through small sample fault data to obtain shape parameters and scale parameters
(2) Substitute the estimated parameters into the model, obtain bootstrap subsamples by Monte Carlo sampling, and estimate the parameters of each group of subsamples as the prior information of Bayesian
(3) Obtain the posterior probability density distribution function of system faults through the Bayesian model

The failure probability density of the Weibull distribution is

$$f(t) = mt^{m-1}\frac{\exp\left[-(t/\eta)^m\right]}{\eta^m}. \tag{2}$$

The reliability function is

$$R(t) = 1 - F(t) = \exp\left[-\left(\frac{t}{\eta}\right)^m\right]. \tag{3}$$

The failure rate function is

$$\lambda(t) = \frac{mt^{m-1}}{\eta^m}, \tag{4}$$

where $t$ is time, $m$ is the shape parameter, and $\eta$ is the scale parameter. A set of shape parameters and scale parameters can be determined by regression analysis on a set of fault data and then sampled by the sampling formula [57]:

$$t(n) = \eta(-\mathrm{len}(e[n]))^{1/m}. \tag{5}$$

Assume that each group of samples obtained by sampling is independent of each other; then, we can perform parameter estimation on them to obtain the parameter estimates of each group. In this way, the reliability function and the failure probability density function are obtained through the Bayesian formula.

*7.3. Fault Diagnosis Based on Big Data.* With the rapid development of big data and electric vehicles, fault detection and diagnosis of electric vehicles based on big data has a wide application prospect. A commonly used method is Artificial Neural Network (ANN). The basic idea is based on a large number of electric vehicle fault data, with the fault data dimension as the network input layer dimension, and the fault category as the output dimension. Through continuous iterative training, the model weights, thresholds, and other parameters are obtained. Then, we can fit the potential relationship between the sample data and the sample label, realize the fault detection and diagnosis, and constantly update the diagnosis database improvement.

The power battery and motor system of electric vehicles are both nonlinear systems. Traditional neural networks cannot adapt well to nonlinear data. Therefore, neurons need to be delinearized by adding activation functions. Common activation functions include ReLU function, sigmoid function, and tanh function, and they are shown as follows:

$$f(x) = \max(x, 0), \tag{6}$$

$$f(x) = \frac{1}{\left(1 + e^{-x}\right)}, \tag{7}$$

$$f(x) = \frac{\left(1 - e^{-2x}\right)}{\left(1 + e^{-2x}\right)}. \tag{8}$$

Common faults of power batteries include abnormal temperature, abnormal voltage, and abnormal temperature and voltage consistency. Common faults in motor systems include abnormal output power. The model needs to determine which type of failure has the greatest probability of occurrence among multiple failure types. Now, the softmax function needs to be introduced:

$$\mathrm{soft\,max}(y_i) = \frac{e^{y_i}}{\sum_{j=1}^{n} e^{y_i}}. \tag{9}$$

The softmax function converts the output of the neural network into a probability distribution to calculate the cross entropy or directly selects the fault type with the highest probability as the final fault diagnosis result.

## 8. Conclusion

In this paper, a complete electric vehicle fault prediction and health management system is established based on the system structure of electric vehicles and the sources of data information. The system mainly includes three levels:

(1) Life prediction of electric vehicles at the factory stage: at the factory stage, a physical model method or a data-driven method is used to obtain the life curve of a single component. Based on this, a linear and nonlinear fusion method is used to obtain the life curve of a system composed of multiple components. The simulation method and the data-driven method are used to obtain the vehicle life prediction curve composed of multiple systems.
(2) Real-time life prediction of running electric vehicles: the data information to be collected from the three electric vehicle systems under real-time running status is summarized. And the filter information, filter type, wrapper type, and embedded type are used to realize the feature extraction of the data information to predict the remaining life of the electric vehicle.
(3) Fault diagnosis of electric vehicle detection process: based on the current situation of the fault database of electric vehicles, fault diagnosis method based on quantitative models, small sample data, and big data are proposed.

The electric vehicle PHM system proposed in this article can realize the whole-life-cycle prognostics and health management of electric vehicles since it supports the detection and prediction for vehicles at factory stage and postfactory stage. This will improve the safety level of electric vehicles and provide reference for the design of other product health management systems in the future. Meanwhile the vehicle users, manufactures, and government can also get benefit from it. For users, the PHM system can help them monitor the status of electric vehicles and identify possible faults, so as to improve the safety level of vehicles. For manufacturers, the PHM system is enabled to establish a more complete vehicle management system, especially in the postfactory stage. For the government, the supporting database of the system can promote research innovation and big-data-related services, which is beneficial to the development of the industry.

## Data Availability

No data were directly used in this study. However, in the design of this paper, we refer to the dataset which comes from the real-time status data record of Shenzhen electric buses. The dataset has not been made available because this dataset in not open yet.

## Conflicts of Interest

The authors declare that there are no conflicts of interest regarding the publication of this paper.

## Acknowledgments

This work was supported by the Science and Technology Innovation Committee of Shenzhen (Grant no. JCYJ20170412172030008) and Shenzhen Knowledge Innovation Plan (Grant no. 20170410195308266).

## References

[1] W. Waag, C. Fleischer, and D. U. Sauer, "Critical review of the methods for monitoring of lithium-ion batteries in electric and hybrid vehicles," *Journal of Power Sources*, vol. 258, no. 14, pp. 321–339, 2014.

[2] L. Chen, Z. Lü, W. Lin, J. Li, and H. Pan, "A new state-of-health estimation method for lithium-ion batteries through the intrinsic relationship between ohmic internal resistance and capacity," *Measurement*, vol. 116, pp. 586–595, 2018.

[3] N. H. Kim, J. H. Choi, and D. An, *Prognostics and Health Management of Engineering Systems: An Introduction*, Springer, Cham, Switzerland, 2016.

[4] G. Niu, *Data-driven Technology for Engineering System Health Management*, Springer, Cham, Switzerland, 2016.

[5] Y. Lei, *Intelligent Fault Diagnosis and Remaining Useful Life Prediction of Rotating Machinery*, Elsevier, Amsterdam, Netherlands, 1st edition, 2016.

[6] J. Lee, F. Wu, W. Zhao, M. Ghaffari, L. Liao, and D. Siegel, "Prognostics and health management design for rotary machinery systems-reviews, methodology and applications," *Mechanical Systems and Signal Processing*, vol. 42, no. 1-2, pp. 314–334, 2014.

[7] M. Brahimi, K. Medjaher, M. Leouatni, and N. Zerhouni, "Development of a prognostics and health management system for the railway infrastructure—review and methodology," in *Proceedings of Prognostics and System Health Management Conference*, Chengdu, China, October 2016.

[8] M. Pecht, "Encyclopedia of structural health monitoring," in *Prognostics and Health Management Of Electronics*John Wiley & Sons, Hoboken, NJ, USA., 2008.

[9] S. B. Johnson, T. Gormley, S. Kessler et al., "Avionics Health Management," in *System Health Management: with Aerospace Applications*, pp. 445–465, John Wiley & Sons, West Sussex, UK, 2011.

[10] S. A. Aye and P. S. Heyns, "An integrated gaussian process regression for prediction of remaining useful life of slow speed bearings based on acoustic emission," *Mechanical Systems and Signal Processing*, vol. 84, pp. 485–498, 2017.

[11] Y. Zhou, M. Huang, Y. Chen, and Y. Tao, "A novel health indicator for on-line lithium-ion batteries remaining useful life prediction," *Journal of Power Sources*, vol. 321, pp. 1–10, 2016.

[12] L. Lu, X. Han, J. Li, J. Hua, and M. Ouyang, "A review on the key issues for lithium-ion battery management in electric vehicles," *Journal of Power Sources*, vol. 226, pp. 272–288, 2013.

[13] M. Esperon-Miguez, P. John, and I. K. Jennions, "A review of integrated vehicle health management tools for legacy platforms: challenges and opportunities," *Progress in Aerospace Sciences*, vol. 56, pp. 19–34, 2013.

[14] Z. Omariba, L. Zhang, and D. Sun, "Review on health management system for lithium-ion batteries of electric vehicles," *Electronics*, vol. 7, no. 5, p. 72, 2018.

[15] R. Xiong, Y. Zhang, J. Wang, H. He, S. Peng, and M. Pecht, "Lithium-ion battery health prognosis based on a real battery management system used in electric vehicles," *IEEE Transactions on Vehicular Technology*, vol. 68, no. 5, pp. 4110–4121, 2019.

[16] K. Liu, K. Li, Q. Peng, and C. Zhang, "A brief review on key technologies in the battery management system of electric vehicles," *Frontiers of Mechanical Engineering*, vol. 14, no. 1, pp. 47–64, 2019.

[17] J. Fan, K. C. Yung, and M. Pecht, "Physics-of-failure-based prognostics and health management for high-power white light-emitting diode lighting," *IEEE Transactions on Device and Materials Reliability*, vol. 11, no. 3, pp. 407–416, 2011.

[18] K. L. Son, M. Fouladirad, and A. Barros, "Remaining useful lifetime estimation and noisy gamma deterioration process," *Reliability Engineering and System Safety*, vol. 149, pp. 76–87, 2016.

[19] W. Wang, "A two-stage prognosis model in condition based maintenance," *European Journal of Operational Research*, vol. 182, no. 3, pp. 1177–1187, 2007.

[20] J. Lin, "A two-stage failure model for bayesian change point analysis," *IEEE Transactions on Reliability*, vol. 57, no. 2, pp. 388–393, 2008.

[21] T. Yuan and Y. Kuo, "Bayesian analysis of hazard rate, change point, and cost-optimal burn-in time for electronic devices," *IEEE Transactions on Reliability*, vol. 59, no. 1, pp. 132–138, 2010.

[22] P. Wang and G. Vachtsevanos, "Fault prognostics using dynamic wavelet neural networks," *Artificial Intelligence for Engineering Design, Analysis and Manufacturing*, vol. 15, no. 4, pp. 349–365, 2001.

[23] G.-W. You, S. Park, and D. Oh, "Real-time state-of-health estimation for electric vehicle batteries: a data-driven approach," *Applied Energy*, vol. 176, pp. 92–103, 2016.

[24] R. Khelif, B. Chebel-Morello, S. Malinowski, E. Laajili, F. Fnaiech, and N. Zerhouni, "Direct remaining useful life estimation based on support vector regression," *IEEE Transactions on Industrial Electronics*, vol. 64, no. 3, pp. 2276–2285, 2017.

[25] J. M. V. Noortwijk, "A survey of the application of gamma processes in maintenance," *Reliability Engineering and System Safety*, vol. 94, no. 1, pp. 2–21, 2009.

[26] Z. Zhang, X. Si, C. Hu, and Y. Lei, "Degradation data analysis and remaining useful life estimation: a review on wiener-process-based methods," *European Journal of Operational Research*, vol. 271, no. 3, pp. 775–796, 2018.

[27] X.-S. Si, W. Wang, C.-H. Hu, M.-Y. Chen, and D.-H. Zhou, "A wiener-process-based degradation model with a recursive filter algorithm for remaining useful life estimation," *Mechanical Systems and Signal Processing*, vol. 35, no. 1-2, pp. 219–237, 2013.

[28] L. Liao and F. Köttig, "A hybrid framework combining data-driven and model-based methods for system remaining useful life prediction," *Applied Soft Computing*, vol. 44, pp. 191–199, 2016.

[29] R. Isermann, "Model-based fault-detection and diagnosis - status and applications," *Annual Reviews in Control*, vol. 29, no. 1, pp. 71–85, 2005.

[30] J. Xu, J. Wang, S. Li, and B. Cao, "A method to simultaneously detect the current sensor fault and estimate the state of energy for batteries in electric vehicles," *Sensors*, vol. 16, no. 8, pp. 1328–1342, 2016.

[31] G. Ablay, "An observer-based fault diagnosis in battery systems of hybrid vehicles," in *Proceedings of the International Conference on Engineering, Energy, and Environment (ICEEE)*, pp. 238–242, Bursa, Turkey, 2013.

[32] Z. Liu, Q. Ahmed, J. Zhang, G. Rizzoni, and H. He, "Structural analysis based sensors fault detection and isolation of cylindrical lithium-ion batteries in automotive applications," *Control Engineering Practice*, vol. 52, pp. 46–58, 2016.

[33] Z. Liu and H. He, "Sensor fault detection and isolation for a lithium-ion battery pack in electric vehicles using adaptive extended Kalman filter," *Applied Energy*, vol. 185, pp. 2033–2044, 2017.

[34] H. Ríos, D. Efimov, and W. Perruquetti, "An adaptive sliding-mode observer for a class of uncertain nonlinear systems," *International Journal of Adaptive Control and Signal Processing*, vol. 32, no. 3, pp. 511–527, 2018.

[35] R. C. M. Yam, P. W. Tse, L. Li, and P. Tu, "Intelligent predictive decision support system for condition-based maintenance," *The International Journal of Advanced Manufacturing Technology*, vol. 17, no. 5, pp. 383–391, 2001.

[36] W. Q. Wang, M. F. Golnaraghi, and F. Ismail, "Prognosis of machine health condition using neuro-fuzzy systems," *Mechanical Systems and Signal Processing*, vol. 18, no. 4, pp. 813–831, 2004.

[37] H. Qiu, H. T. Liao, and J. Lee, "Degradation assessment for machinery prognostics using hidden Markov models," in *Proceedings Of the ASME IDETC-CIE*, pp. 531–537, Hyatt Regency, Chicago, IL, USA, 2005.

[38] K. Goebel, B. Saha, and A. Saxena, "A comparison of three data-driven techniques for prognostics," in *Failure Prevention for System Availability*, pp. 119–131, Society for Machinery Failure Prevention Technology, Savanna Georgia, 2008.

[39] V. A. Skormin, L. J. Popyack, V. I. Gorodetski, M. L. Araiza, and J. D. Michel, "Applications of cluster analysis in diagnostics-related problems," in *Proceedings of IEEE Aerospace Conference*, pp. 161–168, Aspen, CO, USA, 1999.

[40] G. Vachtsevanos, *Intelligent Fault Diagnosis and Prognosis for Engineering Systems*, Wiley, Hoboken, NJ, USA, 2006.

[41] W. Weibull, "A statistical distribution function of wide applicability," *International Journal Of Applied Mechanics*, vol. 13, no. 2, pp. 293–297, 1951.

[42] G. Ye, X. Kong, and W. Sun, "Study of power system transient stability assessment with Monte-Carlo method," *Proceedings of CSU-EPSA*, vol. 24, no. 5, pp. 71–76, 2012.

[43] G. Cheng, L. Li, and Y. Tang, "Reliability analysis of a two-units series system with not be good as new," *Mathematics in Theory and Practice*, vol. 38, no. 10, pp. 77–83, 2008.

[44] Q. Dong, Q. Chen, and R. Liu, "Opportunistic maintenance policy for two-unit series system with a cold standby component," *Operations Research and Management Science*, vol. 26, no. 11, pp. 100–104, 2017.

[45] B. Gu, R. Wang, and X. Xu, "Estimation of parameters for a discrete bivariate distribution in a series system," *Application of Statistics and Management*, vol. 28, no. 3, pp. 428–435, 2009.

[46] M. Dong, "Reliability equivalence factors of a series system with components in gamma distribution," *Journal of Henan University of Science & Technology*, vol. 28, no. 1, pp. 90–93, 2007.

[47] Z. Zhang and Y. Chang, "MRL and MPL functions of parallel systems with INID components under double monitoring," *Communications in Statistics - Simulation and Computation*, vol. 40, no. 9, pp. 1514–1523, 2011.

[48] M. K. Sadegh, "Mean past and mean residual life functions of a parallel system with nonidentical components," *Communications in Statistics—Theory and Methods*, vol. 37, no. 7, pp. 1134–1145, 2008.

[49] S. Li, Y. Li, Y. Chen, and Z. Wei, "Comparisons of series and parallel systems with random and non-random dependent components," *Journal of Shenzhen University Science and Engineering*, vol. 31, no. 3, pp. 312–316, 2014.

[50] A. Naess, B. J. Leira, and O. Batsevych, "System reliability analysis by enhanced Monte Carlo simulation," *Structural Safety*, vol. 31, no. 5, pp. 349–355, 2009.

[51] A. K. S. Jardine, D. Lin, and D. Banjevic, "A review on machinery diagnostics and prognostics implementing condition-based maintenance," *Mechanical Systems and Signal Processing*, vol. 20, no. 7, pp. 1483–1510, 2006.

[52] X.-S. Si, W. Wang, C.-H. Hu, and D.-H. Zhou, "Remaining useful life estimation—a review on the statistical data driven approaches," *European Journal of Operational Research*, vol. 213, no. 1, pp. 1–14, 2011.

[53] Z. Zhou, *Machine Learning*, Tsing University Press, Beijing, China, 2016.

[54] X. Duan and Z. Wang, "Application of bootstrap method in small sample case," *Journal of Ballistics*, vol. 15, no. 3, pp. 1–5, 2003.

[55] H. Dong, X. Jin, Y. Lou, and C. Wang, "Lithium-ion battery state of health monitoring and remaining useful life prediction based on support vector regression-particle filter," *Journal of Power Sources*, vol. 271, pp. 114–123, 2014.

[56] Z. Li, Z. Dai, and Y. Jiao, "Bayes Monte-Carlo reliability assessment method of protection systems with small failure samples," *Proceedings of CSU-EPSA*, vol. 28, no. 5, pp. 9–14, 2016.

[57] Z. Sheng, S. Xie, and C. Pan, *Probability Theory and Mathematical Statistics*, Higher Education Press, Beijing, China, 2009.

Hindawi
Advances in Civil Engineering
Volume 2020, Article ID 8855409, 10 pages
https://doi.org/10.1155/2020/8855409

*Research Article*

# How to Achieve Efficiency and Accuracy in Discrete Element Simulation of Asphalt Mixture: A DRF-Based Equivalent Model for Asphalt Sand Mortar

**Yu Liu,[1] Peifeng Su,[1] Miaomiao Li,[1] Hui Yao,[2] Junfu Liu,[2] Mei Xu,[2] Xiaodong Zhou,[3] and Zhanping You[3]**

[1]*Highway School, Chang'an University, South Erhuan Middle Section, Xi'an, Shaanxi 710064, China*
[2]*Beijing Key Laboratory of Traffic Engineering, College of Metropolitan Transportation, Beijing University of Technology, No. 100, Pingleyuan, Chaoyang, Beijing 100124, China*
[3]*Department of Civil & Environmental Engineering, Michigan Technological University, 1400 Townsend Drive, Houghton, MI 49931, USA*

Correspondence should be addressed to Hui Yao; huiyao@mtu.edu

Received 24 June 2020; Revised 18 November 2020; Accepted 7 December 2020; Published 22 December 2020

Academic Editor: Fan Gu



The clump-based discrete element model is one of the asphalt mixture simulation methods, which has the potential to not only predict mixture performance but also simulate particle movement during compaction, transporting, and other situations. However, modelling of asphalt sand mortar in this method remains to be a problem due to computing capacity. Larger-sized balls (generally 2.0–2.36 mm) were usually used to model the smaller particles and asphalt binder, but this replacement may result in the mixture's unrealistic volumetric features. More specifically, replacing original elements with equal volume but larger size particles will increase in buck volume and then different particle contacting states. The major objective of this research is to provide a solution to the dilemma situation through an improved equivalent model of the smaller particles and asphalt binders. The key parameter of the equivalent model is the diameter reduction factor (DRF), which was proposed in this research to minimize the effects of asphalt mortar's particle replacement modelling. To determine DRF, the DEM-based analysis was conducted to evaluate several mixture features, including element overlap ratio, ball-wall contact number, and the average wall stress. Through this study, it was observed that when the original glued ball diameters are ranging from 2.00 mm and 2.36 mm, the diameter reduction factor changes from 0.82 to 0.86 for AC mixtures and 0.80 to 0.84 for SMA mixtures. The modelling method presented in this research is suitable not only for asphalt mixtures but also for the other particulate mix with multisize particles.

## 1. Introduction

In the past decades, the discrete element method (DEM) has been popularly used for simulating multisize particulate mixtures, such as asphalt mixtures, sands, graded stones, and chemically bounded mixtures [1]. In the simulated model, the discrete elements are applied to represent different components in the mixture. From a simple two-dimensional ideal model [2] to a complex three-dimensional image-based model [3], the DEM model is more and more similar to the real mixture, and the simulation results are more credible [4–6]. Currently, there are two main types of discrete element models which were popularly used for simulating asphalt mixtures in the past decades: the cluster-based models [7, 8] and the clump-based models [9]. The primary goal of these DEM models was to predict mechanical behaviours. Furthermore, with the development of the clump-based model, it became practicable to apply DEM in other studies, for instance, the compaction stage.

In the cluster-based models, both coarse aggregates and asphalt sand mortar are simulated through mono-sized balls which are bounded through contact bonding models [10].

The coarse aggregates and the asphalt sand mortar are distinguished by assigning different stiffnesses and strength properties [11]. After deleting part of balls randomly, asphalt mixture specimens with certain air voids can be obtained [12]. The cluster-based models have the following advantages: (1) coarse aggregate morphological features can be realistically simulated with accurate images of mixtures or coarse aggregates [13]; (2) the volumetric features of coarse aggregates, asphalt sand mortar, and air voids can be modelled with high accuracy [14]. The disadvantages of these models are also obvious: (1) only compacted specimens can be simulated, which means the problems related to the compaction process, segregation, and packing cannot be analysed, and the simulation model applicability is limited by this way of modelling; (2) a large number of elements are needed to ensure reasonable accuracy of simulating asphalt sand mortar; hence, the computing efficiency is relatively low.

The clump-based model is an updated model compared to the cluster-based model, with higher computational efficiency and more possible applications. In the clump-based models, the coarse aggregates are simulated by clumps with realistic particle shapes and sizes [15]. The use of the clump element tremendously increases the computing speed since pebbles within the same clump will not form contact. For fine aggregates, fillers and asphalt are integrally simulated as asphalt sand mortar in two ways for different research goals: (1) mono-sized balls, which are the same as the cluster-based model, can be used for the purpose of mechanical behaviour prediction; (2) equivalent ball elements with same or similar diameters for the studying of particle movements during compaction or other stages. In this way, the number of ball elements was determined by dividing the total volume of asphalt sand mortar by the ball volume.

The use of equivalent ball elements way is a compromise to ensure practical computational efficiency. Researchers mostly replace fine particles (0–2.36 mm) and asphalt with larger size particles (generally 2.0–2.36 mm) since it is unrealistic to generate fine particles with real size and number [9]. Different from the first way, these particles still retain particular properties during compaction. However, this compromise definitely leads to the volumetric problem since larger size balls actually occupy more space in the specimen.

In sum, although the clump-based model provides a way to study particle movements during the compaction stage, the challenging task is to find a potential solution to this dilemma situation: researchers prefer selecting larger size balls (2 mm or larger) to build the equivalent models of asphalt sand mortar for the higher computational efficiency. However, this method is usually empirical and lacks quantitative analysis and verification, which will lead to the following problems: (1) since the ball-ball interactions in the equivalent models are different from those in the asphalt sand mortar, particle-interlocking effects may result in unrealistic mechanical responses. (2) The equivalent model of ball elements has a larger volume than realistic asphalt sand mortar of the same mass. In other words, the equivalent model cannot realistically simulate asphalt sand mortar since they have different volumetric features. (3) With the increasing ball element diameters of the equivalent model, the particle-interlocking effects and volumetric discrepancy become more serious.

Based on the above discussion, the major objective of this research is to provide a potential solution to the dilemma situation through an improved equivalent model of the smaller particles and asphalt binders for the clump-based model. Hence, the asphalt sand mortar can be well simulated during the compaction stage without causing the volumetric problem. In order to minimize the effects of particle interlocking, a key parameter: diameter reduction factor (DRF) is developed to reduce the total volume of the original equivalent ball element model. By proportionally reducing the mortar particle diameter, the DRF method can reduce the interfering caused by replacing asphalt sand mortar with larger particles. Optimum DRF values could minimize the buck volume discrepancy before and after replacing. The DRF value is determined through analysing the overlap ratio of mortar particle and average wall stress, ensuring the volumetric feature of asphalt sand mortar and particle interaction between mortar ball element and coarse particles. The details of the DRF definition and value determination will be introduced in Section 2. Suitable DRFs are recommended for different mixture gradations, and the results are verified in lab tests.

## 2. An Improved Equivalent Model for Simulating Asphalt Sand Mortar

*2.1. Volumetric Testing of Coarse-Grained and Fine-Grained Mineral Mixtures.* The bulk volume of the small-sized particle mixture may be different from a large-sized particle mixture. Even though with the same mass, the difference still occurs in terms of particle-interlocking actions and volumetric features. In order to verify this postulate, an experimental test was conducted; two mineral mixtures that have the same mass were put into the two identical cups, as shown in Figure 1. Mix A is fine-grained with particles from 0.00 mm to 2.36 mm, while the mix B is coarse-grained with particles from 1.18 mm to 2.36 mm. Both of the two mixtures are stacking conditions without compaction; therefore, the packing energy can be assumed to be equal. The bulk volume of mix A and mix B is 85 ml and 100 ml, respectively. The volumetric difference is about 17.9%.

Through this experimental test, it could conclude that the same mass of mixtures may have significantly different volumes. With this conclusion, the authors believe that the larger-sized rigid balls for modelling asphalt mortar may occupy the larger volume in a discrete element model. Therefore, in order to improve the discrete element model accuracy, it is necessary to determine the optimum sizes of rigid balls.

*2.2. Clump-Based DEM Asphalt Mixture Model Establishment.* In this research, the clump-based DEM model of asphalt mixture was built by the following procedures:


Figure 1: Volumetric testing of coarse-grained and fine-grained mixtures.

(1) Coarse aggregates morphological features were obtained through 3D scanning and image processing. Then, virtual sieving tests were carried out to obtain clump templates in PFC [16].

(2) Coarse aggregates (modelled by clump elements) were generated according to the gradation and clump templates, as shown in Figure 2(a).

(3) Asphalt sand mortar (modelled by ball elements) was generated, as shown in Figure 2(b).

(4) The specimen was compacted with hydrostatic pressure, as shown in Figure 2(c).

Note that different colours in Figure 2 represent different particle size groups. Through the above steps, a virtual DEM model with a real particle shape can be built. Parameters used in virtual models are listed in Table 1 [17].

*2.3. Diameter Reduction Factor for Modelling Asphalt Sand Mortar.* In most of the existing studies, the glued rigid balls of diameters from 2.00 mm to 2.36 mm were commonly used to build the equivalent model of asphalt sand mortar. The number of the rigid balls was determined through the following two steps: (1) in the first step, the volume of asphalt sand mortar is calculated from weights and densities of fine aggregates, fillers, and asphalt binder according to the mixture design; (2) in the second step, users may select diameters of the rigid balls (ranging from 2.00 mm to 2.36 mm for instance); the number of the rigid balls is calculated through dividing the total volume of asphalt sand mortar by the individual ball's volume. However, this approach generally ignores the real volume occupied by mortar particles; similar to Figure 1, larger size particles with the same mass will occupy more volume in the specimen and, therefore, change the mixture specimen skeleton and further mechanical performance.

The functions of mortar are the same in both real and virtual specimens: (1) the volume among skeleton particles is occupied; (2) force applied by adjacent particles is transferred. However, the asphalt sand mortar in simulation does not need to be dense without porosity, and it can occupy the same volume to real condition and has enough contacts with adjacent particles to transfer force.

In order to accurately and efficiently simulate asphalt sand mortar, diameter reduction factor (DRF) was recommended in this research:

$$\mathrm{DRF} = \frac{D_i}{D_0}. \tag{1}$$

In equation (1), $D_0$ is the initial diameter and $D_i$ is the reduced diameter. $D_0$ can be a single value (2.00 mm for instance) or a range (from 2.00 mm to 2.36 mm for instance). In this research, $D_0 = 2.00 \sim 2.36$mm. When DRFs are given, the reduced diameter ($D_i$) and the volumetric ratio between the two models after and before diameter reduction can be calculated, as shown in Table 2.

Obviously, with DRFs, the ball element diameters in the equivalent model of asphalt sand mortar can be reduced. As a result, the equivalent model volume is reduced and the particle-interlocking effects can be more realistically simulated.

*2.4. DRF-Based Discrete Element Model for Asphalt Mixture.* This section presented an improved DEM model of asphalt mixture with the following steps:

(1) Graded clumps and balls are generated simultaneously within a cylindrical sample. According to different application requirements, the height and diameter of the sample may be different. In this paper, both the height and diameter of the cylindrical sample are set as 70 mm. The clumps are generated according to shapes and gradation of coarse aggregates with the method presented in Section 2.2. The balls of diameter from 2.00 mm to 2.36 mm are generated with DRF = 1.0 according to the method presented in Section 2.3.

(2) Cycling is performed until clump and ball elements become stable. The sample should be compacted until the designed height is met. Note that the design height in this paper is 70 mm since all the elements are generated according to specimen volume. The compacted sample is the initial sample of asphalt mixture with DRF = 1.0. There is a serious overlap in the initial sample due to interference.

(3) Initial sample model will be restored first, and then, different values are assigned to DRF, as shown in Figure 3. Meanwhile, different colours here in Figure 3 also represent different particle size groups. It should be noted that cycling computation should be performed after a new value is assigned to DRF.

(4) The optimum value of DRF should be recommended according to its overlap condition and internal stress to more realistically simulate asphalt sand mortar. Details on the recommendation will be presented in the next section.

## 3. Discrete Element Simulation and Diameter Reduction Factor Determination

As mentioned above, considering the interactions of glued balls in the equivalent model of asphalt sand mortar, it was

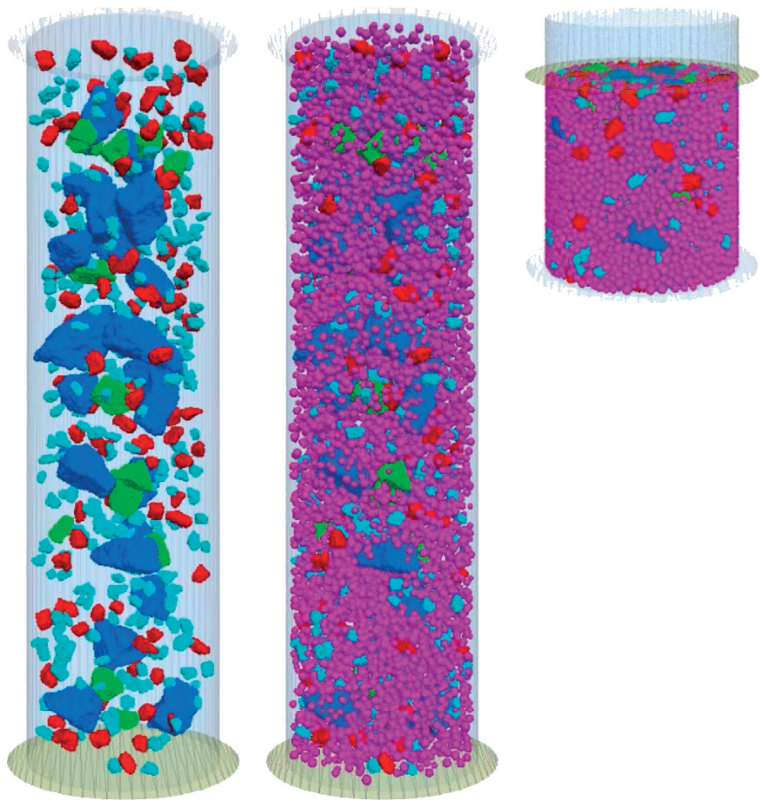

(a) (b) (c)

Figure 2: Clump-based DEM model establishment: (a) coarse particles generation; (b) asphalt sand mortar generation; (c) hydrostatic compaction.

Table 1: Micromodelling parameters.

| Contact types | Friction | Modulus (GPa) |
|---|---|---|
| Aggregate/aggregate | 0.36 | 55 |
| Aggregate/mortar | 0.20 | 29 |
| Mortar/mortar | 0.20 | 20 |
| Mortar/container | 0.15 | 39 |
| Aggregate/container | 0.15 | 100 |

necessary to find suitable DRFs for typical asphalt mixtures. In this section, discrete element modelling of typical asphalt mixtures was performed, and results were analysed to determine DRFs with considerations on volumetric overlapping, ball-wall contact number, and interlocking stress within asphalt sand mortar.

*3.1. Gradation and Volumetric Features of Typical Asphalt Mixtures.* As shown in Figure 4, six types of asphalt mixtures were designed based on the Chinese Technical Specification for Construction of Highway Asphalt Pavements JTG F40-2004. To calculate the volume fractions used in virtual models, some assumptions were made as follows based on the existing researches and specifications:

(1) Coarse aggregates, fine aggregates, and fillers come from rocks whose density is assumed to be 2650 kg/m$^3$.

Table 2: Reduced diameters and volumetric ratios of different diameter reduction factors.

| DRF | $D_i$ (mm) | Volume ratio |
|---|---|---|
| 1.00 | 2.00–2.36 | 1.00 |
| 0.98 | 1.96–2.31 | 0.94 |
| 0.96 | 1.92–2.27 | 0.88 |
| 0.94 | 1.88–2.22 | 0.83 |
| 0.92 | 1.84–2.17 | 0.78 |
| 0.90 | 1.80–2.12 | 0.73 |
| 0.88 | 1.76–2.08 | 0.68 |
| 0.86 | 1.72–2.03 | 0.64 |
| 0.84 | 1.68–1.98 | 0.59 |
| 0.82 | 1.64–1.94 | 0.55 |
| 0.80 | 1.60–1.89 | 0.51 |
| 0.78 | 1.56–1.84 | 0.47 |
| 0.76 | 1.52–1.79 | 0.44 |
| 0.74 | 1.48–1.75 | 0.41 |
| 0.72 | 1.44–1.70 | 0.37 |
| 0.70 | 1.40–1.65 | 0.34 |
| 0.68 | 1.36–1.60 | 0.31 |

(2) The density and content of asphalt binder are assumed to be 1030 kg/m$^3$ and 5%, respectively.

(3) The air voids of all 6 mixtures were assumed to be 4%.

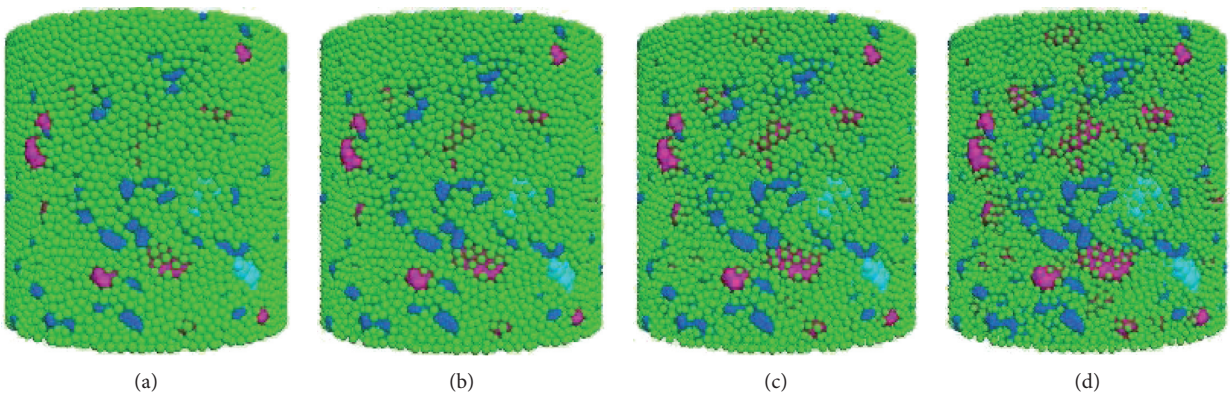


Figure 3: Discrete element models of asphalt mixture with various DRFs. (a) DRF = 1.00. (b) DRF = 0.92. (c) DRF = 0.84. (d) DRF = 0.76.

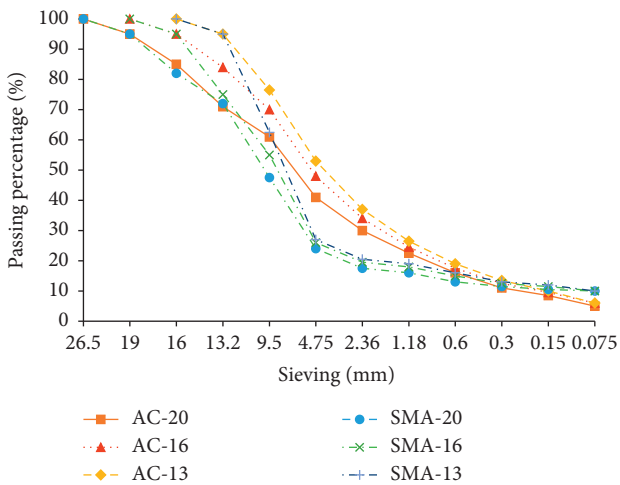


Figure 4: Typical gradation curves.

With the information above, the volume fractions of coarse aggregates, asphalt sand mortar (sum of fillers, fine aggregates, and asphalt binder), and air void contents for all 6 gradations are listed in Table 3. It should be noted that the volumetric parameters used here can be adjusted according to a different situation.

*3.2. Volumetric Overlap Analysis for Determining Diameter Reduction Factors.* Evidently, DRF values represented volumetric features of equivalent models: the decrease in DRF value meant glued ball element diameters were decreasing and then resulted in less overlapping between adjacent discrete elements. In this research, a new concept of "mortar element overlapping ratio" was proposed for determining the rational DRF range.

Figure 5 shows an example to obtain an overlap ratio in PFC. Firstly, the total volume of each mortar element $V_1$ was calculated based on their radiuses, as shown in Figure 5(a). Then, the real volume $V_2$ can be obtained by the built-in function measure sphere, as shown in Figure 5(b) [18]. Therefore, the overlap ratio can be computed by the following equation:

Table 3: Volumetric fractions of mixture components.

| Gradation type | Volume fraction (%) | | |
|---|---|---|---|
| | Coarse aggregates | Asphalt sand mortar | Air voids |
| AC-13 | 54.18 | 41.82 | 4 |
| AC-16 | 56.76 | 39.24 | 4 |
| AC-20 | 60.20 | 35.80 | 4 |
| SMA-13 | 68.37 | 27.63 | 4 |
| SMA-16 | 69.23 | 26.77 | 4 |
| SMA-20 | 70.95 | 25.05 | 4 |

$$\text{overlap ratio} = \frac{V_1 - V_2}{V_1}. \quad (2)$$

As the gradation curves shown in Figure 5 and volumetric fractions listed in Table 2, the discrete element simulation of six typical asphalt mixtures was performed with various DRFs from 0.68 to 1.0, as listed in Table 1. A total of 90 discrete element models were built with the method presented in Section 2, while the coarse aggregates were simulated with clumps, and the asphalt sand mortar was simulated with the DRF-based equivalent model. The discrete element simulation data were analysed, and the curves of the mortar element overlap ratio versus DRFs were plotted, as shown in Figure 6.

From Figure 6, it can be observed as follows: (1) with decreasing DRF, the mortar element overlap ratio decreased from about 12% to less than 0.6%. (2) All 6 gradations had similar curve trends, which firstly linearly decreased to the turning point and then went stabilized. The turning point indicated a critical state that the condition of glued balls started to translate from interlocked to suspended. (3) For AC gradations, the mortar element overlap ratio with DRF values less than 0.80 was almost constant to zero, which meant that 0.80 can be deemed as the optimum value that all glued balls were suspended. (4) SMA gradations were slightly different from AC gradations: curve slopes with DRF values less than 0.76 remained to be nonzero constant. The main reason for this phenomenon was that SMA mixtures had coarser aggregates, and some of the glued balls were interlocking by the strong skeleton and cannot rearrange

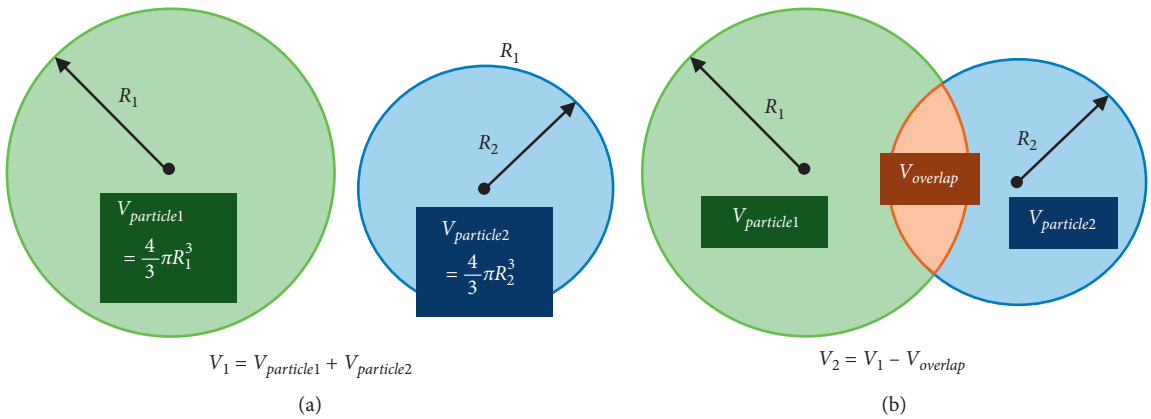


Figure 5: The calculation of mortar overlap ratio. (a)$V_1$ (without overlapping). (b)$V_2$ (without overlapping).

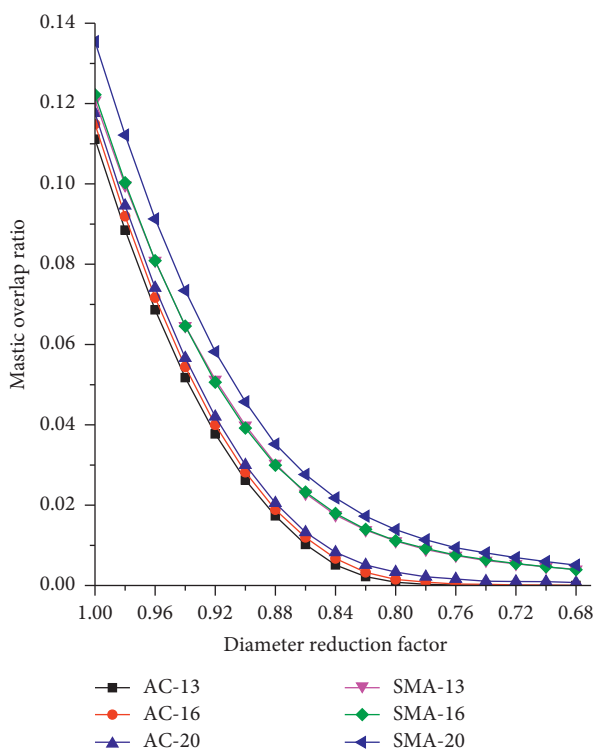


Figure 6: Mortar element overlap ratio of AC gradation and SMA gradation.

with a decreasing diameter. Therefore, 0.76 can be deemed as the value that most glued balls were suspended for SMA gradations.

It should be noted that, since increasing nominal diameter resulted in less glued balls volume fraction, the curves tended to entirely move upward from AC gradation to SMA gradation. However, although the glued ball volumes' difference among three AC gradations was larger than those in SMA gradations, AC gradation curves had little difference within each other while had considerable discrepancy compared to SMA gradations, especially when DRF values were less than a turning point. This discrepancy was mainly caused by different skeleton conditions. AC mixtures and SMA mixtures generally had suspended dense structures and skeleton dense structures, respectively. Therefore, it was easier for glued balls in AC mixtures to rearrange with their decreasing diameter. When the mixture's structure is conveyed to a skeleton dense structure, even a small increase in coarse aggregates will result in a stronger skeleton and overlap ratio, which cannot be eliminated by rearrangement. Based on the above analysis, the recommended low limit of DRF could be determined as 0.76 for all mixtures, which meant the glued ball will be in the suspending state if DRF was over the low limit.

*3.3. Ball-Wall Contact Number Analysis for Evaluating Diameter Reduction Factor.* Similarly, the change in DRF values led to a decreasing ball-wall contact number, which indicated the condition of the ball element changed from an over interlocked state to a suspended state. Therefore, a ball-wall contact number was also applied to determine a reasonable DRF range. For Figure 7, six curves displayed how the ball-wall contact number varies with different DRF values of 6 gradation types.

In Figure 7, it can be found as follows: (1) the general tendency of all six curves was that the ball-wall contact number decreased slowly in the initial stage and then dropped dramatically. This phenomenon indicated glued balls were too small to fill the existing voids after and the ball elements tended to be more suspended and even had few contacts with the boundary wall. Hence, the contact numbers were significantly influenced by glued balls volume. (2) The difference between the two gradation types was obvious. The range of curves was from about 4200 to 600 and from 3400 to over 1000 for AC and SMA mixtures, respectively. Meanwhile, curves of AC mixtures descended faster than SMA mixtures due to different mixture structures. (3) In the same gradation type, the mixture with a distinct maximum nominal particle size had a different glued ball volume, which resulted in the discrepancy of three curves in each gradation group. In other words, the more the volume of ball elements, the more the ball-wall contact number, and the faster the decrease rate.

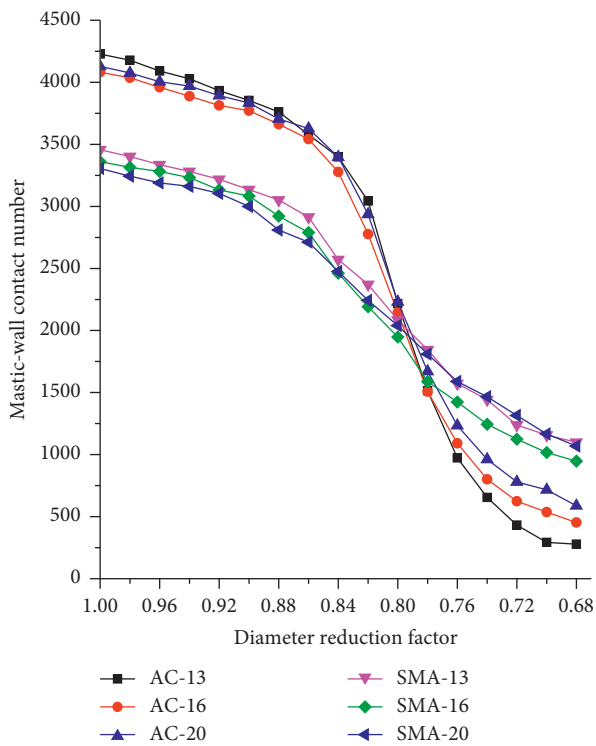


Figure 7: Ball-wall contact number of AC gradation and SMA gradation.

In order to keep glued balls from overpacking, the range of DRF should be determined when the ball-wall contact number started to drop quickly. Therefore, the upper limit of DRF values was chosen as 0.86 for all gradation types.

*3.4. Average Wall Stress Analysis for Evaluating Diameter Reduction Factor.* Redundant glued balls will not only cause volumetric and structure problems in compacted mixtures but also have a significant impact on the interlocking stress state. Therefore, the average wall stress of every specimen was applied to determine the range of DRF values.

In this model, particles were compacted by the top wall. After the size of the mortar element was reduced according to the DRF value, the internal structure changed and the contact stress between particles and walls also decreased. Through the built-in codes [18], the contact force between wall and particles in the $Z$ direction could be recorded, and the wall stress can be calculated according to the following equation:

$$\overline{\sigma_m} = \frac{|F_{tw}| + |F_{bw}|}{\text{wall area}}, \tag{3}$$

where $\overline{\sigma_m}$ means the average wall stress and $F_{tw}$ and $F_{bw}$ represent the forces on the top and bottom wall, respectively. And the following figure shows the recorded results of all 6 gradation mixtures.

From Figure 8, it can be observed as follows: (1) curves of average wall stress firstly decreased rapidly, and then, its descending speed slowed down and gradually tended to be stable. The DRF values of the turning point of AC and SMA gradation were about 0.82 and 0.80, respectively. (2) The

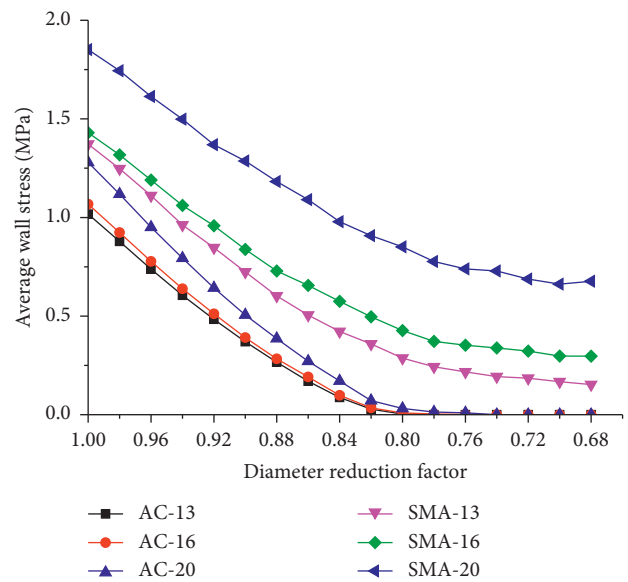


Figure 8: Average wall stress of AC gradation and SMA gradation.

average wall stress of AC gradation was less than SMA gradation dramatically due to different structures. (3) The descending speed of AC curves was larger than SMA curves. The reason was that AC mixtures had more glued balls, and they were more sensitive to the change in DRF values. Note that the determination of the turning point was mainly based on simple observation rather than mathematical methods. The main purpose of this section was to determine a recommended DRF range. Therefore, the turning point was generally selected for convenience. A well-compacted asphalt mixture should have a good interlocking state for all particles. Since the turning point represented the critical state between interlocking and suspending, the optimum DRF value should be bigger than a turning point.

In summary, the analysis of three parameters provided three DRF limits as follows: in Figure 6, DRF should be larger than 0.80 for AC gradation and 0.76 for SMA gradation; in Figure 7, DRF should be less than 0.86 for two gradation types; in Figure 8, DRF should be larger than 0.82 for AC gradation and 0.80 for SMA gradation. Therefore, based on 3 figures, the conservative preliminary DRF ranges were determined as 0.82–0.86 and 0.80–0.84 for AC and SMA gradations, respectively. Note that this recommended range could be adjusted according to a different situation.

## 4. Application and Verification of Diameter Reduction Factor

Based on the above analysis, the range of DRF value could be slightly different for different gradation types due to the differences in mortar volume. Some virtual and lab tests were carried out for verifying the recommended DRF value for different gradation types.

*4.1. Virtual Compaction Tests.* After choosing the midvalue of the recommended gradation range according to

Table 4: Specimen height with different DRFs after virtual static compaction.

| DRF | Compacted specimen height in DEM (mm) | | Height difference between DEM and mixture designed height (%) | |
|---|---|---|---|---|
| | AC-13 | SMA-13 | AC-13 | SMA-13 |
| 0.80 | 65.2 | 68.7 | 6.9 | 1.9 |
| 0.82 | 67.5 | 70.2 | 3.6 | −0.3 |
| 0.84 | 69.6 | 71.3 | 0.6 | −1.9 |
| 0.86 | 71.9 | 72.7 | −2.7 | −3.9 |

(a) (b) (c)

Figure 9: Specimens with different DRFs after indoor Marshall compaction tests.

Technical Specification for Construction of Highway Asphalt Pavements JTG F40-2004, two gradation mixtures were determined as AC-13 and SMA-13. The general generation and compaction procedures were shown in the following part:

Firstly, according to the above volumetric calculation, the volume of coarse aggregates, fillers, asphalt, and air voids can be obtained. Based on the above analysis, DRF in the range of 0.80–0.86 is determined. Hence, there would be 8 specimens generated in this test.

Secondly, coarse-grained aggregates with realistic gradation and particle shapes were generated by clump elements. The asphalt sand mortar was simulated by rigid ball elements with DRF equaling to 1.0.

Thirdly, the specimens were compacted with a static pressure of 600 kPa, and then, the diameters of ball elements were reduced according to different DRFs.

Finally, the compacted specimen heights and height differences between DEM and mixture designed height (70 mm) were recorded, as shown in Table 4.

According to the height differences between mixture designed height and compacted height, 0.84 is the best DRF value for AC-13 while 0.82 for SMA-13. In fact, the DRF value was mainly determined based on the mortar volume of asphalt mixture, and it can be selected in the range of 0.80–0.86. In addition, the more the mortar volume, the bigger the DRF. The consistency between design height and compacted height also proved that the application of DRF improved the accuracy in volume.

*4.2. Indoor Marshall Compaction Tests.* Meanwhile, indoor Marshall compaction tests were also applied to verify the recommended DRF value range. It should be noted that the critical variable here was not the compaction methods but the internal relationship of different mixtures. The influence caused by different compaction methods could be negligible in this problem. Therefore, Marshall compaction tests were carried out to verify the simulation results. In this part, there are three compacted specimens with the same coarse gradation (AC-13) as follows: (1) particles less than 2.36 mm were replaced by fine aggregates in 1.18–2.36 mm with no volume reduction; (2) particles less than 2.36 mm were replaced by the fine aggregate in 1.18–2.36 mm with recommended volume reduction; (3) normal specimen with complete particle sizes. The asphalt content was set to be 5.0%. The final specimens are shown in Figure 9.

After Marshall compaction, the specimens' height is recorded in Table 5:

The following could be observed: (1) without volume reduction, the volume characteristic of the specimen was far from the real situation. (2) The specimen with the recommended volume reduction had a similar height with the specimen in complete gradation.

Table 5: Specimen height with different DRFs after indoor Marshall compaction tests.

| #1 | #2 | #3 |
|---|---|---|
| 7.236 cm | 6.247 cm | 6.309 cm |

## 5. Summary and Conclusion

Based on discrete element modelling, this paper generated a virtual specimen of asphalt mixture including aggregate, asphalt mortar, and air voids and then deeply analysed mortar element overlap ratio and average wall stress in different DRFs. During the process, the findings produced are as follows:

After result analysis, the DRF ranges of mortar elements were recommended for different gradations. Given that the initial mortar element diameter was set as 2.00–2.36 mm for AC gradation, and the DRF range (0.82–0.86) was recommended, while (0.80–0.84) was chosen for SMA gradation.

The virtual specimen of asphalt mixture was created with real particle shape and gradation, and the recommended generation method of asphalt sand mortar is as follows: (1) calculating the real volume of each part in asphalt mixture specimen; (2)building the basic model with coarse aggregates in the calculated volume; (3) generating mortar ball elements in the size of 2.00 mm to 2.36 mm with the initial calculated volume; (4) setting contact models and compacting the mixtures; (5) removing all velocities to make the whole system in a static state; (6) replacing mortar elements with the chosen DRF in the same position.

This article focused on the particle replacement for asphalt mortar. In fact, this method can also be used in other kinds of granular mixtures. The diameter reduction factor can be selected from the recommended range in this article based on fine aggregate volume or conducted a similar virtual test to determine an accurate value.

In conclusion, this article provided a reference for the asphalt mixture simulation in the clump-based discrete element method. The recommended model generation method plays a significant role in DEM further development to solve the problem of asphalt sand mortar dynamic simulation. Both calculation efficiency and enough accuracy were considered in this method, which indicated that DEM could be applied in a more complex situation to deal with more practical problems. However, the current study only focused on solving volumetric problems, and this method still needs to be perfected with consideration of mixture mechanical behaviour. And the in situ replacement method could also be applied to further analysis of asphalt mixtures' gradation in the following papers.

## Data Availability

The data used to support the findings of this study are available from the corresponding author upon request.

## Conflicts of Interest

There are no conflicts of interest regarding the publication of this paper.

## Acknowledgments

This work was supported by the National Natural Science Foundation of China (Grant no. 51978074). The authors also appreciate the funding support from Beijing Key Laboratory of Traffic Engineering, Beijing University of Technology (Grant no. 2018BJUT-JTJD007), and funding support from Beijing Municipal Commission of Transport (Grant no. 40038003201805).

## References

[1] P. A. Cundall and O. D. L. Strack, "A discrete numerical model for granular assemblies," *Géotechnique*, vol. 29, no. 1, pp. 47–65, 1979.

[2] D. O. Potyondy and P. A. Cundall, "A bonded-particle model for rock," *International Journal of Rock Mechanics and Mining Sciences*, vol. 41, no. 8, pp. 1329–1364, 2004.

[3] R. Liu, X. Yin, H. Li et al., "Visualization and quantitative profiling of mixing and segregation of granules using synchrotron radiation X-ray microtomography and three dimensional reconstruction," *International Journal of Pharmaceutics*, vol. 445, no. 1-2, pp. 125–133, 2013.

[4] H. Gao, X. Yang, and C. Zhang, "Experimental and numerical analysis of three-point bending fracture of pre-notched asphalt mixture beam," *Construction and Building Materials*, vol. 90, pp. 1–10, 2015.

[5] Y. Peng, J.-X. Bao, and Z. Wang, "A comparison of two-dimensional and three-dimensional micromechanical discrete element modeling of the splitting tests for asphalt mixtures," in *Proceedings of the 1st International Conference on Transportation Infrastructure and Materials (ICTIM 2016), Xi'an*, China, July 2016.

[6] Y. Peng and J.-X. Bao, "Micromechanical analysis of asphalt-mixture shear strength using the three-dimensional discrete element method," *Journal of Materials in Civil Engineering*, vol. 30, no. 11, Article ID 04018302, 2018.

[7] J. Chen, T. Pan, and X. Huang, "Discrete element modeling of asphalt concrete cracking using a user-defined three-dimensional micromechanical approach," *Journal of Wuhan University of Technology*, vol. 26, no. 6, pp. 1215–1221, 2011.

[8] J. Chen, L.-B. Wang, and X.-M. Huang, "Micromechanical modeling of asphalt concrete fracture using a user-defined three-dimensional discrete element method," *Journal of Central South University*, vol. 19, no. 12, pp. 3595–3602, 2012.

[9] F. Gong, Y. Liu, X. Zhou, and Z. You, "Lab assessment and discrete element modeling of asphalt mixture during compaction with elongated and flat coarse aggregates," *Construction and Building Materials*, vol. 182, pp. 573–579, 2018.

[10] X. Ding, T. Ma, and W. Gao, "Morphological characterization and mechanical analysis for coarse aggregate skeleton of asphalt mixture based on discrete-element modeling," *Construction and Building Materials*, vol. 154, pp. 1048–1061, 2017.

[11] J. Li, J. H. Zhang, G. P. Qian, J. L. Zheng, and Y. Q. Zhang, "Three-dimensional simulation of aggregate and asphalt mixture using parameterized shape and size gradation,"

*Journal of Materials in Civil Engineering*, vol. 31, no. 3, p. 9, 2019.

[12] J. Chen, B. Huang, and X. Shu, "Air-void distribution analysis of asphalt mixture using discrete element method," *Journal of Materials in Civil Engineering*, vol. 25, no. 10, pp. 1375–1385, 2013.

[13] D. Zhang, X. Huang, and Y. Zhao, "Algorithms for generating three-dimensional aggregates and asphalt mixture samples by the discrete-element method," *Journal of Computing in Civil Engineering*, vol. 27, no. 2, pp. 111–117, 2012.

[14] W. Zhou, X. Huang, and L. Wang, "Study on the void reduction behaviour of porous asphalt pavement based on discrete element method," *International Journal of Pavement Engineering*, vol. 18, no. 4, pp. 285–291, 2017.

[15] J.-F. Ferellec and G. R. McDowell, "A method to model realistic particle shape and inertia in DEM," *Granular Matter*, vol. 12, no. 5, pp. 459–467, 2010.

[16] X. Zhou, Y. Liu, and Z. You, "Heavy impact compaction modeling and analysis on unbound paving mixtures," in *Proceedings of the International Conference on Discrete Element Methods*, Dalian, China, August 2016.

[17] F. Gong, X. Zhou, Z. You, Y. Liu, and S. Chen, "Using discrete element models to track movement of coarse aggregates during compaction of asphalt mixture," *Construction and Building Materials*, vol. 189, pp. 338–351, 2018.

[18] Itasca-Consulting-Group, *PFC5.0 Suite Documentation*, Itasca-Consulting-Group, Minneapolis, MI, USA, 2014.

Hindawi
Advances in Civil Engineering
Volume 2020, Article ID 8892686, 20 pages
https://doi.org/10.1155/2020/8892686

*Research Article*

# Damage Identification Method of Beam Structure Based on Modal Curvature Utility Information Entropy

**Chang-Sheng Xiang,[1] Ling-Yun Li,[1] Yu Zhou,[2] and Zi Yuan[1]**

[1]*School of Civil Engineering, Lanzhou University of Technology, Lanzhou 730050, China*
[2]*College of Civil Engineering, Anhui Jianzhu University, Hefei 230601, China*

Correspondence should be addressed to Yu Zhou; yuzhou923@outlook.com

Received 16 July 2020; Revised 14 August 2020; Accepted 5 September 2020; Published 19 September 2020

Academic Editor: Songtao Lv



Generally, the damage of the structure will lead to the discontinuity of the local mode shape, which can be well reflected by the modal curvature of the structure, and the local information entropy of the beam structure will also change with the discontinuity of the mode. In this paper, based on the information entropy theory and combining the advantages of modal curvature index in damage identification of beam structure, the modal curvature utility information entropy index is proposed. The modal curvature curves of nondestructive structures were obtained by fitting the modal curvature curves of damage structures with the gapped smoothing technique to avoid dependence on the baseline data of nondestructive structures. The index comprehensively reflects the damage state of the structure by calculating mutual weight change matrix and the weight-probability coefficient. The performance of the new index was verified by the finite element simulation and model test of simply supported beam, respectively. The results show that the modal curvature utility information entropy index takes advantage of the modal curvature index which is sensitive to damage and can overcome its shortcomings effectively. The index proposed can identify the damage location and damage degree accurately and has certain noise immunity, which provides an effective damage identification indicator for beam structures.

## 1. Introduction

In recent years, high requirements on the integrity and performance of civil engineering structures is increasingly needed, which is reflected in the increasing complexity of civil structures, bridge structures, large stadiums, and tunnels, as well as the increasing service performance and construction scale. The safety of the beam structure is inevitably reduced due to the natural environment, material deterioration, construction defects, overload, and other factors, which may cause serious consequences. Therefore, it is of great practical significance to study the structural health monitoring (SHM) technology [1, 2].

With the use of an advanced and reliable sensor, the SHM technology has been rapid developed [3–5]. The most fashionable approaches in SHM are based on the structure vibration characteristics. These methods depend on the stiffness change on the influence of the dynamic characteristics of structure [6], which get the extensive attention of scholars because it is simple and easy. Common indicators include modal frequency [7], modal displacement [8], and the modal strain energy [9]. In view of the insufficient sensitivity of early damage identification indexes such as natural frequency and modal displacement, Pandey [10] firstly proposed a damage identification method for beam structure based on modal curvature (MC) in 1991, which has been widely applied and extended. Cao et al. [11] expounded the effectiveness of MC index and pointed out that MC is sensitive to measurement noise in waveform. In order to solve this problem, the Teager energy operator together with wavelet transform is tactically utilized to treat modal curvature; thus, a new modal curvature is put up, termed the Teager energy operator-wavelet transform (TEO-WT) modal curvature. It has been found that the combination of

continuous wavelet transform and MC can effectively filter out the modal data containing noise and reduce the impact of noise on the damage identification accuracy [2, 12]. Xu et al. [13] improved the two-dimensional modal curvature by real wavelet transform and complex wavelet transform, and wavelet 2D modal curvature is obtained. Dessi and Camerlengo [14] compared several damage identification methods based on MC and modal strain energy analysis; this analysis intends to point out comparatively the capability of locating and estimating damage of each method along with some critical issues already present with noiseless data. Zhang et al. [15] pointed out the shortcomings of MC index: (1) MC is not sensitive enough to the damage of modal nodes; (2) for the structure with multiple damages, the index of modal curvature difference cannot effectively reflect the damage degree of the structure. In order to improve the damage identification ability of MC index, some scholars obtained the analytical expression of the modal curvature change of the beam damage state by using the perturbation solution of the Euler beam motion equation, and introduced the filtering technology of the modal curvature change to establish the inverse problem of damage positioning based on the modal curvature only [16, 17]. MC index has also been popularized and applied to damage identification of plate structures based on two-dimensional mode curvature [18]. Yang et al. [19] proposed a curvature correction method incorporating bending and torsion effects into damage assessment.

Combining with the advantages of MC index to identify structural damage, entropy theory is introduced into the damage identification of beam structures. Entropy is an important concept to describe system chaos proposed by Clausius in thermodynamics. The physical meaning of entropy has different meanings in different fields, so the application of entropy presents different forms [20–23], and different forms of entropy show a promising prospect in the field of structural damage identification, such as, the transfer entropy, the approximate entropy, the fuzzy entropy and the wavelet entropy. Information entropy was first proposed by Shannon [24], which is used to characterize the disorder degree of the system signal state. Information entropy theory has been applied in the study on surrounding rock stability [25] and material damage [26]. However, relatively few studies have been conducted in the field of beam structure damage. Liu and Wu [27] introduced the theory of information entropy into the dynamic identification of damage to concrete structures, providing a new way of thinking for solving such problems as insufficient sensitivity and difficulty in nonlinear analysis in damage identification. Yang et al. [28] proposed generalized-local information entropy algorithm.

In this paper, on the basis of previous researches, based on the theory of Utility Information Entropy in Information theory, the advantages of MC in structural damage identification is make fully used and the Modal Curvature Utility Information Entropy (MCUIE) index is put forward. The effectiveness of the index is verified by using the finite element model of simply supported beam, and the practicability of the index is verified by the test of simply supported steel beam.

## 2. Theoretical Background

*2.1. Basic Theory of Modal Curvature.* In structural mechanics, the differential equation of transverse vibration of Euler beam is [29]

$$\frac{\partial^2}{\partial x^2}\left(EI(x)\frac{\partial^2 v(x,t)}{\partial x^2}\right)+m(x)\frac{\partial^2 v(x,t)}{\partial t^2}=p(x,t), \quad (1)$$

where $v(x, t)$ is the vertical vibration displacement at the beam section $x$ at time $t$ and $EI(x)$ is the bending stiffness of the section.

In order to better describe the vibration state of the structure, the relationship between variables is expressed in the form of function. After the structure is discretized, the vibration equation of Euler beam in the form of matrix in the elastic range can be obtained:

$$\begin{pmatrix} m(x_1) & & & 0 \\ & m(x_2) & & \\ & & \ddots & \\ 0 & & & m(x_n) \end{pmatrix}\begin{bmatrix} v_1'' \\ v_2'' \\ \vdots \\ v_n'' \end{bmatrix}+\begin{bmatrix} k_{11}[E(x_1)I(x_1)] & k_{12}[E(x_1)I(x_2)] & \cdots & k_{1n}[E(x_1)I(x_n)] \\ k_{21}[E(x_2)I(x_1)] & k_{22}[E(x_2)I(x_2)] & \cdots & k_{2n}[E(x_2)I(x_n)] \\ \vdots & \vdots & \ddots & \vdots \\ k_{n1}[E(x_n)I(x_1)] & k_{n2}[E(x_n)I(x_2)] & \cdots & k_{nn}[E(x_n)I(x_n)] \end{bmatrix}\begin{bmatrix} v_1 \\ v_2 \\ \vdots \\ v_n \end{bmatrix}=\begin{bmatrix} p(x_1,t) \\ p(x_2,t) \\ \vdots \\ p(x_n,t) \end{bmatrix}, \quad (2)$$

where, $x_1, x_2, \ldots, x_n$ is the longitudinal coordinate of node 1, 2, . . ., $n$; $m(x_n)$ is the discrete mass of node $n$; $v_n$ and $v_n''$ are the vertical displacement and vertical acceleration of node $n$, respectively; $k_{ij}(E(x_i)I(x_j))$ is the stiffness coefficient component of the structure, which means the vertical force on node $i$ when element deformation of node $j$ occurs. $p(x_n, {}_t)$ is the external excitation received by node $n$ at time $t$.

From equation (2), it can be seen that the stiffness change at the node of the structure not only affects the displacement and curvature change of itself, but also affects the displacement and curvature of other nodes. As reflected in the practical problem, the modal curvature difference (MCD) at the structural damage will change greatly, but the undamaged part, especially near the damage location, the MCD will often be large, which leads to the misjudgment of damage identification.

The solution of equation (1) can be expressed as the superposition form of each mode:

$$v(x,t) = \sum_{j=1}^{\infty} \varphi_j(x) q_j(t), \tag{3}$$

where $j$ is the number of mode order; $\varphi_j(x)$ and $q_j(t)$ are the $j^{\text{th}}$ mode displacement and mode coordinates of the beam, respectively.

According to the relevant theories of beam bending deformation [15]:

$$\frac{M(x,t)}{EI(x)} = k(x,t) = \frac{\partial^2 v(x,t)}{\partial x^2} = \sum_{j=i}^{\infty} \varphi_j''(x) q_j(t), \tag{4}$$

where $M(x, t)$ is the bending moment of the beam section; $K(x, t)$ ias the curvature of beam vibration curve; and $\varphi_j''(x)$ is the $j^{\text{th}}$ MC.

It is assumed that in the eigenvalue problem, the damage of the beam structure only affects the stiffness matrix, but not the inertia matrix [14]. According to damage mechanics, the constitutive relation of concrete damage is [16]

$$\sigma = E(1-D)\varepsilon, \tag{5}$$

where $D$ is the local damage factor of the structure and $E(1-D)$ is the local stiffness of the structure after damage.

According to equations (4) and (5), with the aggravation of the damage degree of the structure, the damage factor $D$ increases while the local stiffness of the structure decreases, which finally leads to the increase of the MC at the damage.

The simply supported planar beam has negligible shear deformability. As shown in Figure 1, damage is modelled as a localized and uniform reduction of the bending stiffness distribution $K(x)$ along the dimensional coordinate $x$. Thus, the damaged beam of length $L$ is considered as the union of three beam portions as shown in Figure 2, where the shortest one, with a reduced cross section with respect to the others, represents the damaged portion. For each beam portion, $L_i$, $A_i$, and $K_i$ denote the length, cross section area, and bending stiffness, respectively. For generality, it is convenient to formulate identification methods using nondimensional coordinates $\xi$, $\eta$, with $\xi = x/L$ and $\eta = y/L$, and nondimensional variables. For each beam portion of nondimensional length $l_i = L_i/L$ $(i = 1, 2, 3)$, conditions at the edges are defined in terms of the boundary conditions whereas at the interfaces between the beam portions, continuity of displacement $v$, slope $\theta$, bending moment $M$, and shear force $V$ is imposed (all nondimensional). The generic expression of mode shapes in nondimensional form is [30, 31]

$$\begin{aligned} \varphi(x_i) = {} & A \sin a_i x_i + B \cos a_i x_i + C \sin h\, a_i x_i \\ & + D \cos h\, a_i x_i \quad i = 1, 2, 3, \end{aligned} \tag{6}$$

where $A$, $B$, $C$, and $D$ are the coefficients, $a_i^4 = \omega_i^2 m_i / EI_i$ is frequency equations.

The beam boundary conditions in terms of nondimensional mode shapes are expressed as

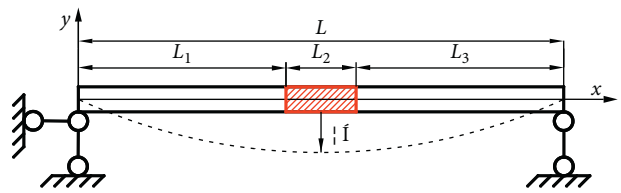


Figure 1: Simply supported beam with the damaged portion in red.

$$\begin{cases} \varphi_1(0) = 0, \\ \varphi_1''(0) = 0, \\ \text{applied in point } O_1, \end{cases} \qquad \begin{cases} \varphi_3(l_3) = 0, \\ \varphi_3''(l_3) = 0, \\ \text{applied in point } O_4. \end{cases} \tag{7}$$

Substituting the generic expression of mode shapes into the set of boundary conditions equation (7), the expressions of natural frequencies and mode shapes can be calculated [30]:

$$\omega_i^n = n^2 \pi^2 \sqrt{\frac{EI_i}{m_i L_i}} \quad (i = 1, 2, 3; n = 1, 2, \ldots, \infty), \tag{8}$$

$$\varphi_n(x_i) = A_n \sin\left(\frac{n\pi L_i}{L}\right) \quad (i = 1, 2, 3; n = 1, 2, \ldots, \infty), \tag{9}$$

where $A_n$ is constant and depends on the initial conditions, whereas at the interfaces, the continuity of displacement, slope, bending moment, and shear force is applied [14]:

$$\begin{cases} \varphi_1(l_1) = \varphi_2(0), \\ \varphi_1'(l_1) = \varphi_2'(0), \\ \varphi_1''(l_1) = \dfrac{K_2}{K_1}\varphi_2''(0), \text{ applied in point } O_2, \\ \varphi_1'''(l_1) = \dfrac{K_2}{K_1}\varphi_2'''(0), \end{cases} \qquad \begin{cases} \varphi_2(l_2) = \varphi_3(0), \\ \varphi_2'(l_2) = \varphi_3'(0), \\ \varphi_2''(l_2) = \dfrac{K_1}{K_2}\varphi_3''(0), \text{ applied in point } O_3. \\ \varphi_2'''(l_2) = \dfrac{K_1}{K_2}\varphi_3'''(0), \end{cases} \tag{10}$$

It is worth underlying that the sudden variation of stiffness implies that curvatures lose continuity as well. The discontinuity in the bending stiffness is reflected sharply on the curvature of the mode shapes as a result of equation (10).

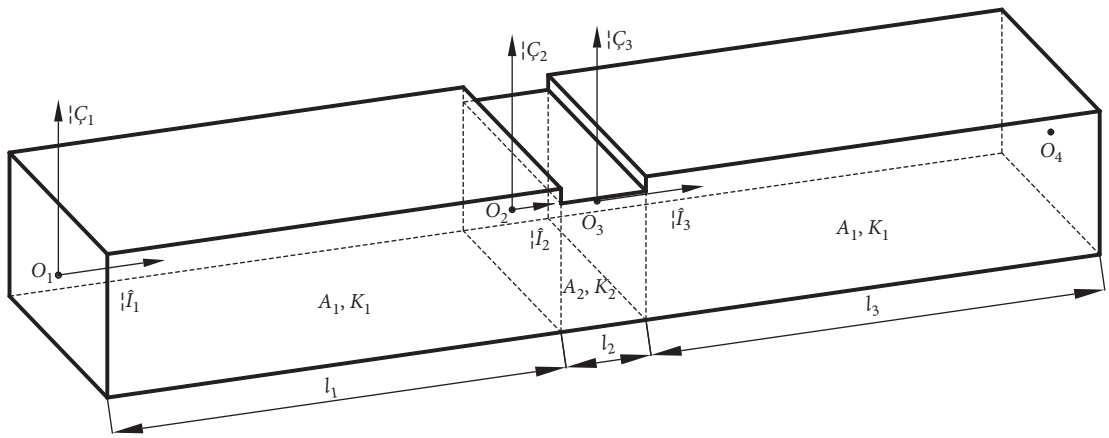


Figure 2: Geometrical nondimensional parameters of the notched beam.

The final expression for the mode-shape curvatures is quite complicate. In practical engineering, the MC of structural modes is generally approximated by the central difference method [10]:

$$\varphi_{ji}'' \approx \frac{2}{h_{i-1}+h_i}\left[\frac{\varphi_{j(i+1)}-\varphi_{ji}}{h_i}-\frac{\varphi_{ji}-\varphi_{j(i-1)}}{h_{i-1}}\right], \tag{11}$$

where $\varphi_{ji}$ represents the mode displacement of the $i^{\text{th}}$ measurement point in the $j^{\text{th}}$ modal and $h_i$ is the distance between the $i^{th}$ measuring point and the $(i\text{-}1)^{\text{th}}$ measuring point.

*2.2. Basic Theory of Information Entropy.* Let the information space of information source $X$ be

$$[X \cdot P]: \begin{cases} X: a_1 a_2 \cdots a_n, \\ p(X): p_1\, p_2 \cdots p_n, \end{cases} \tag{12}$$

where $X$: $a_1\, a_2 \ldots a_n$ is the information source symbol, $p(X)$: $p_1\ p_2\ \ldots\ p_n$ is the probability of the information source symbol, and $0 \le p_i \le 1$.

The total information contained in the information source symbol $a_i$ $(i = 1, 2, \ldots, n)$ is called the self-information $I(a_i)$ of the information source symbol $a_i$, and its mathematical meaning refers to the logarithm of the reciprocal of the prior probability $p(a_i)$ of the information source symbol $a_i$, that is [32],

$$I(a_i) = \log\frac{1}{p(a_i)} = -\log p(a_i) \quad (i = 1, 2, \ldots, n). \tag{13}$$

The self-information function determined by equation (13) shows that the uncertainty of symbol $a_i$ $(i = 1, 2, \ldots, n)$ emitted by information source $X$ is a function of the prior probability $p(a_i)$ of symbol $a_i$, and is uniquely determined by it.

Although the self-information function $I(a_i)$ $(i = 1, 2, \ldots, n)$ can measure the information capacity well, the self-information function is random because of the uncertainty of the source symbol, which means that the source emits a certain symbol $a_i$ $(i = 1, 2, \ldots, n)$, the amount of information provided, and it cannot represent the ability of the entire source to provide information.

In order to represent the information measure of information source $X$, in 1948, Shannon put forward the concept of information entropy [24]. The information entropy of the information source $X$ is defined as statistical average of self-information $I(a_i)$ $(i = 1, 2, \ldots, n)$, which is used to represent the disorder degree and of the signal state of the system, that is [32],

$$\begin{aligned} H(X) &= p(a_1)I(a_1) + p(a_2)I(a_2) + \cdots + p(a_n)I(a_n) \\ &= -p(a_1)\log p(a_1) - p(a_2)\log p(a_2) - \cdots \\ &\quad - p(a_n)\log p(a_n) \\ &= -\sum_{i=1}^{n} p(a_i)\log p(a_i), \end{aligned} \tag{14}$$

where $H(X)$ is the information entropy of the system; $P_i$ is the probability of the $i^{\text{th}}$ information in the information source; and $\log P_i$ is the amount of information provided by the $i^{\text{th}}$ information.

## 3. Calculation Method of MCUIE Index

*3.1. Establish of the Local Probability of MC.* Information entropy is a global parameter, which is capable of representing the overall characteristics of the structure. However, the damage is a local feature of the structure. When the global probability is used to describe the information of the damage point, the information of the damage point will be covered by the boundary effect. Therefore, this paper defines a set composed of $n$ locally adjacent measurement points; $P(x)$ adopts the local probability [28] to represent the proportion of the information amount of the measurement points in the sum of the information amount of the adjacent measurement points and reflects the disorder degree of the signal state of the measurement points:

$$p_i = \frac{\varphi_i''}{\sum_{i=0}^{n} \varphi_i''}, \tag{15}$$

where $\varphi_i''$ is the MC of the $i^{th}$ node and $n$ represents the number of nodes.

When calculating the local probability $P_i$ of the $i^{th}$ node, the front and rear nodes adjacent to the $i$ node are taken as auxiliary calculation points, the calculation points, and auxiliary points form a sliding window to calculate the local probability of each point in turn, as shown in Figure 3.

For the calculation of the local probability of second-order MC, the negative and positive offset will occur near the zero point of the MC, so that the denominator of equation (15) will be reduced to close to zero, and the value of $P_i$ will jump greatly, i.e., "false peak" will appear, affecting the accuracy of structural damage identification. Therefore, it is necessary to process the second-order MC data to eliminate the influence of "false peak". The specific operation step is as follows:

(1) Take the absolute value of the data under a certain damage case and normalize it.

(2) Return the normalized data to the positive and negative states before the absolute value is taken, so as to ensure the change trend of the data remains unchanged.

(3) Add value "1" to the data processed in the previous step to eliminate the offset between the positive and negative data.

(4) Calculate the local probability of the data processed above.

Taking the local probability of MC of damage cases (5(40%), 20(20%), 30(10%), 50(60%); (5(40%) indicates that 40% damage occurred in element 5) as an example, the effect of data processing is illustrated, as shown in Figure 4.

From Figure 4(a), it can be seen that the local probability of the untreated data will show a large peak at the mode node (element 30), which covers the real damage situation. Figure 4(b) shows that the variation trend of the local probability curve of the processed data conforms to the actual situation of the damage.

*3.2. Gapped Smoothing Technique.* Most of the structural damage identification indexes require the modal data before and after the structural damage as input parameters, but the modal parameters of the undamaged structure state are often difficult to obtain. The basic idea of gapped smoothing technique (GST) is that modal characterization such as mode shape and curvature mode shape of a healthy structure has a smooth shape, which can be approximated by a polynomial in two or three variables. For damaged structures, the modal characterization is no longer smooth in the whole space and irregular mutation is induced where local damages exist. With the modal curvature information of the undamaged structure being unknown, the modal curvature value of the damage point of the structure can be removed, and the smooth curve can be fitted by using the gapped smoothing technique to approximate replace the modal curvature curve of the undamaged structure. This technique was originally developed by Ratcliffe [33]. A similar method is the Chebyshev polynomial fitting technique [34]. The curve fitting function is a quartic polynomial described by equation (16), where $F(x)$ is the mode shape curvature of the beam.

$$F(x) = c_4x^4 + c_3x^3 + c_2x^2 + c_1x + c_0. \tag{16}$$

For example, the modal curvature before and after the single point damage of simply supported beam structure is shown in Figure 5. It can be seen that the MC curve at the damage location has a significant mutation. The MC curve equation of the structure in the undamaged state and the approximate modal curvature curve equation of the structure in the undamaged state fitted by gapped smoothing technique are as follows:

$$\begin{aligned} F_1(x) = {} & (-5.642e-8)x^4 + (6.996e-6)x^3 \\ & - (5.009e-5)x^2 - 0.01034x + 0.0102, \end{aligned} \tag{17}$$

$$\begin{aligned} F_2(x) = {} & (-5.601e-8)x^4 + (6.945e-6)x^3 \\ & + (4.984e-5)x^2 - 0.01026x + 0.0101. \end{aligned} \tag{18}$$

The MC curve fitted by the undamaged beam and GST as indicated by equations (17) and (18) is shown in Figure 6. It can be seen that the two curves almost coincide. By using the corrcoef $(X, Y)$ function in MATLAB, the Pearson correlation coefficient of the two curves can be calculated to be equal to 1, i.e., the two curves are completely correlated, indicating that it is feasible to replace the modal curvature curve in the undamaged state of the structure with the MC curve obtained by GST fitting.

*3.3. Calculation of MCUIE Index.* Let the utility space of information source $X$ be

$$[X \cdot W]: \begin{cases} X: a_1a_2 \cdots a_n, \\ W(X): w_{11}w_{ij} \cdots w_{nn}, \end{cases} \tag{19}$$

where $w_{ij} \geq 0\,(i = 1, 2, \ldots, n;\, j = 1, 2, \ldots, n)$ is the utility weight coefficient and represents the relative importance of the source symbol $a_i\,(i = 1, 2, \ldots, n)$ to the source symbol $a_j\,(j = 1, 2, \ldots, n)$.

In this paper, we take the value of pairwise division of the elements in the source symbol as its relative importance; then a mutual weight matrix $H(w)$ of order $n \times n$ can be obtained. In theory, when the structure is damaged, the MC of the damaged node will be changed in the corresponding rows and columns in the mutual weight matrix, while the corresponding rows and columns of the undamaged node will remain unchanged, which indicates that when the damage occurs, the disorder degree of the relative

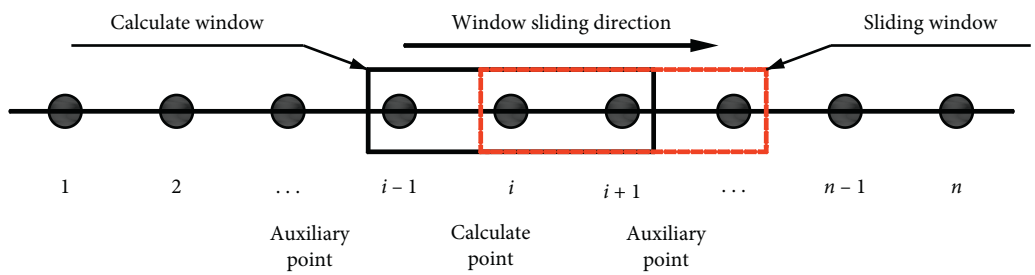


Figure 3: Description of local probability calculation.

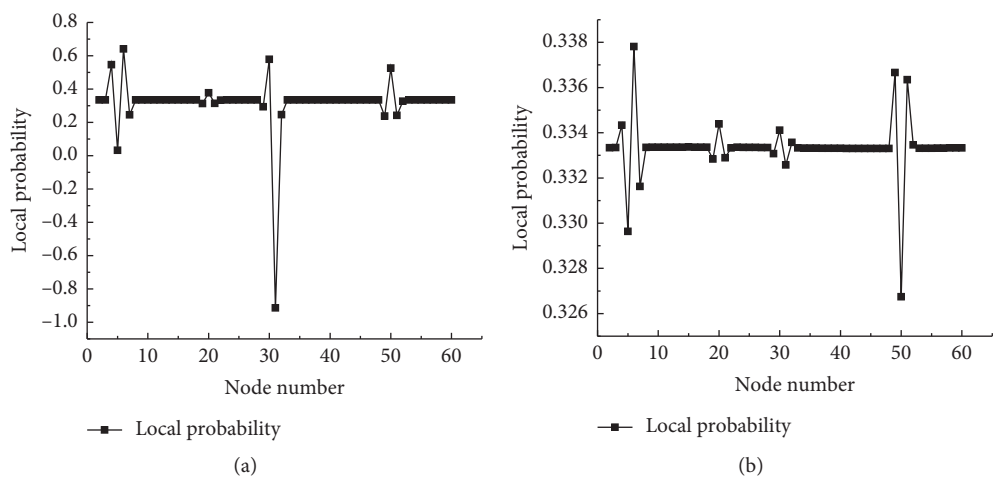


Figure 4: Local probability of modal curvature. (a) Original local probability. (b) Modified local probability.

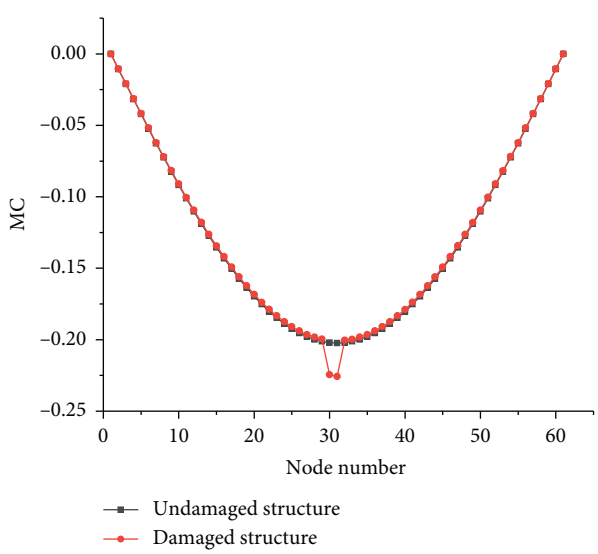


Figure 5: MC curves of structure before and after.

information of the damage node increases. This makes use of the subjective utility value and objective probability information of node modal information.

The expression of mutual weight matrix $H(w)$ is

$$H(w) = \begin{array}{c} \\ a_1 \\ a_2 \\ \vdots \\ a_n \end{array} \begin{array}{c} \begin{array}{cccc} a_1 & a_2 & \dots & a_n \end{array} \\ \begin{bmatrix} a_{11} & a_{12} & \dots & a_{1n} \\ a_{21} & a_{22} & \dots & a_{2n} \\ \vdots & \vdots & \ddots & \vdots \\ a_{n1} & a_{n2} & \dots & a_{nn} \end{bmatrix} \end{array} \tag{20}$$

where $a_{ij} = (a_i/a_j)(i = 1, 2, \dots, n;\ j = 1, 2, \dots, n)$, $n$ is the number of nodes.

Suppose the mutual weight change matrix $\Delta$ before and after structural damage is

$$\begin{aligned} \Delta &= H(w)_u - H(w)_d \\ &= \begin{bmatrix} \Delta_{11} & \Delta_{12} & \cdots & \Delta_{1n} \\ \Delta_{21} & \Delta_{22} & \cdots & \Delta_{2n} \\ \vdots & \vdots & \ddots & \vdots \\ \Delta_{n1} & \Delta_{n2} & \cdots & \Delta_{nn} \end{bmatrix}, \end{aligned} \tag{21}$$

where $H(w)_u$ and $H(w)_d$ are the mutual weight matrix before and after structural damage, respectively; and the

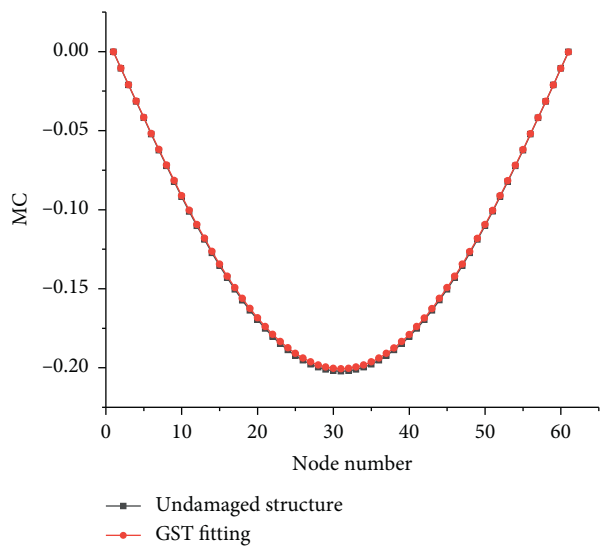


Figure 6: Gapped smoothing technique fitting.

subscripts "$u$" and "$d$" represent the undamaged and damaged states of the structure, respectively.

The MC of the damaged nodes also mutates in the corresponding rows and columns in the mutual weight change matrix, and the degree of mutation is proportional to the mutation value of the MC. When the modal curvature changes at the damage before and after the damage, the MC trend curve of the whole beam will shrink slightly, which indicates that the damage elements affect the stability of the surrounding undamaged elements to some degree, as shown in Figure 7.

To facilitate the explanation of the new index, two functions are defined: sum$(\Delta)$ represents the sum of the elements of the mutual weight change matrix $\Delta$ by rows and mul $(\Delta \cdot p)$ is expressed as the product of the sum of the utility weight coefficients of the source symbol $a_i \quad (i = 1, 2, \ldots, n)$ and the local probability $p_i \quad (i = 1, 2, \ldots, n)$ of the source symbol, i.e., the weighted-probability coefficient.

The weighted sum of mul$(\Delta \cdot p)$ and the self-information $I(a_i) = -\log p_i \quad (i = 1, 2, \ldots, n)$ of the source symbol is defined as the modal curvature utility information entropy of the system

$$\begin{aligned}\mathrm{MCUIE} &= H_W(\mathrm{mul}_1, \mathrm{mul}_2, \ldots, \mathrm{mul}_n; I_1, I_2, \ldots, I_n)\\ &= -\mathrm{mul}_1 \log p_1 - \mathrm{mul}_2 \log p_2 - \cdots - \mathrm{mul}_n \log p_n\\ &= -\{\mathrm{mul}_1 \log p_1 + \mathrm{mul}_2 \log p_2 + \cdots + \mathrm{mul}_n \log p_n\}\\ &= -\sum_{i=1}^{n} \mathrm{mul}_i \log p_i,\end{aligned} \tag{22}$$

that is,

$$\mathrm{MCUIE} = -\sum_{i=1}^{n} mul_i \log p_i. \tag{23}$$

To some degree, the weight-probability coefficient $\mathrm{mul}_i \, (i = 1, 2, \ldots, n)$ reflects the influence of the change of the structure's overall stress characteristics on the deformation of the structure points. The self-information $I(a_i) = -\log p_i \, (i = 1, 2, \ldots, n)$ of the source symbol reflects the amount of information that the changes of structural nodes can provide to identify the overall deformation of the structure.

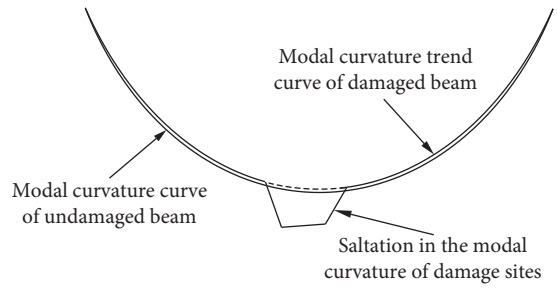


Figure 7: Change of modal curvature cure.

The specific steps of MCUIE index calculation are as follows in Figure 8:

*3.4. Damage Degree Identification Method Based on MCUIE Index.* The MC of element $D(x)$ without damage is $\phi_E$; theoretically, the MC of element $D(x)$ after damage should be mutation from $\phi_{NA}$ to $\phi_{NB}$, and the actual result $\phi_{NE}$ is the average value of $\phi_{NA}$ and $\phi_{NB}$, as shown in Figure 9 [15].

In this paper, by considering the relationship between element damage and "node damage," the MATLAB polynomial fitting method is adopted to obtain the relationship curve between MCUIE peak at the damaged node and element damage degree, so as to judge the damage degree of the structure.

The sum of squared errors (SSE) is used as the index to evaluate the effect of curve fitting:

$$\mathrm{SSE} = \sum_{i=1}^{r} \sum_{j=1}^{ni} \left(x_{ij} - \overline{x}_i\right)^2, \tag{24}$$

where $r$, $ni$, $x_{ij}$, and $\overline{x}_i$ are the total number of observed data, the number of observed data, the fitting data of the $j^{\text{th}}$ data in the $i^{\text{th}}$ population, and the average value of the $i^{\text{th}}$ observation data.

The closer $SSE$ is to 0, the closer the linear correlation between the fitting data and the fitting function is, and the better the fitting effect is.

## 4. Finite Element Numerical Analysis of MCUIE Index

*4.1. Establishment of Simply Supported Beam Model.* The simply supported beam model was established in MIDAS/Civil, and the beam structure was divided into 60 equally spaced elements, as shown in Figure 10. The span of simply supported beam is $L = 6$ m with a section size 0.6 m × 0.4 m. C40 concrete is applied with a elastic modulus $E = 3.25 \times 107$ kN/m$^2$ and Poisson ratio $\mu = 0.2$. The bulk density is $c = 25$ kN/m$^3$ and mass density is 2.549 kN/m$^3$/g.

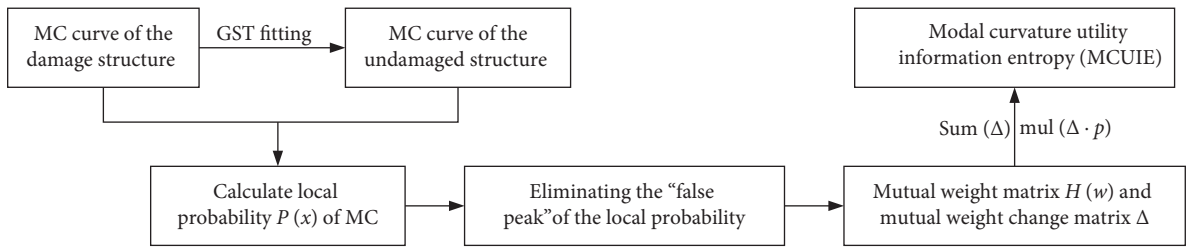


Figure 8: Calculation process of MCUIE index.

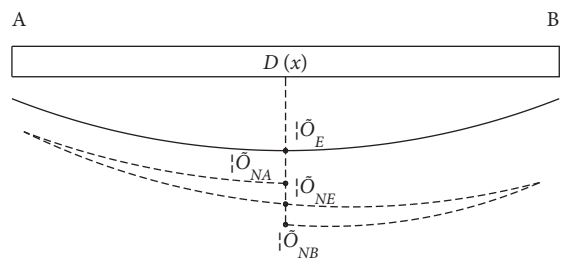


Figure 9: Relationship between element damage and node damage.

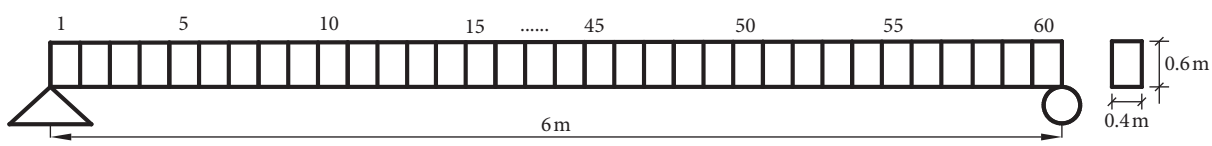


Figure 10: Simply supported beam Finite element model.

Table 1: Damage case studies in simply supported beam.

| Damage case | Damage element | Damage degree (%) |
|---|---|---|
| 1 | 5 20 30 50 | 5 60 30 20 |
| 2 | 5 20 30 50 | 20 40 60 10 |
| 3 | 5 20 30 50 | 40 20 10 60 |
| 4 | 1 20 35 | 10 20 30 40 50 |
| 5 | 30 | 5 10 20 30 40 60 |

Here the damage of the structure is simulated by the reduction of the element elastic modulus.

*4.2. Setting of Damage Cases of Simply Supported Beam Model.* The damage cases of single point, multiple points with the same damage degree, and different damage degrees were set to verify the effectiveness of MCUIE index, and the damage cases of simply supported beam are shown in Table 1.

The calculation results of the first-two order frequencies and periods of the simply supported beam model are shown in Table 2.

By comparison, with the aggravation of the beam structure damage (the degradation of the element stiffness), the natural frequency of the beam structure gradually decreases and the period gradually increases.

*4.3. Damage Identification Results Analysis of MCUIE.* The first-two modal damage identification results are given in this section. Figures 11–13 show the damage identification comparison result of the first-two orders of MCUIE index and MCD index [18] in the above damage cases. When the structure is damaged, the MCUIE curve and MCD curve will undergo saltation at the corresponding damage location.

The identification results of damage cases 1–3 under the MCD are shown in Figures 11(a) and 11(b); the value of MCD index shows an obvious peak at the set damage position, so the damage position of the structure can be located. However, there are anomalies near the supports at both ends of the beam structure, and in the identification results of the second-order modes, the value of MCD index at the damage of the modal nodes is 0. Because the modal curvature at the second-order modal nodes is positive and negative offset, which negatively influences the identification of the relative damage degree of the structure.

In contrast, the MCUIE index is modified by local probability to measure the structural damage from the

Table 2: Modal information of simply supported beam.

| Damage case | First-order frequency (rad/sec) | First-order period (sec) | Second-order frequency (rad/sec) | Second-order period (sec) |
|---|---|---|---|---|
| Undamaged | 167.568 | 0.0375 | 648.129 | 0.00969 |
| Single damage | 166.412 | 0.0377 | 647.713 | 0.00971 |
| Multiple damage | 165.611 | 0.0379 | 643.143 | 0.00977 |

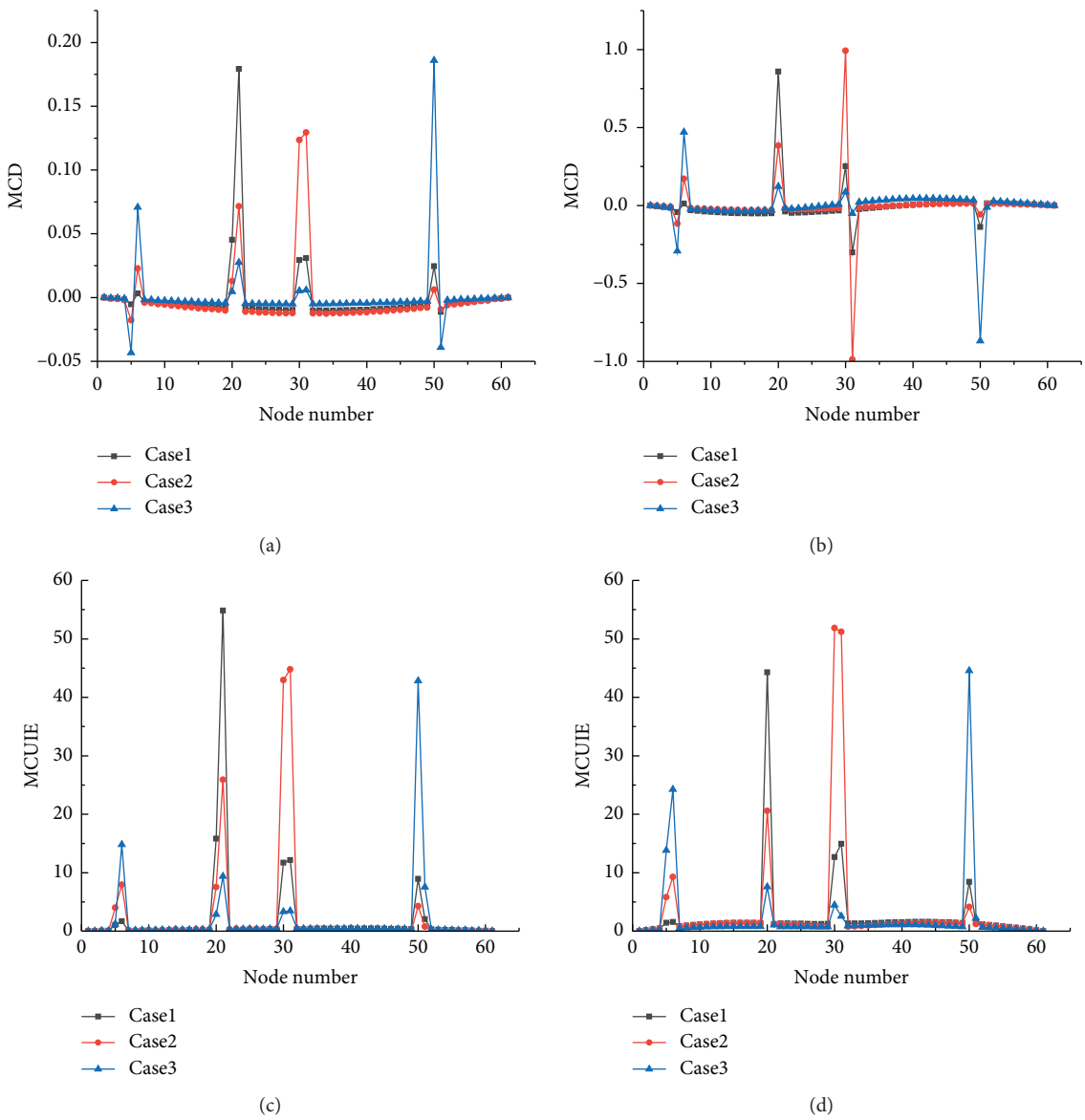


Figure 11: Damage identification results of MCD and MCIUE index of case studies 1–3. (a) First-order MCD. (b) Second-order MCD. (c) First-order MCUIE. (d) Second-order MCUIE.

perspective of probability, it can also accurately locate the damage position in Figures 11(c) and 11(d), and the identification results of the first-two modes can truly reflect the damage situation of the structure without any abnormal. With the increase of the damage degree, the MCUIE index value at the damage location also increases and increases synchronously in accordance with the proportion of the damage degree.

The identification results of case 4 are shown in Figure 12. When the same damage degree occurs at different positions of the structure, the peak value of MCUIE index of each damage position is very close, while the value of MCD index identification results varies greatly.

By comparing Figure 13, it can be seen that in the case of single point damage, the damage identification result of MCUIE index is also better than MCD index. In MCUIE

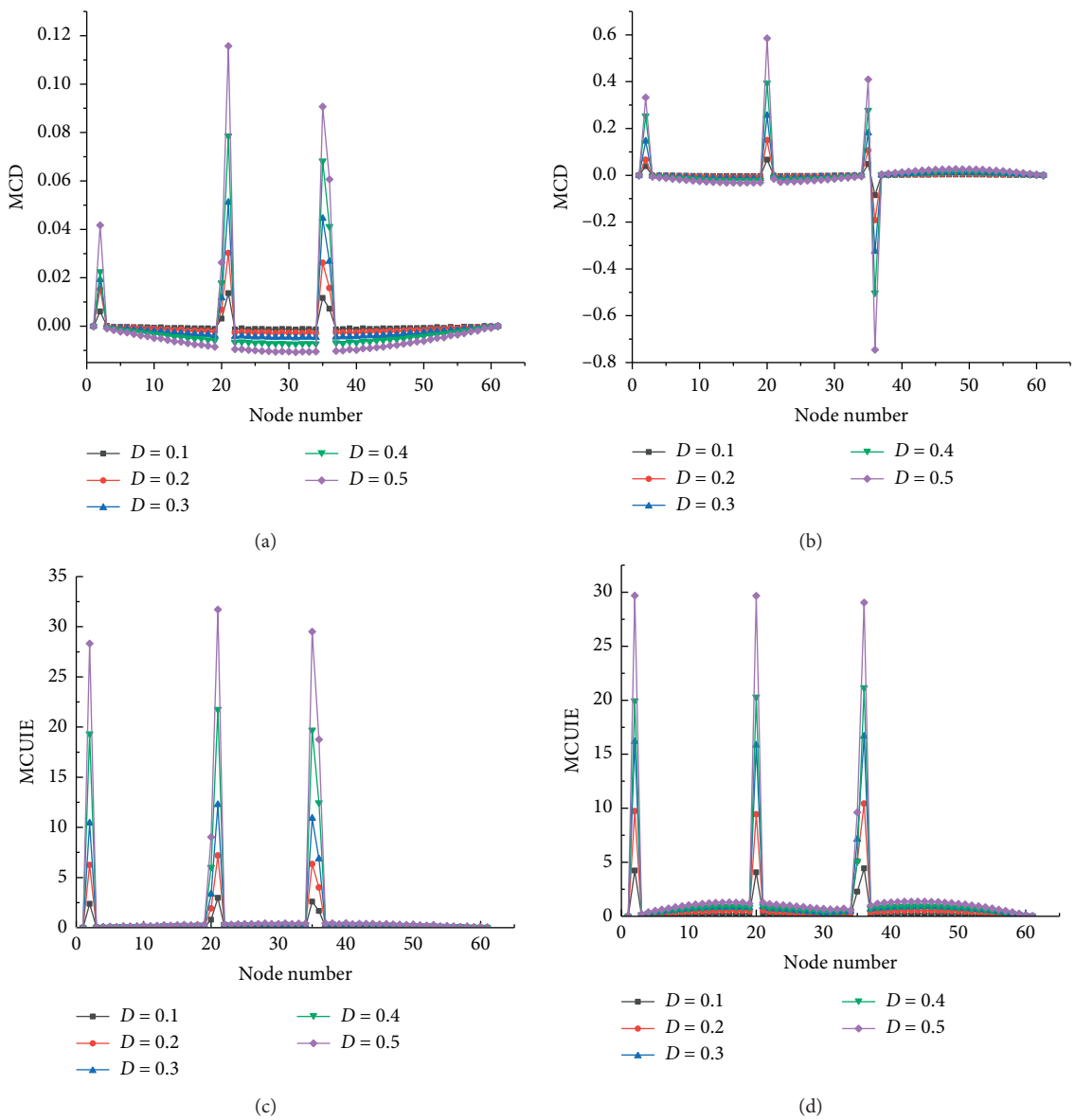


Figure 12: Damage identification results of MCD and MCUIE index of case studies 4. (a) First-order MCD. (b) Second-order MCD. (c) First-order MCUIE. (d) Second-order MCUIE.

index identification, the index has a promising sensitivity to damage when a single point of structure is damaged to a different degree, and with the aggravation of damage, the MCUIE value at the damage position increases in proportion to the damage degree of the structure, which can qualitatively reflect the damage degree of the structure.

*4.4. Calculation of Structural Damage Degree.* Regarding the calculation of damage degree, MATLAB is used in this paper to obtain the relationship curve between the peak value of MCUIE at damage node and damage degree by polynomial fitting method to judge the damage degree of the structure.

When a single damage with different degrees occurs in the structure (Case 5), the peak value of MCUIE at damage node is shown in Table 3 (first-order value). The relation curve of MCUIE peak value and damage degree is fitted, and the polynomial degree is 3; the damage degree function equation of structure when damage occurs in element 30 is obtained:

$$y = 151.2x^3 - 32.68x^2 + 38.88x - 0.2222, \text{SSE} = 4.5853e - 30. \quad (25)$$

The validity of equation (25) was verified by taking the index peak values of 15% and 55% as damage degree in Case 5, respectively. The results are shown in Table 4.

It can be seen from Table 4 that, for the functional equation of damage degree of a single point, the fitting error of both small damage and large damage is less than 10%,

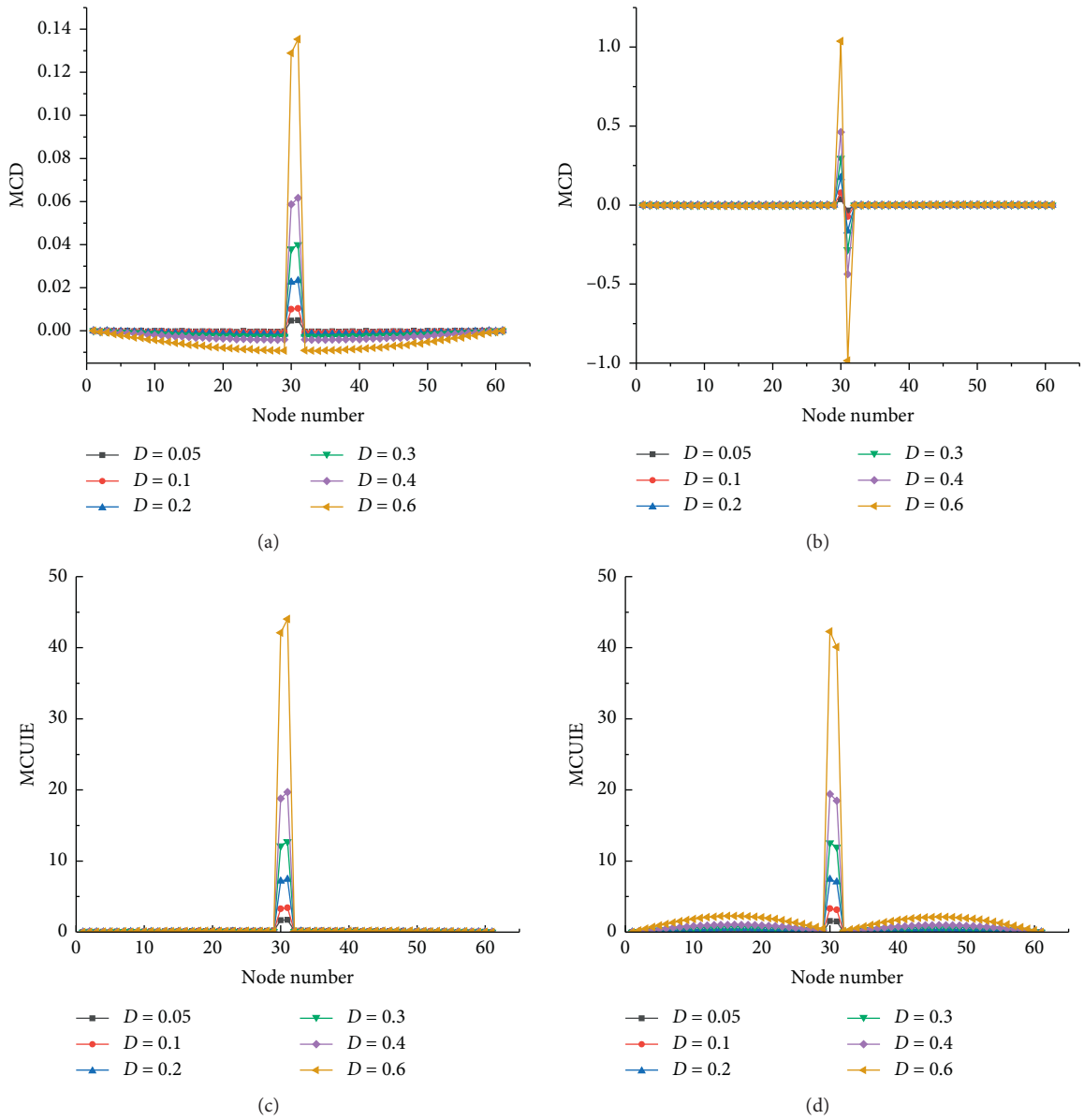


Figure 13: Damage identification results of MDC and MCUIE index of case studies 5. (a) First-order MCD. (b) Second-order MCD. (c) First-order MCUIE. (d) Second-order MCUIE.

Table 3: MCUIE value of Single damage with different damage degrees.

| Damage element | Damage degree (%) | MCUIE value |
|---|---|---|
| 30 | 5 | 1.6591 |
| | 10 | 3.4902 |
| | 20 | 7.4562 |
| | 30 | 12.5832 |
| | 40 | 19.7782 |
| | 60 | 44.0021 |

indicating that equation (25) of damage degree fitting is effective and feasible.

Structural damage relationship fitting curve is shown in Figure 14; as can be seen from the graph, with the increase of damage degree, MCUIE value of damage node increases gradually, when damage degree is greater than 40%, the damage growth curve is nonlinear. Considering the cumulative effect of structure damage, the relationship of damage can be qualitatively verified the rationality of the fitted curve growth trend.

Table 4: Validation of single damage degree function equation.

| Damage element | Damage degree (%) | Calculated value | Fitted value | Identification error |
|---|---|---|---|---|
| 30 | 15 | 5.982 | 5.385 | 9.9 |
| | 55 | 37.855 | 36.432 | 3.8 |

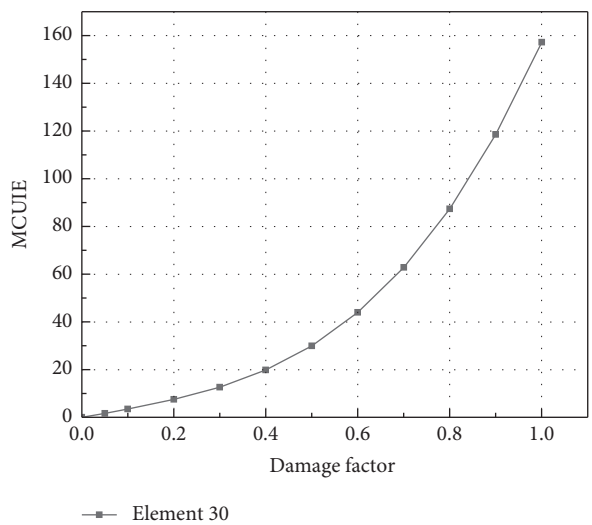


Figure 14: Damage degree fitting curve of single damage.

Table 5: MCUIE value of multidamage with different damage degrees.

| Damage element | MCUIE value of element with different damage degrees | | | | |
|---|---|---|---|---|---|
| | Damage degree (%) | 10 | 20 | 30 | 40 | 50 |
| 1 | | 2.3745 | 6.0944 | 11.533 | 19.3256 | 28.3274 |
| 20 | | 2.9621 | 7.1848 | 13.311 | 21.7613 | 31.7177 |
| 35 | | 2.5933 | 6.3385 | 11.727 | 19.7066 | 29.5062 |

Table 6: Validation of multidamage degree function equation.

| Damage element | Damage degree (%) | Calculated value | Fitted value | Identification error (%) |
|---|---|---|---|---|
| 1 | 15 | 4.484 | 3.918 | 12.6 |
| 20 | 45 | 27.514 | 26.501 | 3.75 |

The damage degree of structure with multiple points and different damage degrees is calculated by taking case 4 as an example. MCUIE peak value of the damaged node is shown in Table 5 (first-order value). The relationship curve between the peak value of MCUIE at damaged node and the damage degree can be obtained by fitting the data in Table 5:

$$y_1 = -42.45x^3 + 130.5x^2 - 0.243x + 1.162, \mathrm{SSE}_1 = 0.0341, \tag{26}$$

$$y_2 = -33.11x^3 + 128.3x^2 + 5.166x + 1.213, \mathrm{SSE}_2 = 0.0219, \tag{27}$$

$$y_3 = 14.74x^3 + 91.73x^2 + 7.677x + 0.918, \mathrm{SSE}_3 = 0.0422. \tag{28}$$

The damage degree fitting equations (26) and (27) of multipoint damage case were verified by taking the index peak values when the damage degrees of element 1 and 20 in case 4 were 15% and 45%, respectively. The results shown in Table 6.

The damage degree fitting curve is shown in Figure 15, comparing the damage degree fitting curves of element 1, 20, and 35, it can be seen that the damage degree fitting curves vary at different positions. Under the same damage degree, the fitting curve of element 35 near the span is above element 1 near the support, indicating that under the same damage degree, the closer the damage node is to the span, the larger the MCUIE is. Besides, with the aggravation of damage, the difference between the two curves becomes larger. Under the same damage degree, the damage degree fitting curve of element 20 is above elements 1 and 35, indicating that the damage of element on both sides of the damage location

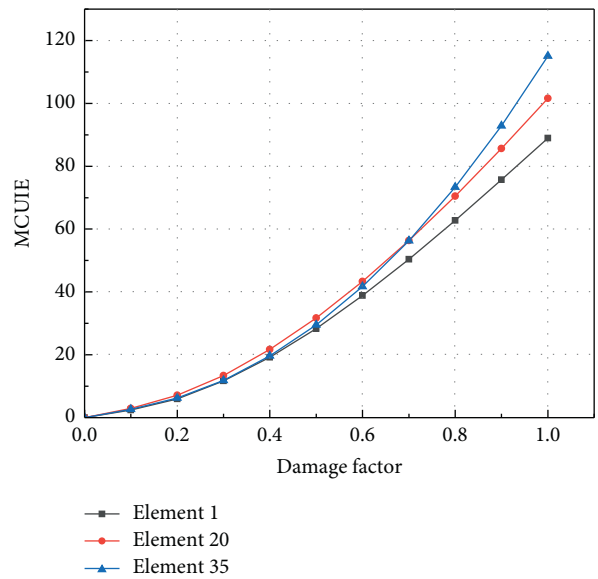


Figure 15: Damage degree fitting curve of multidamage.

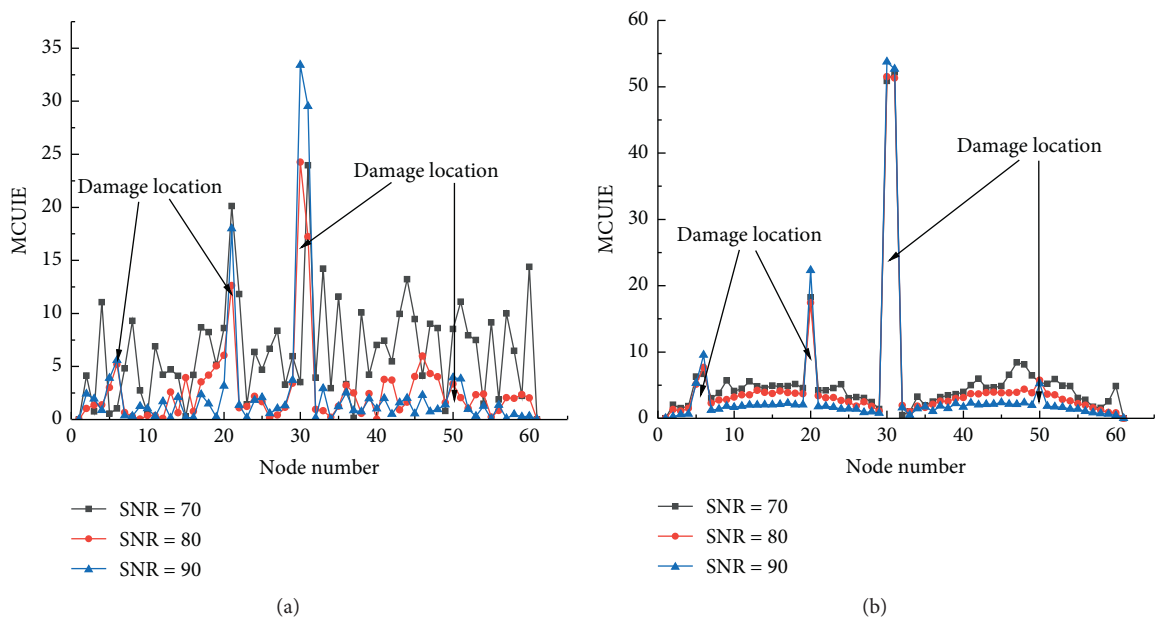


Figure 16: Antinoise verification of MCUIE index. (a) Antinoise verification of first-order. (b) Antinoise verification of second-order.

plays an aggravating role. When the damage degree reaches a certain threshold, the damage degree fitting curve of element 20 is between elements 1 and 35.

*4.5. MCUIE Index Antinoise Performance Verification.* To verify the antinoise performance of MCUIE index, Gaussian white noise with signal to noise ratio (SNR) of 70 dB, 80 dB, and 90 dB was added to the mode shape to simulate the noise interference.

$$\mathrm{SNR} = 10\log_{10}\left(\frac{P_s}{P_n}\right), \tag{29}$$

where $P_s$ is the effective power of the original signal, $P_n$ is the effective power of the noise signal, and the length of the original signal and the noise signal are consistent.

The damage identification results after adding Gaussian white noise to the mode shape of Case 2 are shown in Figure 16.

It can be seen from Figure 16 that MCUIE index has promising antinoise performance, but when the SNR of first-order index is equal 70 dB, the damage identification effect with a small damage degree is unsatisfactory. By comparing the results of antinoise analysis of the first-two order MCUIE indexes, it can be seen that the second-order indexes have

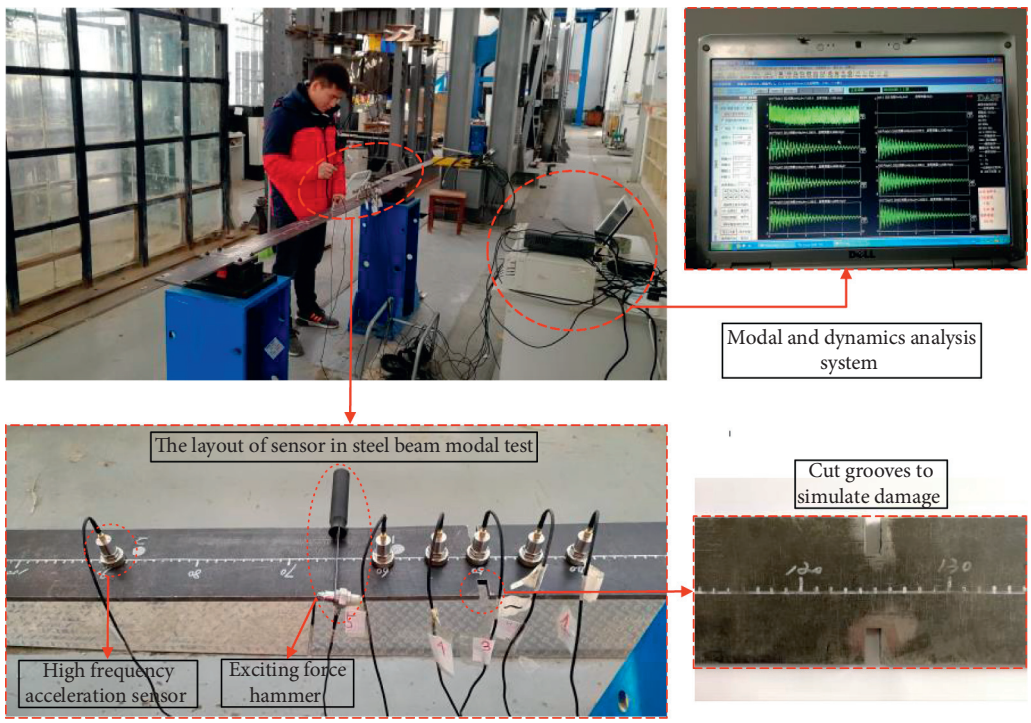


Figure 17: Test site.

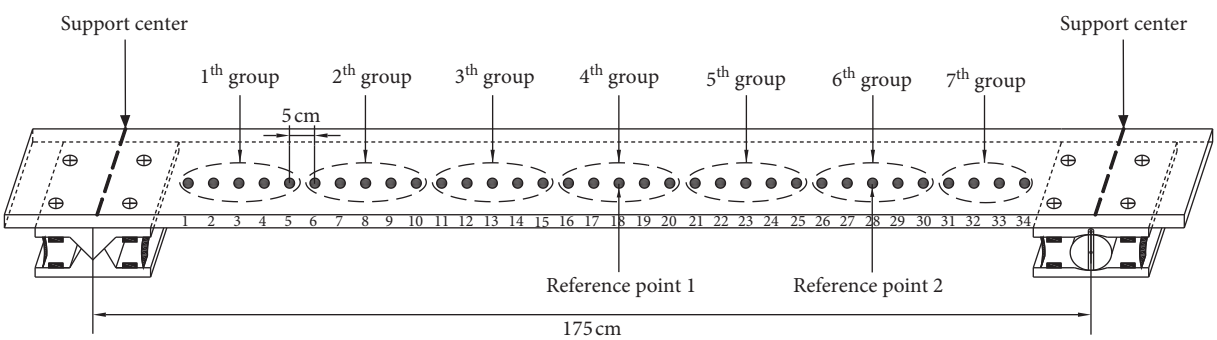


Figure 18: Monitoring point arrangement.

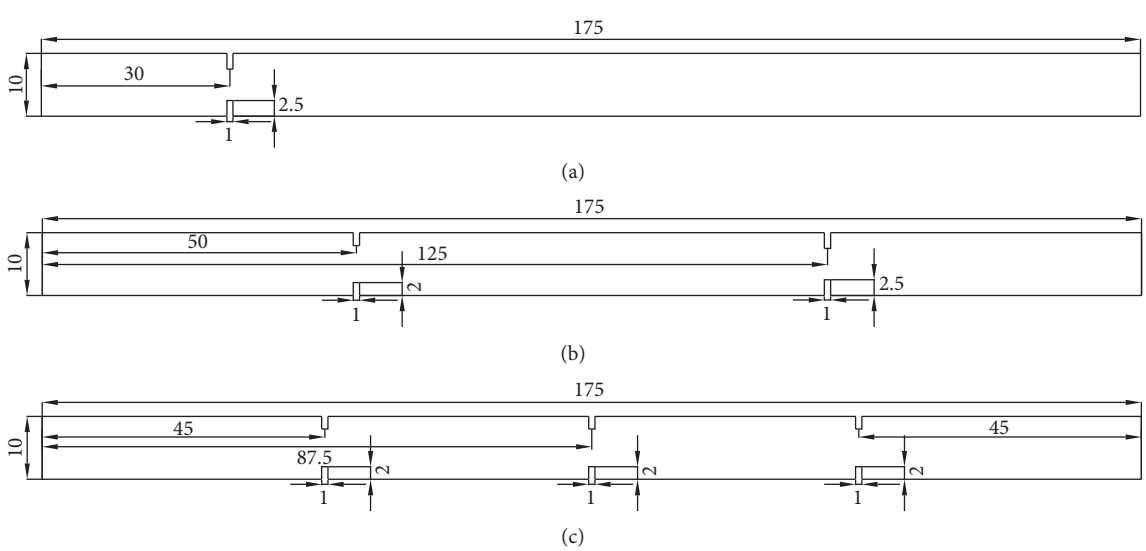


Figure 19: Steel beam damage setting (unit: cm). (a) Single damage. (b) Two damage. (c) Three damage.

Table 7: Test simulation damage cases.

| Damage cases | Cutting cases (incision width of 1 cm) | Damage degree (%) |
|---|---|---|
| 6 | Incision depth was 2.5 cm at 30 cm | 50 |
| 7 | Incision depth was 2.0 cm and 2.5 cm at 50 cm and 125 cm | 40, 50 |
| 8 | Incision depth was 2.0 cm at 45 cm, 87.5 cm and 130 cm | 40 |

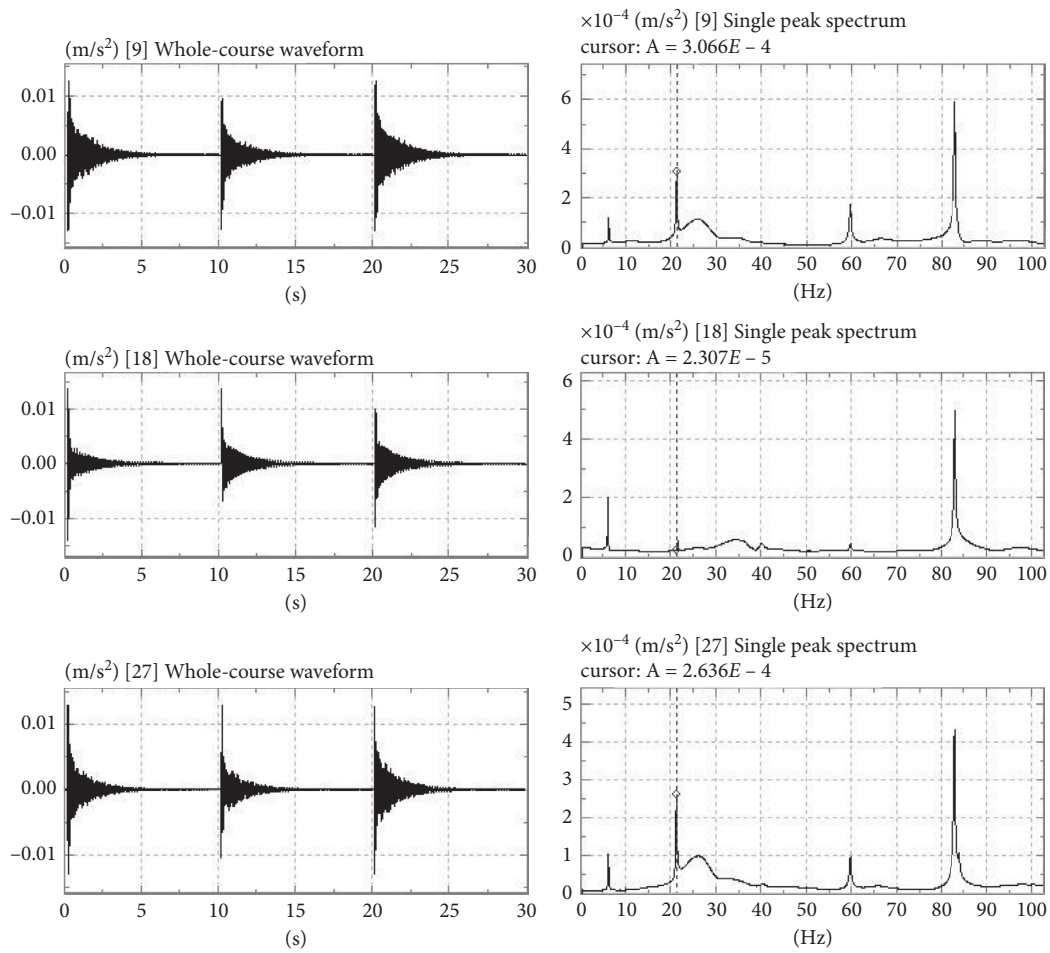


Figure 20: Spectrum curve of undamaged beam.

better antinoise performance, and the minor damage can be effectively identified, and the variation trend of MCUIE peak at the damage node is basically consistent with the variation trend of damage degree.

## 5. Test Verification of Simply Supported Beam

*5.1. Design of Experimental Model.* The model of simply supported steel beam with uniform section is taken as the research object to verify the effectiveness of the MCUIE index. The cross section size of the model is 100 mm × 8 mm, the model span is 175 cm, and 35 elements, 36 nodes are divided. The elastic modulus of the experimental model material $E = 2.0795 \times 108\,\mathrm{kN/m^2}$, the bulk density $c = 76.98\,\mathrm{kN/m^3}$, and Poisson ratio $\mu = 0.3$. The two ends of the steel beam are fixed on the prefabricated hinge support and rolling fabrication by high-strength bolts, and the acceleration sensor is installed at the element node to obtain the modal data of the structure. The single point hammer excitation force multipoint acceleration collected for simply supported steel beam, as shown in Figure 17.

With six acceleration sensors available, in order to obtain the first-two modes information of the structure more accurately, the reference point is set at the "reference point 1" in the midspan position to obtain the first-order mode information of the structure, and the "reference point 2" along the 3/4 of the span direction to obtain the second-order mode information of the structure, as shown in Figure 18.

*5.2. Structural Damage Simulation and Damage Cases Setting.* The section of the beam is symmetrically cut to simulate the damage; the damage form of the simulated steel beam is shown in Figure 19.

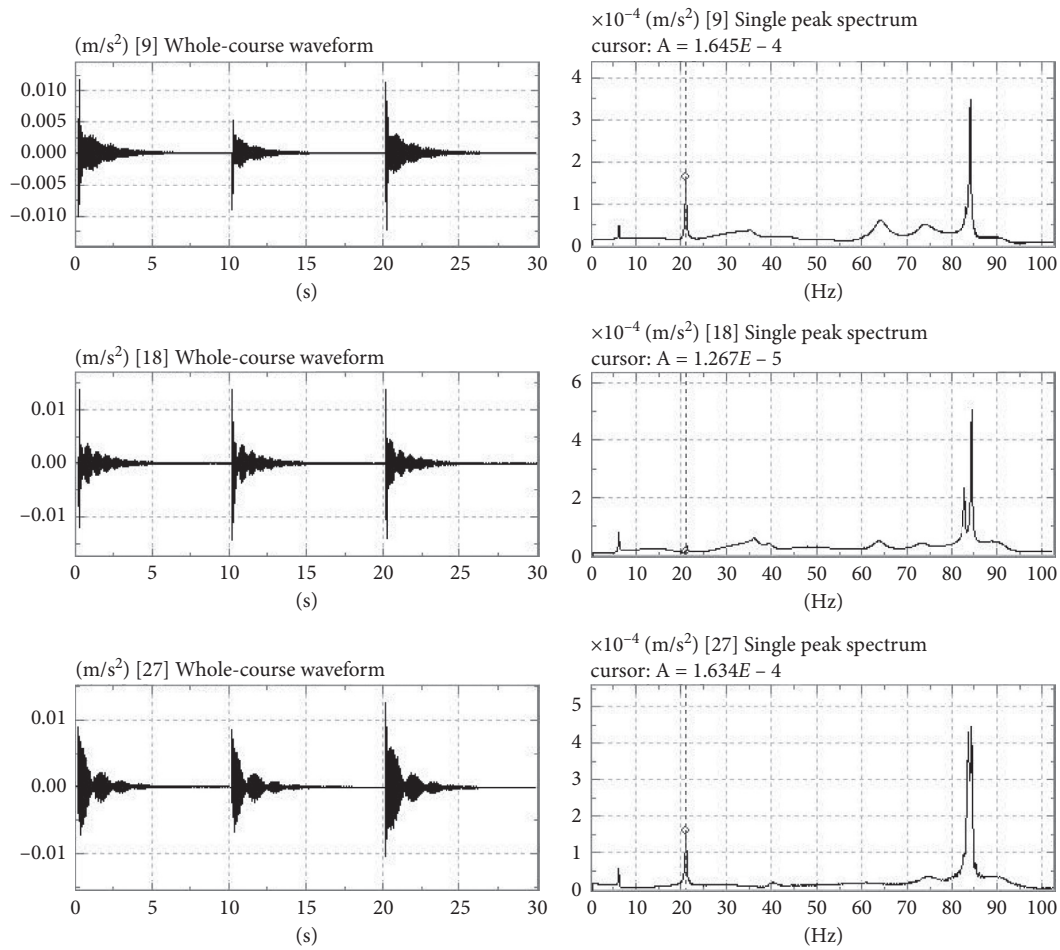


Figure 21: Spectrum curve of case 6.

For any small segment of a simply supported beam of equal section, assuming that the bending moment $M$ is the same everywhere in the section, the maximum total bending deformation of this segment is the sum of the maximum bending deformation of each segment, as shown in the following equation:

$$\frac{L}{EI} = \frac{L_1}{EI_1} + \frac{L_2}{EI_2}, \tag{30}$$

where $EI$ is the equivalent stiffness of any small segment, $EI_1$ and $EI_2$ are stiffness of $L_1$ and $L_2$ segments, respectively. According to equation (30), the damage degree of each damage case can be calculated, and then the damage cases of the simulated steel beam can be obtained, as shown in Table 7.

*5.3. Analysis of MCUIE Method Test Verification.* The random subspace method is used to calculate the modal frequency and mode data of the structure, the acceleration time-history curve is processed by fast Fourier transform, and the corresponding spectrum curve is obtained. The spectrum curve of the undamaged and damaged structure is shown in Figures 20–23.

According to equation (12), the first-two MC of the structure under each damage case can be obtained according to the modal information obtained from the test, as shown in Figure 24 (take the second-order identification result as an example). According to the calculation results of MC of damaged structures, there is an obvious abrupt peak point at the damage location, which can well show the damage location of structures, but the defects of MC index are prominent as well. For example, the linear relationship between the MC value and the damage degree of the damage point is poor, and it is not sensitive to the damage at the mode shape node.

The measured MC of the structure is abnormal near the support, which may be caused by the disturbance of the support link, the field noise, the defect of the test member, and the error of the test instrument, but it has little effect on the effectiveness of the proposed method.

According to the calculation method above, the MCUIE relation curve under each damage case is obtained by processing the measured modal data of the

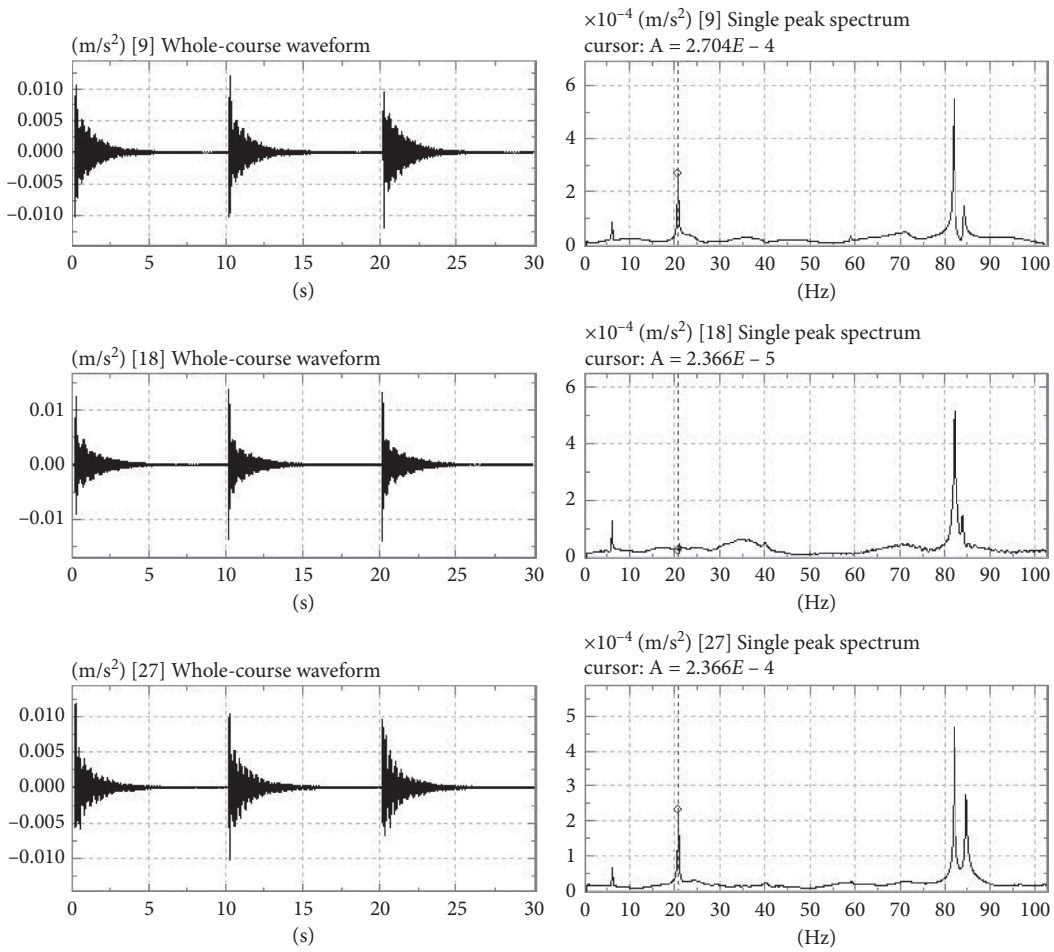


Figure 22: Spectrum curve of case 7.

structure, as shown in the following figure (take the second-order identification result as an example).

Although it is inevitable to be affected by external noise, defects of the specimens. and measurement errors in the process of testing, which may resulting in errors in the test data, the MCUIE index calculated by using the first-two modes information of the test structure can still better identify the damage of the structure. It can be seen from Figure 25 that MCUIE increases with the aggravation of damage degree, and the MCUIE values at different damage locations with the same damage degree have little difference, which can preliminarily reflect the damage degree of the structure.

The first-order damage index peak value was extracted from damage Case 7, and the relationship curve between the index peak value and the damage degree was fitted. Since the damage was two points with different damage degrees, the fitting polynomial degree was 2, and the damage degree fitting equation was as follows:

$$y = 33.14x^2 + 3.574x + 1.02, \mathrm{SSE} = 4.437e - 31. \quad (31)$$

Damage degree fitting curve of Case 7 is shown in Figure 26. Because the measured modal curvature is abnormal near the support, the MCUIE value does not start from 0. Considering the cumulative effect of structural damage, the correctness of the growth trend of the damage assessment function curve can be qualitatively verified.

## 6. Conclusion

Based on the sensitivity of modal curvature to damage, the information entropy index describing the degree of system uncertainty is introduced into the damage identification of beam structure. Combining with the concept of utility information entropy, the MCUIE index is proposed, and the damage identification ability of the new index and MCD is compared and analyzed by using the finite element simulation of simply supported beam.

With gapped smoothing technique adopted, the MC curve of the damaged structure is used to fit a smooth curve to replace the MC curve of the undamaged structure, which avoids the dependence on the baseline data of the undamaged structure. Through polynomial fitting of the relationship between MCUIE peak and damage degree at the damage site, the damage degree fitting equation can be obtained, which can effectively determine the damage degree qualitatively, but needs to

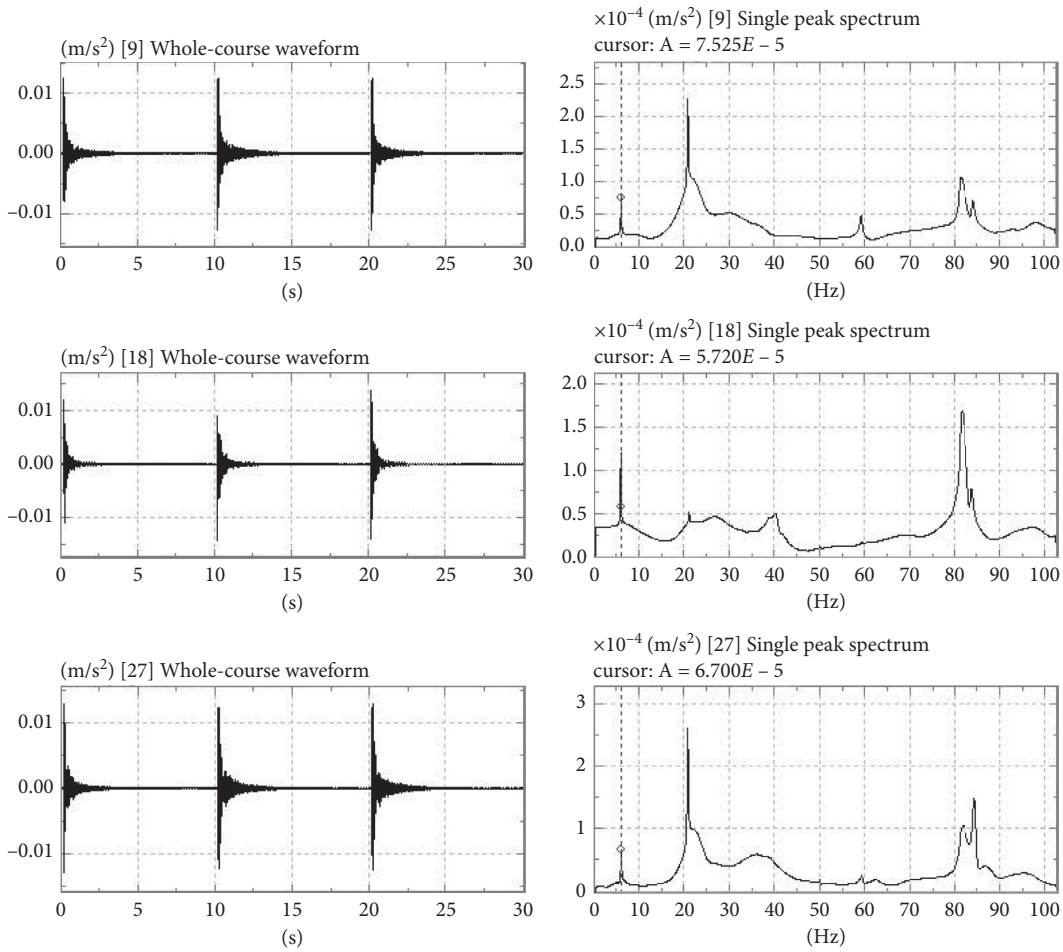


Figure 23: Spectrum curve of case 8.

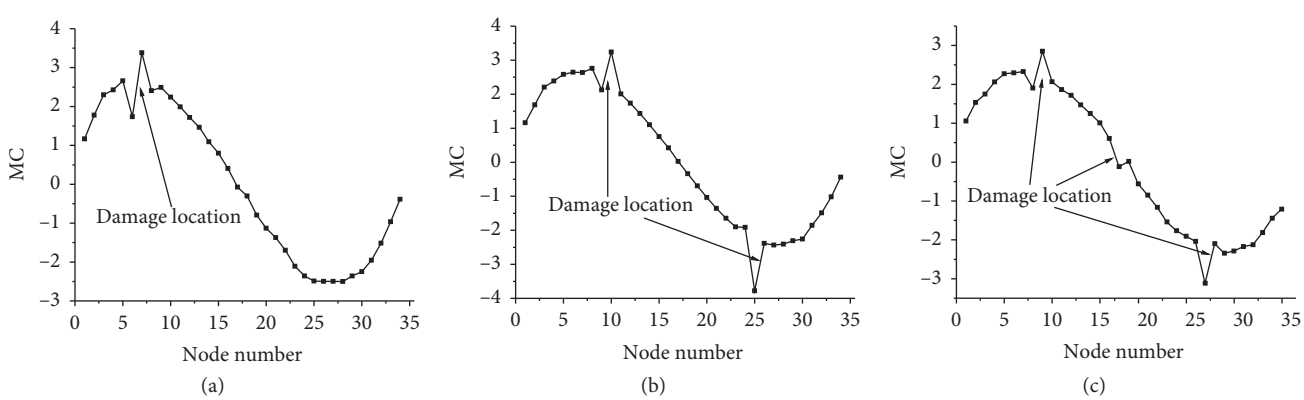


Figure 24: Damage identification result of MC. (a) Case 6. (b) Case 7. (c) Case 8.

be further optimized in the direct quantification of damage degree.

The antinoise performance of MCUIE index is analyzed by adding Gaussian white noise to the modal shapes. The results show that the index has certain noise immunity and the higher-order index has better noise immunity.

The effectiveness of MCUIE index in practical structure is verified by the damage simulation of simply supported beam model and it shows promising damage identification ability. However, due to the nonlinearity, complexity, and uncertainty of the actual structure, MCUIE index needs to be further verified in practical engineering.

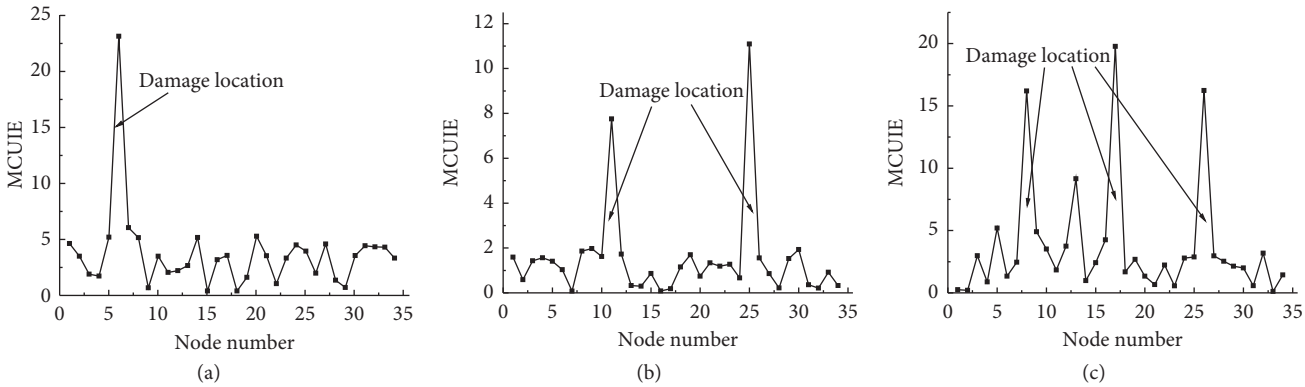


Figure 25: Damage identification result of MCUIE. (a) Case 6. (b). Case 7. (c) Case 8.

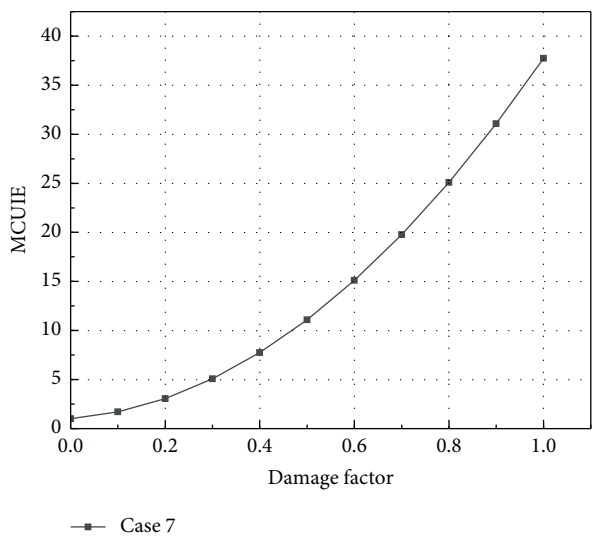


Figure 26: Damage degree fitting curve of case 7.

## Data Availability

All data are available within the article or can be obtained from the corresponding author upon request.

## Conflicts of Interest

The authors declare that there are no conflicts of interest regarding the publication of this paper.

## Acknowledgments

This work was supported by Key Natural Science Project of Anhui Provincial Education Department (KJ2019A0746), Natural Science Foundation of China (51868045), Natural Science Foundation Youth Fund of Anhui Province (2008085QE247), and Startup Fund for Doctor of Anhui Jianzhu University (2019QDZ08).

## References

[1] Y. Zhou, S. Di, C.-S. Xiang et al., "Damage identification in simply supported bridge based on rotational-angle influence lines method," *Transactions of Tianjin University*, vol. 24, no. 6, pp. 587–601, 2018.

[2] F. Han, Q.-J. Zhang, C.-F. Wang et al., "Structural health monitoring of timber using electromechanical impedance (EMI) technique," *Advances in Civil Engineering*, vol. 2020, pp. 1–9, Article ID 1906289, 2020.

[3] W. Fan and P. Qiao, "Vibration-based damage identification methods: a review and comparative study," *Structure Control Health Monitor*, vol. 10, no. 2, pp. 83–111, 2011.

[4] S. Das, P. Saha, and S. K. Patro, "Vibration-based damage detection techniques used for health monitoring of structures: a review," *Journal of Civil Structural Health Monitoring*, vol. 6, no. 3, pp. 477–507, 2016.

[5] Y. Zhou, S.-K. Di, C. Xiang et al., "Beam structure damage detection based on rotational-angle-influence-lines of elastic-constrained-support beam," *Journal of Zhejiang University (Engineering Science)*, vol. 54, no. 5, pp. 879–888, 2020.

[6] M. Bovo, M. Tondi, and M. Savoia, "Infill modelling influence on dynamic identification and model updating of reinforced concrete framed buildings," *Advances in Civil Engineering*, vol. 2020, pp. 1–16, Article ID 9384080, 2020.

[7] X. Zhou, W. Zhang, Y. Gao et al., "An experimental study of the feasibility of identifying the impact damages of reinforced

concrete piers using a modal frequency method," *Advances in Civil Engineering*, vol. 2020, pp. 1–16, Article ID 6365354, 2020.

[8] C.-Y. Kao, X.-Z. Chen, S.-L. Hung, and B. Setiawan, "Two strategies to improve the differential evolution algorithm for optimizing design of truss structures," *Advances in Civil Engineering*, vol. 2020, pp. 1–23, Article ID 4509576, 2020.

[9] W. Fan and P. Qiao, "A strain energy-based damage severity correction factor method for damage identification in plate-type structures," *Mechanical Systems and Signal Processing*, vol. 28, pp. 660–678, 2012.

[10] A. K. Pandey, M. Biswas, and M. M. Samman, "Damage detection from changes in curvature mode shapes," *Journal of Sound and Vibration*, vol. 145, no. 2, pp. 321–332, 1991.

[11] M. Cao, W. Xu, W. Ostachowicz, and Z. Su, "Damage identification for beams in noisy conditions based on teager energy operator-wavelet transform modal curvature," *Journal of Sound and Vibration*, vol. 333, no. 6, pp. 1543–1553, 2014.

[12] Z.-B. Yang, M. Radzienski, P. Kudela, and W. Ostachowicz, "Scale-wavenumber domain filtering method for curvature modal damage detection," *Composite Structures*, vol. 154, pp. 396–409, 2016.

[13] W. Xu, K. Ding, J. Liu, M. Cao, M. Radzieński, and W. Ostachowicz, "Non-uniform crack identification in plate-like structures using wavelet 2D modal curvature under noisy conditions," *Mechanical Systems and Signal Processing*, vol. 126, pp. 469–489, 2019.

[14] D. Dessi and G. Camerlengo, "Damage identification techniques via modal curvature analysis: overview and comparison," *Mechanical Systems and Signal Processing*, vol. 52-53, pp. 181–205, 2015.

[15] J. Zhang, H. Peng, and C. You, "Damage diagnosis of beam structures based on superimposed curvature modal change rate," *Engineering Mechanics*, vol. 29, no. 11, pp. 272–301, 2012.

[16] J. Ciambella and F. Vestroni, "The use of modal curvatures for damage localization in beam-type structures," *Journal of Sound and Vibration*, vol. 340, pp. 126–137, 2015.

[17] J. Ciambella, A. Pau, and F. Vestroni, "Modal curvature-based damage localization in weakly damaged continuous beams," *Mechanical Systems and Signal Processing*, vol. 121, pp. 171–182, 2019.

[18] H. Zhong and M. Yang, "Damage detection for plate-like structures using generalized curvature mode shape method," *Journal of Civil Structural Health Monitoring*, vol. 6, no. 1, pp. 141–152, 2016.

[19] M. Yang, H. Zhong, M. Telste, and S. Gajan, "Bridge damage localization through modified curvature method," *Journal of Civil Structural Health Monitoring*, vol. 6, no. 1, pp. 175–188, 2016.

[20] L. A. Overbey and M. D. Todd, "Dynamic system change detection using a modification of the transfer entropy," *Journal of Sound and Vibration*, vol. 322, no. 1-2, pp. 438–453, 2009.

[21] R. Yan and R. X. Gao, "Approximate entropy as a diagnostic tool for machine health monitoring," *Mechanical Systems and Signal Processing*, vol. 21, no. 2, pp. 824–839, 2007.

[22] C. Lohrmann, P. Luukka, M. Jablonska-Sabuka, and T. Kauranne, "A combination of fuzzy similarity measures and fuzzy entropy measures for supervised feature selection," *Expert Systems with Applications*, vol. 110, pp. 216–236, 2018.

[23] W.-X. Ren and Z.-S. Sun, "Structural damage identification by using wavelet entropy," *Engineering Structures*, vol. 30, no. 10, pp. 2840–2849, 2008.

[24] C. E. Shannon and W. Weaver, "A mathematical theory of communication," *Bell System Technical Journal*, vol. 27, no. 3, pp. 379–423, 1948.

[25] J. Zhou, C. Chen, D. J. Armaghani, and S. Ma, "Developing a hybrid model of information entropy and unascertained measurement theory for evaluation of the excavatability in rock mass," *Engineering with Computers*, vol. 5, pp. 1–24, 2020.

[26] S. F. Karimian, M. Modarres, and H. A. Bruck, "A new method for detecting fatigue crack initiation in aluminum alloy using acoustic emission waveform information entropy," *Engineering Fracture Mechanics*, vol. 223, Article ID 106771, 2020.

[27] G. Liu and Z. Wu, "New thought on dynamic identification technology for damage detection of RC structures by introducing information entropy theory," *Journal of Vibration and Shock*, vol. 30, no. 6, pp. 162–171, 2011.

[28] Z. Yang, X. Chen, Y. Jiang, and Z. He, "Generalised local entropy analysis for crack detection in beam-like structures," *Nondestructive Testing and Evaluation*, vol. 29, no. 2, pp. 133–153, 2014.

[29] R. Craig Roy, "Fundamentals of Structure Dynamics,"China Communications Press, Beijing, China, 1996.

[30] S. Naguleswaran, "Vibration of an euler-bernoulli beam on elastic end supports and with up to three step changes in cross-section," *International Journal of Mechanical Sciences*, vol. 44, no. 12, pp. 2541–2555, 2002.

[31] M. A. Koplow, A. Bhattacharyya, and B. P. Mann, "Closed form solutions for the dynamic response of euler-bernoulli beams with step changes in cross section," *Journal of Sound and Vibration*, vol. 295, no. 1-2, pp. 214–225, 2006.

[32] D. Jiang, "Information Theory and Coding,"University of Science and Technology of China Press, Hefei, China, 2008.

[33] C. P. Ratcliffe, "Damage detection using a modified Laplacian operator on mode shape data," *Journal of Sound and Vibration*, vol. 204, no. 3, pp. 505–517, 1997.

[34] Y. Jiao, H.-B. Liu, Y.-C. Cheng et al., "Damage identification of bridge based on chebyshev polynomial fitting and fuzzy logic without considering baseline model parameters," *Shock And Vibration*, vol. 2015, pp. 1–10, Article ID 187956, 2015.

Hindawi
Advances in Civil Engineering
Volume 2020, Article ID 8825262, 14 pages
https://doi.org/10.1155/2020/8825262

*Research Article*

# Prediction of the Collapse Region Induced by a Concealed Karst Cave above a Deep Highway Tunnel

**Fu Huang, Di Wang, Yuan Feng, and Min Zhang**

*School of Civil Engineering, Changsha University of Science and Technology, Changsha 410114, Hunan, China*

Correspondence should be addressed to Fu Huang; hfcsu0001@163.com

Received 15 July 2020; Revised 7 August 2020; Accepted 24 August 2020; Published 10 September 2020

Academic Editor: Songtao Lv



The presence of a concealed karst cave above a deep highway tunnel may cause the collapse of the rock mass between the karst cave and tunnel during excavation. Rock mass collapse threatens the safety of tunnel construction personnel. A prediction method of the collapse region induced by a concealed karst cave above a deep highway tunnel is proposed on the basis of the upper bound theorem of limit analysis. An analytical expression of the collapse surface is derived from the variational principle. Using the analytical expression of the collapse surface, the shapes of the collapse surfaces are plotted for different rock mass parameters. Moreover, the minimum safe distance between the karst cave and tunnel is defined, and the computational equation of the minimum safe distance is derived. The proposed method is applied in a highway tunnel excavated in a karst terrain as a case study. Based on geological survey report parameters, the shape of the collapse surface and the minimum safe distance between the karst cave and tunnel are obtained. Finally, the collapse surface of the rock mass provided by the proposed approach is compared with that provided by numerical simulation, and the favorable result comparison shows that the proposed method is valid.

## 1. Introduction

Karst caves are widely present in karst terrains, so karst caves are common in the adjacent regions of planned tunnels or even in the excavated regions of planned tunnels. Most highway tunnels are excavated by drilling and blasting methods. If the karst cave is too close to the planned tunnel, the rock mass between the karst cave and the tunnel may collapse under the effect of the blasting shock. Moreover, karst caves can be filled, and the karst cave fill material would rush into the tunnel instantaneously, which would threaten the personal safety of construction personnel. Even if there is no fill material or the volume of fill material in the karst cave is small, the collapse of the rock mass between the karst cave and the tunnel may damage the construction equipment, which would cause delays in the construction period and economic losses. Figure 1 shows a roof collapse induced by a karst cave located above a highway tunnel during tunnel excavation. Therefore, if we can establish a method to predict the potential collapse location and range for the rock mass between the karst cave and the tunnel, we can adopt countermeasures to avoid the occurrence of collapse during tunnel construction in karst terrains.

Because of the lack of understanding of karst characteristics, great difficulties are encountered in tunnel construction in karst terrains. Understanding the features of karst is a key factor for tunnel construction in karst terrains, and many investigators have realized the aforementioned, and great attention has been paid to this issue. Taking the Yichang–Wanzhou railway tunnel as the engineering background, Fan et al. [1] investigated the main features of karst geological disasters. By studying the influence of several unfavorable geological disasters in tunnel construction, the authors proposed treatment methods for large karst caves, and the validity of the proposed methods was verified based on monitoring data. Because a karst cave may cause geohazards during tunnel excavation in karst terrains, Li et al. [2] used ground-penetrating radar and geological drilling to predict the geometric characteristics and locations of karst caves. By applying the proposed techniques in an actual project, Li et al. [2] found that the karst cave location predicted by their technique agreed well with field

Figure 1: Collapse of the roof induced by a karst cave located above a highway tunnel.

observations. Subsequently, Li et al. [3] proposed a new method to study the mechanism of water and mud inrush during tunnel construction in karst terrains. Using a mud inrush computational model, Li et al. [3] investigated the integral sliding stability of the filling media on the basis of the simplified Bishop method, and their results are consistent with the solutions provided by FLAC3D. In a subsequent study, Li et al. [4] developed a method to predict the top of a concealed karst cave based on displacement monitoring during tunnel construction. To verify the validity of the proposed method, the authors compared the results derived from their method with those provided by numerical simulation. More recently, Li et al. [5] designed a true triaxial geomechanical model test to study the stability of the surrounding rock under the effect of a water-bearing cave in front of the tunnel face. To prevent water and mud inrush during tunnel construction in karst terrains, a computational model is established by Wu et al. [6] to calculate the minimum thickness of the rock stratum between the face and the cave under earthquake action. Considering that the tunnel lining and other structures are designed by a similar theory in actual projects, Tian et al. [7] employed a model experiment to study the combined influence of the surrounding rock parameters on tunnel leakage in a karst area.

Although the stability of a tunnel excavated in a karst area has drawn the attention of many scholars, previous studies were carried out on the basis of the numerical simulation technique and model experiments. However, theoretical studies of the collapse mechanism and range of the surrounding rock induced by a concealed karst cave in tunnel construction are rare. Fraldi and Guarracino [8] developed an analytical approach to determine the range and shape of the possible collapse of a cavity roof induced by excavation. Using the variational principle, the researchers obtained the equation of the collapsing block of the cavity roof on the basis of the limit analysis theorem. Because the collapse mechanism of the surrounding rock proposed by Fraldi and Guarracino [8] was constructed by an arbitrary curve, the final result of the collapsing block derived from optimal calculations was not restricted by a predefined line type. As noted by Huang et al. [9], the advantage of this approach is that the final solution of the shape of the collapsing block is consistent with the collapse observed in actual engineering. Due to the remarkable advantage of this approach, numerous scholars have used this approach to study the collapsing blocks of the roof of the tunnel and rectangular cavity under various complex geological conditions [10–17].

Considering that the variational principle is an effective method to determine the collapse region of the surrounding rock in tunnel construction, investigators used this method to study the collapse region induced by a karst cave in a tunnel excavated in a karst area. If a karst cave is present beneath a deep highway tunnel, there is a risk of collapse of the tunnel floor. In view of this problem, Huang et al. [18] derived an analytical expression of the collapse surface of the rock mass under the tunnel floor by using the variational principle and upper bound theorem. Based on this analytical solution, the range of the collapse region was obtained, and the validation of the analytical solution was proved by comparing it with the numerical simulation solution. Consequently, Yang et al. [19] employed the functional catastrophe theory to investigate the collapse region of the rock mass beneath a tunnel floor in Hoek–Brown (H–B) rock media. Considering that the failure pattern of the surrounding rock is different for different pressures of the filler material in a karst cave, Zhang and Yang [20] constructed a new failure mechanism that reflects active and passive failure patterns of the surrounding rock beneath the tunnel floor. Based on the new failure mechanism, the analytical expressions of the rock mass for active and passive failure patterns are derived, and the influence of different rock parameters on failure is obtained by parameter sensitivity analysis.

Presently, studies of the collapse region of the surrounding rock induced by a concealed karst cave focus on the rock mass located beneath the tunnel floor. However, if a concealed karst cave exists above the tunnel roof, the collapse of the rock mass above the tunnel roof occurs much more easily. In actual engineering, the pressure of the filler material in the karst cave, the gravity of the rock mass, and the blasting shock are three adverse factors that can cause the collapse of the rock pillar between the karst cave and the tunnel roof. Under extreme conditions, the three factors may work simultaneously, thereby enhancing the rock mass collapse. Therefore, it is necessary to develop a theoretical method to study the collapse mechanism of the rock mass induced by a concealed karst cave that is present above the tunnel roof.

This paper aims to investigate the collapse mode of the rock mass between the concealed karst cave and tunnel roof within the framework of the upper bound theorem. A failure mechanism is proposed based on the collapse characteristics of the rock mass induced by the concealed karst cave. Using the failure mechanism and variational principle, the analytical equation of the collapse surface of the rock mass is derived, and the range of the collapse region is obtained. To

apply this method in an actual project, the Wuzhishan highway tunnel, excavated in a karst area, is selected as a case study. Based on a geological survey report and the position of the karst cave encountered during tunnel excavation, the failure mechanism in this actual engineering project is established. An analytical equation of the collapse surface of the rock mass above the Wuzhishan tunnel is derived. Furthermore, to validate the presented method, the obtained result is compared with that derived from the numerical simulation technique.

## 2. Collapse Mechanism of a Highway Tunnel Roof Induced by a Concealed Karst Cave

A schematic diagram of the collapse mode of the rock mass under consideration is illustrated in Figure 2. A highway tunnel is excavated in a karst area, and there is a concealed karst cave just above the tunnel. Under the actions of the filler material pressure in the karst cave and construction disturbances, collapse of the rock mass between the karst cave and the tunnel roof occurs. The rock mass in a certain range would move downwards with velocity $v$ relative to the rest of the surrounding rock. Thus, the rock mass in the collapse range is called the collapsing block, and the boundary of the collapse range can be regarded as the collapse surface. Due to the movement of the collapsing block, a relative sliding movement occurs along the collapse surface, and a plastic flow region is formed in this narrow transition layer, where $e_i$ and $n_i$ are the tangential and normal directions of a random point along the collapse surface direction, respectively.

Because the collapse range is unknown, the collapse surface is assumed to consist of two symmetrical arbitrary curves $f(x)$, thus implying that the curves are not of any predefined line type, which is consistent with the rock mass collapse mode observed in actual projects. Moreover, the collapse surface extends from the tunnel roof to the bottom of the karst cave. As the collapse surface consists of arbitrary curves, the karst cave and tunnel roof locations where the rock mass begins to collapse are random. The final collapse surface of the rock mass and the location where collapse occurs are determined by theoretical calculations.

The karst cave is assumed to be a circle for mathematical convenience and the equation of the circle is $g_2(x)$. $H$ denotes the distance between the bottom of the karst cave and the roof of the tunnel and $l_1$ and $l_2$ are the half-widths of the bottom and top of the collapsing block, respectively. Furthermore, a standard internal contour for a two-lane highway tunnel is shown in Figure 3. It can be seen from the figure that the internal contour of the two-lane highway tunnel is a multicircular cross section, which consists of three arc sections. The longest arc is located at the top of the tunnel, and the same two arcs are located at the sidewalls of the tunnel. $O_1$, $O_2$, and $O_3$ are the centers of the three arcs, while $r_1$ and $r_2$ are the radii of the three arcs. Because the rock mass collapse occurs at the roof of the tunnel, the arc at the top of the tunnel would affect the shape and range of the collapsing block. Therefore, this arc is of most concern, and the equation of this arc is assumed to be $g_1(x)$.

## 3. Calculation of the Collapse Surface of a Highway Tunnel Roof Induced by a Concealed Karst Cave

Because of the relative sliding movement between the collapsing block and the rest of the surrounding rock, energy dissipation would occur along the collapse surface. The upper bound theorem states that the upper bound solution of the equation of the collapse surface can be derived from the relation between the rate of total energy dissipation and the rate of external work. Therefore, the energy dissipation of a random point on the collapse surface should be calculated first. According to Chen [21], the rate of energy dissipation of a random point in the plastic flow region can be determined by the plastic stress/strain rate relation. Moreover, the stress/strain rate relation can be deduced from the normality condition related to the yield function. Because most rock masses in deep strata are intact rock or jointed rock masses, it is necessary to employ a suitable failure criterion to estimate the strength and deformability of the rock masses. However, the H–B failure criterion is a criterion developed to evaluate the rock mass strength for both intact rock and jointed rock masses, and the validity of this criterion has been proven by numerous scholars. Therefore, the H–B failure criterion is used here to evaluate the rock mass strength in the influence region affected by excavation. If the rock mass obeys the H–B failure criterion and its associated flow rule, the plastic potential $\Omega$, which is employed to calculate the stress and plastic strain rate relation, can be written in the following form:

$$\Omega = \tau - A\sigma_{ci}\left(\frac{\sigma_n + \sigma_{tm}}{\sigma_{ci}}\right)^B, \tag{1}$$

where $\tau$ is the shear stress, $\sigma_n$ is the normal stress, and $B$ are material constants, $\sigma_{ci}$ is the uniaxial compressive strength, and $\sigma_{tm}$ is the tensile strength of the rock mass.

According to Fraldi and Guarracino [8], the rate of energy dissipation of a random point on the collapse surface is computed by

$$D = \left(\sigma_n \dot{\varepsilon}_n + \tau \dot{\gamma}_n\right)\omega = \left\{\sigma_{tm} - \sigma_{ci}\left[ABf'(x)\right]^{1/(1-B)}\left(1 - B^{-1}\right)\right\}\frac{1}{\sqrt{1 + f'(x)^2}}v, \tag{2}$$

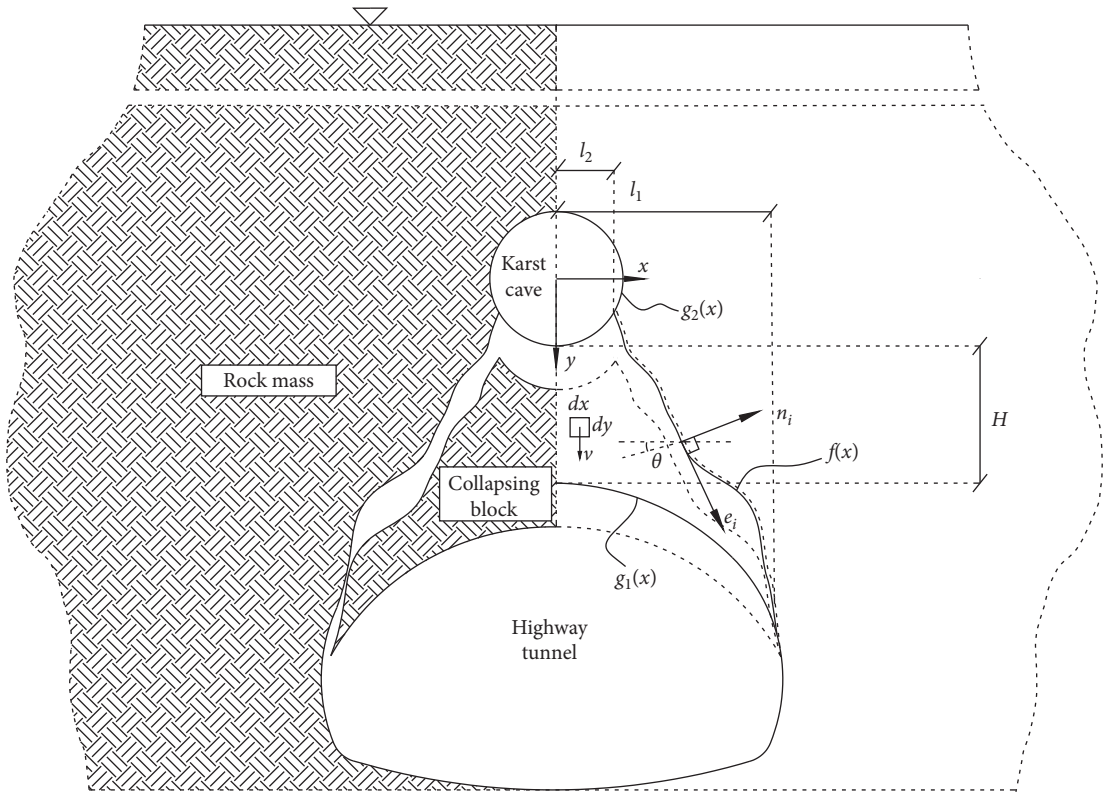


Figure 2: Collapse mechanism of a highway tunnel roof induced by a karst cave.

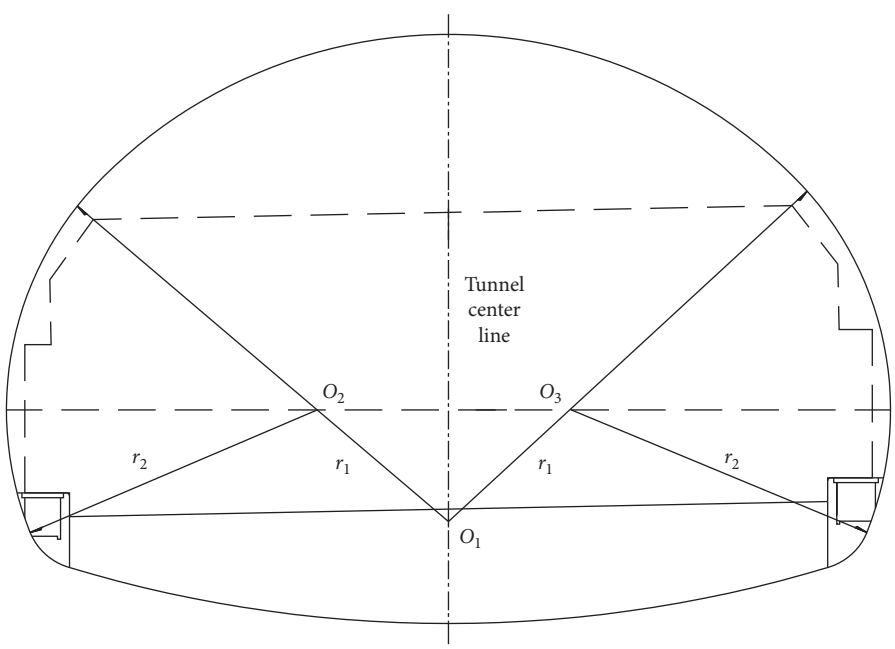


Figure 3: Standard internal contours and construction clearance of a highway tunnel.

where $f'(x)$ is the first derivative of $f(x)$. It can be observed in Figure 1 that the failure mechanism is symmetrical about the $y$-axis, and the energy dissipation and external work rates can be calculated based on half of the failure mechanism for mathematical convenience. The half-rate of energy dissipation along the collapse surface can be obtained by integrating (2) over interval $[l_1, l_2]$, which is expressed in the following form:

$$P_D = \int_{l_2}^{l_1} D\,\mathrm{d}S = \int_{l_2}^{l_1} \left\{\sigma_{tm} - \sigma_{ci}\left[ABf'(x)\right]^{1/(1-B)}\left(1 - B^{-1}\right)\right\} \upsilon \mathrm{d}x. \tag{3}$$

The external forces in this failure mechanism include the gravity of the rock mass, supporting force, and filler material pressure. The total rate of the work in this mechanism is the sum of the rates of work performed by these external forces. The rate of work produced by the self-weight of the half-collapsing block is given by

$$P_\gamma = \left\{\int_0^{l_2} \gamma\left[g_1(x) - g_2(x)\right]\mathrm{d}x + \int_{l_1}^{l_2} \gamma\left[g_1(x) - f(x)\right]\mathrm{d}x\right\} \upsilon, \tag{4}$$

where $\gamma$ is the unit weight of the rock mass. Moreover, the expressions of $g_1(x)$ and $g_2(x)$ are

$$\begin{cases} g_1(x) = H + r_1 + r_3 - \sqrt{r_1^2 - x^2}, \\ g_2(x) = \sqrt{r_3^2 - x^2}, \end{cases} \tag{5}$$

where $r_3$ is the radius of the karst cave. Assuming that the supporting pressure produced by the lining is distributed along the tunnel internal contour in the radial direction, the rate of work for the supporting pressure is

$$P_q = -q\upsilon r_1 \arcsin\frac{l_1}{r_1}, \tag{6}$$

where $q$ is the supporting pressure of the tunnel lining. Assuming that the pressure of the filler material is distributed along the karst cave in the radial direction, the rate of work of the filler material pressure is given by

$$P_T = T\upsilon r_3 \arcsin\frac{l_2}{r_3}, \tag{7}$$

where $T$ is the pressure of the filler material in the karst cave. As stated in the upper bound theorem, the imposed loads cannot be carried by the rock massif; for any assumed failure mechanism, the rate of work conducted by the external forces exceeds the internal rate of energy dissipation. Thus, the first step to calculate the upper bound solution is to establish a virtual work equation composed of the rates of energy dissipation and external work. The virtual work equation, which is the difference between the rate of energy dissipation and the rate of external work, can be written as

$$\xi\left[f(x), f'(x), x\right] = P_D - P_\gamma - P_q - P_T. \tag{8}$$

Substituting equations (3)–(7) into (8), the expression of the virtual work equation is obtained:

$$\begin{aligned} \xi\left[f(x), f\prime(x), x\right] &= \int_{l_2}^{l_1} \left\{\sigma_{tm} - \sigma_{ci}\left[ABf'(x)\right]^{1/(1-B)}\left(1 - B^{-1}\right) + \gamma f(x) - \gamma g_1(x)\right\} \upsilon\,\mathrm{d}x \\ &\quad - \upsilon \int_0^{l_2} \gamma\left[g_1(x) - g_2(x)\right]\mathrm{d}x + q\upsilon r_1 \arcsin\frac{l_1}{r_1} - T\upsilon d_2 \arcsin\frac{l_2}{r_3} \\ &= \int_{l_2}^{l_1} \psi\left[f(x), f'(x), x\right]\upsilon\,\mathrm{d}x - \upsilon \int_0^{l_2} \gamma\left[g_1(x) - g_2(x)\right]\mathrm{d}x + q\upsilon r_1 \arcsin\frac{l_1}{r_1} - T\upsilon r_3 \arcsin\frac{l_2}{r_3}, \end{aligned} \tag{9}$$

where $\psi\left[f(x), f'(x), x\right]$ is a functional that can be written as follows:

$$\psi\left[f(x), f'(x), x\right] = \sigma_{tm} - \sigma_{ci}\left[ABf'(x)\right]^{1/(1-B)}\left(1 - B^{-1}\right) + \gamma f(x) - \gamma g_1(x). \tag{10}$$

Because the virtual work equation includes the first derivative of $f(x)$, the virtual work equation can be regarded as an objective function, which is used to derive the upper bound solution of $f(x)$. Once the virtual work equation is established, the next step is to determine the variable that minimizes or maximizes the objective function. It can be observed that $f(x)$ is the only variable in the objective function $\xi$. Consequently, the real upper bound solution of $f(x)$ is the solution for which the objective function $\xi$ reaches the extremum. Furthermore, the objective function $\xi$ is determined by $\psi$. Therefore, the problem is converted into determining the function $f(x)$ for which $\psi$ reaches the extremum. Based on the variational principle, the functional $\psi$ reaches the extremum when $f(x)$ satisfies the following necessary condition:

$$\frac{\partial\psi}{\partial f(x)} - \frac{\mathrm{d}}{\mathrm{d}x}\left[\frac{\partial\psi}{\partial f'(x)}\right] = 0. \tag{11}$$

Substituting (10) into equation (11), a linear homogeneous second-order differential equation with constant coefficients is obtained:

$$\gamma - \frac{1}{1-B}(AB)^{1/(1-B)}\left[f'(x)\right]^{(2B-1)/(1-B)} f''(x) = 0. \quad (12)$$

By solving this differential equation, the analytical expression of the collapse surface can be written as

$$f(x) = A^{-1/B}\left(\frac{\gamma}{\sigma_{ci}}\right)^{(1-B)/B}\left(x - \frac{c_1}{\gamma}\right)^{1/B} + c_2, \quad (13)$$

where $c_1$ and $c_2$ are two integration constants, and the values of these integration constants can be determined by the boundary conditions. Substituting (13) into (9), the expression of objective function $\xi$ is obtained:

$$\begin{aligned}\xi = {} & (c_2\gamma + \sigma_{tm})(l_1 - l_2)v + \frac{1}{B+1}A^{-1/B}\sigma^{(B-1)/B}\gamma^{1/B}\left[\left(l_1 - \frac{c_1}{\gamma}\right)^{(1+B)/B} - \left(l_2 - \frac{c_2}{\gamma}\right)^{(1+B)/B}\right]v \\ & - \gamma(H + r_1 + r_3)l_1 v + \frac{1}{2}\gamma l_1\sqrt{r_1^2 - l_1^2}v + \frac{1}{2}\gamma r_1^2 \arcsin\left(\frac{l_1}{r_1}\right)v + \frac{1}{2}\gamma l_2\sqrt{r_3^2 - l_2^2}v \\ & + \frac{1}{2}\gamma r_3^2 \arcsin\left(\frac{l_2}{r_3}\right)v + q r_1 \arcsin\left(\frac{l_1}{r_1}\right)v - T r_3 \arcsin\left(\frac{l_2}{r_3}\right)v.\end{aligned} \quad (14)$$

Furthermore, the values of $l_1$ and $l_2$ are undetermined, which means that the karst cave and tunnel roof locations where the rock mass begins to collapse are still unknown. However, the values of $l_1$ and $l_2$ are required to derive the final expression of the collapse surface $f(x)$. Thus, it is necessary to establish the stress boundary condition to determine the values of $l_1$ and $l_2$. Based on the stress distribution rule, there is no distribution of shear stress on the karst cave surface. Therefore, the shear stress of the element at the junction of the collapse surface and the karst cave surface is zero. The stress boundary condition can be expressed as

$$\tau_{xy}\left(x = l_2, y = \sqrt{r_3^2 - l_2^2}\right) = 0, \quad (15)$$

where $\tau_{xy}$ is the shear stress of the element at the junction of the collapse surface and the karst cave surface. According to the equilibrium differential equation, the shear stress of the element mentioned above can be written in the following form:

$$\tau_{xy} = \frac{1}{2}\sigma_n \sin 2\theta - \tau \cos 2\theta, \quad (16)$$

where $\theta$ is the angle between the tangential and vertical directions of a random point on the collapse surface. Based on the trigonometric function, the relationship between $\theta$ and $f\prime(x)$ is given by

$$\begin{aligned}\cos 2\theta &= \frac{f'(x)^2 - 1}{f'(x)^2 + 1}, \\ \sin 2\theta &= \frac{2f'(x)}{f'(x)^2 + 1}.\end{aligned} \quad (17)$$

Substituting equations (16)-(17) and the expression of $f'(x)$ into (15), the value of $c_1$ is obtained as follows:

$$c_1 = \gamma l_2. \quad (18)$$

From Figure 1, it can be seen that a geometric boundary condition should be satisfied. The geometric boundary condition can be expressed as

$$\begin{cases} f(l_1) = H + r_1 + r_3 - \sqrt{r_1^2 - l_1^2}, \\ f(l_2) = \sqrt{r_3^2 - l_2^2}. \end{cases} \quad (19)$$

By substituting (13) and (18) into (19), an equation set that includes three unknowns, $c_2$, $l_1$, and $l_2$, is obtained:

$$\begin{cases} c_2 = \sqrt{r_3^2 - l_2^2}, \\ A^{-1/B}\left(\dfrac{\gamma}{\sigma_{ci}}\right)^{(1-B)/B}(l_1 - l_2)^{1/B} + \sqrt{r_3^2 - l_2^2} = H + r_1 + r_3 - \sqrt{r_1^2 - l_1^2}. \end{cases} \quad (20)$$

Therefore, we have to establish another equation to determine these unknowns. By equating the external rate of work due to external forces to the total internal energy dissipation along the collapse surface, the last equation, which is used to calculate unknowns $c_2$, $l_1$, and $l_2$, is given by

$$\left(\sigma_{tm}+\gamma\sqrt{r_3^2-l_2^2}\right)(l_1-l_2)+\frac{1}{B+1}\sigma_{ci}^{(B-1)/B}A^{-1/B}\gamma^{1/B}(l_1-l_2)^{(1+B)/B}$$
$$-\gamma(H+r_1+r_3)l_1+\frac{1}{2}\gamma l_1\sqrt{r_1^2-l_1^2}+\frac{1}{2}\gamma r_1^2\arcsin\left(\frac{l_1}{r_1}\right)+\frac{1}{2}\gamma l_2\sqrt{r_3^2-l_2^2} \tag{21}$$
$$+\frac{1}{2}\gamma r_3^2\arcsin\left(\frac{l_2}{r_3}\right)+qr_1\arcsin\left(\frac{l_1}{r_1}\right)-Tr_3\arcsin\left(\frac{l_2}{r_3}\right)=0.$$

Combining (20) and (21), a nonlinear equation that can be solved numerically is obtained. Using an iterative algorithm, the numerical solutions of $c_2$, $l_1$, and $l_2$ are obtained. Substituting the values of $c_2$, $l_1$, and $l_2$ into (13), the upper bound solution of the collapse surface $f(x)$ can be expressed as

$$f(x)=A^{-1/B}\left(\frac{\gamma}{\sigma_{ci}}\right)^{(1-B)/B}(x-l_2)^{1/B}+\sqrt{r_3^2-l_2^2}. \tag{22}$$

## 4. The Shape and Range of the Collapse Surface for Different Parameters

The aim of this paper is to study the collapse mode of the rock mass between the concealed karst cave and highway tunnel roof. If the shape and range of the collapse surface are obtained, the collapse mode of the rock mass in this region can be examined intuitively. Based on the analytical equation of collapse surface $f(x)$ expressed in (22), the coordinates of any point on the collapse surface are calculated. Using these point coordinates, the shape and range of the collapse surface can be drawn with the help of computer-aided drawing software. To investigate the influence of different parameters on the collapse surface of the rock mass, the collapse surfaces for parameters corresponding to $A=0.2$–$0.4$, $B=0.6$–$0.8$, $\sigma_{ci}=1$ MPa, $\sigma_{tm}=\sigma_{ci}/100$–$\sigma_{ci}/50$, $T=60$ kPa, $H=13$–$19$ m, $r_1=8.21$ m, $r_3=2.5$ m, and $\gamma=19$–$25$ kN m$^{-3}$ are illustrated in Figures 4–7. Similar to the failure mechanism shown in Figure 2, the collapse surface extends from the tunnel roof to the bottom of the karst cave, which forms an inverted funnel shape. Furthermore, the range of the collapse surface is affected by rock mass parameters $A$, $B$, $\sigma_{ci}$, and $\gamma$. To obtain the change law of the collapse surface range as a function of these parameters, the univariate analysis method is employed in this paper. It can be observed in Figures 4–7 that greater values of $A$ and $\sigma_{tm}$ tend to induce a larger collapse surface range. In contrast, higher values of $B$ and $\gamma$ lead to a decrease in the collapse surface range.

## 5. The Minimum Safe Distance between a Karst Cave and Highway Tunnel

As mentioned above, the distance between a concealed karst cave and the proposed nearby highway tunnel is a major cause that induces the collapse of the rock mass in this region. Numerous investigators have used various methods to study the minimum safe distance between a karst cave and tunnel. However, presently, no theoretical equation can calculate the minimum safe distance between a karst cave and tunnel accurately. To solve this problem, the shapes of the collapse surfaces for different distances between the karst cave and tunnel are investigated. Figure 8 shows that the width of the top of the collapsing block decreases with increasing distance $H$ when the other parameters are fixed. When the distance between the karst cave and tunnel exceeds a critical value, the width of the top of the collapsing block would decrease to zero, which implies that the collapse surface and karst cave intersect at a certain point. If the distance between the karst cave and tunnel continues to increase, the collapse surface would not extend to the karst cave, and the pillar between the karst cave and tunnel will not collapse. Consequently, the critical distance between the karst cave and tunnel for which the collapse surface and karst cave intersect at a certain point can be regarded as the minimum safe distance between the karst cave and highway tunnel. Based on the above assumption, by substituting $l_2=0$ into equations (20)-(21), an equation set that includes two unknowns $l_2$ and $H_{cr}$ is obtained:

$$\begin{cases} A^{-1/B}\left(\dfrac{\gamma}{\sigma_{ci}}\right)^{(1-B)/B}l_1^{1/B}+r_3=H+r_1+r_3\sqrt{r_1^2-l_1^2} \\ (\sigma_{tm}+\gamma r_3)l_1+\dfrac{1}{B+1}\sigma_{ci}^{(B-1)/B}A^{-1/B}\gamma^{1/B}l_1^{(1+B)/B}-\gamma(H+r_1+r_3)l_1 \\ +\dfrac{1}{2}\gamma l_1\sqrt{r_1^2-l_1^2}+\dfrac{1}{2}\gamma r_1^2\arcsin\left(\dfrac{l_1}{r_1}\right)+qr_1\arcsin\left(\dfrac{l_1}{r_1}\right)=0. \end{cases} \tag{23}$$

Because (23) is a nonlinear equation set, the value of $H_{cr}$ can be derived by the numerical method, and $H_{cr}$ is the minimum safe distance between the karst cave and highway tunnel defined in this paper.

Based on the derivation procedure of the minimum safe distance $H_{cr}$, it is found that the value of $H_{cr}$ is determined by several rock mass parameters. Thus, it is necessary to analyze the influence of these parameters on $H_{cr}$. Using (23), $H_{cr}$ for different values of $A$, $B$, $\gamma$, and $\sigma_{tm}$ is plotted in Figure 9. Figure 9 shows that $H_{cr}$ increases with increasing $A$ and $\sigma_{tm}$ but decreases with increasing $B$ and $\gamma$.

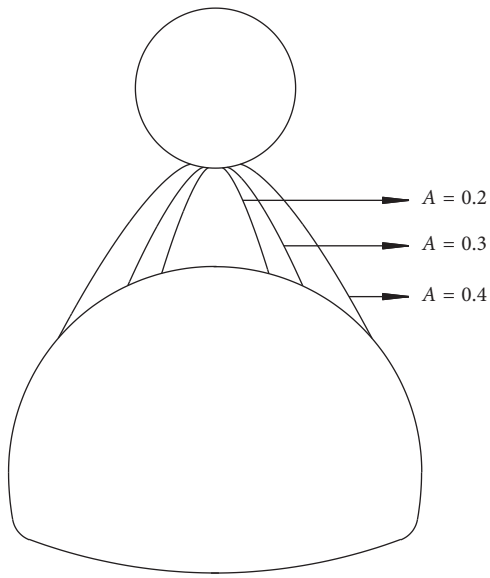


Figure 4: The shape and range of the collapse surface for different values of $A$.

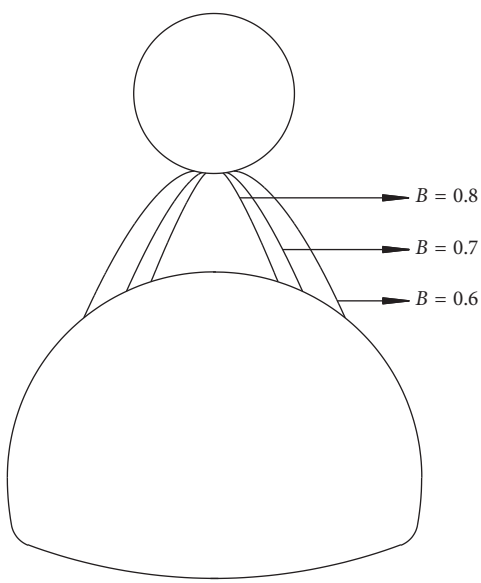


Figure 5: The shape and range of the collapse surface for different values of $B$.

## 6. Application of the Proposed Method in an Actual Engineering Project

To apply the proposed method in actual engineering, a highway tunnel located in a karst area of Guangxi Province is selected as a case study. The engineering geological conditions of this tunnel are described as follows. The Wuzhishan tunnel is a highway tunnel for the Leye-Baise highway in China. The maximum buried depth of the tunnel is 191 m, and the total length is 1230 m. This tunnel is excavated in an area where the surrounding rock has been eroded by tectonic denudation and karst is developed. The principal lithology penetrated by the Wuzhishan tunnel is intermediary weathered limestone and intermediary weathered sandstone. By taking advantage of geophysical prospecting, it was deduced that a karst cave exists above the tunnel roof in the section of KD119 + 319. The engineering geological conditions of this cross section are presented in Figure 10. Figure 10 shows that there is an irregular shape karst cave right above the planned highway tunnel, and the distance between the karst cave and the tunnel is approximately 5.7 m.

Based on the engineering geological and geometric conditions, an upper bound calculation model of this case study is constructed. The shape of the karst cave is simplified as a circle, and the radius of this circle is 3 m. Using the analytical equation of collapse surface $f(x)$ expressed in equation (22) and the rock mass parameters listed in Table 1,

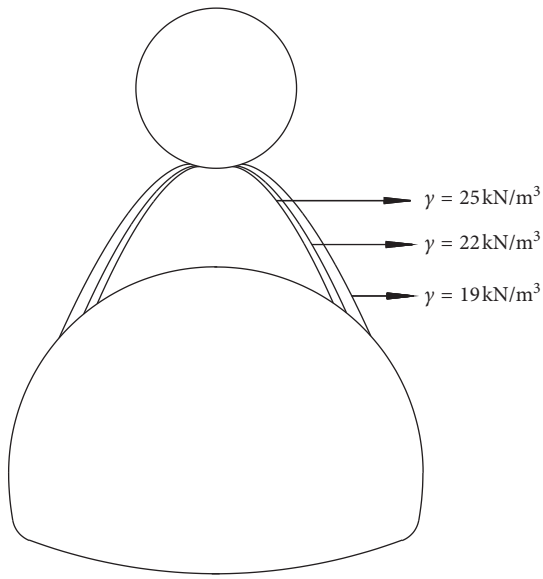


Figure 6: The shape and range of the collapse surface for different values of $\gamma$.

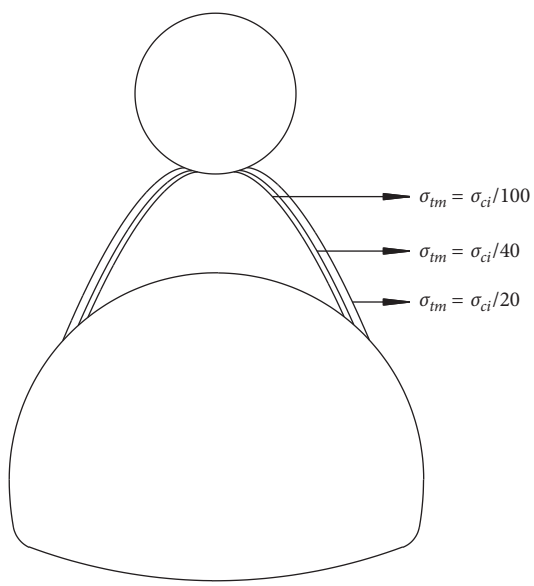


Figure 7: The shape and range of the collapse surface for different values of $\sigma_{tm}$.

the shape and range of the collapse surface for the Wuzhishan tunnel are plotted in Figure 11. From the figure, it is found that a collapse surface extends from the tunnel roof to the bottom of the karst cave, which indicates that the rock mass in this region has a risk of collapse during tunnel excavation. Furthermore, substituting the parameters listed in Table 1 into (23), the minimum safe distance between the karst cave and Wuzhishan tunnel is 5.84 m. According to the definition of the minimum safe distance, rock mass collapse can be avoided if the distance between the karst cave and Wuzhishan tunnel is larger than 5.84 m. Thus, the location of the proposed tunnel can be optimized in the planning stage to reduce the risk of rock mass collapse during tunnel construction.

## 7. Comparison of the Numerical Simulation and Upper Bound Calculation

To verify the proposed method, the results obtained by the upper bound calculation are compared with those provided by numerical analysis using finite difference software FLAC3D. Because the internal contour of the Wuzhishan highway tunnel is multicircular, the tunnel model cannot be constructed by the modeling tool of FLAC3D directly. The tunnel model is constructed by using finite element software ANSYS, and the final model is obtained by importing the data into FLAC3D. The geometrical dimensions of this model are determined by the engineering geological conditions of the Wuzhishan tunnel mentioned above. The

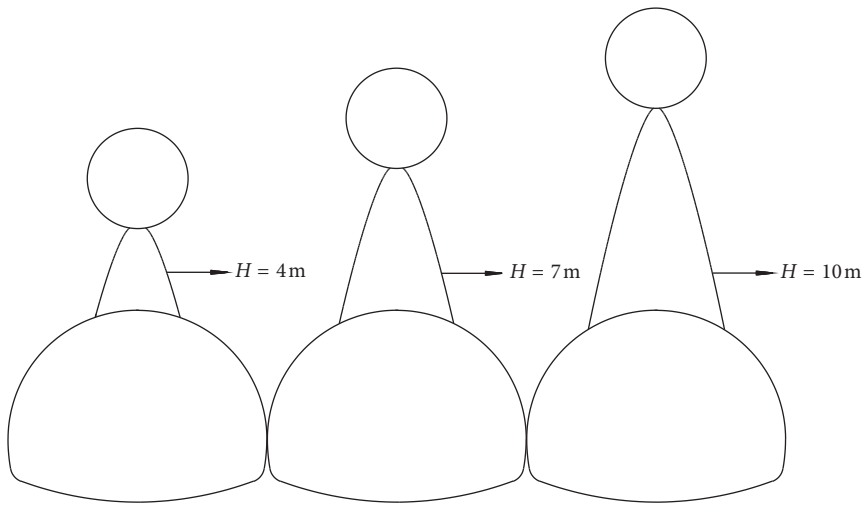


Figure 8: The shape and range of the collapse surface for different values of $H$.

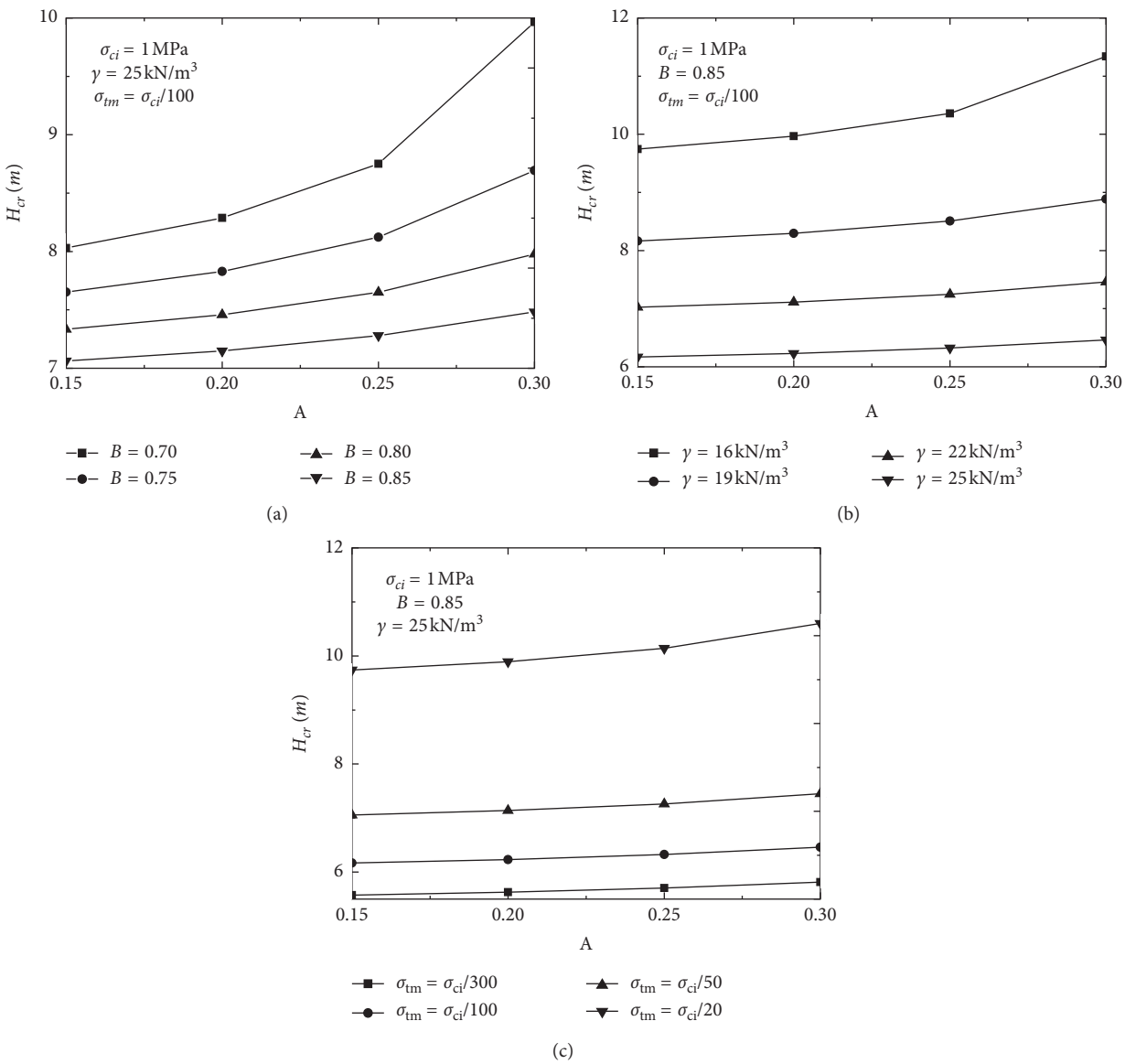


Figure 9: The influence of the different parameters on $H_{cr}$. (a) Influence of the different values of $B$ on $H_{cr}$. (b) Influence of the different values of $\gamma$ on $H_{cr}$. (c) Influence of the different values of $\sigma_{tm}$on $H_{cr}$.

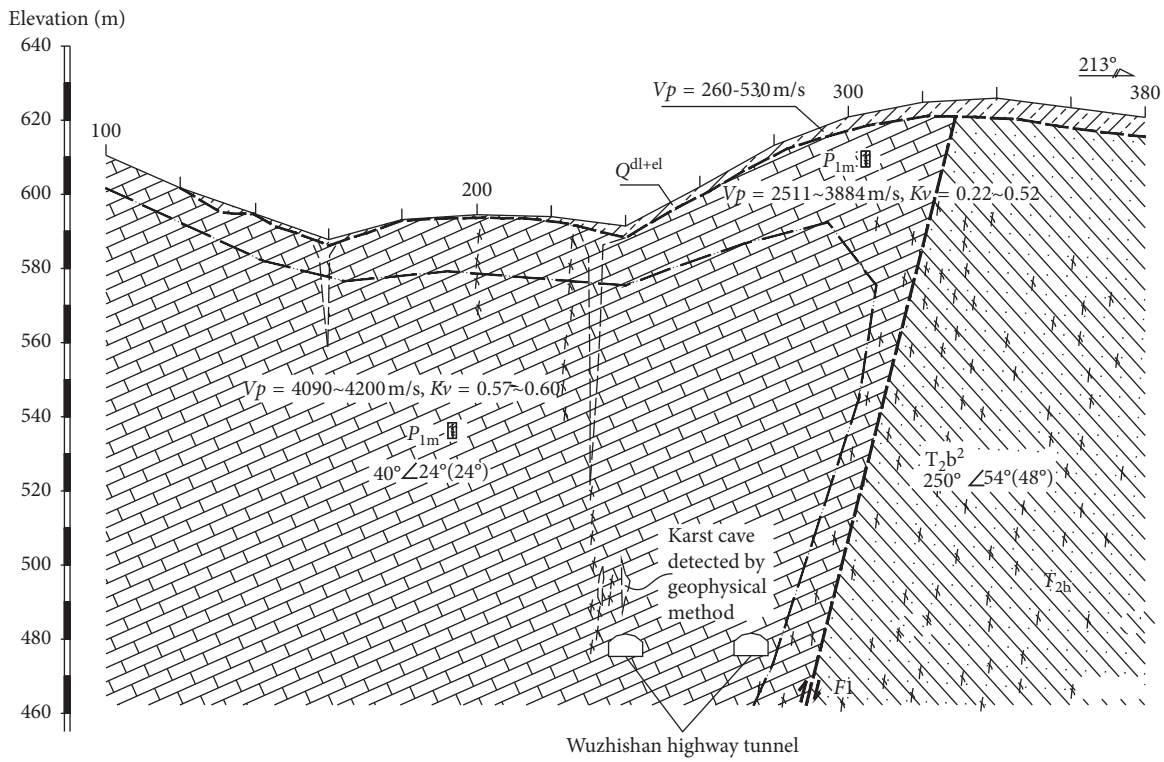


Figure 10: Engineering geological conditions for a certain cross section of the Wuzhishan tunnel.

Table 1: The parameters of rock mass provided by geological survey report of Wuzhishan tunnel.

| $A$ | $B$ | $\mu$ | $\sigma_{ci}$ (MPa) | $\gamma$ (kN/m$^3$) |
|---|---|---|---|---|
| 0.5375 | 0.7816 | 0.3 | 1 | 24 |

whole model is illustrated in Figure 12, and the dimensions of the model are as follows. The dimensions of the numerical model are 80 m in the $X$ direction and 80 m in the $Z$ direction. Because the failure mechanism established in the upper bound calculation is two-dimensional, the dimension of the numerical model in the $Y$ direction is set to 2 m to improve the computational efficiency. The model contains approximately 8823 zones and 13462 nodes. The boundary conditions of the model were assumed as follows: the ground surface is free, and the horizontal displacement in the front and back surfaces and the vertical displacement in the bottom surface of the model are fixed. The multicircular outer contour of the Wuzhishan tunnel is composed of three arc sections. Moreover, the radius of the largest arc is 8.21 m, and the radius of the other two arcs is 5.55 m. To make the numerical model consistent with the upper bound failure mechanism, the karst cave is also assumed to be a circle, and the radius of this circle is 3 m. Based on the geological survey report, the distance between the karst cave and tunnel is approximately 5.7 m. A uniform pressure was applied to the surface of the karst cave to simulate the pressure of the filler material in the karst cave. The excavation process was simplified by assuming that the rock mass located in the excavation region was excavated instantaneously. Simultaneously, a certain uniform pressure was applied to the surface of the excavation region to simulate the supporting pressure produced by the lining of the tunnel, which can be seen in Figure 13.

Because the H–B failure criterion is used in the upper bound calculation, the H–B failure criterion was invoked in the simulation process to compare the upper bound calculation and numerical simulation under the same conditions. Furthermore, the rate of energy dissipation along the collapse surface is associated with the normal stress strain and shear stress strain, and the H–B failure criterion represented by the normal and shear stresses was employed in the upper bound calculation. However, the H–B failure criterion embedded in FLAC3D is represented in terms of the major and minor principal stresses. As the parameters of the H–B failure criterion for the two forms are different, the comparison of the collapse surfaces obtained by the upper bound calculation and numerical simulation cannot be achieved under the same conditions. To solve this discrepancy, Hoek and Brown [22] proposed a method to convert the parameters in one form of the H–B failure criterion into the parameters in another equivalent form. Based on this method, a set of equivalent parameters for the two forms of the H–B failure criterion were obtained, which are summarized in Table 2.

Using the model illustrated in Figure 12 and the parameters listed in Table 3, the rock mass deformation above the tunnel roof during the excavation process is simulated. To obtain the collapse surface of the rock mass in the limit equilibrium state,

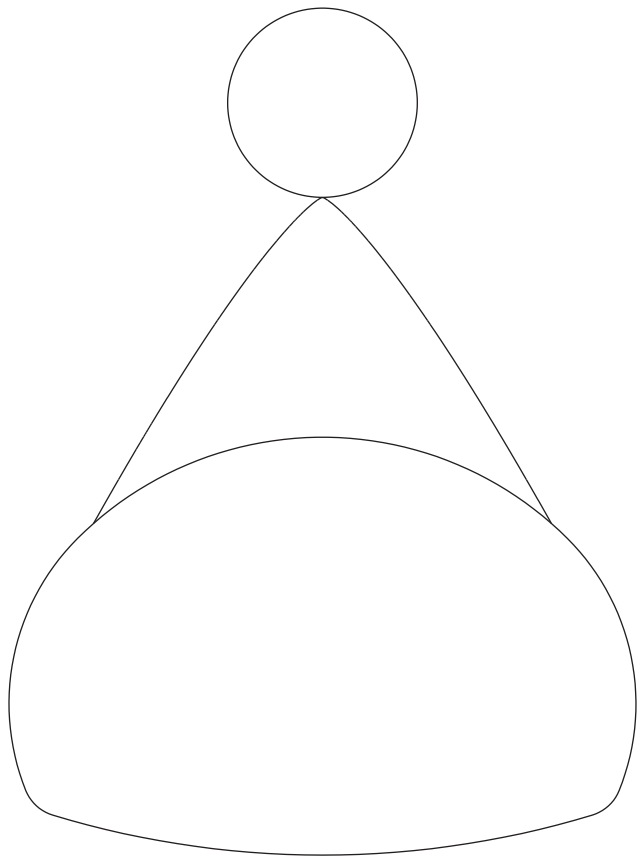

Figure 11: The shape and range of the collapse surface for the Wuzhishan tunnel.

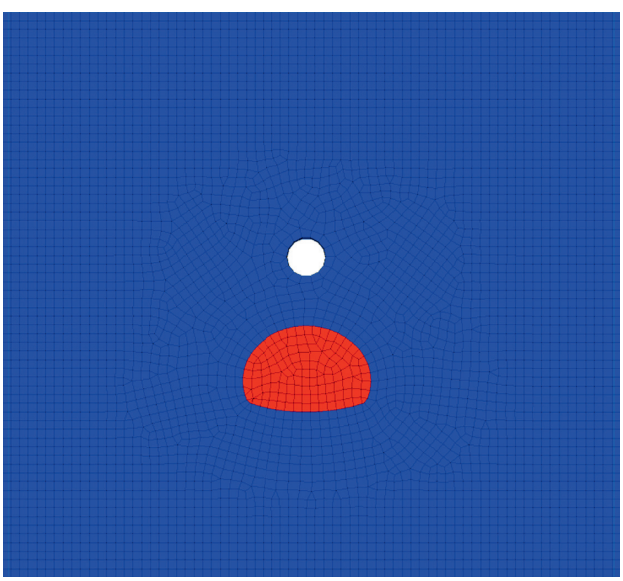

Figure 12: The numerical model of a karst cave above the Wuzhishan tunnel.

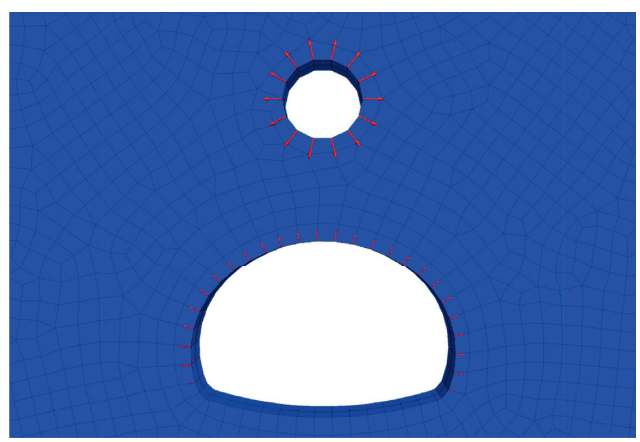

Figure 13: The fill material pressure and supporting pressure in the numerical model.

an indicator should be established to represent the zones in a certain region that enter this state. According to the manual of FLAC3D [23], the failure surface of the rock mass can be determined by the maximum shear strain value, and the maximum shear strain value can be represented by shear strain contours. Furthermore, numerous scholars have also used the shear strain contours provided by FLAC3D to define the failure surfaces of slopes [24–27]. Consequently, the contours of the maximum shear strain increment of the whole model are plotted to determine the collapse surface in the limit equilibrium state, as shown in Figure 14. It is clear that there are two shear failure belts extending from the tunnel roof to the bottom of the karst cave. The shear failure belts are symmetrical about the $z$-axis, whose shape is similar to the collapse surface derived from

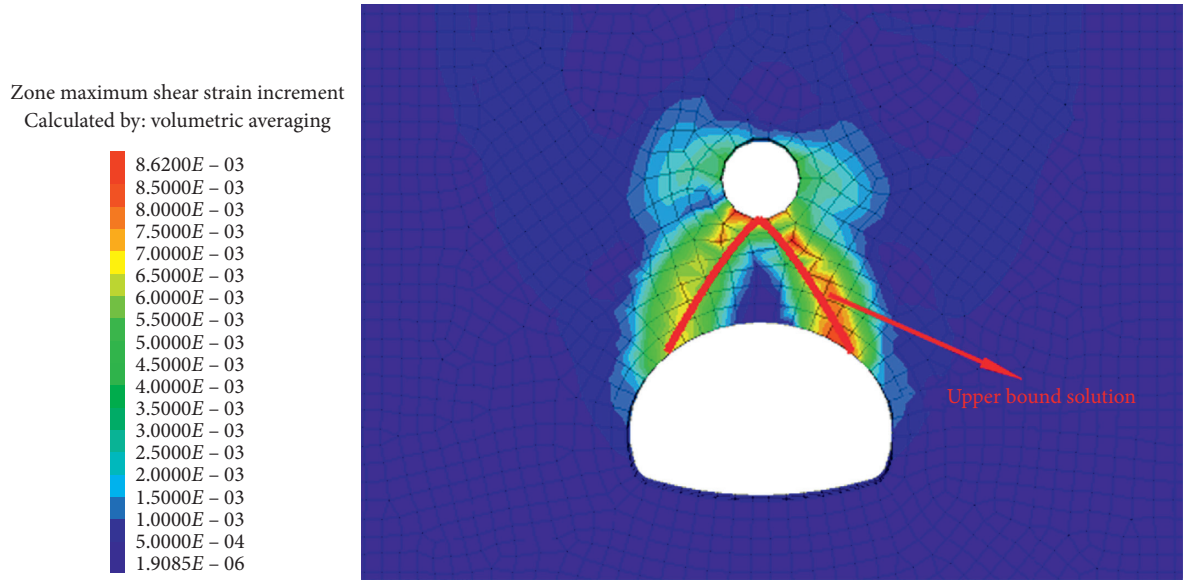


Figure 14: Comparison of the collapse surface of a highway tunnel roof provided by the upper bound theorem and the numerical simulation.

Table 2: Equivalent parameters for the two forms of the H–B failure criterion.

| | |
|---|---|
| $A$ | 0.5375 |
| $B$ | 0.7816 |
| $\sigma_{ci}$ | 1 MPa |
| $\sigma_{tm}$ | $\sigma_{ci}/100$ |
| $a$ | 0.575 |
| $m_b$ | 1.5 |
| $S$ | 0 |
| $\sigma_{ci}$ | 1 MPa |
| $GSI$ | 15 |

Table 3: The parameters used in the numerical simulation.

| $\gamma$ (kN/m$^3$) | $E$ (GPa) | $\mu$ | $\sigma_{ci}$ (MPa) | $A$ | $m_b$ | $s$ |
|---|---|---|---|---|---|---|
| 24 | 0.4 | 0.3 | 1 | 0.575 | 1.5 | 0 |

the upper bound calculation. To better compare the collapse surface provided by the upper bound theorem and that provided by numerical simulation, the upper bound solution of the collapse surface is plotted using red curves and superimposed on Figure 14 with the equivalent parameters listed in Table 2. Clearly, the collapse surface provided by the upper bound calculation approximately coincides with the shear failure belts. The similarity between the collapse surfaces provided by the upper bound solution and numerical simulation shows that the proposed method in this paper is valid.

## 8. Conclusions

For a tunnel excavated in a karst terrain, excavation may induce collapse of the surrounding rock, which poses a threat to the personal safety of construction personnel. A possible prediction method of the collapse region induced by a concealed karst cave above a deep highway tunnel is presented within the framework of the upper bound theorem of limit analysis. A new failure mechanism composed of arbitrary curves is proposed to describe the collapse mode of the rock mass between the karst cave and tunnel. Based on the failure mechanism, an objective function including the equation of the collapse surface is derived from the relation between the rates of total energy dissipation and external work. The analytical expression of the collapse surface is obtained on the basis of the variational principle.

Using the analytical expression of the collapse surface, the shapes of the collapse surfaces for different parameter values are plotted. By studying the change law of the collapse surface as a function of these parameters, it is found that the collapse surface increases with increasing $A$ and $\sigma_{tm}$ but decreases with increasing $B$ and $\gamma$. Furthermore, a definition of the minimum safe distance between the karst cave and tunnel is proposed, and the computational equation of the minimum safe distance is derived.

Based on the geological survey report of a highway tunnel excavated in Guangxi Province, the collapse surface of the rock mass above this tunnel is calculated to verify the practicality of the proposed method. Moreover, the computed result of the proposed approach is compared with that derived from the numerical simulation technique under the same conditions. The similarity between the collapse surface results obtained by the upper bound solution and numerical simulation indicates that the proposed method is valid.

## Data Availability

The data used to support the findings of this study are available from the corresponding author upon request.

## Conflicts of Interest

The authors declare that there are no conflicts of interest regarding the publication of this paper.

## Acknowledgments

This study was supported by the National Natural Science Foundation of China (Grants 51878074 and 51678071). Their financial support is greatly appreciated.

## References

[1] H. B. Fan, Y. H. Zhang, S. Y. He et al., "Hazards and treatment of karst tunneling in Qinling-Daba mountainous area: overview and lessons learnt from Yichang-Wanzhou railway system," *Environmental Earth Sciences*, vol. 77, no. 19, pp. 1–18, 2018.

[2] S. C. Li, Z. Q. Zhou, Z. H. Ye, L. P. Li, Q. Q. Zhang, and Z. H. Xu, "Comprehensive geophysical prediction and treatment measures of karst caves in deep buried tunnel," *Journal of Applied Geophysics*, vol. 116, pp. 247–257, 2015.

[3] S. C. Li, P. Lin, Z. H. Xu et al., "Innovative method for the integral sliding stability analysis of filling media in karst caves and its applications in engineering," *International Journal of Geomechanics*, vol. 17, no. 12, 2017.

[4] S. C. Li, J. Wu, Z. H. Xu, L. Zhou, and B. Zhang, "A possible prediction method to determine the top concealed karst cave based on displacement monitoring during tunnel construction," *Bulletin of Engineering Geology and the Environment*, vol. 78, no. 1, pp. 341–355, 2019.

[5] S. Li, C. Gao, Z. Zhou et al., "Analysis on the precursor information of water inrush in karst tunnels: a true triaxial model test study," *Rock Mechanics and Rock Engineering*, vol. 52, no. 2, pp. 373–384, 2019.

[6] J. Wu, S.-C. Li, Z.-H. Xu, and J. Zhao, "Determination of required rock thickness to resist water and mud inrush from karst caves under earthquake action," *Tunnelling and Underground Space Technology*, vol. 85, pp. 43–55, 2019.

[7] Q. Tian, J. Zhang, and Y. Zhang, "Similar simulation experiment of expressway tunnel in karst area," *Construction and Building Materials*, vol. 176, pp. 1–13, 2018.

[8] M. Fraldi and F. Guarracino, "Limit analysis of collapse mechanisms in cavities and tunnels according to the Hoek-Brown failure criterion," *International Journal of Rock Mechanics and Mining Sciences*, vol. 46, no. 4, pp. 665–673, 2009.

[9] F. Huang, R. C. Ou, Z. L. Li et al., "Limit analysis for the face stability of a shallow-shield tunnel based on a variational approach to the blow-out failure mode," *International Journal of Geomechanics*, vol. 18, no. 6, 2018.

[10] M. Fraldi and F. Guarracino, "Limit analysis of progressive tunnel failure of tunnels in Hoek-Brown rock masses," *International Journal of Rock Mechanics and Mining Sciences*, vol. 50, pp. 170–173, 2012.

[11] K. Guan, W. C. Zhu, L. L. Niu, and Q. Y. Wang, "Three-dimensional upper bound limit analysis of supported cavity roof with arbitrary profile in Hoek-Brown rock mass," *Tunnelling and Underground Space Technology*, vol. 69, pp. 147–154, 2017.

[12] Y. X. Li and C. Yao, "Collapse mechanism of deep tunnels with three-centered arch cross section," *Journal of Central South University*, vol. 23, no. 12, pp. 3293–3301, 2017.

[13] C. Qin and S. C. Chian, "Revisiting crown stability of tunnels deeply buried in non-uniform rock surrounds," *Tunnelling and Underground Space Technology*, vol. 73, pp. 154–161, 2018.

[14] C. B. Qin, S. C. Chian, and X. L. Yang, "3D limit analysis of progressive collapse in partly weathered Hoek–Brown rock banks," *International Journal of Geomechanics*, vol. 17, no. 7, 2017.

[15] C. B. Qin, X. L. Yang, Q. J. Pan, Z. B. Sun, L. L. Wang, and T. Miao, "Upper bound analysis of progressive failure mechanism of tunnel roofs in partly weathered stratified Hoek-Brown rock masses," *International Journal of Rock Mechanics and Mining Sciences*, vol. 74, pp. 157–162, 2015.

[16] H. T. Wang, L. G. Wang, S. C. Li, Q. Wang, P. Liu, and X. J. Li, "Roof collapse mechanisms for a shallow tunnel in two-layer rock strata incorporating the influence of groundwater," *Engineering Failure Analysis*, vol. 98, pp. 215–227, 2019.

[17] X. L. Yang and K. F. Li, "Roof collapse of shallow tunnel in layered Hoek-Brown rock media," *Geomechanics and Engineering*, vol. 11, no. 6, pp. 867–877, 2016.

[18] F. Huang, L. Zhao, T. Ling, and X. Yang, "Rock mass collapse mechanism of concealed karst cave beneath deep tunnel," *International Journal of Rock Mechanics and Mining Sciences*, vol. 91, pp. 133–138, 2017.

[19] X. L. Yang, Z. W. Li, Z. A. Liu, and H. B. Xiao, "Collapse analysis of tunnel floor in karst area based on Hoek-Brown rock media," *Journal of Central South University*, vol. 24, no. 4, pp. 957–966, 2017.

[20] R. Zhang and X. L. Yang, "New 3D failure analysis of water-filled karst cave beneath deep tunnel," *Geomechanics and Engineering*, vol. 18, no. 1, pp. 1–9, 2019.

[21] W. F. Chen, *Limit Analysis and Soil Plasticity*, Elsevier, Amsterdam, Netherlands, 1975.

[22] E. Hoek and E. T. Brown, "Practical estimates of rock mass strength," *International Journal of Rock Mechanics and Mining Sciences*, vol. 34, no. 8, pp. 1165–1186, 1997.

[23] Itasca Consulting Group Inc., *Manual of Fast Lagrangian Analysis of Continua in 3 Dimensions [Computer Program]. Version 5.0*, Itasca Consulting Group Inc., Minneapolis, MI, USA, 2012.

[24] M. Karray, M. N. Hussien, M. Souilem, P. Locat, and R. Mompin, "Adjustment of spectral pseudo-static approach to account for soil plasticity and zone seismicity," *Canadian Geotechnical Journal*, vol. 56, no. 2, pp. 173–186, 2019.

[25] B. Li, Z. Feng, G. Z. Wang et al., "Processes and behaviors of block topple avalanches resulting from carbonate slope failures due to underground mining," *Environmental Earth Sciences*, vol. 75, no. 8, pp. 694–720, 2016.

[26] P. P. Oreste and D. Dias, "Stabilisation of the excavation face in shallow tunnels using fibreglass dowels," *Rock Mechanics and Rock Engineering*, vol. 45, no. 4, pp. 499–517, 2012.

[27] J. Shen and M. Karakus, "Three-dimensional numerical analysis for rock slope stability using shear strength reduction method," *Canadian Geotechnical Journal*, vol. 51, no. 2, pp. 164–172, 2014.

Hindawi
Advances in Civil Engineering
Volume 2020, Article ID 8850436, 11 pages
https://doi.org/10.1155/2020/8850436

*Research Article*

# The Effects of Different Nanoadditives on the Physical and Mechanical Properties of Similar Silty Mudstone Materials

**Ji-jing Wang**,[1] **Zhen-ning Shi**,[2] **Ling Zeng**,[3] **and Shuang-xing Qi**[3]

[1]*School of Traffic & Transportation Engineering, Changsha University of Science & Technology, Changsha 410114, China*
[2]*School of Traffic & Transportation Engineering, National Engineering Laboratory of Highway Maintenance Technology, Changsha University of Science & Technology, Changsha 410114, China*
[3]*School of Civil Engineering, Changsha University of Science & Technology, Changsha 410114, China*

Correspondence should be addressed to Zhen-ning Shi; shizhenning@126.com and Ling Zeng; zl001@csust.edu.cn

Received 18 June 2020; Revised 15 July 2020; Accepted 26 July 2020; Published 11 August 2020

Academic Editor: Songtao Lv



In order to analyze the influence of different nanoadditives on the physical and mechanical properties of similar silty mudstone materials, nano-$TiO_2$ (NTi), nano $Al_2O_3$ (NAl), and nanobentonite (NBe) were added to improve the physical and mechanical properties of silty mudstone similar materials. The physical and mechanical parameters are more in line with silty rock. Finally, nanometer additives suitable for silty mudstone similar materials are determined by conducting density test, natural water absorption test, uniaxial compression test, splitting test, softening coefficient test, expansibility test, and microscopic test. The effects of adding NTi, NAl, and NBe on improving the physical and mechanical properties of silty mudstone similar materials were studied to analyze the influence law of different NTi, NAl, and NBe contents on similar material density, natural water absorption, uniaxial compressive strength, tensile strength, softening coefficient, expansion rate, and other physical and mechanical parameters. The microscopic morphology of similar materials was analyzed by scanning electron microscopy and the mechanism of influence of nanoadditives on the microscopic structure of samples was revealed. The results are as follows. (1) The density of similar materials of silty mudstone increases with the increase of the content of nanoadditive. The natural water absorption rate decreased first and then increased with the increase of the content of nanometer additives, while the softening coefficient decreased with the increase of the content of nanometer additives. The uniaxial compressive strength and tensile strength increased first and then decreased with the increase of the content of nanometer additives. This is due to the incorporation of the nanoadditive amount effective to promote the hydration reaction of gypsum and accelerate the production of cement, while a similar material may be filled in the pores, reducing the internal defects, a similar material to make denser; when excessive dosage, nanoadditives agglomeration occurs, resulting in deterioration of the effect, but will reduce the mechanical properties of similar materials. (2) When the content of NBe is 6%, the physical and mechanical parameters of similar materials can reach or be closer to the silty raw rock except uniaxial compressive strength. The failure mode of the uniaxial compression specimen is also the same as that of the original rock, which can be used as the best choice. The research results laid the foundation for further analysis of NBe application in similar materials.

## 1. Introduction

In the experimental study on the ratio of similar materials in silty mudstone, gypsum is used as the binder, and barite powder is used as the aggregate to make similar materials. Because the physical and mechanical parameters of similar materials such as density, natural water absorption, uniaxial compressive strength, softening coefficient, and swelling are quite different from those of the silty Original rock, they cannot represent the physical and mechanical characteristics of the natural rock and affect the accuracy of model tests. The existing related research shows that choosing appropriate additives to incorporate into similar materials can improve the related physical and mechanical properties of similar materials of silty mudstone [1, 2]. In recent years, with the rapid development of nanotechnology, the production cost

of nanomaterials has been decreasing year by year. At the same time, nanomaterials have shown physical effects that some macroscopic materials do not have, such as small size, large specific surface area, and high surface energy, and have been widely concerned [3]. The nanomaterials, often used as inorganic additives, are being widely used in housing, water conservancy, bridge, municipal, and other projects, which has achieved good application results [4–8].

At present, the appropriate amount of nanoadditives in the existing materials can effectively improve the relevant physical and mechanical parameters of the materials, formulate mixed materials suitable for different needs, and increase the scope of the original materials [9–14]. In terms of improving the cement substrate, Wang et al. found that adding nano-$CaCO_3$ into Portland cement can significantly improve the mechanical properties of cement-based materials and make the cement substrate more uniform. In [15–20], the control effect of mixing nano-$SiO_2$, nano-$TiO_2$, and nano-$Al_2O_3$ materials on water loss in oil well cement slurry was analyzed. The three nanoadditives mentioned above can effectively control the loss of liquid in cement when used separately, among which 3% nano-$SiO_2$ can reduce the amount of loss by 72%, with the most obvious effect. In terms of improving the performance of mixed materials, Anuj [21] found that, in the study of the properties of mixed materials, adding appropriate nanometer additives can not only promote hydration reaction but also play a role in filling the original micropores of the materials, thus improving the internal pore structure and significantly improving the physical and mechanical properties of the materials [22, 23]. In summary, the current research on the improvement of the physical and mechanical properties of related materials by different types of nanoadditives has obtained certain research results [24]. The incorporation of nanoadditives is mainly to improve the physical and mechanical properties of the materials, thereby increasing the range of materials used; however, about incorporating suitable nanoadditives, to improve the physical and mechanical properties of silty mudstone similar materials, studies on the effects of different types of nanoadditives on the physical and mechanical properties of similar silty mudstone materials are rarely involved [25, 26].

In order to deeply analyze the effects of different types of nanoadditives on the physical and mechanical properties of similar silty mudstone materials, based on the existing research results of similar silty mudstone materials [27, 28] on the basis of research results, using common NTi and NAl and Nbe additive for silty mudstone similar to the analysis of the physical and mechanical properties of related materials, and reveal its microcosmic mechanism, the following are carried out. Firstly, the scheme of mixing ratio of similar materials with different dosage of nanoadditives was designed. The effects of nanometer additives on the density, natural water absorption, uniaxial compressive strength, tensile strength, softening coefficient, and expansibility of similar materials were analyzed, and the effects of different nanometer additives on similar materials were analyzed. Finally, the influence mechanism of nanoadditives on the microstructure of silty mudstone was revealed by SEM. It provides some guidance for the application of nanometer additives in similar materials.

## 2. Test Content

### 2.1. Sample Preparation

*2.1.1. Raw Materials.* Similar to the materials of silty mudstone, barite powder is used as aggregate and gypsum is used as cementing material. Among them, the barite powder is produced by Hebei Lingshou, and its particle size is between 2 and 32 $\mu$m. And the chemical composition is shown in Table 1. The cementing material uses ultrahigh-strength gypsum with a particle size between 100 and 600 $\mu$m, and its chemical composition is shown in Table 2. The experiment used tap water for the laboratory.

*2.1.2. Nanometer Additive Material.* The additives mainly include NTi, NAl, and NBe. NTi is a kind of white loose powder material with hydrophilicity, good dispersion, and weather resistance. The particle diameter is between $25 \pm 5$ nm, the relative molecular weight is 79.9, the appearance is white, the specific surface area is 80~85 $m^2/g$, and the purity is greater than 99.9%. NAl is a new type of ultrafine white crystal powder material with a particle size between 30 and 60 nm, a relative molecular weight of 101.96 nm, an average particle size of 50 nm, a specific surface area of 5~10 $m^2/g$, and a purity greater than 99.99%. The particle size of the nanobentonite is between 40~80 nm, with an average particle size of 60 nm. It is a white and light yellow powder with a good ability to bind water. The main composition of the NBe is more than 90% montmorillonite and a small amount of illite, kaolinite, and other minerals.

*2.1.3. Preparation of Similar Materials.* In order to study the physical and mechanical effects of nanomaterial additives (including NTi, NAl, and NBe) on the physical and mechanical effects of similar of silty mudstone, the dosage of different types of nanometer additives was set as 0 (control group), 2%, 4%, 6%, and 8% in the sample preparation process, respectively. The mixing scheme of similar materials is shown in Table 3.

*2.2. Test Plan.* In the process of testing the physical and mechanical properties of similar materials with different nanometer additives, the density, natural water absorption rate, uniaxial compressive strength, tensile strength, softening coefficient, and expansibility of the samples were mainly measured. The specific test plan is shown in Table 4 below. In order to analyze the influence mechanism of nanometer additives on the physical and mechanical properties of similar materials, uniaxial compression tests were carried out on the samples with different dosage of nanometer additives, and SEM tests were carried out on the typical damaged samples. Each group of samples is cured to a specified age in a standard curing box and tested according to the test regulations recommended by the international society for rock mechanics (IRSM) [29]. There are 5 parallel

Table 1: The chemical composition of barite powder (mass fraction) (%).

| $BaSO_4$ | $SiO_2$ | $Fe_2O_3$ | $Al_2O_3$ | Water soluble salt | Other |
|---|---|---|---|---|---|
| 98.00 | 0.40 | 0.05 | 0.01 | 0.20 | <1% |

Table 2: The chemical composition of ultrahigh-strength gypsum (mass fraction) (%).

| $SO_3$ | CaO | $SiO_2$ | $Al_2O_3$ | $Na_2O$ |
|---|---|---|---|---|
| 53.10 | 40.00 | 0.17 | 0.05 | 0.04 |
| $K_2O$ | SrO | $Fe_2O_3$ | MgO | Other |
| 0.04 | 0.04 | 0.03 | 0.02 | <1% |

Table 3: The mixture ratio of similar materials with different dosages of nanoadditives. *Note*. Quality of Barite powder + Quality of Gypsum = 400g.

| Level | Raw material content | | | |
|---|---|---|---|---|
| | Water/(g) | Barite powder/(%) | Gypsum/(%) | Nanometer additive/(g) |
| NA0 | 20 | 36 | 64 | 0 |
| NA1 | 20 | 36 | 64 | 2 |
| NA2 | 20 | 36 | 64 | 4 |
| NA3 | 20 | 36 | 64 | 6 |
| NA4 | 20 | 36 | 64 | 8 |

Table 4: Test schemes.

| Test plan | Expansibility test | Splitting test | Density test | Natural water absorption test | Uniaxial compression test | Softening coefficient test | |
|---|---|---|---|---|---|---|---|
| Test unit number | NTi | A1-1 ~ 1–5 | A2-1 ~ 2–5 | A3-1 ~ 3–5 | A4-1 ~ 4–5 | A5/6–1 ~ 5/6–5 | |
| | NAl | B1-1 ~ 1–5 | B2-1 ~ 2–5 | B3-1 ~ 3–5 | B4-1 ~ 4–5 | B5/6–1 ~ 5/6–5 | |
| | NBe | C1-1 ~ 1–5 | C2-1 ~ 2–5 | C3-1 ~ 3–5 | C4-1 ~ 4–5 | C5/6–1 ~ 5/6–5 | |
| Sample setting within the group | Each group of five diameters of 50 mm and heights of 50 mm sample | Each group of five diameters of 50 mm and heights of 100 mm sample | | | | | |
| Initial state | The standard specimen after curing has reached the age | | | | | | |
| Dry (h) | —— | —— | —— | —— | —— | 48 | —— |
| Flooding (h) | 48 | —— | —— | 48 | —— | —— | 48 |
| Test content | Inflation rate | Tensile strength | First measure the density, then measure the natural water absorption | | SEM test is carried out on damaged samples | | (Saturated) Uniaxial compressive strength |

samples in each group, and the average values of the 3 samples closest to each other are taken as the experimental results. Due to the large number of samples and batch production, only parts of the finished samples are shown (Figure 1).

*2.3. Test Equipment.* According to the test scheme in Table 4, different groups of the standard age samples with different types and dosage of nanoadditives were tested. During the immersion process, the temperature is controlled at 25 ± 5°C by using a three-use water tank (as shown in Figure 2(a)). After immersing the sample for 48 h, it is fully saturated. The device can better control the immersion time and water pressure; during the drying process in the experiment, place the cured standard test in an electric thermostatic drying oven at 60 ± 5°C (as shown in Figure 2(b)) for 48h, then move it to a glass dryer to cool for 48h (as shown in Figure 2(c)). The uniaxial compression test in this paper adopts the MTS-810 electrohydraulic servo system testing machine in the highway engineering experimental center of Changsha University of Science and Technology (as shown in Figure 2(d)) to load the sample. According to the engineering rock mass test method standard, the loading speed of 0.8 MPa/s is set to apply axial pressure to the sample.

Figure 1: Standard samples of similar materials with different contents of nanometer.


Figure 2: Test equipment: (a) three tanks; (b) electric constant temperature drying oven; (c) glass dryer; (d) MTS-810 electrohydraulic servo system testing machine.

## 3. Similar Material Optimization Experiment

*3.1. Effects of Different Nanoadditives on Physical Properties of Similar Materials.* Test the density of similar material samples with different nanoadditive dosages. The test results are shown in Figure 3. (1) With the addition of three nanoadditives in the same amount, compared with the control group, the effects of NAl on the density of similar materials are the most significant, followed by MBe and the minimum is NTi. (2) When the dosage of different nanoadditives increases from 0% to 6%, the density of similar materials increases with the continuous increase of the dosage of nanoadditives. (3) When the dosage is between 6% and 8%, similar materials are gradually increasing trend in density tends to 0. When incorporated into 8%, compared with the control group, NTi, NAl, and NBe, respectively, from 2.01 g/cm$^3$ it increased to 2.16 g/cm$^3$, 2.30 g/cm$^3$, and 2.26 g/cm$^3$. When 6% NBe is added, the density of similar materials is closest to the average density of silty original rocks [30]. It shows that all the three kinds of nanoadditives can effectively fill the pores between barite powder and gypsum particles so that the structure of similar material samples is more compact, and nanoadditives fully fill the pores of similar material samples, increasing the density.

*3.2. Effect of Different Nanoadditives on Natural Water Absorption of Similar Materials.* The natural water absorption rate reflects the water absorption capacity of dry similar material samples, which can effectively reflect the development degree of the material's microcracks. According to the test requirements of "Road Engineering Rock Test Regulations" (JTG E41-2005) [26], the free water absorption method was used to determine the water absorption of similar materials with different types of nanoadditives. The test results are shown in Figure 3.

From the effect of different nanoadditive dosages on the natural water absorption of similar materials, as shown in Figure 4 (1) as the nanoadditive dosage increases, the natural water content of samples of similar materials tends to decrease first and then increase; (2) when the dosage is 4%, the natural water absorption of the similar material sample doped with NTi reaches the minimum, followed by NAl, and the maximum is NBe, which is reduced by 0.23%, 0.12%, and 0.08% compared with the control group; (3) when the doping amount is 8%, the natural water absorption of similar material samples doped with NTi, NAl, and NBe increases from 6.16% to 5.93%, 6.04%, and 6.15% respectively. However, when the doping amount is 6%, the natural water absorption rate of similar material samples is close to the average value of silty raw rocks. It shows that the incorporation of nanoadditives can effectively fill the pores of samples of similar materials and reduce the natural water absorption rate of samples. However, with the increase of nanoadditives, excess nanoadditive materials increase the natural water absorption rate of samples.

*3.3. Effect of Different Nanoadditives on Expansion Rate of Similar Materials.* The specific changes of the expansion rate of similar materials under different nanoadditive dosages are shown in Figure 4. It can be seen from Figure 5 that (1) the expansion rate of samples of similar materials is increasing with the increase of three nanoadditives, in which the addition of NBe has the greatest influence on the expansion rate of the sample, followed by the effect of NAl, and the effect of NTi is the least; (2) compared with the control group, when 8% NTi, NAl, and NBe are added, the expansion rates of similar material samples increase by 0.028%, 0.035%, and 0.078% in sequence; (3) the expansion rate of silty primary rock is about 0.16%, while the similar material after incorporation of 6% NBe is 0.16% close to the original rock. It shows that the incorporation of nano-NBe has the most significant effect on increasing the water absorption expansion rate of similar materials mainly because the NBe itself has strong water absorption expansion characteristics.

*3.4. Effect of Different Nanoadditives on Mechanical Properties of Similar Materials*

*3.4.1. Effect of Different Nanoadditives on the Uniaxial Compressive Strength of Similar Materials.* The MTS-810 electrohydraulic servo system test machine was used to perform uniaxial compressive test on similar materials with different amounts of nanoadditives. Then, select the typical stress-strain curve, the average peak stress, and the typical sample failure form from each group for analysis.

It can be seen from Figures 6(a)–6(c) the curves under the three nanoadditives. Under the condition of incorporation of nanoadditives, the stress-strain curves of all the samples are roughly similar, and all of them undergo the compaction stage, in the elastic stage, plastic deformation stage, and strain softening stage, and when the dosage is 4%, the uniaxial stress of the sample is the largest. When the same nanoadditive is incorporated, for example, when NTi is incorporated into 0%, 2%, 4%, 6%, and 8%, the peak corresponding strains are 1.13%, 1.76%, 1.33%, 1.81%, and 1.31%, respectively. The maximum peak stress is 4.93 MPa, 6.14 MPa, 9.50 MPa, 9.70 MPa, and 6.80 MPa. Compared with the control group, no matter which kind of nanoadditive is added in an appropriate amount, it can improve the uniaxial compressive strength of similar materials to a certain extent.

It can be seen from Figure 6(d) that, under the condition of doping the same nanoadditives, with the increase of the amount of nanoadditives, the uniaxial compressive strength of similar materials showed a trend of first increasing and then decreasing. When it is 4%, the average value of uniaxial compressive strength of similar materials reaches the maximum. It shows that the proper addition of nanoadditives has obvious improvement effect on the uniaxial compressive strength of similar materials, but not as much as possible. There is an optimal dosage of about 4%. The maximum values of NTi, NAl, and NBe are, respectively, 9.70 MPa, 10.58 MPa, and 9.43 MPa.

According to the above stress-strain curve of the sample and the test after the sample is mixed with different nanoadditives, combined with the failure morphology of multiple sets of nanoadditives during the test, it is found that

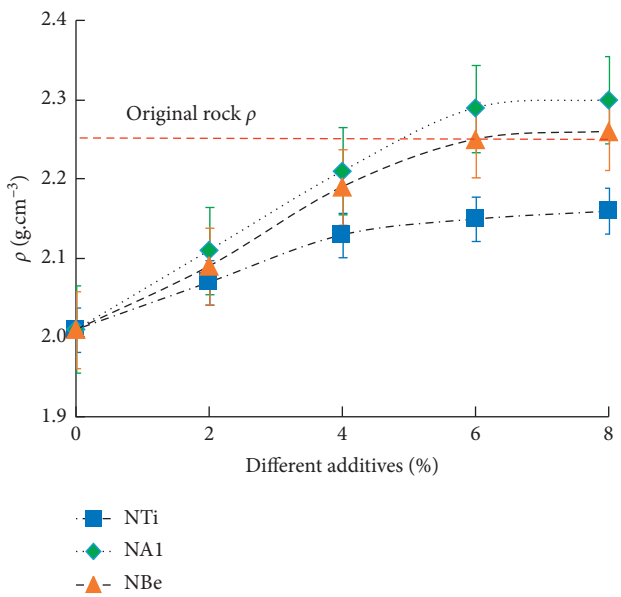


Figure 3: Effects of nanoscale additives on density parameters of similar materials.

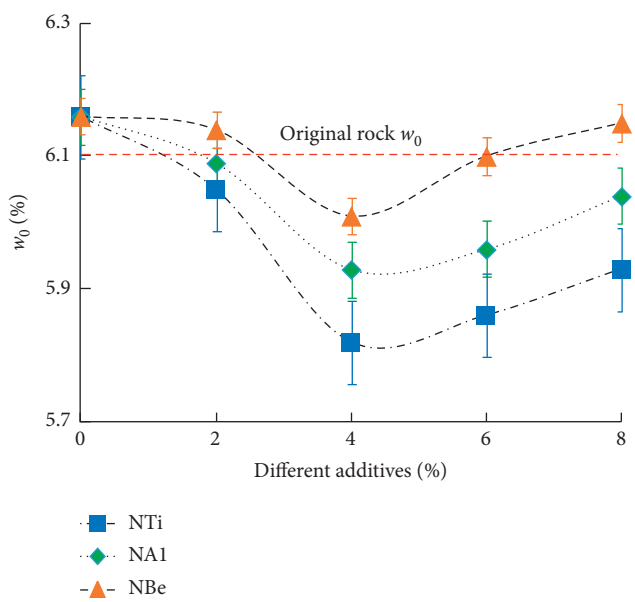


Figure 4: Effects of nanoadditives on natural water absorption parameters of similar materials.

the damage morphology of the sample is mainly affected by nanoadditives which vary considerably and affect the dosage, and the different types of nanoadditives incorporated shape of specimen destruction of substantially identical, and the sample was mostly dominated shear failure. Taking into account the limited space, the following will take NBe as the analysis object; typical damage photos are shown in Figure 7. According to the failure morphology and stress-strain curve of similar material samples after uniaxial compression failure under different NBe contents, as the NBe content increases, the sample cracks crack from the stressed end of the sample and continue to extend to the bottom. The more

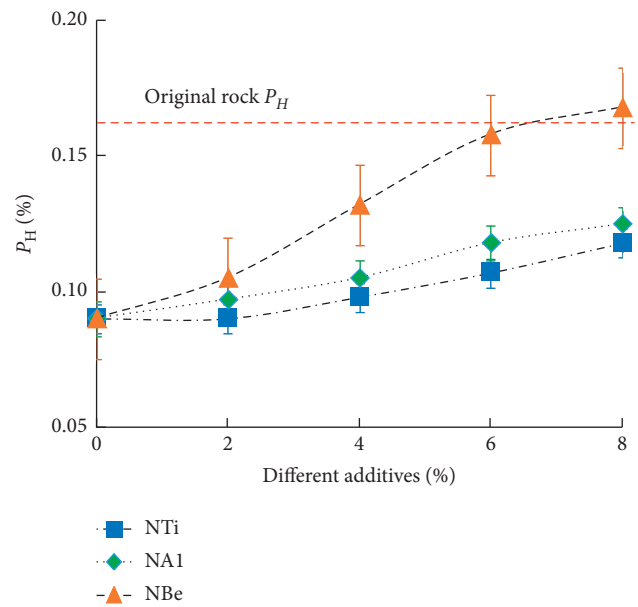


Figure 5: Effects of nanometer additives on expansion rate parameters of similar materials.

obvious the sudden stress drop when the specimen fails, the more obvious the shear failure characteristics. When the dosage is 6%, the destruction characteristics of similar materials in Figure 7(e) are basically the same as those in Figure 7(a).

*3.4.2. Effects of Different Nanoadditives on the Tensile Strength of Similar Materials.* Figure 8 shows the effect of different nanoadditives on the tensile strength of similar materials. It can be seen from Figure 7 that, as the amount of nanoadditives increases, the tensile strength of similar materials increases first and then decreases. When the amount of nanoadditives is 4%, the tensile strength of similar materials reaches the maximum, and NTi, NAl, and NBe are added the maximum value, respectively, is 2.14 MPa, 2.31 MPa, and 2.41 MPa. Later, as the amount of nanoadditives continued to increase, the tensile strength of similar materials decreased significantly. It shows that the incorporation of nanoadditives has a very significant effect on the tensile strength of similar materials; when 6% NBe is incorporated, the tensile strength of similar materials is taken to the average of silty raw rocks.

*3.4.3. Effects of Different Nanoadditives on the Softening Coefficient of Similar Materials.* Figure 9 shows the effect of blending different nanoadditives on the softening coefficient of similar materials. It can be seen from Figure 8 that the incorporation of different nanoadditives reduces the softening coefficient of similar materials. As the amount of nanoadditives increases, the softening coefficient of similar materials continues to decline, but the decline becomes slow. In the process of increasing the additive content from 0% to 4%, the softening coefficient of similar materials is significantly affected; from 4% to 8%, the softening coefficient

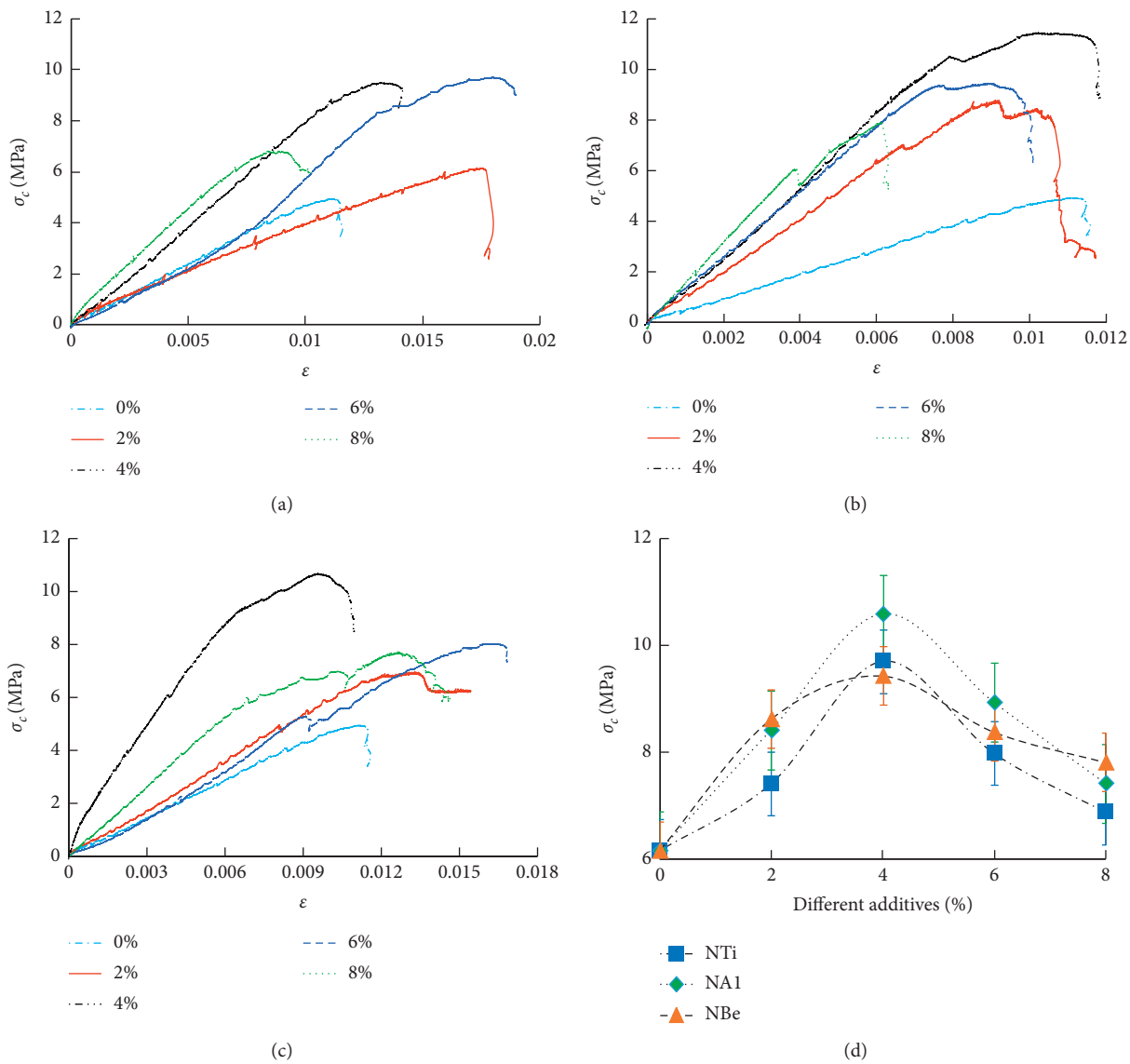


Figure 6: The effects of different nanoadditives on the stress of similar material samples.

gradually stabilizes, and finally the softening coefficient of similar materials after NTi, NAl, and NBe decreased by from 0.70 to 0.51, 0.52, and 0.54; when incorporated NBe is 6%, softening coefficient similar material is closest to the average value of the original rock silty.

In summary, the test results of the density, natural water absorption rate, swelling rate, uniaxial compressive strength, tensile strength, and softening coefficient of similar materials after mixing different nanoadditives can be seen; with the addition of nanoadditives, silt physical and mechanical properties of mudstone similar materials change significantly. When doped with 4% nanoadditives, it can effectively improve the related physical and mechanical properties of similar materials. However, when the dosage is 6%, especially after blending with NBe, all physical and mechanical parameters of similar material samples can reach or be closer to the silty raw rock except uniaxial compressive strength. The failure form of the axial compression specimen is also consistent with that of the original rock and can be used as the best choice. When the 8% nanometer is added immediately, the physical and mechanical properties of the silty mudstone similar materials will change obviously, and it is quite different from the parameters of the silty raw rock.

## 4. Microstructure and Analysis of Similar Material Samples

The nanometer additive added has high surface energy, and the high surface energy effect of nanometer additive in similar materials can be brought into play when added in an appropriate amount. The nanoparticle materials can play the following three effects [31–35]: (1) Size effect: selected raw materials of various particle sizes are above 2 $\mu$m, while additive nanometer average particle size of additive is between 10 and 100 nm. Because of the smaller geometric size

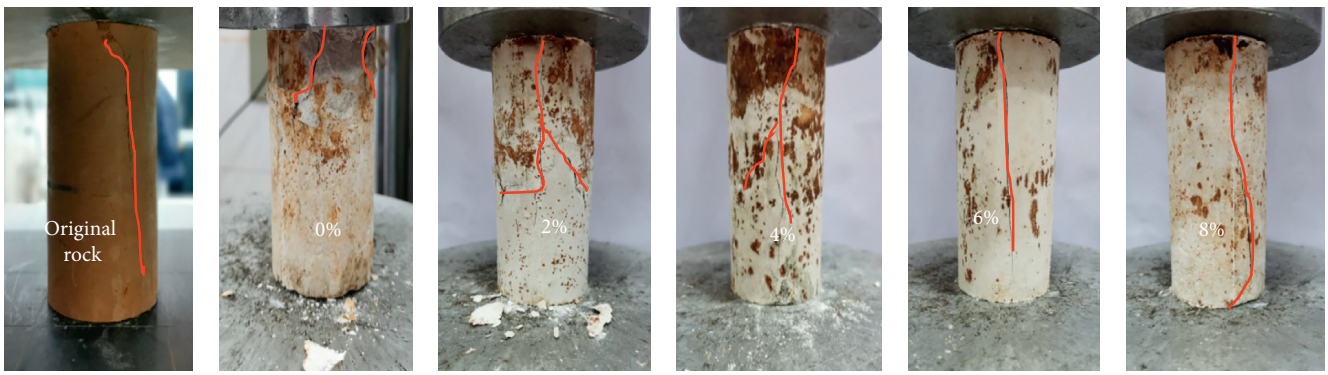


(a) (b) (c) (d) (e) (f)

Figure 7: Shear failure patterns of similar material samples with different NBe contents (water content are controlled at 10% to 12%).

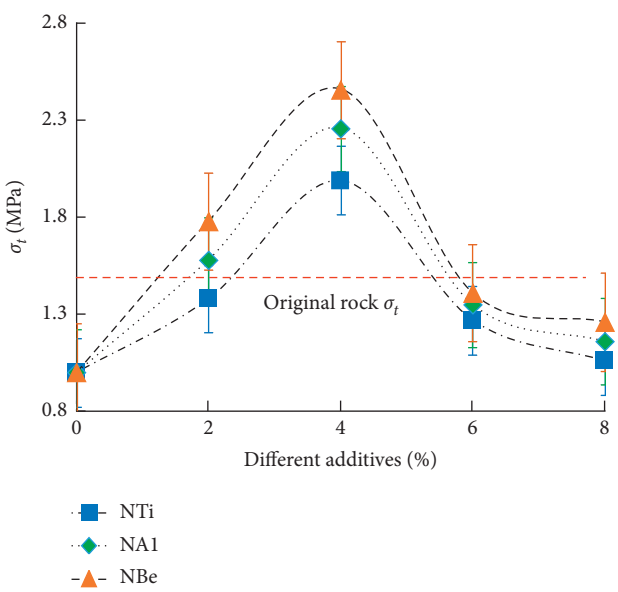


Figure 8: Effects of nanoadditives on uniaxial compressive strength of similar materials.

of nanosized particles, they have stronger adsorption. Adding proper amount of nanometer material into the mixture showed better dispersion. Because the size of nanoparticles is small and the specific surface area is larger, when mixing too much, the particles will adsorb each other and tend to aggregate. (2) Filling effect: the appropriate amount of nanoadditives can optimize the particle gradation of the mixed material, and the nanoparticles have the function of filling the pores, displacing the water in the voids of samples of similar materials, reducing the porosity, and making the maximum pore size and average of the similar materials. The pore size is significantly reduced, improving the internal pore structure of similar materials, resulting in more uniform and dense similar materials. (3) Surface effect: it can be seen from the hydration of gypsum that the barite powder particles in similar materials are wrapped by the gypsum hydration product. The nanoadditive particles are extremely fine and the specific surface area is extremely large, which increases the contact surface with water. The surface of the nanoadditive has high activity and can adsorb a large amount of fine particles, which promotes the hydration reaction of gypsum. As shown in Figure 10, the microscopic structure of similar materials is now observed under 300 times electron microscopy at 0%, 2%, 4%, and 8% of NBe, and the microstructure of similar materials is revealed when nanoadditives are added an influence mechanism.

According to Figure 10, it can be seen that, under the scanning electron microscope at 300 times, the mesostructure structure of similar materials is in silty mudstone under different NBe dosages. As shown in Figure 10(a), when it is 0%, a network structure is formed inside the similar material, and the mesostructure is loose, containing a large number of holes and cracks. From Figure 10(b), when the NBe content is 2%, the internal network structure of similar materials is gradually dense, and the pores of the mesostructure are filled in a large amount, but there are still a lot of pores and cracks. From Figure 10(c), a similar material doped with 4% NBe has the best effect of improving the structure interface and the structure is more dense. The gap between the barite powder and the gypsum hydration product can hardly be seen in the interface transition area. According to Figure 10(d), when the content of NBe is 6%, the structure interface has the best improvement effect, and the structure is more uniform and dense, and the interface transition area is even and smooth, with only a few holes. It shows that the appropriate amount of nanoadditives can promote the hydration reaction of internal gypsum and interweave with the hydration products, thereby forming a dense whole, making the mesostructure of similar materials more uniform and dense. As shown in Figure 10(e), 8% NBe similar material is blended. Because a large amount of nanoparticles will agglomerate, in similar materials, gypsum hydration products will wrap the barite powder particles and nanoagglomerates, and the internal structure will generate a large number of uneven pores. Destroying the dense structure inside similar materials leads to the deterioration of the mechanical properties of similar materials and the decrease of the softening coefficient.

The above analysis revealed the influence mechanism of nanoadditive dosage on the microstructure of similar

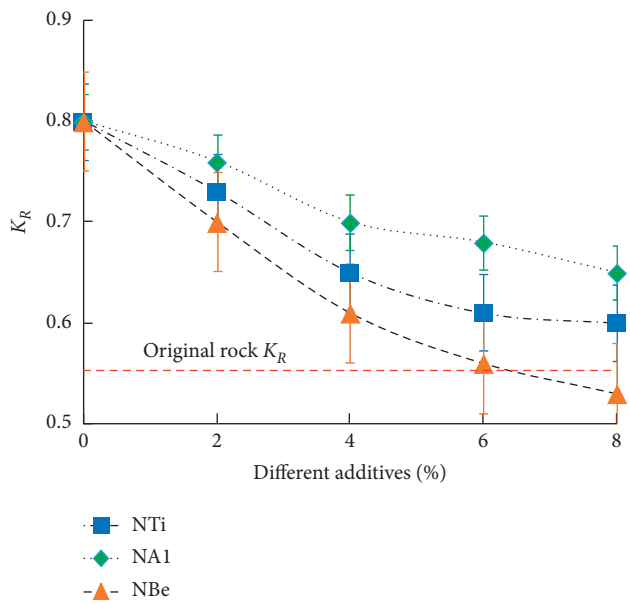


Figure 9: Effect of nanoadditives on softening coefficient of similar materials.

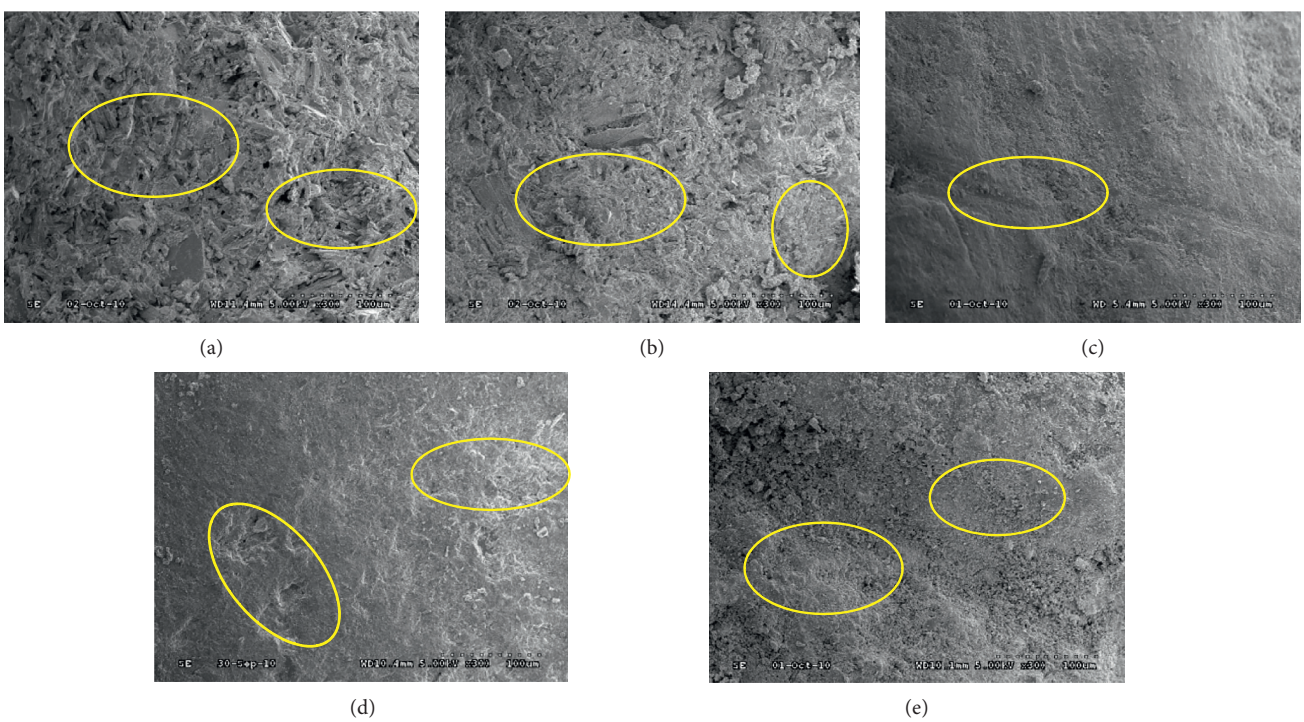


Figure 10: SEM photos of similar material samples with different NBe contents: (a) the structure is loose and contains many holes; (b) the structure gradually compacted and a large number of holes became smaller; (c) the surface is denser and the structure contains more pores; (d) the interface of the structure is smooth and dense with only a few holes; (e) the structure interface is agglomerated and there are many holes (×300 times).

materials, and the following conclusions were drawn: (1) in the control group, only gypsum and water hydration reaction occurred, and a large number of gypsum crystals were generated and interlaced into a network structure. After cementation, there was a certain strength, and the cementation product would have a large number of pores. The mixture of gypsum and barite powder was even. After hydration reaction of gypsum, the barite powder particles were wrapped by cementation, which could improve the compactness, but there would still be a large number of pores and the sample density was small. In this process, the macroscopic mechanical properties of similar materials are mainly affected by cementation. (2) When 2%~6% content is added, on the one hand, nanoparticles can promote the hydration

reaction of gypsum and accelerate the production of cement. On the other hand, the right amount of nanoparticles can fully disperse and fill the pores in similar materials, reduce the water in the pores, and make the materials more dense, and the sample density gradually increases. The macroscopic mechanical strength of similar materials corresponding to this process is further improved. (3) When 6%~8% nanoadditive is added, the nanoparticle agglomeration occurs. The strength of the sample after the nanoadditive agglomeration decreases, and it becomes a primary defect in the similar materials after cementation. Besides, there is a large gap between the nanoadditive particles and the surrounding hydration products, with a poor interface. In this process, the macromechanics of similar material samples weakened to some extent, but too many nanoadditives can still further improve the density, expansion rate, and natural water absorption of similar material samples.

## 5. Conclusions

(1) Compared with the control group, with the addition of nanoadditives, the physical and mechanical properties of similar materials of silty mudstone changed significantly. When 4% nanoadditive is added, the physical and mechanical properties of similar materials can be improved effectively. When 8% nanoadditive is added, the mechanical properties of silty mudstone similar materials deteriorate obviously. This is because adding nanometer additive can effectively promote the hydration reaction of gypsum, accelerate the production of cement, fill the pores of similar materials, reduce internal defects, and make similar materials more compact. When too much is added, the nanoadditive will aggregate and degrade, which will reduce the mechanical properties of similar materials.

(2) When the content of NBe is 6%, all the physical and mechanical parameters of similar materials, except the uniaxial compressive strength, can reach or be closer to the silty original rock, and the failure morphology of uniaxial compression samples is consistent with that of the original rock, which can be used as the best choice. Therefore, appropriate incorporation of NBe can effectively improve the similarity between similar materials and silty rock.

## Data Availability

The data used to support the findings of this study are available from the corresponding author upon request.

## Conflicts of Interest

The authors declare that they have no conflicts of interest.

## Acknowledgments

This study was undertaken with funding from the National Natural Science Foundation of China (Grant nos. 51838001 and 51908069).

## References

[1] C. Wen, S. Jia, X. Fu, L. Meng, and Z. Zhao, "Experimental research and sensitivity analysis of mudstone similar materials based on orthogonal design," *Advances in Materials Science and Engineering*, vol. 2020, Article ID 2031276, 14 pages, 2020.

[2] X. Yang, D. L. Su, B. Zhou et al., "Experiment study on similarity ratio of similar material for model test on red-bed soft rock," *Rock and Soil Mechanics*, vol. 37, no. 8, pp. 2231–2237, 2016.

[3] Y. P. Yang, Y. D. Tang, B. Wang et al., "Impact of size on environmental behavior of metal oxide nanoparticles," *Environmental Science*, vol. 39, pp. 2982–2990, 2018.

[4] W. Jones, A. G. F. Gibb, C. I. Goodier et al., "Nanomaterials in construction-hat is being used, and where?," *Construction Materials*, vol. 172, pp. 49–62, 2016.

[5] B. Han, L. Zhang, S. Zeng et al., "Nano-core effect in nano-engineered cementitious composites," *Composites Part A: Applied Science and Manufacturing*, vol. 95, pp. 100–109, 2017.

[6] B. C. Chen, T. Ji, Q. W. Huang et al., "Review of research on ultrahigh performance concrete," *Archives of Civil and Mechanical Engineering*, vol. 31, pp. 10–24, 2014.

[7] Y. Ruan, B. Han, X. Yu et al., "Mechanical behaviors of nano-zirconia reinforced reactive powder concrete under compression and flexure," *Construction and Building Materials*, vol. 162, pp. 663–673, 2018.

[8] S. Jiang, D. Zhou, L. Zhang et al., "Comparison of compressive strength and electrical resistivity of cementitious composites with different nano- and micro-fillers," *Archives of Civil and Mechanical Engineering*, vol. 18, no. 1, pp. 60–68, 2018.

[9] L. Zeng, L. Xiao, J. Zhang, and H. Fu, "The role of nanotechnology in subgrade and pavement engineering: a review," *Journal of Nanoscience and Nanotechnology*, vol. 20, no. 8, pp. 4607–4618, 2020.

[10] L. Zeng, X. Yao, Q.-F. Gao, H. Bian, and D. Fan, "Use of nanosilica and cement in improving the mechanical behavior of disintegrated carbonaceous mudstone," *Journal of Nanoscience and Nanotechnology*, vol. 20, no. 8, pp. 4807–4814, 2020.

[11] X. Qiu, H. Jiang, and G. Zhang, "Modification effects of nano-CaCO3 on engineering performance of cement grouts," *Journal of Nanoscience and Nanotechnology*, vol. 20, no. 8, pp. 5043–5048, 2020.

[12] L. Zeng, J. Ye, J. Zhang, J. Liu, and C. Jia, "A promising SPEEK/MCM composite membrane for highly efficient vanadium redox flow battery," *Surface and Coatings Technology*, vol. 358, pp. 167–172, 2019.

[13] J. Mostafa, F. Mojtaba, and F. Mohammad, "Effects of fly ash and $TiO_2$ nanoparticles on rheological, mechanical, microstructural and thermal properties of high strength self-compacting concrete," *Mechanics of Materials*, vol. 61, pp. 12–26, 2013.

[14] M.-h. Zhang and H. Li, "Pore structure and chloride permeability of concrete containing nano-particles for pavement," *Construction and Building Materials*, vol. 25, no. 2, pp. 608–616, 2011.

[15] C. Wang, C. Zhang, J. C. Liu et al., "Influence of nano-$CaCO_3$ on hydration characteristic of Portland cement," *Bulletin of the Chinese Ceramic Society*, vol. 35, pp. 824–830, 2016.

[16] S. Lv, C. Xia, H. Liu et al., "Strength and fatigue performance for cement-treated aggregate base materials," *International Journal of Pavement Engineering*, pp. 1–10, 2019.

[17] M. T. Maagi, S. D. Lupyana, and J. Gu, "Effect of nano-$SiO_2$, nano-$TiO_2$ and nano-$Al_2O_3$ addition on fluid loss in oil-well

cement slurry," *International Journal of Concrete Structures and Materials*, vol. 13, p. 62, 2019.

[18] C. C. Liu, S. T. Lv, X. H. Peng et al., "Analysis and comparison of different impacts of aging and loading frequency on fatigue characterization of asphalt concrete," *Journal of Materials in Civil Engineering*, vol. 32, 2020.

[19] J. Zhang, L. Ding, F. Li, and J. Peng, "Recycled aggregates from construction and demolition wastes as alternative filling materials for highway subgrades in China," *Journal of Cleaner Production*, vol. 255, p. 120223, 2020.

[20] J. Zhang, F. Gu, and Y. Zhang, "Use of building-related construction and demolition wastes in highway embankment: laboratory and field evaluations," *Journal of Cleaner Production*, vol. 230, pp. 1051–1060, 2019.

[21] T. Anuj and S. Tarun, "A review study on strength properties of different soils treated with different materials including nanomaterials," *International Journal of Management Technology and Engineering*, vol. 9, pp. 1769–1774, 2019.

[22] K. Nihat and M. Nausad, "A comparative study on the physical and mechanical properties of alkali activated materials," *Sigma Journal of Engineering and Natural Sciences Sigma Mühendislik Ve Fen Bilimleri Dergisi*, vol. 38, no. 2, pp. 649–658, 2020.

[23] J. Qian, Y. Yao, J. Li, H. Xiao, and S. Luo, "Resilient properties of soil-rock mixture materials: preliminary investigation of the effect of composition and structure," *Materials*, vol. 13, no. 7, p. 1658, 2020.

[24] G. Y. Li, P. M. Wang, and X. Zhao, "Mechanical behavior and microstructure of cement composites incorporating surface-treated multi-walled carbon nanotubes," *Carbon*, vol. 43, no. 6, pp. 1239–1245, 2005.

[25] T. Nochaiya and A. Chaipanich, "Behavior of multi-walled carbon nanotubes on the porosity and microstructure of cement-based materials," *Applied Surface Science*, vol. 257, no. 6, pp. 1941–1945, 2011.

[26] B. Zou, S. J. Chen, A. H. Korayem, F. Collins, C. M. Wang, and W. H. Duan, "Effect of ultrasonication energy on engineering properties of carbon nanotube reinforced cement pastes," *Carbon*, vol. 85, pp. 212–220, 2015.

[27] E. Mohseni, M. M. Ranjbar, M. A. Yazdi, S. S. Hosseiny, and E. Roshandel, "The effects of silicon dioxide, iron (III) oxide and copper oxide nanomaterials on the properties of self-compacting mortar containing fly ash," *Magazine of Concrete Research*, vol. 67, no. 20, pp. 1112–1124, 2015.

[28] C.-l. Dong, G.-m. Zhao, X.-y. Lu, X.-r. Meng, Y.-m. Li, and X. Cheng, "Similar simulation device for unloading effect of deep roadway excavation and its application," *Journal of Mountain Science*, vol. 15, no. 5, pp. 1115–1128, 2018.

[29] E. Hoek, D. Wood, and S. Shah, "A modified Hoek-Brown failure criterion for jointed rock masses," in *Proceedings of the Rock Characterization, Symposium Of ISRM*, Thomas Telford Publishing, London, UK, pp. 209–214, September 1992.

[30] J. C. Chen, *Study on Seepage, Mechanical Properties and Fracture Evolution of Silty Mudstone under Hygrothermal Action*, Ph.D. thesis, Changsha University of Science & Technology, Changsha, China, 2019.

[31] A. Nazari and S. Riahi, "Improvement compressive strength of concrete in different curing media by Al2O3 nanoparticles," *Materials Science and Engineering: A*, vol. 528, no. 3, pp. 1183–1191, 2011.

[32] J. Camiletti, A. M. Soliman, and M. L. Nehdi, "Effect of nano-calcium carbonate on early-age properties of ultra-high-performance concrete," *Magazine of Concrete Research*, vol. 65, no. 5, pp. 297–307, 2013.

[33] S. Lv, S. Wang, C. Liu, J. Zheng et al., "Synchronous testing method for tension and compression moduli of asphalt mixture under dynamic and static loading states," *Journal of Materials in Civil Engineering*, vol. 211, pp. 1085–1093, 2018.

[34] I. Mansouri, M. Nejat, S. Shahbazi et al., "Effect of magnetite nanoparticles (ferroferric oxide) on discrete concrete properties," *Proceedings of the Institution of Civil Engineers–Construction Materials*, vol. 172, pp. 95–102, 2018.

[35] G. Prakasam, A. R. Murthy, and M. Saffiq Reheman, "Mechanical, durability and fracture properties of nano-modified FA/GGBS geopolymer mortar," *Magazine of Concrete Research*, vol. 72, no. 4, pp. 207–216, 2020.